UNITED STATES DEPARTMENT OF THE INTERIOR

GEOLOGICAL SURVEY

PROCEEDINGS OF WORKSHOP XVI THE DYNAMIC CHARACTERISTICS OF FAULTING INFERRED FROM RECORDINGS OF STRONG GROUND MOTION VOLUME I

Convened under Auspices of

NATIONAL EARTHQUAKE HAZARDS REDUCTION PROGRAM

Sponsored by

U.S. NUCLEAR REGULATORY COMMISSION

21-23 October 1981

OPEN-FILE REPORT 82-591

Menlo Park, California

1982

CONFERENCES TO DATE

Conference I	Abnormal Animal Behavior Prior to Earthquakes, I Not Open-Filed
Conference II	Experimental Studies of Rock Friction with Application to Earthquake Prediction Not Open-Filed
Conference III	Fault Mechanics and Its Relation to Earthquake Prediction Open-File No. 78-380
Conference IV	Use of Volunteers in the Earthquake Hazards Reduction Program Open-File No. 78-336
Conference V	Communicating Earthquake Hazard Reduction Information Open-File No. 78-933
Conference VI	Methodology for Identifying Seismic Gaps and Soon-to-Break Gaps Open-File No. 78-943
Conference VII	Stress and Strain Measurements Related to Earthquake Prediction Open-File No. 79-370
Conference VIII	Analysis of Actual Fault Zones in Bedrock Open-File No. 79-1239
Conference IX	Magnitude of Deviatoric Stresses in the Earth's Crust and Upper Mantle Open-File No. 80-625
Conference X	Earthquake Hazards Along the Wasatch and Sierra-Nevada Frontal Fault Zones Open-File No. 80-801
Conference XI	Abnormal Animal Behavior Prior to Earthquakes, II Open-File No. 80-453
Conference XII	Earthquake Prediction Information Open-File No. 80-843
Conference XIII	Evaluation of Regional Seismic Hazards and Risk Open-File No. 81-437
Workshop XVI	The Dynamic Characteristics of Faulting Inferred from Recordings of Strong Ground Motion Open-File No. 82-591

Open-File Service Section
Branch of Distribution
U.S. Geological Survey
Box 25425, Federal Center
Denver, Colorado 80225

UNITED STATES

DEPARTMENT OF THE INTERIOR

GEOLOGICAL SURVEY

PROCEEDINGS OF

WORKSHOP XVI

THE DYNAMIC CHARACTERISTICS OF FAULTING

INFERRED FROM RECORDINGS OF STRONG GROUND MOTION

VOLUME I

Convened under Auspices of

NATIONAL EARTHQUAKE HAZARDS REDUCTION PROGRAM

Sponsored by

U.S. NUCLEAR REGULATORY COMMISSION

21-23 October 1981

Editor and Organizer

John Boatwright
U.S. Geological Survey
Menlo Park, CA 94025

Open File Report 82-591

Compiled by
Muriel Jacobson

Menlo Park, California

1982

Acknowledgements

This workshop was financed through the support of the Office of Nuclear Reactor Regulation, United States Nuclear Regulatory Commission. It could not have occurred without the full encouragement and participation of Leon Reiter. Roger Borcherdt was instrumental in helping to set up the workshop and in suggesting topics and participants. Jim Brune also provided important suggestions for topics and participants. The scientists who consented to lead the separate sessions of the workshop, Bill Joyner, Tom Hanks, Jim Brune, Chris Scholz, Paul Spudich and Hiroo Kanamori, are responsible for the smooth running of the sessions and the important discussion of the presentations.

The logistics of gathering and keeping 36 scientists at Lake Tahoe were managed flawlessly by Jessie Reeves and Barbara Charonnat. Without their help and expertise, the workshop would not have been possible. The proceedings were compiled by Muriel Jacobson who caught many mistakes that would have otherwise marred these volumes.

Finally, it is necessary to thank the participants for their interest in the workshop and their indulgence towards its makeshift organization. Workshops of this sort provide a unique opportunity for scientific interaction and discussion. Significant gains towards understanding and predicting strong ground motion were achieved through this interaction. No more satisfying results could have been obtained.

Introduction

The strong ground motions radiated by earthquake faulting are controlled by the dynamic characteristics of the faulting process. Although this assertion seems self-evident, seismologists have only recently begun to derive and test quantitative relations between common measures of strong ground motion and the dynamic characteristics of faulting. Interest in this problem has increased dramatically in past several years, however, resulting in a number of important advances. The research presented in this workshop is a significant part of this scientific development. Watching this development occur through the work of many scientists is exciting; to be able to gather a number of these scientists together in one workshop is a remarkable opportunity.

To construct a dynamic model of faulting requires a description of the dynamic stress drop, the rupture velocity and the rupture complexity over the rupture area. These dynamic characteristics may be considered high-frequency analogs to the more familar static characteristics of the slip and the static stress drop. The spectral model proposed by Boatwright (1982) illustrates the analogy between these two descriptions of the faulting process; where the low-frequency level of the displacement spectrum depends on the product of the slip and the rupture area, the high-frequency level of the acceleration spectrum depends on the product of the dynamic stress drop, the peak rupture velocity and the square root of the rupture area. The dependence on the rupture area is different in the two descriptions because the high-frequency accelerations are incoherent where the low-frequency displacements are coherent.

The distinction between these two descriptions is important for understanding the dynamic description of faulting. The strong ground accelerations radiated by crustal earthquakes depend only indirectly on the static characteristics; similarly, the low-frequency radiation depends only indirectly on the dynamic characteristics. The high or low-frequency seismic radiation may be calculated directly from the dynamic or static description; in this sense, the models should be considered to be frequency-specific descriptions of faulting. To derive relations between these descriptions requires broad-band models of the faulting process. A number of such models have been proposed in the last few years, notably by Aki (1979) and Lay and Kanamori (1981). Because the

resulting relations between the static and dynamic characteristics of faulting are relatively weak, however, these broad-band models are less useful than the frequency specific descriptions of faulting. Scholz (1982) suggests that the static and dynamic characteristics of faulting may differ substantially in earthquakes which rupture through the seismogenic depth of the crust. Using a rupture model with a stress-free boundary condition at depth, Das (1982) demonstrates how the coseismic slip in great earthquakes can overshoot the slip expected for a rupture confined within the seismogenic zone.

The possible discrepancy between the static and dynamic characteristics of great earthquakes confuses the prediction of the strong ground motion radiated by these earthquakes. If measurements of the slip in historic earthquakes cannot be used to estimate the acceleration, then there is no direct means to predict the ground acceleration. This circumstance demonstrates the importance of developing a purely dynamic description of faulting. If acceleration can be calculated directly from the dynamic characteristics of faulting, then it is not necessary to extrapolate a dynamic model from the static characteristics. The natural solution to the problem of predicting strong ground motion is then the evolution and refinement of an appropriate dynamic or high-frequency model of faulting, rather than a broad-band model.

The relations between ground acceleration and the dynamic characteristics of faulting are most readily analyzed in terms of the acceleration radiated by simple kinematic and dynamic source models. In general, these models exhibit the dimensional dependence,

$$\ddot{u} \propto \frac{\Delta\sigma}{\rho R} .$$

Hanks and Johnson (1976) call $\Delta\sigma$ a "dynamic stress difference"; in this discussion it will be considered to be the dynamic stress drop. The linear dependence of the ground acceleration on the dynamic stress drop applies to all of the source models used to estimate source characteristics from recordings of strong ground motion. This relation demonstrates the physical basis of these models; the dynamic stress drop is the force per unit area which accelerates the earthquake focus.

To describe the acceleration radiated by general kinematic and dynamic source models, however, it is also necessary to consider the source size

and the rupture velocity. For coherent rupture models with acceleration spectra which are flat at high frequencies (ω^0), such as the source models of Brune (1970) or Sato and Hirasawa (1973), the strongest acceleration pulses scale linearly with the source radius and the dynamic stress drop. For rupture models with acceleration spectra which falloff as ω^{-1}, or faster, at high frequency, such as Boatwright's (1981) model with gradual healing or McGarr's (1981) asperity model, the acceleration scales linearly with the dynamic stress drop and is independent of the source size. The model proposed by Hanks and Johnson (1976) must exhibit a similar spectral falloff, as the amplitude of the radiated acceleration is independent of the source size. The characteristics of the Hanks and McGuire (1981) model are intermediate to those of the ω^0 and ω^{-1} models; in this model, the acceleration waveform is assumed to be band-limited white noise whose high frequency limit, f_{max}, is determined by the propagation or the recording rather than the source. The peak acceleration and rms acceleration scales approximately as the square root of the source radius.

Madariaga (1977, 1982) and Achenbach and Harris (1978, 1982) consider dynamic models for the acceleration pulses radiated by earthquake faulting. In these models, acceleration pulses are radiated by the stopping or starting of rupture fronts. The scaling of these acceleration pulses is similar to the scaling of the pulses radiated by the kinematic models. The amplitude of the pulses depends on the dynamic stress drop, the source radius and the change in rupture velocity. The peak acceleration of a pulse radiated by an abruptly stopping or starting crack tip is unbounded in the same manner as the strongest pulses radiated by kinematic rupture models with flat acceleration spectra. This singular behavior implies that another parameter, either a source characteristic or a general propagation characteristic, must be introduced to parameterize the peak ground acceleration. If the crack tip decelerates over an interval or duration that depends linearly on the source radius, then the peak and rms acceleration are independent of the source size (Boatwright, 1982) in the same manner as the accelerations radiated by kinematic models whose acceleration spectra fall off as ω^{-1} above the corner frequency.

The regression analyses of Joyner and Boore (1981) and Campbell (1981) provide important information about the range of the dynamic stress drop and the expected stopping and starting behaviors. These analyses show that peak

acceleration is a reasonably predictable function of epicentral distance and source size. In particular, Joyner and Boore (1981) show that peak acceleration increases as the sixth root of the moment; assuming that the stress drop does not depend on the moment, this is equivalent to the square root of the source size. These regressions then indicate that the dynamic stress drop is approximately constant over this set of earthquakes and the average falloff of acceleration spectra at high-frequencies is intermediate to the ω^0 and ω^{-1} models.

This interpretation is partly corroborated by researchers who directly analyze acceleration spectra. The acceleration spectra recorded from moderate California earthquakes are better described, however, as flat or slightly decreasing with frequency up to an abrupt high-frequency limit which is independent of source size. In an analysis of 81 acceleration spectra from 6 large earthquakes, Papageorgiou and Aki (1982b) interprete the abrupt high-frequency falloff as a source characteristic. In their model, the high-frequency limit represents a characteristic stopping length or duration for rupture fronts which is approximately constant for moderate and major earthquakes. Frankel's (1982) analysis of small earthquakes and explosions in the Caribbean and Hanks' (1982) interpretation of 70 acceleration spectra obtained from 8 large aftershocks of the 1975 Oroville earthquake, however, suggest that this high frequency limit is a propagation characteristic. These conflicting interpretations cannot be fully resolved without down-hole or extremely near-field data. Andrews' (1982) analysis of a set of aftershocks of the 1980 Mammoth Lake earthquakes demonstrates the indeterminacy of this problem for far-field data.

Perhaps because their regression models are slightly different, Joyner and Boore (1981) and Campbell (1981) disagree in their predictions of peak acceleration in the near-field of large earthquakes. In order to choose an appropriate regression model, it is necessary to determine and test models for the acceleration time histories expected in the near-field of large earthquakes. Both the duration of strong ground shaking and the radiated power of the motion should be used as constraints for these models. To simplify the following discussion, the term "power" will be used for the time integral of the square of the ground acceleration. The rms acceleration is then the square root of the power divided by the signal duration.

The usual approach to modelling acceleration time histories is to model

the radiation from a complex rupture as the incoherent sum of the radiation from a set of coherent sub-events; this technique generates a composite model of rupture. Gusev (1981) shows that there are two factors which determine the characteristics of the radiation expected from these composite models: the spectral falloff of the radiation from the coherent sub-events and the frequency size distribution of the sub-events. Boatwright (1982) assumes a flat acceleration spectrum for the radiation from the sub-events. This assumption insures that the power radiated by any distribution of sub-events is identical if the distribution is suitably normalized; the power then scales as the square of the dynamic stress drop and the change in rupture velocity times the rupture area, and is independent of the rupture complexity. While Hanks (1979) interpretes the band-limited whiteness of acceleration spectra to imply that the high-frequency character of seismic sources is in some sense "white" or random, he specifies neither the spectral falloff of the radiation nor the frequency-size distribution of the sub-events. Hanks and McGuire (1981) use this composite model to analyze the rms accelerations radiated by 15 Californian earthquakes. Papageorgiou and Aki (1982a) propose a composite model that uses the Sato and Hirasawa (1973) rupture model for the sub-events. The sub-events are assumed to be of a uniform size which corresponds to the barrier interval of the earthquake. Kobayashi et al. (1981) determine envelopes for the acceleration waveforms radiated by an extended rupture process by appropriately delaying and summing envelopes containing the power radiated by the individual segments. Boore and Joyner (1979) consider in detail the radiation from an incoherent rupture model similar to that proposed by Haskell (1966) to show that the power depends on the rupture complexity; this result is conditioned by the assumption that the radiation from the sub-events is independent of the sub-event size.

The observational analyses of Hanks and McGuire (1981) and Papageorgiou and Aki (1982b) indicate that the average dynamic stress drop is approximately constant for those California earthquakes whose records dominate the set of strong motion accelerograms. As demonstrated by Hanks and McGuire (1982), the (dynamic) stress drops determined using the rms accelerations are uncorrelated with the static stress drops of the events. This constant dynamic stress drop is a remarkable and unexpected result; it implies that the dynamic characteristics of faulting are more readily predicted than the static characteristics

and underscores the importance of these dynamic models of faulting in the analysis of ground acceleration.

Altnough these composite models represent an important advance towards predicting the acceleration in the near-field of major earthquakes, there are two phenomena which require further theoretical and observational analysis: the effects of tne rupture velocity and source heterogeneity on the radiated accelerations. The rupture velocity has a twofold effect; not only do the accelerations radiated by a stopping or starting rupture front depend linearly on the change in rupture velocity, but the azimuthal variation of the radiated power and energy (the directivity of the radiated wavefield) is strongly conditioned by the geometry of the rupture propagation and the average rupture velocity.

Even with a dense set of strong motion recordings, however, it is difficult to estimate the average rupture velocity. In an inversion of 26 strong motion accelerograms written by the 1979 Imperial Valley earthquake, Olson and Apsel (1982) obtain a coherent pattern of slip which indicates that the rupture velocity approached the P-wave velocity. In contrast, the rupture model of Hartzell and Helmberger (1982), determined by fitting the displacement pulse shapes at a subset of the stations used by Olson and Apsel (1982), has an average rupture velocity of $.8\beta < v < .9\beta$. Niazi (1982) analyzes the polarity of the ground motion recorded on the USGS differential array to determine an average rupture velocity of $.83\beta$, while Spudich and Cranswick (1982) estimate $v = .78\beta$ from an analysis of the phase velocity across the array. Archuleta and Spudich (1982) obtain $v = .78\beta$ by comparing the components of motion parallel to the fault at stations 6 and 7 of the USGS array.

Estimates of the change of the rupture velocity are similarly difficult. Taking advantage of the excellent azimuthal coverage of the 1980 Livermore Valley earthquakes, Boatwright and Boore (1982) show that the marked directivity in the peak accelerations is consistent with a change of rupture velocity of $.7\beta < \Delta v < .9\beta$. In an analysis of the rms acceleration in 40 P- and S-waves radiated by 10 small earthquakes at Monticello, S.C., Boatwright (1982) obtains $.7\beta < \Delta v < .85\beta$ for the average change of rupture velocity.

The question of the upper bound for the rupture velocity has not been resolved theoretically. Analyzing computational models of fault rupture, Andrews (1976), Das (1976) and Day (1982) conclude that the rupture velocity in the in-

plane direction can exceed the S-wave velocity for weak faults; Virieux and Madariaga (1982) suggest that this result is an artifact of the computational simulation of the rupture process.

As demonstrated by McGarr (1982), peak ground motions can be analyzed by assuming either source heterogeneity or a variable rupture velocity. In his model, the high rupture velocities correspond to a strongly heterogeous source. His analysis of the strong motion recordings of the 1979 Coyote Lake earthquake differs sharply from the analysis of Bouchon (1982), who models the displacements using a smooth rupture model to obtain an estimate of $v = .75\beta$. A similar lack of resolution is demonstrated by the conflicting interpretations of the 1979 Imperial Valley earthquake. The smooth rupture model with a high rupture velocity of Olsen and Apsel (1982) represents a dynamic opposite to the asperity model of Hartzell and Helmberger (1982). As this data set is the most complete set of strong ground motion recordings ever obtained, the non-uniqueness of these rupture models is disconcerting.

The complexity of great earthquakes is readily evident in teleseismic recordings; Kikuchi and Kanamori (1982) have constructed a general technique for analyzing complex ruptures in terms of a heterogeneous distribution of moment. Mori (1982) analyzes the P-waves radiated by the 1965 Rat Island earthquake to show that the sources of the strongest high and low-frequency radiation are spatially distinct; he suggests, however, that the high-frequency radiation is associated with secondary faulting that was triggered by the mainshock. Choy and Boatwright (1982) analyze four events of an extended foreshock sequence of the 1978 Miyagi-Oki earthquake for their dynamic characteristics. The dynamic stress drop of the mainshock is apparently bounded by the dynamic stress drops of the foreshocks.

To predict the strong ground motion in great earthquakes, however, much further work is needed to understand the faulting process. In particular, it is necessary to determine what effect the (teleseismic) rupture complexity has on the near-field ground motion. This requires analyzing both near-field and teleseismic data from the same event. The asperity model of Lay and Kanamori (1981) represents an extremely heterogeneous rupture process; if the dynamic characteristics of faulting are distributed in a similar manner as the moment, this distribution will condition the strong ground motion more strongly than the geometry of the rupture growth.

The problem of determining and constraining a dynamic description of faulting is important to both seismology and earthquake engineering; such a model is necessary both for predicting strong ground motion and for understanding the relationship between the dynamic characteristics of faulting and the rheological character of faults. This second consideration represents a crucial test for dynamic source theory; if the dynamics of faulting, as interpreted from observations of strong ground motion, are consistent with the observed or inferred rheology of crustal faults, as suggested by Fletcher (1982), then it is possible to determine bounds for the strong ground motion from a hypothetical rupture without prior observations of a similar rupture process. McGarr (1982) uses this approach in his prediction of the peak ground acceleration expected from various classes of faults. More detailed models of faulting are required to predict the radiated power and the duration of snaking. While such models are beyond the reach of the research presented in this workshop, these proceedings represent a strong foundation for the further research necessary to realize these goals.

References

Achenbach, J.D. and J.A. Harris (1978). Ray method for elastodynamic radiation from a slip-zone of arbitrary shape, J. Geophys. Res. 83, 2283-2382.

Achenbach, J.D. and J.A. Harris (1982). Focusing of ground motion due to a curved rupture front, Volume I.

Andrews, J.D. (1976). Rupture velocity of plane strain shear cracks, J. Geophys. Res. 81, 3575-3582.

Andrews, J.D. (1982). Separation of source and propagation spectra of seven Mammoth Lake aftershocks, Volume I.

Aki, K. (1979). Characterization of barriers on an earthquake fault, J. Geophys. Res. 84, 6140-6148.

Archuleta, R.J. and P. Spudich (1982). Analysis of near-source static and dynamic measurements from the 1979 Imperial Valley earthquake, Volume II.

Boatwright, J. (1981). Quasi-dynamic models of simple earthquakes: application to an aftershock of tne 1975 Oroville, California, earthquake, Bull. Seism. Soc. Am. 71, 69-94.

Boatwright, J. (1982). A dynamic model for far-field acceleration, Volume I.

Boatwright, J. and D.M. Boore (1982). An analysis of the accelerations radiated by the 1980 Livermore Valley earthquakes for directivity and dynamic source characteristics, Volume I.

Boore, D.M. and W.B. Joyner (1979). The influence of rupture incoherence on seismic directivity, Bull. Seism. Soc. Am. 68, 283-300.

Bouchon, M. (1982). The rupture mechanism of the Coyote Lake earthquake of August 6, 1979, inferred from near field data, Volume II.

Brune J.N. (1970). Tectonic stress and the spectra of seismic shear waves from earthquakes, J. Geophys. Res. 75, 4997-5009.

Campbell, K.W. (1981). Near-source attenuation of peak horizontal acceleration for moderate to large earthquakes, Volume I.

Choy, G.L. and J. Boatwright (1982). Broadband analysis of the extended foreshock sequence of the Miyagi-Oki earthquake of June 12, 1978, Volume II.

Das, S. (1976). A numerical study of rupture propagation and earthquake source mechanism, Ph.D. dissertation, M.I.T.

Das, S. (1982). Numerical experiments to investigate appropriate boundary conditions for modelling very long earthquakes, Volume II.

Day, S.M. (1982). Three dimensional simulation of spontaneous rupture: the effect of non-uniform pre-stress, Volume II.

Fletcher, J.B. (1982). A comparison between the tectonic stress measured In Situ and stress parameters from seismic waves at Monticello, South Carolina: a site of induced seismicity, Volume I.

Frankel, A. (1982). The effects of attenuation and site response on the spectra of microearthquakes in the northeastern Caribbean, submitted to Bull. Seism. Soc. Am. 72.

Gusev, A.A. (1981). A descriptive statistical model for the earthquake source radiation and its application to short-period strong ground estimation, Abstracts of the 1981 IASPEI meeting, Univ. of Western Ont., London, Canada.

Hanks, T.C. and D.A. Johnson (1976). Geophysical assessment of peak accelerations, Bull. Seism. Soc. Am. 66, 959-968.

Hanks, T.C. (1979). b-values and $\omega^{-\gamma}$ seismic source models: implications for tectonic stress variations along active crustal fault zones and the estimation of high-frequency strong ground motion, J. Geophys. Res. 84, 2235-2242.

Hanks, T.C. (1982). f_{max}, Volume I.

Hanks, T.C. and R.K. McGuire (1981). The character of high-frequency strong ground motion, Bull. Seism. Soc. Am. 71, 2071-2095.

Hartzell, S. and D. Helmberger (1982). Strong motion modelling of the Imperial Valley earthquake, Volume II.

Haskell, N.R. (1966). Total energy and energy spectral density of elastic wave radiation from a propagating faults. Part II. A statistical source model, Bull. Seism. Soc. Am. 56, 125-140.

Joyner W.B. and D.M. Boore (1982). Peak horizontal acceleration and velocity from strong motion records including records from the 1979 Imperial Valley, California, earthquake, Volume I.

Lay, T. and H. Kanamori (1981). An asperity model of great earthquake sequences, Ewing Series, 1981.

Kikuchi, M. and H. Kanamori (1982). Inversion of complex body waves, Volume I.

Kobayashi, H., K. Seo and S. Midorikawa (1981). Intensity of strong ground motions due to a predicted earthquake, Abstracts of the 1981 IASPEI meeting, Univ. of Western Ont., London, Canada.

Madariaga, R. (1977). The high-frequency radiation from crack (stress-drop) models of faulting, Geophys. J. 51, 625-652.

Madariaga, R. (1982). A string model for the high-frequency radiation from earthquake faulting, Volume I.

McGarr, A. (1981). Analysis of peak ground motion in terms of a model of inhomogeneous faulting, J. Geophys. Res. 86, 3901-3912.

McGarr, A. (1982). Upper bounds on near-sourcd peak ground acceleration based on a model of inhomogeneous faulting, Volume II.

Mori, J. (1982). Inhomogeneous stress release in the 1965 Rat Island earthquake, Volume II.

Niazi, M. (1982). Source dynamics of the 1979 Imperial Valley earthquake from near-source observations (of ground acceleration and velocity), Volume II.

Olson, A.H. and R.J. Apsel (1982). Finite faults and inverse theory with applications to the 1979 Imperial Valley earthquake, Volume II.

Papageorgiou, A.S. and K. Aki (1982a). A specific barrier model for the quantitative description of inhomogeneous fautling and the prediction of strong ground motion- I. description of the model, Volume I.

Papageorgio, A.S. and K. Aki (1982b). A specific barrier model for the quantitative description of inhomogeneous fautling and the prediction of strong ground motion- II. applications of the model, Volume I.

Sato, T. and T. Hirasawa (1973). Body-wave spectra from propagating shear cracks, J. Physics Earth 21, 415-431.

Scholz, C.H. (1982). Scaling relations for strong ground motion is large earthquakes, Volume II.

Spudich P. and E. Cranswick (1982). Use of near-source seismic-array data to reveal details of earthquake rupture process, Earthquake Notes 53, 39.

Virieux, J. and R. Madariaga (1982). Dynamic faulting studied by a finite difference method, Bull. Seism. Soc. Am. 72, 345-370.

LIST OF PARTICIPANTS

Dr. J.D Achenbach
Technological Institute
Northwestern University
Evanston, Illinois 60201

Dr. Keiiti Aki
Massachusetts Institute of Technology
Dept. of Earth & Planetary Sciences
Cambridge, Massachusetts 02139

Dr. John Anderson
University of California, San Diego
Scripps Institute of Oceanography
La Jolla, California 92093

Dr. Joe Andrews
U.S. Geological Survey
345 Middlefield Road MS 77
Menlo Park, California 94025

Dr. Ralph Archuleta
U.S. Geological Survey
345 Middlefield Road MS77
Menlo Park, California 94025

Dr. John Boatwright
U.S. Geological Survey
345 Middlefield Road, MS77
Menlo Park, California 94025

Dr. David Boore
U.S. Geological Survey
345 Middlefield Road MS 77
Menlo Park, California 94025

Dr. Roger Borcherdt
U.S. Geological Survey
345 Middlefield Road, MS77
Menlo Park, California 94025,

Dr. Michel Bouchon
Laboratoire du Geophysique Interne
IRIGM, BP 53 X
38041 Grenoble, France

Dr. James N. Brune
Institute of Geophysics & Planetary Sciences
Scripps Institute of Oceanography, A-025
University of California, San Diego
La Jolla, California 92093

Dr. Ken Campbell
Tera Corporation
2150 Shattuck Avenue
Berkeley, California 94704

Dr. George Choy
U.S. Geological Survey
Denver Federal Center
Box 25046, MS 967
Denver, Colorado 80225

Dr. Shamita Das
Lamont-Doherty Geological Observatory
Columbia University
Palisades, New York 10964

Dr. Steve Day
Systems, Science & Software
P.O. Box 1620
La Jolla, California 92038

Dr. Neville Donovan
Dames and Moore
1110 Glendon Avenue
Los Angeles, California 90024

Dr. Jon Fletcher
U.S. Geological Survey
345 Middlefield Road, MS77
Menlo Park, California 94025

Dr. Thomas Hanks
U.S. Geological Survey
345 Middlefield Road MS 77
Menlo Park, California 94025

Dr. Steven Hartzell
U.S. Geological Survey
California Institute of Technology
Seismological Laboratory, 252-21
Pasadena, California 91125

LIST OF PARTICIPANTS

Dr. Thomas Heaton
U.S. Geological Survey
California Institute of Technology
Seismological Laboratory, 252-21
Pasadena, California 91125

Dr. Abou-Bakr Ibrahim
P-314 U.S. Nuclear Regulatory Commission
Washington, D.C., 20555

Dr. William Joyner
U.S. Geological Survey
345 Middlefield Road MS 77
Menlo Park, California 94025

Dr. Aladin Kamel
Polytechnic Institute of New York
Route 110
Farmingdale, New York 11735
New York,

Dr. Hiroo Kanamori
California Institute of Technology
Division of Geological & Planetary Sciences
Seismological Laboratory
Pasadena, California 91125

Dr. Allan Lindh
U.S. Geological Survey
345 Middlefield Road MS77
Menlo Park, California 94025

Dr. Raul Madariaga
Institut de Physique du Globe
University of Paris
75230 Paris, Cedex 05, France

Dr. Art McGarr
U.S. Geological Survey
345 Middlefield Road MS 77
Menlo Park, California 94025

Dr. Robin McGuire
ERTEC
1746 Cole Boulevard
Golden, Colorado 80401

Mr. James Mori
Lamont-Doherty Geological Observatory
Columbia University
Palisades, New York 10964

Mr. John Nabelek
Massachusetts Institute of Technology
Cambridge, Massachusetts 02139

Dr. Mansour Niazi
Tera Corporation
2150 Shattuck Avenue
Berkeley, California 94704

Mr. Allen Olson
Scripps Institute of Oceanography
University of California, San Diego
La Jolla, California 92093

Mrs. Jessie F. Reeves
Office of Earthquake Studies
U.S. Geological Survey
345 Middlefield Road MS83
Menlo Park, California 94025

Dr. Leon Reiter
P-314
U.S. Nuclear Regulatory Commission
Washington, D.C., 20555

Dr. Alphonso Z. Reyes
CICESE
Av Espinosa No. 843,
Ensenada, Baja California, MEXICO

Dr. John Rudnicki
Dept. of Civil Eng., The Tech. Inst.,
Northwestern University
2145 Sheridan Road
Evanston, Illinois 60201

Dr. Chris Scholz
Lamont-Doherty Geological Observatory
Columbia University
Palisades, New York 10964

Dr. Phyllis Sobel
P-314 U.S. Nuclear Regulatory Commission
Washington, D.C., 20555

Dr. Paul Spudich
U.S. Geological Survey
345 Middlefield Road MS 77
Menlo Park, California 94025

Dr. Henry Swanger
Systems, Science & Software
P.O. Box 1620
La Jolla, California
FTS 8-(714) 453-0060,

Dr. Jean Virieux
c/o Raul Madariaga
Institut de Physique du Globe
University of Paris
75230 Paris, Cedex 05, France

SEISMOLOGISTS, INNOVATION AND REGULATION

BY
Leon Reiter, Abou-Bakr K. Ibrahim and Phyllis Sobel
Geosciences Branch, U. S. Nuclear Regulatory Commission
Mail Stop P-514, Washington,D.C. 20555
Tel: 301-492-8443

The U. S. Nuclear Regulatory Commission has a vital interest in studies related to understanding the earthquake source mechanism and estimating strong ground motion. We are funding this workshop as a means of better acquainting ourselves with what is current and of stimulating the development of new and innovative techniques. Although there still may exist some misconceptions with regard to the currency and sophistication of our review process many of you are aware that some of the ideas discussed in this workshop have not only been reviewed and utilized by the NRC staff but have also reached the stage of being subjected to intense scientific and regulatory scrutiny at licensing hearings.

For example, presently a licensing board is sitting and deciding on, amongst other issues, the adequacy of the Hanks and McGuire (1981) model in estimating high frequency acceleration from small to modest near-field reservoir-induced earthquakes. Later on we will discuss some of the experience the NRC staff has had in dealing with new techniques and some general guidelines that may be helpful to those who may be called upon to assist us or some other regulatory body in making decisions relating to earthquake design. First, however, it is useful to discuss the role the seismologist plays in the process and some attitudes that we have observed on the part of various members of our community. It must always be remembered that the judgement of seismologists in the design or evaluation process is important in that it is used by engineers as input to a design or analysis procedure of which only the end product gives a measure of the safety with respect to earthquake hazard.

Ground motion parameters (for example magnitude or peak acceleration) may not tell us as much about overall safety as we might like. A structure nominally designed for "0.2g" with one set of engineering procedures may be a safer structure than one designed to "0.4g" utilizing another set of engineering procedures. The better the seismologist understands his role in the process and how the information he provides is used, the more useful his contribution will be. All seismologists however do not have the same view of the part that they play in this process. There are different approaches. Some that we have observed are described below.

1. There are those who apparently think that seismological ground motion parameters directly determine risk. A recurring example of this is the seismologist who views design parameters such as magnitude or peak acceleration as step functions which if exceeded imply imminent failure and catastrophe. There is an increasing amount of evidence to show however that well engineered structures have great ability to withstand large exceedences of design accelerations. A recent example of this is the relatively old El Centro Steam Plant which experienced more than twice its design acceleration of 0.2g in the 1979 Imperial Valley earthquake while sustaining only minor damage.

2. There are many seismologists who honestly admit their lack of knowledge when it comes to relating magnitude or intensity estimates of ground motion to engineering. While this attitude may be better than that described above it is not always useful. On the other side of the fence for example, there often may reside an engineer who claims equal lack of knowledge with respect to seismology. What may develop between these two is a weak link in the chain which could result in serious safety problems or extensive over design. For example if peak acceleration is the scaling parameter used by engineers, the high frequency peaks of short duration observed in the near field of some western U. S. earthquakes cannot be treated in the same manner as the lower-frequency peaks of longer duration estimated in the far field for central U. S. earthquakes. The damage potential associated with a given "peak" in these two situations is very different.

3. The attitude we find the most beneficial is that of the seismologist who knows how the information he generates will be used and tries to parameterize in such a way that will be of use to the engineer. For example duration beyond several cycles has relatively little impact when the design procedure restricts the structures to elastic behavior but it is of the utmost importance in specifying ground motion in liquifaction evaluations. No one wants or expects the seismologist to be a qualified structural or geotechnical engineer but it is remarkable how much more useful seismological input can be when the seismologist is sensitive to the engineers' need. Unfortunately some engineers view with dissatisfaction any incursion by seismologists into their area of expertise. For the decision maker, however, the integrated result and an understanding of how one part of the process affects the other is vital.

Regulators look with ambivalence upon new methodologies in sciences such as seismology. On the one hand it is very useful in dealing with situations that may not have been adequately considered when regulations were written (for example reservoir-induced seismicity) or with new ideas or new data that have changed previous concepts regarding given situations (for example, the discovery of an active fault near a facility). On the other hand they view these new methodologies as unstable, untested from both a scientific and legal standpoint and a departure from the previous methodology which took a long time for them to finally get accustomed to. Those of us anxious for regulators to make greatest use of the new in seismology have to incorporate these methods in a framework that emphasizes reliability, stability and both legal and scientific defendability. Following are common elements of this framework with examples that have been gleaned from the experience of the NRC Geosciences Branch during the past few years.

A. Sensitivity - In any methodology, it is important to know what assumptions are of significance and how they might affect the results. In a new methodology sensitivity studies that demonstrate these effects are particularly important because of the lack of past experience in using these approaches. In 1978 and 1979 the Tennessee Valley Authority developed site specific spectra for rock sites in eastern Tennessee based upon the postulated reoccurrence, near these sites of the 1897 Giles County Virginia earthquake (m_{bLg} = 5.8, Maximum Modified Mercalli Intensity VIII). A new approach was tried in place of what was then the normal practice of scaling a standard spectral

shape to a peak acceleration based upon intensity. All the available accelerograms recorded on rock sites within 25 kilometers of M_L = 5.8 ± 0.5 earthquakeswere processed to produce a site specific spectrum. Figure 1 (Tennessee Valley Authority, 1979) shows the results of this processing under various assumptions. 50% A and 84% A show the 50th and 84th percentile response spectral ordinates of the actual data without any normalization. 84%N is the result of first normalizing the data to the same peak acceleration, calculating the 84th percentile spectral shape and then anchoring it to the median peak acceleration. The response spectrum labelled 50% peak + R.G. 1.60 is derived from anchoring the site independent standard spectral shape described in the U. S. Nuclear Regulatory Commission Regulatory Guide 1.60 to the median peak. The sensitivity to the scaling assumptions is obvious. The spectra labelled Phipps Bend and Sequoyah are design response spectra for two nuclear power plants in the region approved at different times in the past. At their respective times of approval each was considered to be an appropriate representation of an intensity VIII earthquake. The differences in the spectra stem from differences in accepted procedures at the time of review.

B. Uncertainty - In many new (and old) methodologies the choice of input parameters may be controversial with no clear consensus within the seismological community as to which of the parameters is the most appropriate. The lack of stability associated with this situation does not bode well for regulatory positions. If possible, it is always valuable to account for this uncertainty such that small shifts in opinion regarding sensitive input parameters do not lead to large changes in results.

In a program designed to make probabilistic estimates of earthquake hazard at older facilities in the eastern U. S. the NRC (thru Lawrence Livermore National Laboratories and TERA Corporation) embarked on a program which attempted to specifically address this uncertainty. Expert opinion was initially solicited as to what the input parameters might be (for example, source zones, b values and upper magnitude cutoff) what range they might be expected to assume and what credibility could be attached to them. Figure 2 shows a plot of response spectra associated with 1000 year return periods at one site calculated from each expert's input parameters, assumed uncertainty and assigned credibility utilizing a given ground motion model. A single weighted spectrum was also computed utilizing each experts own self ranking. Two years after the first opinion was obtained the experts were polled again as to their choice of input parameters. While some input parameters changed significantly for some experts the incorporation of uncertainty and the balancing effect of different opinions yielded only minor changes in the final results.

C. Multiple Approaches - Very often a new methodology by itself will be associated with sufficient uncertainty as to make the regulators uneasy. Still decisions must be made and cannot be deferred until some time in the future when our knowledge may be more complete. Comparing the results of this new methodology with those from other approaches can result in a more "reliable" decision based upon multiple approaches. Estimating ground motion in the near field, for example, is a difficult and problematic task at best. At the San Onofre site in Southern California the challenge was to estimate ground motion from an M_S = 7.0 earthquake at a distance of 8 km. The NRC staff was able to assess the

adequacy of design by comparing the results of different independent methods. Figure 3 is a plot of the results of three different approaches performed by the applicant and their consultants. One is an empirical approach based upon extrapolating the 84th percentile of the predominently far field data available at the time of the study (Woodward-Clyde Consultants, 1979; Southern California Edison Co. and San Diego Gas and Electric Co., 1980), the second is based upon an extensively investigated theoretical model of ground motion in the vicinity of a rupturing fault (Del Mar Technical Associates, 1978, 1979a, 1979b 1980) and the third is directly based upon data from the Imperial Valley earthquake (Southern California Edison Co. and San Diego Gas and Electric Co. 1980). The response spectrum to which the facility is designed is labelled SONGS 2 & 3 DBE. In the NRC staff's view three different methods each of which alone may not have been able to afford the required amount of certainty could be combined to achieve a higher level of credibility and assurance.

In conclusion we would like to reemphasize that new and innovative methodologies can and are playing a useful role in arriving at regulatory decisions. The extent to which these methodologies can be used in a large part depends upon the extent to which the seismologist recognizes the role that his input plays and the regulators need for reliability, stability and defendability.

REFERENCES

1. Del Mar Technical Associates, 1978, 1979a, 1979b, 1980, Simulation of Earthquake Ground Motions for San Onofre Nuclear Generating Station Unit 1, Final Report, Supplement 1, Supplement II and Supplement III.

2. Hanks T.C. and R. K. McGuire, 1981, The Character of High-Frequency Strong Ground Motion, Bull.Seism. Soc. Am. V71, pp 2071-2095.

3. Southern California Edison Co. San Diego Gas and Electric Company, 1980, San Onofre Nuclear Generating Station Units 2 and 3, Responses to NRC Questions 361.37 through 361.62.

4. Tennessee Valley Authority, 1979, Justification of the Seismic Design Criteria used for the Sequoyah, Watts Bar and Bellefont Nuclear Power Plants Phase II, Responses to NRC Questions 1 through 6.

5. Woodward-Clyde Consultants, 1979 Report of the Evaluation of Maximum Earthquake and Site Ground Motion Parameters Associated with the Offshore Zone of Deformation, San Onofre Nuclear Generating Station: Report for Southern Caifornia Edison Company, June 1979.

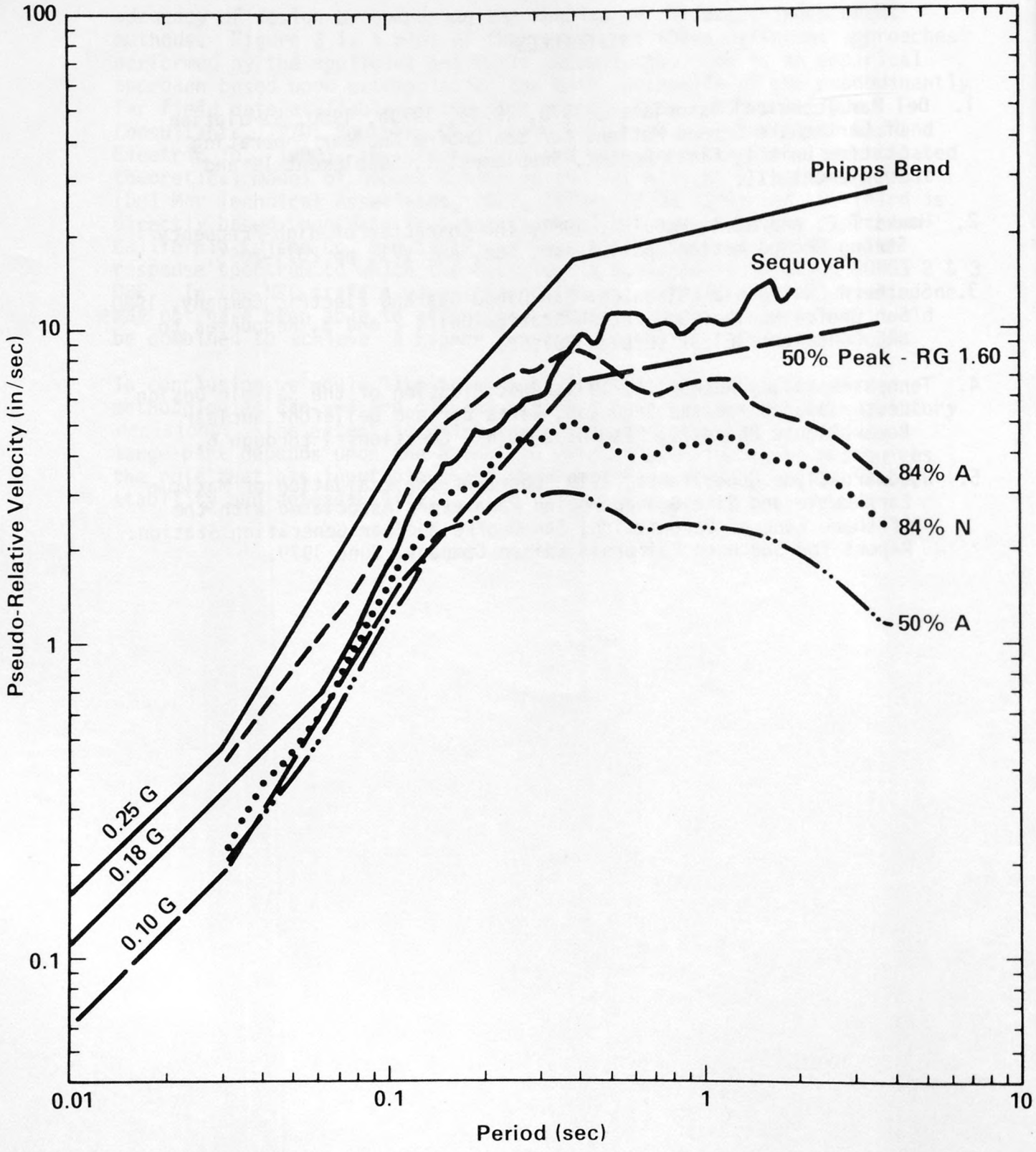

FIGURE 1
COMPARISON OF SEQUOYAH AND PHIPPS BEND DESIGN SPECTRA FOR REINFORCED CONCRETE STRUCTURES WITH VARIOUS SITE SPECIFIC SPECTRA

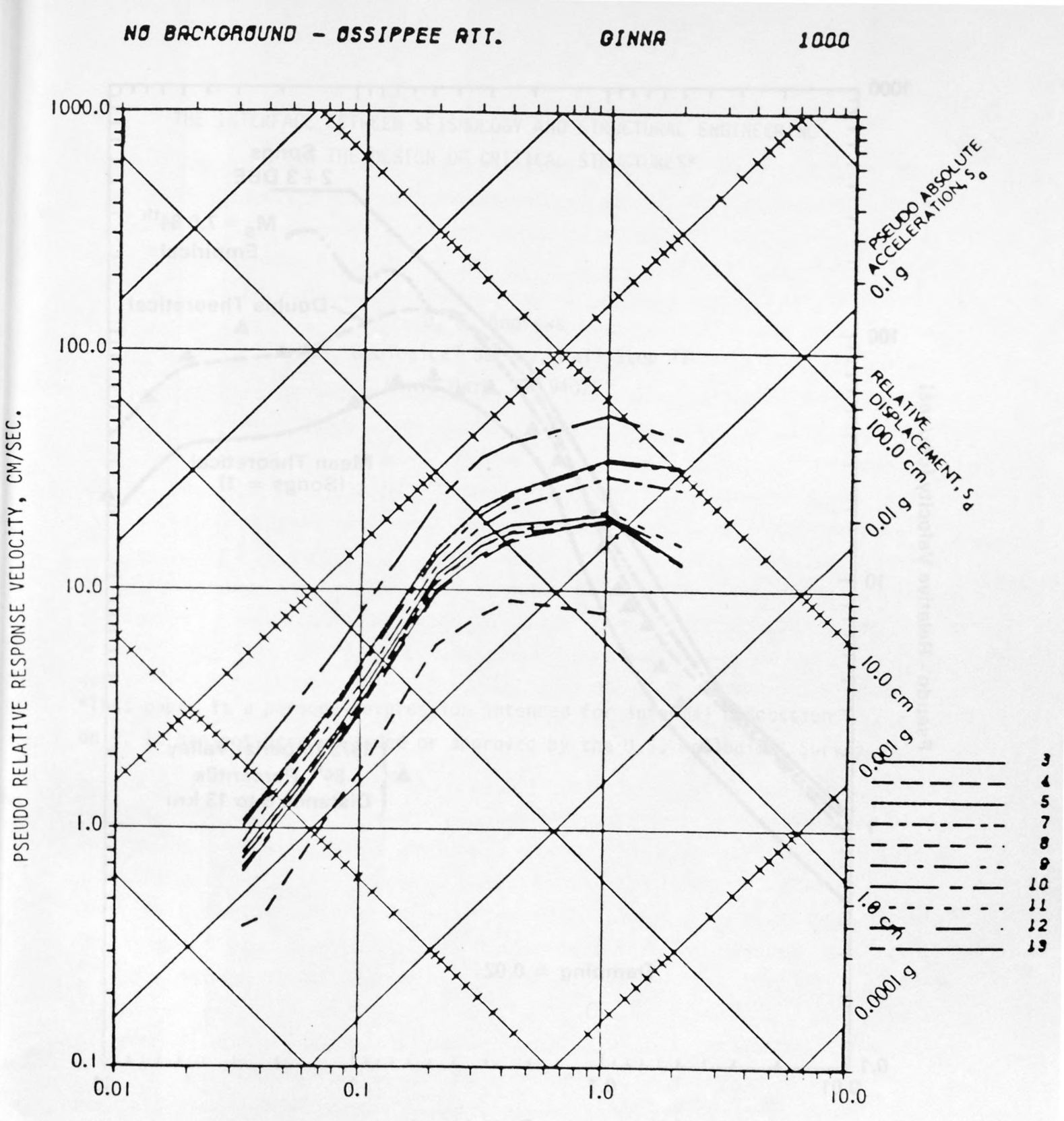

FIGURE 2

RESPONSE SPECTRA ASSOCIATED WITH A 1000 YEAR RETURN PERIOD, FOR THE GINNA N.Y. SITE BASED UPON GIVEN GROUND MOTION MODEL AND INDIVIDUAL EXPERT OPINION. EACH EXPERT IS IDENTIFIED BY A DIFFERENT NUMBER. (NUREG/CR-1582, 1981, SEISMIC HAZARD ANALYSIS APPLICATION OF METHODOLOGY, RESULTS AND SENSITIVITY STUDIES, APPENDIX B).

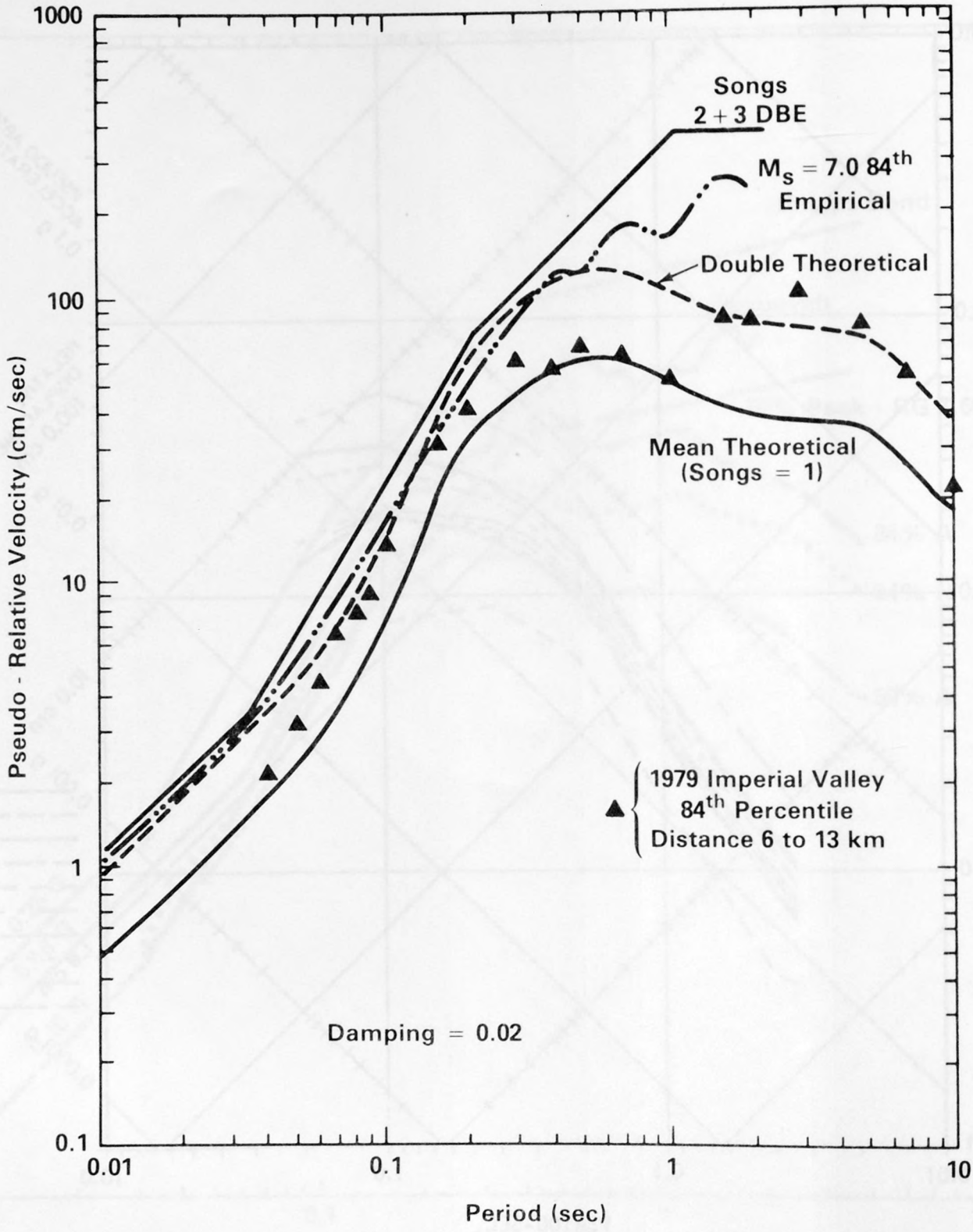

FIGURE 3

COMPARISON OF HORIZONTAL DESIGN GROUND MOTION (DBE) APPROVED FOR SONGS 2 + 3 CONSTRUCTION PERMIT WITH THE EMPIRICAL AND THEORETICAL ESTIMATES AND DATA FROM THE 1979 M_S = 6.9 IMPERIAL VALLEY EARTHQUAKE

THE INTERFACE BETWEEN SEISMOLOGY AND STRUCTURAL ENGINEERING IN THE DESIGN OF CRITICAL STRUCTURES*

D. J. Andrews
U.S. Geological Survey, Mail Stop 77
Menlo Park, CA 94025

*This paper is a personal expression intended for informal discussion only. It has not been reviewed or approved by the U.S. Geological Survey.

In this note I want to state my personal views on what the interface between seismology and structural engineering should be in the design of critical structures and what directions seismological research might take to meet that responsibility.

The ground motion description that a structural engineer needs to have for a particular site consists of the probability per unit time of exceeding any amplitude of response. Approximating a structure as a single-degree-of-freedom oscillator, the description might take the form of a plot such as Figure 1, in which contours of 50% probability of exceedance for given time intervals are ploted in the two-dimensional space of velocity response and oscillator period. This figure might be supplemented with information on the number of cycles of oscillation above any amplitude, stated again in terms of probability per unit time or return period. For a multi-degree-of-freedom structure, relative phases of different Fourier components may be important. It is not possible for seismologists to furnish an infinite ensemble of possible time histories, but high-frequency components may be assumed to have random phases, and structural response may be analyzed in a probabilistic framework.

For simplicity of discussion I will assume that the ground motion specification that an engineer requires has the form of Figure 1. I will also assume that, for random high-frequency motion, a probabilistic relation exists between response spectra and Fourier spectra, the velocity response being proportional to acceleration Fourier amplitude.

Starting from such a specification as Figure 1, the engineer is responsible for designing a structure that has a probability of failure per unit time that is less than an acceptable risk. The definition of acceptable risk is a social and political judgement.

I think that the appropriate interface between engineers and earth scientists is Figure 1. For any particular site, it is the responsibility of geologists and seismologists, working together, to supply the information shown schematically in Figure 1.

In current practice the interface has been the specification of peak acceleration and the pinning of a design spectrum of fixed shape to this

peak. I think there have been two reasons for this. The first is that basic understanding of seismic sources has not reached the point where seismologists are willing to commit themselves to specification of ground motion spectra to be expected in future earthquakes. Seismic engineers, faced with the practical goal of designing structures, have stepped in to fill the void. The second reason is that peak acceleration, being a single number, easily becomes the focus of discussion. A probability function of two independent variables, response amplitude and oscillator period, cannot be bandied about so easily in public debate. The simple concept that force on a structure is proportional to acceleration, which applies to a rigid body or to a flexible structure in the low-frequency limit, continues to be applied at the opposite end of the spectrum.

In order to specify Figure 1, earth scientists need to co-operate at interfaces between their own disciplines. From seismicity and data on geologic slip rates, faults in the region around a site must be assigned a seismic activity specification. By this I mean that for each fault the probability per unit time per unit length of fault for the occurrence of earthquakes must be specified as a function of seismic moment.

The seismologist concerned with source mechanics and propagation of ground motion needs to be able to specify, for any seismic moment and distance from the rupture, a plot such as Figure 2. Here, contours of exceedance probability are plotted in the two-dimensional space of acceleration Fourier amplitude and frequency. These variables are essentially equivalent to those in Figure 1. The essential difference is that Figure 2 needs to be known for any moment and any distance, while Figure 1 applies for all earthquakes that might be experienced at a particular site.

When the specification of Figure 2 for all moments and distances is convolved with the seismic activity specification of the region, the result is Figure 1. As a ground motion seismologist, I consider my goal to be the specification of Figure 2.

A theoretical model relevant to Figure 2 has been in the seismological literature for some years. Aki (1967, 1972) and Brune (1970) have said that in the far field the displacement Fourier amplitude

is flat and proportional to seismic moment at low frequencies and falls off as the reciprocal of frequency squared at high frequency. The corner frequency, the transition between these trends, depends on the duration or length of the earthquake rupture. The acceleration Fourier amplitude is flat above the corner frequency. In the far field it is proportional to

$$|a(\omega)| \propto \frac{\beta}{\rho^2} \frac{1}{r} M_o^{1/3} \sigma^{2/3}$$

and in the near field (on the fault) it is proportional to

$$|a(\omega)| \propto \frac{\beta}{\rho^2} \sigma$$

Here β is shear wave speed, ρ is shear modulus, r is distance, M_o is seismic moment, and σ is a characteristic stress. I do not use the terms stress drop or apparent stress, because I want to leave open the question of data analysis methods. I have confirmed these results in a theoretical model of self-similar irregular fault motion which predicts that this flat spectral trend continues indefinitely toward higher frequencies.

Frequencies of engineering interest are above the corner frequency for large earthquakes. The decrease of velocity response spectra at short periods (high frequency) is due, in this model at least, to anelastic attenuation.

I am not claiming that this ω-squared model is well enough established to serve as a predictor of ground motion for critical structures. I am interested in using this theoretical model, so closely related to Figure 2, as a guide in judging the relevance of research questions.

In order to specify Figure 2 using the ω-squared model, one must know the probability distribution function of characteristic stress. Indeed, characteristic stress is the most important variable.

Strong motion data at locations near an earthquake rupture exist for only a small number of earthquakes. We need to know the variance of spectral levels that can be expected in future earthquakes. Design of structures with very small probability of failure may depend critically

on earthquakes with characteristic stress in the tail of the probability distribution and not at the mean.

The variance of strong motion spectral levels might be estimated from the variance of characteristic stress observed for distant and small earthquakes, if such determinations are reliable. Published values of stress drops vary by two orders of magnitude, but this large variation may be an artifact of data analysis techniques. Recent works by Boatwright (personal communication) and by Hanks and McGuire (1981) show that apparent stress and stress determined from r.m.s. acceleration are more stable quantities. For this reason I believe that data analysis methods used to infer source parameters deserve careful study.

Important research questions in my mind are:

1. How well can source effects be separated from propagation effects in observed seismograms?
2. How well can high-frequency spectral levels be predicted from low- and intermediate-frequency parameters, such as moment and radiated energy?
3. Is characteristic stress correlated with seismic moment?
4. Can spectra be scaled from small earhquakes to large earthquakes?

REFERENCES

Aki, K., Scaling law of seismic spectrum, J. Geophys. Res., 72, 1217-1231, 1967.

Aki, K., Scaling law of earthquake source time-function, Geophys. J., 31, 3-25,1972.

Brune, J. N., Tectonic stress and the spectra of seismic shear waves from earthquakes, J. Geophys. Res., 75, 4997-5009, 1970.

Hanks, T. C. and R. K. McGuire, The character of high-frequency strong ground motion, Bull. Seismol. Soc. Amer., to appear, 1981.

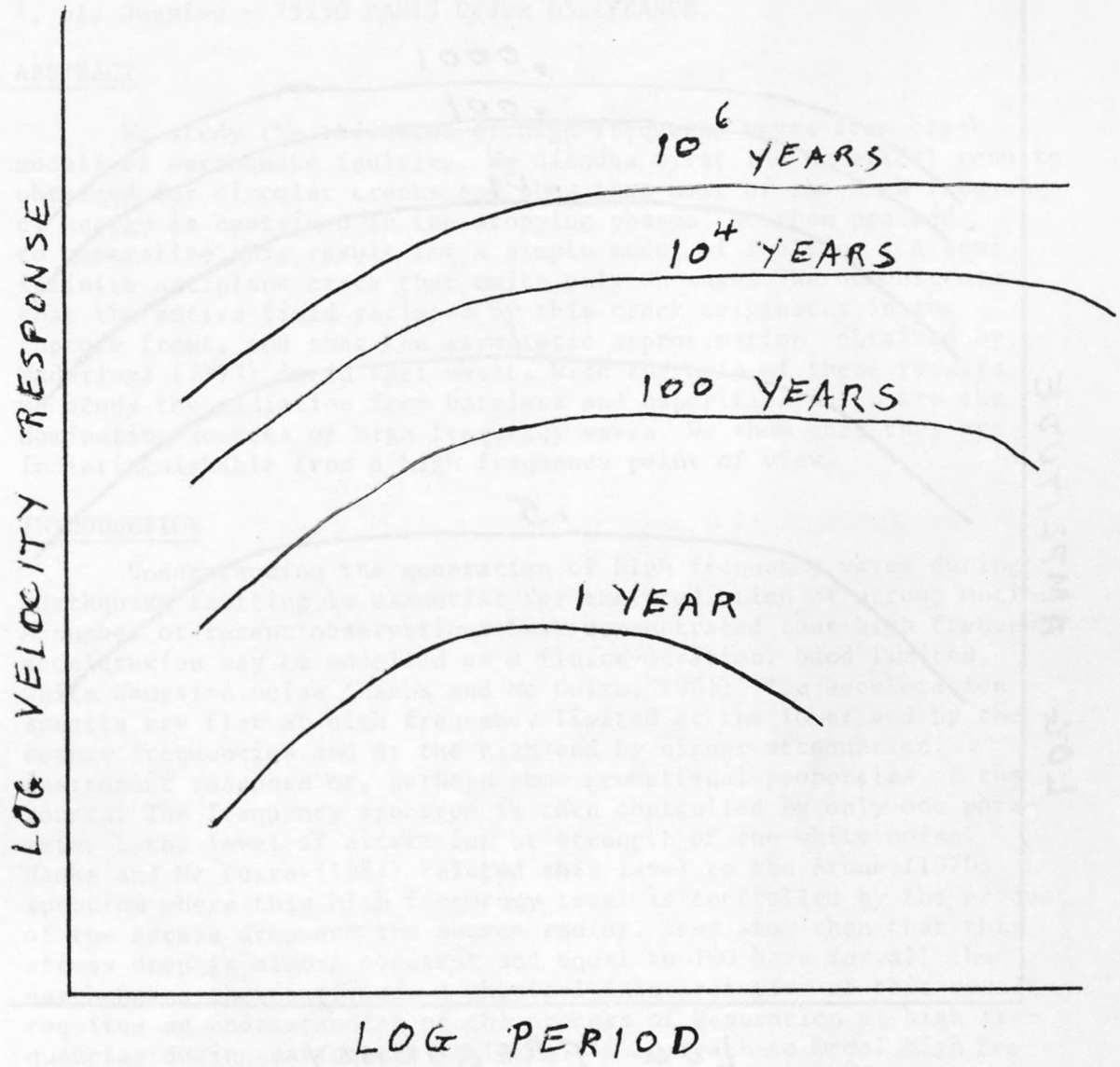

Fig. 1. Schematic plot of contours of 50% probability of exceedance at a particular site for various time intervals as a function of response amplitude and oscillator period.

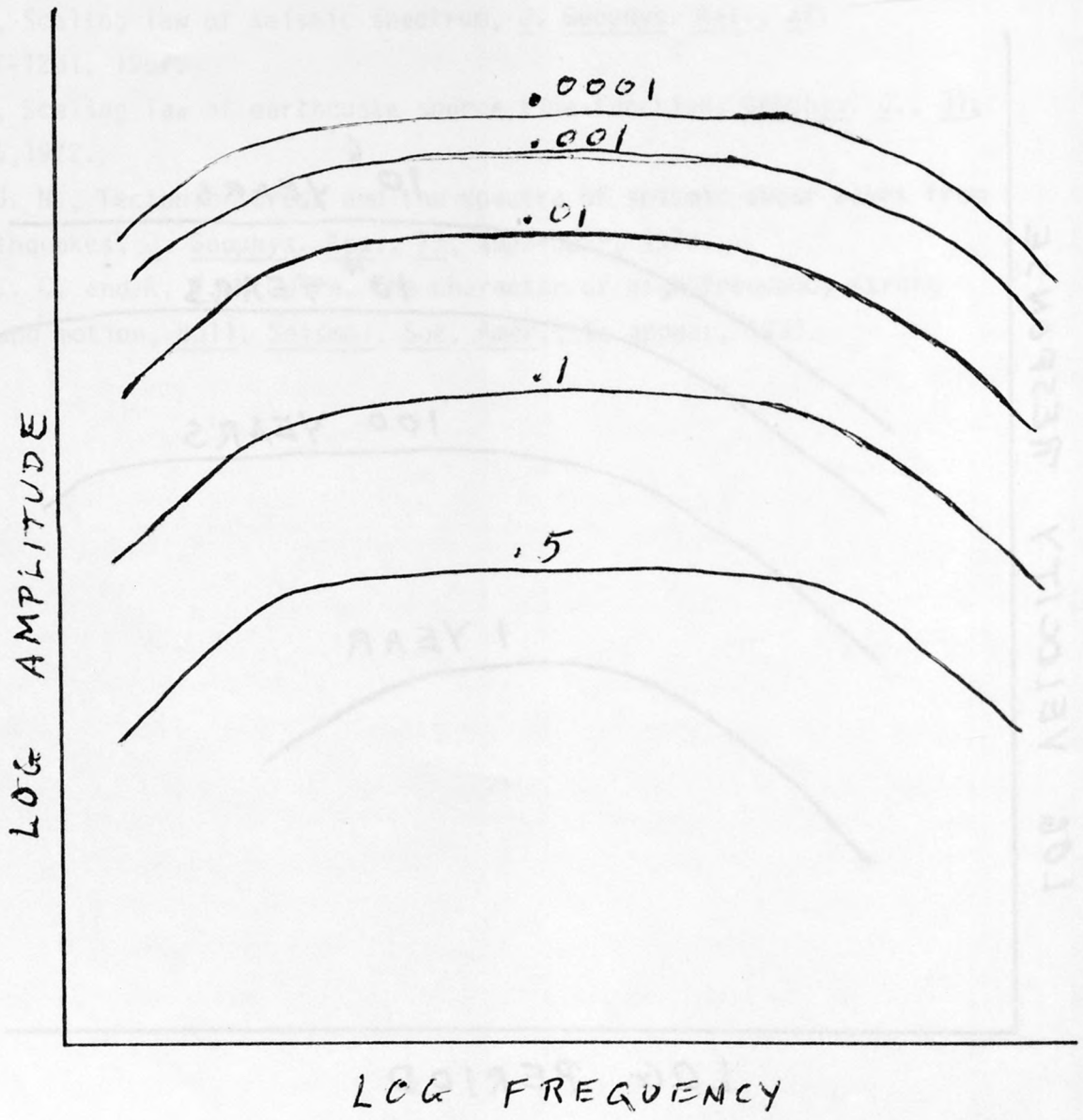

Fig. 2. Schematic plot of exceedance probability for a particular earthquake moment and distance as a function of acceleration Fourier amplitude and frequency.

A STRING MODEL FOR THE HIGH FREQUENCY RADIATION FROM EARTHQUAKE FAULTING.

Raul MADARIAGA
Département des Sciences de la Terre, Université Paris VII and
Institut de Physique du Globe, Université Paris VI
4, pl. Jussieu - 75230 PARIS Cedex 05, FRANCE.

ABSTRACT

We study the radiation of high frequency waves from crack models of earthquake faulting. We discuss first the numerical results obtained for circular cracks and show that most of the high frequency energy is contained in the stopping phases. We then proceed to generalize this result for a simple model of faulting : a semi infinite antiplane crack that emits only SH waves. We demonstrate that the entire field radiated by this crack originates in the rupture front, and that the asymptotic approximation obtained by Madariaga (1977) is in fact exact. With the help of these results we study the radiation from barriers and asperities which are the dominating sources of high frequency waves. We show that they are indistinguishable from a high frequency point of view.

INTRODUCTION

Understanding the generation of high frequency waves during earthquake faulting is essential for the prediction of strong motion. A number of recent observations have demonstrated that high frequency acceleration may be modelled as a finite-duration, band limited, white Gaussian noise (Hanks and Mc Guire, 1981). The acceleration spectra are flat at high frequency limited at the lower end by the corner frequencies and at the high end by either attenuation, instrument response or, perhaps some geometrical properties of the source. The frequency spectrum is then controlled by only one parameter : the level of excitation or strength of the white noise. Hanks and Mc Guire (1981) related this level to the Brune (1970) spectrum where this high frequency level is controlled by the product of the stress drop and the source radius. They show then that this stress drop is almost constant and equal to 100 bars for all the earthquakes they analysed. A physical interpretation of this result requires an understanding of the process of generation of high frequencies during earthquake faulting. An approach to model high fre-
radiation has been to build random models of the slip velocity on the fault and then to calculate the far field radiation (Haskell, 1964 ; Aki, 1967 ; Andrews, 1981). In this approach the underlying stress release mechanism is not taken into account, nor is the causal spreading of the rupture front during faulting.

A different approach, based on dynamical fracture mechanics, was adopted by Madariaga (1977) and Achenbach and Harris (1978). The radiation from a fault is entirely controlled by the slip velocity field in the ruptured portion of the fault. This slip velocity has

a number of universal topological features that should be incorporated into any model of high frequency generation. The most important property is that slip velocity is strongly concentrated behind the the rupture front. Even if there are barriers, asperities, multiple sources or other complexities on the fault, these strong slip velocity concentrations are always present. The radiation of high frequency waves is controlled by the motion of the slip velocity concentrations. Barriers and asperities produce large variations of the intensity of these concentrations and are the source of the high frequency waves. In these notes we shall demonstrate that this is the case for simple coherent models published on the literature, in particular the circular crack model of Madariaga (1976). Then, we shall present a complete approximate study of high frequency radiation from two-dimensional cracks in the presence of asperities and barriers. The extension of these results to three dimensions is possible, provided that a few canonical problems can be solved. We propose that in three dimensions, high frequency waves are generated by the motion of the rupture front, its stopping, acceleration and eventual disappearance at the free surface. This leads to a model where the source of high frequencies at any instant of time is a curved line coinciding with the rupture front. The shape of this line is very general, it may be open or closed. For this reason and to stress its main topological feature , we call this model the string model of high frequency radiation.

HIGH FREQUENCY RADIATION FROM A CIRCULAR CRACK MODEL.

The study reported in this paper was originally motivated by our desire to understand the far field radiation of a simple dynamic circular crack model that we solved numerically (Madariaga, 1976). The far field pulses radiated by this model clearly showed the dominating role of the stopping phases (fig.1). The importance of stopping phases had already been noticed by Savage (1964) in his study of a moving circular dislocation loop. In the following we shall discuss the most salient features of the circular model and attempt to establish the basic physics of high frequency wave excitation.

Let us consider a self-similar circular shear crack. This is a planar rupture that starts from a point and expands radially at a constant rupture velocity v. Slip in the crack is driven by a uniform prestress field that drops to the frictional stress in the broken part of the fault. Static and dynamic stress drop are the same and equal to $\Delta\sigma$. The solution to this problem was obtained by Kostrov (1964) who showed that the slip inside the crack is parallel to the initial traction of the fault and has the typical ellipsoidal shape :

$$\Delta u(r,t) = \frac{\Delta\sigma}{\mu} C \left(v^2 t^2 - r^2\right)^{1/2} \qquad r < vt \qquad (1)$$

where C = C(v) is an alsmot constant function of the rupture velocity. $C(v) \approx 1$ for the whole subsonic rupture velocity range.

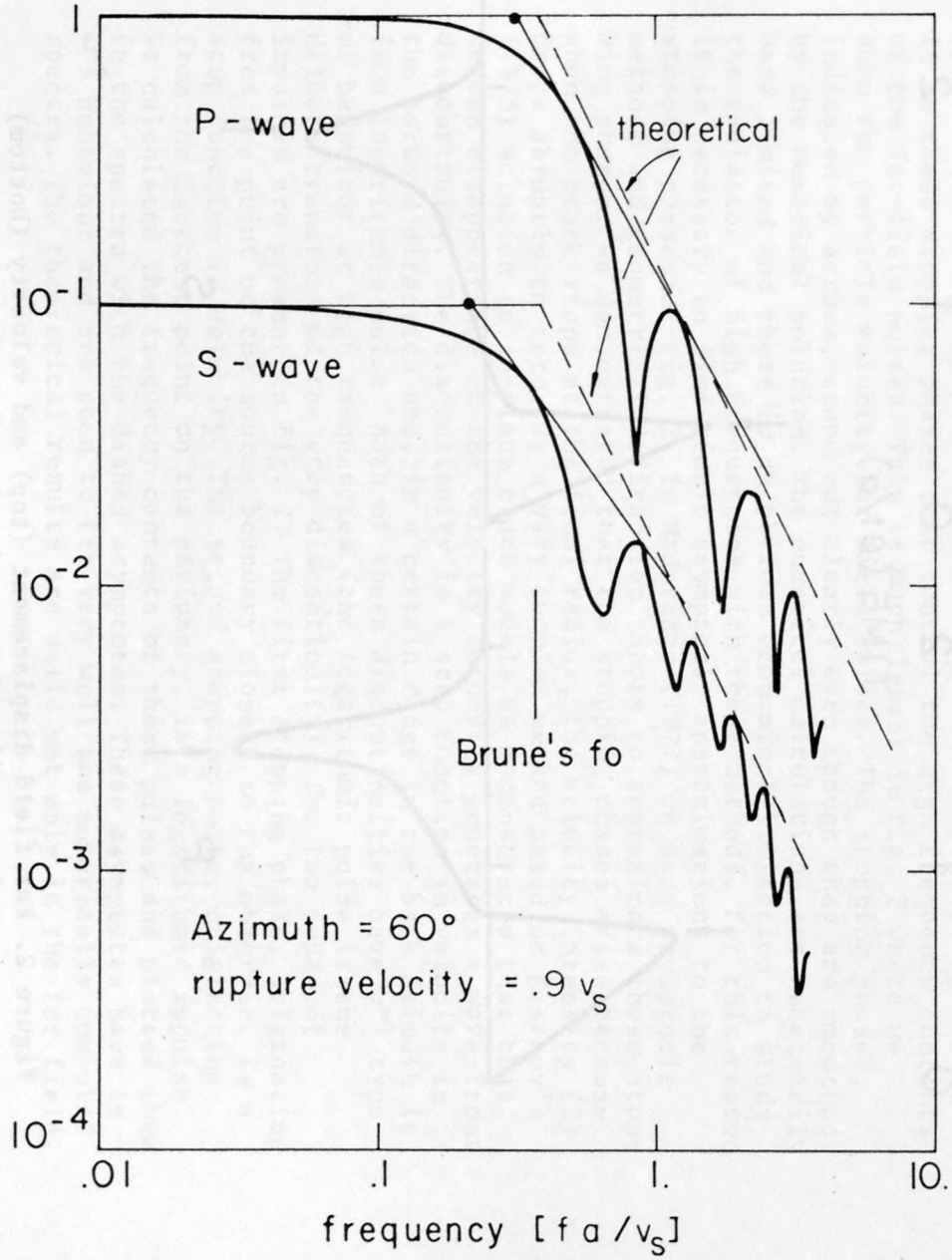

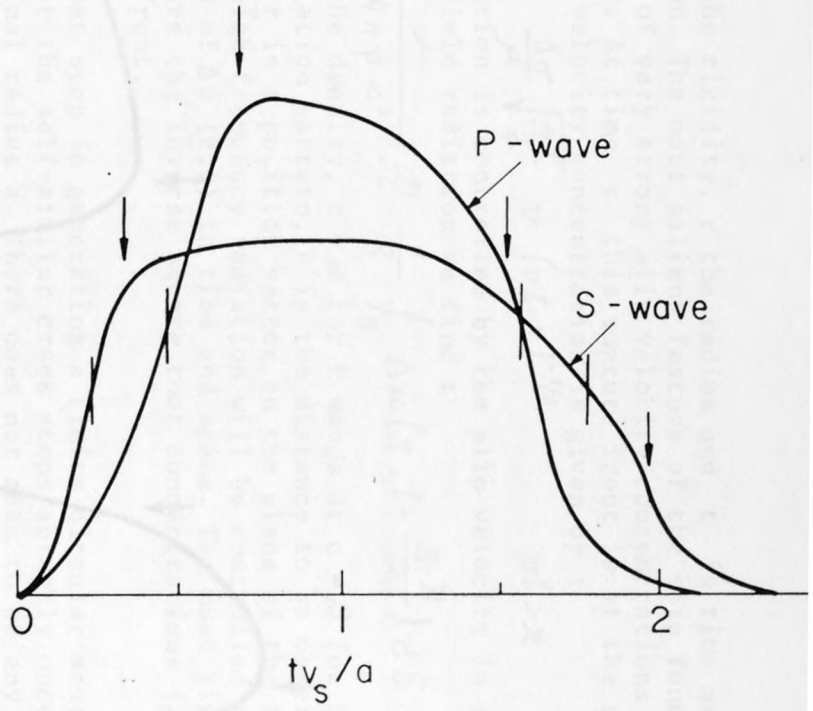

Figure 1. Radiation from a circular crack

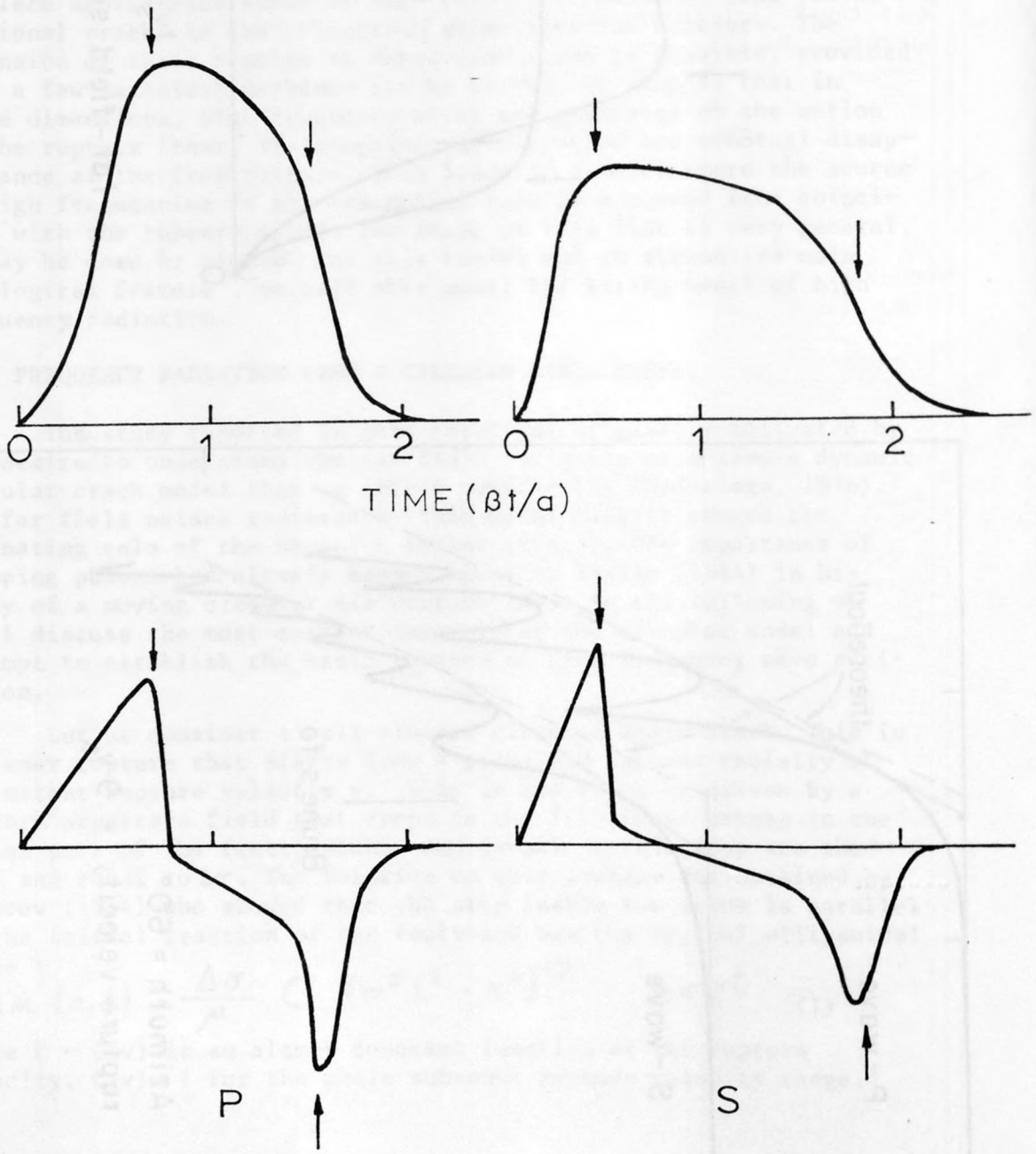

Figure 2. Far field displacement (top) and velocity (bottom) pulses radiated by a circular fault.

In (1) μ is the rigidity, r the radius and t is time measured from the nucleation. The most salient feature of the slip function (1) is the presence of very strong slip velocity concentrations behind the rupture front. At time t this rupture front is at the radius vt and the slip velocity concentration is given by :

$$\Delta \dot{u}(r,t) = \frac{\Delta\sigma}{\mu}\sqrt{\frac{vt}{2}}\; v\,(vt-r)^{-1/2} \qquad vt>r \qquad (2)$$

Seismic radiation is controlled by the slip velocity in the fault. For the far field radiation we find :

$$u(\underline{R},t) = \frac{\mu}{4\pi\rho c^3}\mathcal{R}\;\frac{1}{R}\int_S \Delta\dot{u}\left(\underline{r}, t+\frac{\underline{r}\cdot\hat{\underline{R}}}{c}\right) dS \qquad (3)$$

where ρ is the density, $c = \alpha$ for P waves or $c = \beta$ for S-waves. $\mathcal{R}$ is the radiation pattern, R is the distance to an observer in the direction $\hat{\underline{R}}$, $\underline{r}$ is a position vector on the plane of the fault. Clearly the high frequency radiation will be controlled by the singularities of $\Delta\dot{u}\ (\underline{r},t)$ in time and space. The most singular behaviour of $\Delta\dot{u}$ are the inverse square root concentrations (2) behind the rupture front.

The next step in generating a finite circular source was to assume that the self-similar crack stops abruptly once it has grown to a final radius a. There does not seem to be any way to find an exact solution of this simple model. For this reason it was solved numerically and the slip velocity on the crack integrated numerically in order to find the far field pulses defined in equation 3. The result of these calculations are shown in fig. 1 together with the spectra. The stopping phases are marked in these figures by arrows. It is these stopping phases that control the high frequency contents of the far-field pulses. This is much clearer in fig. 2 where we show the particle velocity far field pulses. The stopping phases, indicated by arrows, stand out clearly even though they are smoothed by the numerical solution. The numerical calculations are necessarily band limited and there is an obvious economical limitation to study the radiation of high frequencies with these methods. For this reason it is necessary to find simple asymptotic approximations to the stopping phases of fig. 2. In Madariaga (1977) we used asymptotic methods and geometrical diffraction theory to approximate these stopming phases. We demonstrated that the stopping phases arise because when the crack stops at the final radius, the velocity intensity (2) drops abruptly to zero. By a very complex method based on Kostrov's (1975) solution to in-plane crack models we demonstrated that this sudden disappearance of the velocity intensity generates a wave-front discontinuity. The discontinuity is a step function in velocity in the forward direction and, in a certain range in the back azimuth it is a logarithmic pulse. Both of these discontinuities have ω^{-1} type of behaviour at high frequencies (the logarithmic pulse is the Hilbert transform of the step discontinuity). The two types of impulses are present in fig. 2. The first stopping phase, originating from the point on the source boundary closest to the observer, is a step function in velocity. The second stopping phase, originating from the farthest point on the periphery, is a logarithmic impulse. We calculated the frequency contents of these pulses and plotted them in the spectra with the dashed asymptotes. These asymptotes have an ω^{-2} behaviour and are seen to fit very well the numerically computed spectra. The theoretical results are valid not only in the far field.

An examination of the near field calculation for a circular crack made by Archuleta and Hartzell (1981) shows that the near field acceleration are completely dominated by strong stopping phases of delta-type of its Hilbert transform, the t^{-1} function. Both of these functions have flat spectra at high frequencies, they only differ in their phases.

We have thus a powerful tool to predict high frequencies when there are jumps in the rupture velocity. All we have to know is the velocity intensity (2) immediately before or after the jump in velocity occurs. We can formulate a simple physical model : high frequencies originate mainly from the rupture front which acts as a curved line source. The wave front discontinuities that dominate high frequency behaviour are generated by sudden changes in rupture velocity of this line source. There are two unsatisfactory aspects of this solution. First, how does stress heterogeneity affect the high frequency radiation ? Do stress concentration (asperities) generate high frequencies that are comparable to those generated by rupture velocity jumps ? In the following we shall study a two-dimensional crack in detail and demonstrate the role of stress heterogeneity, in the generation of high frequency waves.

THE ANTIPLANE STRING MODEL

In order to discuss the main features of the radiation of high frequencies we choose the simplest possible fault configuration : a two dimensional antiplane crack (fig.3). In this model slip occurs only in the y direction while the rupture fronts are infinite straight lines parallel to the y-axis. Only SH waves are generated which simplified enormously the analytical work. Solutions for the plane problem also exist but, although they are more complicated, the basic physics is entirely contained in the simpler antiplane problem. In this two dimensional model the high frequencies originate from the rupture front which are straight lines, i.e. we have a straight string sources.

Consider the geometry shown in fig. 3 : and antiplane rupture moves with an arbitrary rupture velocity $v(x)$ along the x axis. The initial state of stress is a pure shear stress $\sigma^{o}_{yz}(x,z)$. Inside the crack, after the passage of the rupture the stress drops to the dynamic friction $\sigma^{f}_{yz}(x)$. The difference :

$$\tau_{yz}(x) = \sigma^{o}_{yz}(x,0) - \sigma^{f}_{yz}(x) \qquad (1)$$

is the dynamic stress drop, that is the stress that is available to drive the slip on the crack and generate seismic waves. The solution to the general problem of determining the slip velocity for arbitrary motion of the crack tip and heterogeneous stress drop was obtained in the classical work by Kostrov (1966) and discussed in detail by Aki and Richards (1980, p. 884). For a finite crack the solution leads to a multiple diffraction problem by the tips of the crack. For simplicity we shall consider here a semi infinite crack extending along the axis $x < \ell(t)$ where $\ell(t)$ is the current position of the crack tip.

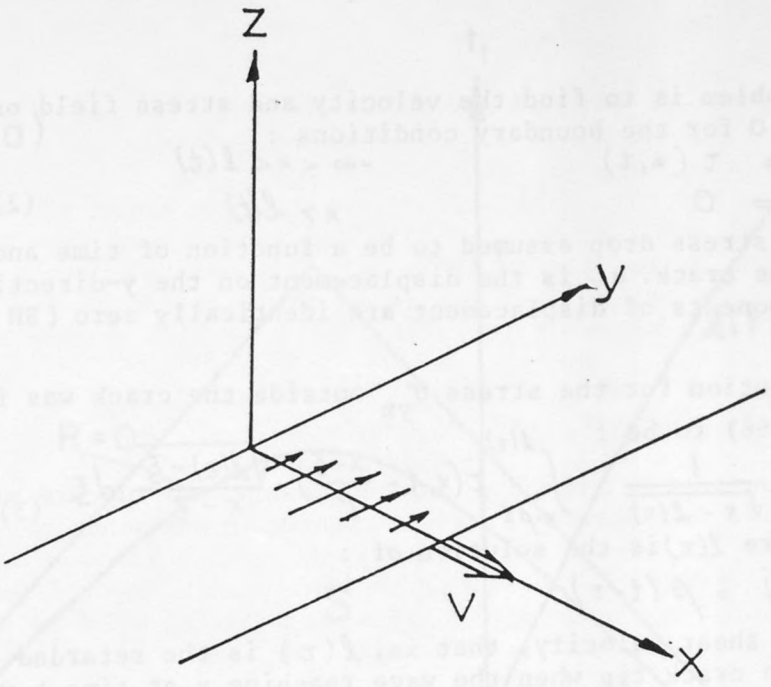

Figure 3a Geometry of the moving antiplane crack.

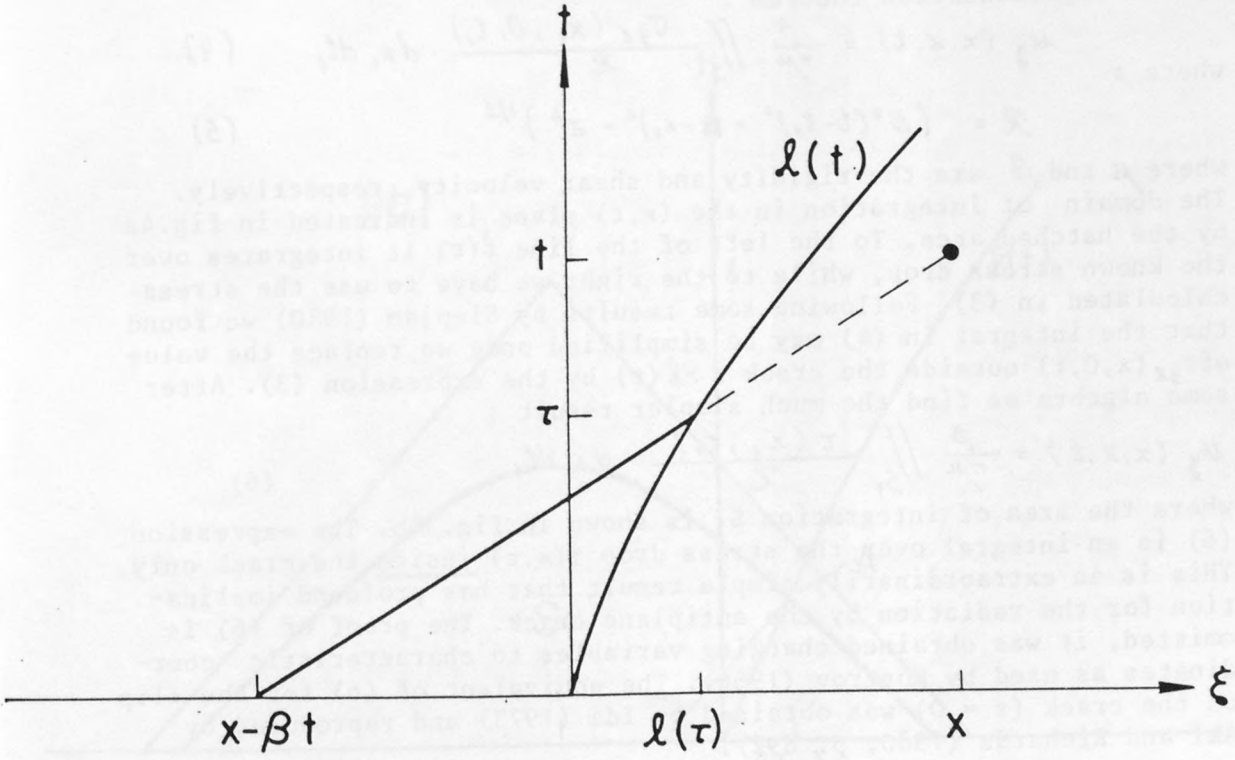

Figure 3b. Integration for the solution of the stress outside the crack.

The problem is to find the velocity and stress field on the half plane $z > 0$ for the boundary conditions :

$$\sigma_{yz}(x,0,t) = \tau(x,t) \qquad -\infty < x < \ell(t)$$
$$u_y(x,0,t) = 0 \qquad x > \ell(t) \qquad (2)$$

where τ is the stress drop assumed to be a function of time and position on the crack. u_y is the displacement on the y-directive, all other components of displacement are identically zero (SH problem).

The solution for the stress σ_{yz} outside the crack was found by Kostrov (1966) to be :

$$\sigma_{yz}(x,0,t) = \frac{1}{\sqrt{x-\ell(\tau)}} \int_{x-\beta t}^{\ell(\tau)} \tau\left(x, t-\frac{x-\xi}{\beta}\right) \frac{\sqrt{\ell(\tau)-\xi}}{x-\xi}\, d\xi \qquad (3)$$

for $x > \ell$, where $\ell(\tau)$ is the solution of :

$$x - \ell(\tau) = \beta(t-\tau)$$

where β is the shear velocity, that is, $\ell(\tau)$ is the retarded position of the crack tip when the wave reaching x at time t was emitted. $\ell(t)$ is the position of the crack tip as a function of time. We assume that $\ell(t)$ is a given monotonically increasing function of time. It may be calculated by a rupture criterion as explained by Kostrov (1966). We assume here that the rupture velocity $\dot{\ell}(t)$ is always subsonic. The integration in eq. (3) is illustrated in fig. 3.

We have now the complete solution for the stress on the line $z = 0$; $\tau(x,t)$ for $x < \ell(t)$ and $\sigma_{yz}(x,0,t)$ for $x > \ell(t)$. The displacement field $u_y(x,z,t)$ inside the half plane $z > 0$ may be calculated by the representation theorem :

$$u_y(x,z,t) = \frac{\beta}{\pi\mu} \iint_S \frac{\sigma_{yz}(x_1,0,t_1)}{\mathcal{R}}\, dx_1\, dt_1 \qquad (4)$$

where :

$$\mathcal{R} = \left(\beta^2(t-t_1)^2 - (x-x_1)^2 - z^2\right)^{1/2} \qquad (5)$$

where μ and β are the rigidity and shear velocity, respectively. The domain of integration in the (x,t) plane is indicated in fig.4a by the hatched area. To the left of the line $\ell(\tau)$ it integrates over the known stress drop, while to the right we have to use the stress calculated in (3). Following some results by Slepjan (1980) we found that the integral in (4) may be simplified once we replace the value of $\sigma_{yz}(x,0,t)$ outside the crack $x > \ell(t)$ by the expression (3). After some algebra we find the much simpler result :

$$u_y(x,z,t) = \frac{\beta}{\pi\mu} \iint_{S_1} \frac{\tau(x_1,t_1)}{\mathcal{R}}\, dx_1\, dt_1 \qquad (6)$$

where the area of integration S_1 is shown in fig. 4b. The expression (6) is an integral over the stress drop $\tau(x,t)$ inside the crack only. THis is an extraordinarily simple result that has profound implication for the radiation by the antiplane crack. The proof of (6) is omitted, it was obtained changing variables to characteristic coordinates as used by Kostrov (1966). The equivalent of (6) for the slip on the crack ($z = 0$) was obtained by Ida (1973) and reproduced by Aki and Richards (1980, p. 892).

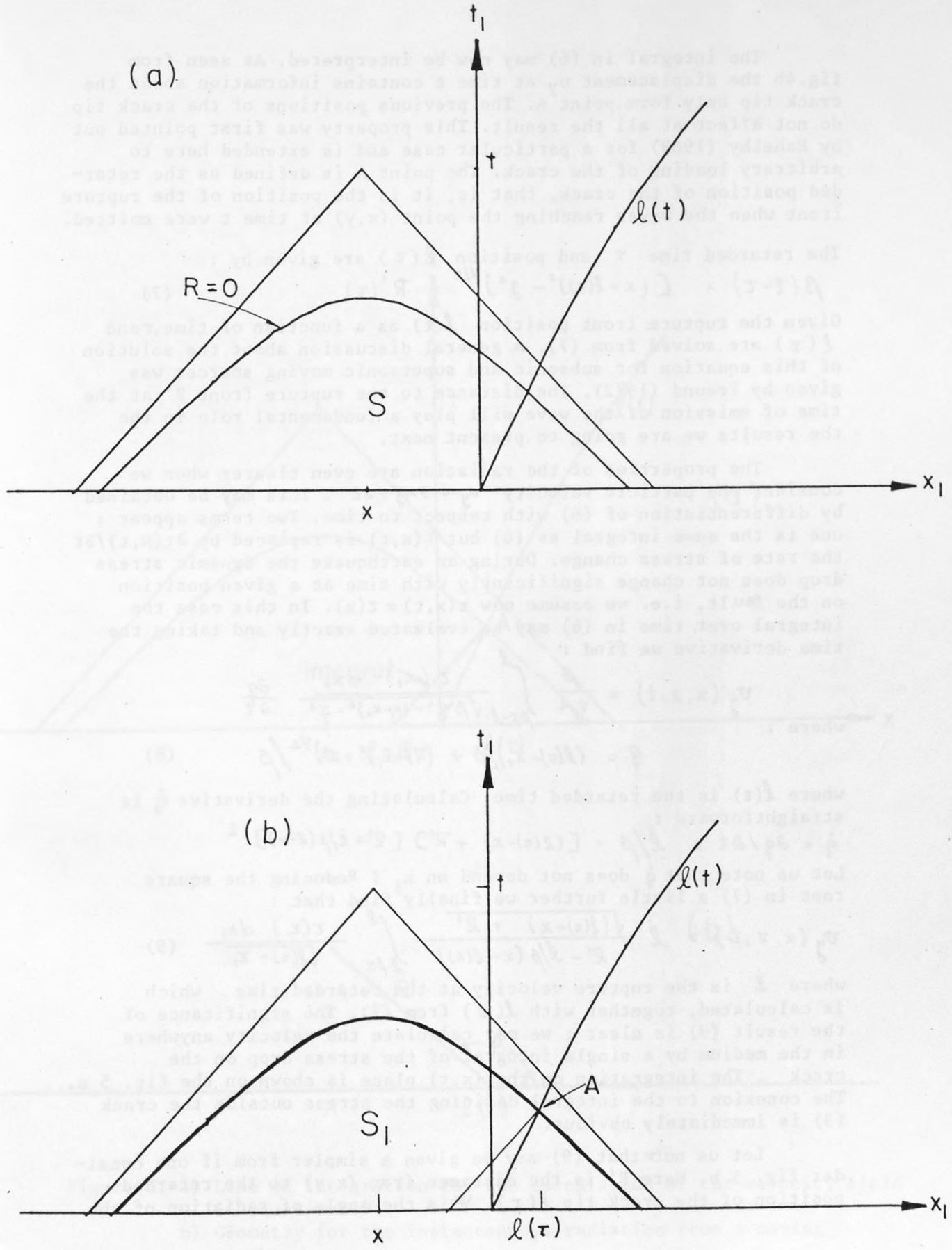

Figure 4. Area of integration on the (x,t) plane for the calculation of displacement away from the crack.

The integral in (6) may now be interpreted. As seen from fig.4b the displacement v_y at time t contains information about the crack tip only form point A. The previous positions of the crack tip do not affect at all the result. This property was first pointed out by Eshelby (1969) for a particular case and is extended here to arbitrary loading of the crack. The point A is defined as the retarded position of the crack, that is, it is the position of the rupture front when the waves reaching the point (x,y) at time t were emitted.

The retarded time τ and position $\ell(\tau)$ are given by :

$$\beta(t-\tau) = [(x-\ell(\tau))^2 - z^2]^{1/2} = R'(\tau) \qquad (7)$$

Given the rupture front position $\ell(t)$ as a function of time, τ and $\ell(\tau)$ are solved from (7). A general discussion about the solution of this equation for subsonic and supersonic moving sources was given by Freund (1972). The distance to the rupture front R' at the time of emission of the wave will play a fundamental role in the the results we are going to present next.

The properties of the radiation are even clearer when we consider the particle velocity $v_y = \partial u_y / \partial t$. This may be obtained by differentiation of (6) with respect to time. Two terms appear : one is the same integral as (6) but $\tau(x,t)$ is replaced by $\partial\tau(x,t)/\partial t$ the rate of stress change. During an earthquake the dynamic stress drop does not change significantly with time at a given position on the fault, i.e. we assume now $\tau(x,t) = \tau(x)$. In this case the integral over time in (6) may be evaluated exactly and taking the time derivative we find :

$$v_y(x,z,t) = \frac{\beta}{\pi\mu} \int_{\beta\tau-\ell}^{\ell} \frac{\tau(x_1)\, dx_1}{\sqrt{\beta^2 q^2 - (x-x_1)^2 - z^2}} \frac{\partial q}{\partial t}$$

where :

$$q = (\ell(\tau)-x_1)/\beta + [(\ell-x_1)^2+z^2]^{1/2}/\beta \qquad (8)$$

where $\ell(\tau)$ is the retarded time. Calculating the derivative $\dot{q}$ is straightforward :

$$\dot{q} = \partial q/\partial\tau = \dot{\ell}/\beta \cdot [(\ell(\tau)-x) + R'][R' + \dot{\ell}/\beta(\ell-x)]^{-1}$$

Let us note that $\dot{q}$ does not depend on x_1 ! Reducing the square root in (7) a little further we finally find that :

$$v_y(x,z,t) = \dot{\ell} \frac{\sqrt{(\ell(\tau)-x) + R'}}{R' - \dot{\ell}/\beta(x-\ell(\tau))} \int_{\ell-\beta\tau}^{\ell} \frac{\tau(x_1)\, dx_1}{\sqrt{\ell(\tau)-x_1}} \qquad (9)$$

where $\dot{\ell}$ is the rupture velocity at the retarded time which is calculated, together with $\ell(\tau)$ from (7). The significance of the result (9) is clear : we may calculate the velocity anywhere in the medium by a single integral of the stress drop on the crack . The integration on the (x,t) plane is shown on the fig. 5 a. The conexion to the integral defining the stress outside the crack (3) is immediately obvious.

Let us note that (9) may be given a simpler from if one consider fig. 5 b. Here R' is the distance from (x,y) to the retarded position of the crack tip $\ell(\tau)$. Ψ is the angle of radiation of the

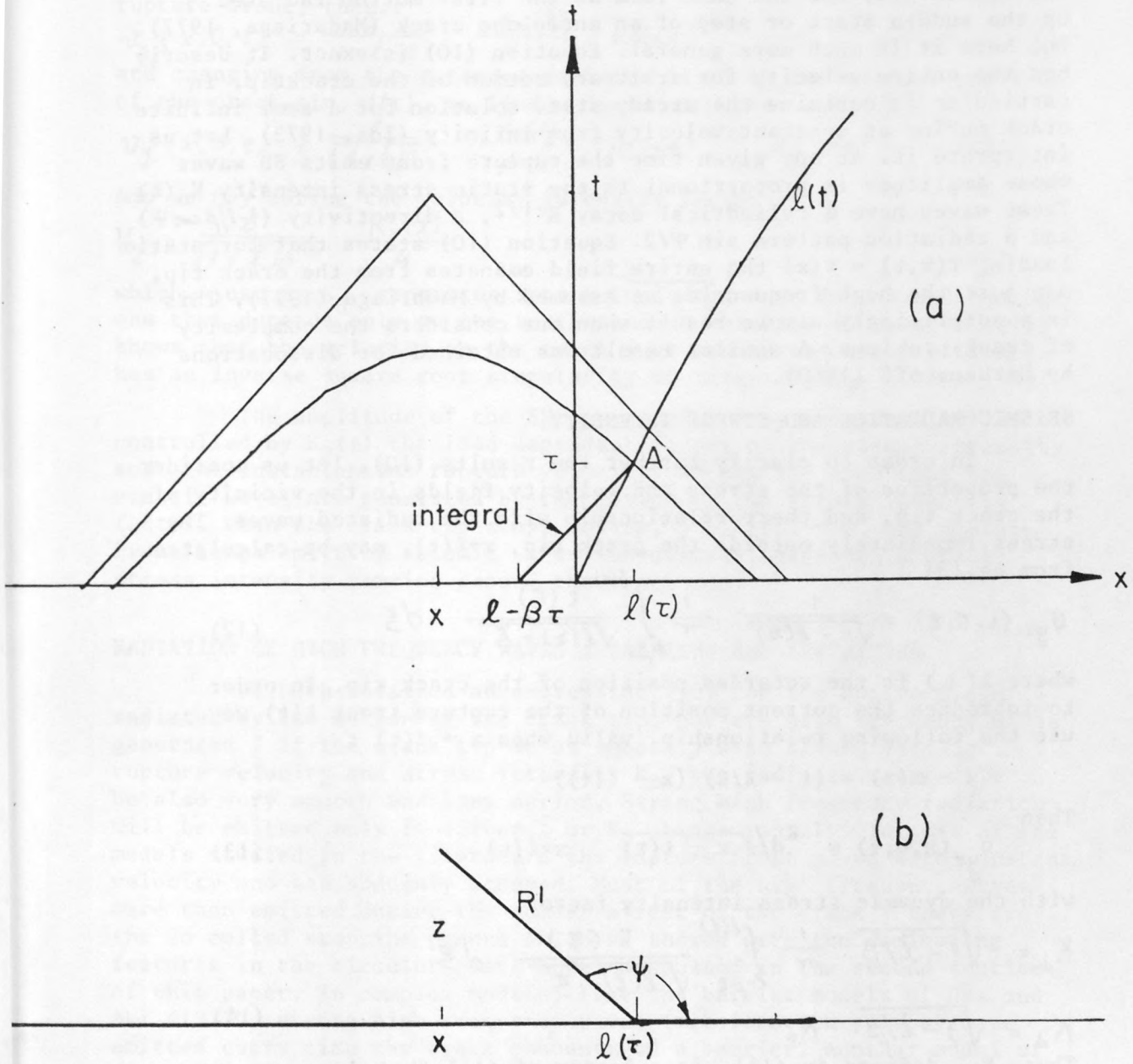

Figure 5. a) Line of integration for the calculation of the velocity field in equation 10.
b) Géometry for the instantaneous radiation from a moving crack.

ray from the retarded position to the observer. Then,

$$v_y(x,z,t) = \dot{\ell}\ \frac{\sin \Psi/2}{1-\dot{\ell}/\beta \cos\Psi}\ \frac{1}{R'^{1/2}}\ \frac{K_o(\ell)}{\mu} \qquad (10)$$

where K_o is the stress intensity of a static crack with its tip at $\ell(\tau)$:

$$K_o(\ell) = \frac{1}{\pi}\int_{\ell-\beta\tau}^{\ell} \frac{\tau(x_1)}{\sqrt{\ell - x_1}}\, dx_1 \qquad (11)$$

The result (10) has the same form as the first motion radiated by the sudden start or stop of an antiplane crack (Madariaga, 1977). But here it is much more general. Equation (10) is exact. It describes the entire velocity for arbitrary motion of the cracktip, in particular it contains the steady state solution for a semi infinite crack moving at constant velocity from infinity (Ida, 1973). Let us interprete it. At any given time the rupture front emits SH waves whose amplitude is proportional to the static stress intensity $K_o(\ell)$. These waves have a cylindrical decay $R^{-1/2}$, a directivity $(1-\dot{\ell}/\beta\cos\Psi)$ and a radiation pattern $\sin\Psi/2$. Equation (10) states that for static loading $\tau(x,t) = \tau(x)$ the entire field emanates from the crack tip, not just the high frequencies as assumed by Madariaga (1977). This is a surprisingly simple result when one considers the complexity of crack problems. A similar result was obtained for dislocations by Markenscoff (1980).

SEISMIC RADIATION AND STRESS INTENSITY.

In order to clarify further the results (10), let us consider the properties of the stress and velocity fields in the vicinity of the crack tip, and their relationship with the radiated waves. The stress immediately outside the crack tip, $x \to \ell(t)$, may be calculated from eq.(3) :

$$\sigma_{yz}(x,0,t) = \frac{1}{\sqrt{x-\ell(\tau)}}\ \frac{1}{\pi}\int_{\ell-\beta\tau}^{\ell(\tau)} \frac{\tau(\xi)}{\sqrt{\ell(\tau)-\xi}}\, d\xi \qquad (12)$$

where $\ell(\tau)$ is the retarded position of the crack tip. In order to introduce the current position of the rupture front $\ell(t)$ we use the following relationship, valid when $x \to \ell(t)$:

$$x - \ell(t) = (1 - \dot{\ell}/\beta)\ (x - \ell(\tau))$$

Then

$$\sigma_{yz}(x,0,t) = K_d/\sqrt{x-\ell(t)} \qquad x>\ell(t) \qquad (13)$$

with the dynamic stress intensity factor

$$K_d = \sqrt{1-\dot{\ell}/\beta}\ \frac{1}{\pi}\int_{\ell-\beta t}^{\ell(t)} \frac{\tau(\xi)}{\sqrt{\ell(t)-\xi}}\, d\xi$$

$$K_d = \sqrt{1-\dot{\ell}/\beta}\ K_o \qquad (14)$$

Thus, K_o, defined in (11), is a factor of (14) that does not depend on the instantaneous value of the rupture velocity . K_o depends only on the load and, for subsonic rupture, it has

no information on the history of rupture. Thus if at time t, $\dot{\ell}$ (t) changes abruptly the dynamic stress intensity K_d does also change because of the factor $\sqrt{1 - \dot{\ell}/\beta}$. The separation of the rupture velocity dependent term from the load dependent term K_o is valid even if the dynamic stress drop varies with time. In that case the definition of K_o has to be modified slightly (Kostrov, 1966).

Let us examine now the velocity field in the vicinity of the crack tip. On the plane of the crack (z = 0), $\psi = \pi/2$ behind the rupture front, then :

$$v_y(x,0,t) = \frac{\dot{\ell}}{1+\dot{\ell}/\beta} \frac{K_o(\ell)}{\mu} (\ell(\tau) - x)^{-1/2} \qquad x < \ell(t)$$

and changing from the retarded position $\ell(\tau)$ to the current position of the crack tip, $\ell(t)$, we find asymptotically for $x \to \ell(t)$:

$$v_y(x,0,t) = \frac{\dot{\ell}}{\sqrt{1+\dot{\ell}/\beta}} \frac{K_o(\ell)}{\mu} (\ell(t) - x)^{-1/2} \qquad x < \ell(t) \qquad (15)$$

And we may define the velocity intensity factor :

$$V_d = \frac{\dot{\ell}}{\sqrt{1+\dot{\ell}/\beta}} \frac{K_o(\ell)}{\mu} \qquad (16)$$

which, just as K_d, separates into a load dependent factor and another one that depends only on the instantaneous velocity $\dot{\ell}$. Equation (15) shows that the velocity on the crack just behind the rupture front, has an inverse square root singularity of intensity V_d.

The amplitude of the SH waves defined by equation (10) is controlled by $K_o(\ell)$ the load dependent factor of the stress intensity and the instantaneous rupture velocity. We may say then that the elastic waves are generated by the motion of the stress intensity factor. When the crack tip stops moving, i.e. $\dot{\ell}(t) = 0$, the rupture front stops emitting seismic a es immediately, although a static stress intensity remains around the crack tip.

RADIATION OF HIGH FREQUENCY WAVES : BARRIERS AND ASPERITIES.

We have obtained an expression (10) for the entire field radiated by the motion of the crack tip. How are high frequency waves generated ? If the crack tip moves smoothly with slowly varying rupture velocity and stress intensity K_o, the radiated waves will be also very smooth and long period. Strong high frequency radiation will be emitted only if either $\dot{\ell}$ or K_o change rapidly. In most of the models studied in the literature the rupture front moved with constant velocity and was suddenly stopped. Most of the high frequency waves were then emitted during the sudden arrest of the crack ; these are the so called stopping phases which we showed were the dominating features in the circular crack model discussed in the second section of this paper. In complex models, like the barrier models of Das and Aki (1977), strong high frequency waves (acceleration pulses) were emitted every time the crack encountered a barrier. Another model of source complexity discussed in the literature is the asperity model of Rudnicki and Kanamori (1981). Depending on the strength of the asperity the strength of radiation will vary. Let us discuss both models in more detail.

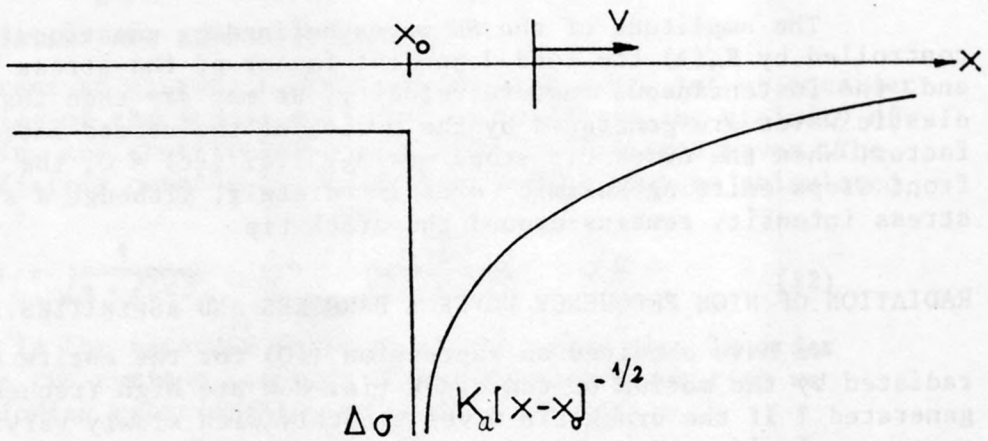

Figure 6. Strong stress heterogeneity (asperity). This type of stress concentration may be created if the area of the fault to the right of x_o was left unbroken during previous faulting episodes.

The Barrier Model

A barrier was defined by Das and Aki (1977) as a region of increased rupture strength on the fault plane. Thus if a rupture moving along the fault encounters a barrier, it will either reduce rapidly its rupture velocity or, at a very strong asperity, stop completely. This will generate strong high frequency waves whose amplitude will be controlled by the jump in rupture velocity. K_o does not change so that, if the position of the barrier on the fault plane is $\ell = \ell_o$, the radiation will be simply :

$$\Delta v_y(x,z,t) = \Delta \left[\frac{\dot{\ell}}{1 - \dot{\ell}/\beta \cos\psi} \right] \frac{\sin \psi/2}{R^{1/2}} \frac{K_o(\ell)}{\mu} \qquad (17)$$

the symbol Δ indicating as jump in the factor inside the brackets. This result was already found by Madariaga (1977) and in a slightly different from by Achenbach and Harris (1978). Therefore, a barrier produces a jump in rupture velocity which in turn produces a jump in the radiated field which is modulated by the directivity. The stopping phase is the limit case of the radiation by an unbreakable barrier, the rupture velocity drops to zero and the radiated wave will be proportional to $\dot{\ell}/(1 - \dot{\ell}/\beta \cos\psi)$ where $\dot{\ell}$ is the rupture velocity just before the crack encounters the barrier. This simple result may be verified in the seismograms calculated by Aki and Das (1977), although their radiation is not exactly like (17) because they took a slice of the two dimensional antiplane crack in order to simulate a finite three dimensional crack.

The Asperity Model.

It has often been suggested in the literature that stress heterogeneity on the fault should be a source of high frequency radiation. We can analyze the effect of these variations in dynamic stress drop with our model. Stress heterogeneity produce variations of the stress intensity K_o, which in turn generates radiated waves. In this fashion stress variation will generate seismic radiation. Let us see this in more detail : K_o depends on the dynamic stress drop via :

$$K_o(x) = \frac{1}{\pi} \int_{x-\beta t}^{x} \Delta\sigma(\xi) \frac{d\xi}{\sqrt{x-\xi}}$$

where as in (9) we assumed that the dynamic stress drop is independent of time. Clearly discontinuities in $\Delta\sigma$ will be reflected in the variation of $K_o(x)$ although K_o will be smoother because of the integration. Therefore, if there is a jump in stress at x_o, $K_o(x)$ will present an $(x-x_o)^{1/2}$ behaviour after the rupture front breaks through x_o. Assuming that the rupture velocity does not change at x_o, the velocity radiation calculated from (10) will present a t type-wavefront. This is weaker wave than the step function fronts created by changes in rupture velocities. There is one case however in which the radiation due to stress heterogeneity will be as strong as that due to rupture velocity jumps. This occurs, as shown in fig. 6, when the rupture front encounters a stress heterogeneity of the type :

$$\sigma(x) = K_a (x - x_o)^{-1/2} \qquad (18)$$

In this case the stress intensity changes at x_o by :

$$K_o(x) = K_a H(x - x_o) \qquad (19)$$

i.e., $K_o(x)$ jumps by the finite amount K_a.

This may appear as an extreme case of heterogeneity, yet it is very likely that it occurs on a fault plane subjected to successive events. Stress singularities of the type (18) are always associated with cracks, so that if the rupture is breaking into a previously unbroken patch it will almost certainly encounter a stress concentration of this kind. This is the case, for instance, in the asperity models studied by Rudnicki and Kanamori (1981) and Mc Garr (1981). In those models an unbroken patch has been left over from previous events on the fault. The stress concentration in the unborken patch presents inverse square root singularities of the type (18) near the borders of the asperity. When the rupture front breaks through the asperity a jump in K_o occurs and a strong jump in particule velocity is radiated. It is very likely, of course, that a jump in velocity will occur at the same time reinforcing even more the high frequency radiation.

In conclusion, there are two ways to produce jumps the particle velocity radiation : in the first, the rupture front encounters a barrier where the strength or rupture resistance increases suddenly, the rupture velocity changes abruptly and a strong wave (step change in particle velocity) is generated. In the second case, the rupture front encounters an asperity due to a previously unbroken ligament on the fault. Whether the rupture velocity changes or not, this generates a step in particle velocity. These two models are undistinguishable from the seismic radiation, unless we can detect the sign of the particle velocity jumps. Particle velocity jumps are associated with ω^{-1}-type high frequency asumptotes in the particle velocity spectrum. In terms of the displacement spectra these jumps create the usual ω^{-2} high frequency asymptotes. In acceleration both barriers and asperities of the type discussed above contribute to a flat high frequency spectrum of the type found by Hanks and Mc Guire 1981) in most accelerograms. Their results may be interpreted as a clear indication that high frequency waves are controlled by the presence of barriers and asperities on the fault plane.

CONCLUSIONS.

The preceding results were derived for the simplest crack model of faulting that we can devise : the antiplane crack. Our result (10) describes completely the radiation from this crack model. Similar results may be obtained for in-plane crack propagation in two dimensions, the radiation of P and SV waves presents the same dynamic characteristics as the SH waves radiated by the antiplane model. The major differences being in the radiation pattern (Madariaga, 1977 and in preparation, 1982). We conclude that for two dimensional

dynamic source models, the strongest possible radiation are jumps in particle velocity, i.e. ω^{-2} high frequency asymptotes in the displacement spectra. The acceleration spectra are therefore flat at high frequencies. A simple interpretation of Hanks and Mc Guire's (1981) results is that high frequency seismic waves are generated by the rupture front when it encounters barriers or asperities.

Seismic radiation is, however, a three-dimensional phenomenon and we must prove that the two dimensional results are applicable to earthquakes. This has already been demnstrated for a curved rupture front by Madariaga (1977) and Harris and Achenbach (1978), under the assumption that the rupture front changes its rupture velocity simultaneously all around the crack edge. This is a highly restrictive assumption and it is necessary to extend this result to more general situations. For instance, when the rupture front encounters a barrier or asperity of a general shape, the rupture velocity change propagates along the border of the barrier or asperity with an apparent velocity which will be very likely supersonic. This problem has no solution yet.

The preceding results were an effort to understand the physics of high frequency excitation during earthquake faulting. We have described the main features that we expect from a single encounter of the rupture front with a barrier or asperity. The result may be generalized and used to explain the high frequency waves and accelerations in the more realistic situation when there is a random distribution of barriers and asperities on the fault. A first step in this direction has been presented by Boatwright (1982).

ACKNOWLEDGEMENTS.

The work presented here was initiated during the author's tenure of a Green scholarship at the Institute of Geophysics and Planetary Physics of the University of California at San Diego. I deeply thank Prof. E. Luco for many helpful discussions on the theory of nearfield radiation.

This research was sponsored by Institut National d'Astronomie et Géophysique (I.N.A.G.) through the ATP Sismogenèse.

Contrib. I.P.G.P. : n° 580

REFERENCES

Achenbach, J.D. and J.A. Harris.- J. Geophys. Res., 83, 2283-2302, 1978.

Aki, K. - J. Geophys. Res., 72, 1217-1231, 1967

Aki, K. and P.G. Richards.-Quantitative Seismology, W.F. Freeman, San Francisco, CA, 1980.

Andrews, D.J. - J. Geophys. Res., 86, 10821-10828,1981.

Archuleta, R. and S. Hartzel. - Bull. Seism. Soc. Am., 71, 939-958, 1981.

Boatwright, J. - This volume, 1982.

Brune, J.N. - J. Geophys. Res., 75, 4997-5009, 1970.

Das, S., and K. Aki. - J. Geophys. Res., 82, 5658-5670, 1977.

Eshelby, J. - Mech. Phys. Solids, 17, 177-197, 1969.

Freund, L.B. - Quart. App. Math., 30, 371-281, 1981.

Hanks, T.C. and R.K. Mc Guire. - Bull. Seism. Soc. Am., 71, 2071-2095.

Haskell, N.R. - Bull. Seism. Soc. Am., 56, 125-140, 1966.

Keller, J.B. - J. Opt. Soc. Am., 52, 116-130, 1962.

Kostrov, B.V. - J. Appl. Math. Mech., 30, 1241-1248, 1966.

Kostrov, B.V. - Int. J. Fracture Mech., 14, 47-56, 1975.

Madariaga, R. - Bull. Seism. Soc. Am., 65, 163-182, 1976.

Madariaga, R. - Geophys. J. Roy. Astr. Soc. 51, 625-652, 1977.

Mc Garr, A. - J. Geophys. Res., 86, 3901-3912, 1981.

Markenscoff, X. - J. Elast. 10, 193-201, 1980.

Rudnicki, J. and H. Kanamori. - J. Geophys. Res., 86, 1785-1793, 1981.

Savage, J. - Bull. Seism. Soc. Am., 56, 577-592, 1966.

Stepjan, L.I. - Theory of Cracks, Sudostrojenje, Leningrad, 1981.

FOCUSING OF GROUND MOTION DUE TO CURVED RUPTURE FRONTS

by

J. D. Achenbach
The Technological Institute
Northwestern University
Evanston, IL. 60201

and

J. G. Harris
Theoretical and Applied Mechanics
University of Illinois
Urbana, Illinois 61801

Abstract

Analytical results are presented which describe ground motions generated by a sudden decrease of the rate of advance of a curved front of a region of sliding in an inclined fault plane. The elastic-wave emission is computed on the basis of two-dimensional canonical problems for slip-displacement distributions near the rupture front, that are consistent with Mode II and Mode III crack propagation models. Ray theory considerations provide modifications to the two-dimensional radiated fields to account for curvature of the front. In the near-field the ground motion is computed by considering the reflection of rays of body-wave motion at the ground's surface. Surface-wave motions are computed in the far-field. Both for the reflection of body waves and for surface waves the curvature of the rupture front gives rise to a focusing effect of the ground motion. This effect appears to be more severe for body waves than for surface waves.

1. Introduction

This paper combines results of dynamic crack propagation with elements of ray theory to compute ground motions generated by elastodynamic radiation due to a sudden change of the rate of advance of a propagating slip zone.

Within the mathematical idealization considered here, the rupture front is a singular curve in the fault plane, which forms the transition from continuous stresses and displacements ahead of the rupture front to conditions of sliding in the slip zone. In recent elastodynamic fracture studies the conditions governing the propagation of such a rupture front have been investigated.

It may be expected that the strongest motions are radiated at abrupt changes of the rupture-front speed. Naturally, the idealizations of a discontinuous rupture-front speed and of a singular rupture front produce more severe motions than would be the case for a gradual change of the speed or for a transition zone of rupture. Hence, the results presented here are upper bounds. In terms of the frequency spectrum one can, however, argue that the results apply in a frequency range higher than the corner frequencies, but still in a range for which the corresponding wavelengths would be sufficiently larger than the distance over which the speed of the rupture front changes drastically as well as the length of a transition zone of rupture.

The computations presented here are based on slip-displacement distributions near the rupture front that are consistent with Mode II and Mode III crack models, which have recently been discussed in the literature. The distribution of slip just behind the rupture front is taken in the general form $\eta^{\kappa/2}$, where η is the distance from the rupture front. For $\kappa = 1$ this distribution corresponds to brittle fracture. By taking $\kappa > 1$, the important case of rupture in the presence of distributions of cohesive tractions at the rupture front is included in the analysis. It is shown that discontinuous changes of the rupture-front speed give rise to the radiation of particle velocities which at the wavefronts are of the forms $(t-s_T r)^{(\kappa+1)/2-1}$ and $(t-s_L r)^{(\kappa+1)/2-1}$, while the corresponding frequency spectra are of order $O[\omega^{-(\kappa+1)/2}]$. Thus, the nature of the elastodynamic radiation strongly depends on the value of κ.

An interesting feature of the results presented in this paper is the focusing of motion caused by the curvature of the propagating rupture front. This kind of focusing should be distinguished from focusing due to propagation of the rupture front, which also occurs for a straight front, and which has been investigated by other authors.

The first crack models of earthquake faulting were two-dimensional and of the Mode III variety; see, e.g., Burridge and Halliday [1971]. Three-dimensional models of the crack-type that have been considered are the ones in which rupture begins at a point and spreads with constant velocity over a circular or elliptic region. These models have recently been discussed in detail by Richards [1976]. They provide valuable insight, but they have the drawback that the solution breaks down at a change of speed of the rupture front. In recent work numerical methods have been used to escape the constraints of these idealized models; see e.g., Madariaga [1976].

In this paper we compute the fields along rays emitted by the rupture front by the use of fields calculated for a semi-infinite crack whose faces are subjected to analogous disturbances. Solutions for the semi-infinite crack geometry can be obtained analytically by application of Laplace transform techniques in combination with the Wiener-Hopf method; see Achenbach [1973]. Wavefront motions can be analyzed directly from the Laplace transforms of the solutions by asymptotic considerations. These wavefront results can be expressed in terms of emission coefficients that relate the emitted fields to the crack opening displacement. Ray-theory considerations provide modifications to the semi-infinite crack results to account for the curvature of the rupture front and for the finite dimensions of the crack. In the usual terminology the results for the corresponding semi-infinite crack problem are referred to as the canonical solutions. The computations described here have been discussed in detail by Achenbach and Harris [1978]. Similar results have been presented by Madariaga [1977].

Recently, Harris and Achenbach [1981] have extended their results to include the interaction of the emitted radiation with the ground's surface in the near-field. Bouchon [1980a, 1980b] has shown by means of three-dimensional computer-plots how significant this interaction can be. In particular his plots demonstrate the amplification of the bulk waves by their reflection from a traction-free surface.

In the near-field the motion of the ground's surface can be readily computed by considering the reflection of rays of body-wave motion. We study the surface motion not only in regions where ordinary reflection takes place, but also in those regions where the angle of incidence of rays of transverse motion exceeds the critical angle. The ordinary reflection problem is readily treated by ray methods. The calculation of the critically reflected rays requires additional analysis, which is briefly reviewed. In the far-field the ground motion is primarily due to surface waves. It is possible to analyze surface waves on the basis of ray theory, see e.g. Keller and Karal [1964]. This requires, however, the tracing of rays in complex space. In this paper we have elected to follow a conceptually simpler method whereby the surface-wave field is expressed in terms of a representation integral over a surface S_i in the interior of the half space which envelops the rupture front. In fact, the surface is taken as a wavefront of the wave motion emitted by the rupture front, and the field on S_i is the one computed earlier by ray methods. The other terms in the representation integral come from the Green's function for the half-space. By the use of asymptotic methods the representation integral can be evaluated to give a simple explicit

form for the surface-wave motion. Details are given for the excitation of Love waves by strike slip over a region with a curved rupture front on an inclined fault plane.

2. Radiation from an expanding slip-zone

The rupture front C of a planar slip-zone is advancing with a normal velocity v. The plane of the slip-zone makes an angle ϕ with the normal to the surface of the half-space. An instantaneous position of C is shown in Fig. 1. In general the radius of curvature of C, which is defined by ρ, may vary along the rupture front. A point on the rupture front C is defined by the polar angle ψ. The unit vector $\hat{\underset{\sim}{t}}(\psi)$ is tangential to C. The plane $N(\psi)$, which is normal to $\hat{\underset{\sim}{t}}(\psi)$, contains a polar coordinate system with its center on the intersection with C. The plane $N(0)$ and its coordinate system (r,θ) are shown in Fig. 1. A second coordinate system (x,y,z) is located with its origin at the intersection of the slip-plane and the surface of the half-space, so that point B has coordinates $(-D\tan\phi, D, 0)$.

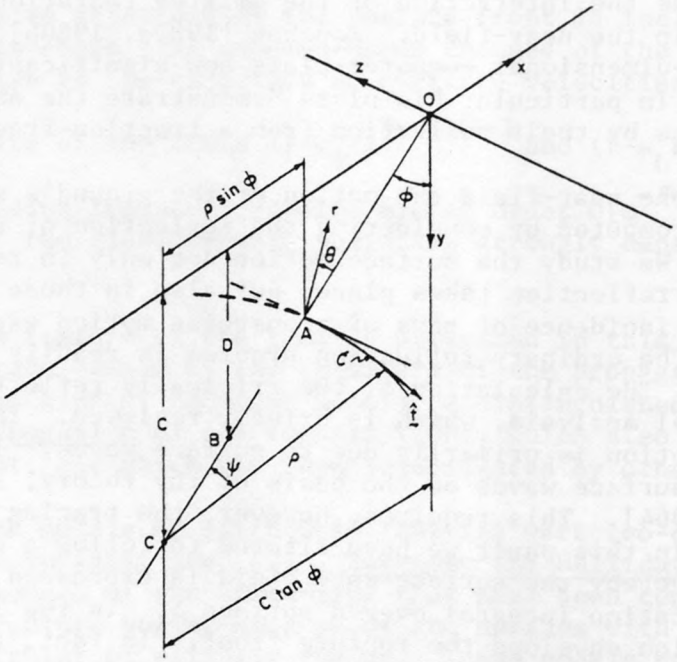

Fig. 1: Rupture front C of a planar slip-zone.

The propagating rupture front emits wave motions, which increase in intensity at a sudden change of the propagation speed v. When the

rupture is brittle, an abrupt change in the speed of the rupture front at time $t = 0$ from v_1 to v_2, where $v_2 < v_1$, causes two step-function discontinuities in the particle velocities to propagate outwards at the longitudinal and transverse wave speeds, respectively. When the rupture process is more gradual, the particle velocities are no longer discontinuous.

We first consider the radiated wave motions before any interaction with the surface of the half-space takes place, i.e., as if the slip zone were located in an unbounded medium. At a change of the rate of advance of the rupture front from v_1 to v_2, the high-frequency emission of wave motion from a point P on the rupture front can be represented by fans of body-wave rays in the plane $N(\psi)$ through P normal to the rupture front. In a two-dimensional geometry expressions for the particle velocity at the relevant wavefronts have been given by Achenbach and Harris [1978]. For a three dimensional geometry these canonical solutions must be adjusted for curvature of the rupture front by multiplication with a factor $(1 + r/\bar{\rho})^{-\frac{1}{2}}$, where

$$\bar{\rho} = \rho(\psi)/\cos\theta \tag{1}$$

The wave motions that are defined in this manner can be longitudinal (L), in-plane transverse (TV) or anti-plane transverse (TH) relative to the plane $N(\psi)$.

For rupture and sliding in Mode II it follows from Achenbach and Harris [1978] that the elastodynamic accelerations radiated from a point on C may be written as

$$\ddot{u}_r(r,\theta,t) = \dot{U}_r^L \, \dot{e}_L(t-s_L r) \tag{2a}$$

$$\ddot{u}_\theta(r,\theta,t) = \dot{U}_\theta^T \, \dot{e}_T(t-s_T r) \tag{2b}$$

where for the special case of $v_2 \equiv 0$ (stopping event)

$$\dot{U}_r^L = r^{-\frac{1}{2}}(1+r/\bar{\rho})^{-\frac{1}{2}} \, E_L^{TV}(\theta) \tag{3a}$$

$$\dot{U}_\theta^T = r^{-\frac{1}{2}}(1+r/\bar{\rho})^{-\frac{1}{2}} \, E_{TV}^{TV}(\theta) \tag{3b}$$

In (2a) and (2b) s_L and s_T are the longitudinal and transverse slowness, respectively; that is, $s_L = 1/c_L$ and $s_T = 1/c_T$ where c_L and c_T are

the corresponding wave speeds. The above expressions are essentially those of equations (38)-(41) of Achenbach and Harris [1978]. The length $\bar{\rho}$, which is given by (1), defines the distance to a caustic. The emission coefficients $E_L^{TV}(\theta)$ and $E_{TV}^{TV}(\theta)$ follow from equations (15) and (28) of Achenbach and Harris [1978] by setting $v_2 \equiv 0$. The superscript TV indicates that the wave motion is generated by Mode-II rupture, while the subscripts L and TV define the nature of the motion in the plane $N(\psi)$. The time dependence of the emitted pulse follows from equation (26) of Achenbach and Harris [1978] as

$$\dot{e}_\beta(t-s_\beta r) = \begin{cases} A\ \delta(t-s_\beta r) & \kappa = 1 \\ A\ \frac{1}{2}(\kappa-1)(t-s_\beta r)^{\frac{1}{2}(\kappa-3)} H(t-s_\beta r) & \kappa > 1 \end{cases} \tag{4a,b}$$

where $\beta = L$ or $\beta = T$, and the constant A is determined by the nature of the crack growth.

For rupture and sliding in Mode-III we have

$$\ddot{u}_\psi(r,\theta,t) = -\dot{U}_\psi^T\, \dot{e}_T(t-s_T r) \tag{5}$$

where $\dot{e}_T$ is defined by (4a,b), and

$$\dot{U}_\psi^T = r^{-\frac{1}{2}}(1+r/\bar{\rho})^{-\frac{1}{2}}\, E_{TH}^{TH}(\theta) \tag{6}$$

The emission coefficient $E_{TH}^{TH}(\theta)$ is simple enough to be written out explicitly:

$$E_{TH}^{TH}(\theta) = \frac{(1+v_1/c_T)^{\frac{1}{2}}\, v_1^{\frac{1}{2}} \sin(\theta/2)}{\sqrt{\pi}\ [1-(v_1/c_T)\cos\theta]} \tag{7}$$

The independent variable in the emission coefficients is the angle θ, which is defined in Fig. 1. For $v_2 \equiv 0$, the parameters are c_L/c_T and v_1/c_T. The ratio c_L/c_T is defined by Poisson's ratio ν; for $\nu = 0.25$ we have $c_L/c_T = \sqrt{3}$. In Figs. 2 and 3 the emission coefficents are plotted versus θ, for $\nu = 0.25$, and for various values of v_1/c_T The emission coefficient for vertically polarized transverse motion is

plotted up to the headwave region, i.e., $0 \leq \theta \leq \theta_{HW}$, where $\theta_{HW} = \cos^{-1}(-c_L/c_T)$. At $\theta = \theta_{HW}$ the emission coefficient though large is bounded. This increase in amplitude near the critical angle has been observed by other authors, see e.g. Cagniard [1962, pp. 161-163]. As expected the absolute magnitudes of the emission coefficients are larger when v_1/c_T is larger.

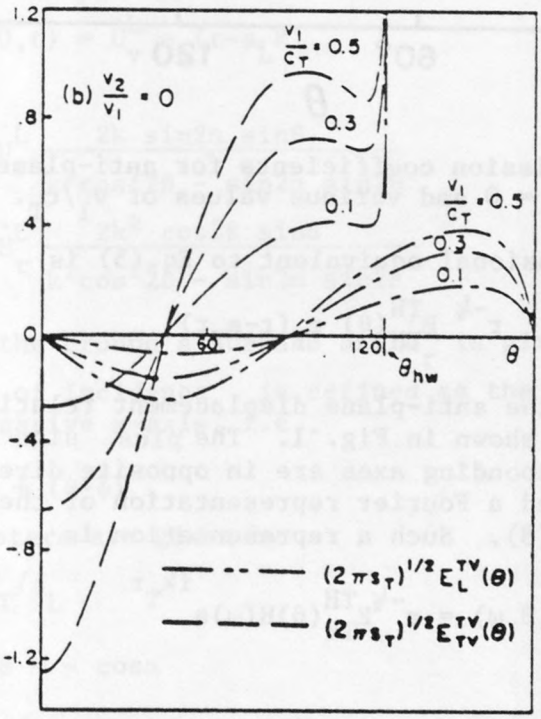

Fig. 2: Emission coefficients for in-plane slip; for $\nu = 0.25$, $v_2 = 0$ and various values of v_1/c_T.

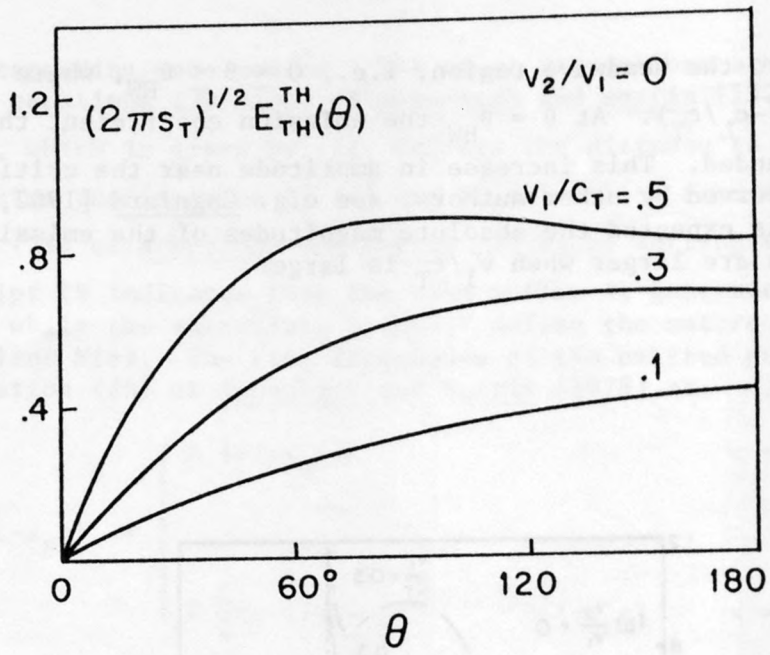

Fig. 3: Emission coefficients for anti-plane slip, $v_2 = 0$ and various values of v_1/c_T.

The two-dimensional equivalent to Eq.(5) is

$$\ddot{w} = r^{-\frac{1}{2}} E_{TH}^{TH}(\theta)\, \dot{e}_T(t-s_T r) \tag{8}$$

Here w(x,y,t) is the anti-plane displacement relative to the (x,y,z) coordinate system shown in Fig. 1. The plus sign appears in Eq.(8) because the corresponding axes are in opposite directions. In the sequel we will need a Fourier representation of the <u>displacement</u> corresponding to (8). Such a representation is

$$w(r,\theta,\omega) = r^{-\frac{1}{2}} E_{TH}^{TH}(\theta) H(\omega) e^{ik_T r} \tag{9a}$$

where

$$H(\omega) = \hat{\dot{e}}_T(\omega)(-i\omega)^{-2} \tag{9b}$$

$$\hat{\dot{e}}_T(\omega) = \begin{cases} A & \kappa = 1 \\ A\Gamma[\frac{1}{2}(\kappa+1)]/(-i\omega)^{\frac{1}{2}(\kappa-1)} & \kappa > 1 \end{cases} \tag{9c}$$

3. Near-Field Ground Motion Caused by Reflection of Body Waves

One of the principles of geometrical elastodynamices, or ray theory, is that the pulse given by (2) behaves locally as a plane wave (Cervaný et al [1977, pp. 26-34 and pp. 53-54]). Therefore the acceleration pulses reflected from the free surface, when a longitudinal acceleration pulse of the form (2) strikes it, can be constructed in the same manner as are reflected plane waves. By adding these reflected pulses to the incident acceleration pulse, the components of the ground's acceleration can be computed. In the plane $N(0)$ we find

$$\ddot{u}_x(x,0,t) = \dot{U}^L_x \dot{e}_L(t-s_L R) \tag{10}$$

$$\ddot{u}_y(x,0,t) = \dot{U}^L_y \dot{e}_L(t-s_L R) \tag{11}$$

where

$$\dot{U}^L_x = \dot{U}^L_r \frac{2k \sin 2\alpha \sin\beta}{k^2 \cos^2 2\beta - \sin 2\alpha \sin 2\beta} \tag{12}$$

$$\dot{U}^L_y = \dot{U}^L_r \frac{2k^2 \cos 2\beta \sin\alpha}{k^2 \cos^2 2\beta - \sin 2\alpha \sin 2\beta} \tag{13}$$

where $r = R$ on the ground's surface and $\dot{U}^L_r$ is given by (4) with $r = R$. Also, the angle of incidence is defined as the angle of the incident ray with the negative x-axis, i.e.,

$$\alpha = \frac{\pi}{2} + (\theta - \phi) \ . \tag{14}$$

The other parameters are given by

$$k = s_T / s_L \tag{15}$$

$$k \cos\beta = - \cos\alpha \tag{16}$$

$$R = y_A / \cos(\theta - \phi) \tag{17}$$

$$y_A = D - b \cos\phi \tag{18}$$

In order to calculate the reflection from the free surface of the incident transverse acceleration given by (3), we were forced to proceed more indirectly than in the previous case because the reflection coefficients become complex when the angle of incidence of the transverse ray, α defined by (9), is less than α^+_{cr} or greater than α^-_{cr}, where α^+_{cr}

and α_{cr}^{-} are the angles of critical reflection. These angles are given by

$$\alpha_{cr}^{+} = \cos^{-1}(1/k), \quad \alpha_{cr}^{-} = \cos^{-1}(-1/k) \ . \tag{19a,b}$$

We proceeded as follows: First the incident pulse was analyzed into its Fourier components. Next, by assuming that each incident component behaves locally as a plane time-harmonic wave, the Fourier components of the reflected pulses were calculated by multiplying each incident component by the appropriate reflection coefficient (transverse or longitudinal). The incident component and the corresponding reflected components were then added together to construct the net Fourier component of the ground's acceleration. Finally, the net acceleration pulse was Fourier synthesized. In this manner the x and y components of the ground's acceleration were calculated to be

$$\ddot{u}_x = |\dot{U}_x^T| \ \{\cos\varepsilon_x \ \dot{e}_T(t-s_T R) + \sin\varepsilon_x \ H[\dot{e}_T(t-s_T R)]\} \tag{20}$$

$$\ddot{u}_y = |\dot{U}_y^T| \ \{\cos\varepsilon_y \ \dot{e}_T(t-s_T R) + \sin\varepsilon_y \ H[\dot{e}_T(t-s_T R)]\} \tag{21}$$

In the above equations the amplitudes $|\dot{U}_x^T|$ and $|\dot{U}_y^T|$, and the phase angles ε_x and ε_y are given by

$$|\dot{U}_x^T| \exp(i\varepsilon_x) = \dot{U}_\theta^T \frac{2k^2 \sin\alpha \ \cos 2\alpha}{k^2\cos^2 2\alpha - \sin 2\alpha \ \sin 2\gamma} \tag{22}$$

$$|\dot{U}_y^T| \exp(i\varepsilon_y) = \dot{U}_\theta^T \frac{2\sin 2\gamma \ \sin\alpha}{k^2\cos^2 2\alpha - \sin 2\alpha \ \sin 2\gamma} \tag{23}$$

respectively. In (20) and (21), $H[\dot{e}_T(t)]$ is the Hilbert transform

$$H[\dot{e}_T(t)] = \frac{1}{\pi} \int_{-\infty}^{\infty} \frac{\dot{e}_T(\xi)\, d\xi}{\xi - t} \ . \tag{24}$$

For the case $\kappa=1$, $\dot{e}_T(t) = A \ \delta(t)$ and $H[\dot{e}_T(t)] = -A \ (\pi t)^{-1}$, and for the case $\kappa=2$, $\dot{e}_T(t) = A \ (4t)^{-1/2} \ H(t)$ and $H[\dot{e}_T(t)] = A \ (-4t)^{-1/2} \ H(-t)$. In the above equations $r = R$ on the ground's surface. The ratio k is given by (15), the angle α by (14), R by (17), and the angle γ follows from the relation

$$\cos\gamma = - k \cos\alpha \ . \tag{25}$$

The term $\dot{U}_\theta^T$ is given by (5) with r = R. For $|k\cos\alpha| > 1$ we have taken

$$\sin\gamma = -i(k^2\cos^2\alpha - 1)^{1/2}. \tag{26}$$

For values of α such that $\alpha_{cr}^+ < \alpha < \alpha_{cr}^-$, the phase angles ε_x and ε_y are 0 or π, thus making the second term in the waveform functions in (20) and (21) zero. In other words, the reflection coefficients for these angles of incidence are real. For $\alpha < \alpha_{cr}^+$ or $\alpha > \alpha_{cr}^-$ the second terms do not vanish. The expressions (20) and (21) then include, however, more effects than are simply described by the critical reflection of the discrete rays. This has been discussed in greater detail by Harris and Achenbach [1981].

Numerical calculations have been carried out for the case that the rupture front is part of an ellipse with major axis a and minor axis b, and for the following values of the parameters:

$$v_1/c_T = 0.5,\ v_2/c_T = 0\ ,\ a/b = 10,\ a/D = 0.2$$

$$\phi = 15^o,\ \nu(\text{Poisson's ratio}) = 0.25 \tag{27}$$

At $\psi = 0$, we then have

$$\rho/D = (a^2/b)/D = 2 \tag{28}$$

The x and y amplitudes $(2\pi s_T D)^{1/2}\ \dot{U}_x^L$ and $(2\pi s_T D)\ \dot{U}_y^L$ of that part of the ground's acceleration caused by the incidence of a longitudinal pulse emitted from point A have been displayed graphically by Harris and Achenbach [1981]. The factor $(2\pi s_T D)^{1/2}$ is a normalization factor. As expected, the addition of the reflected accelerations to the incident acceleration results in an amplification of the latter. However, it is significant to note that the amplitude of the incident field of longitudinal motion has extrema at essentially the same points as the total field. The maxima of the incident field depend on the angular variation of $E_L^{TV}(\theta)$, which is determined by the rupture process.

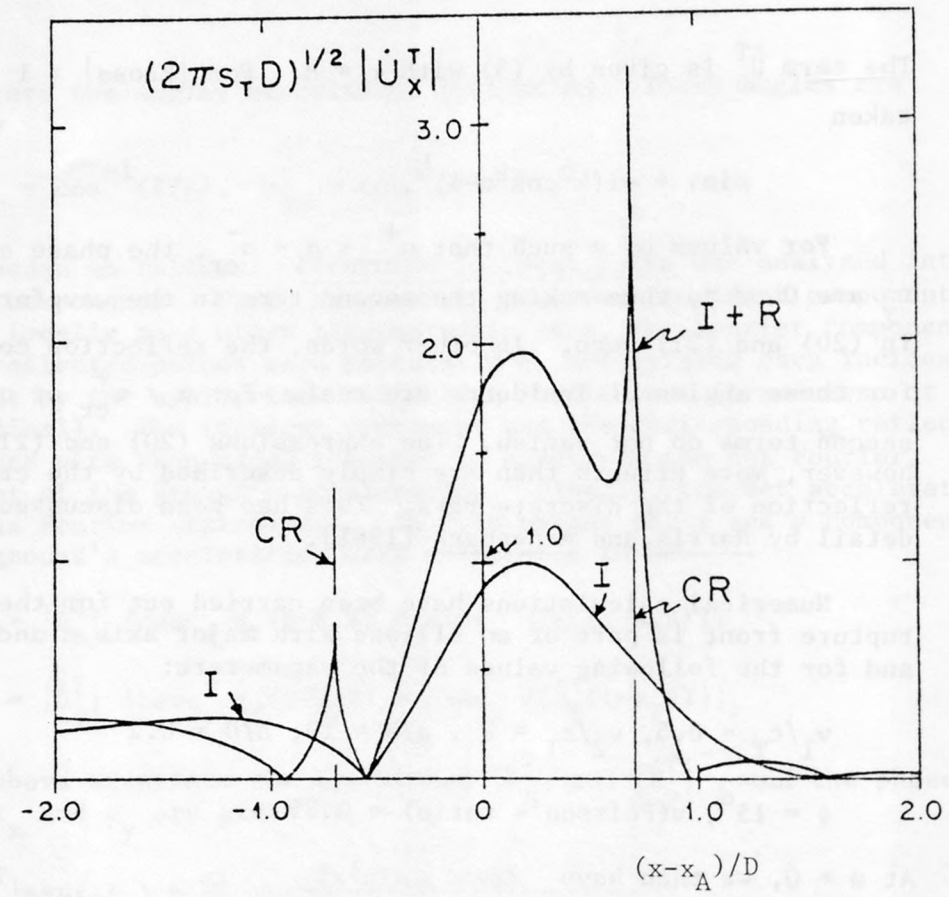

Fig. 4: Amplitude factor of horizontal component of surface acceleration generated by the emitted transverse wave, I = incident wave only, I + R = incident + reflected wave. The lines CR indicate boundaries beyond which critical reflection takes place.

The absolute values of the x and y amplitudes $(2\pi s_T D)^{\frac{1}{2}}|\dot{U}_x^T|$ and $(2\pi s_T D)^{\frac{1}{2}}|\dot{U}_y^T|$ of the ground's acceleration caused by the transverse pulse emitted from point A are plotted in Figs. 4 and 5, respectively. Also plotted are the magnitudes of the x and y components of the incident acceleration pulse of transverse motion evaluated on the surface. For values of $\alpha < \alpha_{cr}^{+}$ or $\alpha > \alpha_{cr}^{-}$ critial reflection takes place, and clearly such reflection takes place over most of the ground's surface. The boundaries beyond which critical reflection takes place are indicated by CR in Figs. 4 and 5. Though the present calculation may not be numerically accurate for points very close to

these boundaries, it may be concluded from examining these figures that the ground's acceleration can be particularly strong near these boundaries. It is also important to note that the magnitude of the ground's acceleration excited by the incident transverse acceleration is greater than that excited by the incident longitudinal acceleration.

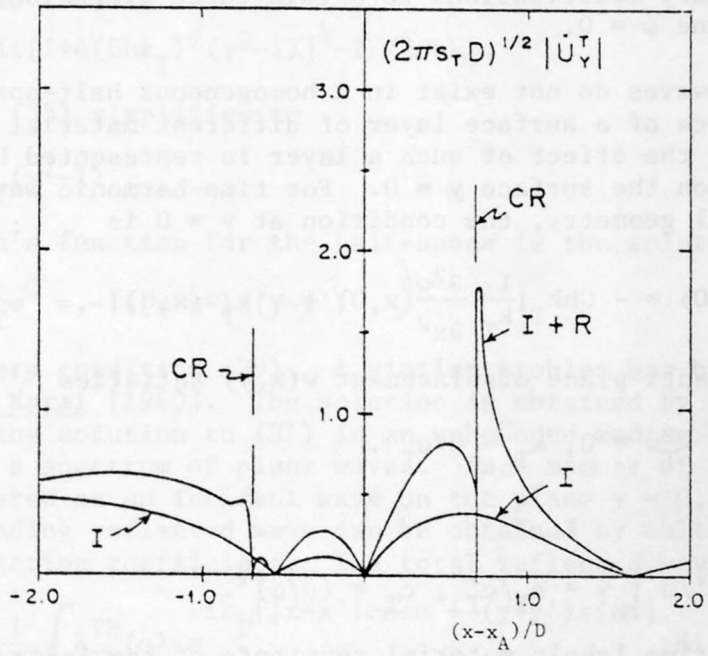

Fig. 5: Amplitude factor of vertical component of surface acceleration generated by the emitted transverse wave, I = incident wave only, I + R = incident + reflected wave. The lines CR indicate boundaries beyond which critical reflection takes place.

In both of the above cases the amplitudes of the surface accelerations in the forward direction become small for $(x - x_A)/D > 4.0$ so that $x \cong 4D + x_A$ is a measure of the extent of the near-field.

The expression given by (4) and (5) becomes unbounded when $r = -\rho(\psi)/\cos\psi$. This relation defines a caustic surface (the envelope of adjacent rays). The results given here are not valid on caustic surfaces. These surfaces are, however, of interest because their presence indicates a focusing effect of the radiated and reflected waves. Thus, for sufficiently large ϕ, there may be zones of severe ground motion in the near field due to focusing caused by curvature of the rupture front.

4. Surface Waves

Body waves radiating from a stopping phase of a rupture front generate surface waves. As an example we consider the excitation of Love waves. In a two dimensional geometry and in the frequency domain, the radiated displacement field is given by (9a). We first consider two-dimensional Love waves excited by (9a), and then indicate the necessary modifications to obtain three dimensional Love waves in the plane $\psi = 0$.

Love waves do not exist in a homogeneous half-space. They require the presence of a surface layer of different material properties. In this paper the effect of such a layer is represented by a boundary condition on the surface $y = 0$. For time-harmonic waves in a two-dimensional geometry, the condition at $y = 0$ is

$$\frac{\partial w}{\partial y}(x,0) = - Ghk_T\left[\frac{1}{k_T}\frac{\partial^2 w}{\partial x^2}(x,0) + \gamma^2 k_T w(x,0)\right] , \tag{29}$$

where the anti-plane displacement $w(x,y)$ satisfies

$$\nabla^2 w + k_T^2 w = 0, \quad k_T = \omega/c_T . \tag{30}$$

In (29):

$$G = \mu'/\mu \; ; \; \gamma = c_T/c_T' \; ; \; c_T = (\mu/\rho)^{1/2}. \tag{31}$$

Here the prime labels material constants of the layer, h is the layer thickness, and (29) is valid for $k_T h << 1$. A brief derivation of (29) has been given by Harris and Achenbach [1982]. An application of the boundary condition can be found in a paper by Simons [1975].

The simplest wave motion satisfying (29) and (30) is a system of incident and reflected plane horizontally polarized transverse waves represented by

$$w = e^{ik_T x\cos\alpha}\left[e^{-ik_T y\sin\alpha} + R_{TH}^{TH}(\alpha)e^{ik_T y\sin\alpha}\right] , \tag{32}$$

where α is the angle of incidence, and $R_{TH}^{TH}(\alpha)$ is the reflection coefficient which is easily obtained as

$$R_{TH}^{TH}(\alpha) = \frac{i\sin\alpha - Ghk_T(\gamma^2-\cos^2\alpha)}{i\sin\alpha + Ghk_T(\gamma^2-\cos^2\alpha)} . \tag{33}$$

Note that $R_{TH}^{TH}(\alpha)$ when viewed as a function of the complex variable α has a pole at $\alpha = \alpha^*$ where

$$i \sin\alpha^* + Ghk_T(\gamma^2-\cos^2\alpha^*) = 0 \ . \tag{34}$$

The presence of a pole in (33) indicates the existence of surface waves. The solution to (34) is

$$\sin\alpha^* = i\{[1+4(Ghk_T)^2(\gamma^2-1)]^{1/2}-1\}/2Ghk_T . \tag{35}$$

For $hk_T << 1$, (35) simplifies to

$$\alpha^* \simeq iGhk_T(\gamma^2-1) \ . \tag{36}$$

The Green's function for the half-space is the solution to

$$\nabla^2 w^G + k_T^2 w^G = - \delta(x-x')\delta(y-y') \ , \tag{37}$$

and the boundary condition (29). A similar problem has been solved by Keller and Karal [1960]. The solution is obtained by first representing the solution to (37) in an unbounded medium as an integral over a spectrum of plane waves. Each member of this spectrum can be considered as an incident wave on the plane $y = 0$, and hence each corresponding reflected wave can be obtained by multiplication with the reflection coefficient. The total reflected wave is

$$w^{GR} = - \frac{i}{4\pi} \int_{\mathcal{B}} R_{TH}^{TH}(\alpha) \, e^{ik_T[|x-x'|\cos\alpha + (y+y')\sin\alpha]} \, d\alpha \ . \tag{38}$$

The contour $\mathcal{B}$ is the Sommerfeld contour in the complex α-plane. By deforming this contour to one of steepest descent we pick up a contribution from the pole at $\alpha = \alpha^*$, when

$$(y+y')/|x-x'| < Ghk_T(\gamma^2-1) \ . \tag{39}$$

The approximation (36) has been used to obtain (39). The pole contribution is the Love-wave part of the Green's function:

$$w^{GL}(\underset{\sim}{x},\underset{\sim}{x}') = \alpha^* \, e^{ik_T[|x-x'|\cos\alpha^* + (y+y')\sin\alpha^*]} \ . \tag{40}$$

In (40) we have again used the approximation (36), and terms of order $O[(hk_T)^2]$ have been neglected in the amplitude.

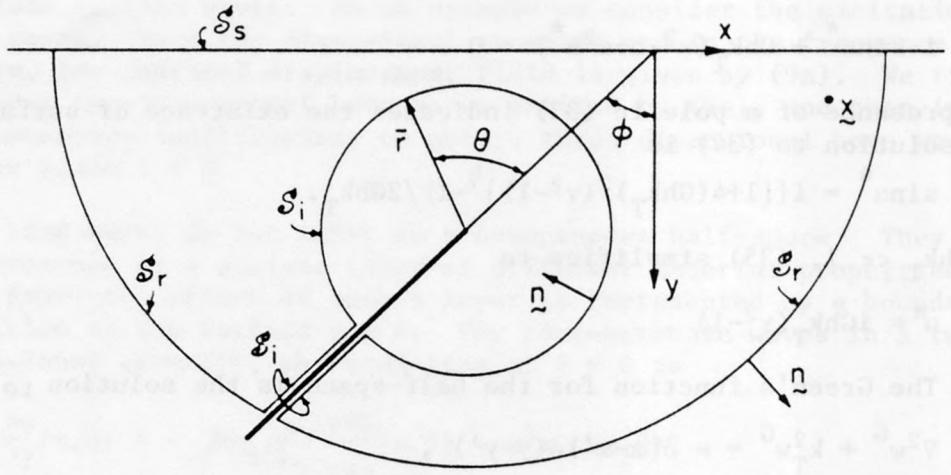

Fig. 6: Surface $S = S_r + S_s + S_i$, where S_i surrounds the rupture front and the fault plane.

Figure 6 shows a cross-sectional view of the surface $S = S_r + S_s + S_i$, with S_i surrounding the rupture front and the fault plane. It is well-known that the displacement at an arbitrary position $\underset{\sim}{x} = (x,y)$ may be expressed in the form

$$w(\underset{\sim}{x}) = \int_{S_i} [w^G(\underset{\sim}{x},\underset{\sim}{x}') \frac{\partial w}{\partial n}(\underset{\sim}{x}') - w(\underset{\sim}{x}') \frac{\partial w^G}{\partial n}(\underset{\sim}{x},\underset{\sim}{x}')] dS(\underset{\sim}{x}') \tag{41}$$

The wavefield $w(\underset{\sim}{x}')$ can be decomposed in three parts, namely,

$$w(\underset{\sim}{x}') = w^I(\underset{\sim}{x}') + w^R(\underset{\sim}{x}') + w^{MS}(\underset{\sim}{x}') \tag{42}$$

Here $w^I(\underset{\sim}{x}')$ represents the radiation from the rupture front in an unbounded medium, $w^R(\underset{\sim}{x}')$ represents the reflection of $w^I(\underset{\sim}{x}')$ from the surface of the half-space and $w^{MS}(\underset{\sim}{x}')$ represents multiple wave interactions between the source and the surface of the half-space. Because $w^R(\underset{\sim}{x}')$ satisfies source-free equations within S_i, the terms

with $w^R(\underset{\sim}{x}')$ in (41) vanish. Next, the terms with $w^{MS}(\underset{\sim}{x}')$ in (41) are neglected. These terms generally are of smaller order of magnitude. Moreover, in the time domain they correspond to disturbances which arrive much later. Finally, because we are interested in the Love-wave contribution to the field $w(\underset{\sim}{x})$, only the Love-wave components of the Green's function need be used in (41). After these simplifications (41) reduces to

$$w^L(\underset{\sim}{x}) = \int_{S_i} [w^{GL}(\underset{\sim}{x},\underset{\sim}{x}') \frac{\partial w^I}{\partial n}(\underset{\sim}{x}') - w^I(\underset{\sim}{x}') \frac{\partial w^{GL}}{\partial n}(\underset{\sim}{x},\underset{\sim}{x}')]dS(\underset{\sim}{x}') \tag{43}$$

In this expression $w^L(\underset{\sim}{x})$ is the Love-wave displacement, S_i is now a curve in the (x,y)-plane surrounding the crack (see Fig. 6), and $w^{GL}(\underset{\sim}{x},\underset{\sim}{x}')$ is the Love-wave component of the two-dimensional Green's function. The latter is defined by equation (40).

To evaluate (43) we take the contour S_i to lie in the far-field where we may approximate $w^I(\underset{\sim}{x})$ by the far-field approximation to the disturbance excited by the advancing rupture front as it changes its rate of advance. It is convenient to take S_i as a wavefront of that disturbance plus some portions along either surface of the fault plane as shown in Fig. 6. Because we are interested in far-field results, we may evaluate (43) by the method of steepest descents. Relative to a coordinate system with origin at the intersection of the plane of the fault with the free surface, the instantaneous position of the rupture front is defined by (-d tanϕ,d). The radius of S_i is $\bar{r}$, as shown in Fig. 6. We also place a polar coordinate system at the rupture front, so that

$$x = -d\tan\phi + r\sin(\phi-\theta),\quad y = d - r\cos(\phi-\theta) \tag{44a,b}$$

The angle is in the range $0 \leq \phi < \pi/2$

Upon substitution of $w^I(\underset{\sim}{x}')$ from (9a) and $w^{GL}(\underset{\sim}{x},\underset{\sim}{x}')$ from (40) into (43) we find for a point to the right of the projection of the rupture front on the surface of the half-space ($x > -d\tan\phi$) the following expression for the Love-wave

$$w^L(x,y) = -ik_T\bar{r}^{\frac{1}{2}}\alpha^* H(\omega)D(d,\alpha^*)W^L(x,y)e^{ik_T\bar{r}}I(\bar{r}) \tag{45}$$

where $H(\omega)$ is defined by (9b), and

$$D(d,\alpha^*) = e^{ik_T d\sin\alpha^*} \tag{46}$$

$$W^L(x,y) = e^{ik_T(|x+d\ \tan\phi|\cos\alpha^* + y\ \sin\alpha^*)} \tag{47}$$

$$I(\bar{r}) = \int_{-\pi}^{\pi} E_{TH}^{TH}(\theta)[\sin(\phi-\theta+\alpha^*)+1]e^{-ik_T\bar{r}\ \sin(\phi-\theta+\alpha^*)}\,d\theta \tag{48}$$

The complex angle α^* is the solution to (35). For large values of $k_T\bar{r}$, Eq.(48) can be evaluated by the method of steepest descent. The saddle point is located at $\bar{\theta} = \phi + \alpha^* - \frac{1}{2}\pi$. We obtain

$$w^L(x,y) \simeq A^{L+}(d,\alpha^*,\phi)H(\omega)W^L(x,y), \tag{49}$$

where

$$A^{L+}(d,\alpha^*,\phi) = 2(-i2\pi k_T)^{\frac{1}{2}}\ \alpha^*\ E_{TH}^{TH}(\phi+\alpha^* - \tfrac{1}{2}\pi)D(d,\alpha^*)\ , \tag{50}$$

and $W^L(x,y)$ is defined by (47). The strength of the Love-wave depends on the depth d through the function $D(d,\alpha^*)$. It should be noted that (49) is independent of $\bar{r}$. The condition that $k_T\bar{r}$ is large does not imply that $k_T d$ is large. In fact, if interest in the time domain is focused on the first Love-wave arrival, the surface S_i may intersect the surface, of the half-space, because the point of steepest descent is also at depth d.

For a fixed point to the left of the rupture front ($x < -d\ \tan\phi$) we find analogously

$$w^L(x,y) \simeq A^{L-}(d,\alpha^*,\phi)H(\omega)W^L(x,y)\ , \tag{51}$$

where

$$A^{L-}(d,\alpha^*,\phi) = 2(-i2\pi k_T)^{\frac{1}{2}}\ \alpha^*\ E_{TH}^{TH}(\phi-\alpha^* + \tfrac{\pi}{2})D(d,\alpha^*)\ . \tag{52}$$

For $|\alpha^*| << 1$, but $\phi \neq \frac{1}{2}\pi$:

$$E_{TH}^{TH}(\phi \pm \alpha \mp \tfrac{\pi}{2}) \simeq E_{TH}^{TH}(\phi \mp \tfrac{\pi}{2}) \tag{53}$$

The amplitude ratio of forward and backward Love-waves then is

$$A^{L+}/A^{L-} = E_{TH}^{TH}(\phi - \tfrac{1}{2}\pi)/E_{TH}^{TH}(\phi + \tfrac{1}{2}\pi)\ , \tag{54}$$

which is the ratio of the values of $E_{TH}^{TH}(\theta)$ in the positive and negatives x-directions.

In first approximation the two-dimensional results (49) and (51) can be generalized to three dimensions by including an appropriate geometrical correction factor. Some details have been given by Achenbach and Harris [1982]. For a circular rupture front of radius a, the coordinate system (r,θ,ψ) is a toroidal coordinate system. In the plane $\psi = 0$ we then find

$$u_3^{L+}(x,y,o) \simeq g^{+}(a,d,\phi,\alpha^*)A^{L+}(d,\alpha^*,\phi)H(\omega)W^{L}(x,y) \tag{55}$$

where A^{L+}, $H(\omega)$ and W^{L} are defined by (50), (9b) and (47), respectively. A comparison of (55) with (49) shows that the three-dimensional solution in the plane of symmetry is obtained as the two-dimensional solution multiplied by an edge curvature factor g^{+}, where

$$g^{+} = \frac{(a\cos\alpha^*)^{1/2}}{[a\cos\alpha^* + (x + d\tan\phi)\sin(\phi+\alpha^*)]^{1/2}} \tag{56}$$

In (56) we have not introduced the simplification of small α^* in order to obtain a more precise interpretation of this factor. For a point of observation behind the rupture front we find analogously

$$u_3^{L-}(x,y,0) \simeq g^{-}(a,d,\phi,\alpha^*)A^{L-}(d,\alpha^*,\phi)H(\omega)W^{L}(x,y) \tag{57}$$

where A^{L-} is defined by (52), and

$$g^{-} = \frac{(a\cos\alpha^*)^{1/2}}{[a\cos\alpha^* + (x+d\tan\phi)\sin(\phi-\alpha^*)]^{1/2}} \tag{58}$$

If the slip zone were completely circular, there would be a second pair of saddle points in the plane $\psi = \pi$. We have, however, ignored these saddle points because we are interested only in emission from a neighborhood of the advancing rupture front nearest to the ground's surface.

5. Discussion

Two assumptions have been made in this paper, namely, $k_T r >> 1$ (say > 10) and $k_T h << 1$ (say < 0.1), where r and h are the distance from the rupture front to the point of observation and the layer thickness, respectively. These assumptions are not mutually exclusive if $h/r << 1$. For a given point of observation and a given h, the angular frequency must, however, be in a frequency window $\omega_{min} < \omega < \omega_{max}$. If we consider frequencies in a realistic range of 1 Hz < f < 15 Hz, the corresponding angular frequencies and acceptable values of r and h can be estimated.

Equations (9a), (49) and (51) show that the frequency dependence of the radiated fields is controlled by $H(\omega)$, which is defined by (9b). Clearly the nature of the rupture process dominates the frequency dependence.

Equations (49) and (51) show that the strength of the Love-wave depends on the boundary condition at y = 0 (through α^*) and the depth of the rupture front (through $D(d,\alpha^*)$). In the far-field the Love-waves will dominate because the body waves suffer sharper geometrical decay.

Equations (56) and (58) show that $g_- \to 1$ and $g_+ \to 1$ as $a \to \infty$. It is noted that g_- remains bounded. There is, however a maximum at $x \simeq -d\tan\phi - a/\sin\phi$. Thus, we note a focusing effect for Love waves, but it is not as pronounced as for body waves generated by the rupture front.

The model that has been explored in this paper may be called the "rupture front" model. It considers the motions that are generated by stopping and starting phases of the rupture front. In stopping and starting phases the rupture front acts as a line of sources. The corresponding motions have been calculated by the use of solutions to canonical problems and some elements of ray theory.

Acknowledgements

The first part of the work reported here was carried out as part of a research project at Northwestern University sponsored by the Division of Earth Sciences of the National Science Foundation. The closing part of the work was carried out as part of a research project at the University of Illinois sponsored by the Solid Mechanics Program of the National Science Foundation (MEA-8104738).

References

Achenbach, J. D., Wave Propagation in Elastic Solids, North-Holland-American Elsevier, Amsterdam-New York, 1973.

Achenbach, J. D., and Harris, J. G., Ray Method for Elastodynamic Radiation from a Slip Zone of Arbitrary Shape, J. Geophys. Res. 83, 2283, 1978.

Bouchon, M., The Motion of the Ground During an Earthquake 1. The Case of a Strike Slip Fault, J. Geophys. Res. 85, 356, 1980a.

Bouchon, M., The Motion of the Ground During an Earthquake 2. The Case of a Dip Slip Fault, J. Geophys. Res. 85, 367, 1980b.

Burridge, R., and Halliday, G.S., Dynamic Shear Cracks with Friction as Models for Shallow Focus Earthquakes, Geophys. J. Roy. Astr. Soc. 25, 261, 1971.

Cagniard, L., Reflection and Refraction of Progressive Seismic Waves (translated from French and revised by E.A. Flinn and C.W. Dix), McGraw-Hill, New York, 1962.

Cervený, V., Molotkov, I. H., and Psencík, I., Ray Method in Seismology, Charles University, Prague 1977.

Harris, J. G., and Achenbach, J. D., Near-Field Surface Motions Excited by Radiation from a Slip-Zone of Arbitrary Shape, J. Geophys. Res. 86, 9352, 1981.

Harris, J. G., and Achenbach, J. D., Love Waves Excited by Discontinuous Propagation of a Rupture Front, submitted for publication, 1982.

Keller, J. B., and Karal, F. C., Jr., Geometrical Theory of Elastic Surface Wave Excitation and Propagation, J. Acoust. Soc. Amer. 36, 32, 1964.

Keller, J. B., and Karal, F. C., Jr., Surface Wave Excitation and Propagation, J. of Appl. Physics 31, 1039, 1960.

Madariaga, R., Dynamics of an Expanding Circular Fault, Bull. Seism. Soc. Amer. 66, 639, 1976.

Madariaga, R., High Frequency Radiation from Crack (Stress Drop) Models of Earthquake Faulting, Geophys. J. R. Astr. Soc. 51, 625, 1977.

Richards, P. G., Dynamic Motions near an Earthquake Fault: A Three Dimensional Solution, Bull. Seism. Soc. Amer. 66, 1, 1976.

Simons, D. A., Scattering of a Love Wave by the Edge of a Thin Surface Layer, J. Appl. Mech. 42, 842, 1975.

A STOCHASTIC FAULT MODEL FOR ESTIMATING NEAR-FIELD PEAK ACCELERATION

by
Henry Jay Swanger

Systems, Science and Software
P. O. Box 1620
La Jolla, CA 92038-1620

We present a simple stochastic model of the generation of high frequency radiation from moderate to large earthquakes. We will assume there exists a simple relationship between the statistics of peak acceleration and the statistics of some unspecified random faulting process. The average far-field dependence of peak acceleration on magnitude is used to infer the statistics governing this unknown process which can be applied to the estimation of the near-field peak acceleration statistics.

We begin with the assumption that, on a small spatial scale, the faulting processes which govern high frequency radiation are independent of magnitude. We assume that the reason larger peak accelerations are observed in the far-field for larger magnitude earthquakes is that the larger faulting area results in a greater probability that at least one fault element will be capable of generating a large peak acceleration. In other words, increasing the area of the fault increases the cumulative probability that a given peak acceleration will be exceeded.

The process suggested above can be expressed as an equation relating differential probabilities and fault area. If p(a) is the cumulative probability that an acceleration a will be exceeded, we express the dependence of p(a) on increasing fault area to be

$$dp(a) = [1 - p(a)]\, q(\hat{a})ds$$

where ds is a differential fault area, $\hat{a}$ is the acceleration scaled back to the source, and $q(\hat{a})$ is a function of the random variable $\hat{a}$ describing the high frequency generation at the source. This expression can be integrated to obtain

$$p(a) = 1 - \exp\left[-\iint_S q(\hat{a})\, ds\right] .$$

This equation relates the cumulative probability to an integral of the unknown source function over the fault area.

In the far-field this relationship can be simplified. If we assume far-field implies that the entire fault surface is roughly the same distance from the observer, we can simplify our relationship to

$$P_{FF}(a) = 1 - \exp\,[Sq(\hat{a})] \quad .$$

At this point, we do not know what kind of statistics will be appropriate in the far-field. The form of q(a) will determine the appropriate statistics. Normally we analyze data using log-normal statistics. If we assume that the averages obtained from data using log-normal statistics also approximate the median levels, we can use

the above expression to determine a form of $q(\hat{a})$ using existing attentuation relationships. If we set p(a) to 0.5, we obtain

$$q(\hat{a}_o) = \frac{- \ln 0.5}{S(a_o)}$$

which relates $q(\hat{a})$ to fault area S and a_o, which is the median value of peak acceleration expected for a fault area S. If we can obtain the median peak acceleration as a function of fault area, we can infer the unknown function $q(\hat{a})$.

A recent study by Joyner and Boore (1981) has suggested an attenuation relationship of the form

$$\log a_o = - 1.02 + 0.249 M - \log r - 0.00255 r$$

where M is moment magnitude and r is distance in km. We can use the last two terms to define our scaling back to the source region. From the definition of M (Hanks and Kanamori, 1979) and scaling law studies of the relationship between moment and fault area (Kanamori and Anderson, 1975), we can derive an approximate relationship between M and S

$$\log S \simeq M - 4.0$$

where S has units of km^2. Using the Joyner and Boore relationship and ignoring the third decimal place, we obtain an approximate relationship between fault area and median peak acceleration of

$$S \simeq \hat{a}_o^4 \quad .$$

This results in q(a) taking the form

$$q(\hat{a}) \simeq \frac{-\ln 0.5}{\hat{a}^4} \quad .$$

If we substitute into our earlier equations, our cumulative probability function takes the form

$$p(a) = 1 - \exp\left[\ln 0.5\ G/a^4\right]$$

where G is the distance attenuation function to the fourth power integrated over the fault surface. Note that this relationship applies to both the near-field and far-field. Fault geometry enters into the equation only through a weighting factor. For a single source-receiver configuration, one needs only to compute this factor once and one obtains the entire probability distribution.

This probability function only includes random effects from source processes. We would expect site and propagation effects to also be of importance. If a probability density function can be inferred for these random processes, it could be convolved with cumulative probability functions given here to obtain total cumulative probabilites.

The intent here is to develop a simple model which can relate the statistics of far-field data to that in the near-field. Here we have presented only the basic concepts behind the model, and they will be developed more completely in a later paper along with applications to near-field estimations of ground motion levels and

their uncertainties. The method suggested is very simple, and more robust approaches along these lines may be required for practical applications. The method can be expanded in many ways. We may wish to include double-couple radiation patterns. This would only change the calculation of the geometrical weight factor. We can also add time domain information and consider the estimation of r.m.s. accelerations and durations.

REFERENCES

Hanks, T. C. and H. Kanamori (1979), "Moment Magnitude Scale," JGR, pp. 2348-2350.

Joyner, W. B. and D. M. Boore (1981), "Peak Horizontal Acceleration and Velocity from Strong-Motion Records Including Records from the 1979 Imperial Valley, California, Earthquake," preprint.

Kanamori, H. and D. L. Anderson (1975), "Theoretical Basis of Some Empirical Relations in Seismology," BSSA, 65, pp. 1073-1098.

PEAK HORIZONTAL ACCELERATION AND VELOCITY FROM STRONG-MOTION RECORDS INCLUDING RECORDS FROM THE 1979 IMPERIAL VALLEY, CALIFORNIA, EARTHQUAKE*

by

William B. Joyner
and
David M. Boore
U.S. Geological Survey, Menlo Park, California

ABSTRACT

We have taken advantage of the recent increase in strong-motion data at close distances to derive new attenuation relations for peak horizontal acceleration and velocity. This new analysis uses a magnitude-independent shape, based on geometrical spreading and anelastic attenuation, for the attenuation curve. An innovation in technique is introduced that decouples the determination of the distance dependence of the data from the magnitude dependence. The resulting equations are

$$\log A = -1.02 + 0.249M - \log r - 0.00255r + 0.26P$$
$$r = (d^2 + 7.3^2)^{1/2} \qquad 5.0 \leq M \leq 7.7$$
$$\log V = -0.67 + 0.489M - \log r - 0.00256r + 0.17S + 0.22P$$
$$r = (d^2 + 4.0^2)^{1/2} \qquad 5.3 \leq M \leq 7.4$$

where A is peak horizontal acceleration in g, V is peak horizontal velocity in cm/sec, M is moment magnitude, d is the closest distance to the surface projection of the fault rupture in km, S takes on the value of zero at rock sites and one at soil sites, and P is zero for 50 percentile values and one for 84 percentile values.

We considered a magnitude-dependent shape, but we find no basis for it in the data; we have adopted the magnitude-independent shape because it requires fewer parameters.

INTRODUCTION

New data, particularly from the 1979 Coyote Lake and Imperial Valley earthquakes in California, provide a much improved basis for making ground-motion predictions at small distances from the source. In this report we update our earlier efforts (Page and others, 1972; Boore and others, 1978; 1980) and we introduce some improvements in statistical technique that should give better determination of the effects of both magnitude and distance on ground motion.

We examine here the dependence of peak horizontal acceleration and peak horizontal velocity on moment magnitude (M), distance, and recording-site geology. The results for velocity should be considered provisional pending the integration of more records. We do not intend to imply a preference for peak horizontal acceleration or velocity as parameters for describing earthquake ground motion; we are simply recognizing their widespread use.

This work differs in several important ways from our previous work. Improvements in statistical analysis techniques permit us to develop prediction equations with an explicit magnitude dependence. The newly available close-in data permit us to extend the prediction equations to zero distance. In doing this we have modified the measure of distance used in the previous work and adopted a different functional form for the prediction equation.

METHOD

We fit the strong motion data by multiple linear regression using the equation

$$\text{Log } y = \sum_{i=1}^{N} a_i E_i - \log r - br + cS \qquad (1)$$

where $E_i = 1$ for earthquake i
$= 0$ otherwise
$S = 1$ for soil sites
$= 0$ for rock sites
$r = (d^2 + h^2)^{1/2}$

y is either peak horizontal acceleration or velocity, N is the number of earthquakes in the data sample, and d is the closest distance from the recording site to the surface projection of the fault rupture. Values for a_i, b, and c are determined by the linear regression for a chosen value of h, and h is determined by a simple search procedure to minimize the sum of squares of the residuals. Once the a_i values are determined they are used to find, by least squares, a first- or second-order polynomial representing the magnitude dependence.

$$a_i = a + bM_i + qM_i^2 \qquad (2)$$

The use of dummy variables such as E_i and S to divide the data into classes is a well known technique in regression analysis (Draper and Smith, 1966, Weisberg, 1980). Similar techniques have been used before for classifying strong-motion data according to site geology (for example, Trifunac, 1976; McGuire, 1978). Extension of the technique by employing the variable E_i has the advantage that it decouples the determination of magnitude dependence from the determination of distance dependence. To see an example of this advantage, note that the data from a single earthquake is typically recorded over a limited range of distance. If the regression analysis were done in terms of magnitude and distance simultaneously, errors in measuring magnitude would affect the distance coefficient obtained from the regression. Another advantage of the approach is that it causes each earthquake to have the same weight in determining magnitude dependence and each recording to have the same weight in determining distance dependence, which intuitively seems appropriate. The method can be considered the analytical equivalent of the graphical method employed by Richter (1935, 1958) in developing the attenuation curve that forms the basis for the local magnitude scale in southern California. The method described here might prove to be useful in the development of local magnitude scales.

The form chosen for the regression is the equivalent of

$$y = \frac{k}{r} e^{-qr}$$

where k is a function of **M** and q is a constant. This corresponds to simple point-source geometric spreading with constant-Q anelastic attenuation. Strictly speaking, this form would apply only to a harmonic component of the ground motion, not to peak acceleration or peak velocity. Since the coefficients are determined empirically, however, we believe the application to peak parameters is an appropriate approximation.

We realize that the rupture surface is not a point source for recording sites close to the rupture in a large earthquake. The source of the peak motion, however, is not the whole rupture surface but rather some more restricted portion of it. Even if rupture were instantaneous over the whole surface, which would seem unlikely, the whole surface could not contribute to the motion at any one time because of finite propagation velocities.

The parameter $\bar{h}$ is introduced to allow for the fact that the source of the peak motion values may not be the closest point on the rupture. If the source of the peak motion were directly below the nearest point on the surface projection of the rupture, the value of $\bar{h}$ would simply represent the depth of that source. In reality the value obtained for $\bar{h}$ incorporates all the factors that tend to limit or reduce motion near the source, including any tendency for the peak horizontal acceleration to be limited by the finite strength of near-surface materials (Ambraseys, 1974). The value of $\bar{h}$ also incorporates any factors that tend to enhance the motion near the source, in particular, directivity (Boore and Joyner, 1978).

We use moment magnitude (Hanks and Kanamori, 1979) defined as

$$\mathbf{M} = 2/3 \log M_0 - 10.7 \qquad (3)$$

where M_0 is seismic moment in dyne cm. We prefer **M** to surface-wave magnitude or local magnitude because **M** corresponds to a well-defined physical property of the source. Furthermore the rate of occurrence of earthquakes with different **M** can be related directly to the slip rate on faults (Brune, 1968; Molnar, 1979; Anderson, 1979; Herd and others, 1981). It has been argued that local magnitude is preferable for use in predicting ground motion for engineering purposes because local magnitude is based on measurements at frequencies in the range of engineering significance. It is not clear that local magnitude is in fact a better predictor of ground motion in that frequency range, but, even if it were, the use of local magnitude for predicting ground motion in a future earthquake might merely have the effect of transferring the uncertainty from the step of predicting ground motion given the local magnitude to the step of predicting the local magnitude. (We have done an analysis predicting peak horizontal acceleration and velocity in terms of Richter local magnitude [Joyner and others, 1981] similar to the analysis presented here in terms of moment magnitude. The results are comparable.)

The closest distance to the surface projection of the fault rupture is taken as the horizontal component of the station distance rather than the epicentral distance or the distance to the surface projection of the center of the rupture, because the latter two alternatives are clearly inappropriate in such important cases as Parkfield 1966 or Imperial Valley 1979 where recording sites are located close to the rupture but far from both epicenter and rupture center. Ideally one would work with the distance to the point on the rupture

that contributes the peak motion, but it would be difficult to determine the location of that point for past earthquakes and in the present state of knowledge impossible for future earthquakes. The use of our measure of distance in the development of prediction equations is the equivalent of considering the placement of strong-motion instruments and the placement of structures as analogous experiments from the statistical point of view.

In our earlier work (Page and others, 1972; Boore and others, 1978; 1980) we used the shortest distance to the rupture as the measure of distance, whereas here we use the shortest distance to the surface projection of the rupture. The reason for the change is the introduction of the parameter h, which makes allowance, among other things, for the fact that the source of the peak motion may lie at some depth below the surface. If we used the former measure of distance for d, then we would be compensating twice for the effect of depth.

To estimate s_y, the standard error of a prediction made using the procedures described here, we use the equation

$$s_y = (s_s^2 + s_a^2)^{1/2}$$

where s_s is the standard deviation of the residuals from the regression described by equation (1) and s_a is the standard deviation of the residuals from the regression described by equation (2). This is based on two assumptions: first, that the error in determining the attenuation curve in equation (1) is negligible compared to the residual of an individual data point relative to that curve and second, that all the variability s_a is due to the stochastic nature of the relationship between a_i and M and none is due to measuring error in a_i or M_i such as might be caused by inadequate sampling. We believe that the first assumption is probably true, and the second, though not strictly true, is close enough to give a satisfactory approximation to s_y.

DATA

The data set for peak acceleration consists of 182 recordings from 23 earthquakes and for peak velocity 62 recordings from 10 earthquakes. Six of the earthquakes in the peak acceleration data set and four of the earthquakes in the peak velocity data set were recorded at only one station. Such data are given zero weight in the analysis. The data sets are restricted to earthquakes in western North America with M greater than 5.0 and to shallow earthquakes, defined as those for which the fault rupture lies mainly above a depth of 20 km. For peak values we use the larger of the two horizontal components in the directions as originally recorded. Others (e.g. Campbell, 1981) have used the mean of the two components. For his data set Campbell reports that, on the average, the larger value for peak acceleration exceeds the mean by 13 percent. The small symbols on Figure 1 show the distribution of the peak acceleration data in magnitude and distance; the large symbols indicate data points not included in our data set but compared with our prediction equations in Table 5. Figure 2 shows the distribution of the peak velocity data in magnitude and distance.

Table 1 lists the earthquakes and gives the source of data used in assigning magnitudes and station distances. For earthquakes through 1975 the sources of strong motion data and geologic site data are given in a previous publication (Boore and others, 1978). Many of the acceleration data for these earthquakes were taken from Volume I of the series "Strong-Motion Earthquake

Accelerograms" published under the direction of D. E. Hudson by the Earthquake Engineering Research Laboratory of the California Institute of Technology. Volume I of that series was used for acceleration instead of Volume II because the procedures used in producing Volume II tended to bias the peak acceleration toward lower values. For more recent earthquakes sources of strong-motion data include Porter (1978), Porcella (1979), Porcella and others (1979), Brady and others (1980), and Boore and Porcella (1981). In addition, unpublished data were made available by the California Division of Mines and Geology, by J. N. Brune for the stations of the cooperative program of the University of California at San Diego and the Universidad Nacional Autonoma de Mexico, and by Kinemetrics Inc. for the Shell Oil Company station at Munday Creek, Alaska. Sources of site descriptions for records obtained since 1975 include the U.S. Geological Survey (1977) and Shannon and Wilson Inc. and Agbabian Associates (1978; 1980a; 1980b). In the case of two stations (290 Wrightwood, California, and 1096 Fort Tejon, California), site classifications made by Boore and others (1978) were changed on the basis of new information given by Shannon and Wilson Inc. and Agbabian Associates (1978; 1980a; 1980b). The strong-motion data and site classifications are given in Table 2. For some of the recent earthquakes geologic data were not available for all sites. Since only acceleration data were available for those earthquakes and since earlier studies (Boore and others, 1980) had shown that peak acceleration is not correlated with geologic site conditions, we proceeded with the analysis without geologic site data for those earthquakes.

The $\mathbf{M}$ values (Table 1) are calculated from seismic moments if moment determinations are available. In cases where they are not available $\mathbf{M}$ is taken to be equal to M_L and the values are enclosed in parentheses in Table 1. The largest such value is 6.2 for the 1972 Managua, Nicaragua, earthquake. This event had an M_s of 6.2 (U.S. Dept. of Commerce, 1973); an M_L of 6.2 was calculated from the strong-motion record at the Esso Refinery (Jennings and Kanamori, 1979).

On the basis of evidence (Boore and others, 1980; Crouse, 1978) suggesting that large structures may bias the ground-motion data recorded at the base of the structure, we excluded from the data set records made at the base of buildings three or more stories in height and on the abutments of dams. We excluded all earthquakes for which the data were in our opinion inadequate for estimating the source distance to an accuracy better than 5 km (see Page et al, 1972, Table 5).

Bias may be introduced into the analysis of strong-motion data by the fact that some operational instruments are not triggered. To avoid this bias we employed the following procedure: For each earthquake the distance to the nearest operational instrument that did not trigger was determined or in some cases estimated. All data from equal or greater distances for that earthquake were excluded. In contrast to our earlier work the cutoff distance was different for each earthquake. For a few records peak accelerations were reported only as "less than 0.05 g." In those cases we noted the smallest distance for such a record and excluded all data recorded at equal or greater distances for that event. There exists a possibility of bias in analyzing peak velocity data because high-amplitude records may have been preferentially chosen for integration. To avoid this bias we noted the distance of the nearest record that had not been integrated, except records for which we knew definitely that the reason they were not integrated had nothing to do with amplitude. We then excluded all velocity data recorded at equal or greater distances for that event.

Recording sites were classified into two categories, rock and soil, using the best available information in the same way as done in earlier work (Boore and others, 1978; 1980). Sites described by such terms as "granite," "diorite," "gneiss," "chert," "graywacke," "limestone," "sandstone," or "siltstone" were assigned to the rock category, and sites described by such terms as "alluvium," "sand," "gravel," "clay," "silt," "mud," "fill," or "glacial outwash" were assigned to the soil category, except that if the description indicated soil material less than 4 to 5 m thick overlying rock, the site was classified as a rock site. Resonant frequencies of soil layers as thin as that would generally be greater than 10 Hz and thereby outside the range of frequencies making up the dominant part of the accelerogram.

RESULTS

The a_i values resulting from the regression analysis of peak acceleration data using equation (1) are plotted against **M** in Figure 3. Earthquakes represented in the data set by only one record are shown in Figure 3 by diamonds and are excluded in the fitting of the polynomial. The coefficient of the second degree term of the polynomial is not significant at the 90 percent level and the term is omitted.

The effect on the final prediction equations of excluding the points represented by the diamonds in Figure 3 is relatively small. The effect on the 50 percentile values ranges from a 40-percent increase at magnitude 5.0 to a 10-percent decrease at magnitude 7.7. The points were excluded in an effort to obtain the best possible estimates of the parameters of the prediction equation. The two lowest points in Figure 3, which represent the two Santa Rosa earthquakes recorded at the same site, are not representative of the earthquakes. In both earthquakes instruments at eight sites recorded higher peak horizontal acceleration than the record included in the data set even though they were at greater distances (Boore and others, 1978). (These other records were excluded because their distances exceeded the distance of the closest operational instrument that did not trigger.)

Combining the results of the analyses using equations (1) and (2), we obtain the following prediction equation for peak horizontal acceleration:

$$\log A = -1.02 + 0.249\,\mathbf{M} - \log r - 0.00255r + 0.26P$$
$$r = (d^2 + 7.3^2)^{1/2} \qquad 5.0 \leq \mathbf{M} \leq 7.7 \qquad (4)$$

where d is defined as in equation (1) and $\bar{P}$ equals zero for 50 percent probability that the prediction will exceed the real value and one for 84 percent probability. The value of P is based on the assumption that the prediction errors are normally distributed, and one could obtain the values of P for other percentiles from a table of the normal distribution function. Because of the limited number of data points, however, the assumption of normality cannot be tested for the tail of the distribution and values of P greater than one should be used with caution. For a few of the recent earthquakes, geologic site data are not available at all sites (Table 2). A preliminary analysis using only the earthquakes for which site data are available indicated that the soil term is not statistically significant for peak acceleration--a conclusion reached in earlier work (Boore and others, 1980)--and it is therefore not included. Equation (4) is illustrated in Figure 4 for the 50 and 84 percentiles. It is of interest to note that the magnitude coefficient is the same, to two decimal places, as that given by Donovan (1973).

The coefficient of P in equation (4) represents s_y, the standard error of an individual prediction, and is determined from a value of 0.22 for s_s, the standard deviation of the residuals from the regression described by equation (1) and a value of 0.13 for s_a, the standard deviation of the residuals from the regression described by equation (2). The value 0.26 obtained for s_y compares well with the value 0.27 obtained by McGuire (1978) using a data set specially constructed to avoid bias in the estimate of residuals caused by multiple records from a single event or by multiple records from the same site of different events.

Residuals of the data with respect to equation (4) are plotted against distance in Figure 5 with different symbols for three magnitude classes. No obvious differences in trend are apparent among the three different magnitude classes, giving no support to the idea that the shape of the attenuation curves depends upon magnitude. Within 10 km the standard deviation appears to be less than the overall average; whether this is the result of the relatively few recordings from a small number of earthquakes or is a general phenomenon awaits further data.

To test further the concept of a magnitude-dependent shape for the attenuation curves, we repeated the analysis of the acceleration data using a magnitude-dependent value of $\underline{h}$ given by

$$h = h_1 \exp(h_2[M - 6.0]) \qquad (5)$$

where h_1 and h_2 are determined by minimizing the sum of squares of the residuals. The expression was written in terms of $[M - 6.0]$ rather than simply M in order to reduce the correlation between h_1 and h_2. We tested the significance of the reduction in variance achieved by going to the magnitude-dependent $\underline{h}$, using an approximate method described by Draper and Smith (1966) for multiple nonlinear regression problems. The reduction in variance is not significant. The distribution of the data set in distance, however, is such that this test is not definitive. The value of $\underline{h}$ has a large effect on the residuals only for values of $\underline{d}$ less than about 10 km. Since $\underline{d}$ is greater than 10 km for most of the data set, changes in h bring relatively small changes in the total variance. A more sensitive test is provided by examining the residuals from equation (4) as a function of magnitude for stations with $\underline{d}$ less than or equal to 10 km (Figure 6). If there is support in the data for a magnitude-dependent $\underline{h}$, it should show as a magnitude dependence in these residuals. A least-squares straight line through the points in Figure 6 has a slope of -0.075, and the standard deviation of the slope is 0.045. A glance at the plot, however, shows that even this marginal relationship depends on a single earthquake, an aftershock of the 1979 Imperial Valley earthquake, which contributes all of the points plotted at $M = 5.0$. If that earthquake is removed, the least-squares straight line through the remaining points has a slope whose value is less than its standard deviation. From this we conclude that the data do not support a magnitude-dependent $\underline{h}$. A theoretical argument based on a stochastic source model predicts a slightly magnitude-dependent shape equivalent to choosing $h_2 = 0.12$ in equation (5). The argument is detailed in the Appendix. The resulting prediction equation gives a value of the 50 percentile peak acceleration, for $M = 7.7$ and $d = 0$ only 16 percent less than that of equation (4). Even if we accepted the model without reservation we would be disinclined to change the prediction equations for a difference so small. Lacking an adequate basis in the data or in theory for choosing between a magnitude-independent and magnitude-dependent shape for the attenuation curve, we have adopted the magnitude-independent shape because it

requires fewer parameters.

In order to demonstrate the sensitivity of the prediction equations to the presence of particular earthquakes in the data set we recomputed the prediction equations repeatedly, each time excluding a different one (or in some cases two) of the earthquakes. This process was carried out for all of the earthquakes that contribute a significant fraction of the data set. The results are given in Table 3, which shows the parameters of the prediction equations and the predicted 50 percentile values of peak acceleration at d = 0 for M = 6.5 and 7.7.

In order to show the effect of h on the residuals, prediction equations were developed for four different values of h bracketing the value determined by least squares. Residuals against these equations are shown in Figure 7. The value of the distance coefficient h determined by least squares is also shown for each value of h, illustrating the coupling between these two parameters.

The a_i values resulting from the regression of peak velocity data using equation (1) are plotted against M in Figure 8. As with peak acceleration earthquakes represented in the data set by only one record are shown by diamonds and are excluded in fitting the straight line. It is apparent that the exclusion of these events has a relatively small effect in determining the line but a rather large effect on the standard deviation of points about the line. The coefficient of the second-degree term of the polynomial fitted to the pluses in Figure 8 is statistically significant and leads to a curve concave upwards. In view of the small number of points we have suppressed the second-degree term. The prediction equation for peak horizontal velocity is

$$\log V = -0.67 + 0.489\,M - \log r - 0.00256r + 0.17S + 0.22P \qquad (6)$$

$$r = (d^2 + 4.0^2)^{1/2} \qquad 5.3 \leq M \leq 7.4$$

where d and S are as defined in equation (1) and P as defined in equation (4). Equation (6) is illustrated in Figure 9.

The soil term in equation (6) is statistically significant at the 98 percent level in contrast to the case of peak acceleration where it is not significant. Similar results have been reported by Duke and others (1972), Trifunac (1976), and Boore and others (1978, 1980). It seems likely that some sort of amplification mechanisms are operating on the longer periods that are dominant on velocity records and that for the shorter periods dominant on the acceleration records these mechanisms are counterbalanced by anelastic attenuation. It is important to note that the determination of the soil effect is dominated by data from southern California where the thickness of low-Q material near the surface is typically large. Net amplification of peak acceleration at soil sites may occur for some other distributions of Q.

The coefficient of P in equation (6) is s_y, the standard error of an individual prediction, and it reflects a value of 0.20 for s_s, the standard deviation of the residuals of the regression of equation (1), and a value of 0.10 for s_a, the standard deviation of the residuals of the regression of equation (2). As with peak acceleration the value of 0.22 for s_y compares reasonably well with McGuire's (1978) value of 0.28.

Residuals of the peak velocity data with respect to equation (6) are plotted against distance in Figure 10 for the three different magnitude classes. As with peak acceleration there are no differences in trend among the different magnitude classes that would support a magnitude-dependent shape for the attenuation curves. As with peak acceleration we further test the

idea of a magnitude-dependent shape by plotting the residuals from equation (6) as a function of magnitude for stations with d less than or equal to 10.0 km (Figure 11). The slope of the least-squares straight line through the points is smaller than its standard error.

The sensitivity of the prediction equations to particular earthquakes in the data set was examined by repeating the computations, each time excluding a different one of the earthquakes. The results are given in Table 4.

In Figure 12 are shown the residuals of peak horizontal velocity for four different values of h bracketing the value determined by least squares. Also shown is the value of the distance coefficient b determined by least squares for each value of h.

DISCUSSION

The prediction equations are presented in terms of moment magnitude for convenience and for ease of comparison with other studies. Seismic moment, however, is the fundamental parameter, and we believe it desirable to repeat the prediction equations, expressed directly in terms of moment.

$$\log A = -3.68 + 0.166 \log M_o - \log r - 0.00255r + 0.26P$$
$$r = (d^2 + 7.3^2)^{1/2} \qquad 23.5 \leq \log M_o \leq 27.6$$
$$\log V = -5.90 + 0.326 \log M_o - \log r - 0.00256r + 0.17S + 0.22P$$
$$r = (d^2 + 4.0^2)^{1/2} \qquad 24.0 \leq \log M_o \leq 27.2$$

(Moment in dyne cm)

The prediction equations are constrained by data at soil sites over the whole distance range of interest for **M** less than or equal to 6.5, the value for the Imperial Valley earthquake. The data set contains no recordings at rock sites with d less than 8 km for earthquakes with **M** greater than 6.0, and caution is indicated in applying the equations to rock sites at shorter distances for earthquakes of larger magnitudes. Some indication of the applicability of the equations under those conditions can be obtained by comparing the predicted and observed values, given in Table 5, for the Pacoima Dam record of the San Fernando earthquake (d = 0.0 km, **M** = 6.6). The Pacoima Dam site is a rock site, but the record was excluded from the data set used in the regression analysis because it was recorded on a dam abutment. The observed values are higher than the predicted values for both acceleration and velocity, but the difference is less than the standard error of prediction (s_y) for velocity and also for acceleration if the observed acceleration is corrected for topographic amplification (Boore, 1973).

For distances less than 40 km from earthquakes with **M** greater than 6.6 the prediction equations are not constrained by data, and the results should be treated with caution. An indication of the applicability of the equation for acceleration in that range of magnitude and distance can be had by comparing predicted and observed values, given in Table 5, for the Tabas, Iran, and Gazli, USSR records. These records were not included in the data set because they did not originate in western North America.

We do not propose use of the prediction equations beyond the magnitude limits of the data set, 7.7 for peak acceleration and 7.4 for peak velocity, but we do note that Figures 3 and 8 show no tendency for either peak acceleration or peak velocity to saturate with magnitude. We do not believe that a valid basis now exists for specifying the behavior of peak acceleration and velocity at magnitudes beyond the limits of our data set. Although it might be argued that peak acceleration and peak velocity should saturate for

the same reason that the body-wave magnitude scale saturates, we are not aware of any careful analysis supporting this argument. We consider the question open. The recent demonstration by Scholz (1981) that mean slip in large earthquakes correlates linearly with fault length will certainly have important bearing on these questions.

The prediction equations predict peak velocities greater than 200 cm/sec for M greater than or equal to 7.0 at close distances. No values that high have ever been observed but we know of no physical reason why they could not occur. At soil sites in an earthquake of M greater than 6.5, the finite strength of the soil might limit the peak acceleration to values smaller than those given by the prediction equations, but determining what that limit would be would require adequate in situ determination of the dynamic soil properties.

On the basis of fewer available data, Trifunac (1976) made estimates comparable to ours for the peak velocity at small distances from earthquakes of magnitude 7.0 and above. Kanamori (1978) gave an estimate of 200 cm/sec for the peak velocity at 10 km from an earthquake like Kern County (M = 7.4), a value somewhat greater than ours (Figure 6). Both Trifunac (1976) and Kanamori (1978) employed the attenuation curve used for local magnitude determinations in southern California. That curve is only weakly constrained by data at short distances. Recent data, especially from the 1979 Imperial Valley earthquake, enable us to develop more closely constrained curves for both acceleration and velocity.

The attenuation relationships developed by Campbell (1981; Campbell and others, 1980) for peak horizontal acceleration are compared in Figure 13 with our results. His definition of peak horizontal acceleration differed from ours in that he used the mean of the two components rather than the larger of the two. To compensate for this we have raised his curves in Figure 13 by 13 percent, a value determined by him. He selected magnitudes to be consistent with a moment-magnitude scale, essentially M_L for $M < 6$ and $M_S > 6$. His measure of distance was "the shortest distance from the site to the rupture zone", whereas our measure is the shortest distance to the surface projection of the rupture. This will make no difference for the large magnitude events, which typically break the surface, but the difference may be significant for the smaller events in which the rupture zone may be at significant depth below the surface. His curve for magnitude 5.5 is cut off at 5 km in Figure 13 because at smaller distances the difference in definition of distance invalidates the comparison. He included only data with distances less than 50 km, which severely limits the number of data points included from higher magnitude events.

The differences shown on Figure 13 are small compared to statistical prediction uncertainty. The most conspicuous difference is the change in shape with magnitude shown by his curves, which may be in part due to the different definition of distance. All things considered we view the relative agreement between the two sets of curves as more significant than the differences. It suggests that the results of both studies are insensitive to rather large variations in method and assumptions.

It is of some interest to consider the physical interpretation of the parameters in the attenuation relationship. If the values agree with what we would expect from other considerations, we gain more confidence that the model, though oversimplified, is appropriate. The value determined for the

attenuation coefficient in the relationship for peak acceleration corresponds to a Q of 700 for an assumed frequency of 4 Hz and 350 for a frequency of 2 Hz. The latter value is probably the more appropriate one to consider because the distant records with frequencies closer to 2 Hz than 4 Hz dominate in the determination of the attenuation coefficient. The value of the attenuation coefficient in the relationship for peak velocity correspond to a Q of 180 for an assumed frequency of 1 Hz. These Q values lie in the range generally considered appropriate on the basis of other data and increase our confidence in the model. The smaller value for velocity than for acceleration is consistent with the frequency dependence of Q described by Aki (1980), but in view of the oversimplified character of the model we do not propose this as evidence for a frequency-dependent Q.

The values of 7.3 and 4.0 km for $\bar{h}$ in the relationships for peak acceleration and peak velocity seem reasonable in the sense that they lie in the range of one quarter to one half of the thickness of the seismogenic zone in California, where most of the data were recorded. Why the value is less for velocity than for acceleration is not clear. It might be argued that the larger value of $\bar{h}$ for peak acceleration represents a limitation in acceleration near the source by the limited strength of the near-surface materials. If that were the case, however, one would expect the attenuation curve for earthquakes of magnitude less than 6 to differ in shape from that of earthquakes greater than 6. Figures 5 and 6 show no evidence of this. Another possibility relates to directivity. The effect of directivity would be to increase the peak velocity preferentially at sites near the fault. This effect would be reflected in a smaller value for $\bar{h}$. Directivity would be expected to have a similar effect on peak acceleration (Boore and Joyner, 1978; Boore and Porcella, 1980), but one might speculate that local variations in the direction of rupture propagation or scattering and lateral refraction might in some way reduce the effect of directivity upon the higher frequency waves dominant in the acceleration record.

The magnitude coefficient in the relationship for peak acceleration is 0.25 and has a standard error of 0.04. It thus differs by little more than one standard error from the value 0.30, which corresponds to the scaling of peak acceleration as $M_o^{1/5}$ derived theoretically by Hanks and McGuire (1981) by treating the acceleration record as a stochastic process. The magnitude coefficient for peak velocity is 0.49 with a standard error of 0.06. It lies within one standard error of the value 0.5, which corresponds to the scaling of peak velocity as $M_o^{1/3}$, appropriate for a deterministic rupture propagating outward from a point (Boatwright, 1980; oral communication, 1981; McGarr, 1981). It seems quite reasonable that the acceleration should look like a stochastic process and the velocity like a deterministic process.

ACKNOWLEDGMENTS

Unpublished strong-motion data were generously supplied to us by the California Division of Mines and Geology, by J. N. Brune on behalf of the University of California at San Diego and the Universidad Nacional Autonoma de Mexico and by Kinemetrics Inc. and the Shell Oil Co. We benefited significantly from discussion with T. C. Hanks. J. Boatwright and C. Rojahn critically reviewed the manuscript and made a number of valuable suggestions. We are indebted to K. W. Campbell for extended helpful discussions.

APPENDIX

The theoretical arguments for a magnitude dependent shape, referred to in the text, are based on consideration of the scaling of peak acceleration with magnitude at close and far distances, and follow from an extension of the reasoning given in Hanks and McGuire (1981). Their stochastic source model predicts that the acceleration time history is to a good approximation a finite-duration sample of band-limited white, Gaussian noise. Using a result from Vanmarcke and Lai (1980), Hanks and McGuire (1981) give the following expression for the peak acceleration at a site whose distance to the source is large compared to the source dimensions

$$A_{max} = A_{rms}\left[2\ln\left(\frac{2S_o}{T_o}\right)\right]^{1/2} \qquad (A1)$$

where A_{rms} is the root-mean-square acceleration, S_o is the duration of the acceleration time history, and T_o is the predominant period of the acceleration.

By the Hanks and McGuire source theory A_{rms} scales as $M_o^{1/6}$ and, given the moment-magnitude relation of equation (3), log A_{rms} is thereby proportional to moment magnitude with a coefficient of 0.25. Using their scaling of S_o in terms of moment and assuming T_o equals 0.2 sec, the logarithm of

$$\left[2\ln\left(\frac{2S_o}{T_o}\right)\right]^{1/2}$$

is approximately proportional to moment magnitude in the range between 6.5 and 7.5 with a coefficient of 0.05. Combining the two factors gives a magnitude coefficient of 0.30 for log A_{max}. (As stated in the text this compares with our value of 0.25, which has a standard deviation of 0.04. The difference is only slightly greater than the standard deviation.)

Further considerations are needed for the magnitude scaling close to the source. At small distance from a large source only a restricted portion of the source has an opportunity to generate the peak accelerations. In other words the effective duration S_o is fixed even as moment magnitude increases. Furthermore since the predominant period T_o in Hanks and McGuire's analysis is independent of magnitude, the bracketed term in equation (A1) will also be magnitude independent. A_{max} at small distance should then scale with magnitude in the same way as A_{rms}, provided that A_{rms} is measured over the restricted portion of the record that corresponds to the effective duration. But A_{rms} measured over a fixed interval should scale with magnitude in the same way as A_{rms} over the whole record scales at distant stations. The difference in magnitude coefficient between near and distant stations is just the quantity

$$\log\left[2\ln\left(\frac{2S_o}{T_o}\right)\right]^{1/2}$$

which we have found to be 0.05 in the magnitude range 6.5 to 7.5. By choosing $h_2 = 0.12$ in our equations we can force the 0.05 difference in magnitude coefficient between near and distant stations.

REFERENCES

Aki, K. (1980). Scattering and attenuation of shear waves in the lithosphere, J. Geophys. Res., v. 85, p. 6496-6504.

Allen, C. R., T. C. Hanks and J. H. Whitcomb (1973). San Fernando earthquake: Seismological studies and their tectonic implications, in San Fernando, California, earthquake of February 9, 1971, v. 3, National Oceanic and Atmospheric Administration, U.S. Department of Commerce, 13-21.

Ambraseys, N. N. (1974). Dynamics and response of foundation materials in epicentral regions of strong earthquakes, Proc. World Conf. Earthquake Eng., 5th, Rome, v. 1, CXXVI-CXLVIII.

Anderson, J. G. (1979). Estimating the seismicity from geological structure for seismic-risk studies, Bull. Seism. Soc. Am., v. 69, 135-158.

Boatwright, J. (1980). A spectral theory for circular seismic sources: simple estimates of source dimension, dynamic stress drop, and radiated seismic energy, Bull. Seism. Soc. Am., v. 70, 1-27.

Bolt, B. A. (1978). The local magnitude M_L of the Kern County earthquake of July 21, 1952, Bull. Seism. Soc. Am., v. 68, 513-515.

Bolt, B. A., T. V. McEvilly, and R. A. Uhrhammer (1981). The Livermore Valley, California sequence of January 1980, Bull. Seism. Soc. Am., v. 71, 451-463.

Bolt, B. A., and R. D. Miller (1975). Catalogue of earthquakes in northern California and adjoining areas, 1 January 1910-31 December 1972, Seismographic Station, Univ. Calif. Berkeley, 567 pp.

Boore, D. M. (1973). The effect of simple topography on seismic waves: implications for the accelerations recorded at Pacoima Dam, San Fernando Valley, California, Bull. Seism. Soc. Am., v. 63, 1603-1609.

Boore, D. M., and W. B. Joyner (1978). The influence of rupture incoherence on seismic directivity, Bull. Seism. Soc. Am., v. 68, p. 283-300.

Boore, D. M., W. B. Joyner, A. A. Oliver III, and R. A. Page (1978). Estimation of ground motion parameters, U.S. Geol. Surv., Circular 795, 43 pp.

Boore, D. M., W. B. Joyner, A. A. Oliver III, and R. A. Page (1980). Peak acceleration, velocity, and displacement from strong-motion records, Bull. Seism. Soc. Am., v. 70, 305-321.

Boore, D. M., and R. L. Porcella (1980). Peak acceleration from strong-motion records: a postscript, Bull. Seism. Soc. Am., v. 70, p. 2295-2297.

Boore, D. M., and R. L. Porcella (1981). Peak horizontal ground motions from the 1979 Imperial Valley earthquake: comparison with data from previous earthquakes, in The Imperial Valley, California earthquake of October 15, 1979, U.S. Geol. Surv. Prof. Paper, in press.

Boore, D. M., and D. J. Stierman (1976). Source parameters of the Pt. Mugu, California, earthquake of February 21, 1973, Bull. Seism. Soc. Am., v. 66, 385-404.

Brady, A. G., P. N. Mork, V. Perez, and L. D. Porter (1980). Processed data from the Gilroy array and Coyote Creek records, Coyote Lake, California earthquake 6 August 1979, U.S. Geol. Surv. Open-File Report 81-42, 171 p.

Brune, J. N. (1968). Seismic moment, seismicity, and rate of slip along major fault zones, J. Geophys. Res., v. 73, p. 777-784.

Bufe, C. G., F. W. Lester, K. M. Lahr, J. C. Lahr, L. C. Seekins, and T. C. Hanks (1976). Oroville earthquakes: normal faulting in the Sierra Nevada foothills, Science, v. 192, 72-74.

Campbell, K. W. (1981). Near-source attenuation of peak horizontal acceleration, Bull. Seism. Soc. Am., v. 71, (in press).

Campbell, K. W., D. K. Davis, and F. W. Brady (1980). Attenuation of peak acceleration in the near-source region of earthquakes (abstract), Trans. Am. Geophys. Union, v. 61, 1035-1036.

Cloud, W. K. (1959). Intensity and ground motion of the San Francisco earthquake of March 22, 1957, in San Francisco earthquake of March, 1957, Calif. Div. Mines Special Report 57, 49-57.

Cloud, W. K., and J. F. Stifler (1976). Earthquakes and the registration of earthquakes from July 1, 1974 to December 31, 1974, Bull. Seismographic Stations, Univ. Calif. Berkeley, v. 44, 86 pp.

Cockerham, R. S., F. W. Lester, and W. L. Ellsworth (1980). A preliminary report on the Livermore Valley earthquake sequence January 24-February 26, 1980, U.S. Geol. Surv. Open-File Report 80-714, 45 p.

Crouse, C. B. (1978). Prediction of free-field earthquake ground motions, Proc. ASCE Geotech. Eng. Div. Specialty Conf. Earthquake Eng. Soil Dynamics, Pasadena, Calif., v. 1, 359-379.

Donovan, N. C. (1973). Earthquake hazards for buildings, in Building Practice for Disaster Mitigation, National Bureau of Standards Building Science Series 46, 82-111.

Draper, N. R. and H. Smith (1966). Applied regression analysis, Wiley, New York, 407 pp.

Duke, C. M., K. E. Johnsen, L. E. Larson, and D. C. Engman (1972). Effects of site classification and distance on instrumental indices in the San Fernando earthquake, University of California, Los Angeles, School of Engineering and Applied Science, UCLA-ENG-7247, 29 p.

Dunbar, W. S., D. M. Boore, and W. Thatcher (1980). Pre-, co-, and postseismic strain changes associated with the 1952 M_L = 7.2 Kern County, California, earthquake, Bull. Seism. Soc. Am., v. 70, 1893-1905.

Ellsworth, W. L. (1975). Bear Valley, California, earthquake sequence of February-March 1972, Bull. Seism. Soc. Am., v. 65, 483-506.

Ellsworth, W. L., R. H. Campbell, D. P. Hill, R. A. Page, R. W. Alewine III, T. C. Hanks, T. H. Heaton, J. A. Hileman, H. Kanamori, B. Minster and J. H. Whitcomb (1973). Point Mugu, California, earthquake of 21 February 1973 and its aftershocks, Science, v. 182, 1127-1129.

Fogleman, K., R. Hansen and R. Miller (1977). Earthquakes and the registration of earthquakes from July 1, 1975 to December 31, 1975, Bull. Seismographic Stations, Univ. Calif. Berkeley, v. 45, 95 pp.

Hamilton, R. M. (1972). Aftershocks of the Borrego Mountain earthquake from April 12 to June 12, 1968, in The Borrego Mountain earthquake of April 9, 1968, U.S. Geol. Surv. Prof. Paper 787, 31-54.

Hanks, T. C., J. A. Hileman, and W. Thatcher (1975). Seismic moments of the larger earthquakes of the southern California region, Bull. Geol. Soc. Am., v. 86, 1131-1139.

Hanks, T. C., and H. Kanamori (1979). A moment magnitude scale, J. Geophys. Res., v. 84, 2348-2350.

Hanks, T. C., and R. K. McGuire (1981). The character of high-frequency strong ground motion, submitted to Bull. Seism. Soc. Am.

Hanks, T. C., and M. Wyss (1972). The use of body-wave spectra in the determination of seismic-source parameters, Bull. Seism. Soc. Am., v. 62, 561-568.

Hart, R. S., R. Butler, and H. Kanamori (1977). Surface-wave constraints on the August 1, 1975, Oroville earthquake, Bull. Seism. Soc. Am., v. 67, 1-7.

Hasegawa, H. S., J. C. Lahr, and C. D. Stephens (1980). Fault parameters of the St. Elias, Alaska, earthquake of February 28, 1979, Bull. Seism. Soc. Am., v. 70, 1651-1660.

Heaton, T. H., and D. V. Helmberger (1979). Generalized ray models of the San Fernando earthquake, Bull. Seism. Soc. Am., v. 69, 1311-1341.

Herd, D. G., W. L. Ellsworth, A. G. Lindh, and K. M. Shedlock (1981). Future large earthquakes in the San Francisco Bay area, submitted to Science.

Jennings, P. C., and H. Kanamori (1979). Determination of local magnitude, M_L, from seismoscope records, Bull. Seism. Soc. Am., v. 69, 1267-1288.

Johnson, L. R., and T. V. McEvilly (1974). Near-field observations and source parameters of central California earthquakes, Bull. Seism. Soc. Am., v. 64, 1855-1886.

Joyner, W. B., D. M. Boore, and R. L. Porcella (1981). Peak horizontal acceleration and velocity from strong-motion records (abs.), Seism. Soc. Am. Earthquake Notes, v. 52, 80-81.

Kanamori, H. (1978). Semi-empirical approach to prediction of ground motions produced by large earthquakes, Proc. NSF Seminar Workshop on Strong Ground Motion, Calif. Inst. of Tech., Pasadena, 80-84.

Kanamori, H., and P. C. Jennings (1978). Determination of local magnitude, M_L, from strong-motion accelerograms, Bull. Seism. Soc. Am., v. 68, 471-485.

Knudson, C. F., and F. Hansen A. (1973). Accelerograph and seismoscope records from Managua, Nicaragua earthquakes, in Managua, Nicaragua earthquake of December 23, 1972, Proc. Earthquake Eng. Research Inst. Conf., v. 1, 180-205.

Lahr, K. M., J. C. Lahr, A. G. Lindh, C. G. Bufe and F. W. Lester (1976). The August 1975 Oroville earthquakes, Bull. Seism. Soc. Am., v. 66, 1085-1099.

Langston, C. A., and R. Butler (1976). Focal mechanism of the August 1, 1975 Oroville earthquake, Bull. Seism. Soc. Am., v. 66, 1111-1120.

Lee, W. H. K., D. G. Herd, V. Cagnetti, W. H. Bakun, and A. Rapport (1979). A preliminary study of the Coyote Lake earthquake of August 6, 1979 and its major aftershocks, U.S. Geol. Surv. Open-File Report 79-1621, 43 p.

Lee, W. H. K., C. E. Johnson, T. L. Henyey, and R. L. Yerkes (1978). A preliminary study of the Santa Barbara, California, earthquake of August 13, 1978, and its major aftershocks, U.S. Geol. Surv. Circular 797, 11 p.

Lindh, A. G., and D. M. Boore (1981). Control of rupture by fault geometry during the 1966 Parkfield earthquake, Bull. Seism. Soc. Am., v. 71, 95-116.

McEvilly, T. V., W. H. Bakun, and K. B. Casaday (1967). The Parkfield, California, earthquakes of 1966, Bull. Seism. Soc. Am., v. 57, 1221-1244.

McGarr, A. (1981). Analysis of peak ground motion in terms of a model of inhomogeneous faulting, J. Geophys. Res., v. 86, 3901-3912.

McGuire, R. K. (1978). Seismic ground motion parameter relations, Proc. Am. Soc. Civil Eng. J. Geotech. Eng. Div., v. 104, 481-490.

Molnar, P. (1979). Earthquake recurrence intervals and plate tectonics, Bull. Seism. Soc. Am., v. 69, 115-133.

Page, R. A., D. M. Boore, W. B. Joyner, and H. W. Coulter (1972). Ground motion values for use in the seismic design of the trans-Alaska pipeline system, U.S. Geol. Surv. Circular 672, 23 pp.

Page, R. A., and W. H. Gawthrop (1973). The Sitka, Alaska, earthquake of 30 July 1972 and its aftershocks (abs.), Seism. Soc. Am. Earthquake Notes, v. 44, 16-17.

Plafker, G., and R. D. Brown, Jr. (1973). Surface geologic effects of the Managua earthquake of December 23, 1972, in Managua, Nicaragua earthquake of December 23, 1972, Proc. Earthquake Eng. Research Inst. Conf., v. 1, 115-142.

Porcella, R. L., ed. (1979). Seismic Engineering Program Report, U.S. Geol. Surv. Circular 818-A, 20 p.

Porcella, R. L., R. B. Matthiesen, R. D. McJunkin, and J. T. Ragsdale (1979). Compilation of strong-motion records from the August 6, 1979 Coyote Lake earthquake, U.S. Geol. Surv. Open-File Report 79-385, 71 p.

Porter, L. D. (1978). Compilation of strong-motion records recovered from the Santa Barbara earthquake of 13 August 1978, Calif. Div. Mines and Geol. Prelim. Report 22, 43 p.

Purcaru, G., and H. Berckhemer (1978). A magnitude scale for very large earthquakes, Tectonophysics, v. 49, 189-198.

Richter, C. F. (1935). An instrumental earthquake magnitude scale, Bull. Seism. Soc. Am., v. 25, 1-32.

Richter, C. F. (1958). Elementary seismology, W. H. Freeman, San Francisco, 768 pp.

Scholz, C. H. (1981). Scaling laws for large earthquakes: consequences for physical models, submitted to Bull. Seism. Soc. Am.

Shannon and Wilson, Inc., and Agbabian Associates (1978). Verification of subsurface conditions at selected "rock" accelerograph stations in California Volume 1, U.S. Nuclear Regulatory Commission NUREG/CR-0055, Clearinghouse, Springfield, VA 22151.

Shannon and Wilson, Inc., and Agbabian Associates (1980a). Verification of subsurface conditions at selected "rock" accelerograph stations in California Volume 2, U.S. Nuclear Regulatory Commission NUREG/CR-0055, Clearinghouse, Springfield, VA 22151.

Shannon and Wilson, Inc., and Agbabian Associates (1980b). Geotechnical data from accelerograph stations investigated during the period 1975-1979, U.S. Nuclear Regulatory Commission NUREG/CR-1643, Clearinghouse, Springfield, VA 22151.

Stierman, D. J., and W. L. Ellsworth (1976). Aftershocks of the February 21, 1973 Point Mugu, California earthquake, Bull. Seism. Soc. Am., v. 66, 1931-1952.

Swanger, H. J., and D. M. Boore (1978). Simulation of strong-motion displacements using surface-wave modal superposition, Bull. Seism. Soc. Am., v. 68, 907-922.

Tocher, D. (1959). Seismographic results from the 1957 San Francisco earthquakes, in San Francisco earthquakes of March 1957, Calif. Div. Mines Special Report 57, 59-71.

Trifunac, M. D. (1972). Tectonic stress and the source mechanism of the Imperial Valley, California, earthquake of 1940, Bull. Seism. Soc. Am., v. 62, 1283-1302.

Trifunac, M. D. (1976). Preliminary analysis of the peaks of strong earthquake ground motion--dependence of peaks on earthquake magnitude, epicentral distance, and recording site conditions, Bull. Seism. Soc. Am., v. 66, 189-219.

Trifunac, M. D., and J. N. Brune (1970). Complexity of energy release during the Imperial Valley, California, earthquake of 1940, Bull. Seism. Soc. Am., v. 60, 137-160.

Trifunac, M. D., F. E. Udwadia (1974). Parkfield, California, earthquake of June 27, 1966: a three-dimensional moving dislocation, Bull. Seism. Soc. Am., v. 64, 511-533.

Tsai, Y.-B., and K. Aki (1969). Simultaneous determination of the seismic moment and attenuation of seismic surface waves, Bull. Seism. Soc. Am., v. 59, 275-287.

Unger, J. D., and J. P. Eaton (1970). Aftershocks of the October 1, 1969, Santa Rosa, California, earthquakes (abstract), Geol. Soc. Am. Abstracts with Programs, v. 2, 155.

Uhrhammer, R. A. (1980). Observations of the Coyote Lake, California earthquake sequence of August 6, 1979, Bull. Seism. Soc. Am., v. 70, 559-570.

U.S. Dept. of Commerce (1973). Earthquake Data Report EDR No. 76-72.

U.S. Geological Survey (1977). Western hemisphere strong-motion accelerograph station list - 1976, U.S. Geol. Surv. Open-File Report 77-374, 112 p.

Vanmarcke, E. H., and S.-S. P. Lai (1980). Strong-motion duration and rms amplitude of earthquake records, Bull. Seism. Soc. Am., v. 70, 1293-1307.

Wallace, T. C., and D. V. Helmberger (1979). A model of the strong ground motion of the August 13, 1978 Santa Barbara earthquake (abs.), EOS Trans. Am. Geophys. Union, v. 60, 895.

Ward, P. L., D. Harlow, J. Gibbs and A. Aburto O. (1973). Location of the main fault that slipped during the Managua earthquake as determined from locations of some aftershocks, in Managua, Nicaragua earthquake of December 23, 1972, Proc. Earthquake Eng. Research Inst. Conf., v. 1, 89-96.

Weisberg, S. (1980). Applied Linear Regression, Wiley, New York, 283 pp.

Table 1. Sources of data used in assigning magnitudes and station distances

Earthquake	M	M_L	Date (GMT) Month	Day	Year	Sources
Imperial Valley, California	7.0	6.4	5	19	40	Trifunac and Brune (1970); Trifunac (1972); Richter (1958); Hanks and others (1975).
Kern County, California	7.4	7.2	7	21	52	Richter (1958); Page, and others (1972); Bolt (1978); Dunbar and others (1980); Hanks and others (1975); Boore and Kanamori (unpublished).
Daly City, California	(5.3)	5.3	3	22	57	Tocher (1959); Cloud (1959).
Parkfield, California	6.1	5.5	6	28	66	McEvilly and others (1967); Lindh and Boore (1981); Trifunac and Udwadia (1974); Tsai and Aki (1969).
Borrego Mountain, California	6.6	6.7	4	9	68	Kanamori and Jennings (1978); Hamilton (1972); Hanks and Wyss (1972); Swanger and Boore (1978); Hanks and others (1975).
Santa Rosa, California (2 events)	(5.6) (5.7)	5.6 5.7	10	2	69	Bolt and Miller (1975); Unger and Eaton (1970); J. D. Unger and J. P. Eaton (written commun., 1976).
Lytle Creek, California	5.3	5.4	9	12	70	T. C. Hanks (written commun., 1971); Hanks and others (1975).
San Fernando, California	6.6	6.4	2	9	71	Allen and others (1973); Heaton and Helmberger (1979).

Table 1. Continued

Earthquake	M	M_L	Date (GMT) Month	Day	Year	Sources
Bear Valley, California	5.3	5.1	2	24	72	Bolt and Miller (1975); Ellsworth (1975); Johnson and McEvilly (1974).
Sitka, Alaska	7.7		7	30	72	Page and Gawthrop (1973); Page (oral commun., 1976); Purcaru and Berckhemer (1978).
Managua, Nicaragua	(6.2)	6.2	12	23	72	Jennings and Kanamori (1979); Plafker and Brown (1973); Ward and others (1973); Knudson and Hansen A. (1973); U.S. Dept. of Commerce (1973).
Point Mugu, California	5.6	6.0	2	21	73	Ellsworth and others (1973); Boore and Stierman (1976); Stierman and Ellsworth (1976).
Hollister, California	(5.2)	5.2	11	28	74	Cloud and Stifler (1976); W.H.K. Lee (written commun., 1976).
Oroville, California	6.0	5.7	8	1	75	Fogleman and others (1977); Bufe and others (1976); Lahr and others (1976); Langston and Butler (1976); Hart and others (1977).
Santa Barbara, California	5.1	5.1	8	13	78	Wallace and Helmberger (1979); Lee and others (1978).
St. Elias, Alaska	7.6		2	28	79	Hasegawa and others (1980); C. D. Stephens (written commun., 1979); J. Boatwright (oral commun., 1979).

Table 1. Continued

Earthquake	M	M_L	Date (GMT) Month	Day	Year	Sources
Coyote Lake, California	5.8	5.9	8	6	79	Uhrhammer (1980); Lee and others (1979).
Imperial Valley, California	6.5	6.6	10	15	79	Kanamori (oral commun., 1981); C. E. Johnson (oral commun., 1979); Boore and Porcella (1981).
Imperial Valley, California aftershock	(5.0)	5.0	10	15	79	C. E. Johnson (oral commun., 1979).
Livermore Valley, California	5.8	5.5	1	24	80	Bolt and others (1981); R. A. Uhrhammer (oral commun., 1981); J. Boatwright (oral commun., 1980).
Livermore Valley, California	5.5	5.6	1	27	80	Bolt and others (1981); R. A. Uhrhammer (oral commun., 1981); J. Boatwright (oral commun., 1980); Cockerham and others (1980).
Horse Canyon, California	(5.3)	5.3	2	25	80	L. K. Hutton (written commun., 1980).

Table 2. Strong-Motion Data

Earthquake	Station[1]	Distance km	Peak Horizontal Acceleration g	Peak Horizontal Velocity cm/sec	Site Condition
Imperial Valley 1940	117	12.0	0.359	36.9	soil
Kern County 1952	1083	148.0	0.014		rock
	1095	42.0	0.196	17.7	soil
	283	85.0	0.135	19.3	soil
	135	107.0	0.062	8.9	soil
	475	109.0	0.054	9.1	soil
	113	156.0	0.014		soil
	1008	224.0	0.018		soil
	1028	293.0	0.010		soil
	2001	359.0	0.004		soil
	117	370.0	0.004		soil
Daly City 1957	1117	8.0	0.127	4.9	rock
Parkfield 1966	1438	16.1	0.411	22.5	rock
	1083	63.6	0.018	1.1	rock
	1013	6.6	0.509	78.1	soil
	1014	9.3	0.467	25.4	soil
	1015	13.0	0.279	11.8	soil
	1016	17.3	0.072	8.0	soil
	1095	105.0	0.012	2.2	soil
	1011	112.0	0.006		soil
	1028	123.0	0.003		soil
Borrego Mountain 1968	270	105.0	0.018		rock
	280	122.0	0.048		rock
	116	141.0	0.011		rock
	266	200.0	0.007		rock
	117	45.0	0.142	25.8	soil
	113	130.0	0.031		soil
	112	147.0	0.006		soil

Table 2. (continued)

Earthquake	Station[1]	Distance km	Peak Horizontal Acceleration g	Peak Horizontal Velocity cm/sec	Site Condition
Borrego Mountain 1968 (continued)	130	187.0	0.010		soil
	475	197.0	0.010		soil
	269	203.0	0.006		soil
	135	211.0	0.013		soil
Santa Rosa 1969 first event	1093	62.0	0.005		soil
Santa Rosa 1969 second event	1093	62.0	0.003		soil
Lytle Creek 1970	111	19.0	0.086	5.6	rock
	116	21.0	0.179		rock
	290	13.0	0.205	9.6	soil
	112	22.0	0.073		soil
	113	29.0	0.045		soil
San Fernando 1971	128	17.0	0.374	14.6	rock
	126	19.6	0.200	8.6	rock
	127	20.2	0.147	4.8	rock
	141	21.1	0.188	20.5	rock
	266	21.9	0.204	11.6	rock
	110	24.2	0.335	27.8	rock
	1027	66.0	0.057	2.8	rock
	111	87.0	0.021		rock
	125	23.4	0.152	18.0	soil
	135	24.6	0.217	21.1	soil
	475	25.7	0.114	14.3	soil
	262	28.6	0.150	14.2	soil
	269	37.4	0.148	5.4	soil
	1052	46.7	0.112	8.5	soil
	411	56.9	0.043	5.0	soil
	290	60.7	0.057	3.8	soil
	130	61.4	0.030	10.4	soil

Table 2. (continued)

Earthquake	Station[1]	Distance km	Peak Horizontal Acceleration g	Peak Horizontal Velocity cm/sec	Site Condition
San Fernando 1971 (continued)	272	62.0	0.027	7.3	soil
	1096	64.0	0.028	1.4	soil
	1102	82.0	0.034	2.5	soil
	112	88.0	0.030		soil
	113	91.0	0.039		soil
Bear Valley 1972	1028	31.0	0.030		soil
Sitka 1972	2714	45.0	0.110		rock
	2708	145.0	0.010		rock
	2715	300.0	0.010		soil
Managua 1972	3501	5.0	0.390		soil
Point Mugu 1973	655	50.0	0.031		rock
	272	16.0	0.130		soil
Hollister 1974	1032	17.0	0.011		rock
	1377	8.0	0.120		soil
	1028	10.0	0.170		soil
	1250	10.0	0.140		soil
Oroville 1975	1051	8.0	0.110	5.0	rock
	1293	32.0	0.040		rock
	1291	30.0	0.070		soil
	1292	31.0	0.080		soil
Santa Barbara 1978	283	2.9	0.210		
	885	3.2	0.390		
	Goleta substation[2]	7.6	0.280		
St. Elias 1979	2734	25.4	0.160		
	Munday Creek[3]	32.9	0.064		
	2728	92.2	0.090		

Table 2. (continued)

Earthquake	Station[1]	Distance km	Peak Horizontal Acceleration g	Peak Horizontal Velocity cm/sec	Site Condition
Coyote Lake 1979	1413	1.2	0.420	43.8	rock
	1445	1.6	0.230	20.5	rock
	1408	9.1	0.130	10.3	rock
	1411	3.7	0.260	32.2	soil
	1410	5.3	0.270	29.4	soil
	1409	7.4	0.260	31.9	soil
	1377	17.9	0.110		soil
	1492	19.2	0.120		soil
	1251	23.4	0.038		soil
	1422	30.0	0.044		soil
	1376	38.9	0.046		soil
Imperial Valley 1979	Cerro Prieto[4]	23.5	0.170		rock
	286	26.0	0.210	9.0	rock
	Meloland Overpass[5]	0.5	0.320		soil
	5028	0.6	0.520	110.0	soil
	942	1.3	0.720	110.0	soil
	Aeropuerto[4]	1.4	0.320		soil
	5054	2.6	0.810	44.0	soil
	958	3.8	0.640	53.0	soil
	952	4.0	0.560	87.0	soil
	5165	5.1	0.510	68.0	soil
	117	6.2	0.400		soil
	955	6.8	0.610	78.0	soil
	5055	7.5	0.260	48.0	soil
	Imperial Co. Center[5]	7.6	0.240		soil
	Mexicali SAHOP[4]	8.4	0.460		soil
	5060	8.5	0.220	37.0	soil
	412	8.5	0.230	44.0	soil
	5053	10.6	0.280	19.0	soil
	5058	12.6	0.380	39.0	soil
	5057	12.7	0.270	46.0	soil
	Cucapah[4]	12.9	0.310		soil
	5051	14.0	0.200	17.0	soil

Table 2. (continued)

Earthquake	Station[1]	Distance km	Peak Horizontal Acceleration g	Peak Horizontal Velocity cm/sec	Site Condition
Imperial Valley 1979 (continued)	Westmoreland[5]	15.0	0.110		soil
	5115	16.0	0.430	31.0	soil
	Chihuahua[4]	17.7	0.270		soil
	931	18.0	0.150	19.0	soil
	5056	22.0	0.150	15.0	soil
	5059	22.0	0.150	15.0	soil
	5061	23.0	0.130	15.0	soil
	Compuertas[4]	23.2	0.190		soil
	5062	29.0	0.130		soil
	5052	32.0	0.066		soil
	Delta[4]	32.7	0.350		soil
	724	36.0	0.100		soil
	Victoria[4]	43.5	0.160		soil
	5066	49.0	0.140		soil
	5050	60.0	0.049		soil
	2316	64.0	0.034		soil
Imperial Valley 1979 aftershock	5055	7.5	0.264		
	942	8.8	0.263		
	5028	8.9	0.230		
	5165	9.4	0.147		
	952	9.7	0.286		
	958	9.7	0.157		
	955	10.5	0.237		
	117	10.5	0.133		
	412	12.0	0.055		
	5053	12.2	0.097		
	5054	12.8	0.129		
	5058	14.6	0.192		
	5057	14.9	0.147		
	5115	17.6	0.154		
	5056	23.9	0.060		
	5060	25.0	0.057		

Table 2. (continued)

Earthquake	Station[1]	Distance km	Peak Horizontal Acceleration g	Peak Horizontal Velocity cm/sec	Site Condition
Livermore Valley 1980 January 24	1030	10.8	0.120		
	1418	15.7	0.154		
	1383	16.7	0.052		
	1308	20.8	0.045		
	1298	28.5	0.086		
	1299	33.1	0.056		
	1219	40.3	0.065		
Livermore Valley 1980 January 27	Fagundes Ranch[5]	4.0	0.259		
	Morgan Terrace Park[5]	10.1	0.267		
	1030	11.1	0.071		
	1418	17.7	0.275		
	1383	22.5	0.058		
	Antioch Contra Loma[5]	26.5	0.026		
	1299	29.0	0.039		
	1308	30.9	0.112		
	1219	37.8	0.065		
	1456	48.3	0.026		
Horse Canyon 1980	5045	5.8	0.123		
	5044	12.0	0.133		
	5160	12.1	0.073		
	5043	20.5	0.097		
	5047	20.5	0.096		
	C168	25.3	0.230		
	5068	35.9	0.082		
	C118	36.1	0.110		
	5042	36.3	0.110		
	5067	38.5	0.094		
	5049	41.4	0.040		
	C204	43.6	0.050		
	5070	44.4	0.022		
	C266	46.1	0.070		

Table 2. (continued)

Earthquake	Station[1]	Distance km	Peak Horizontal Acceleration g	Peak Horizontal Velocity cm/sec	Site Condition
Horse Canyon 1980 (continued)	C203	47.1	0.080		
	5069	47.7	0.033		
	5073	49.2	0.017		
	5072	53.1	0.022		

[1]Station numbers preceded by the letter C are those assigned by the California Division of Mines and Geology. Other numbers are those assigned by the U.S. Geological Survey (1977; the stations not necessarily being U.S.G.S. stations).

[2]Station operated by the Southern California Edison Company.

[3]Station operated by the Shell Oil Company.

[4]Station operated by the Universidad Nacional Autonoma de Mexico and the University of California at San Diego.

[5]Station operated by the California Division of Mines and Geology.

Table 3. The effects of removing individual earthquakes from the data set for peak horizontal acceleration

Data Set	Constant Term $\underline{\alpha}$	Magnitude Coefficient $\underline{\beta}$	h (km)	Distance Coefficient $\underline{b}$	50 percentile Peak Horizontal Acceleration (g) **M** = 6.5 d = 0.0	**M** = 7.7 d = 0.0
All earthquakes	-1.02	0.249	7.3	-0.00255	0.52	1.04
San Fernando earthquake omitted	-0.97	0.240	7.3	-0.00241	0.51	0.99
Parkfield earthquake omitted	-0.87	0.223	8.0	-0.00210	0.46	0.85
Kern Co. earthquake omitted	-0.91	0.232	7.6	-0.00294	0.50	0.94
Coyote Lake earthquake omitted	-0.97	0.244	7.8	-0.00257	0.51	0.99
1979 Imperial Valley mainshock and aftershock omitted	-1.21	0.275	5.6	-0.00255	0.65	1.40
Borrego Mountain earthquake omitted	-0.97	0.240	7.3	-0.00247	0.51	0.99
Livermore Valley earthquakes omitted	-0.99	0.246	7.3	-0.00257	0.53	1.05
Horse Canyon earthquake omitted	-1.11	0.262	6.7	-0.00254	0.56	1.16

Table 4. The effects of removing individual earthquakes from the data set for peak horizontal velocity

Data Set	Constant Term α	Magnitude Coefficient β	h (km)	Distance Coefficient b	Site Effect Coefficient c	50 percentile Peak Horizontal Velocity (cm/sec) **M** = 6.5 d = 0.0 S = 1	**M** = 7.4 d = 0.0 S = 1
All earthquakes	-0.67	0.489	4.0	-0.00256	0.17	116	321
San Fernando earthquake omitted	-0.55	0.465	3.8	-0.00150	0.19	119	313
Parkfield earthquake omitted	-0.62	0.483	4.3	-0.00253	0.17	111	302
Kern Co. earthquake omitted	0.12	0.359	4.2	-0.00338	0.17	97	204
Coyote Lake earthquake omitted	-0.60	0.481	3.9	-0.00248	0.15	119	323
1979 Imperial Valley earthquake omitted	-0.74	0.501	3.4	-0.00250	0.17	140	396

Table 5. Comparison of values given by the prediction equation with values for selected strong motion records not in the data set.

Record	M	d (km)	Observed Value	Predicted Value
Pacoima Dam Abutment, San Fernando Earthquake (Boore and others, 1978)	6.6	0.0		
Peak horizontal acceleration			1.25 g	0.55 g
Peak horizontal acceleration corrected for effect of topography (Boore, 1973)			0.73 g	
Peak horizontal velocity			113 cm/sec	88 cm/sec
Karakyr site, Gazli, USSR, earthquake (Campbell, 1981)	7.0	3.5	0.81 g	0.62 g
Tabas, Iran (Campbell, 1981)	7.7	3.0	0.80 g	0.95 g

Figure 1. Distribution in M and $\bar{d}$ of the data set for peak horizontal acceleration (small symbols). The large symbols show other data points which are compared with the results of the prediction equation in Table 5.

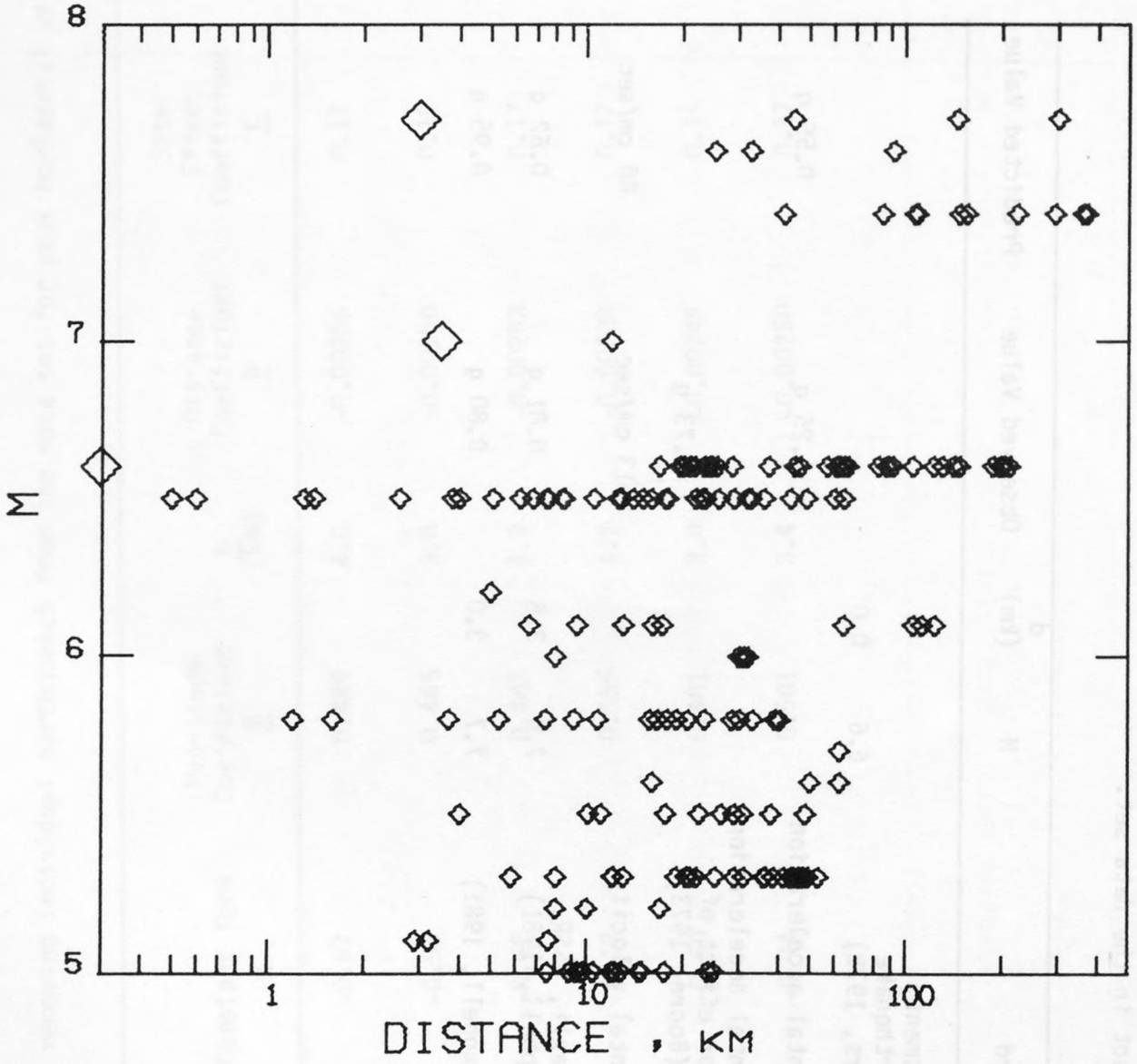

Figure 2. Distribution in M and d of the data set for peak horizontal velocity.

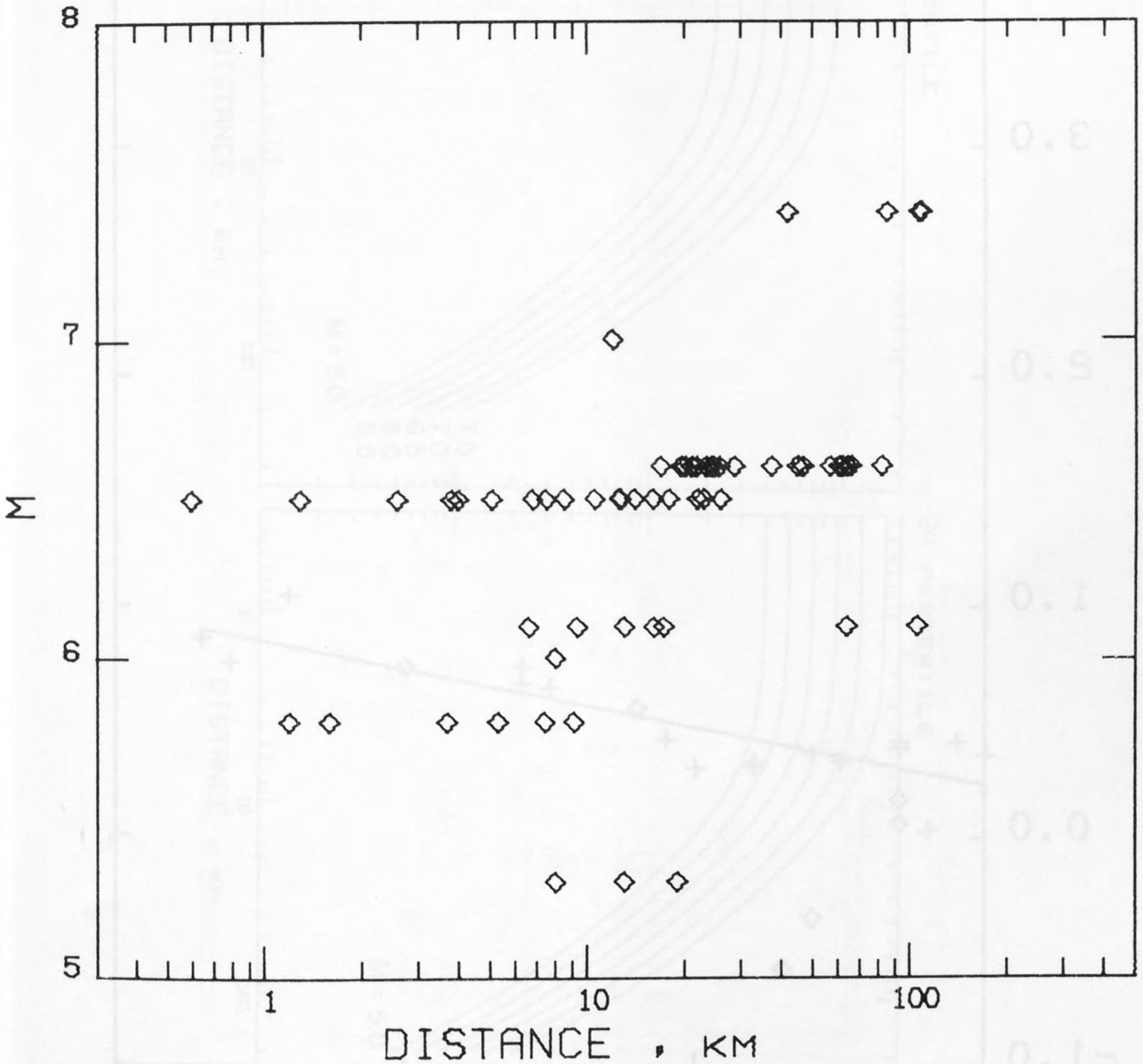

Figure 3. Values of $\underline{a}_i$ for peak horizontal acceleration from the regression analysis of equation (1) plotted against moment magnitude. Diamond symbols are earthquakes represented by only one acceleration value; those events were not used in determining the straight line.

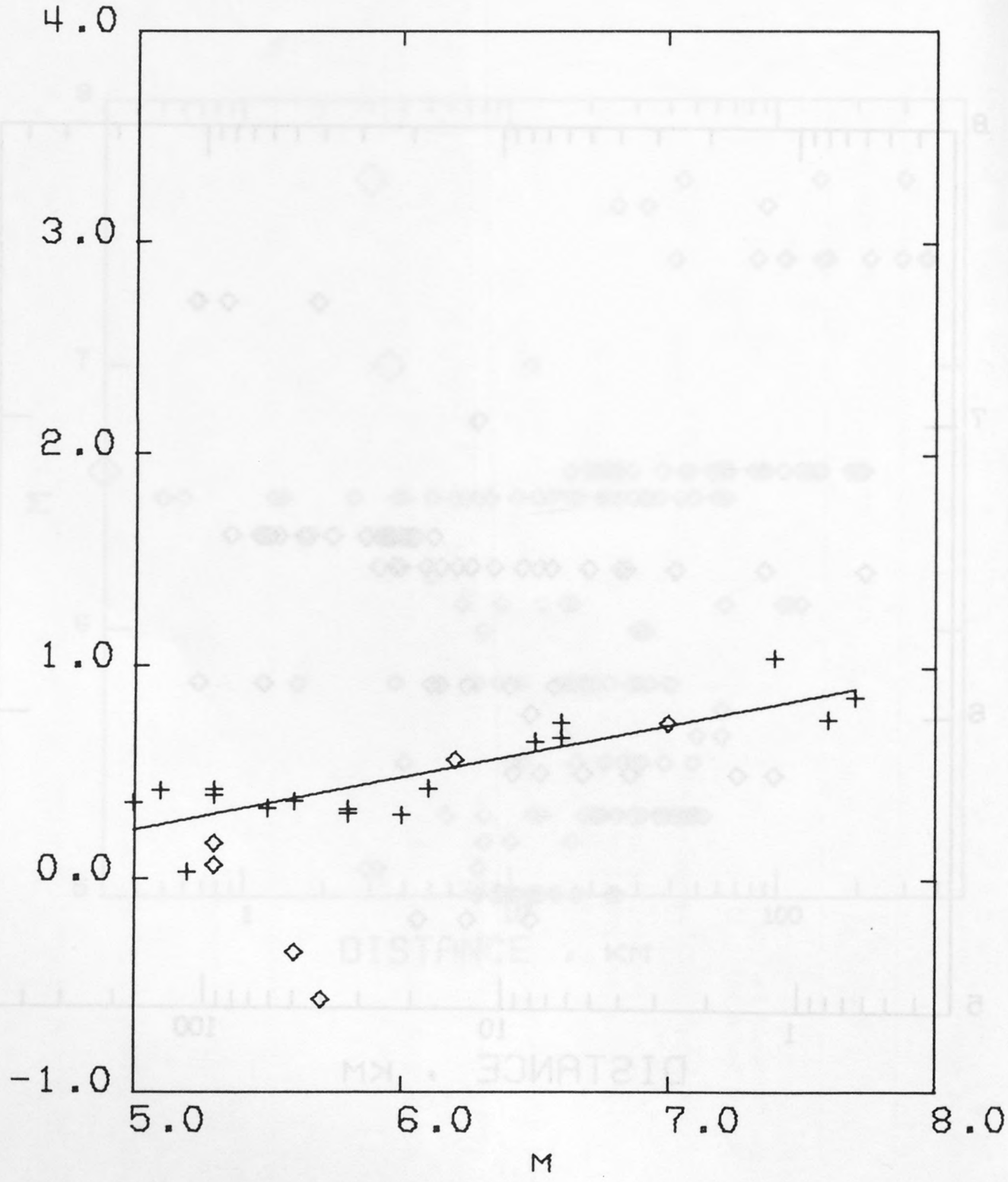

Figure 4. Predicted values of peak horizontal acceleration for 50 and 84 percentile as functions of distance and moment magnitude.

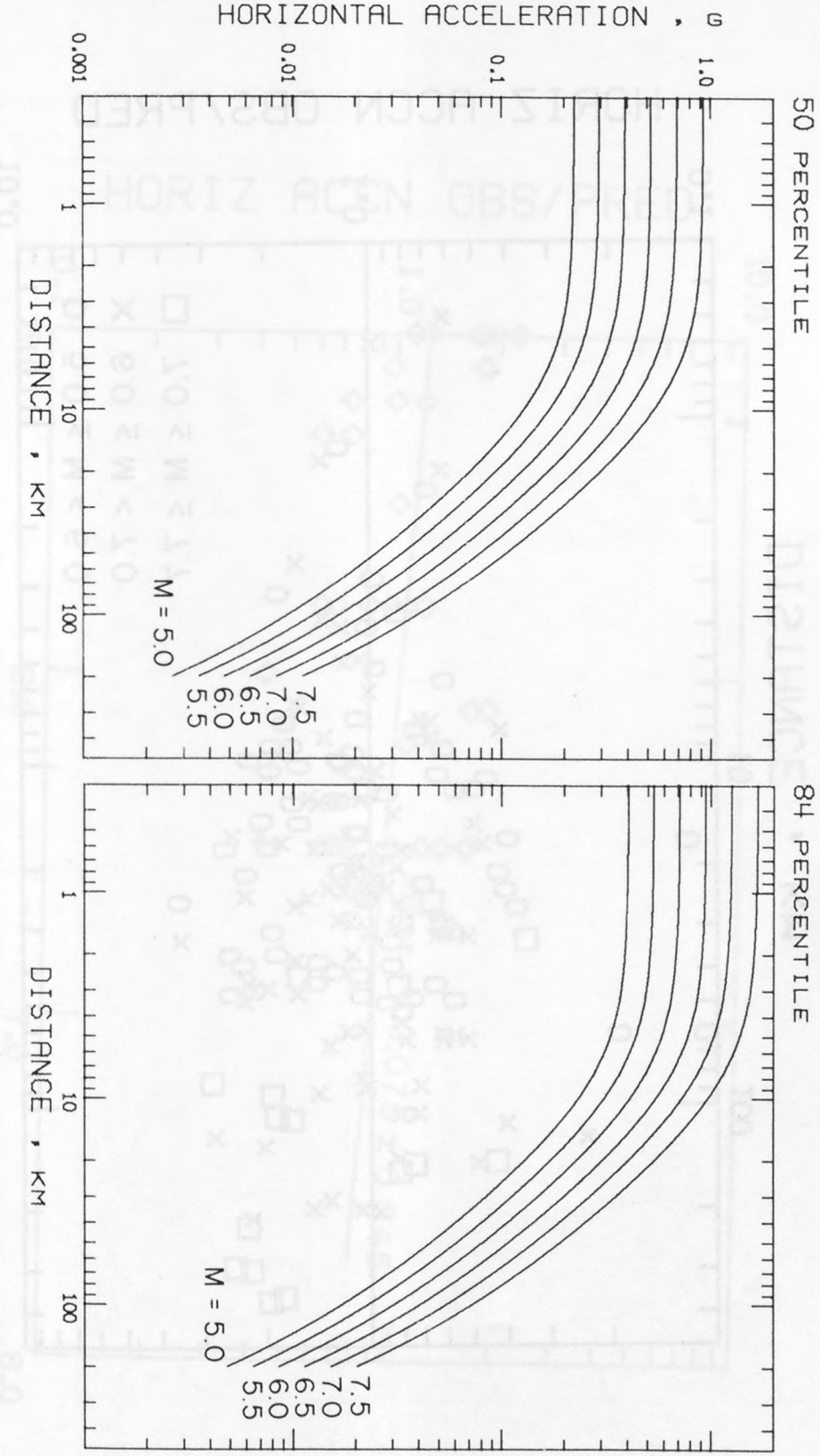

Figure 5. Residuals of peak horizontal acceleration with respect to equation (4) plotted against distance.

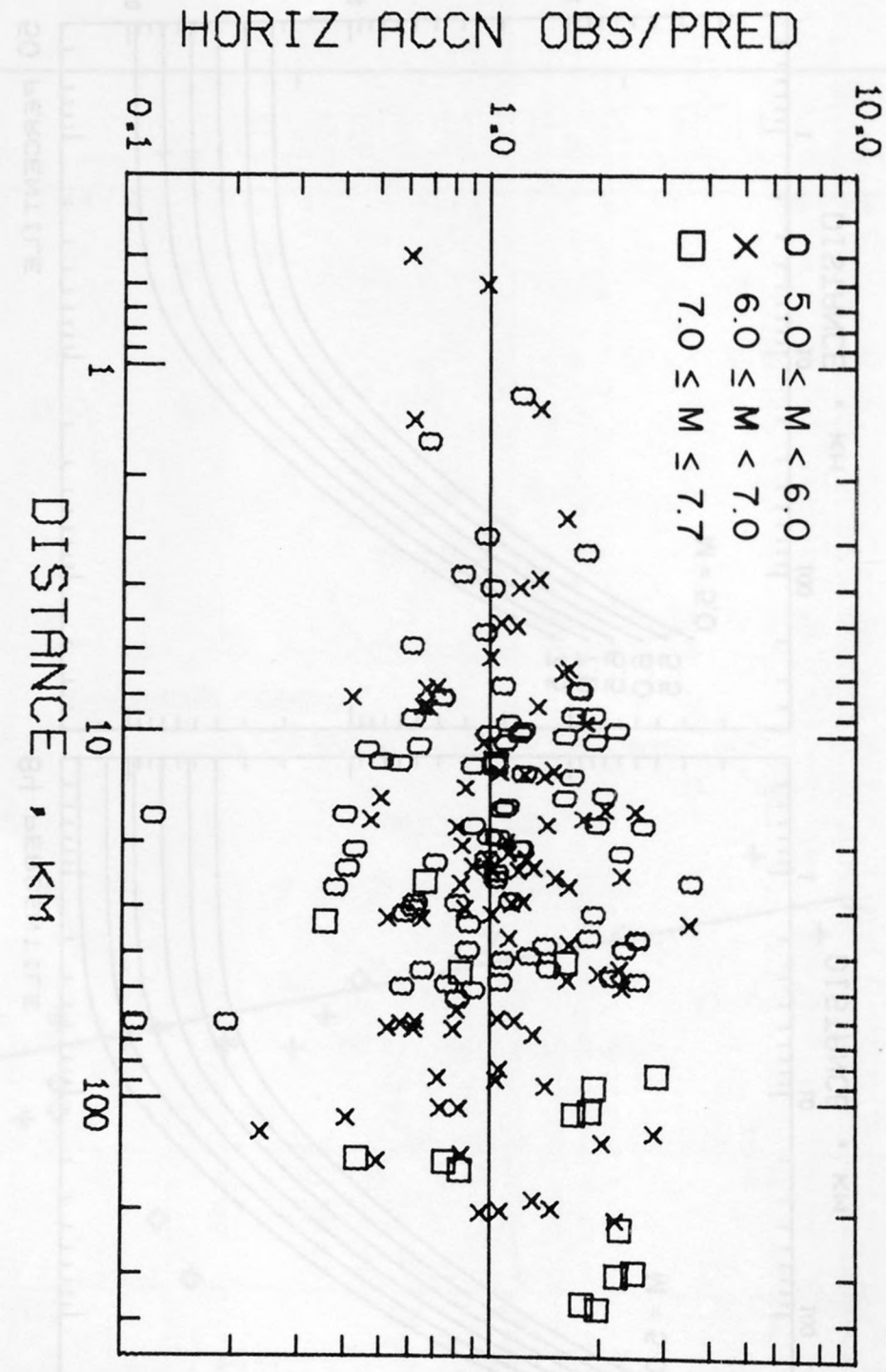

Figure 6. Residuals of peak horizontal acceleration with respect to equation (4) plotted against M for stations with d less than or equal to 10.0 km.

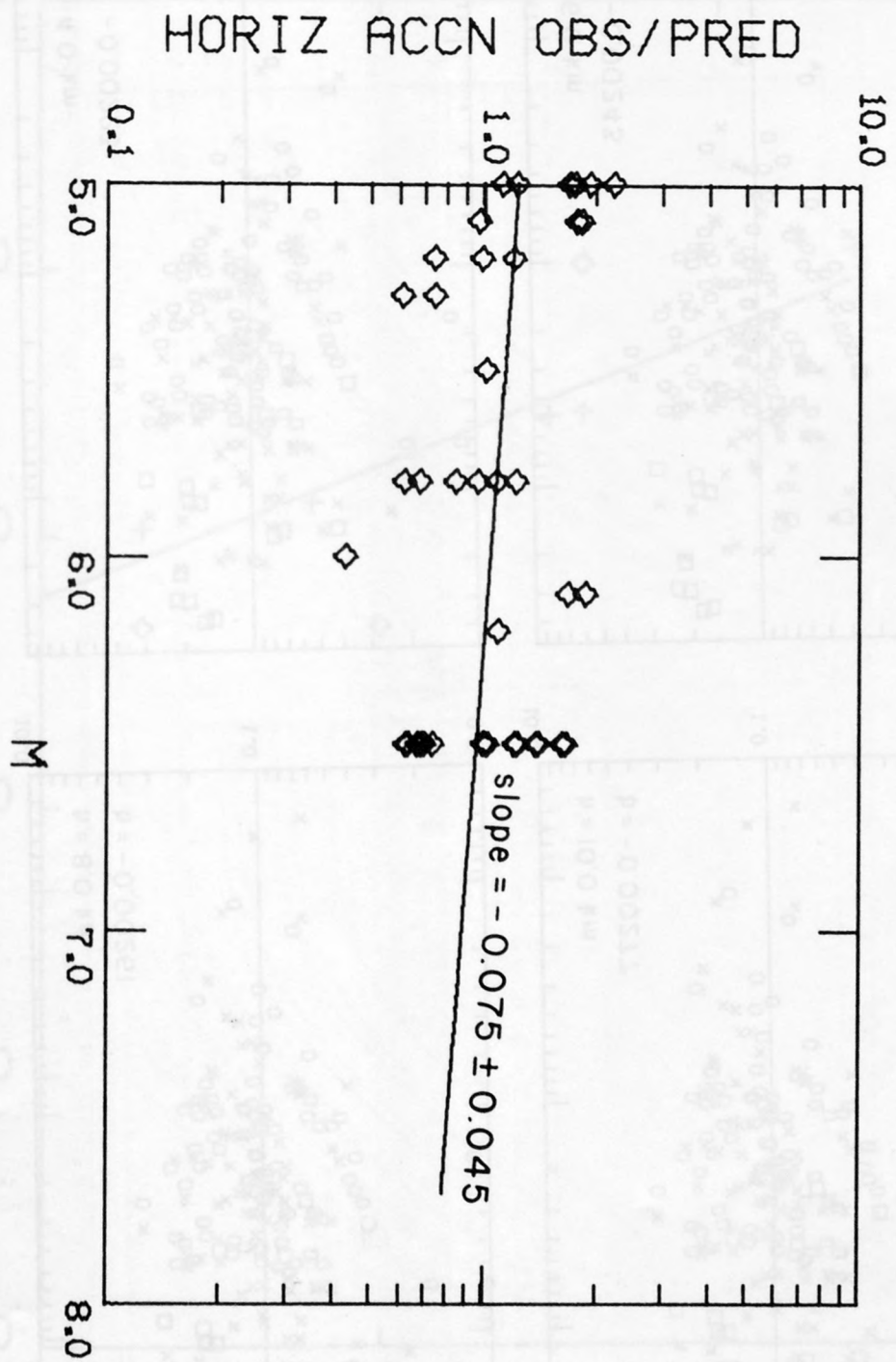

Figure 7. Residuals of peak acceleration with respect to prediction equations developed using the indicated values of $\underline{h}$. Symbols defined as in Figure 5.

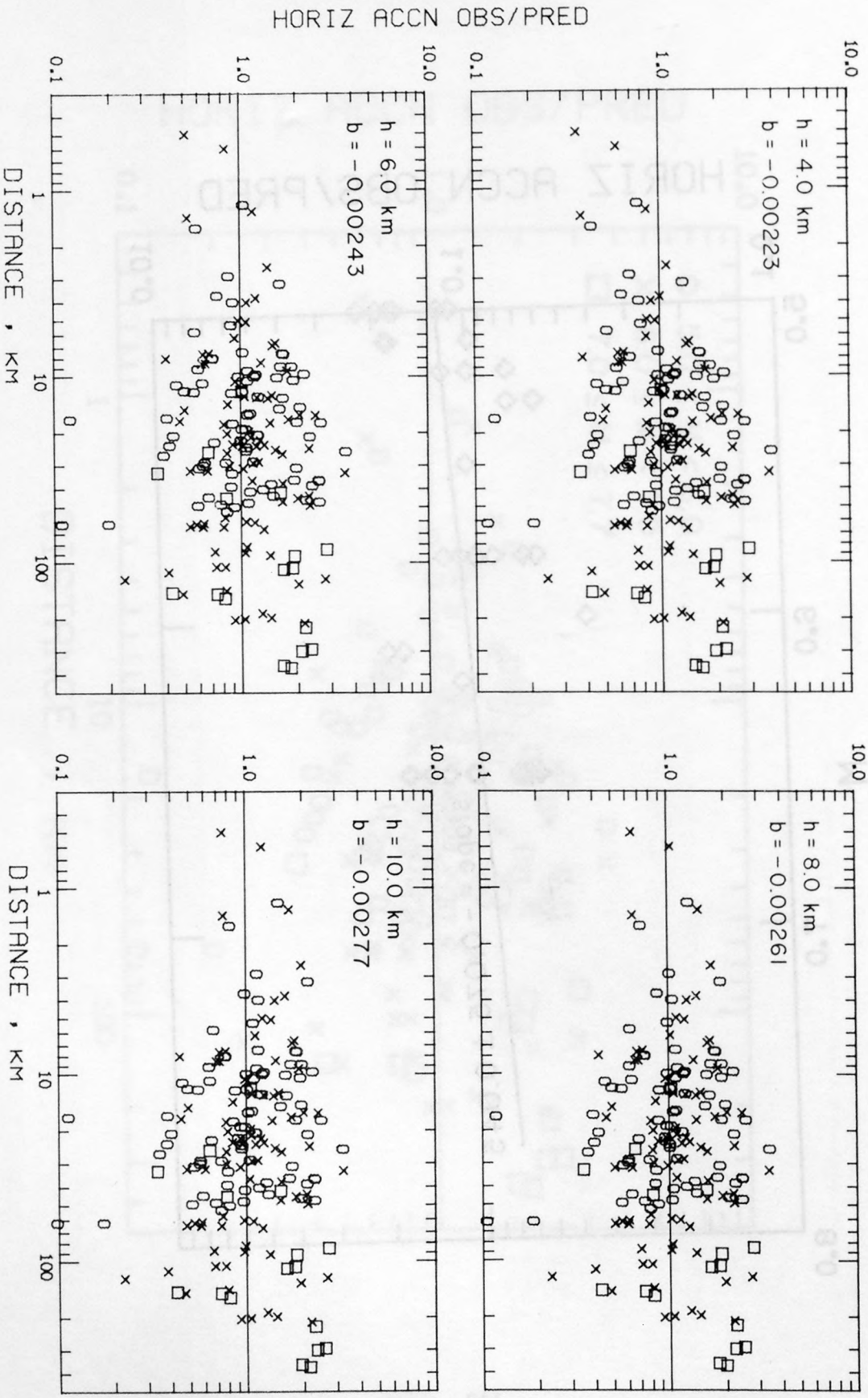

Figure 8. Values of $\overline{a}_i$ for peak horizontal velocity from the regression analysis of equation (1) plotted against moment magnitude. Diamond symbols are earthquakes represented by only one velocity value; those events were not used in determining the straight line.

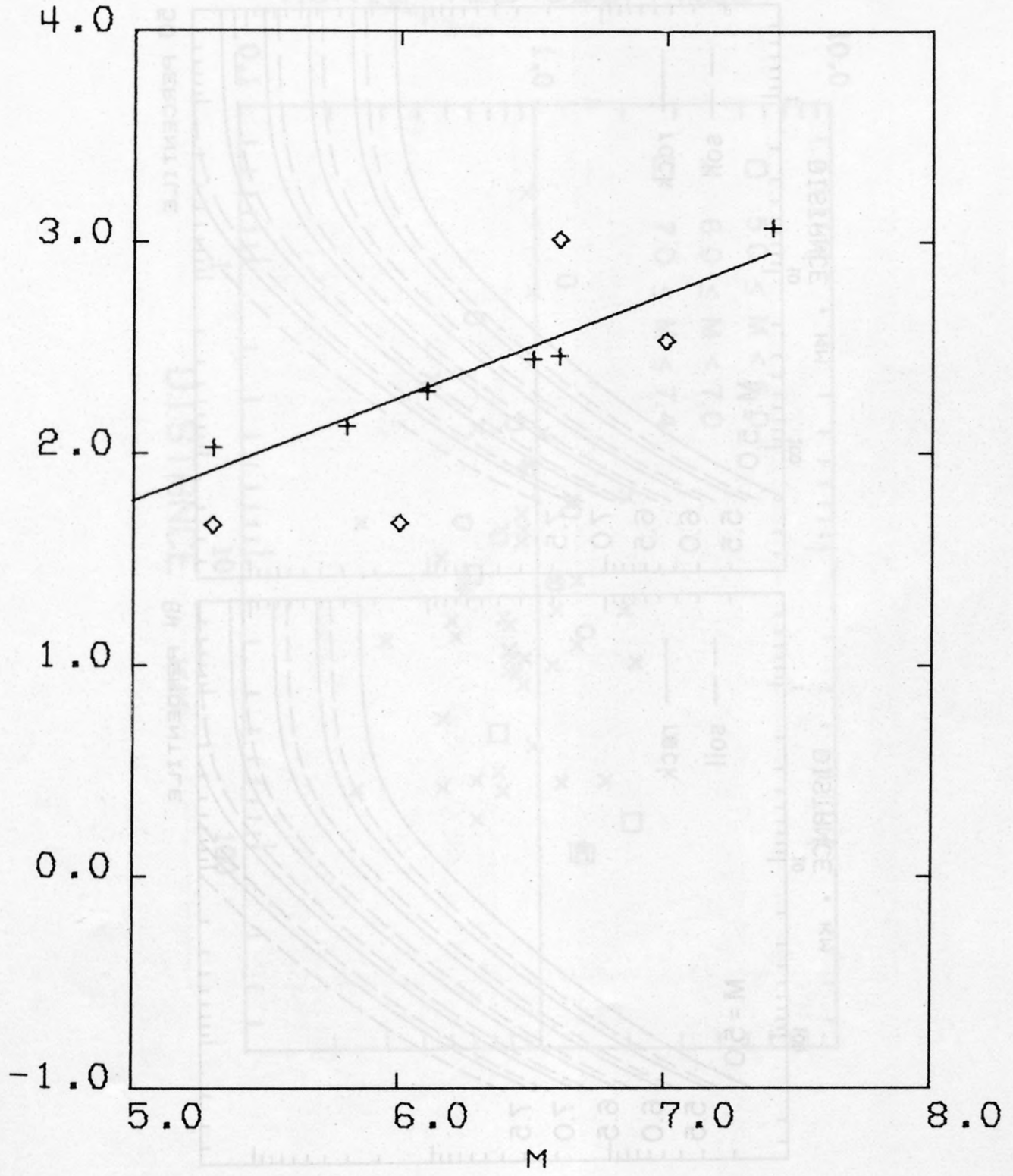

Figure 9. Predicted values of peak horizontal velocity for 50 and 84 percentile as functions of distance, moment magnitude, and geologic site conditions.

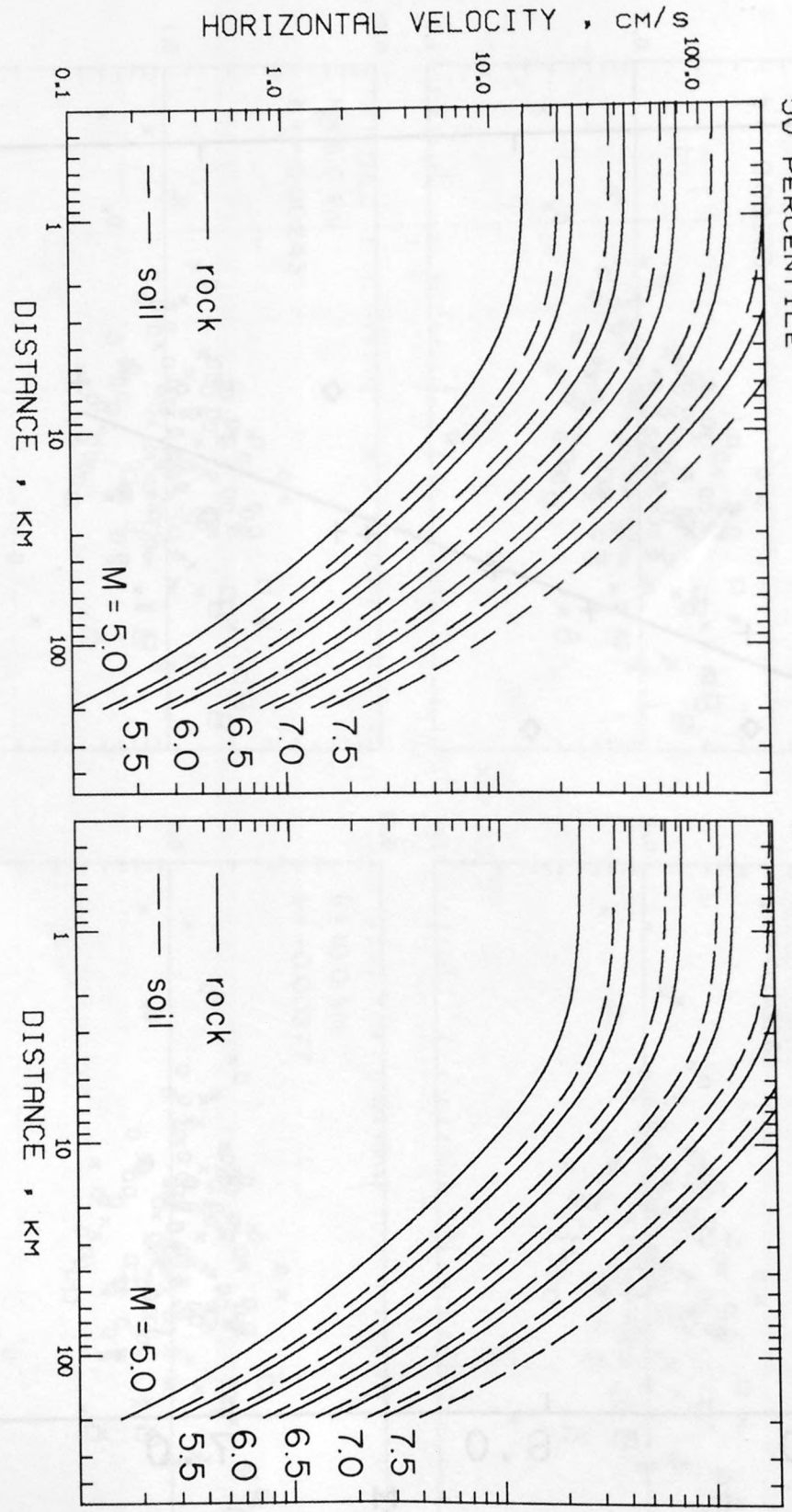

Figure 10. Residuals of peak horizontal velocity with respect to equation (6) plotted against distance.

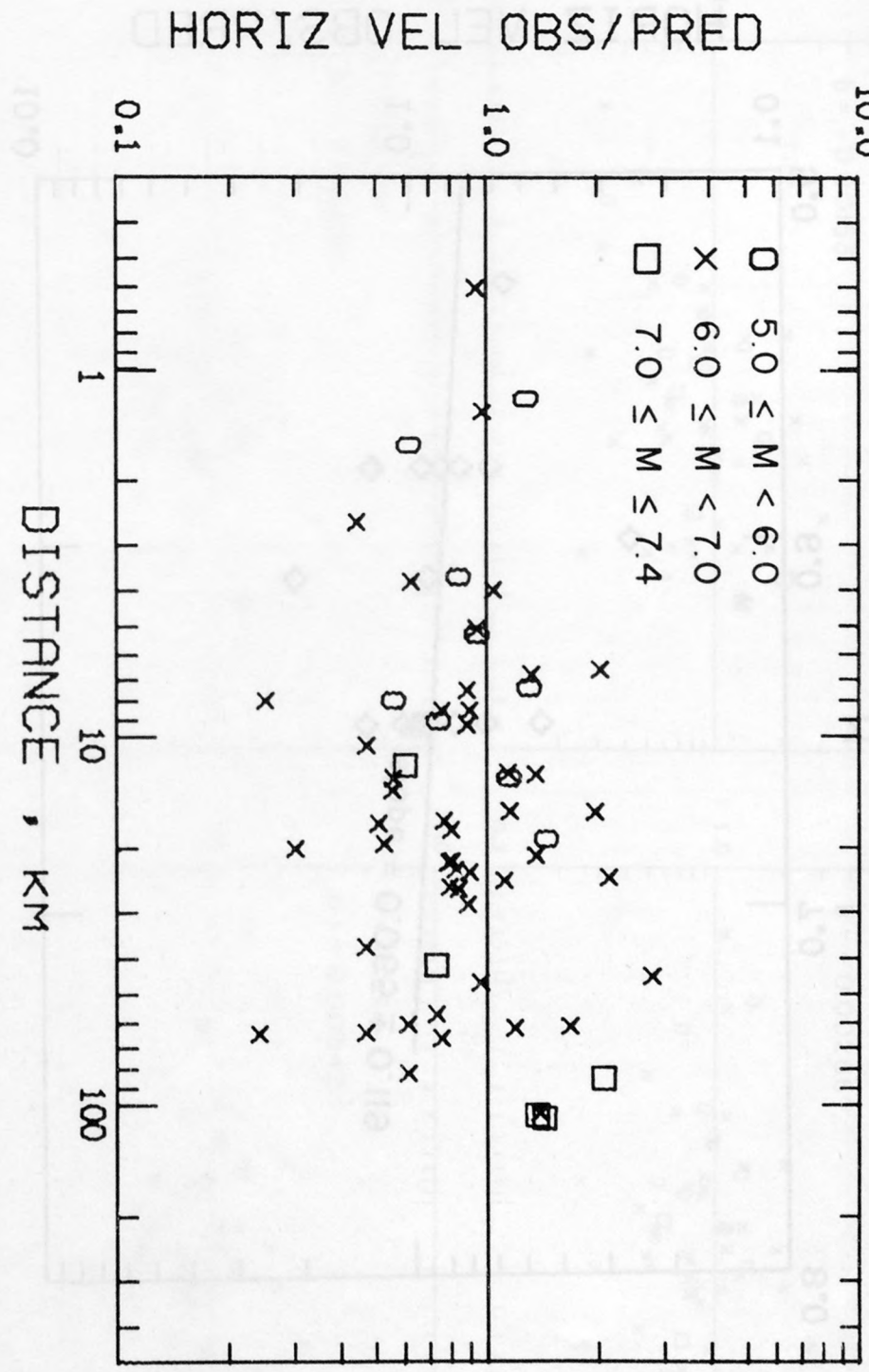

Figure 11. Residuals of peak horizontal velocity with respect to equation (6) plotted against M for stations with d less than or equal to 10.0 km.

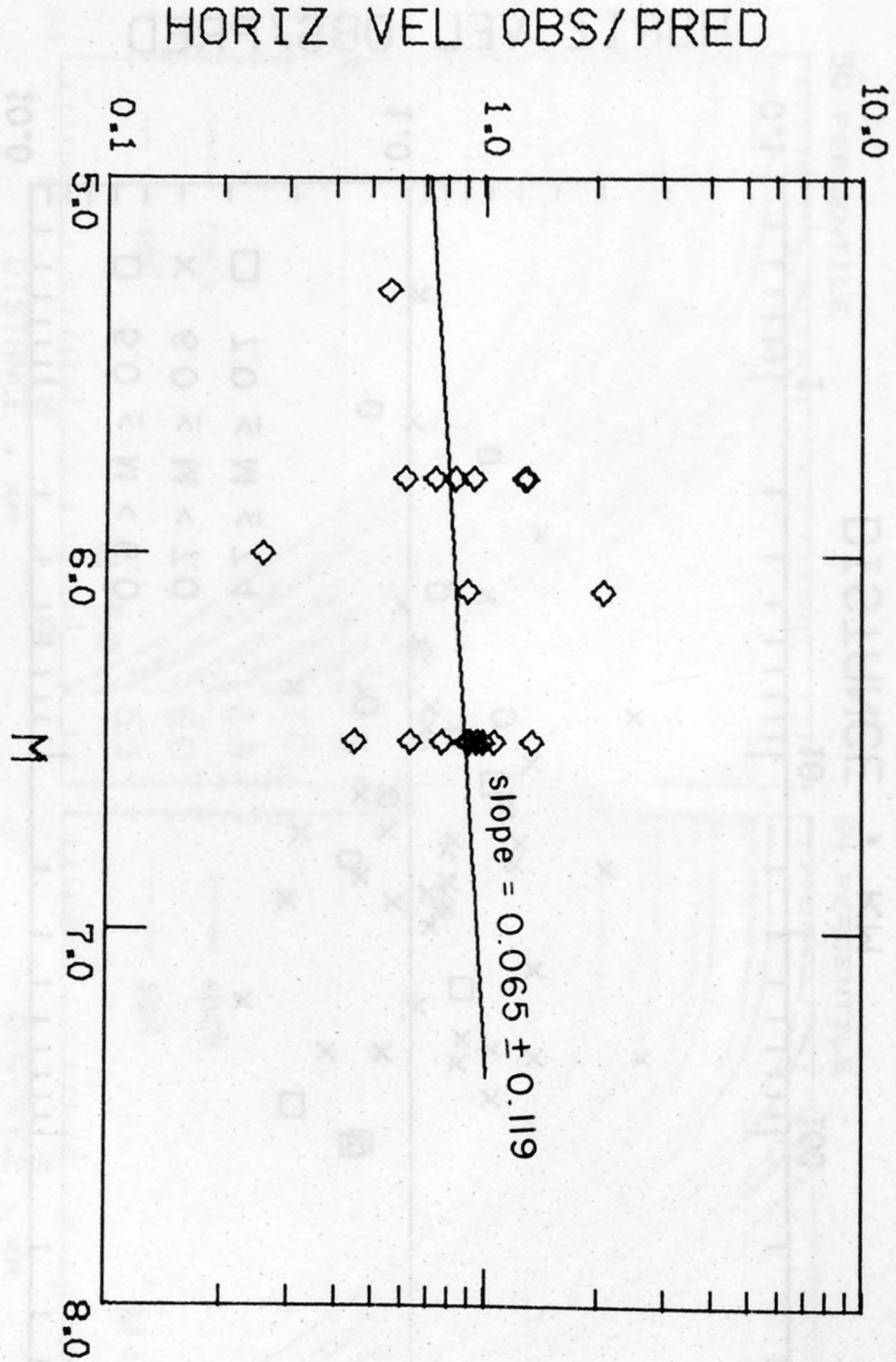

Figure 12. Residuals of peak velocity with respect to prediction equations developed using the indicated values of h. Symbols defined as in Figure 10.

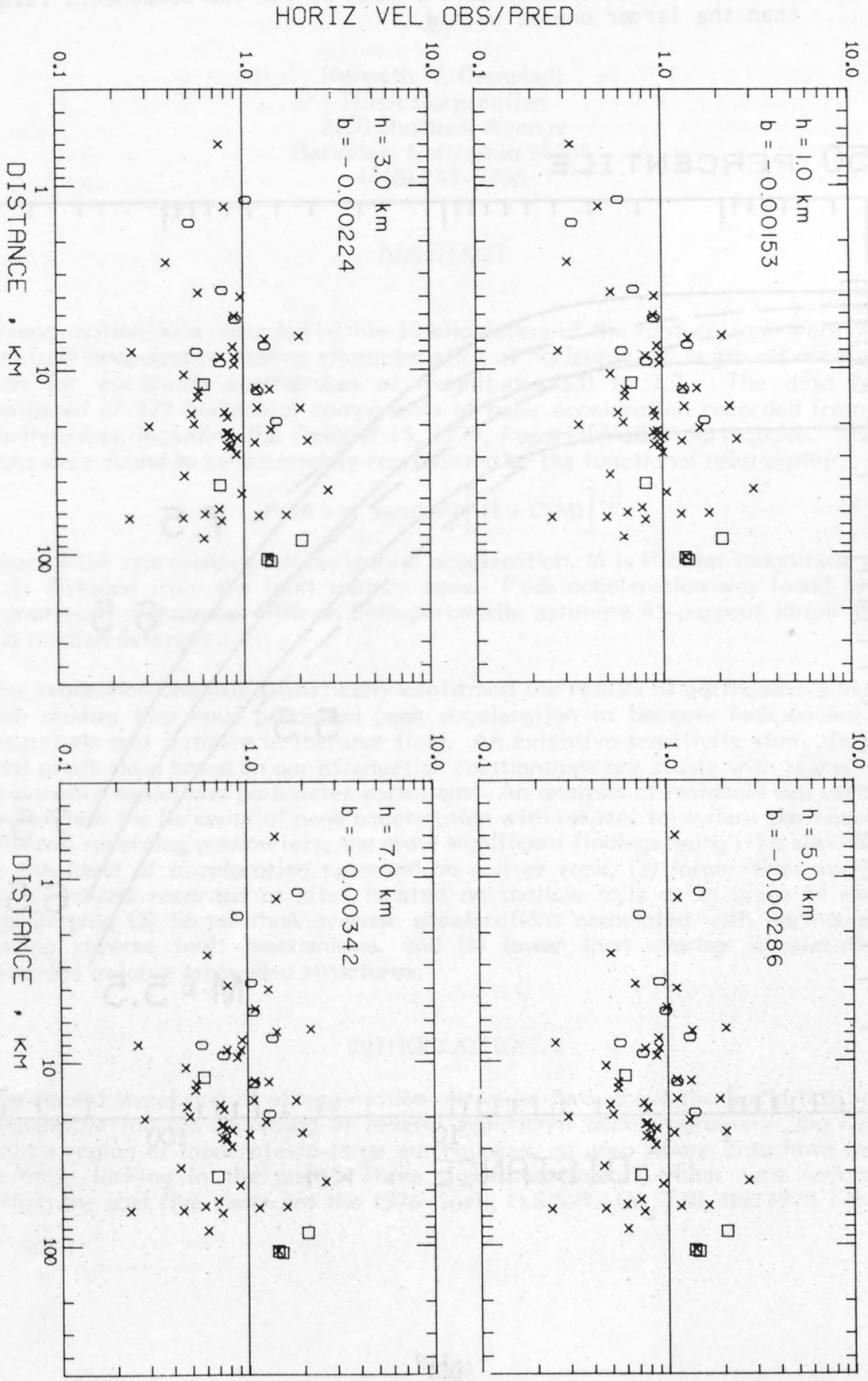

Figure 13. Comparison of attenuation curves for peak horizontal acceleration by Campbell (1980) (dashed lines) with the 50 percentile curves from this report (solid lines). Campbell's curves are raised by 13 percent to compensate for the fact that he defined peak horizontal acceleration as the mean of the two components rather than the larger one as we did.

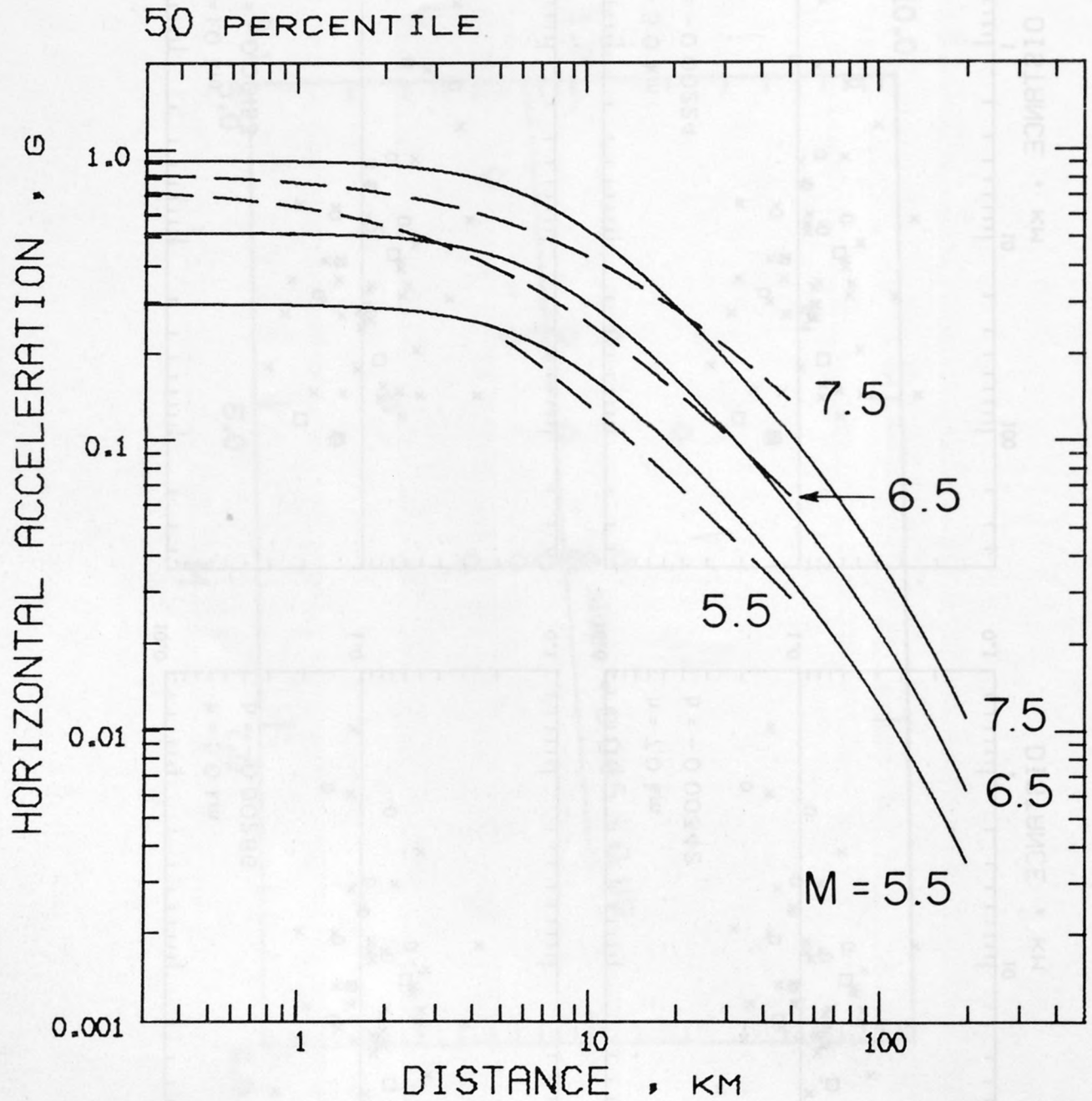

NEAR-SOURCE SCALING CHARACTERISTICS OF PEAK HORIZONTAL ACCELERATION FOR MODERATE-TO-LARGE EARTHQUAKES

by

Kenneth W. Campbell
TERA Corporation
2150 Shattuck Avenue
Berkeley, California 94704
(415) 845-5200

ABSTRACT

Strong-motion data recorded within 50 kilometers of the rupture zone were used to study near-source scaling characteristics of horizontal peak ground acceleration for worldwide earthquakes of magnitudes 5.0 to 7.7. The data base consisted of 229 horizontal components of peak acceleration recorded from 27 earthquakes, including the October 15, 1979, Imperial Valley earthquake. These data were found to be adequately represented by the functional relationship

$$PGA = a \exp(bM) \left[R + C(M) \right]^{-d}$$

where PGA represents peak horizontal acceleration, M is Richter magnitude and R is distance from the fault rupture zone. Peak acceleration was found to be lognormally distributed with an 84th-percentile estimate 45-percent larger than the median estimate.

The regression analysis statistically confirmed the results of earthquake simulation studies that have predicted peak acceleration to become independent of magnitude and distance in the near field. An extensive sensitivity study showed that predictions based on our attenuation relationships are stable with respect to reasonable model and parameter variations. An analysis of residuals was used to investigate the behavior of peak acceleration with respect to various earthquake, site and recording parameters, the more significant findings being (1) a similarity in the level of acceleration recorded on soil or rock, (2) larger than average accelerations recorded at sites located on shallow soils or in areas of steep topography, (3) larger than average accelerations associated with earthquakes having reverse fault mechanisms, and (4) lower than average accelerations recorded in large embedded structures.

INTRODUCTION

The recent expansion of strong-motion networks throughout the world has been responsible for the recording of several significant accelerograms in the near-source region of moderate-to-large earthquakes, an area where data have been severely lacking in the past. Three significant events which have occurred within the past five years are the 1976 Gazli, U.S.S.R., (M_s 7.0), the 1978 Tabas,

Iran, (M_S 7.7) and the 1979 Imperial Valley, U.S.A., (M_S 6.9) earthquakes, each producing accelerograms within ten kilometers of the fault.

These and other recent near-source recordings together with selected near-source data recorded as early as 1933 were used to analyze the behavior of peak horizontal acceleration (PGA) near the causative fault. The goal was to make PGA predictions at these distances as generally reliable as far-field estimates. The study was restricted to the near-source region of earthquakes of magnitude 5.0 or greater to eliminate the small accelerations generally considered to be of little importance in earthquake engineering. This restriction substantially reduced the uncertainty in the analyses and enhanced the statistical significance of the results.

Due to the paucity of near-source data for large earthquakes, the study was not restricted to accelerations recorded in western North America. We acknowledge that the tectonics and recording practices of other countries may be substantially different from those in the western United States, but these possible differences are far outweighed by the important contribution these foreign data make to understanding the behavior of near-source ground motion.

Several factors have minimized the potential bias of the foreign data used in the analyses. First, the restriction to the near-source region has made differences in anelastic attenuation negligible compared to the inherent scatter from other factors. In addition, the foreign data used in this investigation come from events occurring along tectonic plate boundaries which are generally similar to the interplate earthquakes of western North America. Deep subduction events were excluded because of the substantial difference in travel paths and stress conditions compared to the shallow events used in this study. All the foreign data were recorded on instruments having dynamic characteristics similar to those commonly used in the United States to avoid a possible instrument bias for these recordings as is systematically observed for the SMAC strong-motion accelerograph generally used in Japan.

The data base used in the analyses was assembled using criteria designed to select only consistent and quality data in the range of magnitudes and distances of interest for most design applications. The data base consisted of 27 earthquakes representing 229 horizontal components (116 records) of peak ground acceleration recorded at distances from the rupture zone of less than 30 or 50 kilometers, dependent on magnitude. These data were weighted, by earthquake, within several distance intervals to control the effects of well-recorded events such as the 1979 Imperial Valley and the 1971 San Fernando earthquakes.

Two ground motion models were developed and tested in this study. The first was an empirical relationship whose coefficients were determined based solely on regression analysis. Because of the limited amount of data within three to five kilometers of the rupture zone and because our restriction to the near-source region excluded data beyond 50 kilometers, a second ground motion model having specified near-field and far-field properties was developed and compared to the empirical model. As a result, two boundary conditions were applied in the second analysis. First, the far-field attenuation of PGA was constrained to $R^{-1.75}$ based upon the studies of other investigators, and second, PGA at the

fault rupture surface was constrained to a constant value, independent of magnitude, consistent with the physics of the earthquake rupture process.

NEAR-SOURCE DATA BASE

The general data base consists of peak acceleration data recorded in the near-source region of a set of worldwide earthquakes with shallow rupture. It represents available published peak acceleration data recorded in the United States through at least March 1979 that meet the following criteria:

(1) Earthquakes for which either epicenters were determined with an accuracy of 5 kilometers or less, or an accurate estimate of the closest distance to the fault rupture surface was known;

(2) Earthquake magnitude determinations were accurate to within 0.3 units;

(3) Source-to-site distances were within 20, 30, and 50 kilometers for magnitudes less than 4.75, between 4.75 and 6.25, and greater than 6.25, respectively;

(4) Earthquake hypocenters or rupture zones were within 25 kilometers of the ground surface;

(5) Accelerograms had a PGA of at least 0.02 g for one component which triggered early enough in the record to capture the strong phase of shaking; and

(6) Accelerograms were recorded on instruments either in the free field, on the abutments of dams or bridges, in the lowest basement of buildings, or on the ground level of structures without basements.

The data base was developed without any restriction on either the age of the record, the type of recording instrument, the recording site geology, the tectonic province of the earthquake, the earthquake fault type, or the size of the earthquake.

Several significant earthquakes which occurred either outside the United States or since March 1979 and which also met the selection criteria outlined above were included. They were: the August 6, 1979 Coyote Lake (M_L 5.9) and October 15, 1979 Imperial Valley (M_s 6.9) earthquakes in California; the December 10, 1967 Koyna, India, earthquake (M_s 6.5); the December 23, 1972 Managua, Nicaragua, earthquake (M_s 6.2); the October 3, 1974 Lima, Peru, earthquake (M_s 7.6); the May 17, 1976 Gazli, USSR, earthquake (M_s 7.0); and the September 16, 1978 Tabas, Iran, earthquake (M_s 7.7).

Various criteria were applied to the near-source data base in order to select a subset appropriate for the analysis of peak acceleration for moderate-to-large

magnitude earthquakes. The application of these criteria resulted in the selection of 229 horizontal components (116 recordings) of PGA from 27 earthquakes of magnitude 5.0 and greater. A list of these events appears in Table 1. The peak acceleration values, distances and geologic classification for the strong-motion stations are tabulated in the appendix. Figure 1 gives the distribution of recordings with respect to magnitude and distance. The correlation of these two parameters was found to be only six percent. A description of the selection criteria as well as definitions of important parameters of this selected data base are given below.

Peak Acceleration

Peak accelerations scaled from digitized, unprocessed accelerograms* were selected when available, otherwise values were scaled from the original accelerograms. Peak accelerations from fully processed accelerograms were not used because they are generally smaller than those scaled from either the digitized unprocessed or original accelerograms due to the 0.02 second decimation and frequency band-limited filtering of the records. The mean of the two horizontal peak values from an individual recording was used in the analysis because it was found to be a more stable peak acceleration parameter than either the single components taken separately or both components taken together. When only a single horizontal component was available, it was used in lieu of the mean value. The maximum of the two horizontal peak values used by some investigators (e.g., Boore et al., 1980) was found to be on the average 13-percent larger than the mean.

Magnitude

The study was restricted to earthquakes of magnitude 5.0 or greater because they are of greatest concern for most design applications. A magnitude scale which we will refer to as M in this paper was chosen to be generally consistent with both the moment-magnitude scale of Hanks and Kanamori (1979) and the Richter magnitude scale (as interpreted by Nuttli, 1979). It was defined as surface-wave magnitude (M_s) when both local magnitude (M_L) and surface wave magnitude were greater than or equal to 6.0, and it was defined as local magnitude when both magnitudes were below this value. Where M_s or M_L was not available, an appropriate value was estimated based upon empirical relationships among magnitude scales. The 1967 Fairbanks, Alaska, earthquake was the only selected event requiring such a conversion.

The use of M_s for the larger earthquakes not only served as a uniform basis for characterizing the magnitude of worldwide events, but also avoided the saturation effects that have been observed for the M_L and m_b scales (Chinnery, 1978; Kanamori, 1979). Moment magnitude, a scale designed to overcome the deficiencies caused by saturation of the conventional magnitude scales, was not

---

* This refers to the first stage in the routine processing of accelerograms in which the record is digitized and baseline corrected. Unequal digitization intervals are used to preserve the true value of the peaks recorded by the accelerograph.

TABLE I

EARTHQUAKE DATA

Earthquake Name	Date Yr-Mo-Day	Magnitude* (M)	Fault Type	No. of Recordings
Long Beach	33-03-11	6.2	Strike-Slip	3
Helena, Montana	35-10-31	5.5	Normal	1
Imperial Valley	40-05-19	7.1	Strike-Slip	1
Santa Barbara	41-07-01	5.9	Reverse	1
Kern County	52-07-21	7.7	Oblique	1
Daly City	57-03-22	5.3	Strike-Slip	5
Parkfield	66-06-28	6.0	Strike-Slip	4
Fairbanks, Alaska	67-06-21	5.7	Strike-Slip	1
Koyna, India	67-12-10	6.5	Strike-Slip	1
Borrego Mtn.	68-04-09	6.7	Strike-Slip	1
Lytle Creek	70-09-12	5.4	Strike-Slip	4
San Fernando	71-02-09	6.6	Reverse	24
Bear Valley	72-02-24	5.1	Strike-Slip	1
Sitka, Alaska	72-07-30	7.6	Oblique	1
Managua	72-12-23	6.2	Strike-Slip	1
Point Mugu	73-02-21	5.9	Reverse	1
Lima, Peru	74-10-03	7.6	Reverse	2
Hollister	74-11-28	5.1	Strike-Slip	3
Oroville	75-08-01	5.7	Normal	4
Kalapana, Hawaii	75-11-29	7.1	Reverse	2
Gazli, USSR	76-05-17	7.0	Reverse	1
Santa Barbara	78-08-13	5.7	Reverse	6
Tabas, Iran	78-09-16	7.7	Reverse	1
Bishop	78-10-04	5.8	Strike-Slip	4
Malibu	79-01-01	5.0	Reverse	3
St. Elias, Alaska	79-02-28	7.2	Reverse	1
Coyote Lake	79-08-06	5.9	Strike-Slip	9
Imperial Valley	79-10-15	6.9	Strike-Slip	31

* Magnitude (M) was selected to be consistent with the moment-magnitude scale (see text):

$M = M_s$ for magnitudes equal to 6.0 or greater
$M = M_L^s$ for magnitudes less than 6.0

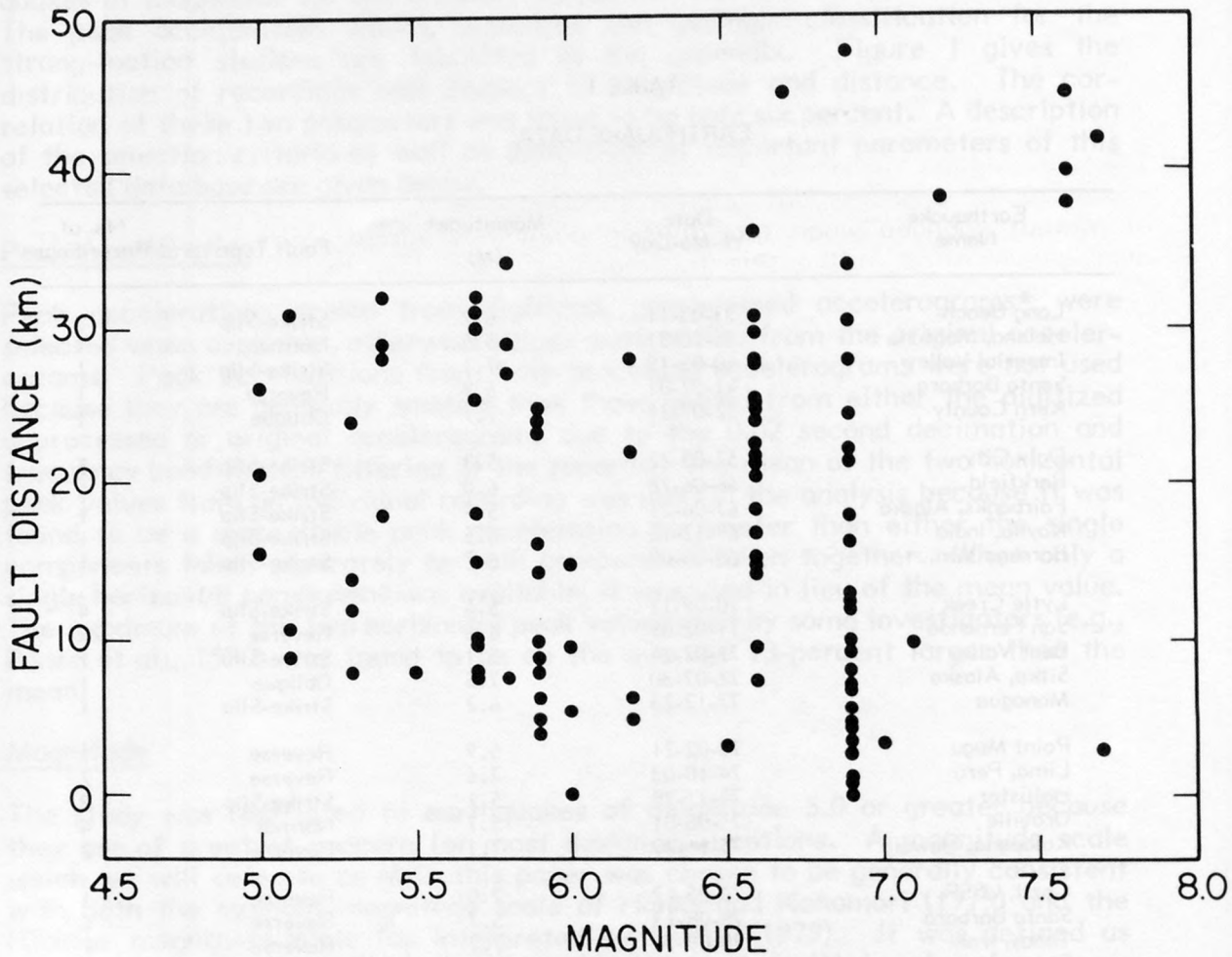

Figure 1. The distribution of strong-motion recordings with respect to magnitude and distance.

used because it was unavailable for many of the events used in this study and in many cases was less reliably determined than either M_L or M_S.

The actual agreement between our selected magnitude M and the moment-magnitude scale was tested by a comparative analysis. For the 18 events in the selected data base for which moment magnitudes were available, the average difference between the two scales was less than 0.2 units, with only two events (1974 Lima, Peru, and 1979 Imperial Valley) deviating by more than 0.3 units. The selected magnitudes were found to be quite insensitive to the actual value chosen as the division point between the choice of M_L or M_S. Of the few values of M that changed when this division point was varied from 5.5 to 6.5, the average variation in the selected magnitude was less than 0.2 units. These variations may be compared with a standard deviation of about 0.25 units for most reported magnitude values.

Source-To-Site Distance

Peak acceleration data were restricted to recording stations for which an accurate estimate of the shortest distance between the station and the fault rupture surface was available or could be determined. We found this distance, hereafter referred to as fault distance, to be statistically superior to either epicentral or hypocentral distance in representing the near-source attenuation characteristics of PGA. Closest distance to the fault rupture is believed to represent a more physically consistent and meaningful definition of distance for earthquakes having extensive rupture zones. These distances were computed from either the surface expression of faulting or the distribution of aftershocks. Consistent with the restriction to the near-source region, data were selected if distances were within 30 kilometers for $M \leq 6.25$ and within 50 kilometers for $M > 6.25$.

Site Geology

Peak accelerations from a wide range of site conditions were included in the analysis so that statistical trends in PGA between various geological classifications could be examined. A description of the classification scheme is found in Table 2. Based on results presented later in this paper, stations known to be situated at sites underlain by shallow soil deposits or extremely soft soils were not included in the final analysis. Statistical analysis has shown that the accelerations recorded at these sites are significantly different from those recorded at the other site conditions.

The Pacoima Dam record of the San Fernando earthquake was specifically excluded from the analysis for several reasons. First, the site experienced extreme topographic amplification (Boore, 1973; Mickey, et al., 1973). Second, the large gradation in wave propagation velocities and the low material damping in the upper 30 meters of rock (Duke et al., 1971) created a condition of extreme high-frequency resonance, thus placing the site in a category similar to shallow soil deposits. Third, there is evidence to suggest that the east-west response of the dam significantly amplified the S74°W component of the recorded motion (Mickey, et al., 1973; Reimer, et al., 1973).

TABLE 2

GEOLOGICAL CLASSIFICATION SCHEME

Site Geology	Description	Classification
Recent Alluvium	Holocene Age soil deposits with rock ≥10 m deep	A
Pleistocene Deposits	Pleistocene Age soil deposits with rock ≥10 m deep	B
Soft Rock	Sedimentary rock, soft volcanics and soft metasedimentary rock	C
Hard Rock	Crystalline rock, hard volcanics and hard metasedimentary rock	D
Shallow Soil Deposits	Holocene or Pleistocene Age soil deposits < 10 m deep overlying Soft or Hard Rock	E
Soft Soil Deposits	Extremely soft or loose Holocene Age soils such as beach sand or recent floodplain, lake, swamp, estuarine, and delta deposits.	F

Instrument Location

In order to assess the effects of the size and embedment of structures on recorded ground motion, peak acceleration data recorded on ground-level and basement-level instruments were selected for analysis. Ground-level instruments included those located on the ground level of buildings without basements, those housed within small shelters in the free field, and a few instruments located near the abutments of dams and bridges. Although the Koyna Dam record was actually located in the lower gallery within the dam, this recording was used in the analysis since it was believed to be representative of the motion at the base of the dam (Krishna et al., 1969).

In order to minimize possible bias associated with the large number of accelerations recorded during the 1971 San Fernando earthquake, we have used the San Fernando data reported by Boore et al. (1980). The criteria they applied lead to the selection of only a few stations from densely instrumented locations, such as downtown Los Angeles, resulting in a reasonable distribution of site types, distances, and instrument locations.

GROUND MOTION MODEL

The mathematical relationship used for modeling the scaling characteristics of near-source peak acceleration is expressed by the following equation:

$$PGA = a \exp(bM) \left[R + C(M)\right]^{-d} \qquad (1)$$

where PGA is peak ground acceleration, R is fault distance and M is magnitude. This functional form was selected because, when used with regression analyses, it is capable of modeling possible nonlinear magnitude and distance scaling effects in the near field that may be supported by the data while incorporating the important features of other empirical relationships. The far-field properties of this relationship are characterized by the coefficient b which controls magnitude scaling, and the coefficient d which controls the geometrical attenuation rate.

The parameter C(M) modulates PGA attenuation at distances close to the fault where little geometrical attenuation is expected (Hadley and Helmberger, 1980). The distance at which the transition from far-field to near-field attenuation occurs is probably proportional to the size of the fault rupture zone, especially fault length for the larger shallow-focus events. Since fault rupture dimensions scale exponentially with magnitude, it would be expected that C(M) also scales exponentially with magnitude, as suggested by Esteva (1970). Therefore, the following relationship was used to model C(M):

$$C(M) = c_1 \exp(c_2 M) \qquad (2)$$

Weighting Scheme

Weights were assigned to each recording to control the influence of the well-recorded earthquakes in the data base. It was thought that these weights should

depend on distance in order to account for the added information on attenuation represented by data from a single earthquake that are well-distributed with respect to distance. Of special concern were the 1971 San Fernando earthquake (24 recordings) and the 1979 Imperial Valley earthquake (31 recordings) which, combined, represent 48 percent of the acceleration data used in this study.

Seven weighting schemes were considered. At the one extreme was an unweighted analysis in which each recording carried an equal weight. In this case, well-recorded earthquakes have their greatest influence. For example, under this scheme, the 1979 Imperial Valley earthquake would have a weight of 27 percent (31 of 116 recordings) whereas the 1978 Tabas event would have a weight of 0.9 percent (1 of 116 recordings). At the other extreme was a weighting-by-earthquake scheme in which each earthquake carried an equal weight in the analysis. Here, well-recorded earthquakes have their least influence in the regressions with, for example, the Imperial Valley and Tabas events each having a weight of about four percent. The five other schemes used a number of distance intervals or bins in determining the weights, with earthquakes being weighted equally within each interval. These included nine-, eight-, seven-, five-and three-bin schemes.

Neither of the two extreme cases was considered to be a reasonable representation of the data. The unweighted case was found to place entirely too much emphasis on the well-recorded data at the expense of significant, singly-recorded events. For instance, Campbell (1980) found this scheme to give results identical to those obtained by removing the large magnitude non-North American events (1976 Gazli, 1978 Tabas, 1974 Lima and 1967 Koyna earthquakes) whose contribution to the magnitude scaling of PGA, especially in the near field, is significant but whose contribution to the data base is only five recordings. On the other hand, weighting-by-earthquake gives the same weight to an event having one recording as it does to a multiply-recorded event. Yet, the singly-recorded event provides no direct information on the attenuation of PGA with distance, and it represents a relatively unstable point estimate of the average PGA that prevailed during the event at that specific distance. Campbell (1980) found the results for the weighting-by-earthquake scheme to be virtually identical to those obtained by removing the 31 records of the 1979 Imperial Valley earthquake from the analysis, thus totally discounting this very significant event.

The nine-bin weighting scheme was chosen for use in this study because it represents a reasonable balance between the two extreme cases discussed above. This approach balanced the important distance attenuation characteristics of well-recorded earthquakes with the near-source magnitude scaling characteristics of the few significant singly-recorded events. To determine the weights the range of distances used in the analysis (0 to 50 kilometers) was divided into nine intervals in which each recording was assigned a relative weighting factor of $1/n_{ij}$, where n_{ij} is the total number of acceleration recordings for the i^{th} earthquake within the j^{th} distance range. The weights were then normalized so that their sum totalled the number of recordings used in the analyses. This assured that the statistics of the analyses would represent the correct number of degrees-of-freedom. The distribution of earthquake recordings within each distance interval is presented in Table 3.

TABLE 3

DISTRIBUTION OF EARTHQUAKE RECORDINGS BY DISTANCE

Distance Range (Km)	Earthquake	No. of Recordings
0 - 2.4	Parkfield 1966	1
	Imperial Valley 1979	6
2.5 - 4.9	Tabas, Iran 1978	1
	Koyna, India, 1967	1
	Gazli, USSR, 1976	1
	Coyote Lake 1979	2
	Imperial Valley 1979	4
5.0 - 7.4	Long Beach 1933	1
	Parkfield 1966	1
	Managua 1972 (m_b 5.6)	1
	Coyote Lake 1979	1
	Imperial Valley 1979	5
7.5 - 9.9	Helena, Montana	1
	Daly City 1957	1
	Parkfield 1966	1
	Hollister 1974	1
	Oroville 1975	1
	Bishop 1978	1
	San Fernando 1971	2
	Coyote Lake 1979	2
	Imperial Valley 1979	2
	Santa Barbara 1978	3
10.0 - 14.0	Imperial Valley 1940	1
	Santa Barbara 1941	1
	Santa Barbara 1978	1
	Hollister 1974	2
	Daly City 1957	3
	Imperial Valley 1979	5
14.1 - 19.9	Parkfield 1966	1
	Fairbanks, Alaska 1967	1
	Lytle Creek 1970	1
	Santa Barbara 1978	1
	Malibu 1979	1
	Coyote Lake 1979	2
	Imperial Valley 1979	2
	San Fernando 1971	7
20.0 - 28.2	Santa Barbara 1978	1
	Daly City 1957	1
	Lytle Creek 1970	1
	Point Mugu 1973	1
	Bishop 1978	1
	Coyote Lake 1979	2
	Long Beach 1933	2
	Malibu 1979	2
	Imperial Valley 1979	4
	San Fernando 1971	10
28.3 - 40.0	Bear Valley 1972	1
	Lima, Peru 1974	1
	St. Elias, Alaska 1978	1
	Lytle Creek 1970	2
	Bishop 1978	2
	Imperial Valley 1979	2
	Oroville 1975	3
	San Fernando 1971	5
40.1 - 56.6	Kern County 1952	1
	Borrego Mountain 1968	1
	Sitka, Alaska 1972	1
	Lima, Peru 1974	1
	Imperial Valley 1979	1

Regression analysis

Two types of analyses were used in conjunction with the mathematical relationship given by Equation 1 to develop ground motion models for peak acceleration. In the first, regression analysis was used to establish all coefficients in the ground motion model. In the second, regression analysis together with certain constraints were used to control the behavior of peak acceleration near the fault rupture surface and in the far field where data were lacking. Consistent with a lognormal distribution of PGA, which was later confirmed by an analysis of residuals, the regression analysis was performed on the logarithmic form of Equations 1 and 2 with peak acceleration in fractions of gravity and distance in kilometers.

Due to the nonlinear form of the distance term, the coefficients were determined from a nonlinear weighted regression analysis using the method of least squares. This analysis resulted in the following expression for the median (50th-percentile) value of PGA:

$$PGA = 0.0159 \exp(0.868M) \left[R + 0.0606 \exp(0.700M)\right]^{-1.09} \qquad (3)$$

All the coefficients were found to be statistically significant at levels of confidence exceeding 99 percent, based on empirical distributions of the coefficients developed using procedures set forth by Gallant (1975). The 84th-percentile value of PGA is obtained by multiplying the median value by a factor of 1.45, which represents a standard error of 0.372 on the natural logarithm of PGA. The goodness-of-fit is represented by an r-square value of 0.81, which indicates that 81 percent of the variance in PGA is explained by the model. Plots of this relationship as a function of distance and magnitude showing the limits of applicability appear in Figures 2 and 3. It should be emphasized that predictions based on this expression represent the mean of the two peak horizontal values from a recording. If an estimate of the maximum value is required, an additional factor of 1.13 should be applied to the predicted values.

The scatter of the observations about their predicted values is shown in Figure 4 where the residuals from the regression analysis are plotted as a function of distance. For this prupose, the residuals have been weighted and normalized to have a mean of 0.0 and a variance of 1.0, as described later in this paper. A comparison of the predictions with the observed accelerations is made in Figures 5 and 6. In Figure 5 the data are grouped into magnitude intervals of 5.0-5.9, 6.0-6.9 and 7.0-7.7 and are plotted as a function of distance. Also plotted as solid lines are predicted curves for the bounding magnitude values of each interval. The dashed lines represent the 84th-percentile and 16th-percentile curves for the upper and lower bounds, respectively. Figure 6 gives a similar comparison versus magnitude for observations grouped into distance intervals of 0-9.9, 10.0-27.9 and 28-50 kilometers. The significant feature of these comparisons is the uniformity with which the predicted curves represent the observed behavior of these data.

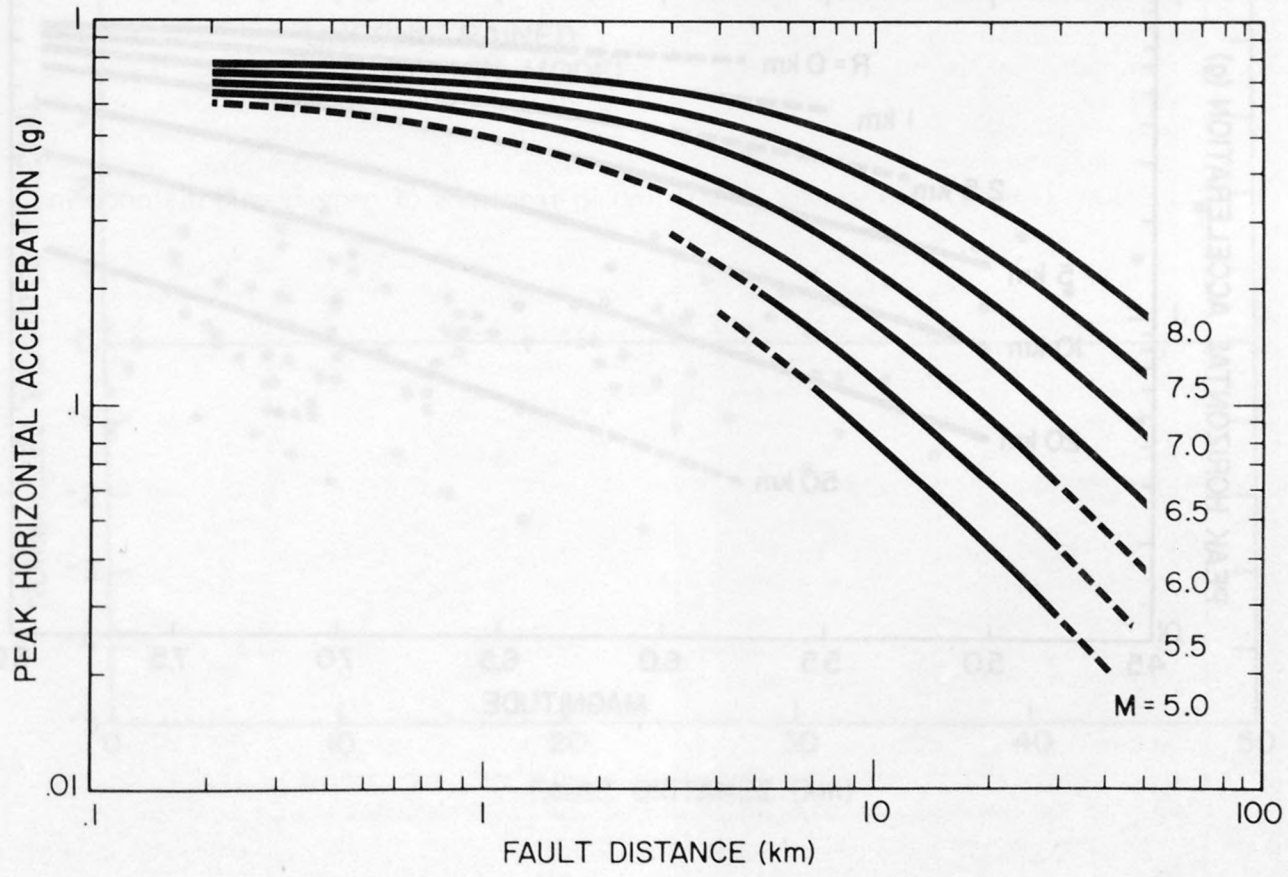

Figure 2. The unconstrained ground motion model (Eq. 3) plotted as a function of fault distance for magnitudes of 5.0 to 8.0. The dashed lines represent extrapolations of limited applicability due to either a lack of data or ambiguity as to the depth of rupture during an event.

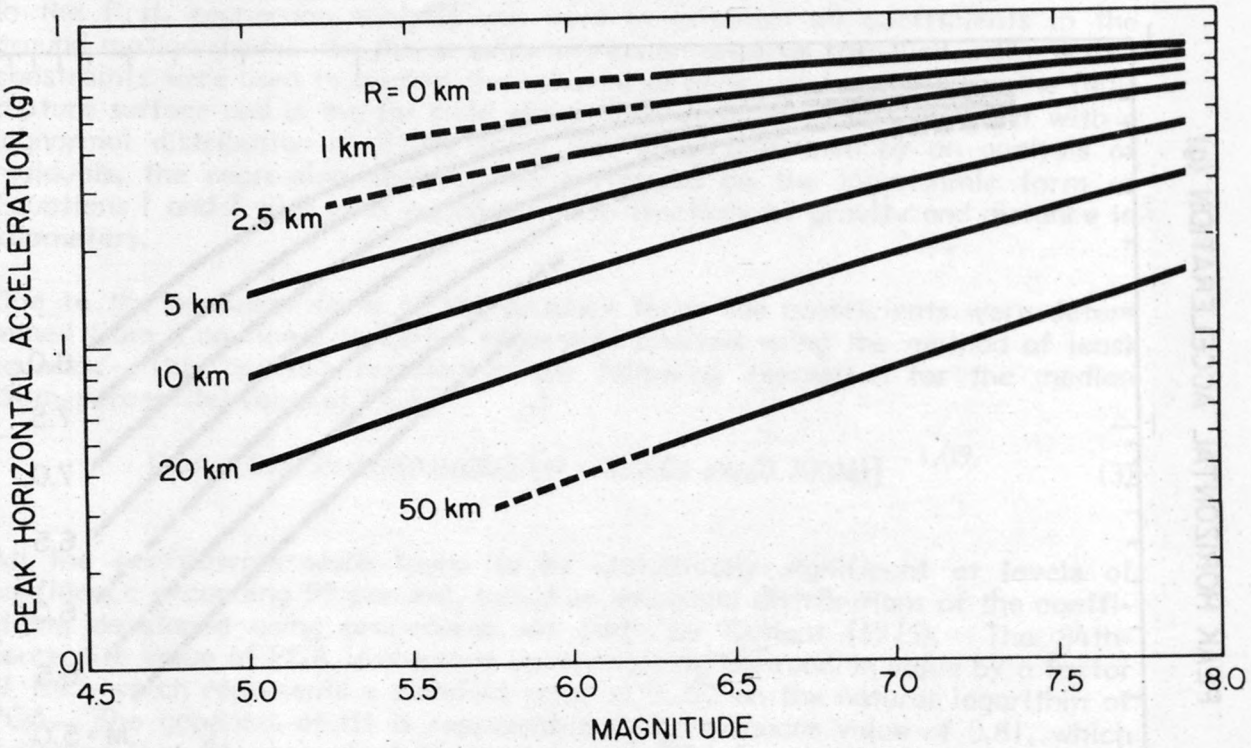

Figure 3. The unconstrained ground motion model (Eq. 3) plotted as a function of magnitude for fault distances of 0 to 50 kilometers. The dashed lines represent extrapolations of limited applicability due to either a lack of data or ambiguity as to the depth of rupture during an event.

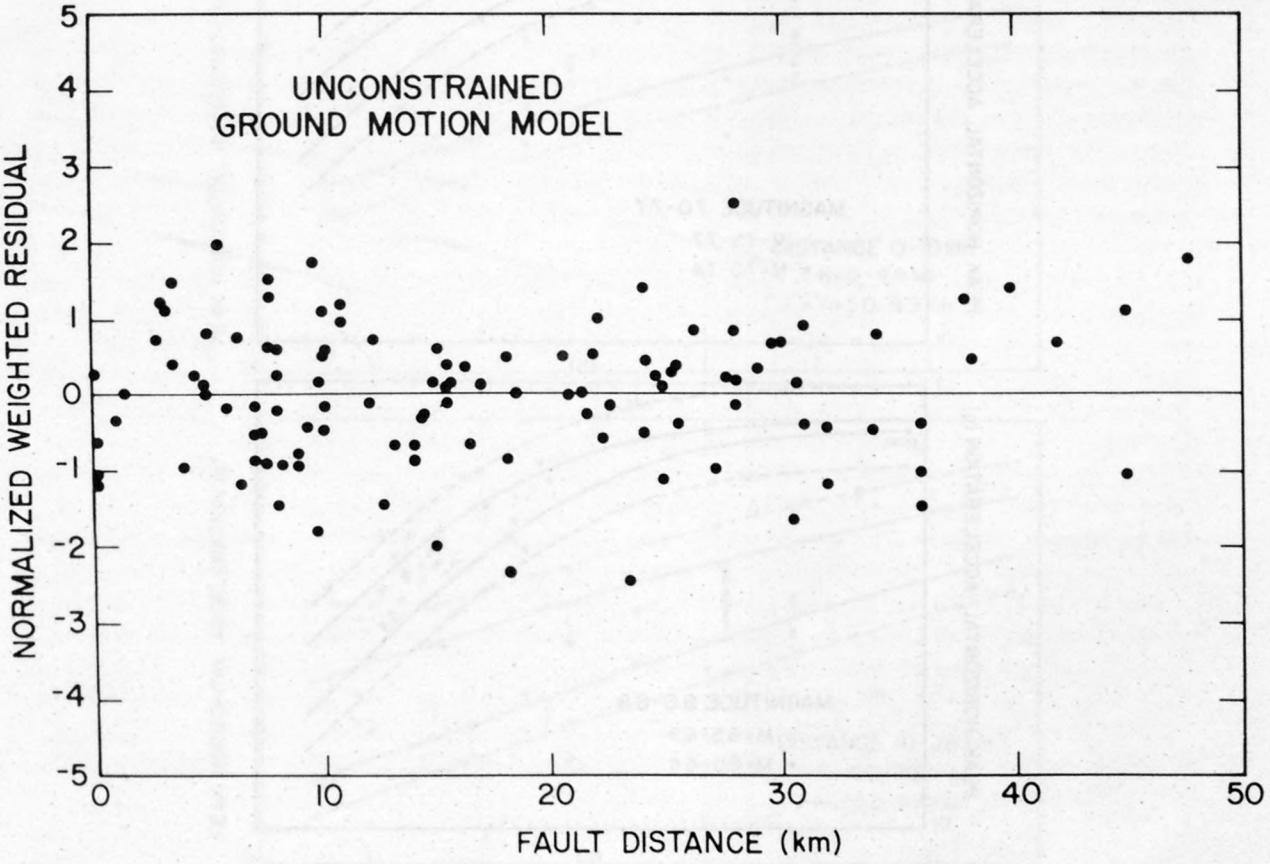

Figure 4. A plot of residuals as a function of fault distance for the unconstrained regression analysis (Eq. 3). The residuals have been weighted and normalized to have a mean of zero and a variance of unity.

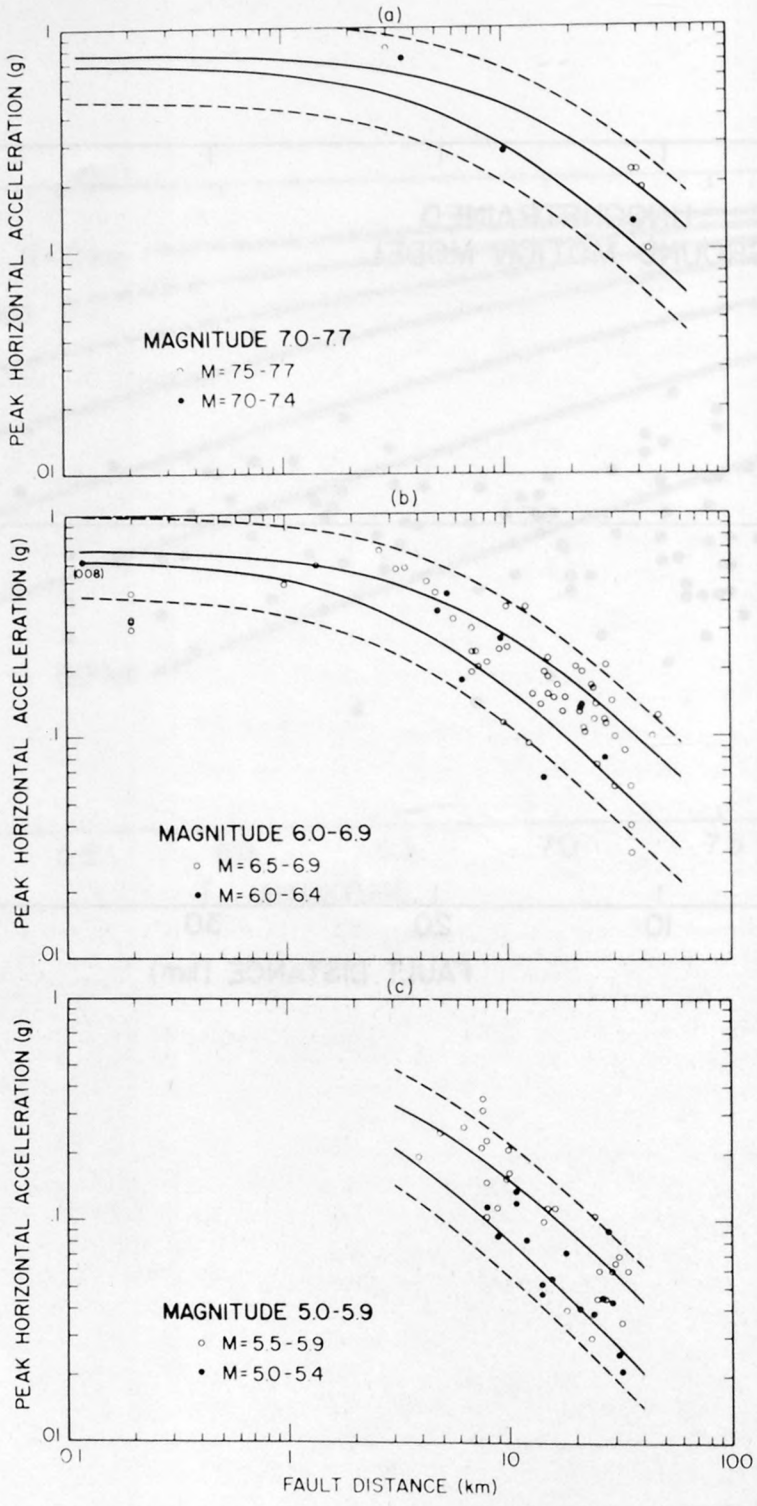

Figure 5. A comparison of the observed values of peak horizontal acceleration with the predictions of Eq. 3 for magnitude intervals of a) M 7.0-7.7, b) M 6.0-6.9 and c) M 5.0-5.9. The solid lines represent the median predictions for the bounding values of magnitude for each interval, and the dashed lines represent the 84th-percentile and 16th-percentile predictions for the upper and lower bound magnitudes, respectively.

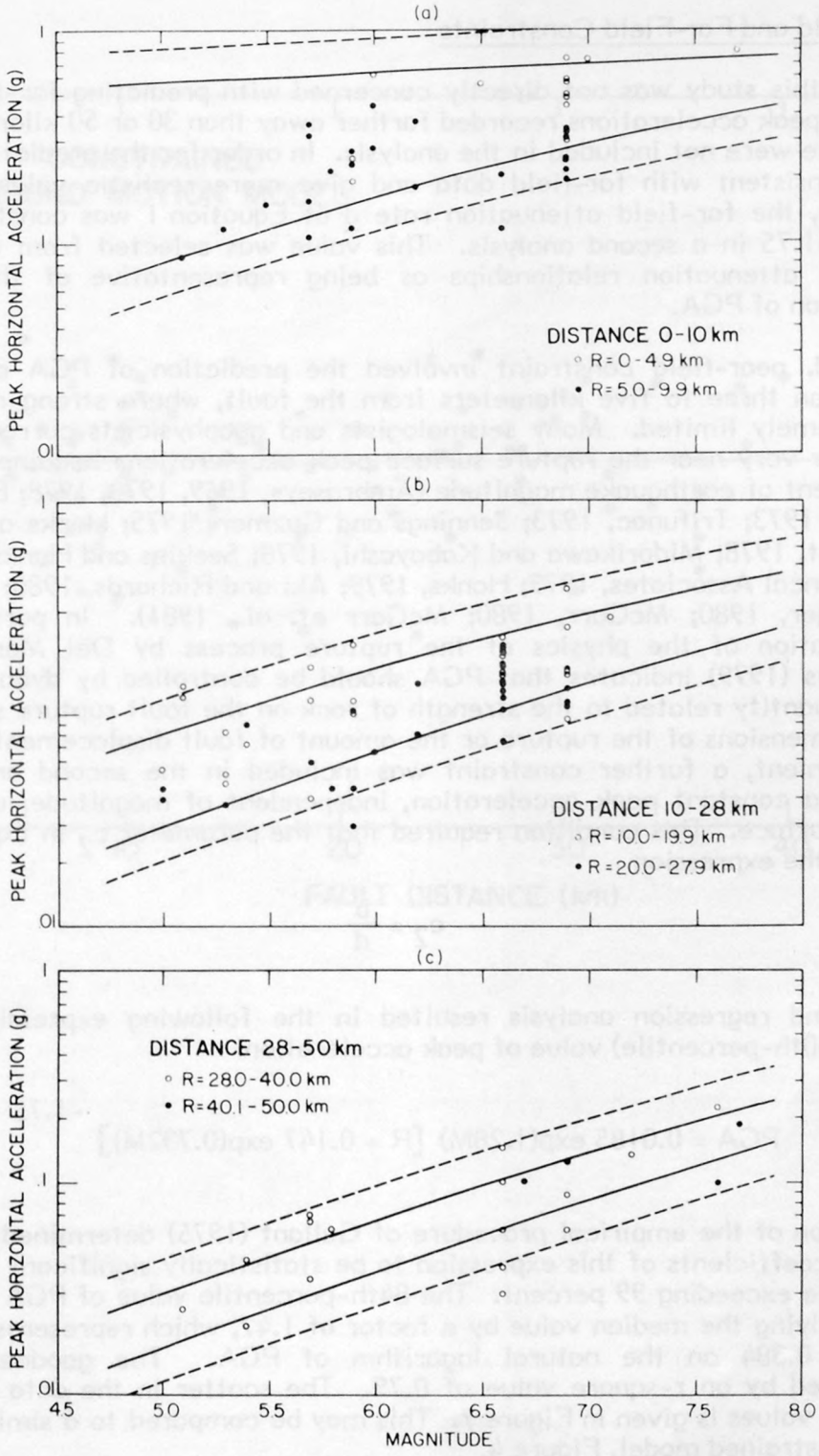

Figure 6. A comparison of the observed values of peak horizontal acceleration with the predictions of Eq. 3 for distance intervals of a) 0-10 km, b) 10-28 km and c) 28-50 km. The solid lines represent the median predictions for the bounding values of distance for each interval, and the dashed lines represent the 84th-percentile and 16th-percentile predictions for the upper and lower bound distances, respectively.

Near-Field and Far-Field Constraints

Because this study was not directly concerned with predicting far-field ground motions, peak accelerations recorded farther away than 30 or 50 kilometers from the source were not included in the analysis. In order for the predictions of PGA to be consistent with far-field data and give more realistic values at larger distances, the far-field attenuation rate $\underline{d}$ of Equation 1 was constrained to a value of 1.75 in a second analysis. This value was selected from a survey of published attenuation relationships as being representative of the far-field attenuation of PGA.

A second, near-field constraint involved the prediction of PGA at distances closer than three to five kilometers from the fault, where strong-motion data are extremely limited. Many seismologists and geophysicists currently believe that at or very near the rupture surface peak accelerations become essentially independent of earthquake magnitude (Ambraseys, 1969, 1973, 1978; Brune, 1970; Dietrich, 1973; Trifunac, 1973; Jennings and Guzman, 1975; Hanks and Johnson, 1976; Bolt, 1978; Midorikawa and Kabayashi, 1978; Seekins and Hanks, 1978; Del Mar Technical Associates, 1979; Hanks, 1979; Aki and Richards, 1980; Hadley and Helmberger, 1980; McGarr, 1980; McGarr et. al., 1981). In particular, the interpretation of the physics of the rupture process by Del Mar Technical Associates (1979) indicates that PGA should be controlled by dynamic stress-drop, a quantity related to the strength of rock on the fault rupture surface, not by the dimensions of the rupture or the amount of fault displacement. Based on this argument, a further constraint was included in the second analysis that required a constant peak acceleration, independent of magnitude, at the fault rupture surface. This condition required that the parameter c_2 in Equation 2 be given by the expression

$$c_2 = \frac{b}{d} \tag{4}$$

The second regression analysis resulted in the following expression for the median (50th-percentile) value of peak acceleration:

$$PGA = 0.0185 \exp(1.28M) \left[R + 0.147 \exp(0.732M)\right]^{-1.75} \tag{5}$$

Application of the empirical procedure of Gallant (1975) determined the unconstrained coefficients of this expression to be statistically significant at levels of confidence exceeding 99 percent. The 84th-percentile value of PGA is obtained by multiplying the median value by a factor of 1.47, which represents a standard error of 0.384 on the natural logarithm of PGA. The goodness-of-fit is represented by an r-square value of 0.79. The scatter in the data about their predicted values is given in Figure 7. This may be compared to a similar plot for the unconstrained model, Figure 4.

A comparison of the ground motion model given by Equation 5 and that given by the unconstrained analysis is made in Figure 8. Differences between these models are found to be relatively small compared to the standard error

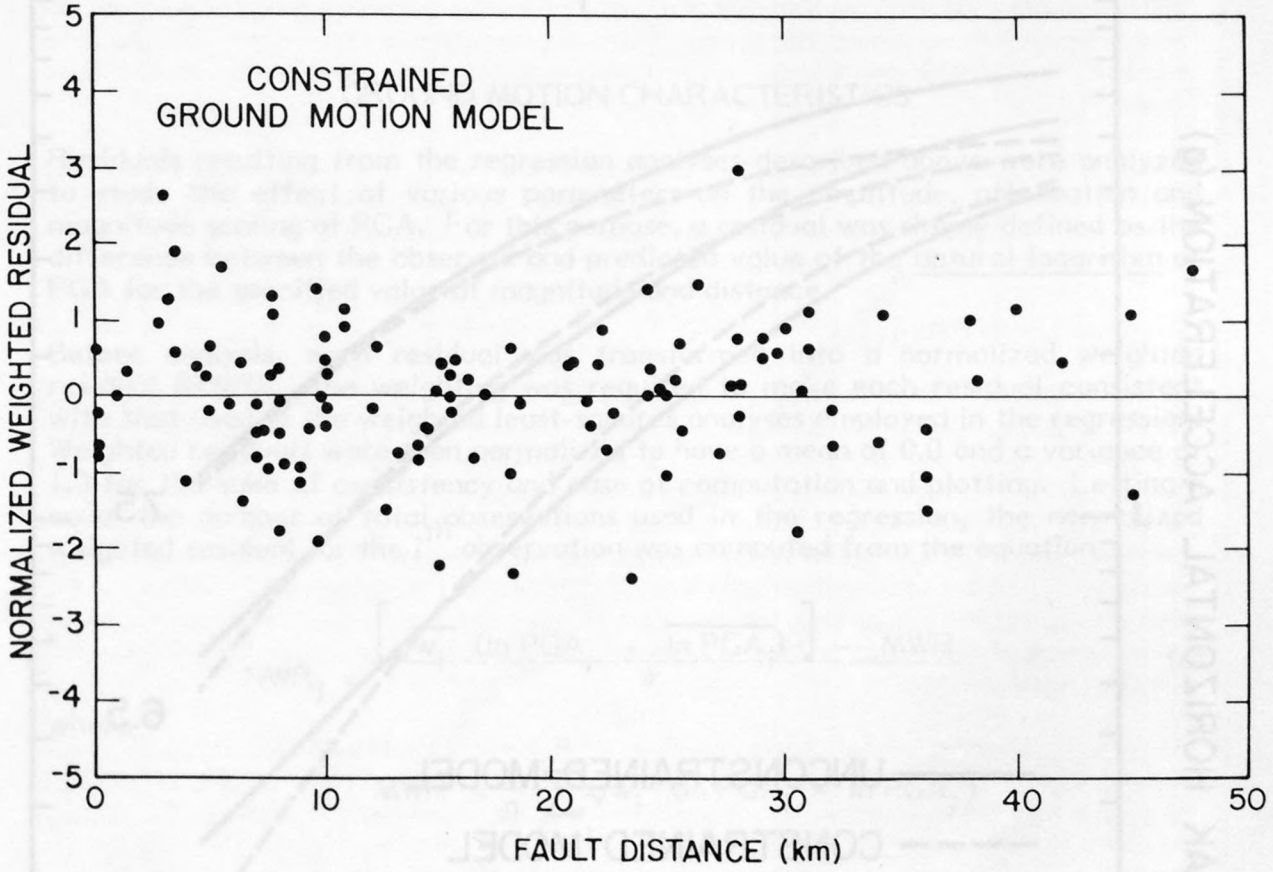

Figure 7. A plot of residuals as a function of fault distance for the constrained regression analysis (Eq. 5). The residuals have been weighted and normalized to have a mean of zero and a variance of unity.

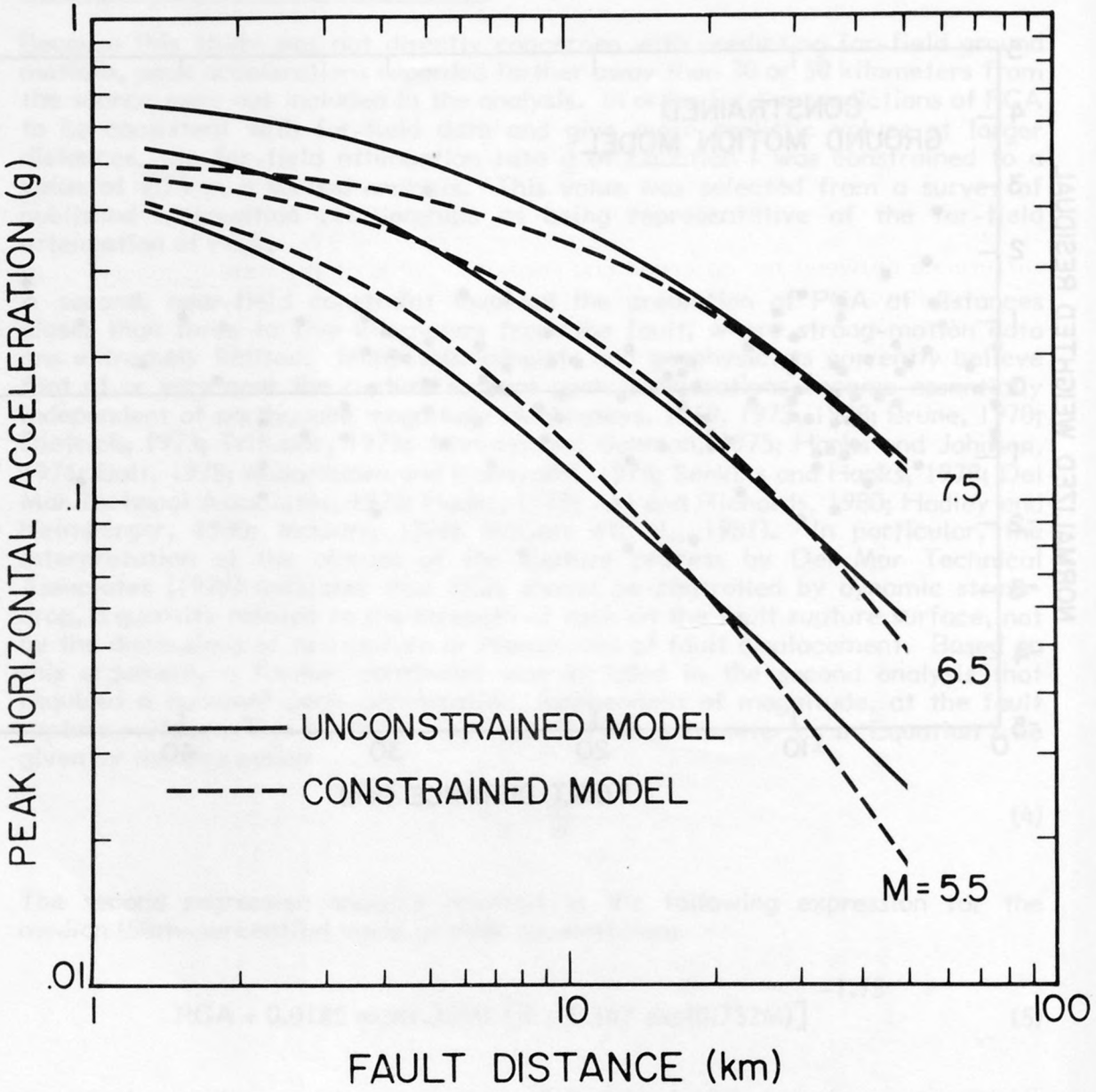

Figure 8. A comparison of the unconstrained and constrained ground motion models for magnitudes of 5.5, 6.5 and 7.5.

associated with their predictions. This reflects a large reduction in magnitude scaling in the near field that is statistically supported by the data.

GROUND MOTION CHARACTERISTICS

Residuals resulting from the regression analyses described above were analyzed to study the effect of various parameters on the amplitude, attenuation and magnitude scaling of PGA. For this purpose, a residual was simply defined as the difference between the observed and predicted value of the natural logarithm of PGA for the specified value of magnitude and distance.

Before analysis, each residual was transformed into a normalized weighted residual (NWR). The weighting was required to make each residual consistent with that used in the weighted least-squares analyses employed in the regression. Weighted residuals were then normalized to have a mean of 0.0 and a variance of 1.0 for the sake of consistency and ease of computation and plotting. Letting n equal the number of total observations used in the regression, the normalized weighted residual for the i^{th} observation was computed from the equation

$$NWR_i = \frac{\left[\sqrt{w_i}\ (\ln PGA_i - \overline{\ln PGA_i})\right]}{\sigma} - MWR \qquad (6)$$

where

$$MWR = \frac{1}{n}\sum_{i=1}^{n}\sqrt{w_i}\ (\ln PGA_i - \overline{\ln PGA_i})$$

$$\sum_{i=1}^{n} w_i = n$$

In these expressions w_i is the weight used in the regression analysis, $\ln PGA$ is the observed value, $\overline{\ln PGA}$ is the predicted value, σ is the standard error of the regression, and MWR is the mean weighted residual.

Three types of analyses were used to test the effect of various parameters on PGA. In the first analysis, the mean normalized weighted residual (MNWR) for each subset, selected on the basis of the parameter under study, was compared to a value of 0.0 appropriate for the entire population, where MNWR is given by the expression

$$MNWR = \frac{1}{n_j}\sum_{i=1}^{n_j} NWR_i \qquad (7)$$

and n_j represents the number of observations in subset j. In the second analysis, the variance of each subset was compared to the population variance of 1.0. The

third analysis consisted of visual inspection of the normalized weighted residuals plotted as a function of distance, magnitude and predicted value together with an accompanying correlation analysis to determine possible trends between the residuals and these three variables. Standard hypothesis testing techniques were used to test the significance of observed variations (e.g., Bowker and Lieber-mann, 1972).

For the purposes of this study, differences in the residuals were neglected if they were not found to be significant at a level of confidence of 90 percent or greater. Those parameter subsets found to be significantly different from the population are discussed below.

Distribution of Residuals

In order to test for potential biases in the predictions given by Equations 3 and 5 regarding magnitude, distance or predicted acceleration, plots of the normalized weighted residuals with respect to these three parameters were carefully inspected. Two such examples of these plots appear as Figures 4 and 7. If there were systematic trends in the data that were not accounted for by our statistical analysis, such trends would be evident from these plots. However, the residuals were found to be uniformly distributed with respect to magnitude, distance and the predicted accelerations. A correlation analysis confirmed that the residuals were uncorrelated with respect to these variables at a greater than 99-percent level of confidence.

Many of the statistical tests used in the analysis of residuals required the assumption that the residuals be distributed normally. Since the regression analysis was performed on the logarithm of peak acceleration, this would require PGA to be lognormally distributed. The observed distribution of the normalized weighted residuals of the regression leading to Equation 3 is given in the insert of Figure 9. Visual inspection of this histogram would appear to confirm the assumption of normalcy. A more statistical validation may be obtained from the normal probability plot presented in the same figure where the normal score, an estimate of the cumulative distribution function of the residuals, is plotted against the normalized weighted residuals. The linear trend of this plot again suggests that the residuals are normally distributed. A Kolmogorov-Smirnov test confirmed that the assumed normal distribution fell within the 90-percent confidence limits of the actual distribution, a criterion commonly used in engineering applications; thus, PGA could be accepted as being lognormally distributed. Similar results were obtained for the constrained model (Equation 5).

Site Geology Effects

As has been noted by other investigators (e.g., Boore et al., 1980; Crouse, 1978), the potential effects of site geology were subject to possible contamination by structural effects. For instance, most of the recordings in the data base used for analysis were obtained in buildings sited on soil. Furthermore, the larger the building, the more likely the instrument was located in a basement. Thus, the effects of site geology, building size and instrument location were found to be extensively interrelated. We attempted to segregate the effects of site geology

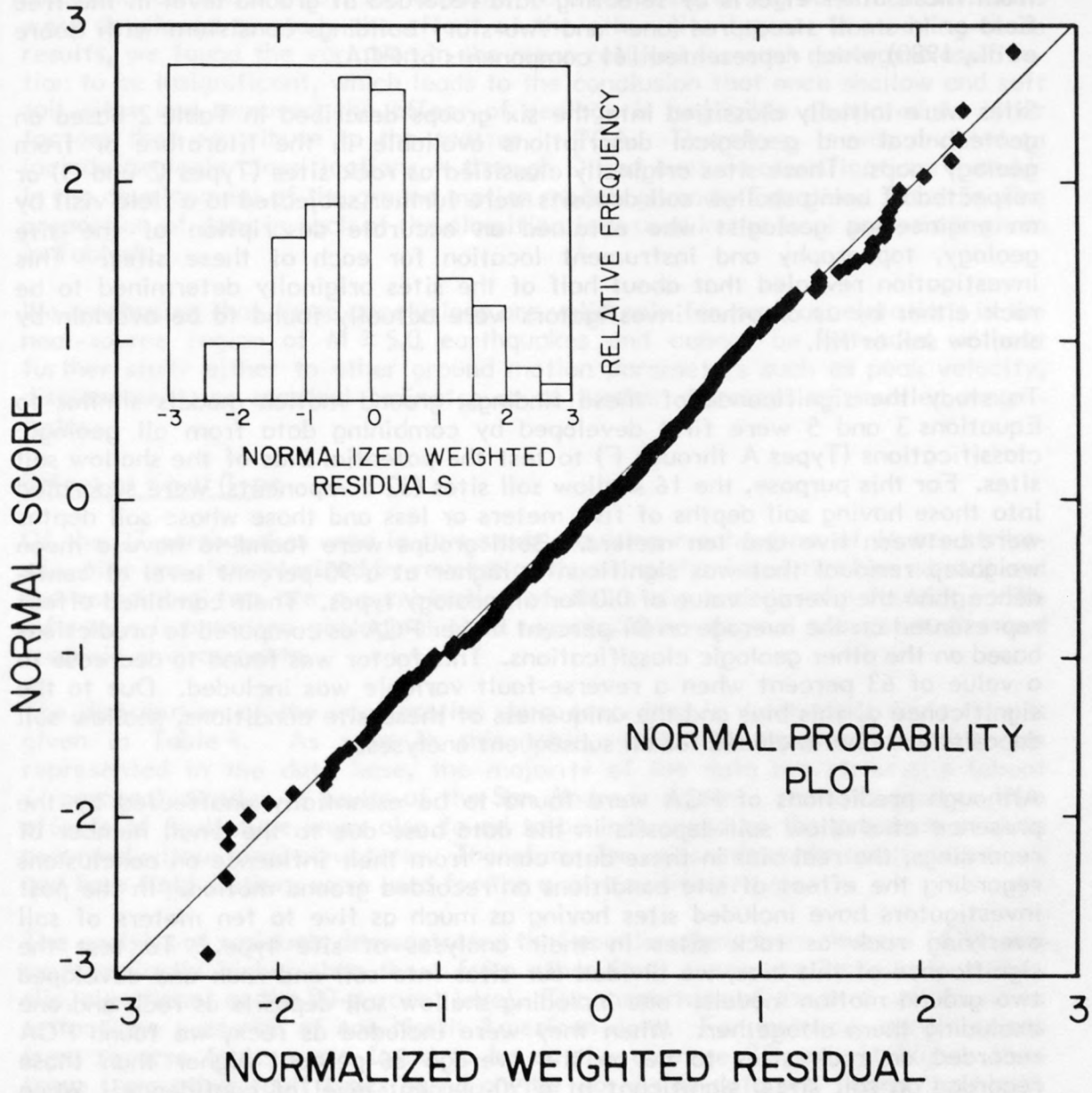

Figure 9. A normal probability plot comparing the observed distribution of residuals for the unconstrained ground motion model with that based on a normal distribution. Residuals have been weighted and normalized to have a mean of zero and a variance of unity.

from these other effects by selecting data recorded at ground level in the free field or in small structures (one- and two-story buildings consistent with Boore et al., 1980) which represented 161 components of PGA.

Sites were initially classified into the six groups described in Table 2 based on geotechnical and geological descriptions available in the literature or from geology maps. Those sites originally classified as rock sites (Types C and D) or suspected of being shallow soil deposits were further subjected to a field visit by an engineering geologist who obtained an accurate description of the site geology, topography and instrument location for each of these sites. This investigation revealed that about half of the sites originally determined to be rock either by us or other investigators were actually found to be overlain by shallow soil or fill.

To study the significance of these findings, ground motion models similar to Equations 3 and 5 were first developed by combining data from all geologic classifications (Types A through F) to test the potential bias of the shallow soil sites. For this purpose, the 16 shallow soil sites (32 components) were separated into those having soil depths of five meters or less and those whose soil depths were between five and ten meters. Both groups were found to have a mean weighted residual that was significantly higher at a 90-percent level of confidence than the average value of 0.0 for all geology types. Their combined effect represented on the average an 84-percent higher PGA as compared to predictions based on the other geologic classifications. This factor was found to decrease to a value of 63 percent when a reverse-fault variable was included. Due to the significance of this bias and the uniqueness of these site conditions, shallow soil deposits were not included for all subsequent analyses.

Although predictions of PGA were found to be essentially unaffected by the presence of shallow soil deposits in the data base due to the small number of recordings, the real bias in these data came from their influence on conclusions regarding the effect of site conditions on recorded ground motion. In the past investigators have included sites having as much as five to ten meters of soil overlying rock as rock sites in their analyses of site type. To test the significance of this bias, we divided our sites into soil and rock and developed two ground motion models: one including shallow soil deposits as rock and one excluding them altogether. When they were included as rock, we found PGA recorded on rock sites to be on the average 26-percent higher than those recorded on soil sites, significant at a 90-percent level of confidence. When shallow soil sites were excluded, differences in accelerations recorded on soil and rock were not found to be statistically significant, consistent with the findings of Boore et al. (1980).

The Punaluu, Hawaii site founded on beach sand was the only strong motion station recording a $M \geq 5.0$ earthquake that was classified as a soft soil deposit. The mean horizontal PGA recorded at this site was found to be about 30-percent lower than that predicted by Equation 3. Since soft soil deposits represent a unique site condition not encountered in most siting studies, this site was not included in all subsequent regression analyses.

Once shallow soil and soft soil deposits were removed, new ground motion models were developed to study the effect of the other site types. In studying these results, we found the variation in the mean residual for each geology classification to be insignificant, which leads to the conclusion that once shallow and soft soil sites are removed the effect of geology is negligible compared to other factors that contribute to the scatter in PGA. Therefore, it was decided to include geologic classifications A through D and exclude classifications E and F in the development of the ground motion models given by Equations 3 and 5. The proportion of data in each of the classifications used in the final analysis is given in Table 4.

We emphasize that these conclusions are valid only for peak accelerations in the near-source region of $M \geq 5.0$ earthquakes and cannot be extended without further study either to other ground motion parameters such as peak velocity, displacement, or spectral ordinates or to further distances or smaller magnitudes.

Effect of Fault Type

Of the 27 earthquakes used in this study, faulting mechanisms of 14 are strike-slip, nine are characterized by reverse or thrust mechanisms, two are normal and the remaining two are a combination of strike-slip and dip-slip faulting. The inference is based on geological field reports, seismological source studies and tectonic environments.

The distribution of the acceleration data according to earthquake fault type is given in Table 4. As seen in this table, while all types of faulting are represented in the data base, the majority of the data are strike-slip (about 61 percent), similar to faults of the San Andreas system. As with geology, the effects of fault type were also found to be influenced by the presence of data recorded within large structures. Therefore, for uniformity only small structures and free-field stations were used for the analysis of fault type.

The analysis of residuals demonstrated that accelerations from reverse faults are systematically higher than those from other fault types, predominantly strike-slip, significant at the 90-percent level. The magnitude of the bias was found to reflect the presence of non-North American data. For instance, accelerations from reverse faults were found to be on the average 28-percent higher than those from other fault types based on the worldwide data set. When non-North American data were removed, this factor reduced to 17 percent. These differences are indicative of the strong bias introduced by the 1974 Lima, the 1976 Gazli, and the 1978 Tabas earthquakes which all had reverse source mechanisms.

Building Effects

In order to isolate the effects of building size and embedment from geologic effects, the data base was divided into four subgroups, all situated on soil (Types A and B), represented by embedded and ground-level recordings in small (one- or two-story) buildings or free-field stations and in large (three- to twenty-story) buildings.

TABLE 4

DISTRIBUTION OF RECORDINGS WITH RESPECT TO GEOLOGY AND FAULT TYPE

Parameter	Number of Recordings	Percent of Total
Geological Classification		
Recent Alluvium	71	61
Pleistocene Deposits	22	19
Soft Rock	14	12
Hard Rock	9	8
Fault Type Classification		
Strike-Slip	69	59
Reverse	40	35
Normal	5	4
Oblique	2	2

The effects of both embedment and building size were studied by regression analysis of the above selected data. Due to limitations in these data, valid comparisons could only be made between small building/free-field recordings (58 recordings) at ground level and recordings obtained in the lowest basement of large buildings (20 recordings). This comparison indicated that PGA recorded in the basement of large buildings was on the average 24-percent lower than those recorded at ground level, significant at the 90-percent level of confidence. This value is somewhat less than the average reduction of 34 percent reported in a case study by Darragh and Campbell (1981) for a similar comparison of peak accelerations recorded by nearby ground-level and embedded instruments.

Effect of Steep Topography

A site investigation by an engineering geologist identified seven stations (representing 13 components of PGA) in the data base considered to be located within an area of steep topographic relief, defined as the top or side of a steep ridge, hill or slope. In addition, four stations classified as shallow soil deposits and the Pacoima Dam station were also found to be located in areas of steep topographic relief.

A statistical analysis of the seven stations used in the regression revealed that their mean residual was significantly higher than that for the entire data set, this bias being significant at the 90-percent level. Due to the small number of stations, however, the magnitude of this bias is probably not reliable and is not reported here. Similar results were obtained for the 11 topographically affected stations when shallow soil sites were included in the regression analysis. When the topographically affected stations were excluded from the analysis, predictions of PGA were found to be essentially unaffected, a result of the relatively small number of such records.

Although this bias could be the result of factors other than topography, such an explanation for the above results is not considered reasonable. Of the seven stations used in the analyses, three are located on abutments of dams, two are located in small buildings, and two are located in large buildings. Of the five earthquakes represented, two of them (7 components) have reverse or thrust mechanisms and three of them (6 components) have strike-slip mechanisms. While all of the stations are located on rock, four are situated on hard rock and three on soft rock.

The Pacoima Dam recording from the 1971 San Fernando earthquake has been the subject of much investigation in the past. The strong-motion station is located on a narrow rocky ridge near the south abutment of a 113-meter-high thin concrete arch dam. Boore (1973) used a simple topographic model together with finite difference techniques to estimate the effect of the instrument location on the recorded accelerations. He found that the peak acceleration from the S16^{o}E component of the accelerogram may have been amplified by as much as 50 percent due to the effect of topography.

Mickey et al. (1973) empirically studied the combined effects of topography, response of the dam, and local geological conditions on the Pacoima Dam recording. They simultaneously recorded eight aftershocks (M_L 2.7-3.7) at three

stations on the dam crest, at the strong-motion station and at a free-field site located on rock on the valley floor downstream from the dam. Their results indicated an average amplification of 75 percent in the peak motion recorded at the strong-motion station as compared to the free-field site for the S16°E component and an average amplification of 190 percent for the S74°W component. The large amplification for the S74°W component was thought to be due in part to the response of the dam, as interpreted from the recordings obtained on the crest of the dam and studies by Reimer et al. (1973).

If we apply the average amplification factor obtained by Mickey et al. (1973) to the peak horizontal acceleration of 0.43 g predicted by Equation 3 for the Pacoima Dam strong-motion site (M_S = 6.6, R = 3.2 km), we obtain a value of 1.0 g. If we further take into account a 17 to 28 percent increase in PGA due to the reverse mechanism of the San Fernando event, we obtain a PGA of 1.17 g to 1.28 g, values consistent with the mean peak horizontal acceleration of 1.25 g recorded during this event. Therefore, we find our predictions quite consistent with the Pacoima Dam recording when account is taken for the unusual site conditions at the station.

More evidence in support of an anomalously high PGA for the Pacoima Dam recording is the Koyna Dam recording obtained during the M_S 6.5 Koyna, India, earthquake of 1967, a strike-slip event of almost the same magnitude as the San Fernando earthquake. This station, located near the base of the dam and about three kilometers from the rupture surface, recorded a mean peak horizontal acceleration of 0.56 g, less than half of that obtained at the Pacoima Dam site.

SENSITIVITY STUDIES

A study was conducted to determine the sensitivity of the predictive ground motion models (Equations 3 and 5) with respect to the data base, selection criteria and various assumptions incorporated in the analyses. Studies were concentrated in six main areas: (1) the effect of the functional form of the scaling relationships, (2) the effect of the far-field attenuation rate, (3) the effect of the data selection criteria, (4) the effect of using fault distance, (5) the effect of large structures, and (6) the effect of the definition of PGA.

Functional Form

In addition to the unconstrained and constrained models defined by Equations 3 and 5, respectively, four additional scaling models were proposed and developed for this study to check the sensitivity of the results to the selected form of the ground motion models.

Four of the six models involved the choice of the parameter C(M) in Equations 1 and 2. In the first, the unconstrained model, the parameters c_1 and c_2 were allowed to be statistically fit by the regression analysis. In the second, the constrained model, c_2 was determined by Equation 4. In the third model, C(M) was constrained to be a constant independent of magnitude (i.e., $c_2 = 0$). In the fourth model, C(M) was set equal to zero and the remaining constants fit by the

regression. In all but the constrained model, the far-field attenuation rate was determined from the regression analyses. Near-field properties of the four models involving the choice of C(M) are described in Table 5.

A fifth model, with properties similar to a relationship proposed by Donovan and Bornstein (1978), was a log-linear relationship of the form

$$\ln PGA = A + BM + \ln R\,[D + EM + F(\ln R)] \tag{8}$$

This model was chosen for comparison with Equation 1 because (1) it provided a totally different functional form and, thus, an independent approach, (2) it could incorporate magnitude and distance scaling as a function of distance, and (3) its coefficients could be determined using linear regression analyses.

A sixth model was based on the functional form proposed by Joyner and Boore (1981),

$$PGA = a \exp(bM)\, R'^{-d} \exp(eR') \tag{9}$$

$$R' = \sqrt{R^2 + C(M)^2}$$

To accommodate magnitude and distance scaling as a function of distance, C(M), as defined by Equation 2, was used in place of Joyner and Boore's constant coefficient h in the expression for R'. Due to a lack of far-field data in our data base, an initial analysis indicated that the coefficient e should be set equal to zero. The remaining coefficients in the expression were then determined from weighted nonlinear regression analysis as was applied in the development of the unconstrained model.

Median predictions at six kilometers for magnitudes 6.5, 7.0 and 7.5 for these various models are presented in Table 6. Also included in this table are the ratios of the median plus one-standard-deviation estimates to the median value and the r-square values (goodness of fit) of the regression.

The results of an F-test on the mean square errors from each of these models as compared to the unconstrained model indicated at a 90-percent confidence level that only the C(M) = zero model had a significantly larger variance. However, the inadequacy of both this and the C(M) = constant model in characterizing the near-source behavior of PGA is discussed in some detail in the Discussion. The log-linear model was found to give results consistent with the unconstrained model. However, since its mathematical form provided little insight into the behavior of near-source accelerations as compared to Equation 1, the log-linear model was not explored further in this study. The Joyner and Boore model was found to give predictions about eight-percent higher than the unconstrained model due to a more abrupt transition from near-field to far-field attenuation properties.

The sensitivity to the simultaneous application of both near-field and far-field constraints in the development of the constrained model was tested by applying each constraint separately. In the first test, total magnitude saturation was required at the fault rupture surface by imposing the constraint given by Equation 4. In the second test, the far-field attenuation rate d was constrained

TABLE 5

NEAR-FIELD PROPERTIES OF THE FOUR GROUND-MOTION MODELS CONTAINING THE FUNCTION C(M)

Model	C(M)	Remarks
Unconstrained	$c_1 \exp(c_2 M)$	Near-field scaling of PGA is statistically determined.
Constrained	$c_1 \exp(bM/d)$	Near-field scaling is constrained to make PGA independent of magnitude at the fault rupture surface.
C(M) = constant	c_1	Near-field scaling of PGA with distance is statistically determined; near-field scaling with magnitude is constrained to be equal to far-field scaling, i.e., exp (bM).
C(M) = zero	0	Near-field scaling of PGA with both distance and magnitude is constrained to be equal to far-field scaling, i.e., $\exp(bM)R^{-d}$.

TABLE 6

SENSITIVITY RESULTS FOR VARIATIONS IN FUNCTIONAL FORM

Model	Peak Acceleration at 6 km(g)			$\frac{\text{Median} + 1\sigma}{\text{Median}}$	r^2
	6.5	7.0	7.5		
Unconstrained	0.31	0.39	0.48	1.45	0.81
Constrained	0.32	0.37	0.41	1.47	0.79
C(M) = Constant	0.30	0.42	0.59	1.47	0.79
C(M) = 0	0.23	0.32	0.43	1.58	0.70
Log-Linear	0.31	0.38	0.47	1.45	0.82
Joyner and Boore	0.33	0.42	0.52	1.45	0.81

to 1.75. By applying each constraint separately, the predictions at a distance of six kilometers were found to agree closely with those of the unconstrained model, varying by five percent or less for magnitudes of 6.5 to 7.5.

Far-Field Attenuation Rate

The far-field attenuation rate $\bar{d}$ was constrained to a value of 1.75 in the development of the constrained model consistent with other investigators' far-field studies. The sensitivity of the predictions of the constrained model to this assumption in the near field was studied by varying the assumed value of $\bar{d}$. In the first analysis we allowed the parameter to be fit by the regression, which selected a significantly smaller value of 1.07. This unrealistic value of $\bar{d}$ reflects the limitation of near-source data in defining a far-field attenuation rate. Two additional analyses constrained this parameter to values of 1.5 and 2.0, respectively. The range of values selected represent a reasonable variation of this parameter, as determined from a literature survey of available attenuation models.

The results of the analyses are presented in Table 7. Variations in predictions of PGA at six kilometers for magnitudes of 6.5 to 7.5, as compared to the constrained model, are less than eight percent, demonstrating relative insensitivity to this parameter. An F-test on the mean square errors also confirmed that there was no significant difference among these models at the 90-percent confidence level.

Data Selection Criteria

Peak acceleration data were excluded from analysis for a variety of reasons. The impact of excluding these data on the predictions of PGA for moderate to large magnitude earthquakes is assessed in this section.

There are essentially two classes of data of $M \geq 5.0$ that were excluded from analysis. The first class (hereafter referred to as Class I) represents data that were originally included as part of the general near-source data base, but were subsequently excluded from the selected data base used in the regression analyses. These data met all the general criteria outlined in the beginning of the section describing the near-source data base but did not pass the subsequent criteria used to select data for analysis. The second class of data (hereafter referred to as Class II) were originally excluded as part of the near-source data base, not passing the general criteria.

Class I Data: A summary of Class I data together with a brief description of the reasons for their exclusion is summarized in Table 8. They are represented by relatively modern events, being recorded within the last 13 years.

The impact of excluding shallow soil sites was assessed by an analysis limited to data from small structures and free-field sites consistent with our analyses on geologic effects. Regressions based on the unconstrained model were compared to a similar regression that included the 16 recordings from shallow soil sites. Predictions of PGA at a distance of six kilometers for magnitudes of 6.5 to 7.5

TABLE 7

SENSITIVITY RESULTS FOR VARIATIONS IN FAR-FIELD ATTENUATION RATE FOR THE CONSTRAINED MODEL

Attenuation Rate (d)	Peak Acceleration at 6 km(g)			$\frac{\text{Median} + 1\sigma}{\text{Median}}$	r^2
	6.5	7.0	7.5		
1.07	0.31	0.39	0.45	1.46	0.81
1.50	0.32	0.37	0.42	1.47	0.79
1.75*	0.32	0.37	0.41	1.47	0.79
2.00	0.31	0.36	0.39	1.48	0.78

*Value of d used in the development of the constrained model

TABLE 8

A SUMMARY OF CLASS I DATA EXCLUDED FROM ANALYSIS OF PGA

Description	No. of Events	No. of Recordings	Magnitude Range (M)	Distance* Range (km)	Acceleration Range (g)
Shallow Soil Sites	7	16	5.0-7.1	4-36	.06-.42
Fault Distance Unavailable	11	19	5.0-5.3	2-28**	.02-.35
Pacoima Dam Site, 1971 San Fernando Earthquake-- Extreme Topographic Amplification	1	1	6.6	3.2	1.25
1971 San Fernando Earthquake Data--Excluded from Boore et al. (1980)	1	39	6.6	19-50	.05-.27
Punaluu Site, 1975 Kalapana, Hawaii Earthquake-- Loose Beach Sand	1	1	7.1	27	.11

* Fault Distance

** Epicentral Distance

were found to increase by less than five percent, this accompanied by a ten-percent increase in the standard error and a six-percent decrease in the goodness of fit. The small variation in the predictions is essentially due to the small number of such recordings, since, on the average, observed PGA for the shallow soil sites were found to be 84-percent higher than predicted values based on the other geologic classifications.

San Fernando earthquake data were selected using the criteria set forth by Boore, et al. (1980) in an attempt to minimize the impact of large clusters of predominantly tall buildings in areas such as downtown Los Angeles. We found 39 recordings, excluding the Pacoima Dam record, meeting our selection criteria that were originally excluded from the analysis. We found that by including these data in the analysis, the predictions were essentially unchanged. This is believed to be principally due to the effect of the weighting scheme, which was designed to control the influence of well-recorded earthquakes.

The exclusion of the Pacoima Dam recording* of the 1971 San Fernando earthquake, although justified in a previous section, is relatively controversial, since it represents the largest horizontal peak recordings of acceleration obtained thus far in the world. However, the addition of this station resulted in only a five-percent increase in predicted PGA at six kilometers for magnitudes of 6.5 to 7.5.

Sensitivity to the exclusion of data for which fault distances were not available is not as straightforward to analyze, since these data could not simply be added to the selected data and the analysis repeated. It was decided that the best analysis would be one in which the observed value of PGA would be compared to predictions based on epicentral distance given by Equation 10. Such a comparison is shown in Figure 10, where the average observed horizontal PGA is plotted versus that predicted by Equation 10.

This figure indicates that the observations are distributed evenly about their median predictions (solid line) and, therefore, are found to be consistent with the rest of the data in the selected data base. Furthermore, we find that seven observations fall outside the plus and minus one-standard-deviation predictions (dashed lines), whereas about six would be expected from a log-normal distribution. This indicates that the scatter in these data are also consistent with that represented by the selected data base. Therefore, we conclude that the inclusion of these data would probably have a negligible effect on the results of this study.

The effect of excluding the Punaluu, Hawaii recording from the analysis was not studied. This recording is low with respect to its prediction based on the unconstrained and constrained models. However, since it represents only one recording, no significant reduction in the median predictions of PGA would be expected if it were included.

---

* We have shown in a previous section that the recorded value of 1.25 g at the Pacoima Dam station is consistent with our predictions when empirical adjustments for the unusual site conditions at this station are applied.

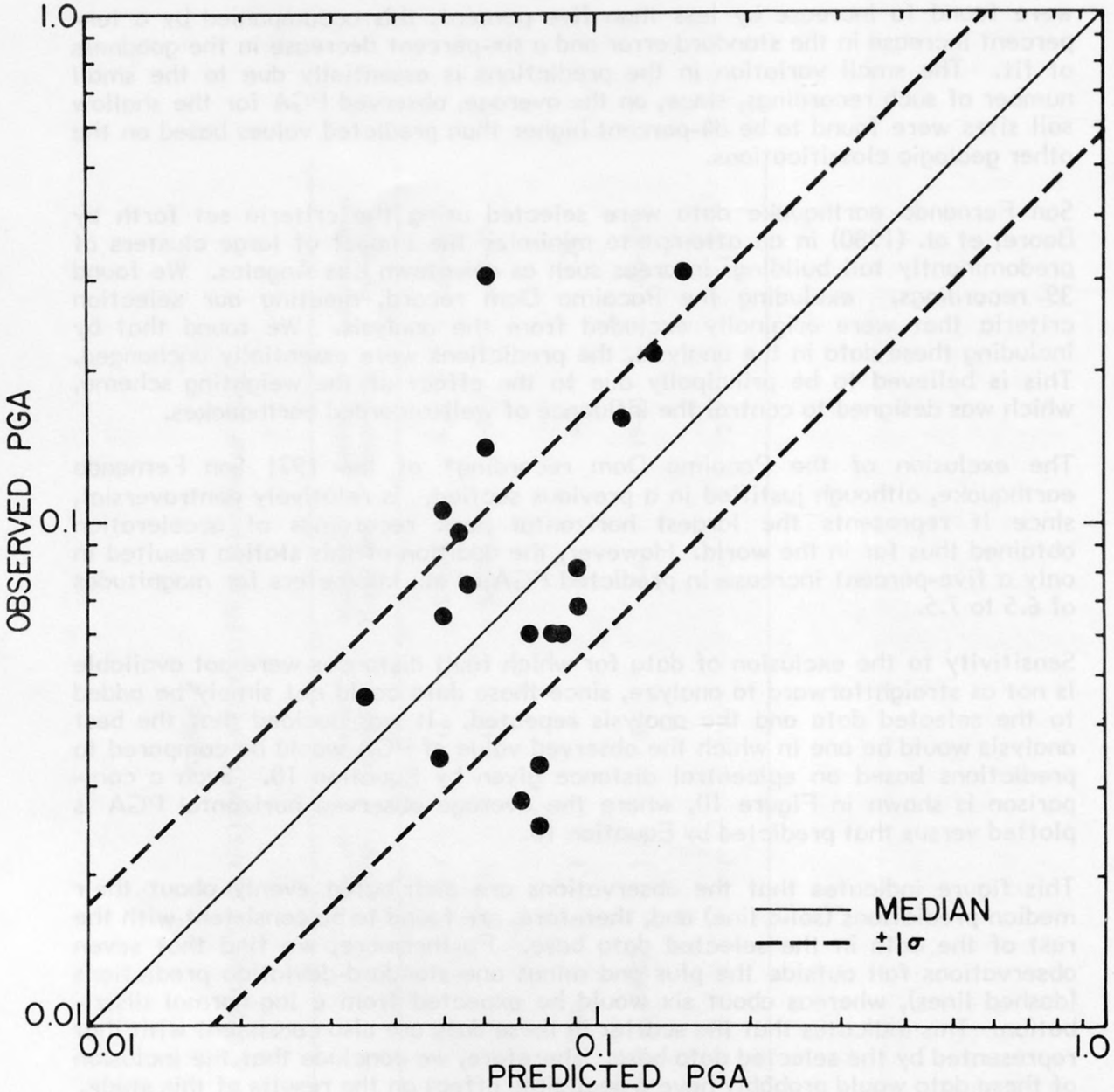

Figure 10. A comparison of observed versus predicted peak accelerations for excluded Class I data with unknown fault distance.

Class II Data: These data, summarized in Table 9, are primarily composed of older recordings obtained from 1933 through 1967. They were excluded from the near-source data base for such reasons as imprecise magnitude determinations, late instrument triggering, inaccurate locations, and undeterminable fault distances. Further discussion is presented below.

The triggering mechanism of the older USGS strong-motion instruments caused relatively large trigger delays with the result that many of the older near-source recordings begin well within the strong phase of shaking. This, of course, results in unreliable estimates of peak acceleration from these recordings and would tend to underestimate the actual PGA.

Due to limited distribution of local seismometer networks in southern and northern California prior to a few decades ago, magnitude determinations generally were reported to the nearest one-half magnitude unit, which by our criteria represents an unacceptable level of uncertainty. The lack of an adequate distribution of seismometers also resulted in errors in epicentral locations of 15 kilometers or greater for certain older earthquakes. Most often, focal depths could not be sufficiently determined from these data and were therefore constrained to 16 kilometers in order to determine the epicenter. Such errors are unacceptably large for meaningful analyses of peak accelerations within 30 or 50 kilometers of the source, and therefore, these data were not used in our near-source studies. Furthermore, the unavailability of aftershock data of sufficient quality and completeness precluded the determination of fault distances for many of these older recordings.

In addition, three recent earthquakes were excluded from analysis. One was excluded because the accuracy of the location was unknown. The other two were excluded because in one case the largest component was less than 0.02 g, and in the other case, both components were less than 0.05 g, their actual values being unknown.

Class II data were analyzed in a manner similar to the Class I data for which significant distances were not available. The mean observed horizontal PGA was compared to that predicted by Equation 10 based on epicentral distance. This comparison is shown in Figure 11. Although we find the observations to be distributed fairly evenly about the median predictions (solid line), twice as many fall below the minus one-standard-deviation prediction than above the plus one-standard-deviation level (dashed lines). Furthermore, one would expect ten values to fall outside these limits assuming a log-normal distribution of PGA, whereas 16 are observed. The bias, then, appears to be associated with lower than average observed accelerations and increased scatter in the observations as was originally expected.

We may conclude from this comparison that median predictions would probably not be affected substantially by including Class II data in the analyses. If any effect is expected, it would probably be to lower the median predictions somewhat. It would appear, however, that the uncertainty in these predictions would be increased by including these data, widening the standard error bounds.

TABLE 9

A SUMMARY OF CLASS II DATA EXCLUDED FROM ANALYSIS OF PGA

Description	No. of Events	No. of Recordings	Magnitude Range (M)	Distance* Range (km)	Acceleration Range (g)
Inaccurate Location; Late Trigger; Imprecise Magnitude; No Fault Distance	25	28	5.0-7.1	6-66	.01-.31
Quality Unknown	1	1	5.0	26	.04
PGA Unknown (<.05 g)	1	1	5.2	13	--
PGA Less Than .02 g	1	1	5.2	17**	.01

* Epicentral Distance

** Fault Distance

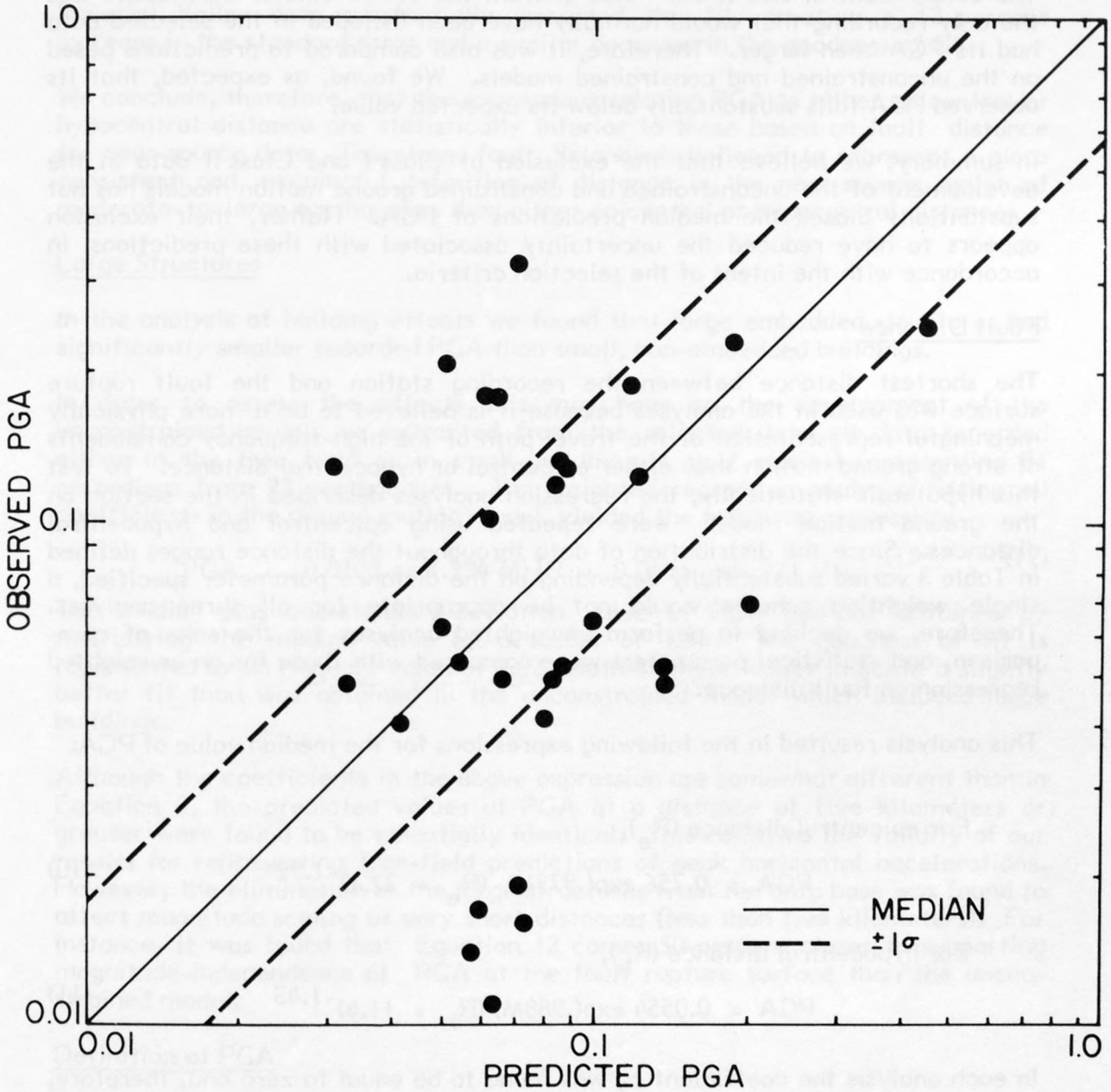

Figure 11. A comparison of observed versus predicted peak accelerations for excluded Class II data with unknown fault distance.

The SAGO Central site (PGA < 0.02 g) from the 1974 Hollister earthquake was the only recording that would normally have been included in the selected data had its PGA been larger. Therefore, it was also compared to predictions based on the unconstrained and constrained models. We found, as expected, that its observed PGA falls substantially below its expected value.

In summary, we believe that the exclusion of Class I and Class II data in the development of the unconstrained and constrained ground motion models has not substantially biased the median predictions of PGA. Rather, their exclusion appears to have reduced the uncertainty associated with these predictions, in accordance with the intent of the selection criteria.

Fault Distance

The shortest distance between the recording station and the fault rupture surface was used in the analyses because it is believed to be a more physically meaningful representation of the travel path of the high-frequency components of strong ground motion than either epicentral or hypocentral distance. To test this hypothesis statistically, the regression analyses described in the section on the ground motion model were repeated using epicentral and hypocentral distances. Since the distribution of data throughout the distance ranges defined in Table 3 varied substantially depending on the distance parameter specified, a single weighting scheme would not be appropriate for all three analyses. Therefore, we decided to perform unweighted analyses for the sake of comparison, and statistical parameters were compared with those for an unweighted regression on fault distance.

This analysis resulted in the following expressions for the median value of PGA:

For epicentral distance (R_e),

$$PGA = 0.756 \exp(.979M) \ (R_e + 32.1)^{-1.92} \tag{10}$$

For hypocentral distance (R_h),

$$PGA = 0.0554 \exp(.988M) \ (R_h + 11.4)^{-1.43} \tag{11}$$

In each analysis the coefficient c_2 was found to be equal to zero and, therefore, is not included in the above expressions. Both equations are represented by a standard error corresponding to a multiplicative factor of 1.67 and an r-square value of 0.57. This corresponds to a 33-percent increase in the standard error and a 27-percent decrease in the r-square (i.e., goodness of fit) as compared to the unweighted, unconstrained model. An F-test on the ratio of the mean square errors confirmed that the increase in the variances are statistically significant at a greater than 99-percent level of confidence.

A similar analysis was performed for the 1979 Imperial Valley earthquake (M_s 6.9) using data recorded within 50 kilometers of the fault (see Appendix). This event produced the most extensive set of strong-motion recordings within 20 kilometers of the fault rupture surface of any earthquake in history. As with

the entire data base, replacing fault distance by epicentral distance for the Imperial Valley data substantially worsened the fit, creating a 13-percent increase in the standard error and a similar decrease in the goodness of fit.

We conclude, therefore, that the expressions relating PGA to either epicentral or hypocentral distance are statistically inferior to those based on fault distance for near-source data. Therefore, fault distance is believed to represent a more consistent and meaningful definition of distance in the near-source region of moderate-to-large earthquakes than either epicentral or hypocentral distance.

Large Structures

In the analysis of building effects we found that large embedded structures had significantly smaller recorded PGA than small, non-embedded buildings.

In order to assess the effects this may have on the development of the unconstrained model, we extracted from the selected data all data recorded either in the free field or in small buildings (1 to 2 stories) representing 81 recordings from 23 earthquakes. The weighted regression analysis, fitting all coefficients in the ground motion model, yielded the following expression:

$$PGA = 0.0109 \exp(.994\ M)\,[R + 0.0491 \exp(.771\ M)]^{-1.19} \qquad (12)$$

The median plus one-standard-deviation value of PGA may be obtained by multiplying the median value by a factor of 1.44. The goodness of fit is represented by an r-square value of 0.82. Both of these values indicate a slightly better fit than was obtained in the unconstrained model which included large buildings.

Although the coefficients in the above expression are somewhat different than in Equation 3, the predicted values of PGA at a distance of five kilometers or greater were found to be essentially identical. This confirms the validity of our results for representing free-field predictions of peak horizontal accelerations. However, the elimination of the large structures from the data base was found to affect magnitude scaling at very short distances (less than five kilometers). For instance, it was found that Equation 12 comes 50-percent closer to supporting magnitude-independence of PGA at the fault rupture surface than the unconstrained model.

Definition of PGA

In essence the use of both horizontal components by most investigators in the development of ground motion models has resulted in the prediction of the mean of the two horizontal components of peak ground acceleration (hereafter referred to as mean PGA). Although unbiased estimates of this mean PGA are obtained in such an analysis, the inclusion of both components as independent data points when in fact they are correlated affects the statistics of the regression analysis. To study this effect the regression analyses resulting in Equations 3 and 5 were repeated using both horizontal components.

As expected, the use of the mean PGA was found to give median predictions of PGA that did not differ from those developed from both components. On the contrary the statistics of the regression analysis were found to vary significantly from the previous analyses. This is explained by the substantial increase in the number of data points and the increased scatter inherent in replacing the mean PGA by its two components. The most significant differences were found in (1) the standard error and goodness-of-fit parameters and (2) the statistical tests of significance.

By using both components of PGA, the standard deviation of the residuals was found to increase by nine percent. This would result in a median plus one-standard-deviation value of PGA that is 1.50 times the median for the unconstrained model and 1.52 times the median for the constrained model. The goodness-of-fit (r-square) was found to decrease by about four percent.

Statistical tests used to test for significant differences in the mean residual between a subset (e.g., geologic classification, fault-type classification, etc.) and the entire data set were found in some cases to result in different conclusions regarding the significance of observed differences when both components were used. The arbitrary increase in the number of points made it less difficult to reject the hypothesis that the mean residual of a subset was no different than that for the entire data set. In other words, the test allows smaller observed differences in order to reject the hypothesis at a specified level of confidence.

Regression analyses on each individual peak horizontal component were associated with standard errors and goodness-of-fit parameters between those obtained for both horizontal components and for mean PGA. The reduction in scatter associated with mean PGA as compared to that obtained for either horizontal component can probably be attributed to an averaging of azimuthal differences between components, which is associated with the random nature of their orientation, among the various recording stations and earthquakes used in the study.

DISCUSSION

The near-source data compiled for this study, of which most have become available only within the last several years, have served as a basis for empirically establishing PGA behavior near a fault. The mathematical relationship used to model this behavior (Equations 1 and 2) was chosen to accommodate any differences in distance and magnitude scaling in the near field required by the data. Physical insight into the observed near-field behavior of PGA is best accomplished from an investigation of the function C(M).

The value of C(M) determines the distance range for which the transition from near-field to far-field attenuation occurs. The tendency for less attenuation of PGA in the near field for values of C(M) greater than zero, which lead to finite values of PGA at the source, is what we define as distance saturation in this

study. Empirical justification for distance saturation comes from both the 1979 Imperial Valley (IV-79) earthquake and the near-source data compiled for this study.

The IV-79 data, plotted in Figure 12, show a definite trend in support of the saturation of PGA at small distances. To quantify this we performed a regression analysis on the IV-79 horizontal accelerations, including data as far as 100 kilometers from the fault in order to empirically constrain the far-field attenuation rate. For this purpose the functional forms given by Equations 1 and 2 were used, where the magnitude coefficients, $\underline{b}$ and c_2, were set equal to zero to reflect the attenuation for a specific earthquake. This analysis resulted in a C-value of 20 kilometers and a far-field geometrical attenuation rate $\underline{d} = -1.77$, values consistent with those found for the constrained ground motion model, Equation 5. The relationship developed from this analysis appears in Figure 12 as the solid curve, with the dashed lines representing the one-standard error bounds.

Values of C(M) for the unconstrained and constrained scaling relationships were found to be magnitude-dependent. These values, given in Table 10, are found to be substantially greater than zero, further supporting distance saturation of PGA in the near field. The sensitivity of these results to the IV-79 data was studied by removing this event and repeating the analyses. The values of C(M) obtained from this analysis are compared with those obtained by including the IV-79 data in Table 10. The similarity in these values confirms the tendency for all near-source data to support the saturation of PGA with distance; the 1979 Imperial Valley earthquake is not unique in this respect.

The differences in the numerical values of C(M) between the constrained and unconstrained ground motion models were found to be a result of the differences in their far-field attenuation rates. These rates required that PGA be proportional to $R^{-1.09}$ in the unconstrained relationship and to $R^{-1.75}$ for the constrained model. The larger attenuation rate, assumed for the latter model in order to make it compatible with other far-field studies, resulted in larger C(M) values in order to accommodate the distance saturation effects required by the near-source data. The similarity between the value of C(M) obtained for the IV-79 event and that computed from the constrained model (C(M) = 23 kilometers for M_s 6.9) is consistent with this finding since the far-field attenuation rate of these two relationships were found to be virtually identical.

The statistical significance of the observed distance saturation characteristics of PGA was studied by standard hypothesis testing techniques (Bowker and Lieberman, 1972). To isolate these characteristics from any magnitude saturation characteristics, a relationship constraining C(M) to be independent of magnitude was developed and tested. A statistical analysis of the value of C given by this relationship found it to be significantly greater than zero at a level of confidence exceeding 99 percent. A second analysis compared the variance obtained from this constant-C model with another model where C(M) was constrained to a value of zero, thereby eliminating any distance saturation. An F-test found the variance associated with this zero-C model to be significantly greater than the variance of the constant-C relationship at a 95-percent level of

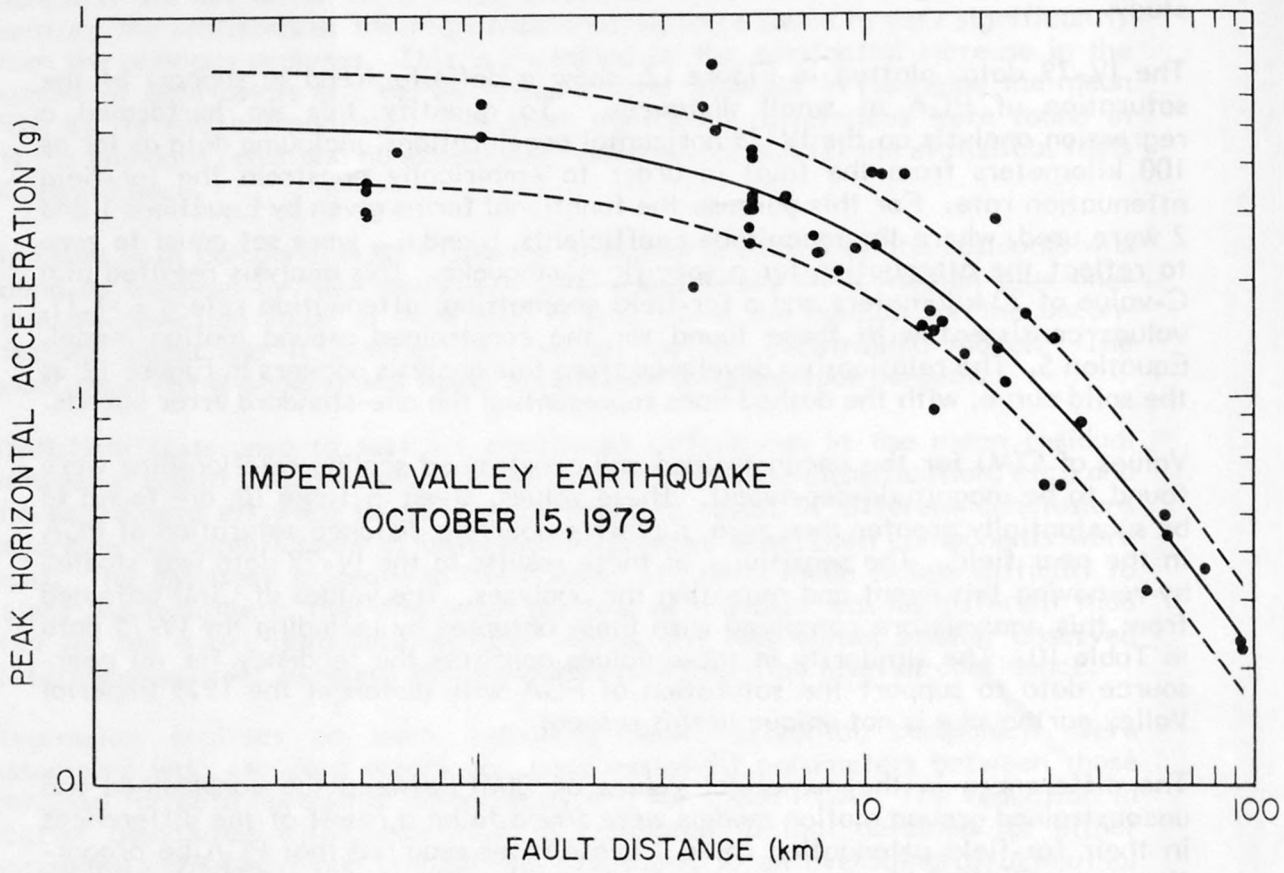

Figure 12. Observed and predicted mean horizontal peak accelerations for the October 15, 1979, Imperial Valley earthquake plotted as a function of distance from the fault. The solid curve represents the median predictions based on the observed values, and the dashed curves represent the standard error bounds for the regression.

TABLE 10

DISTANCE SATURATION CHARACTERISTICS
OF NEAR-SOURCE ACCELERATIONS

Ground Motion Model	M	C(M) (kilometers)
Unconstrained		
Including 1979 Imperial Valley Earthquake	5.5	3
	6.5	6
	7.5	12
Excluding 1979 Imperial Valley Earthquake	5.5	3
	6.5	6
	7.5	11
Constrained		
Including 1979 Imperial Valley Earthquake	5.5	8
	6.5	17
	7.5	36
Excluding 1979 Imperial Valley Earthquake	5.5	7
	6.5	16
	7.5	37

confidence. Therefore, both tests statistically confirmed the importance of distance saturation in modeling the near-source attenuation of peak acceleration.

The exponential function of magnitude adopted for C(M) was designed to accommodate possible variations in magnitude scaling with distance. Values of c_2 greater than zero indicate less dependence on magnitude as distance becomes smaller. This characteristic of PGA we define as magnitude saturation, with total saturation referring to a constant value of PGA at the fault rupture surface.

The degree to which magnitude saturation is supported by the data may be conveniently expressed by a parameter referred to as the degree of magnitude saturation (DMS) which is defined as

$$DMS = \frac{c_2 d}{b} \times 100 \qquad (13)$$

where the terms on the right-hand side of the expression represent coefficients of the ground motion model defined in Equations 1 and 2. When DMS =0% ($c_2 = 0$), the model predicts constant magnitude scaling at all distances, thereby rejecting magnitude saturation effects. When DMS = 100% ($c_2 = b/d$), the model predicts a reduction in magnitude scaling with decreasing distance leading to total magnitude saturation at the fault rupture surface. This latter constraint was used in the development of Equation 5.

The degree to which the near-source data support magnitude saturation was found to be influenced by the presence of large structures and by the rupture mechanism of the earthquakes. The results of this study appear in Table 11. The unconstrained model was found to support an 88-percent degree of magnitude saturation without any regard to building or fault-type effects. When large buildings (number of stories greater than two) were removed, this value increased to 93 percent. When reverse-fault biases were accounted for through a scaling variable, the data were found to support total magnitude saturation at the fault rupture surface consistent with the assumption used to develop the constrained model. Therefore, near-source data are found to support the saturation of peak acceleration with magnitude.

The statistical significance of the magnitude saturation characteristics of PGA comes from an analysis of the coefficient c_2 which determines the magnitude dependence of C(M). Statistical analysis found c_2 to be significantly greater than zero at levels of confidence exceeding 99 percent (Table 11). This value is significantly higher than the traditional 90-percent confidence test and establishes the importance of magnitude saturation effects in modeling the near-source behavior of PGA.

Additional statistical support is reflected in the level of confidence in the observed differences between the variances of each model listed in Table 11 and that of the constant-C model described previously. The constant-C model, while accommodating distance saturation, was constrained to exclude any magnitude

TABLE II

MAGNITUDE SATURATION CHARACTERISTICS
OF NEAR-SOURCE ACCELERATIONS

Structure Size	Fault-Type Scaling Variable	Degree of Magnitude Saturation	Confidence Level	
			Reduction in Variance	coefficient c_2
All Sizes	Not Included	88%	61%	>99%
Small	Not Included	93%	69%	>99%
Small	Included	100%	75%	>99%

saturation effects. As seen in Table 11, the highest level of confidence determined from an F-test, which corresponded to a 14-percent reduction in the variance, comes from the model that excludes large structures and provided for scaling by fault type. Although not passing the traditional 90-percent confidence test, the computed value of 75 percent demonstrates a relatively significant reduction in the variance. With the amount of scatter inherent to peak acceleration data, confidence levels much higher than 75 percent are probably not possible until more data within five kilometers or so from the fault rupture surface become available.

Independent justification of magnitude and distance saturation of peak acceleration in the near field comes from the earthquake modeling studies of Del Mar Technical Associates (1979) and Hadley and Helmberger (1980). They used numerical modeling techniques to simulate the complex physical processes that would occur during moderate-to-large earthquakes in the hopes of gaining an understanding of the behavior of the high frequency components of ground motion near a fault. They found peak accelerations scaled from their simulated accelerograms to become independent of both magnitude and distance in the near field in support of saturation. In particular, Hadley and Helmberger (1980) suggest from their results that empirical attenuation relationships of the form $PGA \propto (R+C)^{-d}$ as used in this study should incorporate a magnitude-dependent function of C in order to account for this near-field behavior. Therefore, we may conclude that the near-source behavior of peak acceleration empirically predicted by our relationships is consistent with physical earthquake processes.

The sensitivity of our predictions to various assumptions used in the development of the ground motion models was studied to test the reliability of these relationships. As described previously, these studies included the effect of model variations, far-field attenuation rate, parameter definitions, and data selection criteria. Near-field predictions of acceleration based on these studies were found to fall well within the one-standard error bounds of Equations 3 and 5 with variations generally less than five to ten percent. Of particular interest was the similarity in the predictions given by the ground motion models used in this study with predictions based on identical analyses using our data and the mathematical form of the relationships proposed by Donovan and Bornstein (1978) and Joyner and Boore (1981). In the latter analysis, our data were found to statistically support an exponential function of magnitude for the depth coefficient h, as defined by the investigators of that study, reflecting the significant magnitude saturation characteristics of these near-source data.

Data from the United States that were excluded from the analysis for reasons other than their failure to meet magnitude and distance constraints were studied to assess their potential impact on the results. They were compared either to predictions based on Equation 3 if fault distance was known or to predictions based on epicentral distance if fault distance was not known. This comparison found the excluded data to be generally consistent with the median estimates of PGA but demonstrating a larger degree of scatter. Therefore, their exclusion apparently has not systematically biased the estimates but rather has reduced the uncertainty associated with these predictions in accordance with the intent of the selection criteria.

Our ground motion models may be compared with a recent study by Joyner and Boore (1981) who used both recently available near-source data and far-field data to establish a relationship for the scaling of peak horizontal acceleration as a function of moment magnitude (Kanamori and Hanks, 1979) and closest distance from the surface projection of the fault rupture surface. Predictions based on their relationship are compared to those given by the unconstrained attenuation model (Equation 3) in Figure 13. Since their analysis used only the maximum horizontal component of peak acceleration, their values were reduced by 12 percent so they could be directly compared to our predictions of mean peak horizontal acceleration.

Inspection of Figure 13 finds their predicted values to deviate from ours by generally less than one-half of a standard error, relatively good agreement considering the differences in the data sets. Only slight differences in the shape of the curves at distances less than 50 kilometers result from the difference in the functional form of their distance term. Their distance term is defined as the square root of the sum of squares of distance and a depth term, and causes the transition from near-field attenuation to far-field attenuation to occur more abruptly than does our distance term.

The largest difference in the two relationships is in the amount of magnitude scaling at distances less than about 10 kilometers. The Joyner and Boore (1981) relationship provides for constant magnitude scaling at all distances (0-200 kilometers), independent of magnitude, corresponding to a 77-percent increase in peak acceleration per magnitude unit. Our data, on the other hand, supported reduced magnitude scaling in the near field, the amount of the reduction being dependent on the size of the event. Our relationship gives a 114-percent increase in peak acceleration from M6.5 to M7.5 at 50 kilometers, decreasing to a 48-percent increase for the same magnitude interval at a distance of five kilometers.

A thorough understanding of the differences in magnitude scaling between the two relationships would require a detailed comparison of the data sets and statistical techniques used in each analysis which is beyond the scope of this study. As suggested by Joyner and Boore (1981), part of the difference may be due to their definition of distance. Their use of closest distance to the surface projection of the fault rupture surface would give smaller distances than would our definition for the smaller magnitude events not accompanied by surface rupture. As a result, their data would be expected to support a larger degree of magnitude scaling between moderate and large earthquakes in the near field. For earthquakes exceeding magnitudes 6.0 to 6.3, which generally rupture to the ground surface, their definition of distance becomes consistent with ours and might then be expected to support reduced magnitude scaling in the near field. To understand the effect of distance definition on the near-source behavior of PGA, we developed a ground motion model from our data, using closest distance to the surface projection of the fault rupture zone, and compared it to the unconstrained relationship given by Equation 3. As expected, we found that by using this alternate distance definition the degree of magnitude saturation decreased, whereby magnitude scaling within ten kilometers of the fault increased for the smaller magnitude earthquakes. However, we find that both the predictions and magnitude scaling of peak acceleration for the larger events

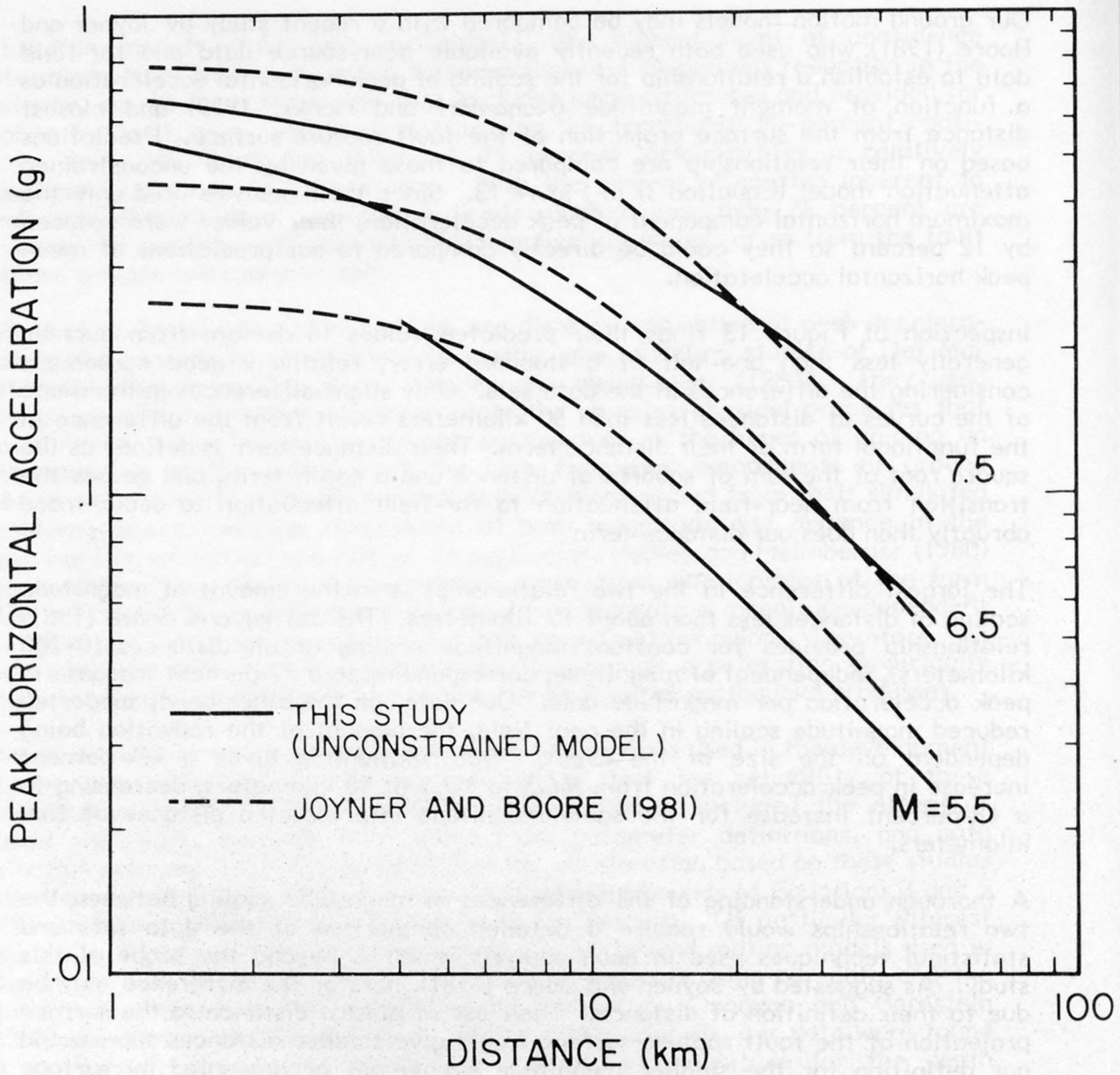

Figure 13. The unconstrained ground motion model (solid curve) compared with the attenuation relationship (dashed curve) developed by Joyner and Boore (1981). The Joyner and Boore predictions of the maximum horizontal component have been reduced by 12 percent so that they may be compared with the predictions of the mean horizontal peak acceleration given by the unconstrained model.

remained the same. Although the physically-based concept of total magnitude saturation at zero distance is no longer appropriate for the smaller events using this alternate distance definition, it is important that reduced magnitude scaling for the larger events continued to be statistically supported by our near-source data strengthening our conclusions regarding the near-source behavior of peak acceleration. Therefore, we conclude that differences in analysis techniques and data selection criteria must be responsible for differences in predicted magnitude scaling characteristics between the two studies.

CONCLUSIONS

Based upon the results of the analyses, the sensitivity studies, and the discussions presented in this report, we offer the following conclusions with regard to the characteristics of horizontal peak ground acceleration (PGA) recorded in the near-source region of moderate to large earthquakes:

- The results of this study have established that accelerations tend to saturate with increasing magnitude at small distances. Conclusions regarding magnitude saturation of PGA were found to be influenced by the effects of fault type and building size. When the analysis was restricted to small structures and fault type was treated as a variable, the unconstrained model was found to support complete saturation of PGA at the fault rupture surface, consistent with the assumption used in the development of the constrained model.

- Both the 1979 Imperial Valley earthquake data and the results of this study were found to support saturation of acceleration with decreasing distance. This confirms the inappropriateness of a linear extrapolation of far-field data in estimating near-source accelerations.

- Based on the data compiled for this study, there was found to be no significant difference between accelerations recorded on rock or soil once shallow soil sites were removed. PGA from shallow soil sites were found to be 63- to 84-percent higher than those from either soil or rock sites.

- A 24-percent reduction in PGA was found to exist for recordings obtained in the basement of large buildings, when compared to ground-level recordings in small (1- and 2-story) buildings or in the free field.

- An extensive sensitivity analysis has established the robustness of the PGA ground motion models developed in this study. Predicted accelerations for variations in parameter values, ground motion models and data selection criteria were found to fall well within the one-

standard-deviation estimates given by the unconstrained and constrained models, their variations being generally less than five to ten percent.

- Sensitivity studies confirmed the adequacy of the weighting scheme in controlling the effect of well-recorded events. The chosen scheme was found to represent a reasonable balance between the contributions to distance attenuation inherent in well-recorded earthquakes and the contributions to magnitude scaling, especially at small distances, offered by significant but more poorly recorded events.

- Non-North American accelerations, primarily from reverse-type faults, were found to be systematically high relative to the primarily strike-slip North American data. Reverse-fault data were found to be 17- to 28- percent higher than data from other fault types.

- Accelerations recorded at sites located within areas of steep topographic relief were found to be significantly higher than the average. The Pacoima Dam accelerations recorded during the 1971 San Fernando earthquake are found to be consistent with those predicted by the unconstrained model when empirically-derived corrections for topography, site conditions, response of the dam, and fault type are accounted for.

- A comparative analysis of several distance definitions found ground motion models based on fault distance, as defined in this study, to be far superior to those based on either epicentral or hypocentral distance. Use of these latter distance definitions resulted in a 33-percent increase in the scatter and a 27-percent decrease in the goodness of fit.

- Data from the United States that were excluded based on the selection criteria set forth in this study were not found to vary systematically from their predicted values. Rather, their exclusion has reduced the uncertainty associated with these predictions in accordance with the intent of the selection criteria.

- The results from the constrained model for very small distances were found to be insensitive to the specified far-field acceleration attentuation rate over the range 1.0 to 2.0. Separate application of the near-field and far-field constraints used in the development of the constrained model yielded predictions relatively consistent with the unconstrained model.

- Statistical assumptions regarding the lognormal distribution of PGA were confirmed, verifying the use of various statistical tests employed throughout the analyses that required this assumption.

REFERENCES

Aki, K., and P. Richards (1980), "Quantitative Seismology Theory and Methods," Vol. II, W.H. Freeman and Company, San Francisco.

Ambraseys, N.N. (1969), "Maximum Intensity of Ground Movements Caused by Faulting," Proc. Fourth World Conf. Earthquake Engr., Santiago, Chile, Vol. I, pp. 154-171.

Ambraseys, N.N. (1973), "Dynamics and Response of Foundation Materials in Epicentral Regions of Strong Earthquakes," Proc. Fifth World Conf. Earthquake Engr., Rome, Italy, Vol. I, pp. 126-148.

Ambraseys, N.N. (1978), "Preliminary Analysis of European Strong-Motion Data 1965-1978," Bulletin of European Assoc. for Earthquake Engineers, 4:17-37.

Bolt, Bruce A. (1978), "Fallacies in Current Ground Motion Prediction," Proc. Second Int'l Conf. on Microzonation, San Francisco, California, Vol. II, pp. 617-633.

Boore, D.M. (1973), "The Effect of Simple Topography on Seismic Waves: Implications for the Accelerations Recorded at Pacoima Dam, San Fernando Valley, California," Bull. Seism. Soc. Am., 63:1603-1609.

Boore, D.M., W.B. Joyner, A.A. Oliver III and R.A. Page (1980), "Peak Acceleration, Velocity, and Displacement from Strong-Motion Records," Bull. Seism. Soc. Am., 70(1):305-321.

Bowker, A.H. and G. J. Liebermann (1972), "Engineering Statistics," Prentice-Hall, Inc., Englewood Cliffs, New Jersey.

Brune, J.N. (1970), "Tectonic Stress and the Spectra of Seismic Shear Waves from Earthquakes," J. Geophys. Res., 75(26):4997-5009.

Campbell, Kenneth W. (1980), "Attenuation of Peak Horizontal Acceleration Within the Near-Source Region of Moderate to Large Earthquakes," TERA Corporation Technical Report 80-1, Berkeley, California.

Chinnery, Michael A. (1978), "Measurement of m_b with a Global Network," Tectonophysics, 49:139-144.

Crouse, C.B. (1978), "Prediction of Free-Field Earthquake Ground Motions," Proceedings of Specialty Conference on Earthquake Engineering and Soil Dynamics, ASCE, Pasadena, California, Vol. I, pp. 359-379.

Darragh, R.B. and K.W. Campbell (1981), "Empirical Assessment of the Reduction in Free Field Ground Motion Due to the Presence of Structures," (abstract), Earthquake Notes, 52(1):18.

Del Mar Technical Associates (1979), "Simulation of Earthquake Ground Motions for San Onofre Nuclear Generating Station Unit I, Supplement I," Del Mar Technical Associates Report to Southern California Edison Company, Del Mar, California.

Dietrich, J.H. (1973), "A Deterministic Near-Field Source Model," Proc. Fifth World Conf. Earthquake Engr., Rome, Italy, Paper 301.

Donovan, N.C., and A.E. Bornstein (1978), "Uncertainties in Seismic Risk Procedures," Journal of the Geotechnical Engineering Division, ASCE, 104 (GT7):869-887.

Duke, C. M., J. A. Johnson, Y. Kharraz, K. W. Campbell, and N. A. Malpiede (1971), "Subsurface Site Conditions and Geology in the San Fernando Earthquake Area," School of Engineering and Applied Science Report UCLA-ENG-7206, University of California, Los Angeles.

Esteva, Luis (1970), "Seismic Risk and Seismic Design Criteria for Nuclear Power Plants," The MIT Press (Edited by Robert J. Hansen), Cambridge, Massachusetts, pp. 142-182.

Gallant, A.R. (1975), "Nonlinear Regression," The American Statistician, 29(2): 73-81.

Hadley, D.M. and D.V. Helmberger (1980), "Simulation of Strong Ground Motions," Bull. Seism. Soc. Am., 70(2):617-630.

Hanks, T.C. and H. Kanamori (1979), "A Moment Magnitude Scale," J. Geophys. Res., 84: 2348-2350.

Hanks, T.C. and D.A. Johnson (1976), "Geophysical Assessment of Peak Accelerations," Bull. Seism. Soc. Am., 66:959-968.

Hanks, T.C. (1979), "b Values and ω^{-2} Seismic Source Models: Implications for Tectonic Stress Variations Along Active Crustal Fault Zones and the Estimation of High-Frequency Strong Ground Motion," J. Geophys. Res., 84(B5): 2235-2242.

Jennings, P.C. and R.A. Guzman (1975), "Seismic Design Criteria for Nuclear Power Plants," Proceedings of U.S. National Conference on Earthquake Engineering, EERI, Ann Arbor, Michigan, pp. 474-483.

Joyner, W.B. and D.M. Boore (1981), "Peak Horizontal Acceleration and Velocity from Strong-Motion Records Including Records from the 1979 Imperial Valley, California, Earthquake," Bull. Seism. Soc. Am., Vol. 71 (in press).

Kanamori, Hiroo (1979), "A Semi-Empirical Approach to Prediction of Long-Period Ground Motions from Great Earthquakes," Bull. Seism. Soc. Am., 69(6):1645-1670.

Krishna, J., A.R. Chandrasekaran, and S.S. Sanai (1969), "Analysis of Koyna Accelerogram of December 11, 1967," Bull. Seism. Soc. Am., 59:1719-1731.

McGarr, A. (1981), "Analysis of Peak Ground Motion in Terms of a Model of Inhomogenous Faulting," J. Geophys. Res., 86:3901-3912.

McGarr, A., R.W.E. Green and S.M. Spottiswoode (1981), "Strong Ground Motion of Mine Tremors: Some Implications for Near-Source Ground Motion Parameters," Bull. Seism. Soc. Am., 71(1): 295-319.

Mickey, W.V., V. Perez and W.K. Cloud (1973), "Response of Pacoima Dam to Aftershocks of San Fernando Earthquake," in the San Fernando, California, Earthquake of February 9, 1971, EERI/NOAA, Vol. II, pp. 403-415.

Midorikawa, S. and H. Kabayashi (1978), "On Estimation of Strong Earthquake Motions with Regard to Fault Rupture," Proc. Second Int'l Conf. on Microzonation," San Francisco, California, Vol. II, pp. 825-836.

Nuttli, O.W. (1979), "The Relations of Sustained Maximum Ground Acceleration and Velocity to Earthquake Intensity and Magnitude," in State-of-the-Art for Assessing Earthquake Hazards in the United States, U.S. Army Engineer Waterways Experiment Station, Vicksburg, Miss., Misc. Paper S-73-1, Report 16.

Reimer, R.B., R.W. Clough and J.M. Raphael (1973), "Evaluation of the Pacoima Dam Accelerogram," Proc. Fifth World Conf. Earthquake Engr., Rome, Italy, Paper 293.

Seekins, L.C. and T.C. Hanks (1978), "Strong-Motion Accelerograms of the Oroville Aftershocks and Peak Acceleration Data," Bull. Seism. Soc. Am., 68(3):667-689.

Trifunac, M.D. (1973), "Analysis of Strong Earthquake Ground Motion," Int. J. Earthq. Engr. Struct. Dyn., 2:59-69.

ACKNOWLEDGEMENTS

The author wishes to thank Ann Bornstein for the development and application of the statistical packages used in this study and for providing computer analysis support. I would also like to recognize the efforts of the following people for their assisstance in various aspects of the study: Mark Polit and Bob Darragh--

technical support, Dr. Mansour Niazi and Don Michniuk--seismology, C. Marshall Payne--engineering geology, and Brian Davis and Dan Moore--statistics. My appreciation also goes to Dr. Stewart Smith, Dr. Gerald Frazier, Don K. Davis and Lawrence H. Wight for their helpful suggestions throughout this project. Financial support was provided by Southern California Edison Company, Rosemead, California, under the management of H. Gene Hawkins and by the Pacific Gas and Electric Company, San Francisco, California, under the management of Frank Brady.

remained the same. Although the physically-based concept of total magnitude saturation at zero distance is no longer appropriate for the smaller events using this alternate distance definition, it is important that reduced magnitude scaling for the larger events continued to be statistically supported by our near-source data strengthening our conclusions regarding the near-source behavior of peak acceleration. Therefore, we conclude that differences in analysis techniques and data selection criteria must be responsible for differences in predicted magnitude scaling characteristics between the two studies.

REFERENCES

Aki, K., and P. Richards (1980), "Quantitative Seismology Theory and Methods," Vol. II, W.H. Freeman and Company, San Francisco.

Ambraseys, N.N. (1969), "Maximum Intensity of Ground Movements Caused by Faulting," Proc. Fourth World Conf. Earthquake Engr., Santiago, Chile, Vol. I, pp. 154-171.

Ambraseys, N.N. (1973), "Dynamics and Response of Foundation Materials in Epicentral Regions of Strong Earthquakes," Proc. Fifth World Conf. Earthquake Engr., Rome, Italy, Vol. I, pp. 126-148.

Ambraseys, N.N. (1978), "Preliminary Analysis of European Strong-Motion Data 1965-1978," Bulletin of European Assoc. for Earthquake Engineers, 4:17-37.

Bolt, Bruce A. (1978), "Fallacies in Current Ground Motion Prediction," Proc. Second Int'l Conf. on Microzonation, San Francisco, California, Vol. II, pp. 617-633.

Boore, D.M. (1973), "The Effect of Simple Topography on Seismic Waves: Implications for the Accelerations Recorded at Pacoima Dam, San Fernando Valley, California," Bull. Seism. Soc. Am., 63:1603-1609.

Boore, D.M., W.B. Joyner, A.A. Oliver III and R.A. Page (1980), "Peak Acceleration, Velocity, and Displacement from Strong-Motion Records," Bull. Seism. Soc. Am., 70(1):305-321.

Bowker, A.H. and G. J. Liebermann (1972), "Engineering Statistics," Prentice-Hall, Inc., Englewood Cliffs, New Jersey.

Brune, J.N. (1970), "Tectonic Stress and the Spectra of Seismic Shear Waves from Earthquakes," J. Geophys. Res., 75(26):4997-5009.

Campbell, Kenneth W. (1980), "Attenuation of Peak Horizontal Acceleration Within the Near-Source Region of Moderate to Large Earthquakes," TERA Corporation Technical Report 80-1, Berkeley, California.

Chinnery, Michael A. (1978), "Measurement of m_b with a Global Network," Tectonophysics, 49:139-144.

Crouse, C.B. (1978), "Prediction of Free-Field Earthquake Ground Motions," Proceedings of Specialty Conference on Earthquake Engineering and Soil Dynamics, ASCE, Pasadena, California, Vol. I, pp. 359-379.

Darragh, R.B. and K.W. Campbell (1981), "Empirical Assessment of the Reduction in Free Field Ground Motion Due to the Presence of Structures," (abstract), Earthquake Notes, 52(1):18.

Del Mar Technical Associates (1979), "Simulation of Earthquake Ground Motions for San Onofre Nuclear Generating Station Unit I, Supplement I," Del Mar Technical Associates Report to Southern California Edison Company, Del Mar, California.

Dietrich, J.H. (1973), "A Deterministic Near-Field Source Model," Proc. Fifth World Conf. Earthquake Engr., Rome, Italy, Paper 301.

Donovan, N.C., and A.E. Bornstein (1978), "Uncertainties in Seismic Risk Procedures," Journal of the Geotechnical Engineering Division, ASCE, 104 (GT7):869-887.

Duke, C. M., J. A. Johnson, Y. Kharraz, K. W. Campbell, and N. A. Malpiede (1971), "Subsurface Site Conditions and Geology in the San Fernando Earthquake Area," School of Engineering and Applied Science Report UCLA-ENG-7206, University of California, Los Angeles.

Esteva, Luis (1970), "Seismic Risk and Seismic Design Criteria for Nuclear Power Plants," The MIT Press (Edited by Robert J. Hansen), Cambridge, Massachusetts, pp. 142-182.

Gallant, A.R. (1975), "Nonlinear Regression," The American Statistician, 29(2): 73-81.

Hadley, D.M. and D.V. Helmberger (1980), "Simulation of Strong Ground Motions," Bull. Seism. Soc. Am., 70(2):617-630.

Hanks, T.C. and H. Kanamori (1979), "A Moment Magnitude Scale," J. Geophys. Res., 84: 2348-2350.

Hanks, T.C. and D.A. Johnson (1976), "Geophysical Assessment of Peak Accelerations," Bull. Seism. Soc. Am., 66:959-968.

Hanks, T.C. (1979), "b Values and ω^{-2} Seismic Source Models: Implications for Tectonic Stress Variations Along Active Crustal Fault Zones and the Estimation of High-Frequency Strong Ground Motion," J. Geophys. Res., 84(B5): 2235-2242.

Jennings, P.C. and R.A. Guzman (1975), "Seismic Design Criteria for Nuclear Power Plants," Proceedings of U.S. National Conference on Earthquake Engineering, EERI, Ann Arbor, Michigan, pp. 474-483.

Joyner, W.B. and D.M. Boore (1981), "Peak Horizontal Acceleration and Velocity from Strong-Motion Records Including Records from the 1979 Imperial Valley, California, Earthquake," Bull. Seism. Soc. Am., Vol. 71 (in press).

Kanamori, Hiroo (1979), "A Semi-Empirical Approach to Prediction of Long-Period Ground Motions from Great Earthquakes," Bull. Seism. Soc. Am., 69(6):1645-1670.

Krishna, J., A.R. Chandrasekaran, and S.S. Sanai (1969), "Analysis of Koyna Accelerogram of December 11, 1967," Bull. Seism. Soc. Am., 59:1719-1731.

McGarr, A. (1981), "Analysis of Peak Ground Motion in Terms of a Model of Inhomogenous Faulting," J. Geophys. Res., 86:3901-3912.

McGarr, A., R.W.E. Green and S.M. Spottiswoode (1981), "Strong Ground Motion of Mine Tremors: Some Implications for Near-Source Ground Motion Parameters," Bull. Seism. Soc. Am., 71(1): 295-319.

Mickey, W.V., V. Perez and W.K. Cloud (1973), "Response of Pacoima Dam to Aftershocks of San Fernando Earthquake," in the San Fernando, California, Earthquake of February 9, 1971, EERI/NOAA, Vol. II, pp. 403-415.

Midorikawa, S. and H. Kabayashi (1978), "On Estimation of Strong Earthquake Motions with Regard to Fault Rupture," Proc. Second Int'l Conf. on Microzonation," San Francisco, California, Vol. II, pp. 825-836.

Nuttli, O.W. (1979), "The Relations of Sustained Maximum Ground Acceleration and Velocity to Earthquake Intensity and Magnitude," in State-of-the-Art for Assessing Earthquake Hazards in the United States, U.S. Army Engineer Waterways Experiment Station, Vicksburg, Miss., Misc. Paper S-73-1, Report 16.

Reimer, R.B., R.W. Clough and J.M. Raphael (1973), "Evaluation of the Pacoima Dam Accelerogram," Proc. Fifth World Conf. Earthquake Engr., Rome, Italy, Paper 293.

Seekins, L.C. and T.C. Hanks (1978), "Strong-Motion Accelerograms of the Oroville Aftershocks and Peak Acceleration Data," Bull. Seism. Soc. Am., 68(3):667-689.

Trifunac, M.D. (1973), "Analysis of Strong Earthquake Ground Motion," Int. J. Earthq. Engr. Struct. Dyn., 2:59-69.

ACKNOWLEDGEMENTS

The author wishes to thank Ann Bornstein for the development and application of the statistical packages used in this study and for providing computer analysis support. I would also like to recognize the efforts of the following people for their assisstance in various aspects of the study: Mark Polit and Bob Darragh--technical support, Dr. Mansour Niazi and Don Michniuk--seismology, C. Marshall Payne--engineering geology, and Brian Davis and Dan Moore--statistics. My appreciation also goes to Dr. Stewart Smith, Dr. Gerald Frazier, Don K. Davis and Lawrence H. Wight for their helpful suggestions throughout this project. Financial support was provided by Southern California Edison Company, Rosemead, California, under the management of H. Gene Hawkins and by the Pacific Gas and Electric Company, San Francisco, California, under the management of Frank Brady.

APPENDIX

STRONG MOTION DATA

EARTHQUAKE NAME	DATE YR-MO-DY	MAGNITUDE[a] (M)	USGS NO.	STATION NAME	FAULT[b] DISTANCE	GEOLOGY[c] CLASS	PEAK GROUND ACCELERATION (g)	
Long Beach	33-03-11	6.2	131	Long Beach Pub Utl Blg	6.4	B	.20	.16
Long Beach	33-03-11	6.2	136	LA Subway Terminal	28.0	C	.098	.064
Long Beach	33-03-11	6.2	288	Vernon CMD Terminal	22.0	A	.15	.13
Helena, Montana	35-10-31	5.5	2229	Helena Mont Fed Bldg	8.0	D	.15	.15
Imperial Valley	40-05-19	7.1	117	El Centro Sta 9	10.0	A	.35	.21
Santa Barbara	41-07-01	5.9	283	Sta Barbara Courthouse	10.0	B	.24	.18
Kern County	52-07-21	7.7	1095	Taft Lincoln School	42.0	A	.197	.177
Daly City	57-03-22	5.3	1049	Oakland City Hall	24.0	B	.047	.029
Daly City	57-03-22	5.3	1065	SF Alexander Bldg	14.0	A	.055	.050
Daly City	57-03-22	5.3	1078	SF So Pacific Bldg	14.0	A	.049	.046
Daly City	57-03-22	5.3	1080	SF State Bldg	12.0	A	.103	.062
Daly City	57-03-22	5.3	1117	SF Golden Gate Park	8.0	C	.126	.105
Parkfield	66-06-28	6.0	1013	Cholame-Shandon Sta 2	0.08	A	.73	.51
Parkfield	66-06-28	6.0	1014	Cholame-Shandon Sta 5	5.5	A	.47	.40
Parkfield	66-06-28	6.0	1015	Cholame-Shandon Sta 7	9.6	B	.28	.27
Parkfield	66-06-28	6.0	1016	Cholame-Shandon Sta 12	14.9	A	.072	.06
Parkfield	66-06-28	6.0	1438	Cholame-Shandon Temblor	10.6	E	.41	.29
Fairbanks, Alaska	67-06-21	5.7	2721	Fairbanks Duck Hall	15.0	D	.14	.09
Koyna, India	67-12-10	6.5	9000	Koyna Dam (Gallery 1A)	3.2	D	.63	.49
Borrego Mtn	68-04-09	6.7	117	El Centro Sta 9	45.0	A	.142	.061
Lytle Creek	70-09-12	5.4	111	Cedar Sprng Miller Cyn	18.0	D	.086	.059
Lytle Creek	70-09-12	5.4	113	Colton SCE Substation	29.0	A	.045	.041
Lytle Creek	70-09-12	5.4	116	Devils Canyon filter plant	19.0	E	.18	.17
Lytle Creek	70-09-12	5.4	274	Hall of Rcrds San Bern	28.0	A	.12	.06
Lytle Creek	70-09-12	5.4	278	Puddingstone Resevoir	32.0	C	.022	.02
Lytle Creek	70-09-12	5.4	290	Wrightwood	15.0	E	.21	.14
Lytle Creek	70-09-12	5.4	557	Cedar Springs Pump Plant	18.0	E	.073	.062
San Fernando	71-02-09	6.6	104	Santa Anita Dam	27.9	D	.24	.18
San Fernando	71-02-09	6.6	110	Castaic Old Rdg. Rt.	22.8	E	.39	.32
San Fernando	71-02-09	6.6	121	Fairmont Reservoir	32.1	E	.17	.15

APPENDIX
(CONT.)

EARTHQUAKE NAME	DATE YR-MO-DY	MAGNITUDE[a] (M)	USGS NO.	STATION NAME	FAULT[b] DISTANCE	GEOLOGY[c] CLASS	PEAK GROUND ACCELERATION (g)	
San Fernando	71-02-09	6.6	125	Lake Hughes Sta 1	29.6	A	.17	.12
San Fernando	71-02-09	6.6	126	Lake Hughes Sta 4	24.9	E	.19	.16
San Fernando	71-02-09	6.6	127	Lake Hughes Sta 9	22.6	E	.16	.15
San Fernando	71-02-09	6.6	128	Lake Hughes Sta 12	18.7	E	.37	.28
San Fernando	71-02-09	6.6	133	LA Hollywd Storage Bld	21.3	A	.15	.11
San Fernando	71-02-09	6.6	135	LA Hlywd Strge PE Lot	20.5	A	.22	.19
San Fernando	71-02-09	6.6	137	LA Water and Power	24.1	C	.20	.14
San Fernando	71-02-09	6.6	141	LA Griffith Park Observ	16.9	D	.18	.16
San Fernando	71-02-09	6.6	181	LA 1640 Marengo	25.2	B	.14	.14
San Fernando	71-02-09	6.6	190	LA 2011 Zonal	25.5	C	.08	.07
San Fernando	71-02-09	6.6	220	LA 3838 Lankershim	15.4	C	.18	.13
San Fernando	71-02-09	6.6	229	LA 5250 Century	36.1	B	.06	.06
San Fernando	71-02-09	6.6	241	LA 8244 Orion	7.5	A	.27	.14
San Fernando	71-02-09	6.6	244	LA 8639 Lincoln	36.1	B	.04	.04
San Fernando	71-02-09	6.6	247	LA 9841 Airport Blvd	36.1	B	.03	.03
San Fernando	71-02-09	6.6	253	LA 14724 Ventura	15.4	A	.26	.19
San Fernando	71-02-09	6.6	262	Palmdale Fire Sta	27.6	A	.13	.11
San Fernando	71-02-09	6.6	264	Pasadena Millikan Lib	21.8	B	.21	.18
San Fernando	71-02-09	6.6	266	Pasadena CIT Seismo Lab	18.4	D	.19	.11
San Fernando	71-02-09	6.6	267	Pasadena Jet Prop Lab	14.8	B	.22	.17
San Fernando	71-02-09	6.6	269	Pearblossom Pump Plant	35.5	E	.15	.10
San Fernando	71-02-09	6.6	279	Pacoima Dam	3.2	E	1.25	1.24
San Fernando	71-02-09	6.6	288	Vernon CMD Terminal	30.7	A	.11	.09
San Fernando	71-02-09	6.6	458	LA 15107 Van Owen	9.7	A	.12	.11
San Fernando	71-02-09	6.6	461	LA 15910 Ventura	14.3	A	.15	.13
San Fernando	71-02-09	6.6	466	LA 15250 Ventura	15.4	A	.23	.14
San Fernando	71-02-09	6.6	475	Pasadena Athenaeum Cit	22.5	B	.11	.10
San Fernando	71-02-09	6.6	482	Alhambra 900 S Fremont	24.8	B	.13	.11
Bear Valley	72-02-24	5.1	1028	Hollister City Hall	31.0	A	.03	.02
Sitka, Alaska	72-07-30	7.6	2714	Sitka Alaska Mag Obs	45.0	A	.11	.09

APPENDIX
(CONT.)

EARTHQUAKE NAME	DATE YR-MO-DY	MAGNITUDE[a] (M)	USGS NO.	STATION NAME	FAULT[b] DISTANCE	GEOLOGY[c] CLASS	PEAK GROUND ACCELERATION (g)	
Managua	72-12-23	6.2	3501	Managua Esso Refinery	5.0	A	.39	.34
Point Mugu	73-02-21	5.9	272	Port Hueneme Naval Lab	24.0	A	.13	.08
Lima, Peru	74-10-03	7.6	4302	Lima Geophysical Inst	38.0	B	.24	.21
Lima, Peru	74-10-03	7.6	4304	Lima Huaca Residence	40.0	B	.25	.20
Hollister	74-11-28	5.1	1028	Hollister City Hall	10.8	A	.17	.10
Hollister	74-11-28	5.1	1250	Gilroy Gavilian Col	10.8	B	.14	.10
Hollister	74-11-28	5.1	1377	San Juan Bautista	8.9	A	.12	.05
Oroville	75-08-01	5.7	1051	Oroville Seismo Sta	8.0	D	.11	.10
Oroville	75-08-01	5.7	1291	Marysville	30.0	A	.07	.06
Oroville	75-08-01	5.7	1292	Chico	31.0	A	.08	.06
Oroville	75-08-01	5.7	1293	Paradise KEWG Transmtr	32.0	C	.04	.03
Kalapana, Hawaii	75-11-29	7.1	2803	Panalu, Hawaii	27.0	F	.12	.10
Kalapana, Hawaii	75-11-29	7.1	2808	Hilo, Hawaii	45.0	E	.22	.11
Gazli, USSR	76-05-17	7.0	9110	USSR, Karakyr	3.5	C	.81	.65
Santa Barbara	78-08-13	5.7	106	Cachuma Dam Toe	25.9	E	.07	.07
Santa Barbara	78-08-13	5.7	885	Goleta UCSB Phys Plant	7.7	A	.39	.24
Santa Barbara	78-08-13	5.7	941	Gibraltar Dam R Abut	18.1	C	.04	.04
Santa Barbara	78-08-13	5.7	5093	Goleta UCSB North Hall	7.7	B	.44	.27
Santa Barbara	78-08-13	5.7	5135	Juncal Dam A	25.4	C	.06	.
Santa Barbara	78-08-13	5.7	5137	Sta Barbara Freitas	10.1	B	.22	.11
Santa Barbara	78-08-13	5.7	9019	Sta Barbara Courthouse	9.8	B	.21	.10
Santa Barbara	78-08-13	5.7	9022	Goleta Substation	11.8	E	.28	.24
Tabas, Iran	78-09-16	7.7	9124	Iran, Tabas	3.0	A	.80	.
Bishop	78-10-04	5.8	1325	Benton Jct 6 + 120	34.2	A	.06	.06
Bishop	78-10-04	5.8	1444	Long Valley Dam	7.6	C	.26	.170
Bishop	78-10-04	5.8	1490	Mammoth Lakes High Sch	29.0	A	.07	.05
Bishop	78-10-04	5.8	9030	Bishop	27.1	A	.06	.03
Malibu	79-01-01	5.0	657	Santa Monica 201 Ocean	20.7	B	.05	.03
Malibu	79-01-01	5.0	757	Sepulveda Control Facl	26.2	B	.06	.03
Malibu	79-01-01	5.0	5079	Kilpatrick Boys School	20.2	E	.07	.06

APPENDIX
(CONT.)

EARTHQUAKE NAME	DATE YR-MO-DY	MAGNITUDE[a] M	USGS NO.	STATION NAME	FAULT[b] DISTANCE	GEOLOGY[c] CLASS	PEAK GROUND ACCELERATION (g)	
Malibu	79-01-01	5.0	5080	Monte Nido Fire Sta	15.6	C	.06	.05
Malibu	79-01-01	5.0	5081	Topanga Fire Sta	18.1	E	.09	.07
St. Elias, Alaska	79-02-28	7.2	2734	Icy Bay	38.3	A	.16	.11
Coyote Lake	79-08-06	5.9	1251	Corralitos	23.3	C	.03	.
Coyote Lake	79-08-06	5.9	1377	San Juan Bautista	14.4	A	.11	.09
Coyote Lake	79-08-06	5.9	1408	Gilroy Array Sta 1	8.9	C	.13	.10
Coyote Lake	79-08-06	5.9	1409	Gilroy Array Sta 2	8.0	A	.26	.20
Coyote Lake	79-08-06	5.9	1410	Gilroy Array Sta 3	6.3	A	.27	.26
Coyote Lake	79-08-06	5.9	1411	Gilroy Array Sta 4	4.9	A	.26	.24
Coyote Lake	79-08-06	5.9	1413	Gilroy Array Sta 6	4.0	E	.42	.34
Coyote Lake	79-08-06	5.9	1422	Halls Valley	24.8	A	.05	.04
Coyote Lake	79-08-06	5.9	1445	Coyote Creek	3.9	B	.23	.16
Coyote Lake	79-08-06	5.9	1492	San Juan Baut Overpass	16.2	B	.12	.11
Imperial Valley	79-10-15	6.9	117	El Centro Sta 9	5.8	A	.40	.27
Imperial Valley	79-10-15	6.9	286	Superstition Mtn USAF	24.5	D	.21	.12
Imperial Valley	79-10-15	6.9	412	El Centro Sta 10	8.2	A	.23	.20
Imperial Valley	79-10-15	6.9	724	Niland	34.0	A	.10	.074
Imperial Valley	79-10-15	6.9	931	El Centro Sta 12	18.0	A	.15	.11
Imperial Valley	79-10-15	6.9	942	El Centro Sta 6	1.4	A	.72	.45
Imperial Valley	79-10-15	6.9	952	El Centro Sta 5	1.0[d]	A	.56	.40
Imperial Valley	79-10-15	6.9	955	El Centro Sta 4	4.4	A	.61	.38
Imperial Valley	79-10-15	6.9	958	El Centro Sta 8	3.5	A	.64	.50
Imperial Valley	79-10-15	6.9	5028	El Centro Sta 7	0.2	A	.52	.36
Imperial Valley	79-10-15	6.9	5051	Parachute Test Site	13.1	A	.20	.11
Imperial Valley	79-10-15	6.9	5052	Plaster City	30.5	A	.07	.05
Imperial Valley	79-10-15	6.9	5053	Calexico Fire Station	10.1	A	.28	.22
Imperial Valley	79-10-15	6.9	5054	Bonds Corner	2.8	A	.81	.66
Imperial Valley	79-10-15	6.9	5055	Holtville Post Office	7.3	A	.26	.22
Imperial Valley	79-10-15	6.9	5056	El Centro Sta 1	16.4[d]	A	.15	.15
Imperial Valley	79-10-15	6.9	5057	El Centro Sta 3	9.3[d]	A	.27	.22

EARTHQUAKE NAME	DATE YR-MO-DY	MAGNITUDE[a] M	USGS NO.	STATION NAME	FAULT[b] DISTANCE	GEOLOGY[c] CLASS	PEAK GROUND ACCELERATION (g)	
Imperial Valley	79-10-15	6.9	5058	El Centro Sta 11	12.2	A	.38	.38
Imperial Valley	79-10-15	6.9	5059	El Centro Sta 13	21.5	A	.15	.12
Imperial Valley	79-10-15	6.9	5060	Brawley Airport	7.0	A	.22	.17
Imperial Valley	79-10-15	6.9	5061	Calipatria Fire Sta	22.2	A	.13	.09
Imperial Valley	79-10-15	6.9	5062	Salton Sea	28.0	A	.13	.10
Imperial Valley	79-10-15	6.9	5066	Coachella Canal Sta 4	47.7	A	.14	.11
Imperial Valley	79-10-15	6.9	5090	ICSB	7.0	A	.319	.291
Imperial Valley	79-10-15	6.9	5115	El Centro Sta 2	10.2[d]	A	.43	.33
Imperial Valley	79-10-15	6.9	5154	ICSB Free Field	7.0	A	.243	.237
Imperial Valley	79-10-15	6.9	5165	Dogwood Road	4.8	A	.51	.37
Imperial Valley	79-10-15	6.9	9028	Westmoreland Fire Sta	12.6	A	.106	.081
Imperial Valley	79-10-15	6.9	9031	Meloland Ovrps Footing	0.2	A	.326	.279
Imperial Valley	79-10-15	6.9	9032	Meloland Ovrps Abut 1	0.2	A	.408	.264
Imperial Valley	79-10-15	6.9	9033	Meloland Ovrps Abut 3	0.2	A	.359	.303

[a] Magnitude (M) selected to be consistent with the moment magnitude scale (see text):

$M = M_L$ for magnitudes less than 6.0
$M = M_S$ for magnitudes 6.0 or greater

[b] Fault distance is defined as the shortest distance between the recording station and the fault rupture surface.

[c] Geology classification (see Table 2):

A -- Recent Alluvium
B -- Pleistocene Deposits
C -- Soft Rock
D -- Hard Rock
E -- Shallow Soil
F -- Soft Soil

[d] Consistent with our definition of fault distance, distances were measured from the rupture surface of the Brawley Fault.

ATTENUATION OF VERTICAL ACCELERATION AND A REVIEW OF ATTENUATION EQUATION PROCESSES

by Neville C. Donovan*

SUMMARY

Historically, vertical acceleration attenuation has been given little attention in structural design because the vertical force produced by earthquakes is only in addition to permanent gravity loadings. A request for a vertical attenuation equation as part of a recent consulting project together with the recent publications of equations for horizontal attenuation by others (1,3,4,5) led to this review of the consistencies and inconsistencies in developing attenuation equations.

The data set used was an expansion of that produced by Joyner and Boore so that additional components of motion were also included. The resulting attenuation equation for vertical acceleration using all the instrumental values from the data set (Table 1) was:

$$y = 37.3 \quad \exp[0.76\ M_L]\ D^{-1.27}$$

where y is vertical acceleration in cm/sec^2 and M_L is local magnitude. The distance D is $(R^2 + 7.0^2)^{1/2}$ where R is the shortest distance to the surface projection of the fault plane in kilometers. The total size of the data set was not sufficient to show conclusive effects of site conditions but the available evidence points to larger vertical acceleration on soil sites than on sites with rock. Because vertical accelerations have more high frequency motion than horizontal accelerations the truncation produced by record processing to uniform time steps can be more severe with vertical accelerations. This truncation has an average reduction to the peak values of 26 percent.

INTRODUCTION

The difficulties of producing attenuation equations for acceleration and velocity are well recognized by those involved in their development. Unfortunately the difficulties are seldom discussed and are rarely considered or understood by subsequent users. The fact remains however that such relationships often form the interface between geophysicists and seismologists and the engineering fraternity. The difficulties of communication between the respective groups can only be compounded when the limitations of the development and the resultant end use are not understood by the respective professional groups.

By using the Joyner and Boore data set as the basis upon which to compile the vertical acceleration list, it became apparent that the data set had serious limitations. These limitations consist of two types. The first type of limitation is that intrinsic to any set where the range of data is not consistent from one event to the other. The second type of limitation is that imposed by the data set development itself. To avoid some difficulties and criticisims that had been made of earlier data compilation Joyner and Boore followed a strict set of rules in compiling their data list. Strict compliance with these rules has posed some additional problems by limiting the size of their data set.

THE DATA SET

Joyner and Boore included peak acceleration values from 182 recordings of motions in the Western United States in their data set. The site classification breakdown for acceleration gave 96 stations with soil profiles and 29 with rock. The remaining 57 were not classified. The data set also included 62 peak ground velocity values of which 46 were on soil sites and 16 on rock sites.

As a means of providing a data set for vertical acceleration in a relatively short time it was decided to use the magnitude and distance data set of Joyner and Boore as a starting point and add the additional component values to their basic set. The expanded data set is shown in Table 1. From left to right the data consist of moment and local magnitude, Station number as listed by the US Geological Survey, the distance in kilometers, six acceleration components and two horizontal velocities, the earthquake date and site characterization with 1 for a rock site and 2 for a soil site. The acceleration values are in two groups of 3 with the two horizontal values followed by the vertical value. The first group of these accelerations is instrumental peak readings and the second set has the peak values from the processed records with uniform digitization time intervals. Those data lines which conclude with an asterisk are data sets in which the peak horizontal velocity was not produced by the component of the record with the largest acceleration.

As a first step to examining the data base some preliminary ratios and their mean values were computed. Such actions are frequently used in an empirical way with strong motion data. These ratios are summarized in Table 2. Of interest is the ratio between the two peak horizontal uncorrected acceleration values of 1.41. This agrees well with the average 13 percent difference between the Joyner and Campbell equations where Campbell considered both peak values. The difference between uncorrected and corrected peak values is also of engineering importance as spectral values and analyses based on digitized data should be scaled to the average of corrected value peaks rather than to the direct peak instrumental quantity.

JOYNER AND BOORE EQUATION

The Joyner and Boore equations have evolved through 3 separate publications. A graphical comparison of the equations for the first and third generations is shown on Figures 1 and 2 for acceleration and velocity respectively.

The first version used M_L rather than moment magnitude which is used in the most recent revision. However a scatter diagram (Figure 3) comparing the two magnitude values available in the data set does not suggest any reason why the results should be different and when the simple equation form:

$$y = b_1 e^{b_2 M} D^{-b_3} \qquad (1)$$

where D = square root of $(d^2 + 7^2)$ is fitted using both local and moment magnitude little difference in results is apparent. Figure 4 shows that the direct effect of a moment or local magnitude choice is very small. By providing equal weighting for each event in developing the attenuation curve shape Joyner and Boore permitted the larger magnitude events which only have data from distances in excess of 40 kilometers to have an unreasonably large effect on the shape of the equation in the near field. The difference between the usage of the two magnitude assumptions is especially apparent in Figure 2 for velocity attenuation. As the data set only contained 16 values on rock sites, the large site effect value has little statistical significance.

In fitting attenuation equations where the effect of a soil profile might be considered there is an optional choice available. The data may be separated and an attenuation relationship considered independently for each set or some part of the relationship may be fixed for all sets and the data made to fit this form. Joyner and Boore chose the latter option. Although this form may produce a neater appearing final result a consequence of this force fit is often considerable divergence of values predicted by the equation at the limits of the data range. This may be partly the reason for the very different results shown on Figure 5 where the Joyner velocity equation is compared with directly derived values for soil and rock. The number in each line of the key on figures such as Figure 5 shows the number of values available for use in each derivation.

VERTICAL ACCELERATION ATTENUATION

Vertical acceleration is usually not given much consideration in structural design. Any structure must withstand at least unit gravity so the additional loading in the vertical direction need not be given the detailed attention that must be given to horizontal acceleration in seismic areas. Common practice is to assume a vertical acceleration which is two-thirds of the horizontal acceleration. Studies have shown this to be generally conservative and in agreement with the ratios listed in Table 2.

However, for a recent project involving the use of seismic bearings a more direct approach to the vertical acceleration was considered. Seismic bearings reduce the horizontal seismic loading. This removes the usual additional strength requirements needed for the horizontal acceleration so that the possible effects of loading produced by the vertical acceleration may be enhanced. Vertical acceleration and attenuation must therefore be examined more carefully.

The data list in Table 1 contains a total of 123 uncorrected or Volume 1 points and 78 corrected or Volume 2 points for the vertical acceleration. The results of a direct fit using the attenuation Equation 1 to the sites with identifiable soil or rock profiles and the total data set are shown on Figures 6 and 7 for the uncorrected and corrected data respectively. It is readily apparent from an examination of either of these figures that the free form attenuation equations for rock sites and soil sites are different in shape. By contrast, Figure 8 shows the result of a comparable analysis of the corrected mean peak horizontal acceleration values. The Joyner and Boore horizontal acceleration data set does not show a dependence on instrument station site profiles.

In the near field at distances less than 10 kilometers, the vertical acceleration attenuation equation for rock sites gives results significantly less than the comparable equation for soil sites. The distance exponent for rock sites is much smaller than that for soil sites. The decision could be readily made, as was done by Joyner and Boore, that the form of the equation should be similar for soil and rock sites. It is a simple exercise to constrain the distance exponent of the rock data equation to be equal to that of the soil data and derive a new equation. The results of such an exercise are shown for the uncorrected and corrected data respectively on Figures 9 and 10. What has resulted from this revision is an apparent reversal of roles. Because a larger distance exponent was forced on the rock site data a compensating larger magnitude term also resulted so that the rock site equation now gives higher computed values than the soil equation at large magnitudes and values that are between 2 and 3 times as large as the least-square fit data.

The data set shows differences between vertical acceleration attenuation relationships for soil or rock sites, but the data set is not large enough to define this difference. For any definitive study, the data set should be extended.

The importance of considering corrected data and relations based on mean sets of values for engineering design must be emphasized. This difference is evident in Figure 11 where the uncorrected and corrected vertical acceleration equations from Figures 6 and 7 are compared. If standard processing techniques are averaged to produce digitized records at finer time intervals this effect will be minimized. At the present time however the available time-histories do show different values between the two record sets and the difference must be recognized to avoid unnecessary conservatism.

When new attenuation equations are released there is a tendency to discard older versions without comparison. Additional information applied to an evolutionary process is most helpful and this is perhaps shown by a comparison on Figure 12 between an earlier horizontal attenuation equation by Donovan and Bornstein (1978) and the Joyner & Boore equation. Several critics using isolated values claimed the Donovan & Bornstein relationship gave low values which were non-conservative. The Joyner & Boore curves have a different numerical form but except in the very near field compare reasonably well with the earlier relationship. The comparison could also be extended to include results by Campbell (1981).

CONCLUSIONS

Attenuation equations can give wide results which are to a large extent controlled by the assumption of those developing them and the constraints resulting from the numerical form chosen. The following conclusions reached in the course of this study are believed pertinent, although not all have been fully discussed above.

1) The data set used is large enough to demonstrate the difference between vertical acceleration attenuation on different soil profiles, but not large enough to define the difference.

2) Forcing the data to fit a particular data form may result in a wide divergence of the results at the extremities of the data field.

3) Far field data from events which do not have comparable and compensating near field data can bias near field results unrealistically. Kern County 1952 is such an event and the reported results of Joyner and Boore show markedly different results when this event is excluded.

4) The choice of a distance constant controls the values in the near field and the far field but does not affect the results in the center of the data field.

5) The standard deviation of the derived equation is only mildly sensitive to the choice of distance constant.

6) The data set used is insensitive to the use of moment or local magnitude. This raises the question whether the introduction of the new term which is not widely understood outside the profession at this time is a positive step.

Campbell, K.W. (1981), "Near-Source Attenuation of Peak Horizontal Acceleration", Bulletin of the Seismological Society of America, Vol. 71, #6, December, pp. 2039-2070

Donovan, N.C. & A.E. Bornstein, "Uncertainties in Seismic Risk Procedures," Journal of the Geotechnical Division, ASCE Vol. 104, GT7, Proc. Paper 13896, July 1978, pp. 869-887

Joyner, W.B., D.M. Boore and R.L. Porcella (1981), "Peak Horizontal Acceleration and Velocity from Strong Motion Records," Seismological Society of America, Abstracts of 76th Annual Meeting Earthquake Notes, Vol. 52, #1, pp. 30-81

Joyner, W.B., D.M. Boore and R.L. Porcella (1981), "Peak Horizontal Acceleration and Velocity From Strong Motion Records Including Records from The 1979 Imperial Valley, California, Earthquake, United States Geological Survey, Open File Report, March, pp. 81-365

Joyner, W.B. and D.M. Boore (1981), "Peak Horizontal Acceleration and Velocity From Strong Motion Records Including Records from The 1979 Imperial Valley, California, Earthquake, Bulletin of the Seismological Society of America, Vol. 71, #6, December, pp. 2011-2038

Table 1

FILE CONTAINS 182 LINES ARRANGED IN 16 COLUMNS.

THE DATA ARE ARRANGED AS FOLLOWS :

1 - 3	MOMENT MAGNITUDE
4 - 6	LOCAL MAGNITUDE
7 - 10	INSTRUMENT STATION NUMBER (USGS)
11 - 15	DISTANCE IN KILOMETERS FROM THE VERTICAL PROJECTION OF THE FAULT
16 - 20	LARGER PEAK HORIZONTAL ACCELERATION (UNCORRECTED RECO
21 - 25	LESSER PEAK HORIZONTAL ACCELERATION (UNCORRECTED RECO
26 - 30	PEAK VERTICAL ACCELERATION (UNCORRECTED RECO
31 - 35	LARGER PEAK HORIZONTAL ACCELERATION (CORRECTED RECORD
36 - 40	LESSER PEAK HORIZONTAL ACCELERATION (CORRECTED RECORD
41 - 45	PEAK VERTICAL ACCELERATION (CORRECTED RECORD
46 - 50	LARGER PEAK HORIZONTAL VELOCITY (CM/SEC)
51 - 55	LESSER PEAK HORIZONTAL VELOCITY (CM/SEC)
56 - 61	DATE OF EARTHQUAKE (MONTH/DAY/YEAR)
62 - 64	INSTRUMENT SITE PROFILE TYPE : 1 = ROCK SITE 2 = SOIL SITE
65 - 68	EARTHQUAKE RECROD SEQUENCE NUMBER (1 TO 23) THE EVENTS BY NAME ARE AS FOLLOWS :

	1	6.4 IMPERIAL VALLEY	1940
	2	7.2 KERN COUNTY	1952
	3	5.3 DALY CITY	1957
	4	5.5 PARKFIELD	1966
	5	6.7 BORREGO MOUNTAIN	1968
	6	5.6 SANTA ROSA	1969
	7	5.7 SANTA ROSA	1969
	8	5.4 LYTLE CREEK	1970
	9	6.4 SAN FERNANDO	1971
	10	5.1 BEAR VALLEY	1972
	11	7.7 SITKA, ALASKA	1972
	12	6.2 MANAGUA, NICARAGUA	1972
	13	6.0 POINT MUGU	1973
	14	5.2 HOLLISTER	1974
	15	5.7 OROVILLE	1975
	16	5.1 SANTA BARBARA	1978
	17	7.6 ST. ELIAS, ALASKA	1979
	18	5.9 COYOTE LAKE	1979
	19	6.6 IMPERIAL VALLEY	1979
	20	5.0 IMPERIAL VALLEY	1979
	21	5.5 LIVERMORE VALLEY	1980
	22	5.6 LIVERMORE VALLEY	1980
	23	5.3 HORSE CANYON	1980

70	ASTERISK DENOTES RECORDS WHERE THE LARGER PEAK VELOCITY IS PRODUCED BY THE LESSER PEAK ACCELERATION

Table 1

7.06.4	117	12.0	.359	.224	.278	.348	.214	.210	36.9	33.4	51940	2 *
7.47.2	1083	148.0	.014	.012	.006						72152	1
	1095	42.0	.196	.176	.123	.179	.156	.105	17.7	15.7		2
	283	85.0	.135	.090	.051	.131	.090	.044	19.3	11.8		2
	135	107.0	.062	.044	.022	.059	.042	.021	8.9	6.6		2 *
	475	109.0	.054	.048	.033	.047	.053	.030	9.1	6.2		2
	113	156.0	.014									2
	1008	224.0	.018									2
	1028	293.0	.010									2
	2001	359.0	.004									2
	117	370.0	.004									2
5.35.3	1117	8.0	.127	.105	.051	.105	.083	.037	4.9	4.6	32257	1 *
6.15.5	1438	16.1	.411	.282	.165	.347	.269	.132	22.5	14.5	62766	1
	1083	63.6	.018	.016	.007	.014	.012	.006	1.1	.8		1
	1013	6.6	.509		.349	.489		.206	78.1			2
	1014	9.3	.467	.403	.181	.434	.356	.119	25.4	23.2		2
	1015	13.0	.279	.276	.138	.275	.237	.079	11.8	10.8		2
	1016	17.3	.072	.066	.061	.064	.053	.045	8.0	7.0		2
	1095	105.0	.012	.008	.007	.011	.008	.006	2.2	2.1		2
	1011	112.0	.006									2
	1028	123.0	.003									2
6.66.7	270	105.0	.018								40968	1
	280	122.0	.048	.042	.064	.046	.040	.055	4.2	3.7		1
	116	141.0	.011									1
	266	200.0	.007									1
	117	45.0	.142	.061	.036	.130	.057	.030	25.8	14.7		2
	113	130.0	.031	.024	.022	.022	.029	.022	3.5	2.7		2 *
	112	147.0	.006									2
	130	187.0	.010	.010	.006	.010	.009	.005	3.2	2.9		2
	475	197.0	.010									2
	269	203.0	.006									2
	135	211.0	.013	.012	.005	.013	.011	.005	3.2	2.4		2
5.65.6	1093	62.0	.005								100269	2
5.75.7	1093	62.0	.003								100269	2
5.35.4	111	19.0	.086	.057	.093	.071	.056	.060	5.6	2.0	91270	1
	116	21.0	.179	.170								1
	290	13.0	.205	.146	.093	.198	.142	.054	9.6	8.9		2
	112	22.0	.073	.062	.044	.071	.057	.038	4.0	2.9		2
	113	29.0	.045	.039	.042	.041	.036	.034	2.6	1.9		2
6.66.4	128	17.0	.374	.288	.164	.353	.283	.107	14.6	12.8	20971	1
	126	19.6	.200	.159	.170	.171	.146	.154	8.6	5.7		1 *
	127	20.2	.147	.131	.089	.122	.112	.073	4.8	4.5		1
	141	21.1	.188	.180	.138	.180	.170	.120	20.5	14.5		1
	266	21.9	.204	.096	.093	.192	.089	.085	11.6	6.0		1
	110	24.2	.335	.289	.180	.315	.271	.156	27.2	16.5		1
	1027	66.0	.057	.030	.050	.048	.021	.039	2.8	1.1		1
	111	87.0	.021	.020	.010							1
	125	23.4	.152	.120	.100	.148	.111	.095	18.0	14.4		2
	135	24.6	.217	.187	.119	.210	.170	.090	21.1	16.5		2
	475	25.7	.114	.103	.106	.109	.095	.095	14.3	8.0		2

Table 1

	262	28.6	.150	.118	.105	.130	.114	.088	14.2	9.3		2 *
	269	37.4	.148	.100	.060	.123	.093	.048	5.4	4.4		2
	1052	46.7	.112	.087	.041	.105	.086	.036	8.5	6.1		2 *
	411	56.9	.043	.025	.020	.041	.025	.019	5.0	4.1		2
	290	60.7	.057	.047	.037	.058	.043	.023	3.8	2.6		2 *
	130	61.4	.030	.029	.016	.029	.029	.017	10.4	7.4		2 *
	272	62.0	.027	.026	.011	.026	.026	.011	7.3	5.5		2
	1096	64.0	.028	.023	.018	.025	.021	.016	1.4	1.3		2
	1102	82.0	.034	.030	.020	.027	.026	.013	2.5	1.9		2 *
	112	88.0	.030	.030	.010							2
	113	91.0	.039	.034	.026	.038	.031	.020	2.6	2.2		2
5.35.11028		31.0	.030			.163	.088	.070	6.9	2.6	22472	2
7.77.72714		45.0	.110			.093	.071	.047	10.8	9.3	73072	1 *
	2708145.0		.010									1
	2715300.0		.010									2
6.26.23501		5.0	.390	.340		.358	.324	.304	35.1	30.3	122372	2
5.66.0	655	50.0	.031								22173	1
	272	16.0	.130	.080								2
5.25.21032		17.0	.011								112874	1
	1377	8.0	.120	.050		.114	.045	.046	7.2	2.4		2
	1028	10.0	.170	.100		.166	.091	.067	11.5	5.6		2
	1250	10.0	.140	.100		.137	.095	.029	3.9	3.2		2
6.05.71051		8.0	.110	.100					5.0		80175	1
	1293	32.0	.040	.030								1
	1291	30.0	.070	.060								2
	1292	31.0	.080	.060								2
5.15.1	283	2.9	.210	.100	.080	.204	.101	.077	15.2	6.5	81378	
	885	3.2	.390	.240					20.9	8.2		
		7.6	.280	.240		.345	.288	.135	39.6	26.1		
7.67.62734		25.4	.160	.110							22879	
		32.9	.064									
	2728	92.2	.090									
5.85.91413		1.2	.420	.340	.170	.417	.321	.150	43.8	25.1	80679	1
	1445	1.6	.230	.160	.100	.250	.140	.103	20.5	11.5		1
	1408	9.1	.130	.100	.080	.113	.085	.059	10.3	4.0		1
	1411	3.7	.260	.240	.440	.251	.233	.417	32.2	25.0		2
	1410	5.3	.270	.260	.150	.257	.250	.139	29.4	16.9		2 *
	1409	7.4	.260	.200	.180	.254	.190	.165	31.9	10.2		2
	1377	17.9	.110	.090	.120							2
	1492	19.2	.120	.080	.060							2
	1251	23.4	.038									2
	1422	30.0	.044	.050	.030							2
	1376	38.9	.046									2
6.56.66604		23.5	.170								101579	1
	286	26.0	.210	.120	.090	.193	.110	.077	9.0	5.0		1
	5155	.5	.320									2
	5028	.6	.520	.360	.650	.462	.370	.513	107.8	45.0		2
	942	1.3	.720	.450	1.740	.436	.376	1.695	108.7	63.1		2
	6616	1.4	.320	.279								2
	5054	2.6	.810	.660	.470	.786	.587	.354	44.0	43.6		2

Table 1

	958	3.8	.640	.500	.550	.610	.466	.414	53.0	47.7	2
	952	4.0	.560	.400	.710	.527	.383	.441	87.0	43.9	2 *
	5165	5.1	.510	.370	.930	.486	.352	.658	68.0	42.5	2 *
	117	6.2	.400	.270	.380						2
	955	6.8	.610	.380	.320	.493	.356	.203	78.0	37.0	2 *
	5055	7.5	.260	.220	.310	.251	.217	.228	48.0	44.6	2 *
	5154	7.6	.240								2
	6619	8.4	.460								2
	5060	8.5	.220	.170	.180	.221	.165	.153	37.0	35.3	2
	412	8.5	.230	.200	.150	.226	.171	.105	44.0	42.0	2 *
	5053	10.6	.280	.220	.210	.275	.201	.183	19.0	16.0	2
	5058	12.6	.380	.380	.160	.382	.362	.140	39.0	35.0	2
	5057	12.7	.270	.220	.150	.267	.222	.132	46.0	37.0	2
	6617	12.9	.310								2
	5051	14.0	.200	.110	.160	.204	.109	.155	17.0	14.6	2 *
	5169	15.0	.110								2
	5115	16.0	.430	.330	.170	.413	.315	.110	31.0	27.0	2 *
	6621	17.7	.270								2
	931	18.0	.150	.110	.080	.141	.116	.067	19.0	18.0	2 *
	5056	22.0	.150	.150	.100	.142	.139	.044	15.0	11.0	2
	5059	22.0	.150	.120	.060	.139	.117	.043	15.0	14.0	2 *
	5061	23.0	.130	.090	.070	.128	.078	.055	15.0	12.0	2
	6622	23.2	.190								2
	5062	29.0	.130	.100	.060						2
	5052	32.0	.066	.050	.030	.057	.043	.027	5.8	3.2	2
	6605	32.7	.350								2
	724	36.0	.100								2
	6610	43.5	.160								2
	5066	49.0	.140	.110	.040	.128	.116	.038	16.0	13.0	2
	5050	60.0	.049	.040	.030						2 *
	2316	64.0	.034	.030	.020						2
5.05.05055		7.5	.264	.116	.042					101579	2
	942	8.8	.263	.175	.080						2
	5028	8.9	.230	.147	.086						2
	5165	9.4	.147	.146	.103						2
	952	9.7	.286	.235	.117						2
	958	9.7	.157	.128	.056						2
	955	10.5	.237	.168	.079						2
	117	10.5	.133	.078	.086						2
	412	12.0	.055	.051	.026						2
	5053	12.2	.097	.011	.034						2
	5054	12.8	.129	.074	.052						2
	5058	14.6	.192	.098	.063						2
	5057	14.9	.147	.103	.039						2
	5115	17.6	.154	.089	.054						2
	5056	23.9	.060	.033	.033						2
	5060	25.0	.057	.045	.043						2
5.85.51030		10.8	.120							12480	
	1418	15.7	.154	.060	.030						
	1383	16.7	.052	.040	.030						

Table 1

	1308	20.8	.045	.040	.020	
	1298	28.5	.086	.050	.040	
	1299	33.1	.056	.050	.030	
	1219	40.3	.065			
5.55.6		4.0	.259	.220	.100	12680
		10.1	.267	.190	.080	
	1030	11.1	.071			
	1418	17.7	.275			
	1383	22.5	.058			
		26.5	.026	.040	.010	
	1299	29.0	.039			
	1308	30.9	.112			
	1219	37.8	.065			
	1456	48.3	.026			
5.35.35045		5.8	.123	.088	.063	22580
	5044	12.0	.133	.118	.058	
	5160	12.1	.073	.067	.041	
	5043	20.5	.097	.076	.101	
	5047	20.5	.096	.096	.051	
	933	25.3	.230	.110	.090	
	5068	35.9	.082	.050	.049	
	901	36.1	.110	.080	.170	
	5042	36.3	.110	.094	.034	
	5067	38.5	.094	.060	.020	
	5049	41.4	.040	.032	.016	
	5005	43.6	.050	.050	.060	
	5070	44.4	.022	.017	.028	
	5091	46.1	.070	.030	.050	
	5006	47.1	.080	.070	.060	
	5069	47.7	.033	.028	.011	
	5073	49.2	.017	.016	.011	
	5072	53.1	.022	.016	.022	

TABLE 2
MEAN VALUES AND MEAN RATIO VALUES*

QUANTITY	NO. OF VALUES	MEAN VALUE
UNCORRECTED DATA		
Peak Horizontal Acceleration	182	0.154g
Lesser Peak Horizontal Acceleration	136	0.129g
Peak Vertical Acceleration	123	0.122g
Vertical/Peak Horizontal Acceleration	123	0.622
Vertical/Mean Peak Horizontal Acceleration	122	0.703
Ratio of Peak Horizontal Acceleration	136	1.406
CORRECTED DATA		
Peak Horizontal Acceleration	78	0.201g
Lesser Peak Horizontal Acceleration	77	0.151g
Peak Vertical Acceleration	78	0.131g
Peak Horizontal Velocity	80	22.0 cm/sec
Lesser Peak Horizontal Velocity	78	14.9 cm/sec
Vertical/Peak Horizontal Acceleration	78	0.597
Vertical/Mean Peak Horizontal Acceleration	77	0.669
Ratio of Peak Horizontal Acceleration	77	1.337
Ratio of Peak Velocities	78	1.506
CORRECTED AND UNCORRECTED		
Ratio of Peak Horizontal Acceleration	78	1.07
Ratio of Peak Vertical Acceleration	71	1.26

*instrument soil profile not considered

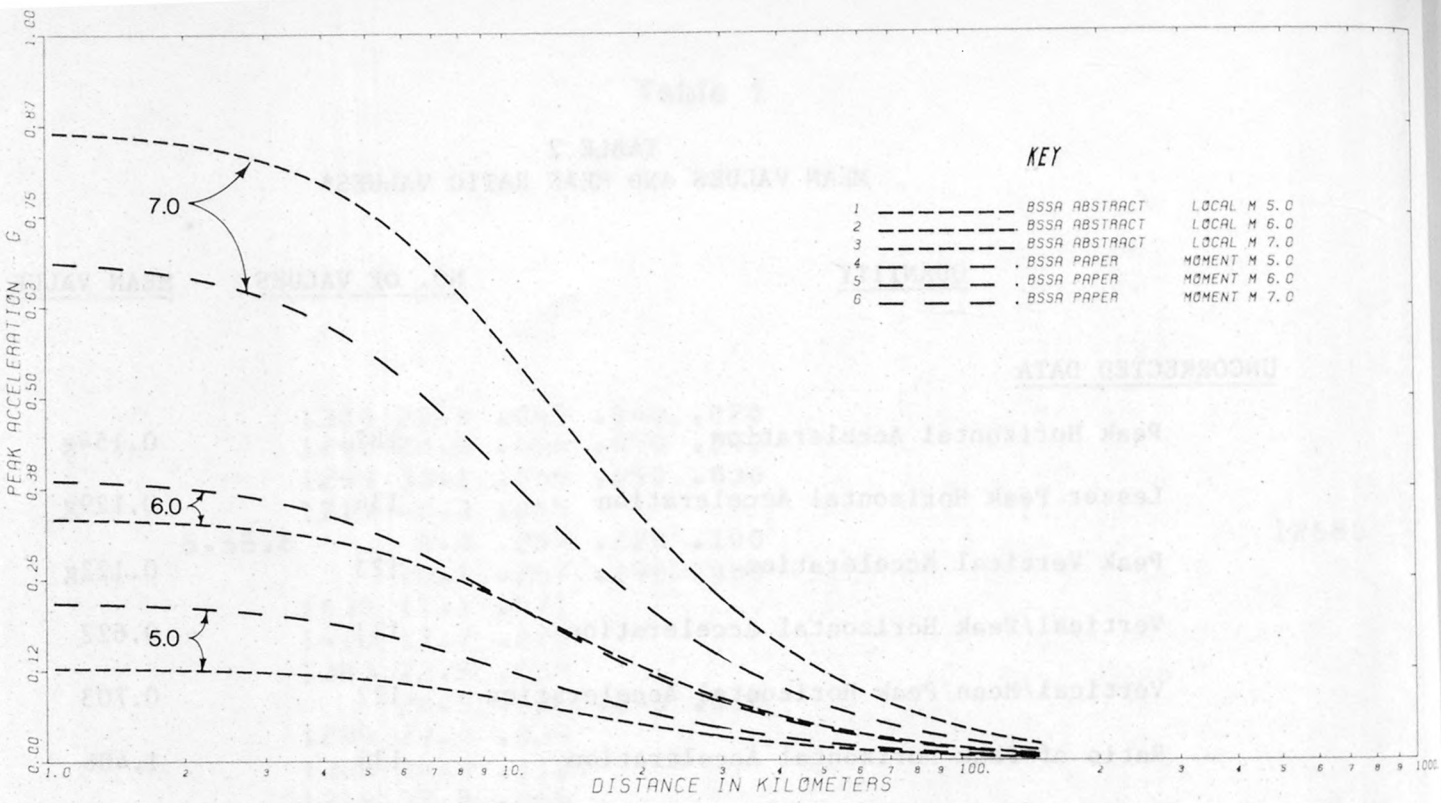

JOYNER & BOORE EQUATIONS BASED ON LOCAL MAGNITUDE AND MOMENT MAGNITUDE (PEAK ACCELERATION)

FIG. 1

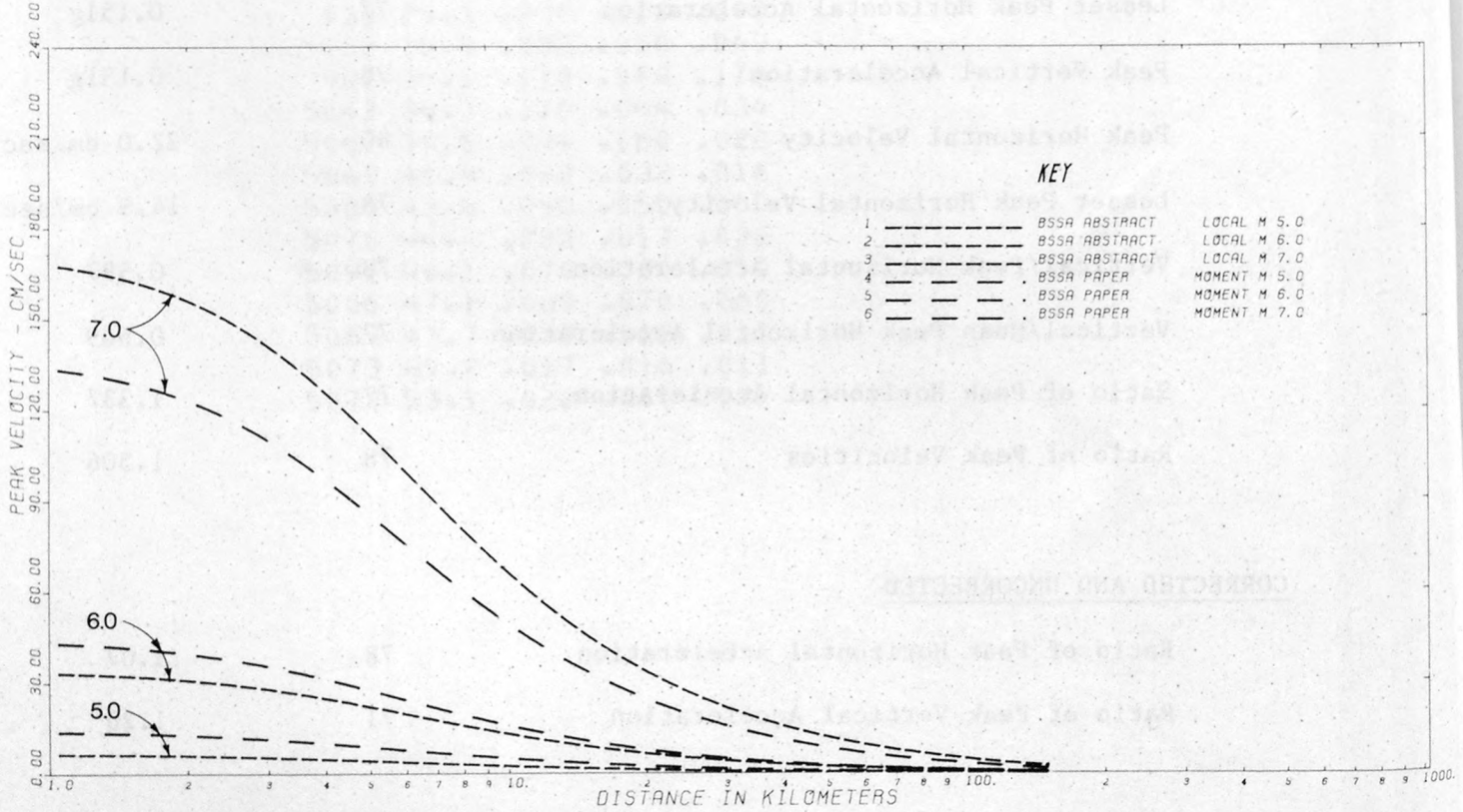

JOYNER & BOORE EQUATIONS BASED ON LOCAL MAGNITUDE AND MOMENT MAGNITUDE (PEAK VELOCITY)

FIG. 2

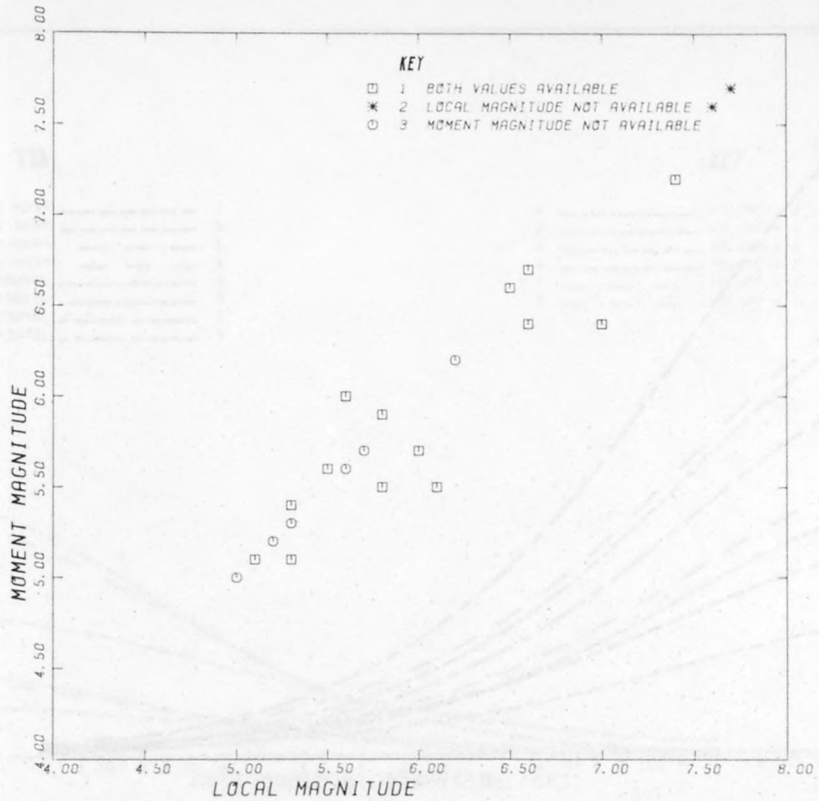

SCATTER DIAGRAM COMPARING LOCAL MAGNITUDE AND MOMENT MAGNITUDE VALUES IN JOYNER & BOORE DATA SET

FIG. 3

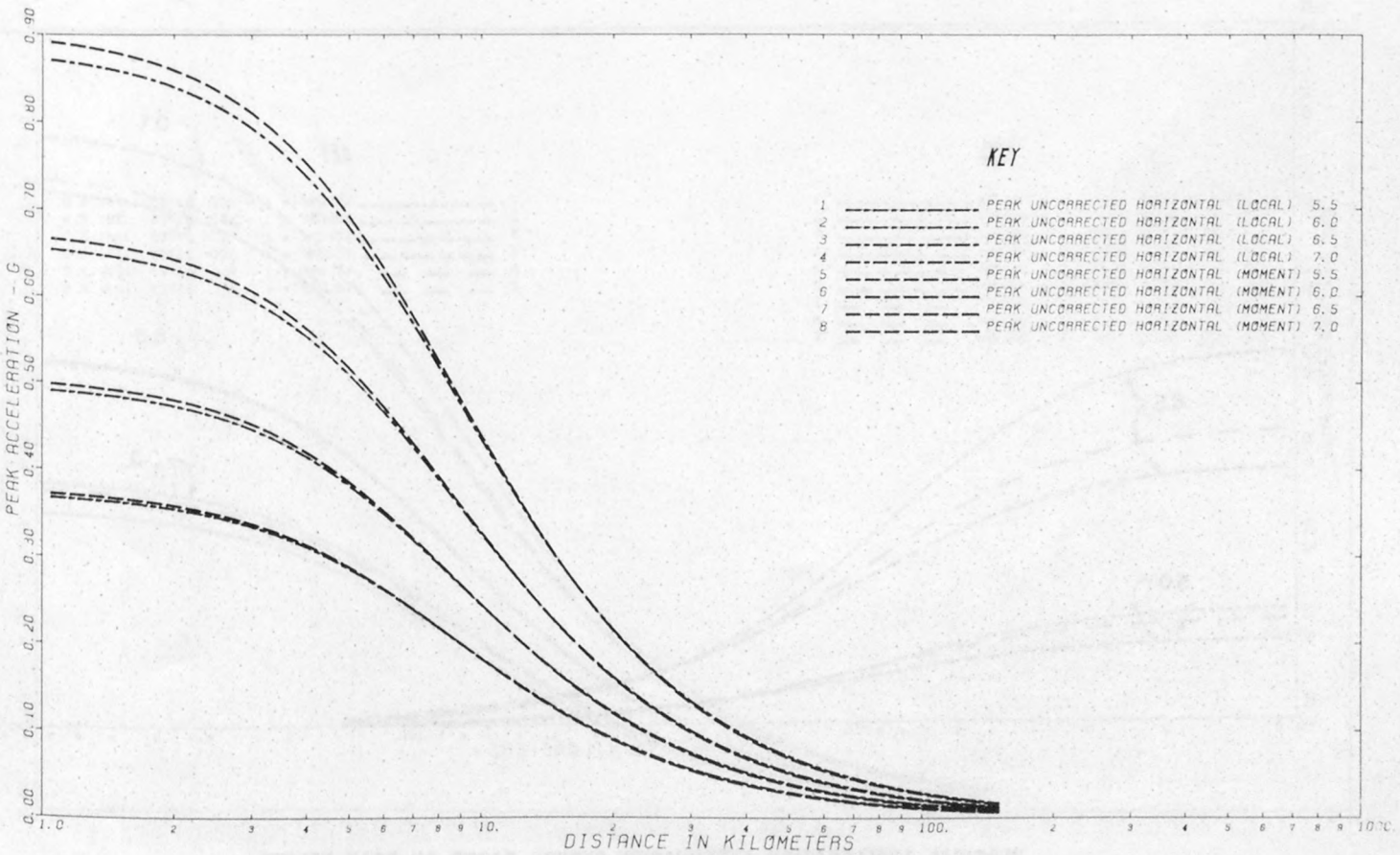

DIRECT FIT OF DATA FOR PEAK ACCELERATION ASSUMING LOCAL MAGNITUDE AND MOMENT MAGNITUDE OPTIONS

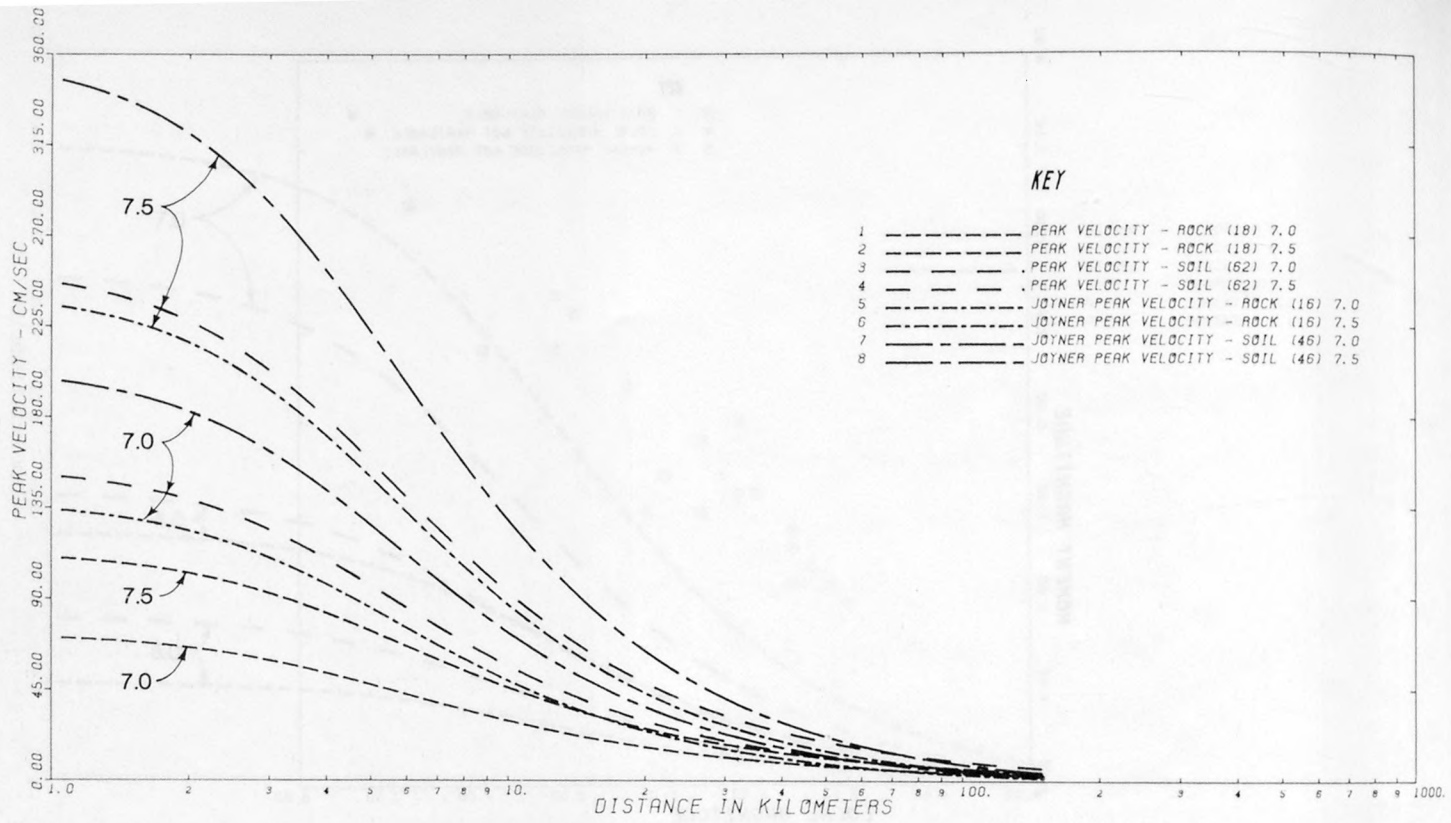

COMPARISON OF DIRECTLY DERIVED VELOCITY EQUATIONS WITH THOSE PRESENTED BY JOYNER & BOORE
(NOTE THAT NUMBER LISTED IN PARENTHESIS IN KEY IS SIZE OF AVAILABLE DATA SET)

FIG. 5

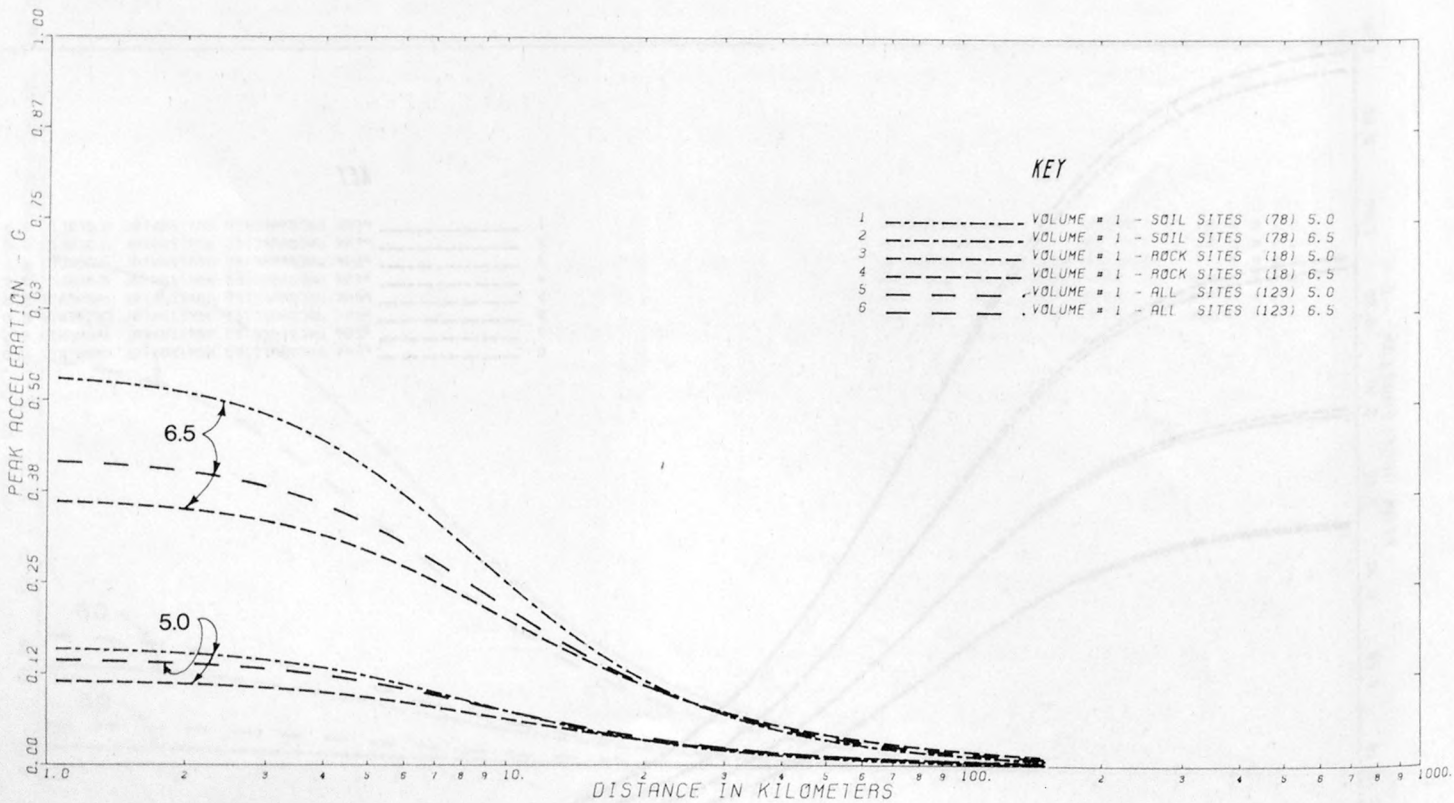

VERTICAL ACCELERATION ATTENUATION CURVES BASED ON PEAK VALUES

FIG. 6

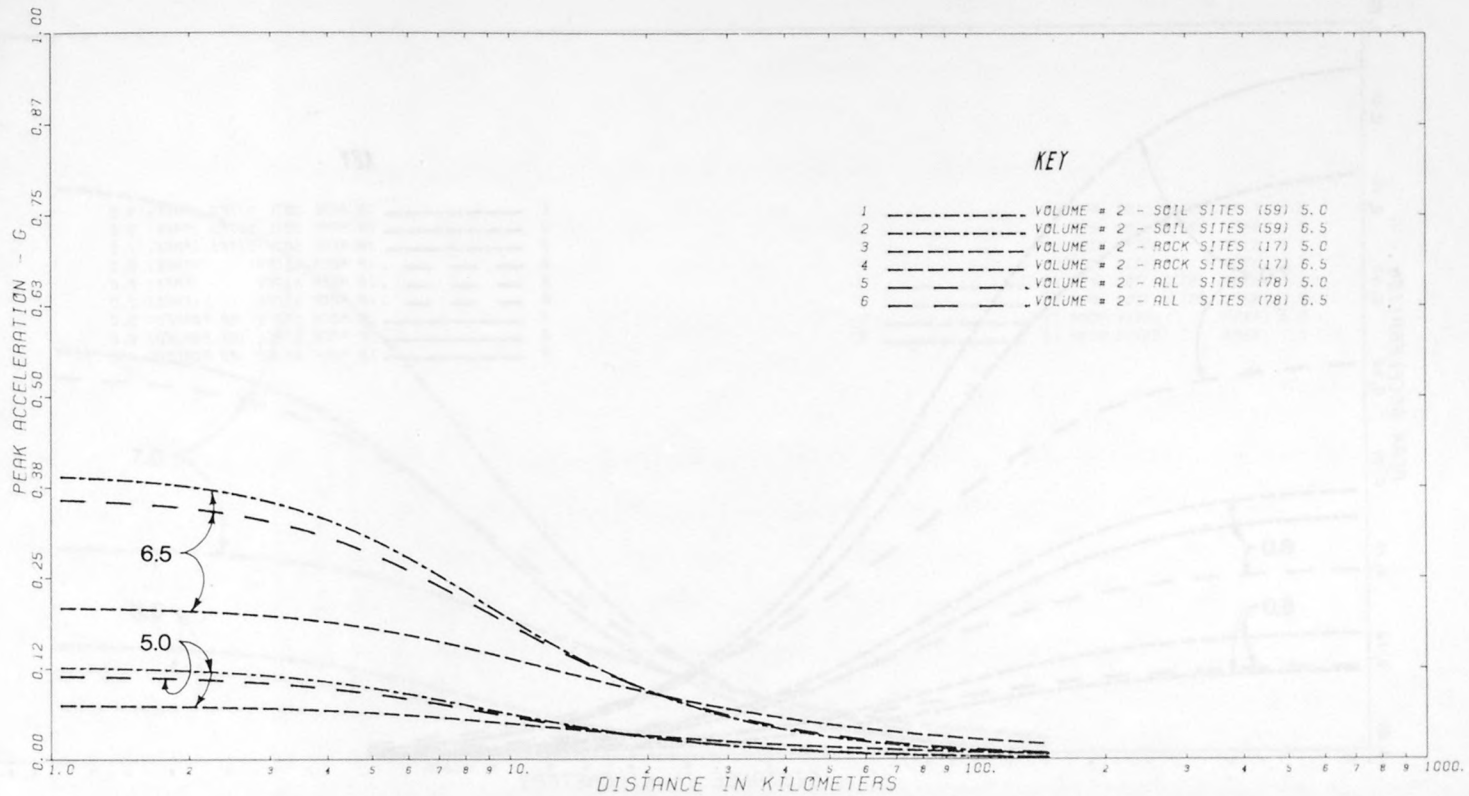

VERTICAL ACCELERATION ATTENUATION CURVES BASED ON PEAK VALUES OF UNIFORMLY DIGITIZED AND PROCESSED RECORDS

FIG. 7

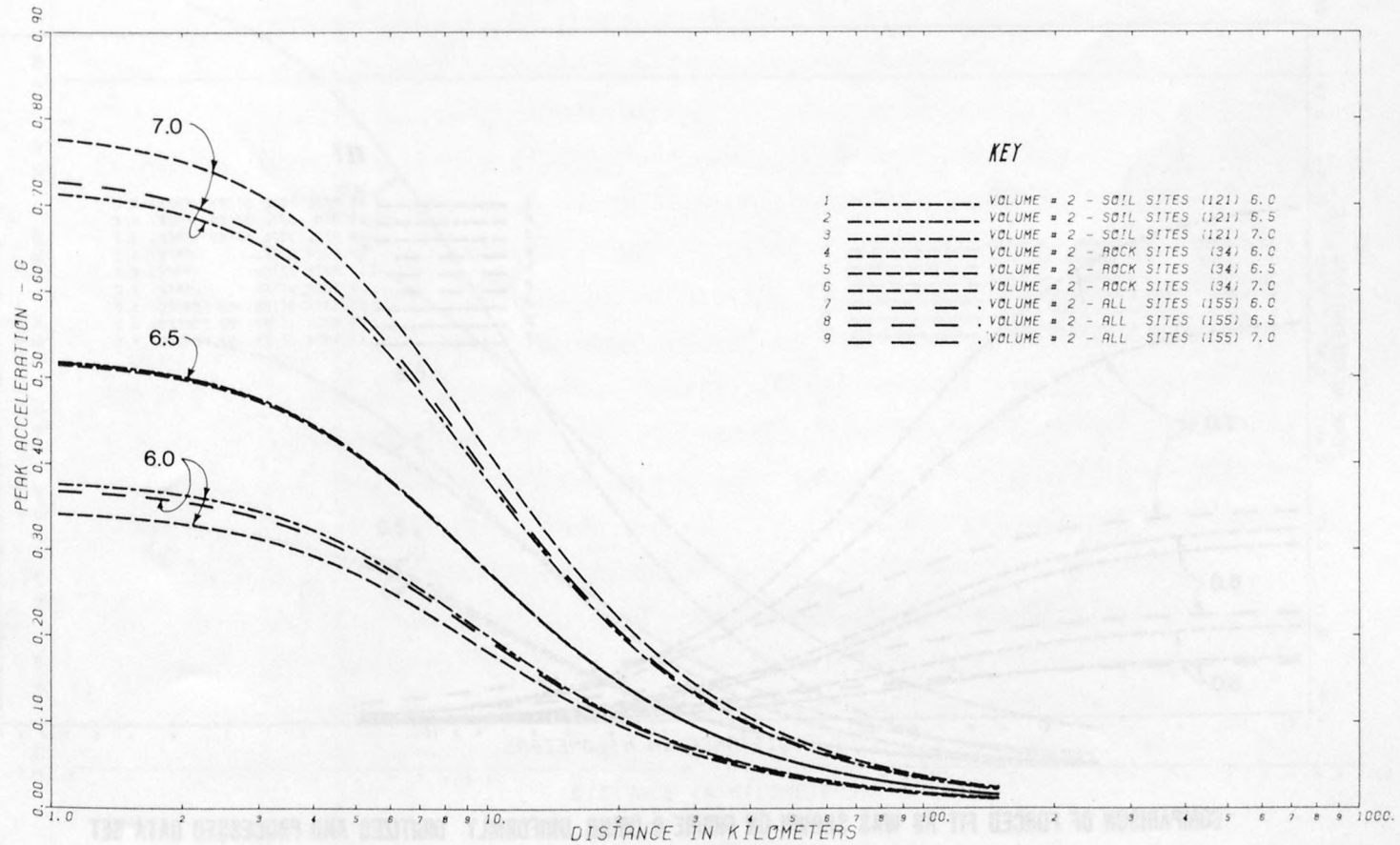

MEAN PEAK HORIZONTAL ATTENUATION CURVES BASED ON AVERAGE PEAK VALUES OF UNIFORMLY DIGITIZED AND PROCESSED RECORDS

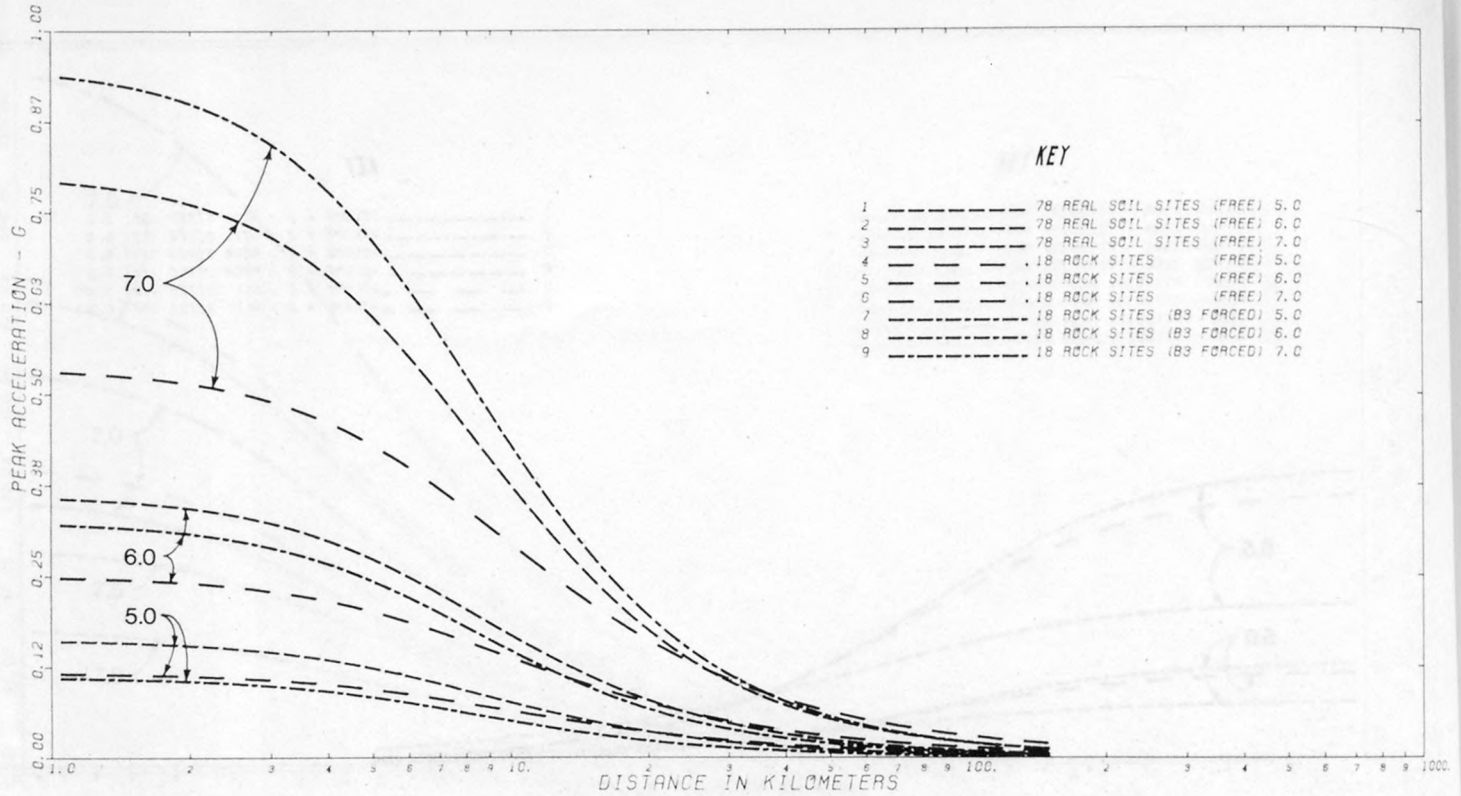

COMPARISON OF LEAST SQUARES FIT OF VERTICAL ACCELERATION DATA WITH RESTRAINED DISTANCE ATTENUATION COEFFICIENT ATTENUATION CURVE FOR ROCK SET TO SAME DISTANCE TERM AS SOIL DATA

FIG. 9

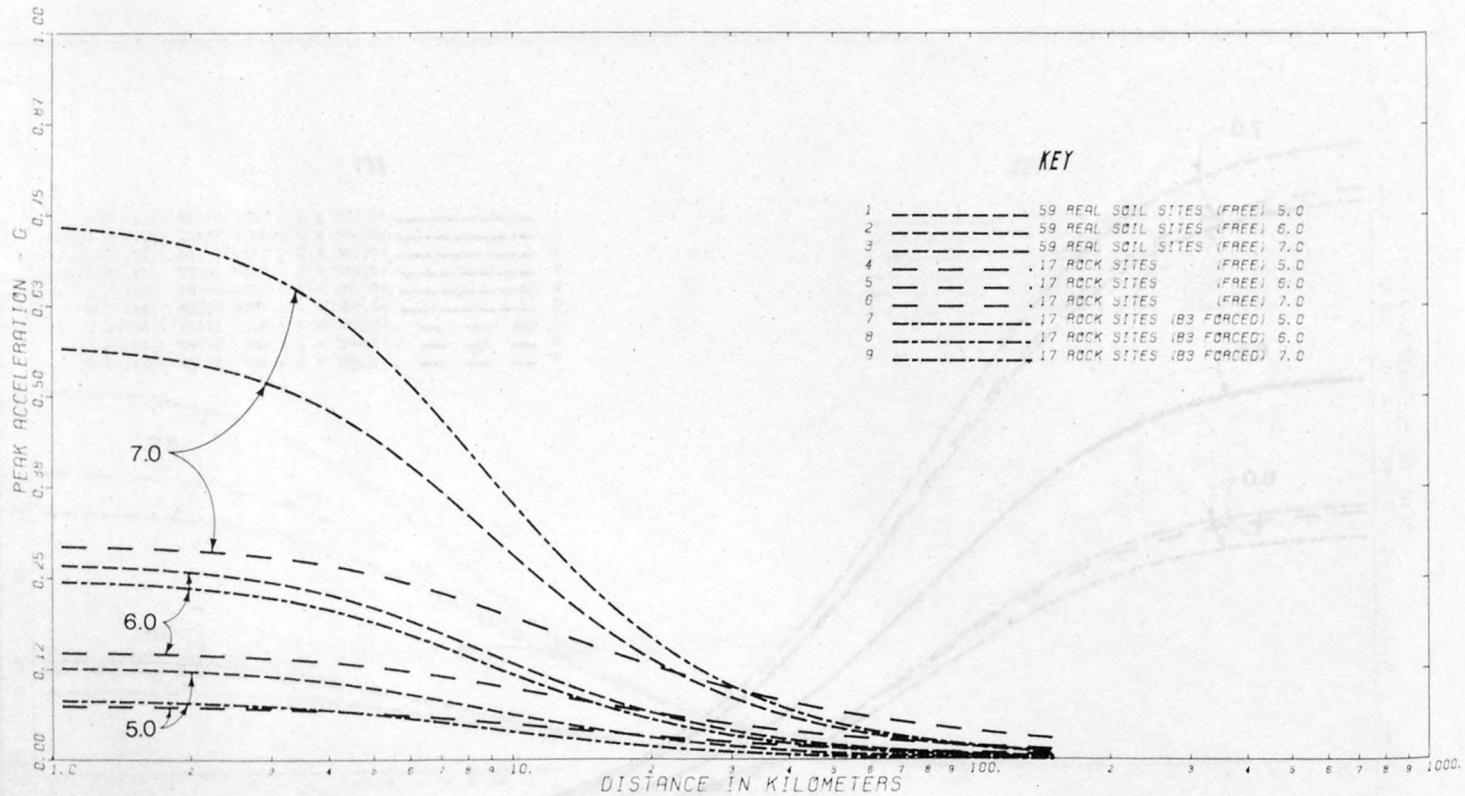

COMPARISON OF FORCED FIT AS WAS SHOWN ON FIGURE 9 USING UNIFORMLY DIGITIZED AND PROCESSED DATA SET

FIG. 10

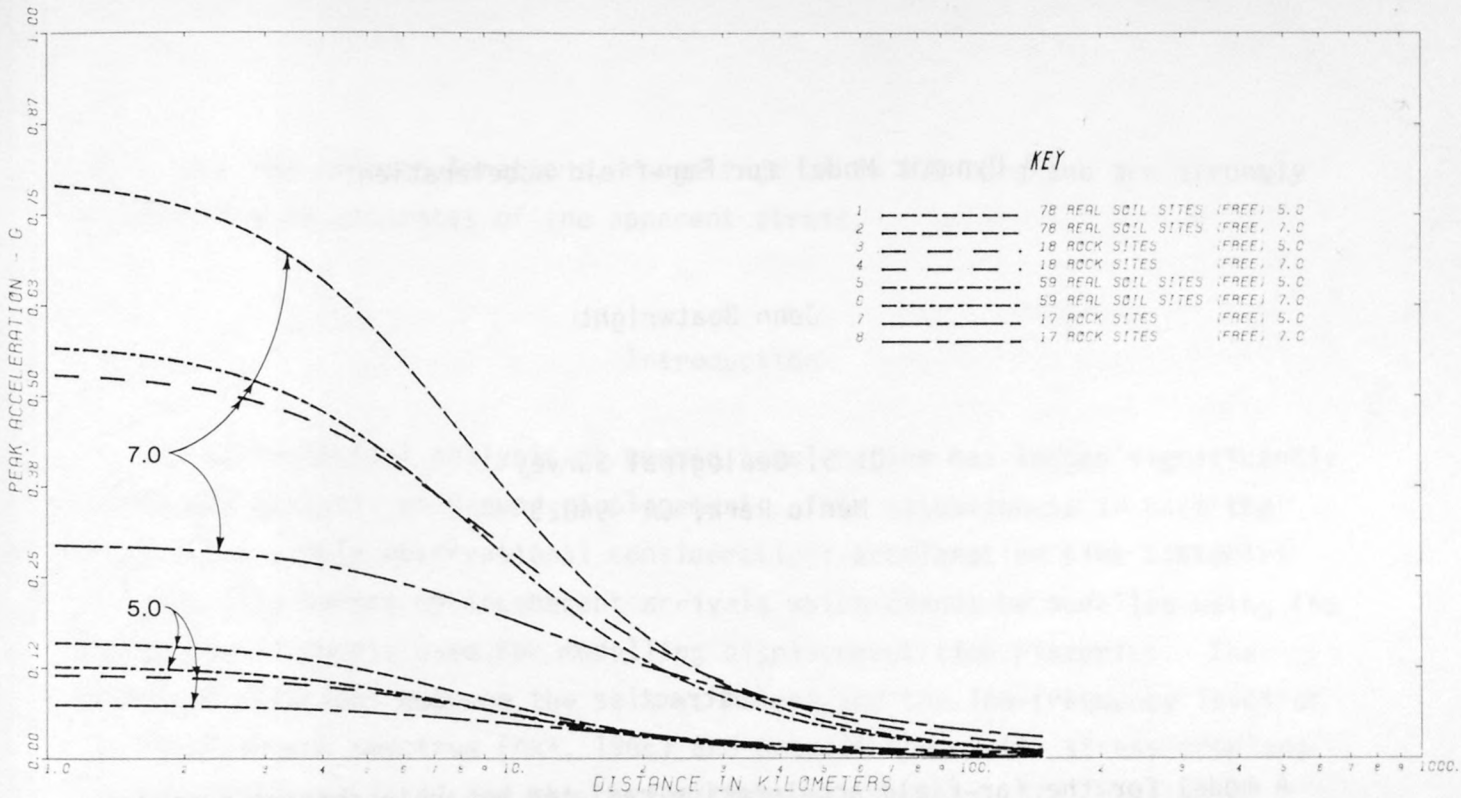

COMPARISON OF ATTENUATION CURVES FOR VERTICAL ACCELERATION EQUATIONS USING UNCORRECTED PEAK VALUES AND PEAK VALUES OF UNIFORMLY DIGITIZED AND PROCESSED DATA

FIG. 11

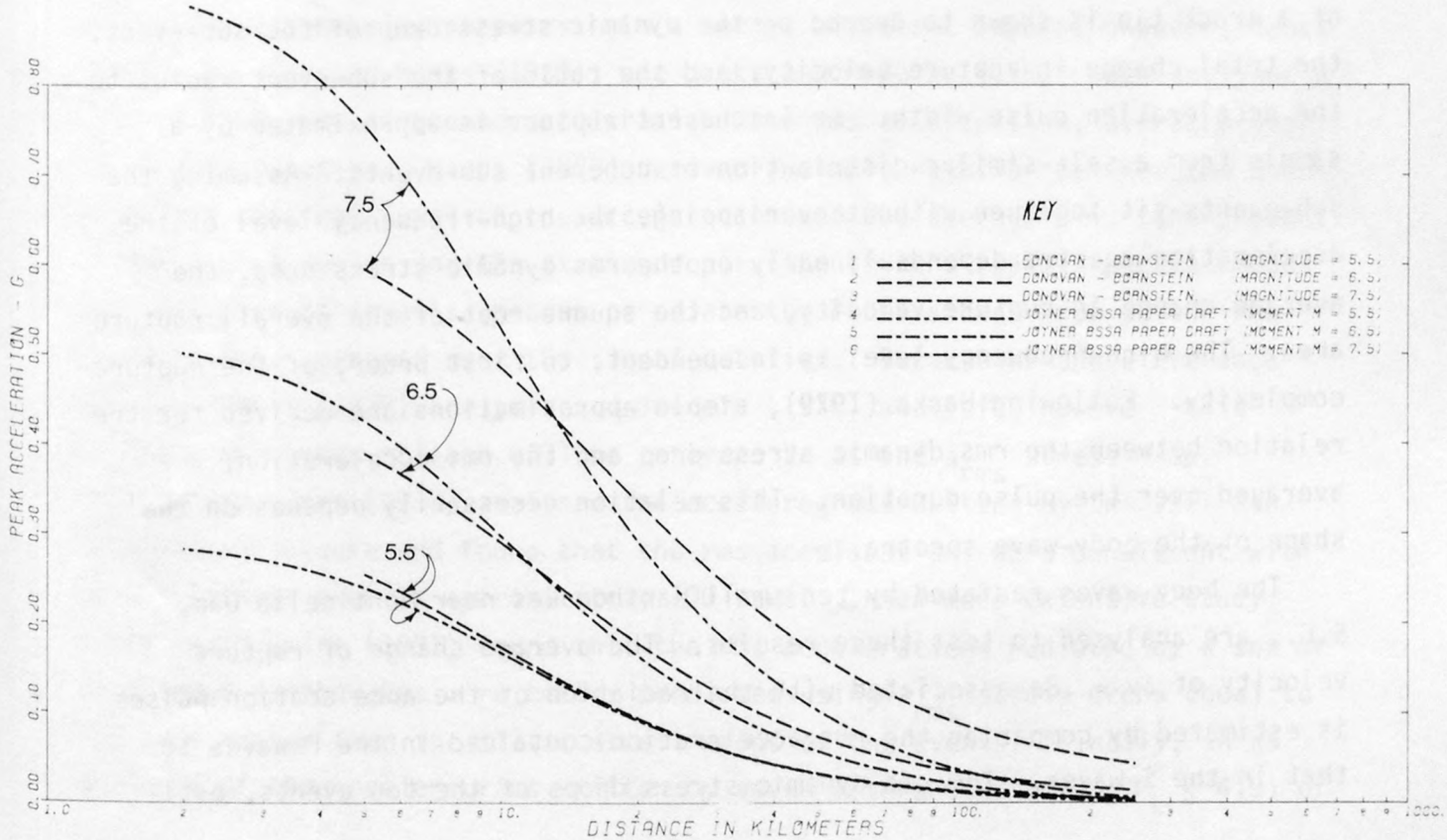

COMPARISON OF DONOVAN AND BORNSTEIN ROCK AND STIFF SOIL ATTENUATION EQUATION (1978) WITH JOYNER & BOORE ATTENUATION EQUATION (1981)

A Dynamic Model for Far-field Acceleration

John Boatwright

U. S. Geological Survey
Menlo Park, CA 94025

Abstract

A model for the far-field acceleration radiated by an incoherent rupture is constructed by combining Madariaga's (1977) theory for the high-frequency radiation from crack models of faulting with a simple statistical source model. By extending Madariaga's results to acceleration pulses with finite durations, the peak acceleration of a pulse radiated by a single stop or start of a crack tip is shown to depend on the dynamic stress drop of the sub-event, the total change in rupture velocity, and the ratio of the sub-event radius to the acceleration pulse width. An incoherent rupture is approximated by a sample from a self-similar distribution of coherent sub-events. Assuming the sub-events fit together without overlapping, the high-frequency level of the acceleration spectra depends linearly on the rms dynamic stress drop, the average change in rupture velocity, and the square root of the overall rupture area. The high-frequency level is independent, to first order, of the rupture complexity. Following Hanks (1979), simple approximations are derived for the relation between the rms dynamic stress drop and the rms acceleration, averaged over the pulse duration. This relation necessarily depends on the shape of the body-wave spectra.

The body-waves radiated by ten small earthquakes near Monticello Dam, S.C., are analysed to test these results. The average change of rupture velocity of $\Delta v = .8\beta$ associated with the radiation of the acceleration pulses is estimated by comparing the rms acceleration contained in the P-waves to that in the S-waves. The rms dynamic stress drops of the ten events, esti-

mated from the rms accelerations, range from .4 to 1.9 bars and are strongly correlated with estimates of the apparent stress.

Introduction

The seismological analysis of ground acceleration has lagged significantly behind the analysis of ground displacement. This situation is in part the result of a simple observational consideration: acceleration time histories are generally bursts of incoherent arrivals which cannot be modelled using the simple source models used for modelling displacement time histories. The important relations between the seismic moment and the low-frequency level of the displacement spectrum (Aki, 1966) and between the static stress drop and the low-frequency level and the corner frequency (Brune, 1970) have also focussed seismological attention on observations of ground displacement rather than ground acceleration.

The only datum uniformly retrieved from strong motion accelerograms is the peak acceleration, which is the customary parametrization of strong ground motion for engineering purposes. In a series of recent papers, however, Hanks (1979), McGuire and Hanks (1980), and Hanks and McGuire (1981) have analysed a different measure of ground acceleration: the rms acceleration, averaged over the signal duration. Hanks (1979) derived a simple relation between the high-frequency spectral level of the acceleration and the average slip (the product of the source radius and the strain drop) using Brune's (1970) spectral model and then used Parseval's theorem to relate the Brune stress drop to the rms acceleration, averaged over the signal duration. Because of the difference between Hanks' (1979) analysis and Brune's (1970) analysis, however this estimate of stress release will be referred to as the a_{rms} stress drop. McGuire and Hanks (1980) analysed the accelerograms written by the 1971 San Fernando earthquake and found that the rms accelerations were consistent with an a_{rms} stress drop of approximately 100 bars. In an more extensive study, Hanks and McGuire (1981) found that the rms accelerations radiated by a set of nine large earthquakes were better predicted using a_{rms} stress drops equal to 100 bars rather than the static stress drops of the events. Finally, in an analysis of the accelerograms written by seven aftershocks ($4.0 \leq M_L \leq 4.9$) of

the 1975 Oroville earthquake, they obtained very constant estimates of stress release by inverting the rms accelerations to directly estimate the a_{rms} stress drops.

In a related study of these aftershocks, Boatwright (1982) compared these a_{rms} stress drops to estimates of the dynamic stress drop (Boatwright, 1980), the apparent stress, the static stress drop, and the Brune stress drop. The a_{rms} stress drops were strongly correlated with the dynamic stress drops and the apparent stress, weakly correlated with the Brune stress drops and were uncorrelated with the static stress drops. The correlations between the a_{rms} stress drops, the dynamic stress drops and the apparent stress were approximately independent of the complexity of the rupture process.

The results of these papers suggest two further conclusions: that the rms acceleration is controlled by the dynamic stress drop rather than the static stress drop, and that the apparent range of the dynamic stress drop is more narrow than the range associated with the static stress drop. The implied difference between these two measures of stress release is an important one for observational source theory. There are two reasons for this difference; first, the dependence of the estimate of the average static stress drop on the cube of the estimate of the source radius introduces a substantial uncertainty into the analysis for the static stress drop; and second, the estimate of the average static stress drop depends strongly on the geometry of the stress release (Madariaga, 1979), while the estimate of the average dynamic stress drop is approximately independent of this geometry.

The model presented in this paper uses Madariaga's (1977) results for the acceleration pulses radiated by rupture fronts which start or stop abruptly. The acceleration radiated by a complex rupture is modelled as a incoherent group of these pulses; the sub-events which radiate the pulses are assumed to cover the rupture area without overlapping. The resulting description of the far-field acceleration depends only on the dynamic characteristics of faulting, i.e., the dynamic stress drop, the average change of rupture velocity and the rupture area. This purely dynamic basis represents a useful counterpoint to Hanks' (1979) extrapolation of Brune's (1970) spectral model. In particular, the high-frequency level of the acceleration spectrum is shown to depend on the product of the rms dynamic stress drop and the square root of the rupture area rather than the ratio of the moment to the rupture area. This relation-

ship is independent of the rupture complexity and can be used to predict the rms acceleration for body-waves with a wide range of spectral shapes. While the results for the rms acceleration are dimensionally similar to those of Hanks (1979), the dynamic model provides a more physical understanding of the acceleration radiated by earthquake faulting.

A Representation for Acceleration Pulses

In this analysis, the high-frequency seismic radiation from a dynamic earthquake rupture is modelled using the acceleration pulses radiated by the starting and stopping of the crack tip as it ruptures through regions of varying fracture strength. In his paper on the "high-frequency radiation from crack (stress drop) models of earthquake faulting", Madariaga (1977) demonstrates how abrupt changes in the rupture velocity radiate acceleration pulses (stress waves). To use Madariaga's results for the acceleration pulses radiated by 3-D rupture fronts, however, it is necessary to specify both the crack half-length and the radius of curvature of the rupture front (see Madariaga, 1977, eq. (46)). By assuming a semi-circular geometry for the rupture front, these two parameters are coalesced to a single parameter, the radius of the crack front. Because a wide range of rupture geometries can be approximated by summing semi-circles of variable size and orientation, this geometrical constraint is assumed to be sufficiently general.

The spectral excitation of the acceleration, $\ddot{u}_c(r,\omega)$, radiated in an elastic whole-space by the abrupt acceleration or deceleration of a semi-circular rupture front of radius r is given by Madariaga, eq. (50), as

$$\ddot{u}_c(r,\omega) = \frac{\Delta\sigma}{\mu} \frac{R^c}{R} \Delta v \, r \, , \qquad (1)$$

where $\Delta\sigma$ is the dynamic stress drop, μ is the rigidity, Δv is the change of rupture velocity, R is the distance to the observer, and c is the wave velocity. The superscripts and subscripts refer to the wavetype (P, SV or SH), where the directions of shear-wave motion are defined relative to the crack plane rather than the surface of the earth. The generalized radiation pattern,

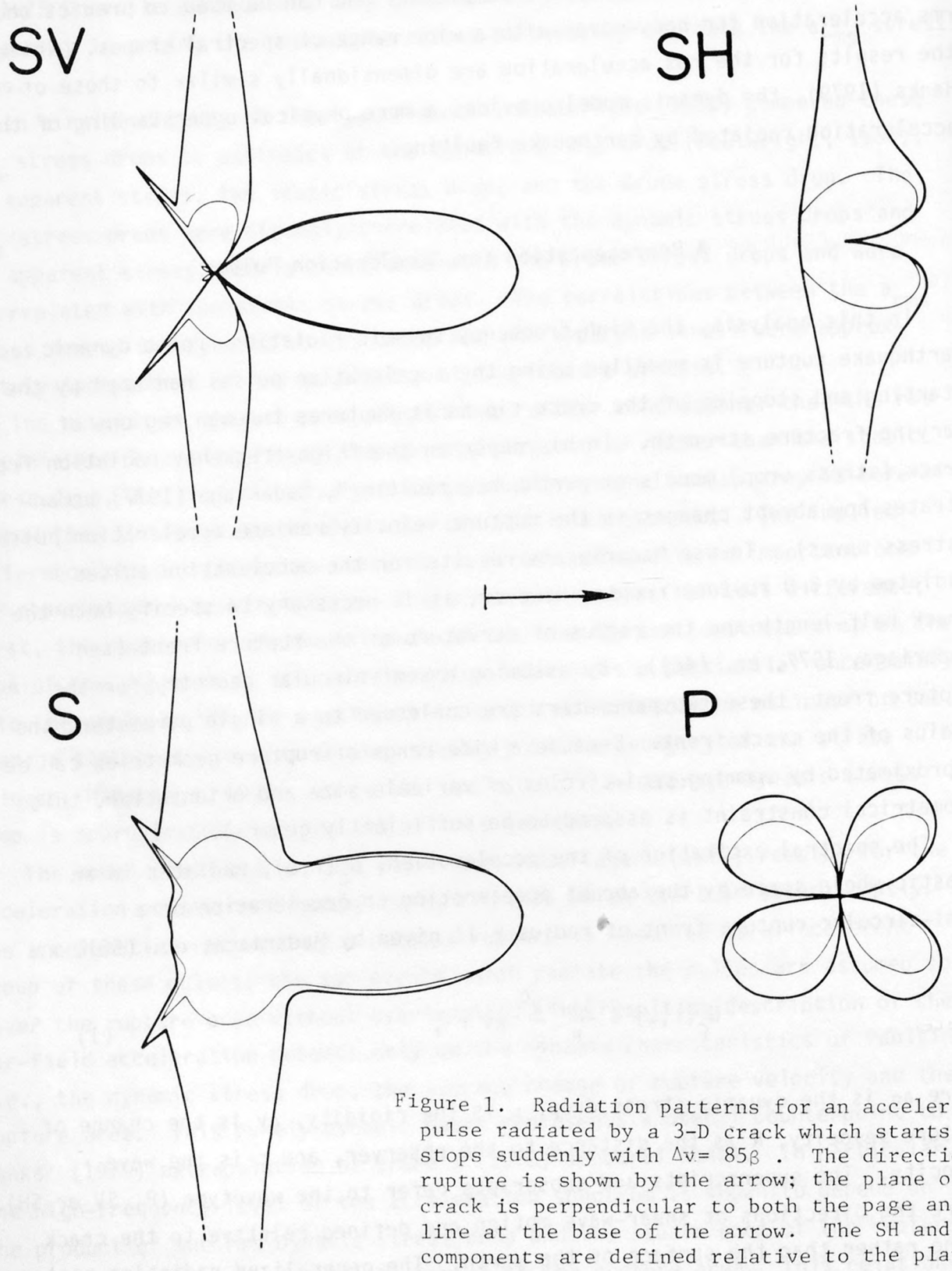

Figure 1. Radiation patterns for an acceleration pulse radiated by a 3-D crack which starts or stops suddenly with $\Delta v = 85\beta$. The direction of rupture is shown by the arrow; the plane of the crack is perpendicular to both the page and the line at the base of the arrow. The SH and SV components are defined relative to the plane of the crack; the S-wave pattern is the square root of the sum of the squares of the two S-wave components. The P-wave radiation patterns have been multiplied by a factor of five. The lighter lines are the 2-D radiation patterns, which lack the geometrical focussing in the direction $\theta = 0$.

$$R^C = \frac{k_C \, F^C(\theta,\phi) \, D^C(\psi)}{1 - \frac{\Delta v}{c} \cos\psi} , \qquad (2)$$

is markedly different from the usual double-couple radiation pattern, $F^C(\theta,\phi)$, where θ is the takeoff angle measured from the fault normal and ϕ is the azimuth. Eq. (2) shows that the double-couple radiation patterns are modified by two important factors: $(1 - \frac{\Delta v}{c} \cos\psi)^{-1}$ is the directivity function introduced by Ben-Menahem (1961), and $D^C(\psi)$ is a diffraction factor that depends on the angle ψ between the takeoff angle and the direction of crack growth and is given in Madariaga's eqs. (51), (35) and (36). k_C is a dimensionless coefficient defined in Madariaga's eqs. (49) and (4).

In Figure 1, these radiation patterns are plotted for a 3-D crack with a change of rupture velocity $\Delta v = .85\beta$. The only significant difference between these 3-D results and the 2-D radiation patterns plotted as lighter lines in Figure 1 is the presence of the caustic at $\theta = 0$. The location of this caustic is a result of the assumed stopping behavior; it represents the simultaneous arrival of the acceleration pulses radiated all of the rupture front. Achenbach and Harris (1978, 1982) show that this location can vary considerably for more general stopping behaviors and geometries.

An important aspect of these radiation patterns is their dependence on the rupture velocity through the directivity factor. To consider this dependence, the radiation patterns have been averaged over the focal sphere for a range of rupture velocities from $.65\beta$ to $.92\beta$ (the Rayleigh wave velocity for a Poisson solid). The coefficients, k_C, were assumed to be constants: $k_{SH} = .2$ and $k_P = k_{SV} = .35$. The results for each of the wavetypes are shown in Figure 2, along with the mean values for F^C. The high-frequency S-wave radiation is a strong function of the change of rupture velocity for rupture velocities greater than $.8\beta$. The ratio $\bar{R}^S/\bar{R}^P$ varies by a factor of 2 over the range $.75\beta < \Delta v < .9\beta$; in a later section, this variation is used to estimate the average change of rupture velocity for a set of small earthquakes.

As Madariaga (1977) points out, the spectral excitation in eq. (1), corresponding to a purely impulsive time function, should be considered as an upper bound for the high-frequency excitation of an acceleration pulse. If the change of rupture velocity is not perfectly abrupt, or if there is a

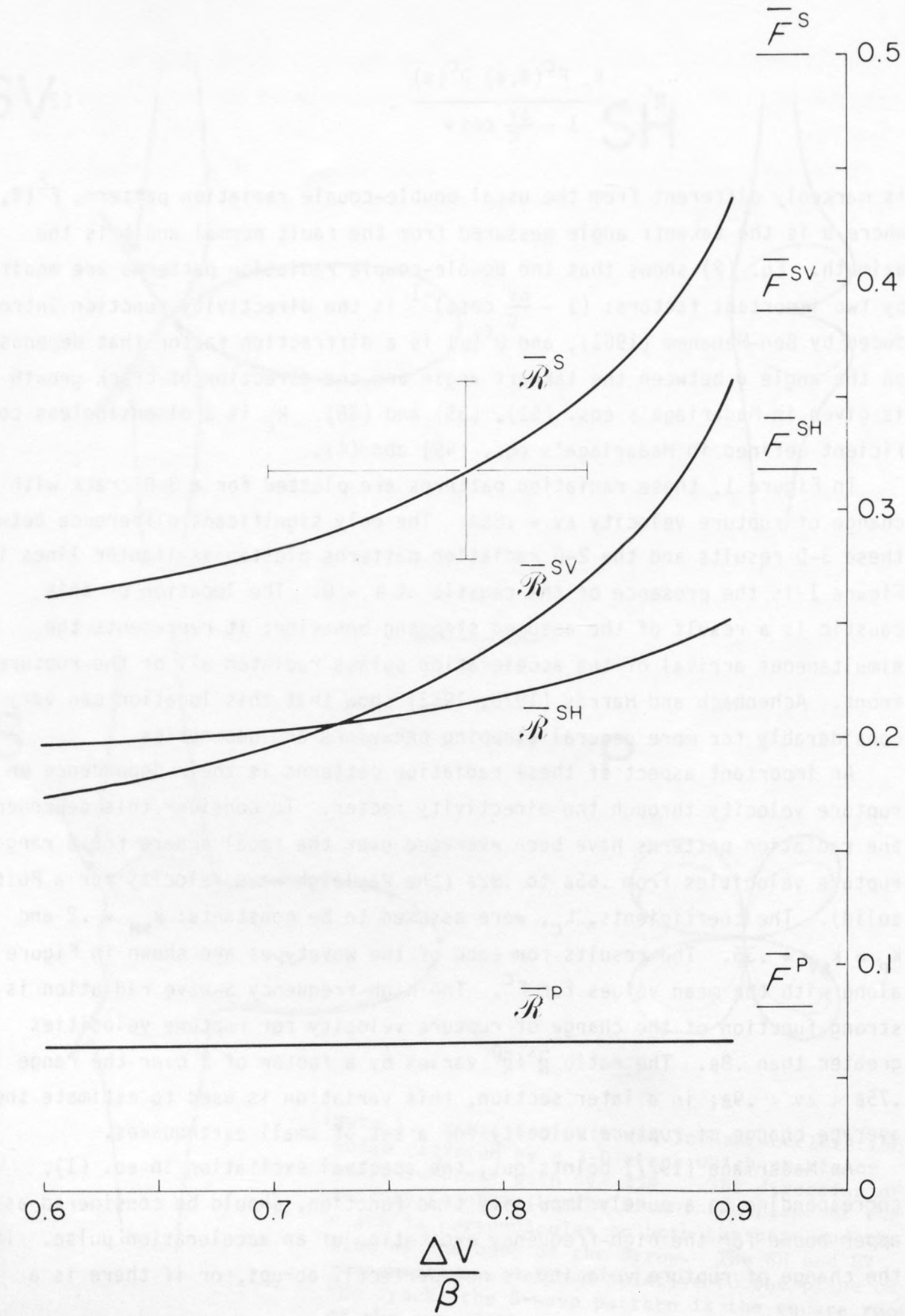

Figure 2. The mean (average absolute value) acceleration pulse radiation patterns, $\overline{R}^c$, plotted as functions of the change in rupture velocity. Because of the directivity in eq. (2), $\overline{R}^S$ is a strong function of Δv. The mean double-couple radiation patterns are shown for comparison. The error bars show a measurement of $\overline{R}^S$ and the resulting estimate of $\Delta v/\beta$ calculated from an analysis of 10 small earthquakes in Monticello, S.C.

subsonic phase delay in the acceleration along the rupture front, then the acceleration pulse will have a finite duration and the spectral excitation will naturally falloff above some frequency. To model the resulting acceleration pulse, it is useful to introduce the pulse shape,

$$\ddot{u}_c(r,t) = \begin{cases} 0 & t < 0 \\ \frac{\Delta\sigma}{\mu} \frac{R^c}{R} \Delta v \frac{r}{\zeta} e^{-t/\zeta} & t > 0 \ . \end{cases} \qquad (3)$$

The peak acceleration occurs at t = 0 and depends linearly on the dynamic stress drop, the change of rupture velocity and ratio of the sub-event radius to the width of the acceleration pulse. This ratio has dimensions of velocity and may be considered to be a measure of the relative abruptness of the behavior of the crack tip. The functional form of eq. (3) is entirely ad hoc. While the finite width of observed acceleration pulses may be assumed to result from the gradual acceleration and incoherent behavior of actual 3-D crack tips, this specific form is motivated only by its relative simplicity. It is the minimum-phase wavelet that corresponds to a low-pass Butterworth filter with an angular corner frequency at $1/\zeta$. The fourier transform of this pulse shape is simply

$$h(\zeta\omega) = (1 + (\zeta\omega)^2)^{-\frac{1}{2}} \ . \qquad (4)$$

Above the angular frequency $1/\zeta$, the excitation of the acceleration spectrum decays as ω^{-1}; this corresponds to a falloff of ω^{-3} in the displacement spectrum.

Combining eqs. (1) and (4) gives a general representation for the spectral excitation radiated by a semi-circular rupture front of radius r which stops or starts gradually with a total change of rupture velocity equal to Δv;

$$\ddot{u}_c(r,\omega) = \frac{\Delta\sigma}{\mu} \frac{R^c}{R} \Delta v \ r \ h(\zeta\omega) \ . \qquad (5)$$

In the following analysis, this representation will be used to model the high frequency radiation from the rupture stops and starts in an incoherent rupture

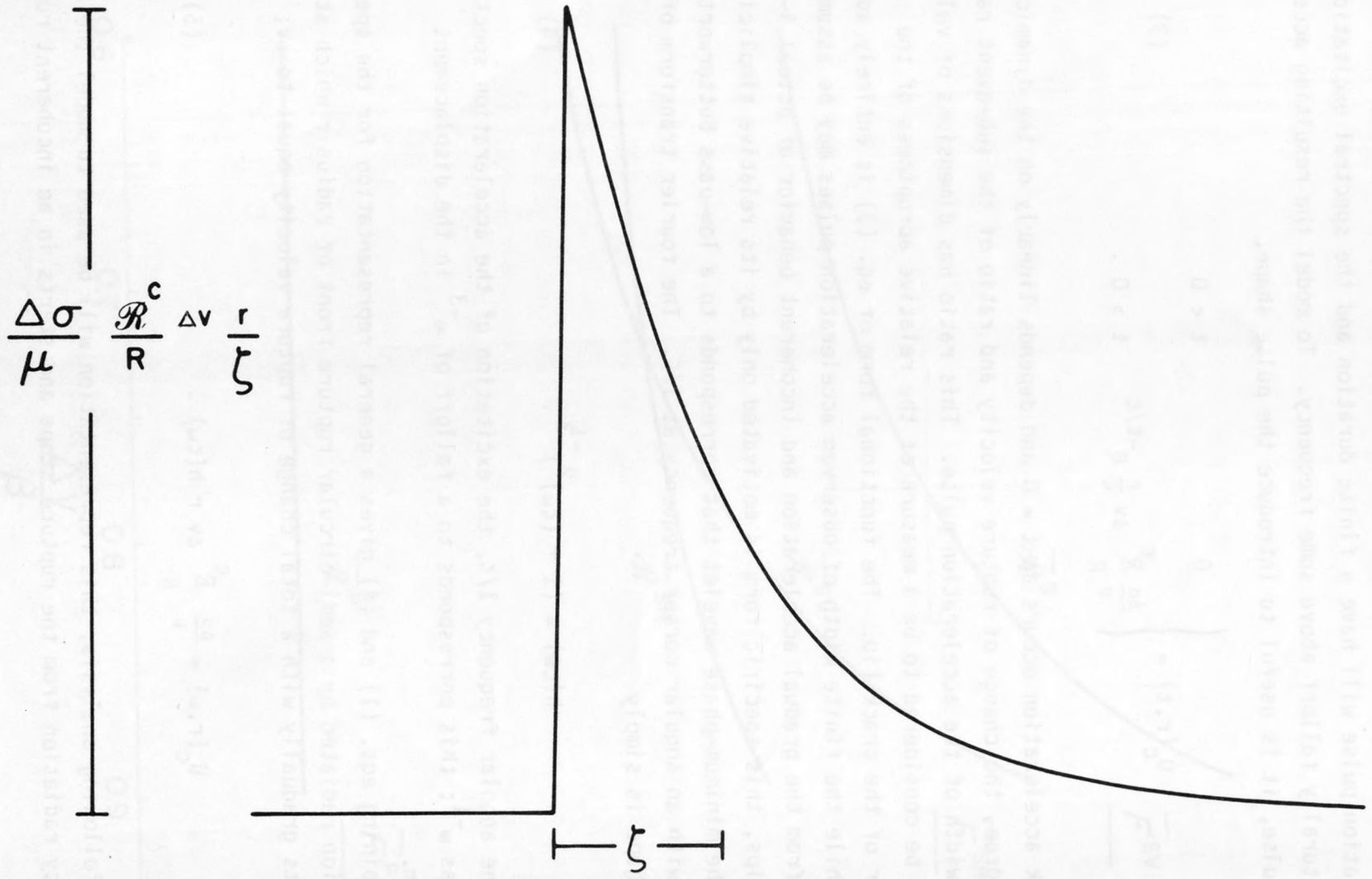

Figure 3. Model for the acceleration pulse radiated during the acceleration or deceleration of a 3-D crack tip. The area of the pulse shape is constrained by eq. (1); the width ζ corresponds to the duration over which the crack tip stops.

process. Because of the ad hoc nature of the acceleration pulse shape introduced in eq. (3), the validity of this representation at very high frequencies ($\omega >> 1/\zeta$) is suspect. As Madariaga (1977, p. 642) states, however, the results are asymptotic approximations for the radiation at wavelengths longer than the distance over which the strength and the rupture velocity change." In the following analysis, eq. (5) is assumed to be valid for the frequency range, $\pi v/r < \omega < 1/\zeta$.

The High-Frequency Radiation from a Coherent Sub-Event

In the rupture model proposed in this paper, the source incoherence is assumed to be the result of the discontinuous growth of rupture over the fault plane. The assumption of this rupture complexity defines an essentially causal model of an incoherent source. The high-frequency radiation from such a source model may be approximated by summing the high-frequency radiation from a set of coherent sub-events. The rupture velocity of the sub-events is assumed to be constant and less than the Rayleigh wave velocity; each change of rupture velocity is assumed to be a complete acceleration or deceleration. The resulting composite source model is a crude but useful approximation of a complex rupture.

Before considering composite models of a complex rupture process, however, it is necessary to model the high-frequency radiation expected from a coherent sub-event in terms of the representation presented in the last section. Figure 4a shows the S-wave acceleration waveform radiated at a takeoff angle of $\theta = 30^{\circ}$ by a circular version of the kinematic rupture model of Boatwright (1981). The two negative pulses are the stopping phases from the near and far perimeters of the rupture. The width of these two pulses is the result of a gradual stopping behavior incorporated into the rupture model.

It is apparent from this synthetic accelerogram that the total acceleration radiated by this rupture model is not well modelled if only the stopping phases are considered; it is also necessary to model the pulse radiated by the growth of rupture over the fault plane, i.e., the initial square-wave in the accelerogram. The spectral excitation of this pulse is dimensionally identical to the excitation given in eq. (5). For S-waves averaged over the focal

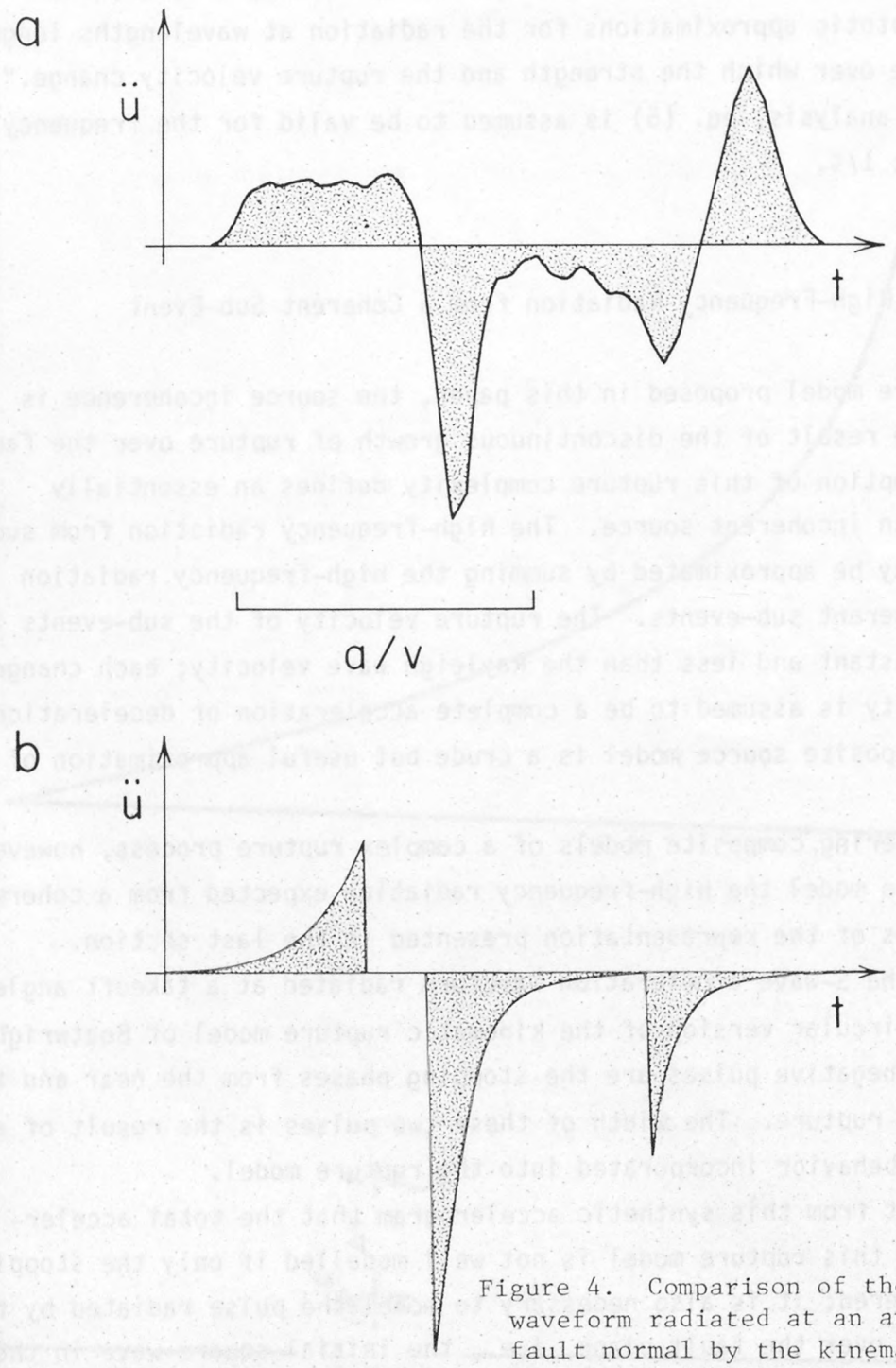

Figure 4. Comparison of the S-wave acceleration waveform radiated at an angle of 30^{o} from the fault normal by the kinematic model of Boatwright (1981) with v = .75β (4a) with an acceleration waveform composed of three acceleration pulses (4b). The second positive in the accelerogram is radiated by the coherent healing of the rupture model. The phase delays and the widths of the acceleration pulses were chosen arbitrarily (see text).

sphere, the integral of the square of the acceleration in this nucleation pulse, from a rupture with an average rupture velocity of $v = .75\beta$, is equal to that of a starting phase with $\zeta = r/2\pi v$. This comparision implies that it is necessary to add a third acceleration pulse to account for this nucleation phase. The positive pulse that follows the second stopping phase in the synthetic accelerogram is the result of the coherent healing assumed for the kinematic model and cannot be modelled using the acceleration pulses described by eq. (5).

Figure 4b shows an accelerogram made up of three acceleration pulses arranged to approximate the kinematic accelerogram. The relative phase delays of the acceleration pulses were arbitrarily chosen to be either maximum or minimum phase. For the starting phase, $\zeta = r/2\pi v$, while for the stopping phases, $\zeta = r/4\pi v$. The positive healing pulse has not been modelled.

Under the assumption that these three pulses arrive incoherently with evenly distributed positive and negative polarities, the expected power spectrum is the sum of the power spectra expected from each pulse (Lee, 1960, p. 241); that is,

$$E(\ddot{u}_c(\omega)^2) = \sum_{i=1}^{3} E(\ddot{u}_c(r,\omega)^2) = 3\left(\frac{\Delta\sigma}{\mu}\frac{\bar{R}^c}{R}\Delta v r h(\zeta\omega)\right)^2 . \qquad (6)$$

The dependence of the spectral excitation on sub-event radius in eq. (1) implies that the expected power spectrum depends on the area of the sub-event, as shown in eq. (6). This dependence prefigures the results obtained using the statistical source description presented in the next section.

Although the high-frequency radiation expected from a single coherent sub-event has been calibrated using a circular rupture which nucleates at a point and stops at a fixed perimeter, this model for the total acceleration radiated by a sub-event can be used to describe a wide range of rupture behaviors. The coherent initiation of rupture along a semi-circular perimeter radiates an equally strong acceleration pulse as the stopping of rupture on the same perimeter. Figure 5 shows three sub-events with markedly different rupture behaviors; the perimeters on which the rupture starts are shown as dashed lines, while the perimeters on which the rupture stops are solid. In the first sub-event, the rupture nucleates in the center and stops at both sides;

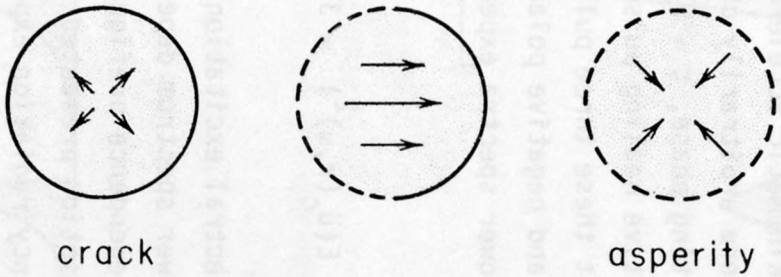

Figure 5. A range of equivalent sub-event rupture behaviors. The dashed and solid perimeters indicate rupture starts and stops, respectively; the arrows show the direction of rupture growth. The first sub-event corresponds to a crack model, the third to an asperity failure, and the second to a mixed mode.

in the second, the rupture starts at one side and stops at the other side; and in the third, the rupture starts at both sides and implodes into the center. The first sub-event is a model of a crack, or barrier controlled rupture, while the third sub-event is a model of an asperity failure (Das and Kostrov, 1982). To prove that the high-frequency radiation from these two sub-events is equivalent, note that the rupture behavior in the asperity failure is approximately the time inverse of the behavior of the crack model. The aspects of rupture which are not equivalent under time inversion, i.e., the healing of the crack and the equilibration of displacement outside the asperity, are low-frequency effects. The total acceleration radiated by the second sub-event, with the mixed rupture behavior, is also approximately equal to the acceleration radiated by the other two sub-events. Madariaga (1982) similarly argues that crack (or barrier) models and asperity models are indistinguishable with regard to their total high-frequency radiation.

An Incoherent Source Model

Following the sense of the arguments articulated by Hanks (1979) and Andrews (1980) for a set of earthquakes occurring within a specific fault area, the distribution of rupture areas of the sub-events comprising a complex rupture process is assumed to be approximately self-similar. Then the number of sub-events with radius greater than or equal to r occurring within a complex rupture of total area $A = \pi a^2$ is proportional to

$$N \propto \frac{A}{r^2} . \tag{7}$$

Using a cutoff radius, $a_o \leq r$, for the minimum size of the sub-events gives the simplified frequency-radius density function,

$$dN = \begin{cases} 0 & r < a_o \\ k \dfrac{a^2}{r^3} \, dr & a_o < r < a \\ 0 & a < r . \end{cases} \tag{8}$$

This sub-event distribution is normalized by setting the expectation of the sum of the sub-event rupture areas equal to the total rupture area. Such a normalization implies that the total rupture area is approximately covered by non-overlapping sub-events. The expectation of the sum of the sub-event rupture areas is simply

$$E(\pi r^2) = \int_{a_o}^{a} \pi \, k \, \frac{a^2}{r} \, dr \, , \tag{9}$$

and the distribution is appropriately normalized when

$$k = 1/\ln(a/a_o) \, . \tag{10}$$

The expected number of sub-events depends on the ratio of the overall source radius to the cut-off radius:

$$E(N) = \int_{a_o}^{a} k \, \frac{a^2}{r^3} \, dr = \frac{k}{2}\left(\frac{a^2}{a_o^2} - 1\right) . \tag{11}$$

For $a/a_o = 10$, $N \simeq 17$, for $a/a_o = 5$, $N \simeq 6$ and for $a/a_o = 1$, $N = 1$. As a_o decreases to zero, the expected number of sub-events grows without bound.

Figure 6 presents three realizations of this statistical model. The set of sub-event radii were generated using the density function in eq. (8) and the ratio $a/a_o = 5$. The sub-event areas were then arranged into approximately equidimensional areas. The velocity waveforms radiated by the sources shown in Figures 6a and 6b would be relatively complex, while the velocity waveforms from the source shown in Figure 6c would be relatively simple, as they would be dominated by the contribution from the largest sub-event.

Note that the eventual geometry of stress release on the fault surface is not assumed to be identical to the geometry of the sub-events. The equivalence of the high-frequency radiation expected from crack and asperity-type sub-events implies that the geometry of the sub-events only provides a bound for the final geometry of stress release. This result is demonstrated in Figure 6, where the sub-event perimeters have been drawn to indicate rupture starts and stops; the fracture barriers which remain unbroken through the rupture process

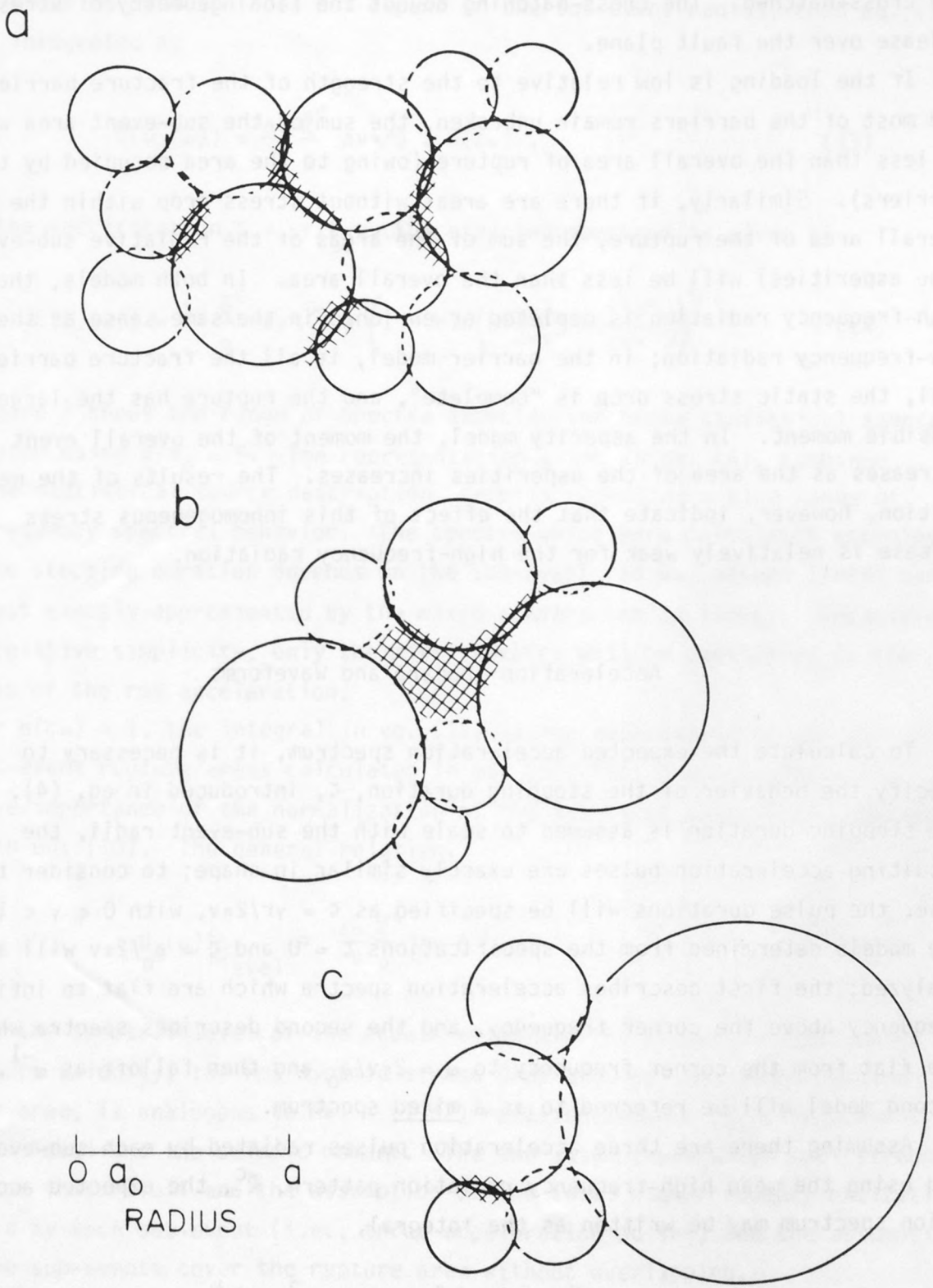

Figure 6. Three sub-event realizations generated from the same sub-event distribution. For this distribution, a_o = a/5, as shown on the scale. The sub-events were arranged arbitrarily into approximately equidimensional areas. The perimeters or the sub-events are marked to indicate rupture starts and stops; the barriers unbroken at the end of the faulting are cross-hatched to show the final geometry of stress release for each of the ruptures.

are cross-hatched. The cross-hatching bounds the final geometry of stress release over the fault plane.

If the loading is low relative to the strength of the fracture barriers and most of the barriers remain unbroken, the sum of the sub-event area will be less than the overall area of rupture (owing to the area occupied by the barriers). Similarly, if there are areas without stress drop within the overall area of the rupture, the sum of the areas of the radiative sub-events (the asperities) will be less than the overall area. In both models, the high-frequency radiation is depleted or enriched in the same sense as the low-frequency radiation; in the barrier model, if all the fracture barriers fail, the static stress drop is "complete", and the rupture has the largest possible moment. In the asperity model, the moment of the overall event increases as the area of the asperities increases. The results of the next section, however, indicate that the effect of this inhomogeneous stress release is relatively weak for the high-frequency radiation.

Acceleration Spectra and Waveforms

To calculate the expected acceleration spectrum, it is necessary to specify the behavior of the stopping duration, ζ, introduced in eq. (4). If the stopping duration is assumed to scale with the sub-event radii, the resulting acceleration pulses are exactly similar in shape; to consider this case, the pulse durations will be specified as $\zeta = \gamma r/2\pi v$, with $0 < \gamma < 1$. The models determined from the specifications $\zeta = 0$ and $\zeta = a_0/2\pi v$ will also be analyzed; the first describes acceleration spectra which are flat to infinite frequency above the corner frequency, and the second describes spectra which are flat from the corner frequency to $\omega = 2\pi v/a_0$ and then falloff as ω^{-1}. The second model will be referred to as a mixed spectrum.

Assuming there are three acceleration pulses radiated by each sub-event, and using the mean high-frequency radiation pattern, $\bar{R}^c$, the expected acceleration spectrum may be written as the integral,

$$E(\ddot{u}_c(\omega)) = \frac{\Delta\sigma}{\mu}\frac{\bar{R}^c}{R}\,\Delta v\left(3\int_{a_0}^{a} h^2(\zeta\omega)\,k\,\frac{a^2}{r}\,dr\right)^{1/2}. \qquad (12)$$

If the stopping duration does not depend on the sub-event radius, then eq. (12) may be integrated as

$$E(\ddot{u}_c(\omega)) = \frac{\Delta\sigma}{\mu}\frac{\bar{R}^c}{R}\,\Delta v\sqrt{3}\;a\;h(\zeta\omega)\;. \qquad (13)$$

Using the specification $\zeta = \gamma r/2\pi v$, the expected spectrum is given by

$$E(\ddot{u}_c(\omega)) = \frac{\Delta\sigma}{\mu}\frac{\bar{R}^c}{R}\,\Delta v\sqrt{3}\;a\left(1 + k\ln\left(h(\frac{\gamma a\omega}{2\pi v})/h(\frac{\gamma a_o\omega}{2\pi v})\right)\right)^{\frac{1}{2}}\;. \qquad (14)$$

Figure 7 shows the range of spectra expected for these statistical sources, calculated using $a/a_o = 5$. The representation given in eq. (4), combined with the statistical source description, permits modelling a wide range of high-frequency spectral behavior. The spectra which were calculated assuming that the stopping duration depends on the sub-event radius (dashed lines) can be almost exactly approximated by the mixed spectra (solid lines). Because of their relative simplicity, only the mixed spectra will be considered in the analysis of the rms acceleration.

For $h(\zeta\omega) = 1$, the integral in eq. (12) is the expectation of the sum of the sub-event rupture areas calculated in eq. (9); this demonstrates the relative importance of the normalization of the sub-event distribution determined in eq. (10). The general relation,

$$\ddot{u}_c(\omega)\Big|_{level} \simeq \frac{\Delta\sigma}{\mu}\frac{\bar{R}^c}{R}\,\Delta v\,A^{\frac{1}{2}}\;, \qquad (15)$$

between the spectral level of the acceleration and the product of the change of rupture velocity, the rms dynamic stress drop and the square root of the rupture area, is analogous to Aki's (1967) relation between the displacement spectral level and the seismic moment. The two assumptions which most strongly condition this result are the assumption of the total high-frequency excitation radiated by each sub-event (i.e., three acceleration pulses) and the assumption that the sub-events cover the rupture area without overlapping.

To complete this description of the expected acceleration spectra, it is necessary only to appropriately constrain the long-period behavior. The

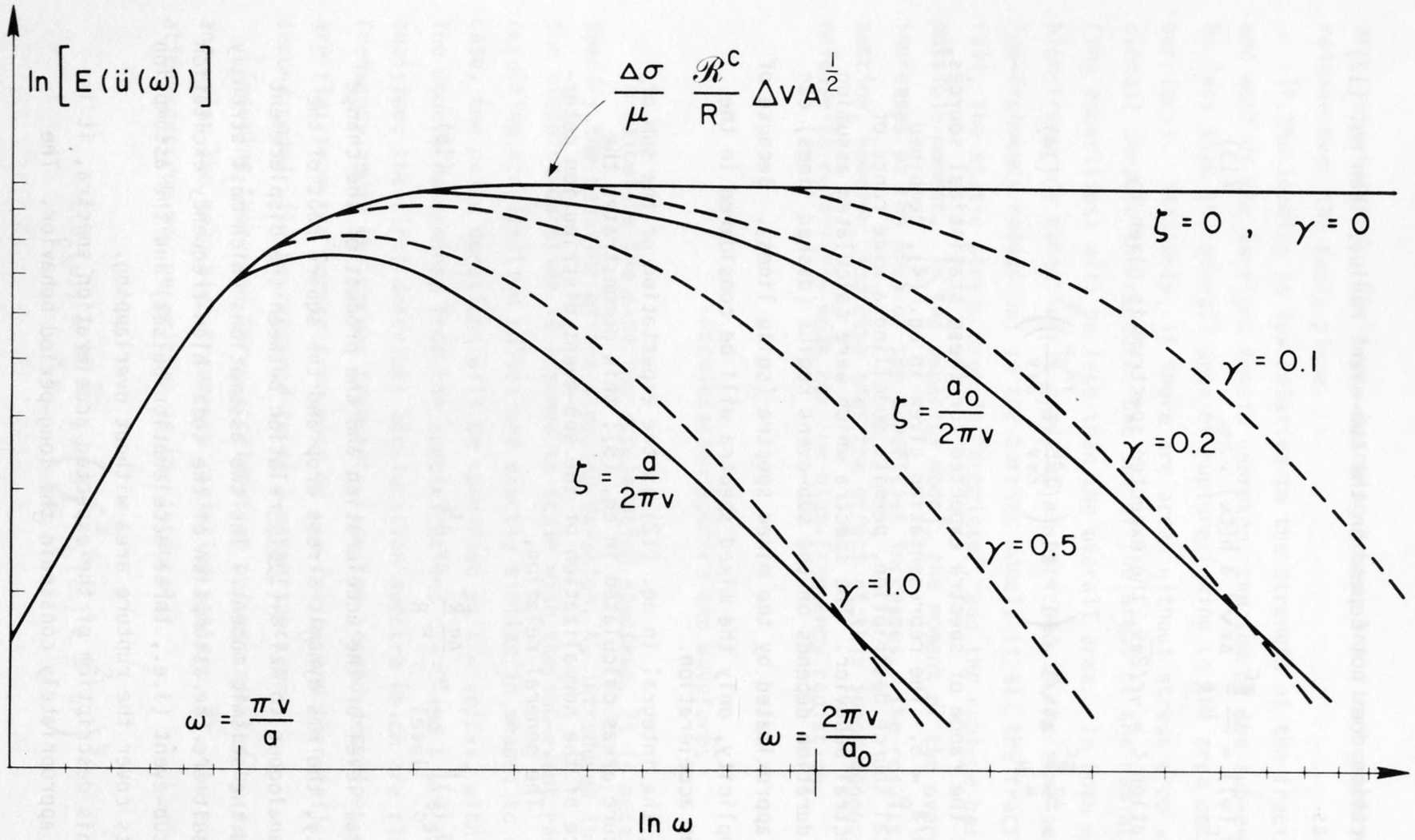

Figure 7. The range of expected acceleration spectra, normalized to the same pulse duration, $\tau = 2a/v$, or inverse corner frequency. The solid lines are calculated for models where the high-frequency corner at $1/\zeta$ did not vary with source size, while the dashed lines were calculated assuming that $\zeta = \gamma r/2\pi v$, for the values of γ shown. Varying the ratio a_0/a, which controls the expected complexity of the rupture process, does not change the expected spectral level.

displacement spectrum of far-field body-waves is flat at low-frequencies; this suggests using a high-pass filter of the form,

$$(\frac{\omega\tau}{2\pi})^2 h^2(\frac{\omega\tau}{2\pi}) = \left((\frac{2\pi}{\omega\tau})^2 + 1\right)^{-1}, \qquad (16)$$

where τ is the signal duration; in this analysis, the signal duration is assumed to be twice the rupture duration (Boatwright, 1980), i.e.,

$$\tau = 2\,\frac{a}{v}\,, \qquad (17)$$

where v is the average rupture velocity. For $v = .75\beta$, this spectral model is identical to Brune's (1970) model.

To invert measurements of the acceleration spectral level, $|\ddot{u}_c(\omega)|$, for estimates of the rms dynamic stress drop, eq. (17) can be combined with eq. (15) to obtain the general relation,

$$\Delta\sigma = 1.13\,\frac{\rho\beta^2}{v\Delta v}\,\frac{R}{\bar{R}^c}\,\frac{|\ddot{u}_c(\omega)|}{\tau}\,. \qquad (18)$$

The values of $\bar{R}^c$ plotted in Figure 2 should be modified to account for the free surface. It is important to point out, considering Figure 3, that this estimate can only be used to determine a lower bound for the rms dynamic stress drop from acceleration spectra which are not flat for some frequency above the corner frequency (i.e. peaked acceleration spectra) unless the attenuation in the region is sufficiently well known.

To calculate synthetic accelerograms for a rupture made up of N sub-events, it is necessary to determine an array of arrival times for the 3N pulses, as eq. (15) specifies only the amplitude spectra. The arrival times are assumed to be uniformly distributed within the pulse duration. While Madariaga's results (1977, eqs. (36) and (37)) indicate that there is little phase variation for acceleration pulses radiated by abrupt rupture starts or stops, it is reasonable to include some phase variability in the generalization given in eq. (4), as shown in Figure 4b. Assuming a distribution for the relative phase delay of the pulse shape, $0 < \delta < 2\pi$, gives a continuum of pulse shapes,

$$h(t,\delta) = \cos\delta \frac{e^{-t/\zeta}}{\zeta} + \sin\delta\, H\left[\frac{e^{-t/\zeta}}{\zeta}\right] , \qquad (19)$$

where H[ ] signifies a Hilbert transform. A sampling from these shapes will be used to model the 3N acceleration pulses.

The accelerograms plotted in Figures 8a, b and c were generated using the sub-event realizations shown in Figure 1. The dynamic stress drop and the rupture velocity were assumed to be constant over the set of sub-events, and the high-frequency corner was specified as $\zeta = r/4\pi v$. For an actual rupture process, this high-frequency corner probably varies substantially from pulse to pulse. In Figures 8d, e and f, the same accelerograms are plotted after having been high-pass filtered using eq. (16) and convolved with a constant Q attenuation operator with $t^* = \zeta/50$.

These filtered synthetic accelerograms are weak fascimilies of recorded ground accelerations. In particular, the low-frequency character of the accelerograms written by actual earthquakes is missing from these synthetics. In order to supply such character, however, information concerning the overall growth and stopping of the rupture must be incorporated into the model. Such a refinement is beyond the scope of this paper, but should be included in any attempt to predict acceleration in the near-field.

Estimates of rms Acceleration

To estimate the expected rms acceleration, averaged over the pulse duration, it is necessary to calculate the integral of the square of the acceleration (hereafter referred to as the power) in a single attenuated acceleration pulse. Multiplying eq. (5) by the attenuation response, $\exp(-\omega t^*/2)$, gives the "observed" spectral excitation,

$$\ddot{u}_c(r,\omega) = \frac{\Delta\sigma}{\mu} \frac{\bar{R}^c}{R} \Delta v\, r\, h(\zeta\omega)\, e^{-\omega t^*/2} \qquad (20)$$

The power can then be calculated from Parseval's Theorem;

$$\int_0^\tau \ddot{u}_c^2(r,t)\, dt = \frac{1}{\pi}\left(\frac{\Delta\sigma}{\mu} \frac{\bar{R}^c}{R} \Delta v\, r\right)^2 \int_0^\infty h^2(\zeta\omega)\, e^{-\omega t^*} d\omega . \qquad (21)$$

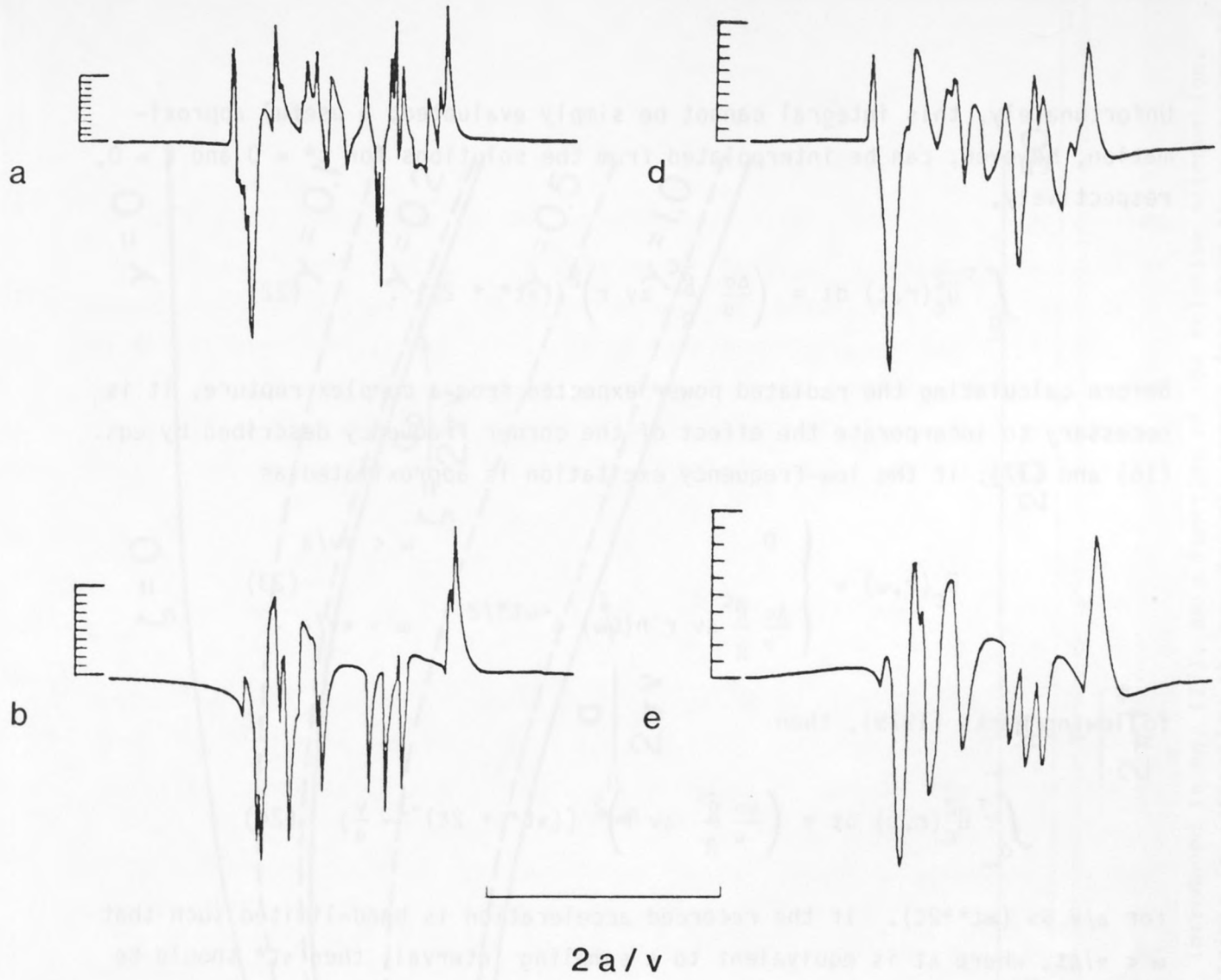

Figure 8. Accelerograms generated from the three sub-event realizations shown in Figure 6. The column on the left shows the set of acceleration pulses generated from the set of sub-events, assuming a slight variability of phase and amplitude. The realizations are ordered from most to least complex. The column on the right shown the resulting accelerogram after both high-pass filtering (at one second) to stimulate the appropriate low-frequency behavior of the displacement spectrum and filtering with a causal Q operator whose $t^* = T/50$.

Unfortunately, this integral cannot be simply evaluated; a useful approximation, however, can be interpolated from the solutions for $t^* = 0$ and $\zeta = 0$, respectively,

$$\int_0^\tau \ddot{u}_c^2(r,t)\, dt \simeq \left(\frac{\Delta\sigma}{\mu}\,\frac{\bar{R}^c}{R}\,\Delta v\, r\right)^2/(\pi t^* + 2\zeta)\ . \qquad (22)$$

Before calculating the radiated power expected from a complex rupture, it is necessary to incorporate the effect of the corner frequency described by eqs. (16) and (17); if the low-frequency excitation is approximated as

$$\ddot{u}_c(r,\omega) = \begin{cases} 0 & \omega < \pi v/a \\ \dfrac{\Delta\sigma}{\mu}\,\dfrac{\bar{R}^c}{R}\,\Delta v\, r\, h(\zeta\omega)\, e^{-\omega t^*/2} & \omega > \pi v/a\ . \end{cases} \qquad (23)$$

following Hanks (1979), then

$$\int_0^\tau \ddot{u}_c^2(r,t)\, dt \simeq \left(\frac{\Delta\sigma}{\mu}\,\frac{\bar{R}^c}{R}\,\Delta v\, r\right)^2 \left[(\pi t^* + 2\zeta)^{-1} - \frac{v}{a}\right] \qquad (24)$$

for $a/v >> (\pi t^* + 2\zeta)$. If the recorded acceleration is band-limited such that $\omega < \pi/\Delta t$, where Δt is equivalent to a sampling interval, then πt^* should be replaced by Δt in eqs. (22) and (24).

The expected rms acceleration may be calculated by taking the square root of the expected power divided by the signal duration,

$$E(a_{rms}) = \left[3E\left(\int_0^\tau \ddot{u}_c^2\, dt\right)/\tau\right]^{1/2}\ , \qquad (25)$$

where $\tau = 2a/v$ is the signal duration given in eq. (17). If the acceleration spectrum falls of as ω^{-1} above $\omega = 1/\zeta$, the rms acceleration is given by

$$E(a_{rms}) = .87\,\frac{\Delta\sigma}{\mu}\,\frac{\bar{R}^c}{R}\, v\Delta v\, [\tau/(\pi t^* + 2\zeta) - 2]^{1/2} \qquad (26)$$

for $\tau > 4(\pi t^* + 2\zeta)$. Compressing this general result into a form analogous to eq. (8) of McGuire and Hanks (1980), gives

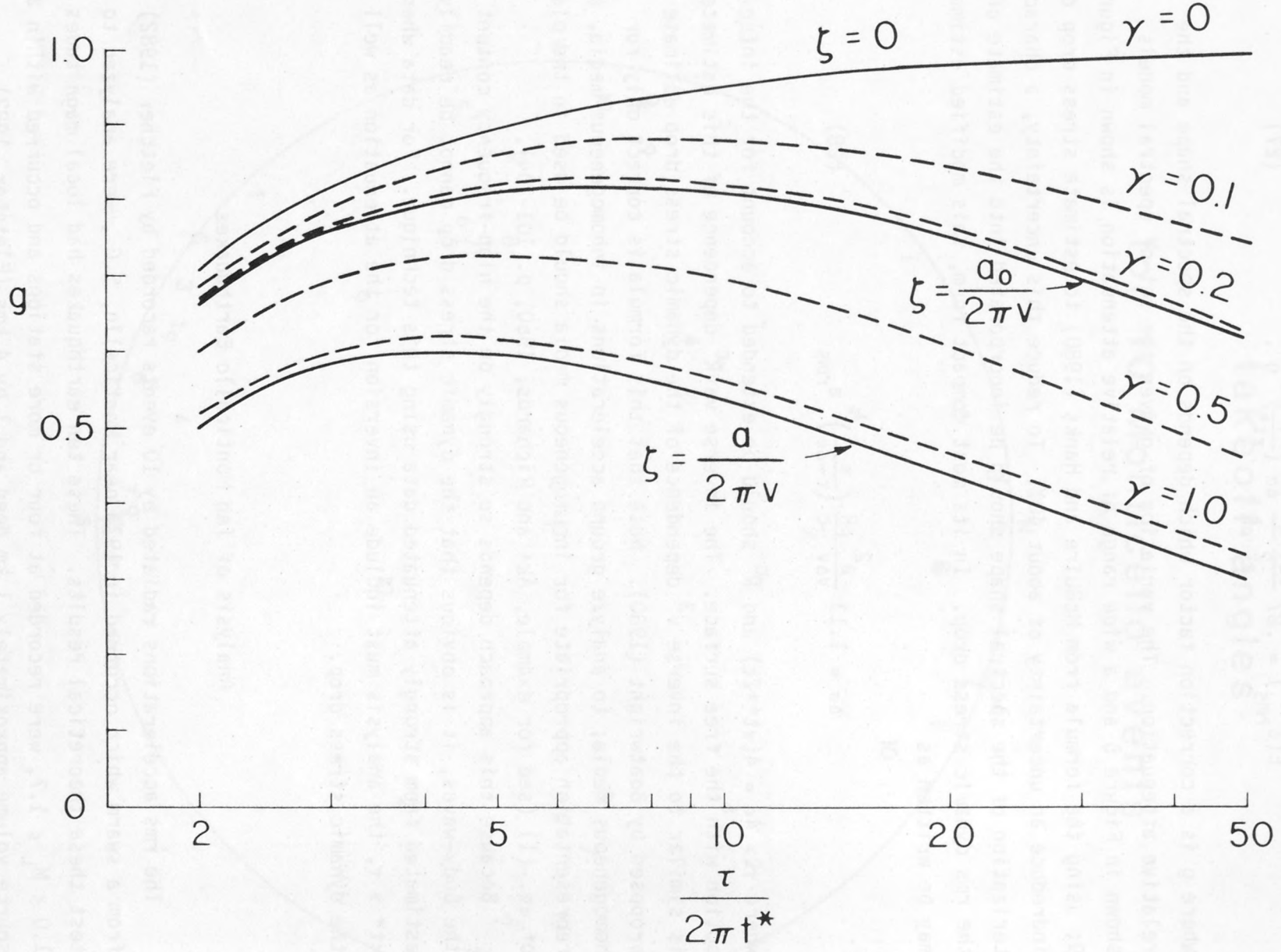

Figure 9. Variation of the correction factor, g, introduced in eq. (27), as a function of the relative attenuation, τ/t^* The range of g is a measure of the uncertainty in estimating the rms dynamic stress drop from the measurements of the rms acceleration without considering the spectral shape. The solid and dashed lines correspond to the special models shown in Figure 7.

$$E(\ddot{a}_{rms}) = .87 \frac{v\Delta v}{\beta^2} \frac{\bar{R}^c}{\rho R} \Delta\sigma \left(\frac{\tau}{\pi t^*}\right)^{\frac{1}{2}} g \ , \qquad (27)$$

where g is a correction factor which depends on the spectral shape and the relative attenuation. The variation of g over the set of spectral models shown in Figure 5 and a wide range of relative attenuation is shown in Figure 9; using the formula from McGuire and Hanks (1980) to estimate stress drop can indroduce an uncertainty of about 40%. To reduce this uncertainty, a characterization of the spectral shape should be incorporated into the estimate of the rms dynamic stress drop. In its most compact form, this modified estimate may be written as

$$\Delta\sigma = 1.13 \frac{\beta^2}{v\Delta v} \frac{\rho R}{\bar{R}^c} \left(\frac{\varepsilon}{\tau - 2\varepsilon}\right)^{\frac{1}{2}} a_{rms} \qquad (28)$$

where $\tau > 4\varepsilon = 4(\pi t^* + 2\zeta)$ and $\bar{R}^c$ should be extended to account for the interaction with the free surface. The inverse $v\Delta v\bar{R}^c$ dependence of this estimate is similar to the inverse v^3 dependence of the dynamic stress drop estimate proposed by Boatwright (1980). Note that this formula is correct only for homogeneous media; to analyze ground accelerations in inhomogeneous media, a representation appropriate for inhomogeneous media should be used in the place of eq. (1) (see for example, Aki and Richards, 1980, p. 101-104).

Because this approach depends so strongly on the high-frequency content of the body-waves, it is obvious that the dynamic stress drop cannot be readily estimated from strongly attenuated data using this technique. For data where $\pi t^* > \tau$, the analysis must include an inversion for the attenuation as well as the dynamic stress drop.

Analysis of Ten Monticello Earthquakes

The rms accelerations radiated by 10 events recorded by Fletcher (1982) from a swarm which occurred in 1978 near Monticello, S.C., were analyzed to test these theoretical results. These ten earthquakes had local magnitudes of $1.0 \lesssim M_L \lesssim 1.7$, were recorded at four or more stations and occurred within a source volume approximately 1 km deep and 1 by 4 kms (Fletcher, 1982).

takeoff angles

for 10 Monticello events

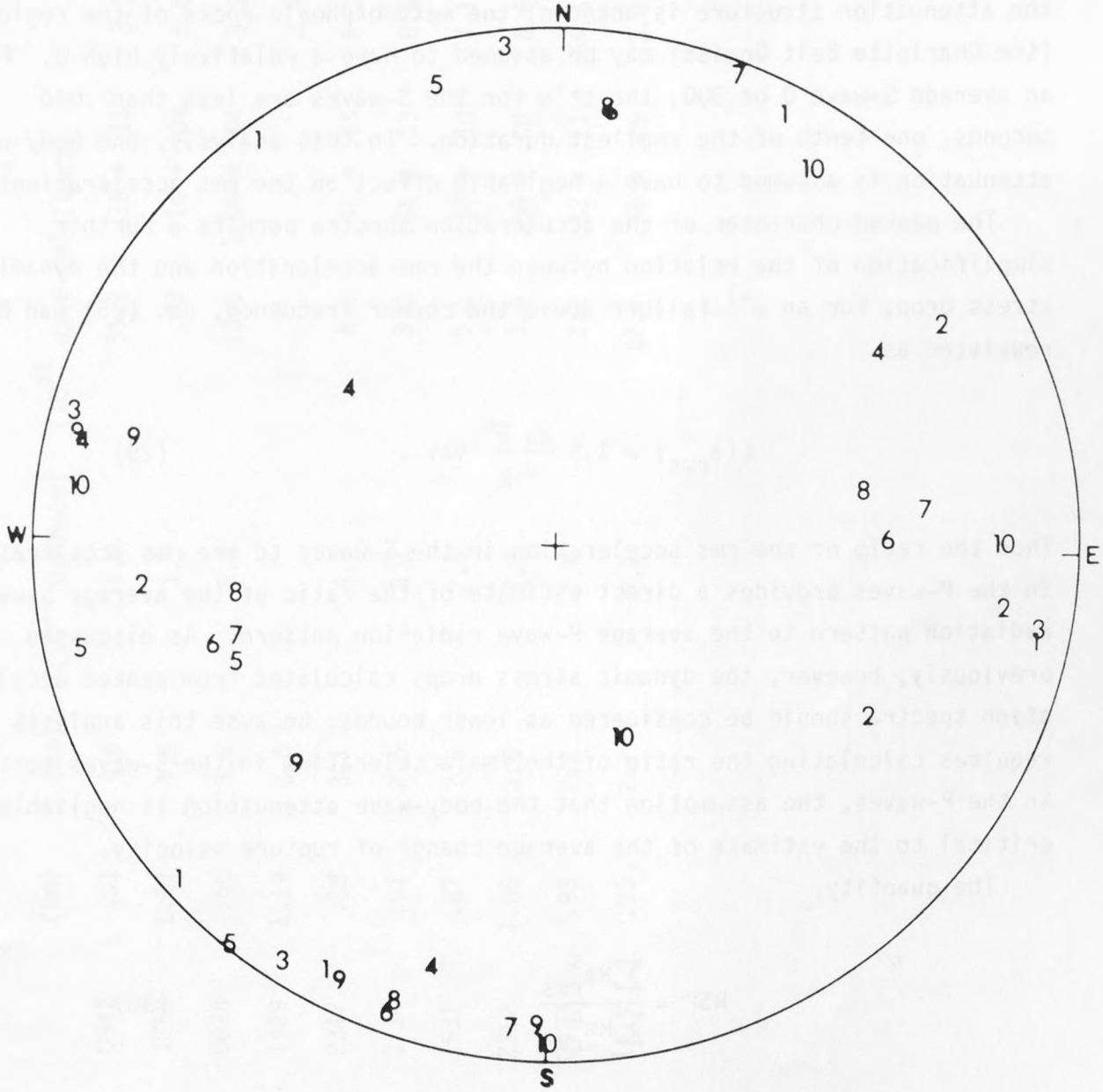

Figure 10. Takeoff angles of the 80 body-waves analyzed. In general, each takeoff angle corresponds to both a P-wave and an S-wave. The numbers refer to the event which radiated the body-wave, as numbered in Table 1 (in chronological order).

Figure 10 shows a composite plot of the takeoff angles of the P and S-waves from the ten events. Although these directions are not distributed uniformly in takeoff angle, the earthquakes exhibit a wide range of focal mechanisms (Fletcher, 1982); in the following analysis, the sampling of the focal sphere is assumed to be uniform.

The acceleration spectra of these body-waves are generally peaked, falling off as ω^{-1} above corner frequencies from 10-40 Hz (Fletcher, 1982). Although the attenuation structure is unknown, the metamorphoric rocks of the region (the Charlotte Belt Gneiss) may be assumed to have a relatively high Q. For an average S-wave Q of 300, the t*'s for the S-waves are less than .006 seconds, one tenth of the smallest duration. In this analysis, the body-wave attenuation is assumed to have a negliable effect on the rms accelerations.

The peaked character of the acceleration spectra permits a further simplification of the relation between the rms acceleration and the dynamic stress drop; for an ω^{-1} falloff above the corner frequency, eq. (25) can be rewritten as

$$E(a_{rms}) = 1.5 \frac{\Delta\sigma}{\mu} \frac{\bar{R}^C}{R} V\Delta V \ . \qquad (29)$$

Thus the ratio of the rms acceleration in the S-waves to the rms acceleration in the P-waves provides a direct estimate of the ratio of the average S-wave radiation pattern to the average P-wave radiation pattern. As discussed previously, however, the dynamic stress drops calculated from peaked acceleration spectra should be considered as lower bounds; because this analysis requires calculating the ratio of the rms acceleration in the S-waves to that in the P-waves, the assumption that the body-wave attenuation is negliable is critical to the estimate of the average change of rupture velocity.

The quantity,

$$RSP = \frac{\sum Ra^S_{rms}}{\sum Ra^P_{rms}} \qquad (30)$$

was calculated for each event; these estimates are listed in Table 1. Here a^S_{rms} is the square root of the sum of the square acceleration of the S-waves on

Table 1

Event	Date	Time	Depth	$\bar{R}$	M_o	E_s	τ_a	RSP	$\overline{Ra}_{rms}$	$\Delta\sigma_{rms}$
	(julian)		(km)	(km)	(10^{17} dyne-cm)	(10^{11} dyne-cm)	(bars)		(10^5 cm/sec^2)	(bars)
1	138	0942	.51	4.6	18.0	35.2	.39 ± .11	3.7	2.3 ± .4	1.3 ± .2
2	138	1258	1.37	4.5	1.9	.73	.16 ± .04	5.6	.7 ± .1	.4 ± .05
3	141	0026	.60	3.6	5.7	13.6	1.04 ± .64	3.3	2.6 ± .5	1.4 ± .3
4	145	1429	1.19	2.8				2.9	1.7 ± .5	.9 ± .3
5	149	2347	.88	3.1	4.3	4.9	.48 ± .15	6.1	1.9 ± .3	1.0 ± .15
6	150	0714	.91	2.5	3.1	3.0	.56 ± .13	8.4	2.0 ± .4	1.1 ± .2
7	150	1531	.87	2.6	2.6	5.1	.56 ± .10	7.1	2.5 ± .6	1.4 ± .3
8	150	2352	1.06	2.6	2.2	3.8	.58 ± .09	6.6	2.2 ± .5	1.3 ± .3
9	151	0433	.93	2.2	1.4	2.2	.32 ± .11	4.6	1.4 ± .4	.8 ± .2
10	151	1619	.95	2.7	7.7	12.4	.98 ± .45	3.0	3.4 ± .6	1.9 ± .3

the two horizontal components while a^{p}_{rms} is the rms acceleration of the P-waves on the vertical component. The ten estimates were averaged logarimthically to obtain RSP = 4.8 ± .6, which in turn gives $\bar{R}^{s}$ = .32 ± .04. As shown on Figure 3, the average change of rupture velocity is then .8β where the 85 confidence interval is .7 < Δv/β < .85.

To calculate the dynamic stress drop from the rms accelerations using eq. (29), it is necessary to estimate the average rupture velocity. Interpreting the ω^{-3} spectral falloff to represent a gradual arrest of rupture over an interval $\zeta > a/\pi v$, implies $v < 5\Delta v/6$ for a rupture which begins with a high rupture velocity. If the rupture accelerates during the initial growth, then the average rupture velocity is less than this limit. For this analysis, the average rupture velocity is assumed to be .6β.

The resulting estimates of rms dynamic stress drop are listed in Table 1, along with the values of $\overline{\bar{R}^{s}Ra^{c}_{rms}/\bar{R}^{c}}$, denoted as $\overline{Ra}_{rms}$ for simplicity. The estimates of the moment, the radiated seismic energy and the apparent stress, taken from Boatwright and Fletcher (1982) are also listed in Table 1.

Figure 10 compares the dynamic stress drops obtained from the analysis of the rms acceleration to estimates of the apparent stress, as obtained from the seismic moment and the radiated energy. The scale for the estimates of the apparent stress is multiplied by a factor of two.

The events are plotted as a function of hypocentral depth with the scale adjusted in the depth range of .8-1.0 kms in order to separate the five events at this depth. The choice of hypocentral depth as the independent variable is somewhat arbitrary, but it shows the only obvious trends in the estimates of stress release. The two estimates of stress release have a correlation coefficient of ρ = .9, calculated without assuming that the component regressions pass through the origin. The small relative uncertainties of the estimates of dynamic stress drop (≈20%) suggest that measurements of the rms acceleration in body-waves can be inverted for robust estimates of stress release for small events ($M_L \leq 2$) as well as for the larger events ($M_L \geq 4$) analyzed by Hanks and McGuire (1981). As discussed throughout this section, however, these estimates can only be considered as lower bounds for the rms dynamic stress drop, as the acceleration spectra were peaked at the corner frequency.

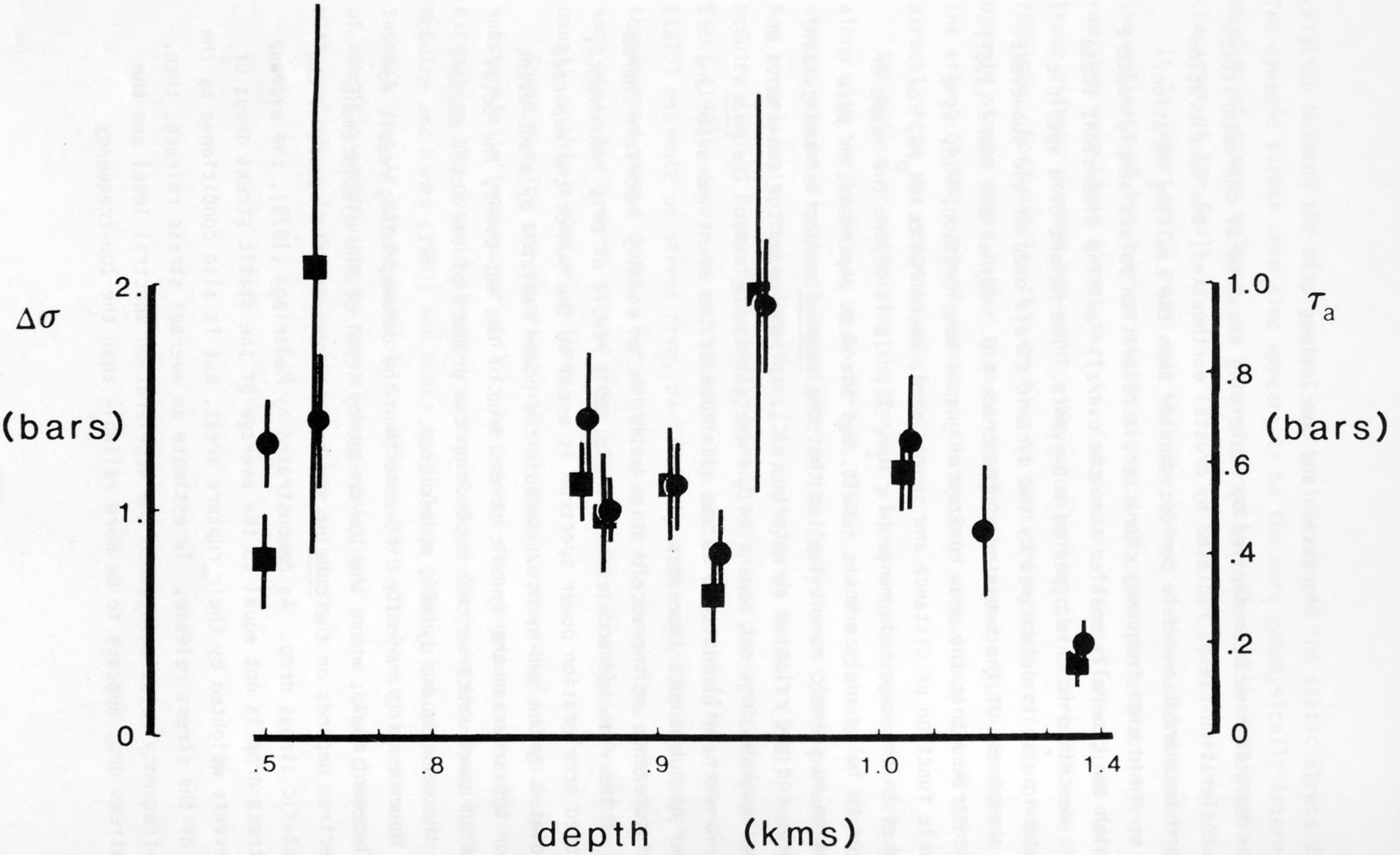

Figure 11. Comparison of the dynamic stress drops estimated from the rms accelerations in the P and S-waves (circles) to the apparent street (squares), as a function of the hypocentral depth. Note the change of depth scale between .8 and 1.0 kms.

Discussion and Conclusions

These results have been derived by exploiting two general characteristics of the acceleration fields radiated by crustal earthquakes; the acceleration pulses are incoherent and have periods shorter than the faulting duration. Because of their high-frequency character, acceleration pulses sample rupture areas which are generally smaller than the overall faulting dimension; these areas are described in this paper as sub-events. The height of a specific acceleration pulse is determined by the dynamic stress drop of the sub-event and the abruptness of the behavior of the crack tip. Joyner and Boore (1981) have demonstrated that the peak horizontal ground acceleration, PGA, is a predictable function of distance and source size, where PGA $\propto \ln M_0/6$, for earthquakes in the magnitude range ($4 \leq M_L \leq 7$). It is beyond the scope of this paper to fully analyze their result, but the weak dependence of peak acceleration on seismic moment implies that the <u>average</u> product of the dynamic stress drop and the relative abruptness (r/ζ), as sampled by the sub-events of these earthquakes, does not depend on the overall source size. The <u>peak</u> product, however, will increase as the magnitude of the event increases and the number of sub-events increases.

The incoherence of the acceleration pulses is an equally important characteristic of the radiated acceleration field; as a result of this incoherence, the expected acceleration power spectrum is equal to the sum of the expected power radiated by the sub-events. Because the power radiated by a sub-event depends on the area and the dynamic stress drop of the sub-event, the total acceleration power spectrum then depends on the product of the total rupture area and the mean square dynamic stress drop.

This dependence is markedly different than the corresponding result for the displacement field, where the low-frequency level of the displacement power spectrum depends on the <u>cube</u> of the rupture area and the square of the average static stress drop. As demonstrated by Madariaga (1979), the average static stress drop is not equal to the average of the static stress drops of the sub-events weighted by their rupture areas, but is also conditioned by the geometry of the stress release. To estimate an average stress release, then, the high-frequency relation between the acceleration spectral level and the dynamic stress drop appears to be more reliable than the low-frequency

relation between the displacement spectral level and the static stress drop. The dynamic stress drop also appears to be the more geophysically interesting measure of stress release, as it more directly reflects the reological character of the fault.

It is important to point out that the effect of the rupture geometry on the estimate of the average static stress drop cannot be extracted from the radiated wave-field alone; that is, independent information such as maximum trace offset, average sub-event size, or extent of the aftershock zone is required. Fortunately, this problem is obviated by this estimate of the dynamic stress drop; rather than correcting the average static stress drop for the effect of the rupture geometry, the dynamic stress drop can be estimated directly from the recorded acceleration.

The method of estimating the dynamic stress drop presented in this paper, along with the technique of Boatwright (1980) and the estimate of the apparent stress, assume a critical importance in the analysis of source parameters. Not surprisingly, these techniques, as employed by Frankel (1981), Hanks and McGuire (1981), Boatwright (1982), Mori (1980), and Linde, Stefansson and Sacks (1980), appear to be statistically better conditioned than the Brune (1970) estimate of stress drop, particularly with regard to the range of thereturned stress drops. For earthquakes of the same size, occurring in the same area, the dynamic stress drops appear to be extremely well constrained, usually within a factor of three.

These results are important not only because they imply that we can substantially improve our ability to predict strong ground motion by estimating the dynamic stress drop expected for large earthquakes, following McGuire and Hanks (1980) and Hanks and McGuire (1981), but also because they suggest that it may be possible to address the tectonic significance of a set of specific earthquakes by correlating variations in the dynamic stress drop with variations in source mechanism, size and depth.

Acknowledgements

Over the course of this research, I have profitted from conversations with Joe Andrews, Shamita Das, Alexander Gusev and Chris Scholz. The manuscript was critically reviewed by Tom Hanks, Dave Boore and Paul Richards. While not responsible for the prose style, Tia Lombardi helped ease some of its initial angularity.

Bibliography

Achenbach, J.D. and J.A. Harris (1978). Ray method for elastodynamic radiation from a slip-zone of arbitrary shape, J. Geophys. Res. 83, 2283-2302.

Aki, K. (1966). Generation and propagation of G waves from the Niigata earthquake of June 16, 1964. 2. Estimation of earthquake movement, released energy, and stress-strain drop from G wave spectrum, Bull. Earth. Res. Inst. 44, 23-88.

Aki, K. and P.G. Richards (1980). Quantitative Seismology: Theory and Methods, W.H. Freeman and Company, San Francisco, Ca.

Andrews, D.J. (1981). A stochastic fault model: 1. static case, J. Geophys. Res. 86, p. 3867-3877.

Boatwright, J. (1980). A spectral theory for circular seismic sources; simple estimates of source dimension, dynamic stress drop and radiated seismic energy. Bull. Seism. Soc. Am. 70, 1-27.

Boatwright, J. (1982). The effect of rupture complexity on estimates of the stress release, in preparation.

Boatwright, J. and J.B. Fletcher (1982). The partition of radiated seismic energy between P-waves and S-waves, in preparation.

Ben-Menahem, A. (1961). The radiation of seismic surface waves from finite moving sources, Bull. Seism. Soc. Am. 51, 401-435.

Brune, J.N. (1970). Tectonic stress and the spectra of seismic shear waves from earthquakes, J. Geophys. Res. 75, 4997-5009.

Das, S. and B.V. Kostrov (1982). Breaking of a single asperity. I- rupture process, submitted to EOS.

Fletcher, J.B. (1982). A comparision between the tectonic stress measured in-situ and stress parameters from seismic waves at Monticello, South Carolina: a site of induced seismicity, sumitted to Bull. Seism. Soc. Am.

Frankel, A. (1981). Source parameters and scaling relationships of small earthquakes in the northeastern Caribbean, Bull. Seism. Soc. Am. 71, 1173-1191.

Hanks, T.C. (1979). b-values and $\omega^{-\gamma}$ seismic source models: implications for tectonic stress variations along active crustal fault zones and the estimation of high-frequency strong ground motion, J. Geophys. Res. 84, 2235-2242.

Hanks, T.C. and D.A. Johnson (1976). Geophysical assessment of peak accelerations, Bull. Seism. Soc. Am. 66, 959-968.

Hanks, T.C. and R.K. McGuire (1981). The character of high-frequency strong ground motion, Bull. Seism. Soc. Am. 71, in press.

Joyner, W.B. and D.M. Boore (1981). Peak horizontal acceleration and velocity from strong motion records including records from the 1979 Imperial Valley earthquake, Bull. Seism. Soc. Am. 71, in press.

Linde, A.T. , R. Stefansson and I.S. Sacks (1980). A technique for high relative accuracy in the determination of earthquake stress drops, EOS 61, 294.

Madariaga, R. (1976). Dynamics of an expanding circular fault, Bull. Seism. Soc. Am. 66, 639-666.

Madariaga, R. (1977). High-frequency radiation from crack (stress-drop) models of earthquake faulting, Geophys. J. 51, 625-652.

Madariaga, R. (1979). On the relation between seismic moment and stress drop in the presence of stress and strength heterogeneity, J. Geophys. Res. 84, 2243-2250.

Madariaga, R. (1982). A string model for the high-frequency radiation from earthquake faulting, submitted to BSSA.

McGuire, R.K. and T.C. Hanks (1980). RMS accelerations and spectral amplitudes of strong ground motion during the San Fernando, California, earthquake, Bull. Seism. Soc. Am. 70, 1997-1919.

Mori, J. (1980). Effective stress drops of moderate earthquakes in the eastern Aleutians, EOS 61, 294.

Analysis of the Ground Accelerations Radiated by the 1980 Livermore Valley Earthquakes for Directivity and Dynamic Source Characteristics

John Boatwright
David M. Boore
U.S. Geological Survey
Menlo Park, California 94025

Abstract

The strong motion accelerograph recordings of the January 24, 1980, mainshock and the January 27, 1980, aftershock of the Livermore Valley earthquake sequence are analysed for systematic variations indicative of either site effects or directivity. The variation of the peak accelerations with epicentral azimuth is apparently reversed for the two events; the mainshock accelerations are larger to the south, and the aftershock accelerations are larger to the northwest. Forming the ratio of the peak accelerations from the two events, after correcting for the epicentral distance, eliminates the site effects to first order. The results of this analysis indicate that source directivity can cause a total variation of a factor of ten in the peak accelerations. Correlation of this variation with the spatial extent of the aftershock sequences following these events suggests that the strong directivity in the radiated accelerations is the result of unilateral ruptures in both events.

The accelerograms recorded at 10 stations within 35 km of the events were digitized to analyze the azimuthal variation of the rms acceleration, the peak velocity and the radiated energy flux. The variation of rms acceleration correlates almost exactly with the variation of the peak accelerations. This correlation is analysed using both deterministic and stochastic models for the acceleration waveforms. The peak velocities, corrected for epicentral distance, vary with azimuth by a factor of five for both events, while the azimuthal variation of the radiated energy flux is a factor of 30 for the

mainshock and 15 for the aftershock. The peak velocities are strongly correlated with the radiated energy flux. The radiated seismic energies are estimated to be $6.3 \pm 2.0 \times 10^{20}$ dyne-cm for the mainshock and $3.2 \pm .6 \times 10^{20}$ dyne-cm for the aftershock.

Introduction

Directivity, i.e., the azimuthal variation of the radiated seismic energy due to the geometry of the rupture growth, has long been recognized at intermediate periods (several tens of seconds) in teleseismic recordings of large earthquakes (e.g., Benioff, 1955). The existence of strong directivity effects at shorter periods, especially at periods of engineering interest, is a matter of current debate. Recordings of ground accelerations from several recent earthquakes in California including the 1971 San Fernando (McGuire and Hanks, 1980), 1979 Coyote Lake (Archuleta, 1979), and Imperial Valley (Swanger et al., 1981), have been interpreted as showing directivity. Although convincing, the evidence is not indisputable. Objections that have been raised to this interpretation appeal to considerations of the heterogeneity of the stress release in an extended rupture and of systematic effects due to radiation pattern, local soil amplification, foundation-soil interaction and anelastic attenuation. While these competing effects cannot possibly obviate all the observations of directivity, they make the direct quantification of directivity difficult.

In this paper we present what appears to be unambiguous evidence for directivity in the accelerations radiated by two earthquakes which occurred near Livermore Valley, California, during January 1980. The analysis for directivity is enhanced by the good azimuthal coverage, the moderate size of the faults relative to the distance to the stations, and the fact that many stations recorded both events. By comparing the accelerations recorded at the same stations, it is possible to eliminate many of the difficulties associated with analysing data from a single event. The peak acceleration data were first presented as part of a letter to the editor by Boore and Porcella (1980); this paper presents a more complete analysis of these accelerations.

While peak acceleration is the most prevalent quantification of strong

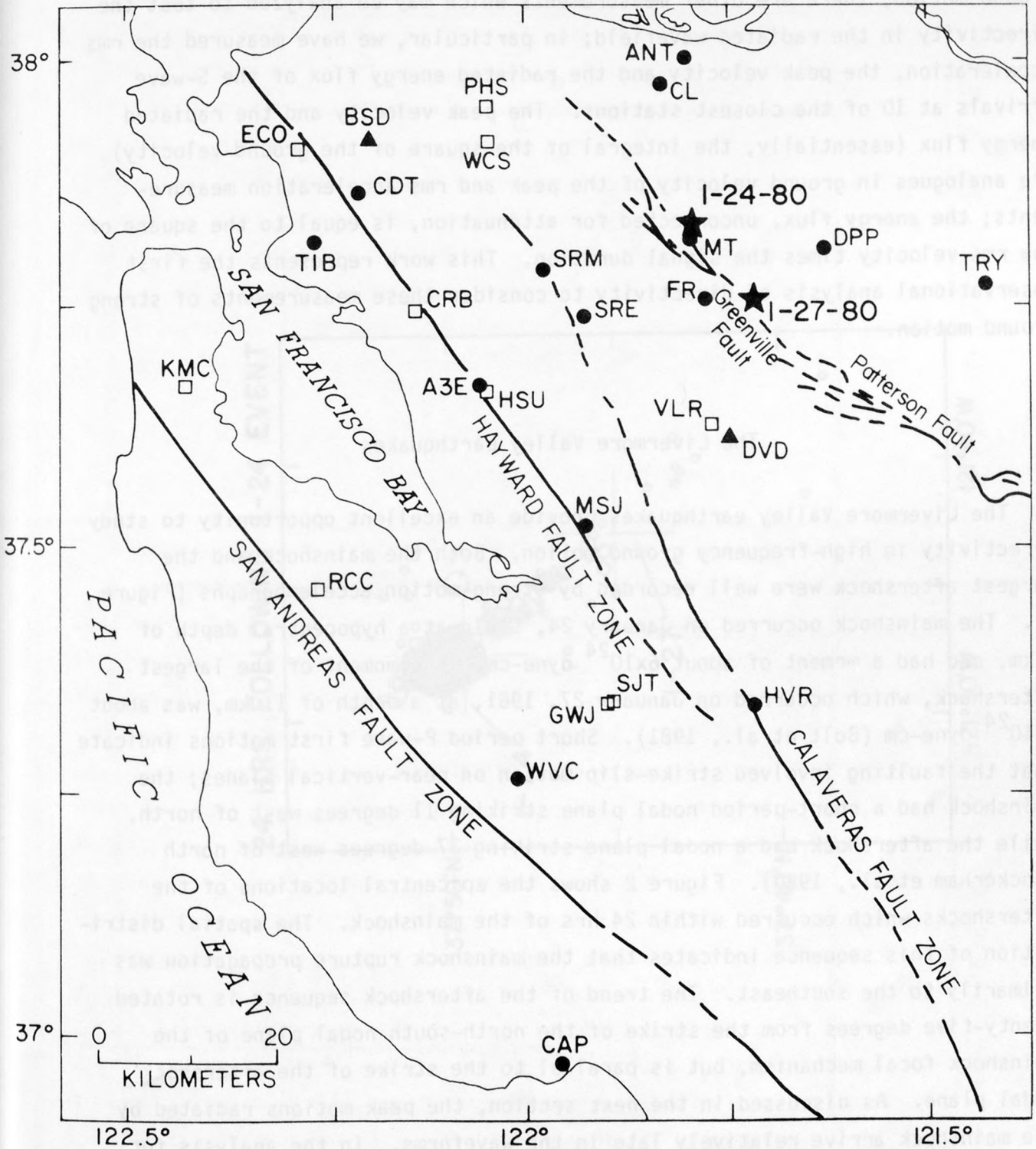

Figure 1. Location map, adapted from McJunkin and Ragsdale (1980). Epicenters of 1/24, 1/27 events (Cockerham et al., 1980) shown by stars. Permanent and temporary accelerograph stations shown by three- and two-letter designations, respectively (Switzer et al., 1981; McJunkin and Ragsdale, 1980). Temporary stations were installed after 1/24 event. Structure type indicated by symbol: circle--building less than 3 stories; square--building taller than 2 stories; triangle--dam abutment or toe.

ground motion, there are other measurements which may be analyzed to test the directivity in the radiated wavefield; in particular, we have measured the rms acceleration, the peak velocity and the radiated energy flux of the S-wave arrivals at 10 of the closest stations. The peak velocity and the radiated energy flux (essentially, the integral of the square of the ground velocity) are analogues in ground velocity of the peak and rms acceleration measurements; the energy flux, uncorrected for attenuation, is equal to the square of the rms velocity times the signal duration. This work represents the first observational analysis of directivity to consider these measurements of strong ground motion.

The Livermore Valley Earthquakes

The Livermore Valley earthquakes provide an excellent opportunity to study directivity in high-frequency ground motion. Both the mainshock and the largest aftershock were well recorded by strong-motion accelerographs (Figure 1). The mainshock occurred on January 24, 1981, at a hypocentral depth of 8 km, and had a moment of about 6×10^{24} dyne-cm. The moment of the largest aftershock, which occurred on January 27, 1981, at a depth of 11 km, was about 2×10^{24} dyne-cm (Bolt et al., 1981). Short period P-wave first motions indicate that the faulting involved strike-slip motion on near-vertical planes; the mainshock had a short-period nodal plane striking 11 degrees west of north, while the aftershock had a nodal plane striking 37 degrees west of north (Cockerham et al., 1980). Figure 2 shows the epicentral locations of the aftershocks which occurred within 24 hrs of the mainshock. The spatial distribution of this sequence indicates that the mainshock rupture propagation was primarily to the southeast. The trend of the aftershock sequence is rotated twenty-five degrees from the strike of the north-south nodal plane of the mainshock focal mechanism, but is parallel to the strike of the aftershock nodal plane. As discussed in the next section, the peak motions radiated by the mainshock arrive relatively late in the waveforms. In the analysis for the directivity, these motions are assumed to be radiated by the section of the fault which strikes to the southeast; the P-wave focal mechanism is assumed to correspond only to a small initial rupture event.

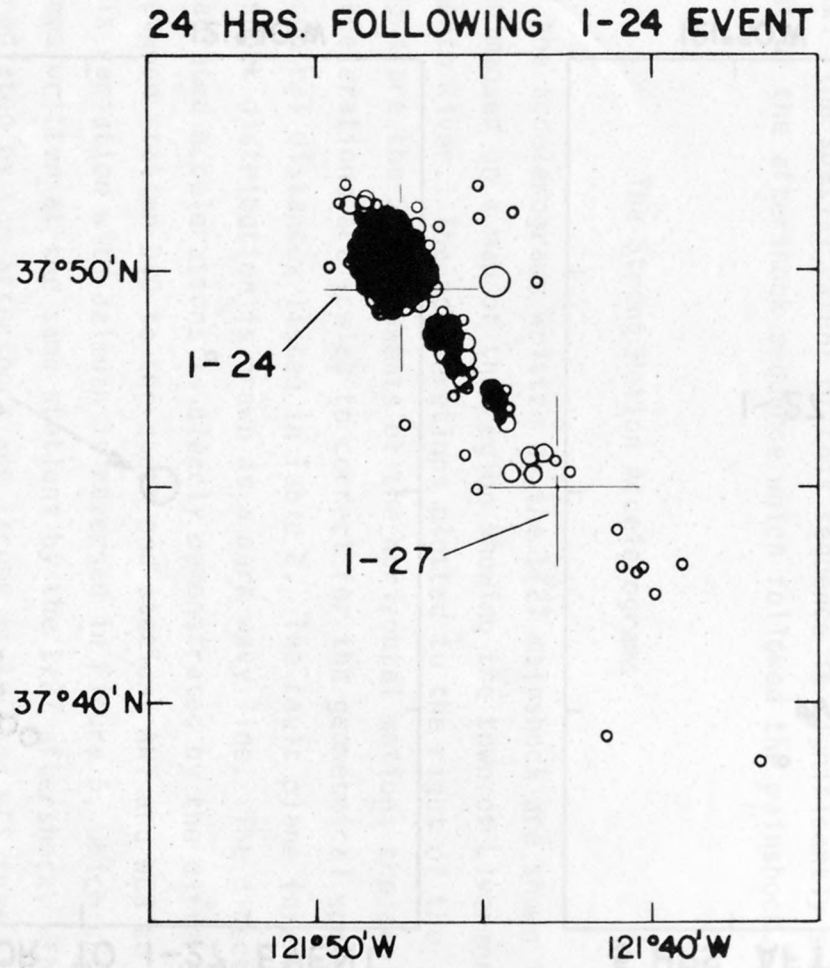

Figure 2. Aftershocks for 24 hours following the 1-24 event, with magnitude shown by symbol size (o for $M_L \geq 2.0$, ○ for $M_L \geq 4.0$). Locations of 1/24 and 1/27 events indicated by crosses.

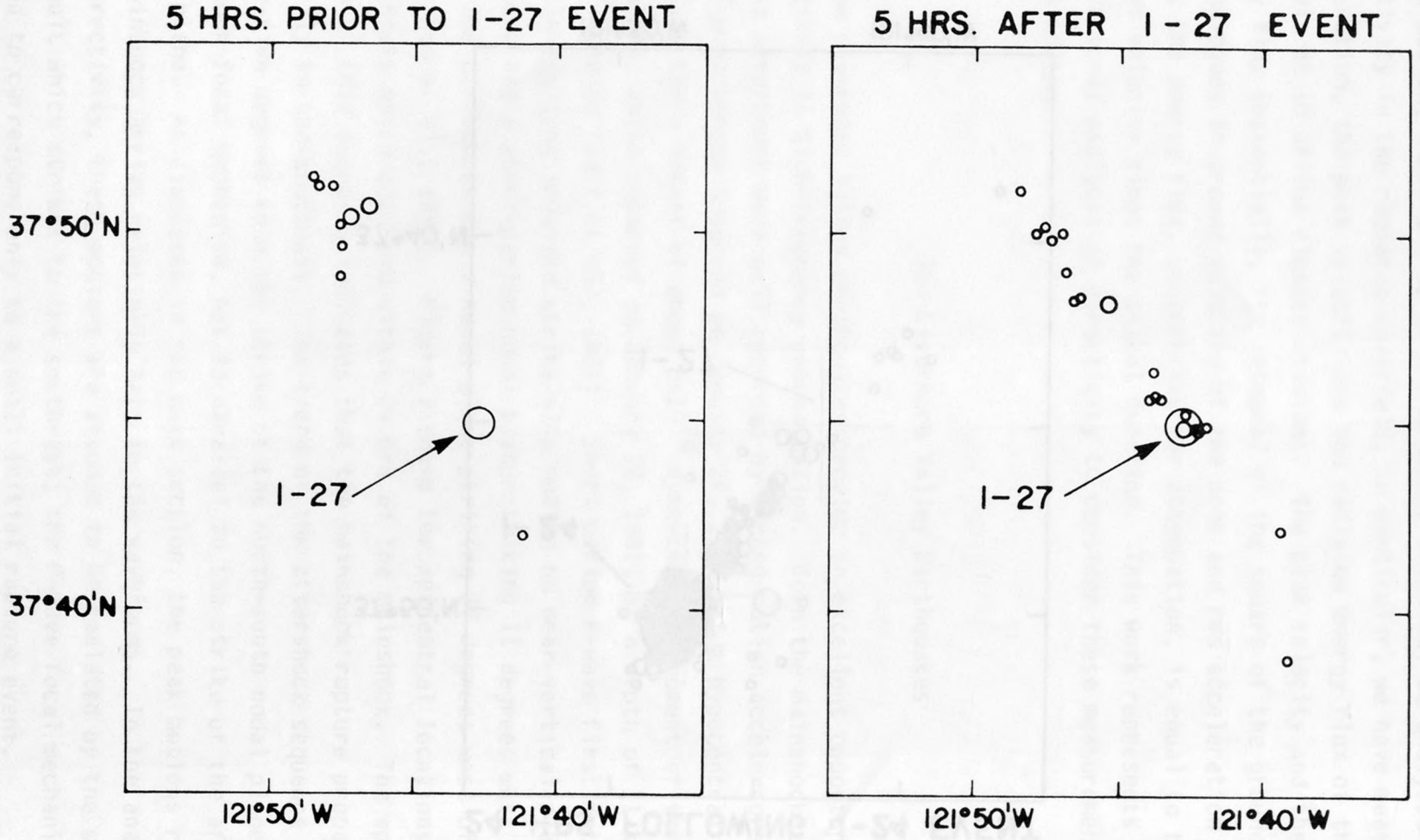

Figure 3. Aftershocks for 5-hour periods before and after 1/27 event (shown by largest symbol).

Figure 3 shows the seismicity pattern for a 5 hour period on either side of the 1/27 aftershock; 2 and 24 hour periods show similar patterns. The rupture in the aftershock appears to have propagated to the northwest; this result is inferred from the cluster of small earthquakes to the northwest of the epicenter. As Figure 2 shows, however, the region of supposed aftershocks of the January 27 event is also the site of aftershock activity following the mainshock. This coincidence implies that these clusters could represent a similar response to the loading of an unruptured ligament or asperity between the two events, and not indicate rupture propagation to the northwest in the 1/27 aftershock. The spatial extent of this sequence is significantly smaller than the extent of the aftershock sequence which followed the mainshock.

The Strong Motion Accelerograms

A subset of the accelerograms written by the 1/27 mainshock are shown in Figure 4, superimposed on a map of the region showing the town of Livermore and the Sacramento River. The accelerations plotted to the right of the station locations are the SH components of the horizontal motion; the amplitudes of the accelerations are scaled to correct for the geometrical spreading using the hypocentral distances listed in Table 2. The fault plane inferred from the aftershock distribution is drawn as a dark wavy line. The directivity in the radiated accelerations is clearly demonstrated by the difference in amplitude between station DVD to the south and stations ANT and WCS to the northwest. This variation with azimuth is reversed in Figure 5, which shows the accelerograms written at the same stations by the 1/27 aftershock. The accelerations radiated by the aftershock are larger at ANT and WCS than at DVD while they are approximately the same for the stations to the east and west. In addition to the strong difference in the azimuthal variation of the amplitudes radiated by the two earthquakes, there is a significant difference in the character of the acceleration waveforms. The peak accelerations in the mainshock accelerograms are embedded late in the waveforms, while the peak accelerations in the aftershock accelerograms occur as the second pulse of the waveform, with the exception of the accelerogram recorded at DVD. This difference is the result of the complexity of the rupture process of the mainshock

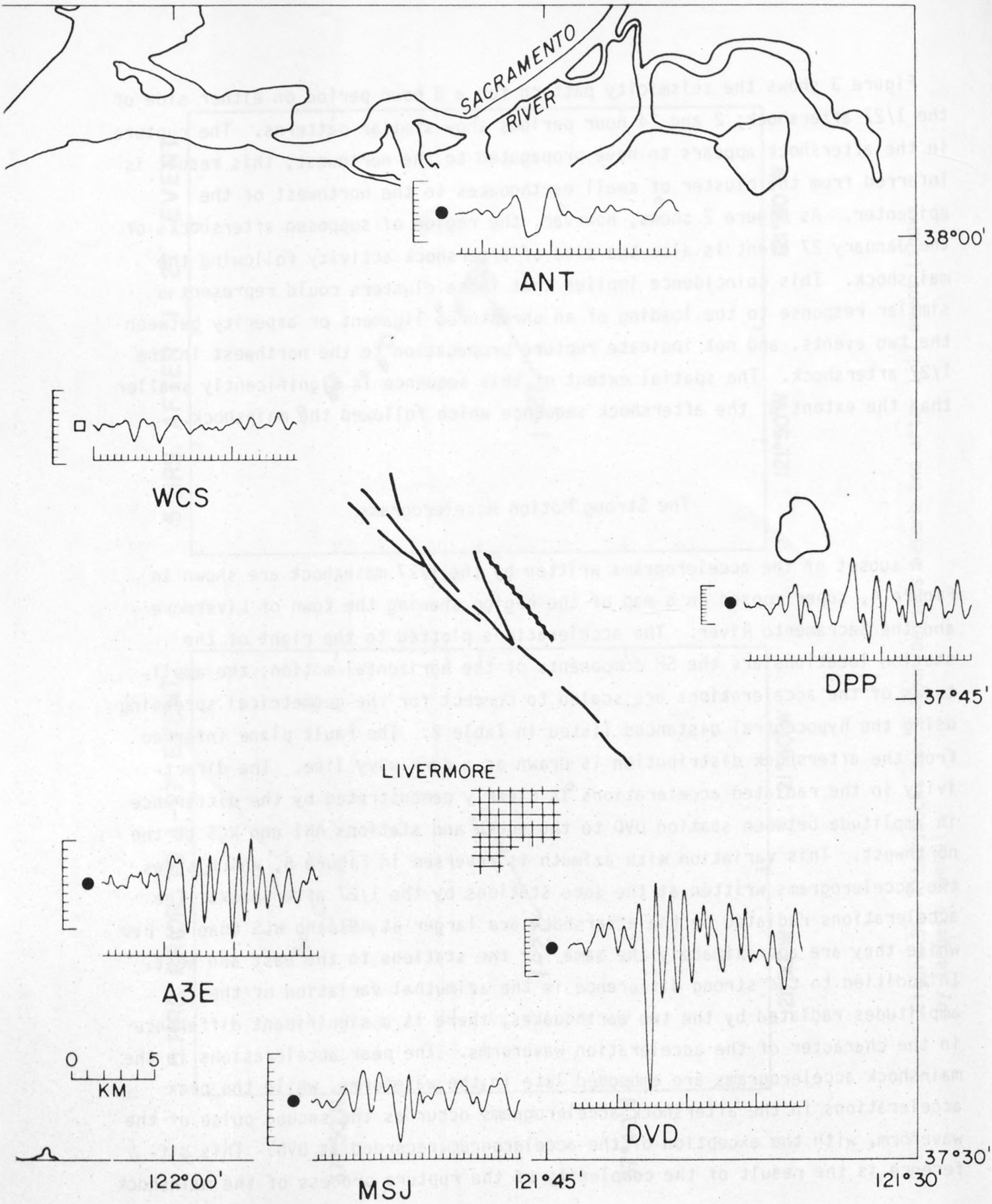

Figure 4. Selected SH accelerograms of the 1/24 mainshock superimposed on a map of the Livermore area, showing the directivity in peak motions and relative complexity of the mainshock accelerograms. The acceleration scales have been adjusted to compensate for the expected 1/R geometrical spreading; each scale has 100 cm/sec^2 between the large tick marks.

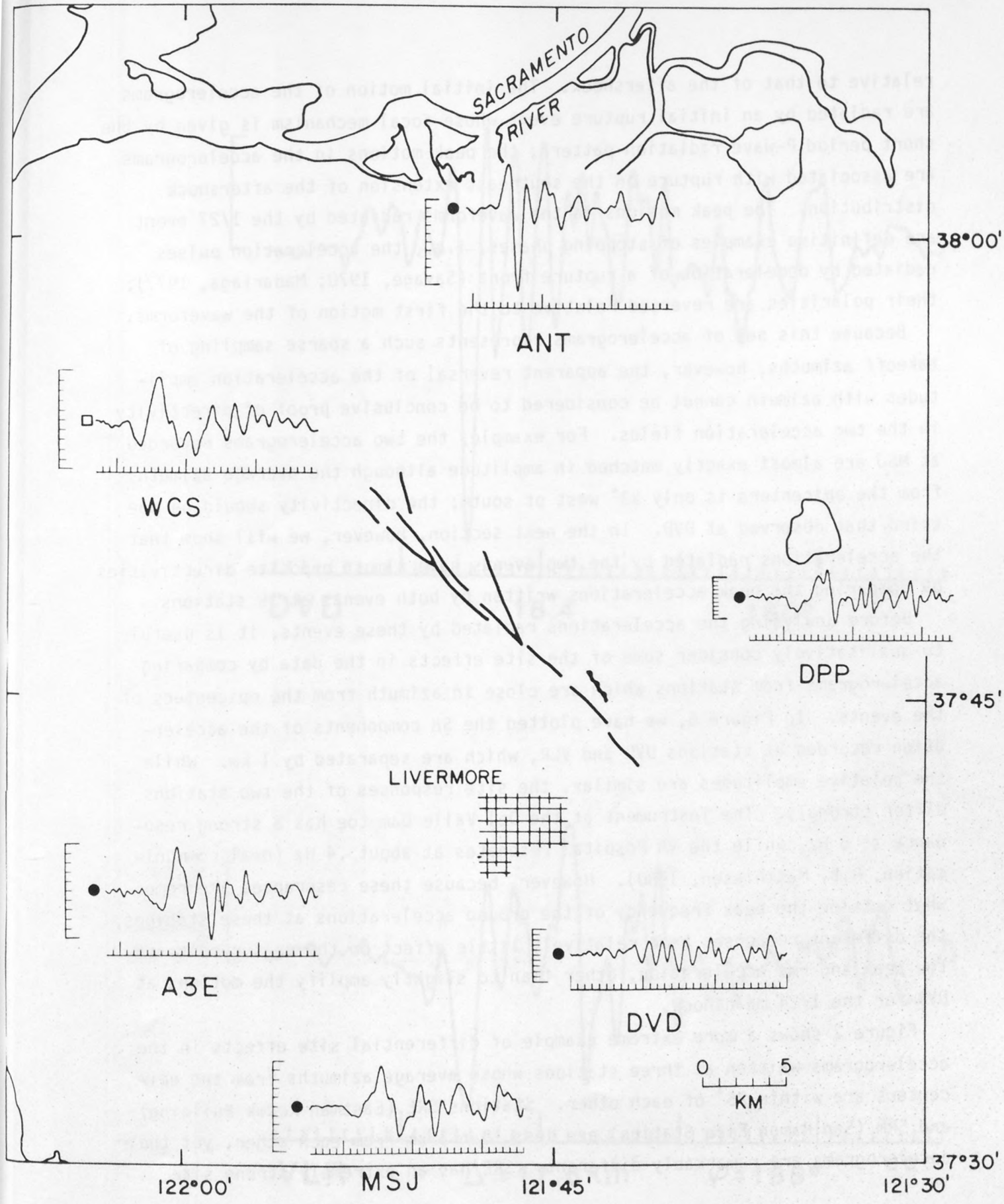

Figure 5. Selected SH accelerograms of the 1/27 aftershock. The acceleration scales have been adjusted as in Figure 4. Note the strong amplification to the northwest, relative to the 1/24 accelerograms.

relative to that of the aftershock. The initial motion of the accelerograms are radiated by an initial rupture event whose focal mechanism is given by the short period P-wave radiation pattern; the peak motions in the accelerograms are associated with rupture on the southeast extension of the aftershock distribution. The peak motions in the waveforms radiated by the 1/27 event are definitive examples of stopping phases, i.e., the acceleration pulses radiated by deceleration of a rupture front (Savage, 1970; Madariaga, 1977); their polarities are reversed relative to the first motion of the waveforms.

Because this set of accelerograms represents such a sparse sampling of takeoff azimuths, however, the apparent reversal of the acceleration amplitudes with azimuth cannot be considered to be conclusive proof of directivity in the two acceleration fields. For example, the two accelerograms recorded at MSJ are almost exactly matched in amplitude although the average azimuth from the epicenters is only 33° west of south; the directivity should be one third that observed at DVD. In the next section, however, we will show that the accelerations radiated by the two events have almost opposite directivities by comparing the peak accelerations written by both events at 19 stations.

Before analysing the accelerations radiated by these events, it is useful to qualitatively consider some of the site effects in the data by comparing accelerograms from stations which are close in azimuth from the epicenters of the events. In Figure 6, we have plotted the SH components of the acceleration recorded at stations DVD and VLR, which are separated by 1 km. While the relative amplitudes are similar, the site responses of the two stations differ strongly. The instrument at the Del Valle Dam toe has a strong resonance at 8 Hz, while the VA Hospital resonates at about .4 Hz (oral communication, R.B. Matthiesen, 1980). However, because these resonances are somewhat outside the peak frequency of the ground accelerations at these stations, the different responses have relatively little effect on the measurements of the peak and rms acceleration, other than to slightly amplify the motions at DVD for the 1/24 mainshock.

Figure 7 shows a more extreme example of differential site effects in the accelerograms written at three stations whose average azimuths from the epicenters are within 25° of each other. Stations SRE (Eastman Kodak Building) and SRM (San Ramon Fire Station) are less than 5 km from each other, yet their accelerograms are remarkably different. SRE has an extremely strong site

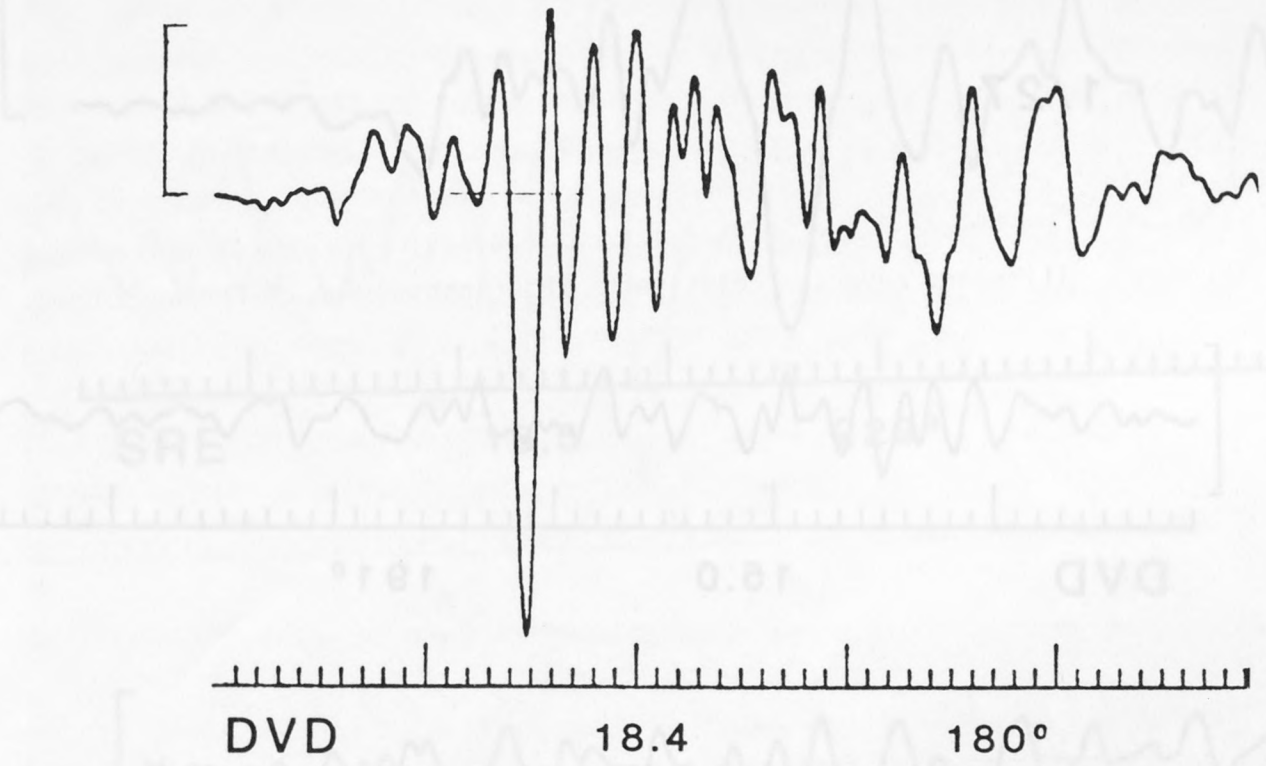

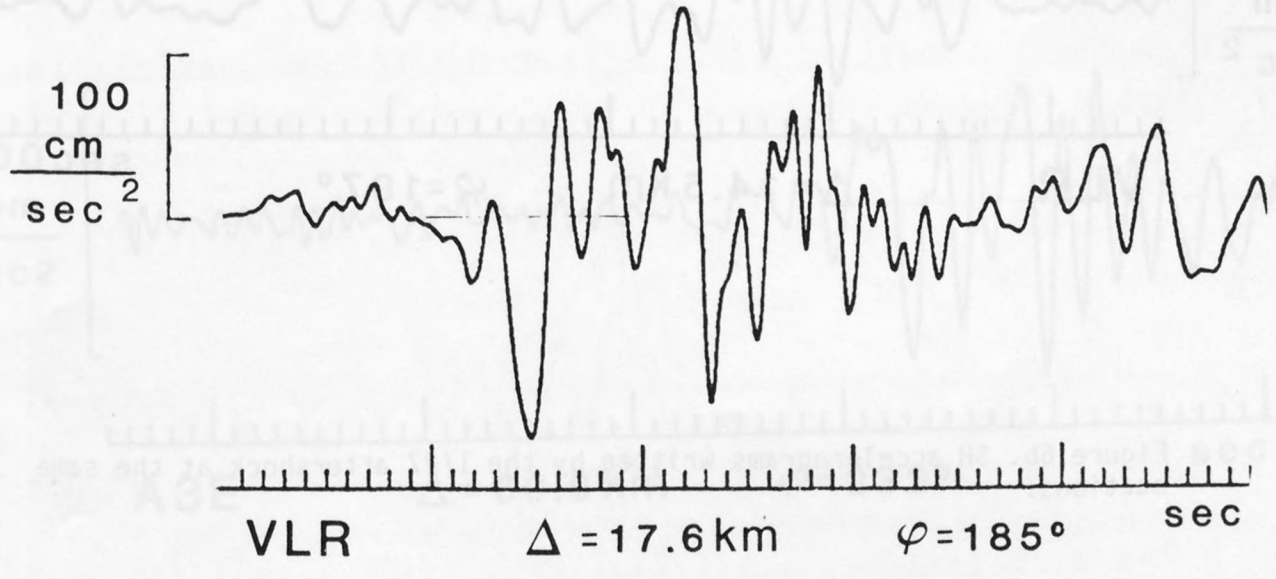

Figure 6a. SH accelerograms of the 1/24 mainshock recorded at stations DVD and VLR. The scales are adjusted as in Figures 4 and 5. Distance and azimuth from the epicenter are indicated below the accelerograms.

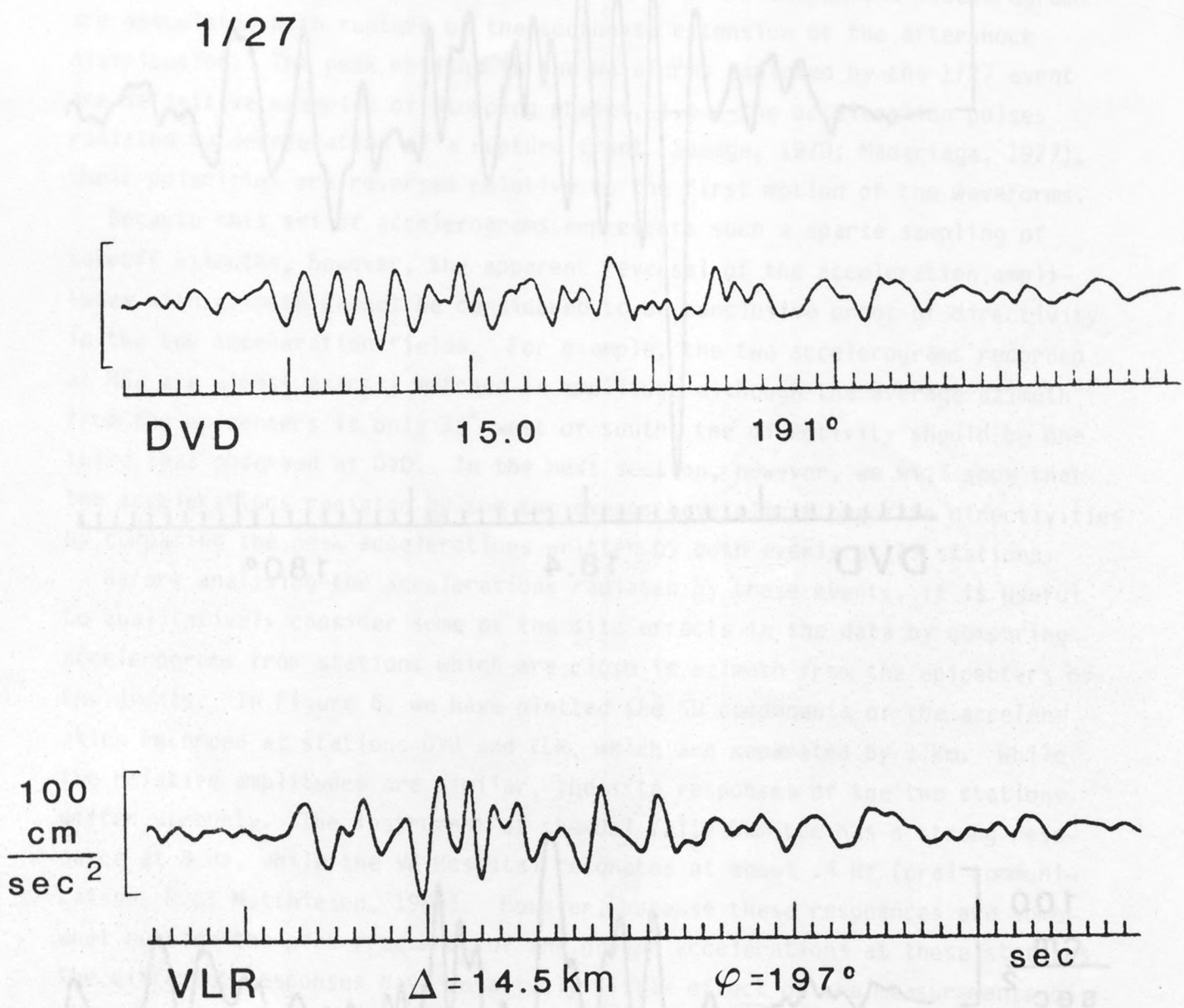

Figure 6b. SH accelerograms written by the 1/27 aftershock at the same stations.

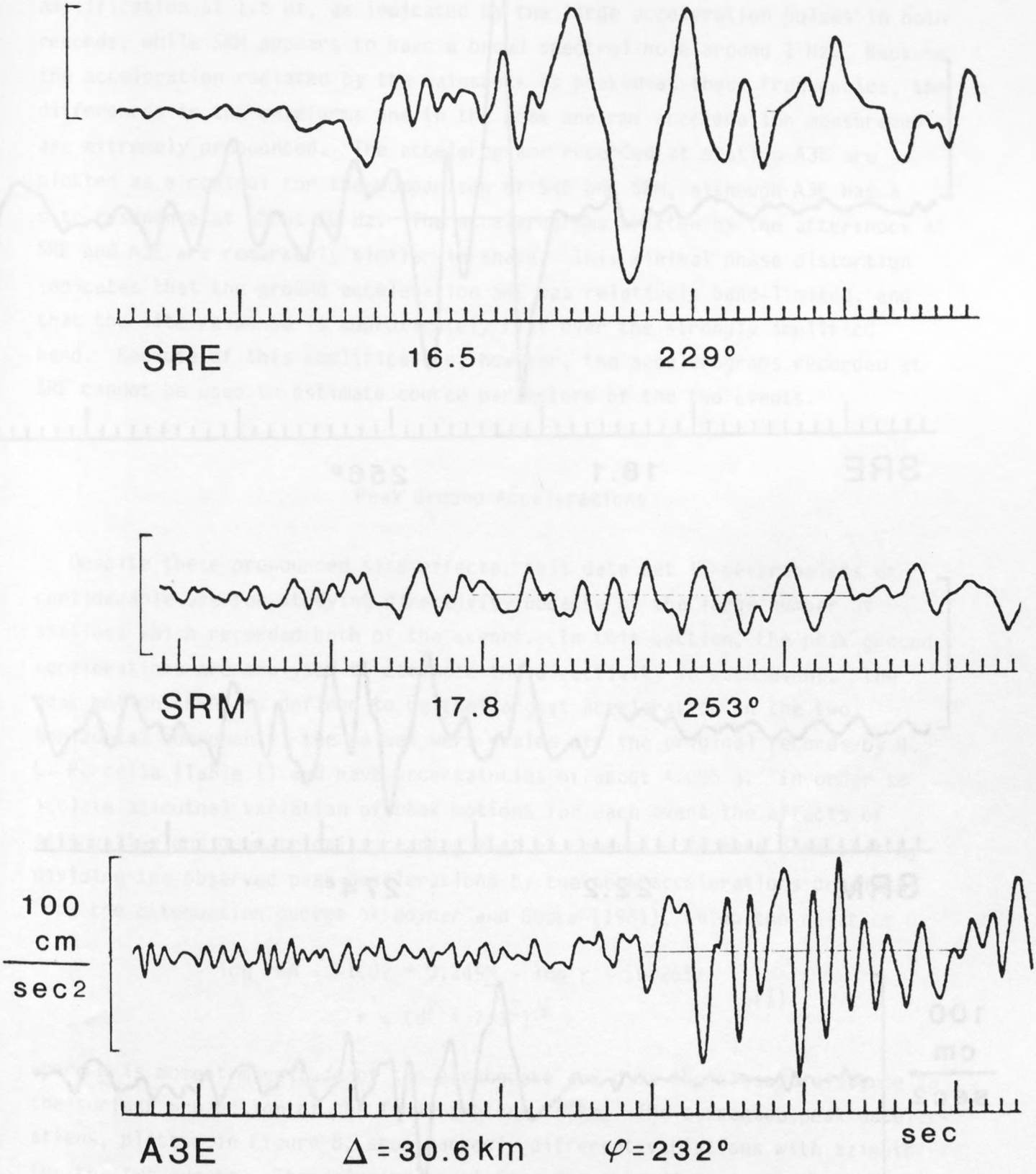

Figure 7a. SH accelerograms of the 1/24 mainshock recorded at stations SRM, SRE and A3E.

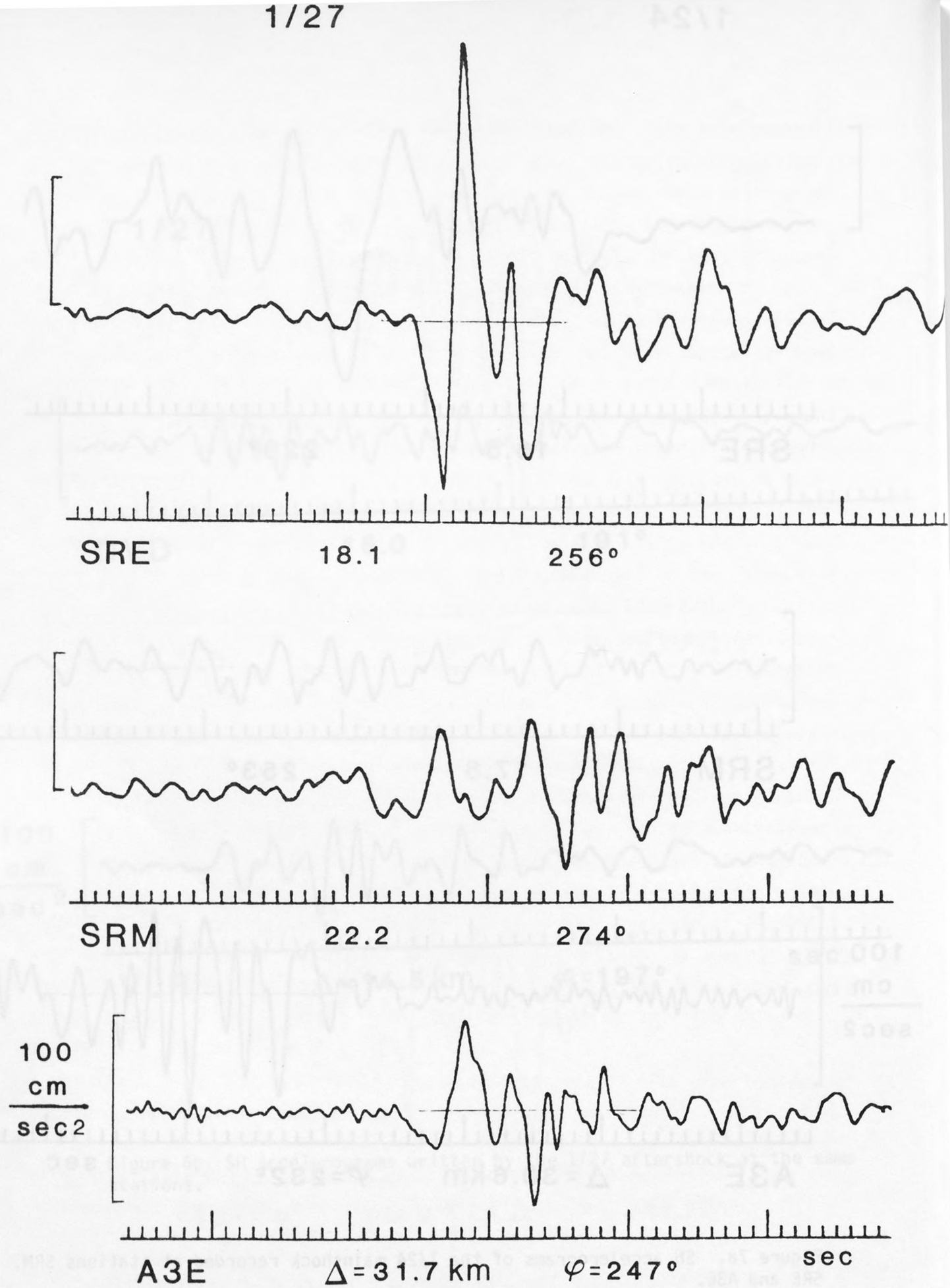

Figure 7b. SH accelerograms written by the 1/27 aftershock.

amplification at 1.5 Hz, as indicated by the large acceleration pulses in both records, while SRM appears to have a broad spectral hole around 1 Hz. Because the acceleration radiated by the mainshock is peaked at these frequencies, the differences in the waveforms and in the peak and rms acceleration measurements are extremely pronounced. The accelerograms recorded at station A3E are plotted as a control for the comparison of SRE and SRM, although A3E has a site resonance at about 10 Hz. The accelerograms written by the aftershock at SRE and A3E are remarkably similar in shape. This minimal phase distortion indicates that the ground acceleration SRE was relatively band-limited, and that the site response is approximately flat over the strongly amplified band. Because of this amplification, however, the accelerograms recorded at SRE cannot be used to estimate source parameters of the two events.

Peak Ground Accelerations

Despite these pronounced site effects, this data set is nevertheless of considerable use for studying directivity because of the large number of stations which recorded both of the events. In this section, the peak ground accelerations are analysed to estimate the directivity in each event. The peak motion (PGA) is defined to be the largest acceleration on the two horizontal components; the values were scaled off the original records by R. L. Porcella (Table 1) and have uncertainties of about ±.005 g. In order to isolate azimuthal variation of peak motions for each event the effects of attenuation and geometrical spreading must be removed. We have done this by dividing the observed peak accelerations by the peak accelerations predicted from the attenuation curves of Joyner and Boore (1981), using the relation

$$\log PGA = -1.02 + 0.249\underline{M} - \log r - .00255r \qquad (1)$$

$$r = (d^2 + 7.3^2)^{\frac{1}{2}}$$

where $\underline{M}$ is moment-magnitude of the earthquake and d is the closest distance to the surface projection of the fault rupture in km. The corrected peak accelerations, plotted in Figure 8, show markedly different variations with azimuth for the two events. The azimuthal variation for recordings in the basements

of large and small structures is approximately the same, but the two sets of data differ from one another by a constant factor. This is consistent with analyses of the accelerations from other earthquakes (primarily the 1971 San Fernando event); on the average, the peak accelerations recorded in the basements of tall buildings are less than those recorded in small structures: Boore et al., (1980) find the difference to be .2 log units for the San Fernando data. Considering this effect of structure size, the estimates of the total azimuthal variation of the peak accelerations yields a factor of eight for the mainshock (.9 log units) and a factor of five for the aftershock (.7 log units).

A critical consideration in this analysis is the effect of the radiation patterns. It is extremely difficult to fit nodes (predicted at 188° and 278°) within the measurements of peak acceleration shown in Figure 8 for each earthquake. While such an observation does not rule out the possibility that the radiation patterns exerts some influence on these results, the dense sampling of station azimuths from 180° to 300° indicates that the radiation patterns are significantly obscured and may be regarded as a secondary effect. The effect of the radiation patterns on the radiated accelerations is weakened by two effects; body-wave scattering at high frequencies and the general complexity of dynamic rupture, as reflected in the radiated acceleration, can be expected to significantly obscure the radiation pattern. Also, the peak S-wave motion on the two horizontal components is measured without regard to whether it is SH or SV motion. Hanks and McGuire (1981) reached a similar conclusion in their analysis of the accelerograms written by the Oroville aftershocks.

As stated earlier, it is difficult to estimate directivity for single events: apparent azimuthal variations can be caused by coarse sampling of radiation patterns, improper distance corrections and by azimuthally-dependent geology or structure-size distributions as in the 1971 San Fernando earthquake, where deep sedimentary basins and many high rise buildings are located to the south of the epicenter. To eliminate these effects, to first order, we consider the ratio of peak motions at those stations that recorded both events (Figure 9). The similar epicentral distances makes this ratio relatively insensitive to the attenuation relation used to correct for epicentral distance. The results plotted in Figure 9 show a strong azimuthal

Table 1

Peak Acceleration Data

STATION	STRUCTURE[1] TYPE	1/24 EVENT d[2] (km)	1/24 EVENT ϕ	1/24 EVENT pga[3] (g)	1/27 EVENT d (km)	1/27 EVENT ϕ	1/27 EVENT pga (g)
A3E	1	30.6	232°	0.065	31.7	247°	0.065
ANT	1	21.0	354°	0.045	28.4	345°	0.112
BSD	3	38.4	284°	0.016	45.2	291°	0.044
CAP	1	92.0	191°	0.023	NO RECORD		
CDT	1	38.4	277°	0.020	NO RECORD		
CRB	2	33.4	253°	0.016	37.2	265°	0.026
DPP	1	11.3	80°	0.12	9.9	56°	0.071
DVD	3	18.4	180°	0.26	15.0	191°	0.047
ECO	2	45.9	280°	0.005	52.4	286°	0.010
GWJ	2	51.1	195°	0.011	48.4	199°	0.005
HSU	2	30.4	231°	0.048	31.4	247°	0.059
HVR	1	49.3	176°	0.093	NO RECORD		
KMC	2	60.4	252°	0.017	63.7	259°	0.012
MSJ	1	32.0	209°	0.056	30.4	217°	0.039
PHS	2	27.6	300°	0.033	35.5	305°	0.035
RCC	2	59.7	226°	0.011	59.4	234°	0.003
SJT	2	51.0	194°	0.023	48.3	199°	0.006
SRE	1	16.5	229°	0.154	18.1	256°	0.275
SRM	1	17.8	253°	0.052	22.2	274°	0.058
TIB	1	NO RECORD			47.9	276°	0.026
TRY	1	28.8	93°	0.086	NO RECORD		
VLR	2	17.6	185°	0.17	14.5	197°	0.059
WCS	2	26.0	290°	0.032	33.4	298°	0.057
WVC	1	62.4	202°	0.018	60.2	206°	0.012
CL	1	STATION NOT INSTALLED			24.1	339°	0.026
FR	1	STATION NOT INSTALLED			4.1	246°	0.259
MT	1	STATION NOT INSTALLED			8.1	314°	0.267

NOTES FOR TABLE 1:

1. Station identification, coordinates, and structure type (1 = buildings less than or equal to 2 stories, 2 = buildings larger than 2 stories, 3 = dam toe or abutment) from Switzer et al., (1981). CL, FR, MT are temporary stations installed after the 1-24 event (McJunkin and Ragsdale, 1980).

2. Closest horizontal distance and azimuth from source to station, assuming faults extending from (37.827°N, 121.787°W) to (37.783°N, 121.746°W) and (37.750°N, 121.713°W) to (37.768°N, 121.729°W) for 1-24, 1-27 events, respectively. Fault locations based on earthquake locations by Cockerham et al., (1980).

3. Peak ground acceleration (pga), largest of the two horizontal components scaled from original records by R. L. Porcella.

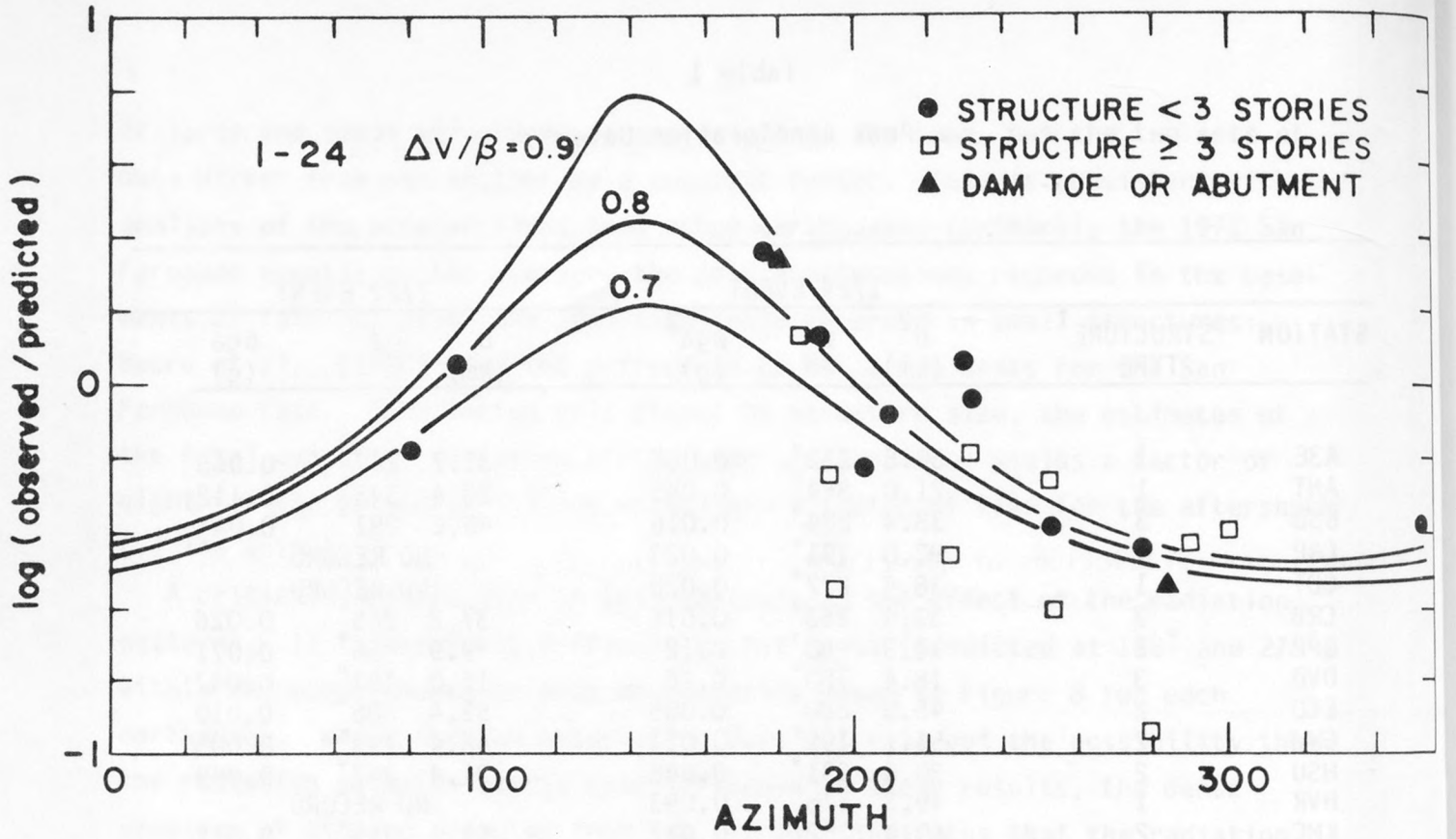

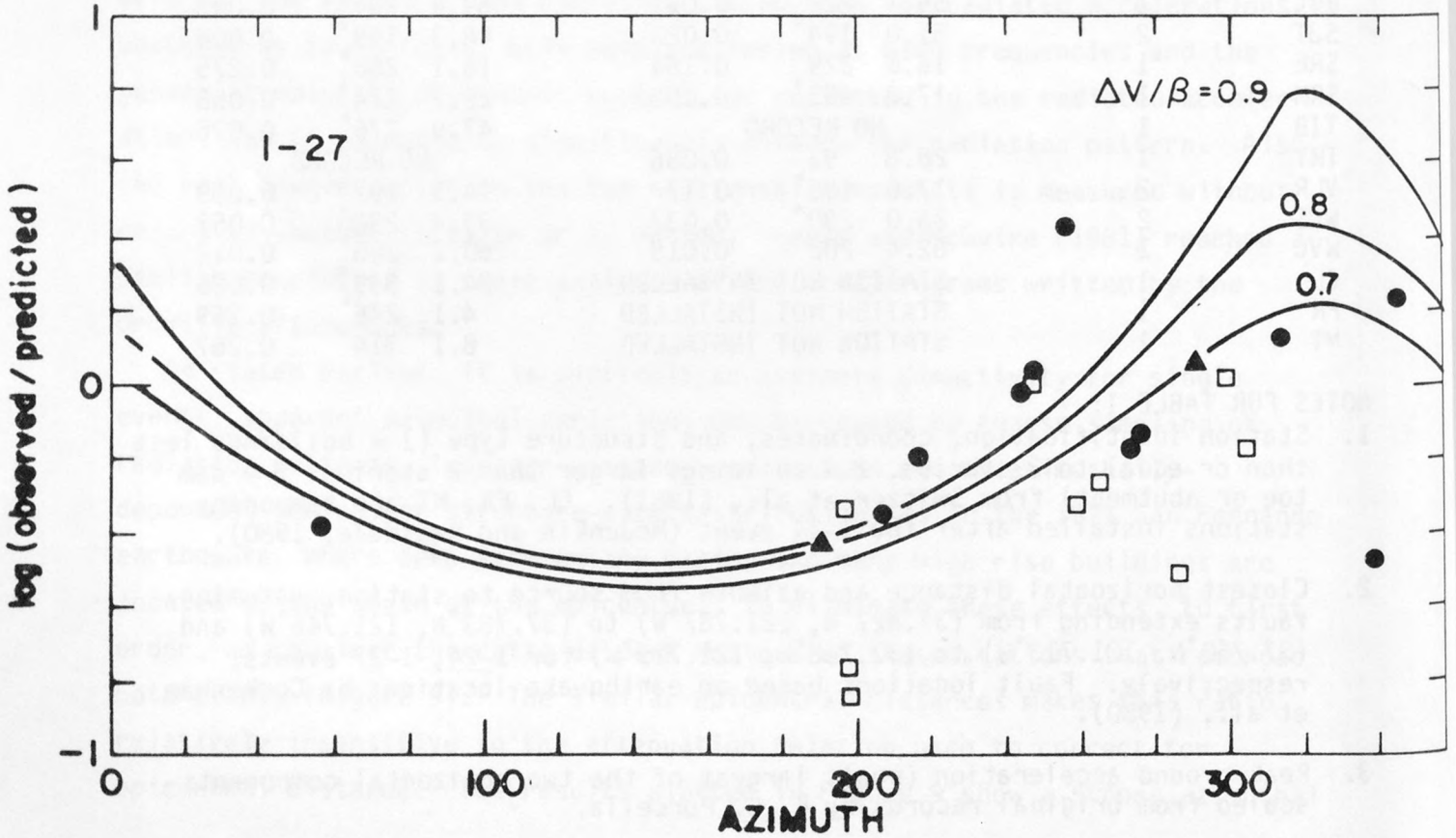

Figure 8. The logarithms of the observed peak acceleration divided by the predicted peak acceleration, plotted against azimuth from source to receiver. The predicted motions are estimated from eq. (1), using moment magnitudes of 5.8 and 5.5 for the 1/24 and 1/27 events. The curves superimposed on the data are the theoretical predictions determined from eq. (2) adjusted to the data.

dependence, with a total variation of a factor of 30 (one and a half logarithmic units). Because we are using the ratio of the peak motions recorded at these stations, this variation can only result from the directivity in the two events. If the dominant motion of the mainshock occurred on the same fault plane as the aftershock, as suggested by the aftershock sequence following the mainshock, this ratio also eliminates any bias which might result from the effect of the radiation pattern.

Having established directivity in the ground acceleration for the Livermore Valley earthquakes, it is important to analyse this azimuthal variation using theoretical predictions of directivity to fit the data. As a simple model for the variation of the peak ground acceleration, we consider the directivity function,

$$D^S(\psi) = [1 - \frac{\Delta v}{\beta}\cos\psi]^{-1} \qquad (2)$$

(Madariaga, 1977; Boatwright, 1982) where Δv is the change of rupture velocity associated with the radiation of the acceleration pulse, β is the shear wave velocity at the source and ψ is the angle between the direction of rupture and the takeoff direction of the ray. This equation is strictly applicable only if the peak accelerations are measured from the acceleration pulse radiated by the same faulting event. Although this is true for the peak accelerations radiated by the aftershock, as shown in Figure 5, it may not be true for the mainshock accelerograms. In calculating the theoretical curves the takeoff angles of the rays are assumed to be horizontal, so that ψ is the angle between the rupture direction, ϕ_r, and the azimuth to the station, ϕ. The rupture directions were assumed to be aligned with the southeastward extension of the distribution of aftershocks for the mainshock ($\phi_r = 143^\circ$) and with the northwest ($\phi_r = 323^\circ$) for the aftershock. The theoretical curves calculated for a range of rupture velocities are plotted on Figures 8 and 9. The curves in Figure 8 were adjusted vertically to the small structure data. Although it is not possible to choose between the changes of rupture velocity used to generate the theoretical curves because the maxima of the theoretical variation is not sampled, the overall fit for the mainshock is surprisingly good. The fit of the theoretical curves to the aftershock data, however, is less convincing, owing to the increase in the scatter of the data.

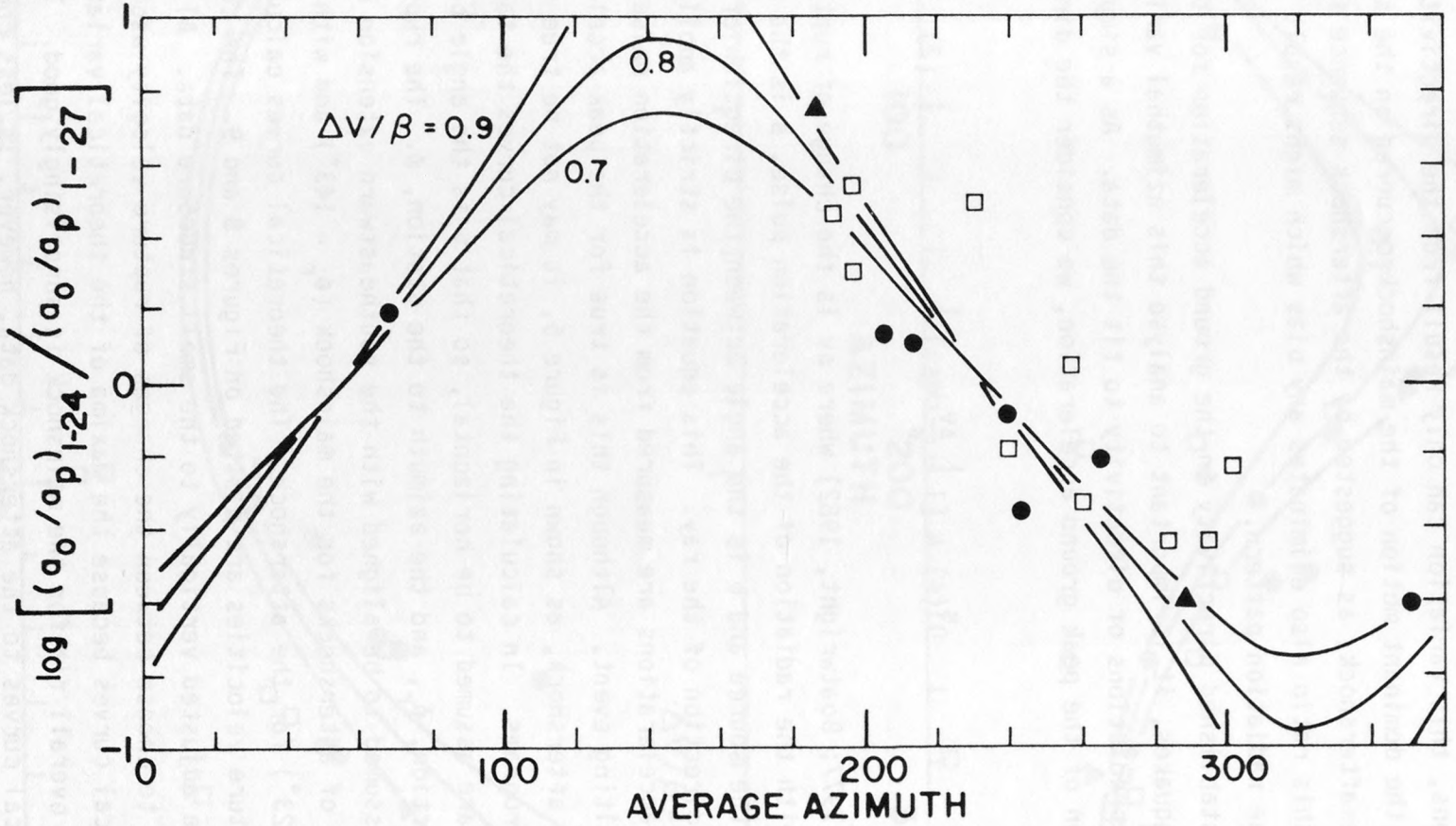

Figure 9. The logarithms of the ratio of peak accelerations from 1/24 and 1/27 events corrected for distance with theoretical curves determined for various changes of rupture velocity superimposed.

The fit of the theoretical curves to the ratios of the peak accelerations recorded at the same stations, shown in Figure 9, is remarkable, as there were no free parameters which were varied to obtain this fit. Considering only the small-structure and dam sites data, the change of rupture velocity is constrained to be greater than .7β. The takeoff angles of the shear waves recorded at stations within 20 kms of the epicenters are significantly different from horizontal (written communication, R. Cockerham, 1981); this effect and the possibility of a non-horizontal direction of rupture, indicate that the theoretical curves calculated from eq. (2) represent upper bounds for the directivity expected for a specific change of rupture velocity. Thus $\Delta v = .7\beta$ is a strong lower bound for the change of rupture velocity.

To determine the variation of peak acceleration which may result from differential site effects, it is useful to analyse the distribution of the logarithms of the products, at each station, of the corrected peak accelerations shown in Figure 8. Assuming that the directivity in the two events is equal in amplitude and exactly reversed as implied by the fit in Figure 9, the standard deviation of this distribution is equal to twice the variation which may be attributed to site effects. This gives an estimate of a factor of three (half a log unit) for the total (peak to peak) variation expected from site effects.

RMS Accelerations

The rms accelerations of the SH components of the shear waves radiated by the mainshock and the largest aftershock have been measured for a subset of the stations which recorded the two events. The stations chosen for this analysis represent as complete an azimuthal distribution as possible; they also represent most of the strong-motion stations within 35 kms of the two events.

While mostly SH motion, the shear waves are not perfectly polarized; as the SH component is always the largest component of motion, however, this analysis is consistent with the previous analysis of the peak ground acceleration. The measurements of a_{rms} and the durations used to calculate them are shown in Table 2. The choice of the interval over which the square of the acceleration

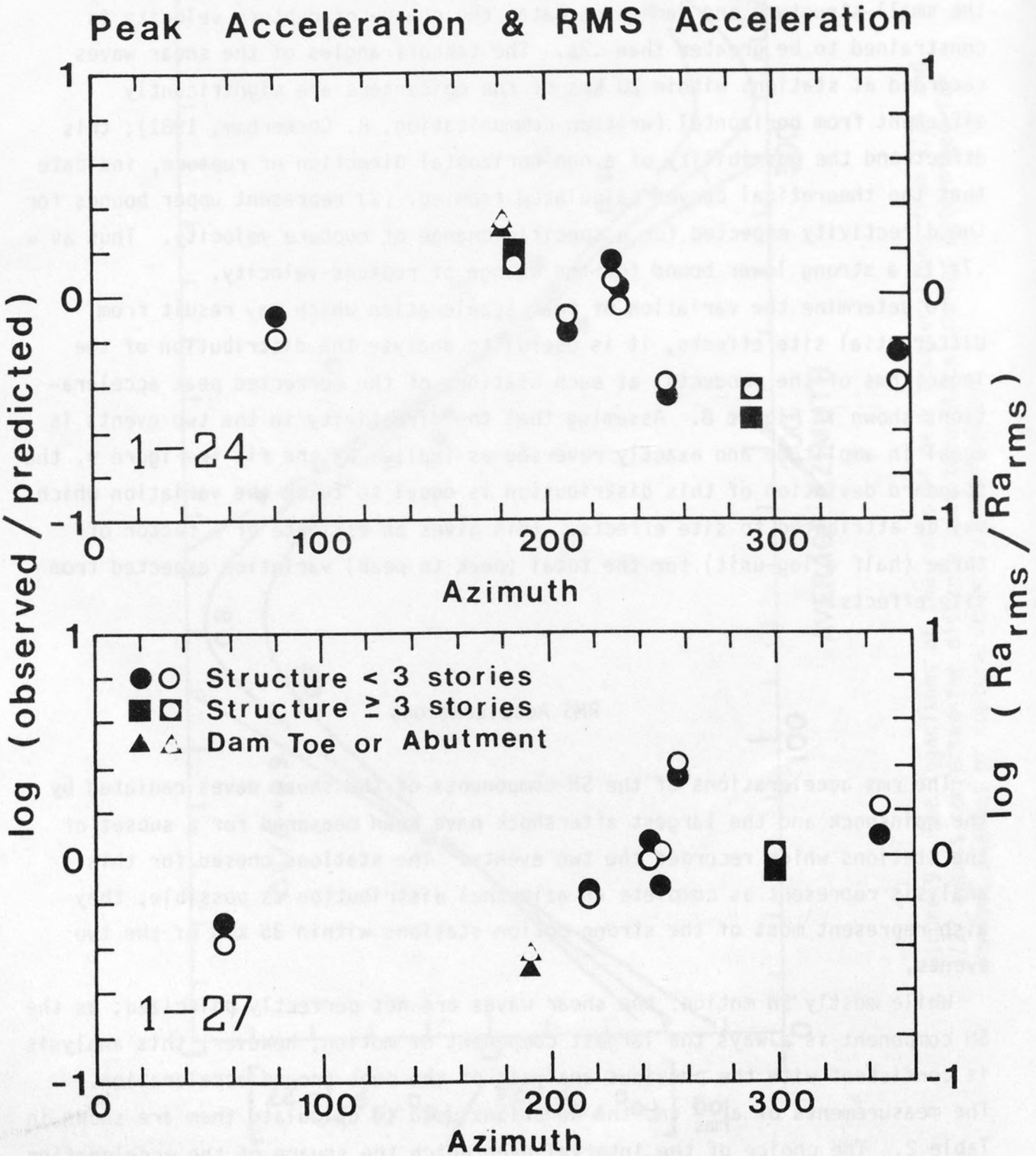

Figure 10. Comparision of corrected peak ground acceleration and rms acceleration for the 10 stations at which the rms acceleration was measured. The rms accelerations are corrected for hypocentral distance and divided by the mean, $\overline{Ra}_{rms}$. The filled symbols are the corrected rms accelerations; the open symbols are the corrected peak accelerations.

is averaged was made in a subjective fashion, where the direct S-wave is enclosed as closely as possible. As discussed by McGuire and Hanks (1980) and McCann and Boore (1982), this technique, though subjective, is reasonably well conditioned; varying the duration has little effect on the rms estimates.

To consider the variation of these measurements with azimuth, the effect of geometrical spreading is removed by multiplying the rms acceleration by the hypocentral distance. The resulting estimates are then averaged to obtain the mean $\overline{Ra}_{rms}$, and the logarithm of the ratio of each estimate of Ra_{rms} to this mean is calculated. These values are plotted in Figure 10, along with the logarithms of the observed peak accelerations divided by the predicted peak accelerations, taken from Figure 8, for the same stations. The corrected a_{rms} values track the corrected peak acceleration values extremely well; for only four of the measurements are these corrected values more than 25% from each other.

The correlation is striking and somewhat stronger than that shown by Hanks and McGuire (1981) for the accelerograms written by the 1975 Oroville aftershock sequence. Using this correlation to extrapolate the variation of the corrected peak accelerations shown in Figures 8 and 9 to the corrected rms accelerations, we then estimate a directivity effect of a factor of 10 (peak to peak) for measurements of rms acceleration from a strongly unilateral event.

As demonstrated by Boatwright (1982), the rms acceleration may be used to estimate the rms dynamic stress drop averaged over the rupture area. The relation between the rms acceleration and the rms dynamic stress drop depends in general on the behavior of the acceleration spectrum. For acceleration spectra which falloff as ω^{-1} above the corner frequency and are not strongly attenuated, the relation

$$\Delta\sigma = \frac{2}{3}\frac{\rho}{\bar{R}^s}\frac{\beta^2}{v\Delta v}\overline{Ra}_{rms} \qquad (3)$$

(Boatwright, 1982) can be used to estimate the rms dynamic stress drop, $\Delta\sigma$. Using $\rho = 2.7$ gm/cm^3 and $\beta = 2.8$ km/sec for the density and average shear wave velocity, and assuming $v = .75\beta$ is the average rupture velocity, $\Delta v = .85\beta$ is the change of rupture velocity associated with the radiated accelerations, and $\bar{R}^s = .54$ is the average high-frequency radiation pattern for SH waves from

a strike-slip fault (see Boatwright, 1982, Figure 2), multiplied by two to account for the free-surface. Estimating the dynamic stress drop from $\overline{Ra}_{rms}$ gives $\Delta\sigma$ = 300±64 bars for the mainshock and 259±40 bars for the aftershock.

This estimate of the dynamic stress drop for the aftershock can be tested against the initial slope technique proposed by Boatwright (1980), using the relation

$$\tau_e = \rho \left(\frac{\beta}{v}\right)^3 \frac{R}{F^c}(1-k^2)^2 \left\langle \frac{\dot{u}}{t} \right\rangle. \qquad (4)$$

In this equation, $k = \frac{v}{c}\sin\theta$, where θ is the angle between the takeoff direction of the ray and the normal to the fault surface. The measurements of the initial slope of the velocity waveforms, $\left\langle \frac{\dot{u}}{t} \right\rangle$, are listed in Table 2 along with the resulting estimates of the dynamic stress drop. The radiation pattern correction, F^S = .78, is the average over the focal sphere of the absolute value of the SH radiation pattern, multiplied by two to correct for the effect of the free surface. The measurements of the initial slope were corrected for attenuation by subtracting t*/2 (= T/2Q where T is the travel time and Q = 200) from the duration over which the slope was estimated. The resulting estimate of the dynamic stress drop is 231±28 bars, slightly less than the estimate of the rms stress drop determined from the rms accelerations.

To consider if the estimates of the rms dynamic stress drop are effected by the attenuation, it is necessary to calculate the ratio of the rupture duration to the attenuation duration, t*. Assuming an average shear wave Q of 200 for the Franciscan sediments of the Livermore Valley gives t*'s from .02 secs to .06 secs, which are substantially less than the rupture durations of approximately .75 secs for the mainshock and .55 secs for the aftershock, estimated as half of the interval used to calculate a_{rms}. Thus, the frequency band of the recorded accelerations, 1 Hz to 8 Hz, is more strongly controlled by the source characteristics than by the propagation characteristics. This conclusion, however, depends strongly on the assumption that the average shear wave Q is greater than 200.

Table 2

RMS Acceleration data

STATION	1/24 EVENT			1/27 EVENT					
	R^1 (km)	τ (sec)	a_{rms} (cm/sec^2)	R (km)	τ (sec)	a_{rms} (cm/sec^2)	$\langle \frac{u}{t} \rangle$	θ	τ_e (bars)
A3E	31.6	1.26	27.0	33.5	1.33	19.8	18.4	10°	372
ANT	22.5	1.60	22.5	30.4	.90	35.2	47.4	85°	175
DPP	13.8	1.61	46.3	14.6	.95	31.1	31.2	35°	189
DVD	20.1	1.20	84.9	18.4	1.34	15.2	RECORD NOT ANALYSED		
MSJ	33.0	1.43	17.6	32.2	1.53	17.8	13.9	35°	185
SRE	18.3	1.87	56.6	21.0	1.04	89.3	109.1	22°	1213
SRM	19.5	2.09	16.5	22.9	1.70	28.1	RECORD NOT ANALYSED		
VLR	19.3	1.47	60.8	18.2	1.30	17.4	RECORD NOT ANALYSED		
WCS	27.2	1.53	8.7	35.1	1.14	21.9	21.7	40°	213
FR	STATION NOT INSTALLED			11.7	.88	89.9	77.0	50°	252

NOTE FOR TABLE 2:
1. Hypocentral distance computed from nearest epicentral distances listed in Table 1 and the hypocentral depths of 8 km for the mainshock and 11 km for the aftershock.

Table 3

Peak Acceleration Pulse Data

STATION	1/24 EVENT			1/27 EVENT		
	a_{max} (cm/sec^2)	ζ (sec)	ζa_{max} (cm/sec)	a_{max} (cm/sec^2)	ζ (sec)	ζa_{max} (cm/sec)
A3E	69±3	.10±.02	6.9±1.6	48±3	.17±.05	8.2±2.4
ANT	40±2	.23±.05	9.2±2.0	97±3	.13±.02	12.6±2.0
DPP	121±3	.16±.02	19.4±3.1	65±4	.17±.07	11.4±3.0
DVD	260±5	.14±.02	36.4±4.8	41±2	.21±.03	8.6±1.4
MSJ	48±2	.14±.02	6.7±1.1	44±2	.22±.03	9.7±1.5
SRE	154±3	.28±.05	43.1±8.3	235±5	.16±.02	37.6±4.5
SRM	33±2	.13±.03	4.3±1.2	56±5	.15±.02	8.4±1.5
VLR	135±3	.19±.02	25.6±3.1	54±2	.10±.03	5.4±1.0
WCS	22±2	.12±.02	2.7±0.6	45±2	.21±.02	9.5±1.1
FR	STATION NOT INSTALLED			178±4	.15±.02	26.7±3.5

Theoretical Relations between Peak and RMS Acceleration

The striking correlation between the peak accelerations and the rms accelerations shown in Figure 10 suggest that the ratio of these measurements be directly compared to predictions from theoretical models of the accelerations waveforms. We will consider two models for this relation: the deterministic model proposed by Boatwright (1982) and the stochastic model proposed by Hanks and McGuire (1981). From eq. (6) of Boatwright (1982), the peak acceleration radiated by sub-event of radius r' and dynamic stress drop $\Delta\sigma'$ may be written as,

$$a_{max} = \frac{\Delta\sigma'}{\mu} \frac{R^S r'}{R \zeta} \Delta v \qquad (5)$$

where ζ is the width of the acceleration pulse, ζa_{max} is the area under the acceleration pulse and μ is the rigidity. Dividing the area of the acceleration pulse by the rms acceleration and assuming that the dynamic stress drop of the strongest sub-event is greater than or equal to the rms dynamic stress drop of the overall event, eqs. (3) and (5) determine an upper bound for the radius of the sub-event which radiated the peak acceleration:

$$\frac{\zeta a_{max}}{a_{rms}} = \frac{2}{3} \frac{\Delta\sigma'}{\Delta\sigma} \frac{r'}{v} \qquad (6)$$

This relation is dimensionally similar to eq. (25) of McGarr (1981) which relates the asperity radius to the ratio of the peak velocity to the peak acceleration. Because it uses the area of the peak acceleration pulse rather than the peak acceleration, however, it is approximately independent of the attenuation. Note that the use of eq. (3) presumes that the effect of the attenuation on the rms acceleration is minimal.

Figure 11 shows the necessary measurements as made on a number of the accelerograms written by the 1/27 aftershock. The measurements are listed in Table 3. The peak accelerations were calculated from the rotated SH components rather than using the values listed in Table 1; if the rms accelerations were calculated from the components on which the peak accelerations were originally measured, the results would be identical. The only anomalous pulse area is the

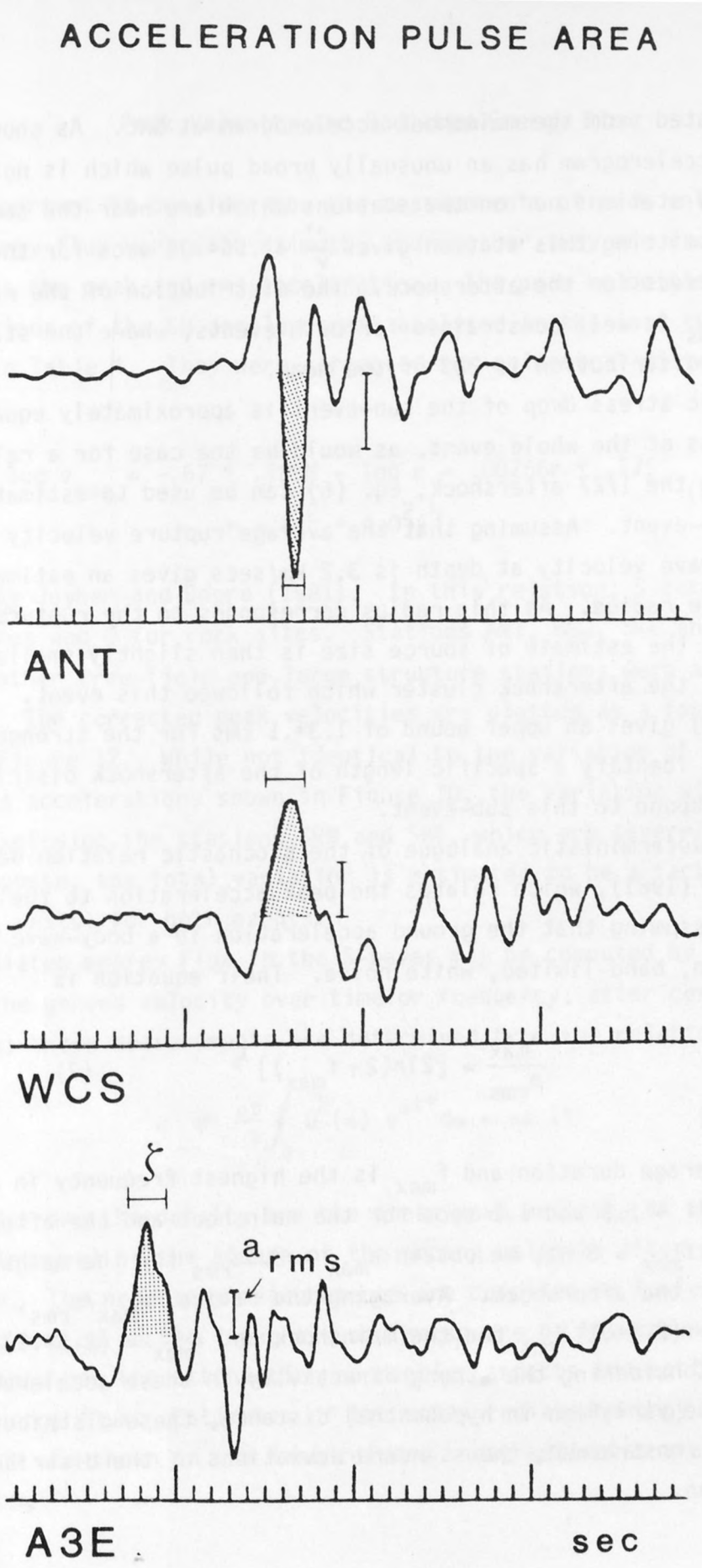

Figure 11. The measurements of pulse width and peak acceleration for three of the accelerograms written by the 1/24 aftershock, shown relative to the rms acceleration level for each pulse.

pulse area estimated from the mainshock accelerogram at SRE. As shown in Figure 7, this accelerogram has an unusually broad pulse which is not seen on any of the nearby stations nor on the stations which are near the same azimuth from the event; omitting this station gives $\frac{r'}{v} < .56 \pm .04$ secs for the mainshock and $\frac{r'}{v} < .62 \pm .04$ secs for the aftershock. The distribution of the ratios of pulse area to a_{rms} is well constrained for both events, where the standard deviation of the distribution is 22% of the mean.

If the dynamic stress drop of the sub-event is approximately equal to the rms dynamic stress of the whole event, as would be the case for a relatively simple event like the 1/27 aftershock, eq. (6) can be used to estimate the radius of the sub-event. Assuming that the average rupture velocity is $.75\beta$ where the shear wave velocity at depth is 3.2 km/secs gives an estimate of $1.5 \pm .1$ kms for the radius. As this radius corresponds to the rupture length to the northwest, the estimate of source size is then slightly smaller than spatial extent of the aftershock cluster which followed this event. For the mainshock, eq. (6) gives an upper bound of $1.3 \pm .1$ kms for the strongest sub-event. We cannot identify a specific length of the aftershock distribution which might correspond to this sub-event.

Eq. (6) is a deterministic analogue of the stochastic relation derived by Hanks and McGuire (1981), which relates the peak acceleration to the rms acceleration by assuming that the ground acceleration in a body-wave arrival is finite-duration, band-limited, white noise. Their equation is

$$\frac{a_{max}}{a_{rms}} = [2\ln(2\tau f_{max})]^{\frac{1}{2}} \qquad (7)$$

where τ is the average duration and f_{max} is the highest frequency in the recording. Using $\tau = 1.5$ and 1.1 secs for the mainshock and the aftershock, respectively, and $f_{max} = 8$ Hz, we obtain $a_{max} = 2.5a_{rms}$ for the mainshock and $a_{max} = 2.4a_{rms}$ for the aftershock. Averaging the ratios, a_{max}/a_{rms}, for each event gives $a_{max} = (2.5 \pm .1)a_{rms}$ for the mainshock and $a_{max} = (2.5 \pm .1)a_{rms}$ for the aftershock. Considering the strong directivity in these accelerations and the factor of three variation in hypocentral distance, these distributions are surprisingly well constrained; the standard deviations of the distributions are 15% of the mean.

Peak Velocity and Radiated Energy Flux

It is important to consider how the measurements of peak velocity and radiated energy flux vary with azimuth, and whether they are as strongly correlated as the peak and rms acceleration. The peak velocities, measured on the integrations of the SH accelerograms analysed in the last two sections, are listed in Table 4. They were corrected for epicentral distance using the relation,

$$\log v_{max} = -.67 + .489\underline{M} - \log r - .00256r + .17S \qquad (8)$$
$$r = (d^2 + 4.0^2)^{\frac{1}{2}}.$$

determined by Joyner and Boore (1981). In this relation, S takes a value of 1 for soil sites and 0 for rock sites. Stations ANT, MSJ, SRE and SRM are soil sites; the other free-field and large structure stations were assumed to be rock sites. The corrected peak velocities are plotted as a function of azimuth in Figure 12. While not identical to the variation of the corrected peak and rms accelerations shown in Figure 10, the variation with azimuth is similar. Excluding the stations SRM and SRE, which are severely contaminated by site response, the total variation is estimated to be a factor of five (.7 logarithmic units) for both events.

The radiated energy flux in the S-waves may be computed by integrating the square of the ground velocity over time or frequency, after correcting for the attenuation; these measurements are determined from the relation,

$$\varepsilon = \frac{\rho\beta}{\pi}\int_0^\infty \dot{u}^2(\omega)\, e^{\omega t^*} d\omega = \rho\beta\, I^* \qquad (9)$$

where ρ and β are the density and the shear wave velocity at the receiver and I^* is the integral of the square of the ground velocity after correcting for attenuation. The necessary measurements are compiled in Table 4; both the uncorrected and corrected integrals of the square of the ground velocity are listed to show how the attenuation correction affects the estimate of the radiated energy flux. Estimates of the total radiated energy determined from each station are shown in the last column; these estimates are determined from the relation,

Table 4

Peak Velocity and Energy Flux Data

STATION	1/24 EVENT				1/27 EVENT			
	v_{max} (cm/sec)	I (cm^2/sec)	I* (10^{20} dyne-cm)	E_s	v_{max} (cm/sec)	I (cm^2/sec)	I* (10^{20} dyne-cm)	E_s
ANT	3.9	8.2	17.7	5.9	3.7	6.6	11.3	4.3
A3E	4.5	7.0	9.6	1.6	6.0	6.4	12.4	3.8
DPP	7.1	22.5	31.3	2.0	5.5	13.3	16.6	1.2
DVD	15.8	81.9	111.2	15.2	2.1	2.2	3.4	.4
MSJ	3.9	5.6	13.0	4.7	4.5	8.1	12.9	4.5
SRE	21.1	214.4	253.3	28.5	17.5	82.2	115.4	17.1
SRM	2.3	3.4	5.7	.7	3.7	9.2	14.6	2.6
VLR	14.1	92.5	115.4	14.5	2.6	2.7	4.8	.5
WCS	2.3	1.1	1.9	.5	4.9	12.2	19.1	7.9
FR	STATION NOT INSTALLED				12.4	30.5	41.2	1.9

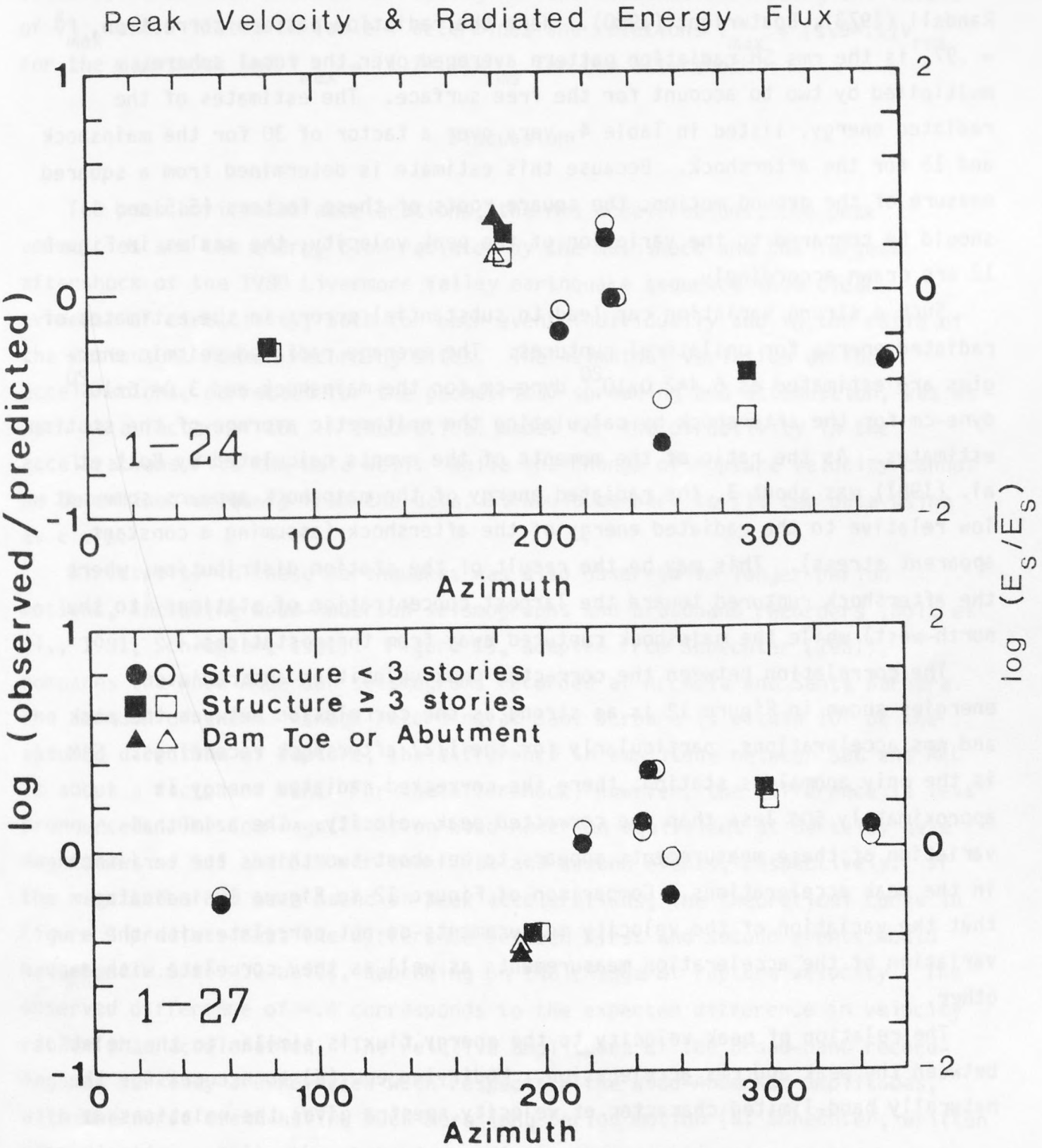

Figure 12. Corrected peak velocity and radiated energy estimates plotted against azimuth for 10 stations. The stations SRE (at 229° and 256°) and SRM (at 253° and 274°) have anomalous site responses. The filled symbols are the corrected radiated energy estimates; the open symbols are the corrected peak velocities. Note the strong correlation for the 1/27 data.

$$E_s = 2\pi \left(\frac{R}{F^S}\right)^2 \varepsilon \ , \qquad (10)$$

Randall (1973), Boatwright (1980). Here the radiation pattern correction, F^S = .97, is the rms SH radiation pattern averaged over the focal sphere, multiplied by two to account for the free surface. The estimates of the radiated energy, listed in Table 4, vary over a factor of 30 for the mainshock and 15 for the aftershock. Because this estimate is determined from a squared measure of the ground motion, the square roots of these factors (5.5 and 4) should be compared to the variation of the peak velocity; the scales in Figure 12 are drawn accordingly.

Such a strong variation can lead to substantial errors in the estimates of radiated energy for unilateral ruptures. The average radiated seismic energies are estimated as $6.4\pm2.0\times10^{20}$ dyne-cm for the mainshock and $3.0\pm.6\times10^{20}$ dyne-cm for the aftershock by calculating the arithmetic average of the station estimates. As the ratio of the moments of the events calculated by Bolt et al. (1981) was about 3, the radiated energy of the mainshock appears somewhat low relative to the radiated energy of the aftershock (assuming a constant apparent stress). This may be the result of the station distribution, where the aftershock ruptured toward the largest concentration of stations (to the north-west) while the mainshock ruptured away from these stations.

The correlation between the corrected peak velocities and radiated energies shown in Figure 12 is as strong as the correlation between the peak and rms accelerations, particularly for the 1/27 aftershock recordings. SRM is the only anomalous station; there the corrected radiated energy is approximately 50% less than the corrected peak velocity. The azimuthal variation of these measurements appears to be about two thirds the variation in the peak accelerations. Comparison of Figure 12 to Figure 10 indicates that the variation of the velocity measurements do not correlate with the variation of the acceleration measurements as well as they correlate with each other.

The relation of peak velocity to the energy flux is similar to the relation between the peak and rms acceleration. Modifying eq. (6) to account for the naturally band-limited character of velocity spectra gives the relations

$$v_{max} \cong \gamma \, v_{rms} = \gamma \left(\frac{I}{\tau}\right)^{\frac{1}{2}} \qquad (10)$$

where $1.66 < \gamma < 2.14$ for velocity spectra which falloff between ω^{-2} and ω^{-1} above the corner frequency. Here I is the integral of the square of the ground velocity determined without correcting for the attenuation. Using the values of v_{max} and I listed in Table 4 determines the relations $v_{max} = (1.9 \pm .1)v_{rms}$ for the mainshock and $v_{max} = (1.7 \pm .1)v_{rms}$ for the aftershock.

Discussion

The peak horizontal accelerations, the rms accelerations, the peak velocities and the energy flux radiated by the mainshock and the largest aftershock of the 1980 Livermore Valley earthquake sequence show clear evidence of directivity, both for each event individually and in the ratio of the motions at common recording sites. The azimuthal variation of the accelerations, corrected for the geometrical spreading and attenuation, was as much as a factor of 10. A theoretical model for the directivity in the accelerations fits the data well. While the change of rupture velocity cannot be determined uniquely from the data, it would be hard to fit the data using $\Delta v < .7\beta$.

Directivity in these earthquakes was also observed in longer period motions, including Wood-Anderson seismographs and broadband recorders (Bolt et al., 1981; Schechter, 1981). Figure 13, adapted from Schechter (1981), compares the Wood-Anderson seismograms recorded at Arcadia and Santa Barbara. The azimuth of the mainshock recording at Sant Barbara is within 10° of the assumed direction of rupture; the difference in amplitude between SBC and ARC is about a factor of ten. For the aftershock, however, the difference is less pronounced. The low-magnification Wood-Anderson equivalent at Berkeley gave magnitudes of 5.5 and 5.9 for the first and second events, respectively. If the magnitudes had been based on peak accelerations, the theoretical curve in Figure 9 predicts that the difference between first and second events would have been -.5 to -.7 units, depending on the change of rupture velocity. The observed difference of -.4 corresponds to the expected difference in velocity rather than acceleration. The relative amplitudes of the broad-band recordings at Berkeley are reversed with respect to the Wood-Anderson amplitudes, with the first event having much more long period motion (B. Schechter, written communication, 1981); this behavior reflects the relative size of the moments

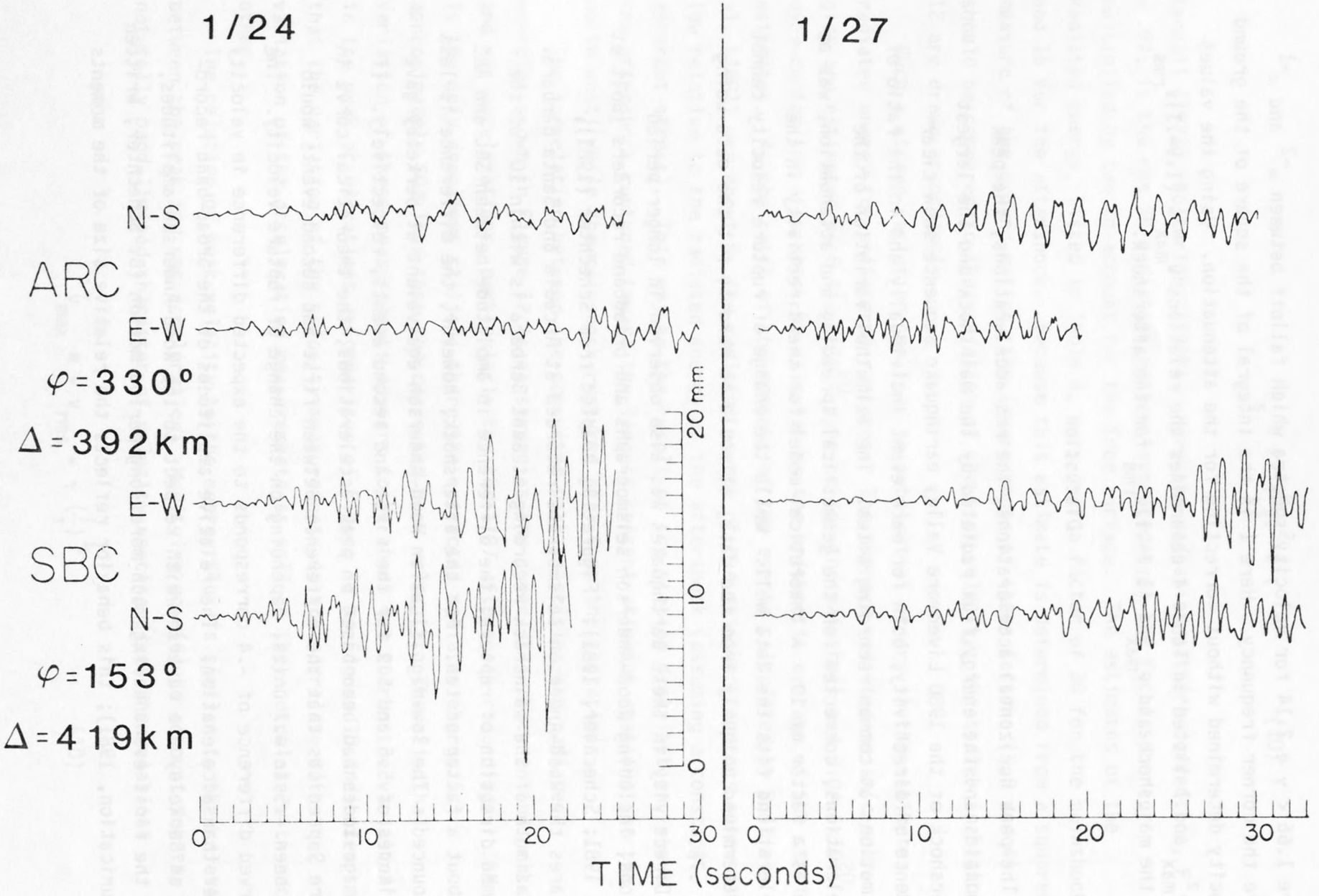

Figure 13. Wood-Anderson seismograms of the 1/24 mainshock and the 1/27 aftershock recorded at Arcadia and Santa Barbara (reprinted from Schechter, 1981).

of the two events.

The strong directivity in the peak accelerations radiated by these earthquakes implies that both events had unilateral ruptures. Consider the dependence of peak acceleration on the dynamic characteristics of the sub-event implied by eq. (3), where the peak acceleration depends linearly on the asperity radius and the dynamic stress drop. For an incoherent rupture in which the dynamic stress drop is approximately constant over the component sub-events, the directivity in the radiated peak accelerations must be similarly reflected in the relative asymmetry of the rupture process. Either the sub-event which radiated the peak accelerations was the largest by a factor of five, or all the large sub-events of the rupture process ruptured in the same direction.

A similar argument can be made concerning the directivity in the rms acceleration measurements. Because the rms acceleration uses the mean of the square of the acceleration, it is very sensitive to the strongest sub-event. For complex events, then, both the peak and rms acceleration should be generally insensitive to directivity, except in the case of a simple event or a purely unilateral rupture. The fact that the peak and rms accelerations show such strong directivity implies that the rupture processes of these earthquakes were unilateral.

Conclusions

Although we have established the significant impact that directivity had on the S-waves in accelerograms from the 1980 Livermore Valley earthquakes, we make no claim for being the first to establish conclusively directivity at high frequencies. For example, Bakun et al., (1978) showed clear directivity effects in a study of P waves from two small magnitude earthquakes (M = 3.0 and 2.0) in central California. However, this analysis is the first to clearly demonstrate directivity in the high-frequency accelerations which are of interest to seismic engineers. Moreover, the measurements analysed in this study, that is, peak and rms acceleration, peak velocity and radiated energy flux, are considerably more important to engineering than the duration and frequency of zero crossing measurements analyzed by Bakun et al. (1978).

The correlations determined in this analysis between the peak and rms accelerations, and the peak velocities and the radiated energy flux, imply that the measurements of peak aceleration and peak velocity made on a large number of accelerograms and seismograms can be used to determine source parameters such as the dynamic stress drop and the radiated seismic energy if the signal durations are also measured. In particular, the relation between peak velocity and radiated energy flux might be used to supplant the Gutenberg-Richter magnitude-energy relationship (Richter, 1958).

While it is possible that a future earthquake might exhibit a more extreme directivity in its radiated wavefield, it is suggested that this data set be used to establish operative bounds for the expected effect of directivity. For peak and rms acceleration, the maximum total variation is a factor of ten, or a factor of three amplification of the mean. For peak velocity, the total variation is a factor of five, while the energy flux can vary by a factor of thirty. Finally, differential site effects, including soil and structural resonances, can be expected to amplify or decrease motions by a factor of two.

Acknowledgements

We thank Rob Cockerham for the aftershock locations which are shown in Figures 2 and 3, Ron Porcella for the peak acceleration measurements, and Bruce Schechter for use of the Wood-Anderson recordings shown in Figure 13. This paper has been critically reviewed by Art McGarr and Paul Spudich, whose comments have helped us to improve it significantly.

References

Archuleta, R. J. (1979). Rupture propagation effects in the Coyote Lake earthquake (abs.), EOS (Trans. Am. Geophy. Un.) 60, 890.

Bakun, W. H., R. M. Stewart, and C. G. Bufe (1978). Directivity in the high-frequency radiation of small earthquakes, Bull. Seism. Soc. Am. 68, 2353-1263.

Benioff, H. (1955). Mechanism and strain characteristics of the White Wolf fault as indicated by the aftershock sequence, Earthquakes in Kern County, California during 1955 (G.B. Oakeshott, ed.), Cal. Div. Mines Bull. 171, 199-202.

Boatwright, J., (1980). A spectral theory for circular seismic sources: simple estimates of source dimension, dynamic stress drop and radiated seismic energy, Bull. Seism. Soc. Am. 70, 1-27.

Boatwright, J., (1982). A dynamic model for far-field acceleration, Bull. Seis. Soc. Am. 72, in press.

Bolt, B. A., T. V. McEvilly, and R. A. Uhrhammer (1981). The Livermore Valley, California, sequence of January 1980, Bull. Seism. Soc. Am. 71, 451-463.

Boore, D. M. and R. L. Porcella (1980). Peak acceleration from strong-motion records: a postscript, Bull. Seism. Soc. Am. 70, 2295-2297.

Boore, D. M., W. B. Joyner, A. A. Oliver III, and R. A. Page (1980). Peak acceleration, velocity, and displacement from strong-motion records, Bull. Seism. Soc. Am. 70, 305-321.

Cockerham, R. S., F. W. Lester, and W. L. Ellsworth (1980). A preliminary report on the Livermore Valley earthquake sequence January 24-February 26, 1980, U.S. Geol. Surv. Open-File Report 80-714.

Hanks, T.C. and R.K. McGuire (1981). The character of high-frequency strong ground motion, Bull. Seis. Soc. Am. 71, 2071-2096.

Heaton, T. H. and D. V. Helmberger (1979). Generalized rays models of the San Fernando earthquake, Bull. Seism. Soc. Am. 69, 1311-1341.

Joyner, W. B. and D. M. Boore (1981). Peak horizontal acceleration and velocity from strong-motion records including records from the 1979 Imperial Valley, California, earthquake, Bull. Seism. Soc. Am. 71, 2011-2038.

Madariaga, R. (1977). High-frequency radiation from crack (stress-drop) models of faulting, Geophys. J. 51, 625-652.

McCann, M. and D. M. Boore (1982). Variability in ground motions: root mean square accelerationsand peak acceleration for the 1971 San Fernando, California, earthquake, submitted to Bull. Seis. Soc. Am.

McGarr, A. (1981). Analysis of peak ground motion in terms of a model of inhomogeneous faulting, Jour. Geophys. Res. 86, 3901-3912.

McGuire, R. N. and T. C. Hanks (1980). RMS accelerations and spectral amplitudes of strong ground motion during the the San Fernando, California, earthquake, Bull. Seism. Soc. Am. 70, 1907-1919.

McJunkin, R. D. and J. T. Ragsdale (1980). Strong-motion records from the Livermore earthquake of 24 and 26 January 1980, Calif. Div. Mines and Geology Preliminary Report 28.

Randall, M. J. (1973). The spectral theory of seismic sources, Bull. Seism. Soc. Am. 63, 1133-1144.

Savage, J. C. (1968). The stopping phase on seismograms, Bull. Seism. Soc. Am. 58, 47-58.

Schechter, B. (1981). Source parameters and directivity of the Livermore earthquakes of 1980 (abs.), Earthquake Notes 52, 83.

Swanger, H. J., S. M. Day, J. R. Murphy, and R. Guzman (1981). State-of-the-Art study concerning near-field earthquake ground motion, U.S. Nuclear Reg. Comm. NUREG/CR-1978.

Switzer, J., D. Johnson, R. Maley, and R. Matthiesen (1981). Western hemisphere strong-motion accelerograph station list-1980, U.S. Geol. Surv. Open-File Report 81-664.

A Comparison between the Tectonic Stress Measured In Situ and Stress Parameters from Induced Seismicity at Monticello Reservoir, South Carolina

Jon B. Fletcher
U.S. Geological Survey
345 Middlefield Road
Menlo Park, CA 94025

Abstract

During May and early June, 1979, five three-component digital seismographs were deployed near the Monticello Reservoir, S.C. to determine the stress drops of reservoir-induced earthquakes and compare them with earlier hydrofracture stress measurements of Zoback and Hickman (1982). Records for 327 events were obtained; 10 of these events, each recorded on four or more stations, were analyzed to determine stress drops. Depths for the ten events ranged from 0.5 to 1.4 km. Fault-plane orientations were calculated from an inversion of the body-wave displacements: individual radiation pattern corrections were applied in calculating the moments at each station. Final estimates of seismic moment, source radius, and stress drop were obtained by averaging logarithmically the estimates from each component for each event. Moments of the ten digitally-recorded earthquakes ranged from 2.4×10^{17} to 2.6×10^{18} dyne-cm for the P-wave data and from 3.3×10^{17} to 4.7×10^{18} dyne-cm for the S wave data. The stress drops (S wave data only) generally ranged from about .3 to 4 bars. Four earthquakes were recorded by a strong motion instrument at the dam site. Magnitudes (**M**) for these events ranged from 2.8 to 3.0. Moments taken as averages of the values from each component ranged from 1.7 to 3.4×10^{20} dyne-cm. and the stress drops drops from 13 to 92 bars. Large differences between the corner frequencies of the two components (factors of 2.5 and 4 for two of the events) correspond to a large relative uncertainty for these stress drop values. Nevertheless, tens of bars of stress are apparently being released for the largest events in the Monticello sequence but only a few bars are being released for the smaller

magnitude events.

In comparison, the in-situ stress data measured in two holes give an estimate of shear stress of about 45 bars at 0.2 km depth and 30 to 70 bars at 1 km deptn in the northern hole and from 15-20 bars near the surface to almost 70 bars at deptn in the soutnern hole. The variation in shear stress inferred from in-situ measurements at 1 km depth indicates an inconsistency between the tnrust-faulting mechanisms of the earthquakes and the state of stress which is more consistent with thrust faulting at 0.2 km depth and strike-slip or normal faulting below. Thus the estimates of shear stress from in-situ measurements is of the same order as the stress drop of the **M** ≈ 2.8-3.0 events but about one order of magnitude larger than the stress drops obtained for the smaller events.

Introduction

The effect of tne level of regional tectonic stress on the magnitude and character of an associated earthquake is a critical link in our attempt to understand tne physics of earthquake rupture, fault dynamics, and the generation of seismic waves. Hanks and Tnatcher (1972) point out that only stress differences $\sigma_1-\sigma_2$ or $\sigma_1-\sigma_f$ (σ_1 is initial stress, σ_2 is final stress, and σ_f is the frictional stress) can be determined from seismic waves, leaving the possibility that earthquakes have stress differences of only a few bars in regions that are acted on by driving stresses of the order of a kilobar because the σ_f or σ_2 may also be of the order of a kilobar. The subject is further complicated by the lack of quantitative stress information for many seismically active areas where stress drops could be measured. For example, studies that attempt to infer the state of stress in the earth's upper lithospnere in the region seaward of oceanic trenches appear sharply divided between nign regional compressive stress (Hanks, 1971; Watts and Talwani, 1974) and low compressive stresses (Parsons and Molnar, 1976) and again between nign shear stresses (Scholz et al., 1979) and low stresses (Lachenbrucn et al., 1980) on interplate fault zones. Some attempts, however, nave been made to relate in-situ stress measurements to estimates of stress differences from seismic waves.

Wyss and Molnar (1972) related seismic stress parameters (Healy et al.,

1968) to a minimum estimate of shear stress from fluid pressures and rates of injection at the Denver Arsenal (Evans 1966, 1966b). Their experiment, however, may be improved upon in several aspects. First, to determine the size of the source radius of the two events analyzed they used the extent of the aftershock zone which may not have a direct relation to the source size (Fitch and Scholz, 1971). Second, the two events occurred after the main injection period and thus their relation to the stress determined from the injection history is indirect. Nevertheless, they found that for two earthquakes which have M_L's of 5.3 and 5.0, the stress drops were 22 and 3 bars. Compared to the initial stress of 203 bars, the stress released during the event is a very small proportion of the initial stress (about 0.1 and 0.02 respectively).

McGarr et al., (1979) report on a comparison between stress drops of mining-induced tremors in a deep South African gold mine and the relevant in-situ stress and rock properties. Stress drops were determined from surface seismograms and ranged from 5 to 50 bars for events that ranged in magnitude from 0 to 3 (Spottiswoode et al. 1975). In-situ stresses were determined using an over-coring stress relief technique that gave shear stresses (including the stress caused by the mining) of about 700 bars at a depth of 3.2 km which is similar to that at which earthquake stress drop values are available. Fault gouge taken from two excavated shear zones was also analyzed to establish the average driving stress necessary to create the new fault zones, and McGarr et al., (1979) found that at a depth of 2 km, the average driving stress was about 400 bars. In this case most of the stress has apparently been expended in creating the fault zone, and that the lower seismic stress drops reflect the larger areas of induced stress caused by the mining. An important result of the Monticello experiment is the high efficiency of stress release and the comparison between the mechanism of induced seismicity at Monticello (high pore pressure) and the South African gold mines (mining-induced stresses causing failure in dry, previously unfractured rock).

At Monticello, five event-triggered digital cassette seismographs were deployed for about one month in the epicentral region to obtain a suite of seismograms for a small group of events from which seismic stress drop data could be determined with reasonable accuracy. Individual focal mechanisms

were determined for ten events using the vector displacements of the P and S waves from 4 or 5 stations using a new inversion technique (Caterina et al., 1981) for a simple double-couple source which should be appropriate for these small events (magnitudes are all less than about $M \cong 1.7$). Estimates for seismic moment, source radius, and stress drop are obtained for each event by averaging the individual values; radiation pattern corrections are applied to data from each station. Strong motion accelerographs of four events with magnitudes ranging from 2.8 to 3.0 extended the moment range of the total data set from a few parts in 10^{18} dyne-cm to about 3×10^{20} dyne-cm. These values of stress are then compared to the in-situ levels of stress as reported by Zoback and Hickman, (1981).

Induced Seismicity at Monticello

Monticello is located in the Charlotte Belt Gneiss, a regional body of epidote amphibolite facies metamorphic rocks that is frequently intruded by granodiorite, granite, and migmatitic bodies. The seismic activity appears to be associated with the fractured migmatitic zones (Talwani et al., 1978). Between December 1977 and early February 1978, the depth of the reservoir at Monticello increased from 20 m to 52 m. Earthquake activity increased shortly after the filling began in mid-December 1977 and a high rate of seismicity was sustained during most of the month of February, sometimes exceeding 100 events/day (see fig 1). The in-situ stress measurements were made in July 1978, in the hole nearest the seismicity studied in this paper. Another hole was drilled and hydrofractured at the south end of the reservoir in January 1979, but this well is further from the epicenters. The recording of the earthquakes occurred during the month of May and early June, 1979, almost a year and a half after the beginning of the induced seismicity.

Instrumentation

Five digital event recorders (Sprengnether DR100) were deployed around the epicentral region of the most active area in May and early June, 1979 (see figure 2). Each station had three orthogonal geophones with natural periods of about 2 Hz. The output of the velocity transducers, which were damped at about 0.7 of critical, were amplified with a variable-gain pre-amplifier with steps every 6 db from 0 to 120 db, before entering an anti-aliasing filter. This allowed a close match of background and expected signal levels to the sensitivity of the analog to digital converter (A/D) to maximize the system's dynamic range. The A/D has 12 bits yielding 72 db dynamic range and resolution. The anti-aliasing filter is a Butterworth low-pass filter of 5 orders (30 db/octave roll-off rate) with corners at 50 or 70 Hz. Stations DUC and SNK had the 70 Hz filters while the others had 50 Hz corners. Sampling rates for these five stations is 200 samples/sec./channel. A broader band system was also used that consisted of a single vertical-component Ranger seismometer matched to a variable gain pre-amplifier that had 6 db steps from 0-60 db (usually operated with all 60 db). A Butterworth low-pass filter was used to prevent aliasing with a corner at 120 Hz. The output of the filter was then digitized at a rate of 600 samples/sec. The broad-band system was used to investigate the effect of the lower bandwidth of the other recording systems on the character of the seismograms as it is generally believed that earthquakes in the eastern part of the United States and Canada (Marion and Long, 1980) are of a higher frequency content than in other sections of the country (such as central California). This belief is based on several factors which include lower attenuation of the older Paleozoic rocks, shallower depths in some cases (e.g. Blue Mountain Lake, New York, Sbar et al, 1972, and Monticello, South Carolina) and a compressive stress regime that would suggest a predominance of impulsive thrust-type mechanisms (Sbar and Sykes, 1973; Sykes and Sbar, 1974).

Table 1 lists the events recorded at the 8 different sites occupied during the 27 days of the experiment. Records were obtained for 327 events, 52 of which were recorded on three or more stations. All events for which there were four or more unclipped records were analyzed for source parameters as this appeared to be the minimum number that would yield reasonably reliable

hypocenter locations and focal mechanism solutions. The activity varied substantially during the month with three major peaks. A high failure rate of the geophones (due to overwound coils) caused many of the records obtained early in the first peak in activity to be unusable either due to a low clipping level or to dead components. The data recovery improved so that by the second swarm, five complete stations were operating. All of the events contained in the main data set came from the second and third swarms.

Clock corrections were made in the field by comparing the internal one pulse/sec time mark against WWVB time code on a portable strip chart recorder and by simply recording WWVB on a data channel. Geophone coil constants, damping, and natural period were determined or set at the factory and these settings were confirmed using shake table testing in Menlo Park. The ground velocity can be determined from the digital data by normalizing the integer data with the sensitivity of the A/D (2048. = 10. volts), the amplifier gain, and the geophone velocity sensitivity (0.50 volts/cm/sec.). Thus the corrected ground velocity time series shown later are not corrected for the frequency response of the instrument or anti-alias filter but otherwise represent the ground velocity within the limits of about 2 to 50 Hz. The spectra of these time series, however, are corrected for the response of the filter and the sensor.

Earthquake Locations

Hypocenters were calculated with the computer program HYPOINVERSE (Klein, 1978) using both P and S wave arrival times at the local array of event recorders as well as some data from a more regional network of short period geophones (P. Talwani, Personal communication). A well log from the site of the in-situ stress measurement was used to construct the velocity-depth profile shown in figure 3 to a depth of about 1 km. A regional refraction survey (Talwani, et al 1980) has been used for the velocities below 1 km. Figure 2 shows the epicenters for those earthquakes which had three or more readings and whose solution appeared to be stable. Most of the activity is located along the northwestern edge of the reservoir. Although there is

diffuse seismicity at most of the western end of the reservoir, a concentration of epicenters exists near the 81°20' longitude between stations DUC and SNK. Two cross sections in figure 4, a N-S and an E-W profile, show that the depths extend from within a few tenths of a kilometer of the surface (average errors in depth are estimated to be 0.3 to 0.5 km from the stability of the depth when small changes in the velocity model are made) to about 1.5 km. The cross sections do not show a single seismic zone that would suggest a through-going fault. The depths of the events studied in more detail later range from 0.5 to 1.4 km. These events occur predominantly in the central cluster, but also include the most northerly event and three located beneath the lake.

Interpretation of Seismograms

The suite of seismograms obtained at Monticello provides a unique set of digital ground-motion time-histories for eastern United States earthquakes, in which the character of the arrivals can be quantitatively investigated in detail. For this study we are primarily concerned with the character of the P and S waves and any other secondary phases that may contaminate their spectra. These seismograms were obtained at unusually close distances in a region where the attenuation is low.

Figure 5 shows all of the velocity traces for an earthquake that occurred on Julian Day 151 at 16 hours, 19 minutes (events will be identified by the tag Julian day, hour, and minute, or in this case 151 16.19). Its depth and approximate magnitude are 0.95 km and 1.5 respectively (all magnitudes noted for these events are computed from the moments using the formula $\mathbf{M} = (\log M_0 - 16.)/1.5$, Hanks and Kanamori, 1979). At the closest station SNK, (epicentral distance is 0.3 km) the P wave is easily identified as the first arrival on the vertical component and is characterized by its remarkable impulsiveness. The pulse shape is symmetric (the down swing has the same snape as the upswing). In displacement its shape would be a simple unipolar pulse in the down direction. An oscillation with a period of 0.28 s immediately follows the P wave on the vertical and is also clearly present on

the North-South (N-S) component. As this oscillation is not visible on the other records for this event, it may be a site effect at SNK.

After the P wave, the 3 hz oscillation and abundance of secondary arrivals on all of the components at SNK makes the identification of the S wave difficult but the largest arrival on the W-E component is the best interpretation. At the same time on the N-S component, the record has a sharp change in cnaracter suggesting that arriving S wave energy is coupling into surface waves at that point in the record. There is a marked similarity between the P wave and the S wave pulse shapes.

At 2.4 km epicentral distance the amount of long period energy is reduced considerably in comparison with the records at SNK as shown by the records at DUC. Again the P wave is easily discerned but the S wave is now separated enough that it too is easily identified on the N-S component. At station LKS, epicentral distance of 2.7 km, the general character has not changed from that at DUC and SNK but the S wave is a broader pulse than observed at the closer stations. It is identified only on the N-S component which is about 10° in azimuth from pure transverse. The records at CEM are noteworthy because of the near nodal character of the P wave and the pure SH character of the S wave. Two phases that follow the S wave on the W-E component are apparent and may be SH multiples in the top layers. These multiples are not readily apparent on the other records, possibly due to the strong SH radiation at CEM. The most distant station is JAB at 4.0 km. Here the P and S waves no longer appear as simple isolated pulses but as more of a wavelet. This is particularly true for the S wave which no longer has an impulsive beginning. On the vertical component, the P wave is impulsive but is followed by a moderate coda of its own.

The use of horizontals allows us to identify the S wave by its polarization and determine its arrival time and character. However, in at least two earthquake prediction experiments (Blue Mountain Lake, New York and Lake Jocasee, South Carolina) the arrival times of the S waves were picked from vertical component seismographs. We can use these records from Monticello to see if the S waves can be accurately picked from the vertical component records compared to the arrival of the S waves on the horizontals. The resolution of these time measurements is about 0.01 secs. At station DUC the arrival of the S wave appears at about the same time on both the vertical

and horizontal components. At LKS, the first arrival of the S wave is ambiguous. The larger upward pulse on the north component is preceeded by a smaller arrival with the opposite polarity (see fig. 5). The smaller arrival is coincident with the best pick for the S wave on the vertical component. The large pulse on the north component, however, lags the apparent S wave on the vertical component by about 0.04 sec. At CEM the first arriving S wave energies are impulsive and the vertical S wave leads that of both horizontals by 0.02 sec. At JAB the first arriving energies of the S waves are not as clear as at CEM, but measurement of similar pulses in each of the waveforms on the vertical and north component suggests that again the apparent S wave on the vertical leads that of the horizontals by about 0.04 sec. This suggests that beyond some fairly short distance (3.0 km or 3 times the depth) the arrival time of the S wave on a vertical component seismograph will be difficult to pick to an accuracy greater than about 0.02 to 0.04 sec.

Azimuthal Variation of Corner Frequencies and Pulse Widths

Pulse shapes provide the basic data set from which we calculate source parameters. However, pulse shapes can be described (not necessarily equivalently) by either a set of measurements made in the time domain (area under the curve of the displacement pulse shape, and pulse duration) or in the frequency domain (asymptotic long-period level of the displacement spectra and corner frequency). Describing pulse shapes in the time domain has the advantage that if the body waves are at all impulsive, the pulse duration can be much more accurately measured than the corner frequency. The disavantages are 1) the pulses are sometimes not well defined because of interferring multiple arrivals and/or surface waves, and 2) the theory used here (Brune, 1970) is derived in terms of the spectral measurements and there is an ambiguity in the relationship between pulse duration and corner frequency especially when the pulses are not symmetric because of directivity effects. In the frequency domain (spectra of the P and S waves for event 151 16.19 are shown in fig. 6) the long-period spectral level is relatively simple to estimate, but the corner frequency can often be difficult to accurately

determine. Further, both measurements can be contaminated by later arrivals and surface waves. To provide a stable estimate of the long-period part of the spectra, a segment of time domain data at least three times larger than the pulse duration is used to calculate the Fourier coefficients.

Table 2 compares the important time domain and frequency domain data for event 151 16.19 to provide a basis for choosing a set of measurements for this study that will yield the most robust stress drop estimates and also be the most directly comparable to results of other studies. Except for station DUC, P-wave long-period spectral levels all appear close to the pulse areal values. For the S waves, however, two of the long-period spectral levels differ by more than a factor of two from the pulse areal values. This suggests that as the pulse dimensions are relatively unambiguously determined,these two spectral values are being contaminated by later arrivals. This shift would cause an over estimate of the moment from S wave data compared to P wave data.

Reciprocal P-wave corner frequencies are larger than the durations for two of the five stations and reciprocal S-wave corner frequencies are larger than tne durations at three stations although three of the five stations have values that are fairly similar. In both sets, tne durations are more nearly constant than the corner frequencies. Nevertheless, to preserve our ability to compare these results with others in the literature and because there is apparently no consistent relationship between the two data sets, we will continue to use the corner frequency as the parameter from which source radius is calculated.

The azimuthal variation of corner frequency can also be used to estimate rupture propagation. From table 2 the S wave corner frequencies (S waves are more sensitive to directivity than P waves) appear shorter to the west and northwest and longer to the east. This pattern is also mirrored in the pulse durations. If pulse widtns are shortened in the direction of rupture propagation, the direction of rupture is to the northwest away from the reservoir. It is important to note that there does not appear to be any correlation of pulse duration or corner frequencies with distance, suggesting tnat attenuation has little or no effect on the character of these body waves.

Focal Mechanisms

Focal mechanisms were calculated for each of ten events by inverting the displacement amplitudes of P and S waves for the six terms of the moment tensor (Caterina et al, 1982). This program inverts for a double-couple point source in a homogeneous half-space overlain by a surface layer of lower velocity. Corrections for the coupling between P and SV at the free surface (Aki and Richards, 1979) are included and appear to be essential in obtaining reliable solutions. The assumption of a homogeneous half-space does not include the reversal in sign for SV waves that go through a turning point. A sign reversal in SV that would not be appropriate for a situation which had strictly upgoing rays was therefore incorporated . To avoid this problem, the S waves may be entered as unsigned amplitudes. To investigate this effect, two inversions were performed on the same event, the first with signed S-wave amplitudes and the second with unsigned amplitudes. If the error is measured by the fit (defined as when a synthetic is within a factor of three of the observed amplitude) and the root-mean-square error (RMS) of the amplitude residuals, then the case with the signed amplitudes had a better focal mechanism solution. The case with the unsigned amplitudes, however, attained the convergency criteria faster (in 2 iterations instead of 3) than with signed amplitudes. If only P-wave signs are used, the inversion program will find an answer more easily (i.e. with fewer iterations) than if S-wave signs are also used, but the solution may not be as accurate as when the signs of S-waves are used to help constrain the solution. For the ten events in this study, signed amplitudes were generally used when possible except when a convergence was not obtained or the "fit" was unusually poor, in which case the most dubious signs were deleted and the inversion retried. For the 151 04.33 event, the mechanism using signed amplitudes was sufficiently poor that all S-wave signs were deleted. This solution produced a lower RMS error, even though the fit was not better. The mechanism is more nearly pure thrust using unsigned amplitudes and this solution was used in computing source parameters for the 151 04.33 event. This inversion program was only used to find the orientation of the fault plane because of a suspected error in the part of the program that computed the scalar moment and because the moment is more accurately determined from the displacement pulse area.

As a consequence of the severity of the P-SV free-surface coupling which diminisnes SV beyond about 40° (angle of incidence measured from the downward vertical), the amount of ray steepening is an important parameter to the program. The velocity of the surface layer was varied to control the amount of refraction and to achieve the best fit to the data. A final model of a 5.6 km/sec layer over a 6.2 km/sec half-space was used for all inversions. Changes in the velocity model will also effect the estimate of depth which in turn will alter the take-off angles. The result is that not only are the dips of the fault planes inaccurately determined by the inversion program but the program will not converge as fast because the solution is constrained to orthogonal fault planes. All but three events are within the major cluster near stations DUC and SNK and because of the distribution of stations, should have comparatively well-determined depths. Events 149 23.47 and 138 09.42, however, are outside the array of stations used to locate the event, and for event 138 12.58 the closest station is at least 2 km away, suggesting that for these events the depths and their focal mechanisms may not be as accurately determined. All of the solutions are thrust-type mechanisms, in agreement with Talwani et al (1979), but the strike and dip of the fault planes vary considerably. Visual inspection of the first motion data for some of the events suggests that the variations are real and not an artifact of the phase problems associated with SV.

Source Parameters

Seismic moments were determined from the formula,

$$M_o(\alpha,\beta) = 4\pi\rho(\alpha,\beta)^3 R A_o / R_{\theta\phi},$$

where ρ = 2.9 gm/cc, α = 6 km/sec, β = 3.5 km/sec, R = hypocentral distance, A_o is area of the displacement pulse, and $R_{\theta\phi}$ is the radiation pattern correction which includes the effect of the free surface.

Source radii and stress drops were determined using the usual formula from the Brune (1970, 1971) source model for S waves and as extended to P waves by

Hanks and Wyss (1972). Estimates of the moment, source radius, and stress drop were obtained separately for P and S waves for each event by averaging logarithmically the individual estimates of the moment at each station (e.g. $\bar{M}_0(\alpha)$, $\bar{M}_0(\beta)$), averaging the source radii (e.g. $\bar{r}_0(\alpha)$, $\bar{r}_0(\beta)$), and then using the average values in one calculation to compute the stress drop

$$\Delta\sigma(\alpha,\beta) = \frac{7}{16} \frac{\bar{M}_0(\alpha,\beta)}{\bar{r}_0(\alpha,\beta)^3} \quad .$$

Table 3 gives the moment, source radius, and stress drop for each event.

The two estimates of the moment are remarkably close (within one standard deviation of each other) for all ten events. The S waves always have smaller source radii than the equivalent P wave data, which means that the ratio of the P wave corner frequency to S wave corner frequency is usually less than 1.73 but greater than one. Consequently, the stress drops for the S wave data are always larger than for the P waves and vary between 0.3 and 3.6 bars. As the theoretical basis is more rigorous for S waves, we will use the S wave data as the representative data for later comparison.

Strong Motion Records

Four strong motion accelerograms were recovered from a Kinemetrics SMA-1 located at the dam site near the southern end of the reservoir (see figure 2). A radio time standard was not recorded on the accelerograms, leaving the correlation between the earthquake catalogue and the strong motion records somewhat tenuous. Nevertheless, the correlation between the first, third, and fourth accelerograms, each of which had peak accelerations above 0.2 g, and the largest events in their corresponding time period (between visits for maintenance) seems fairly certain. The other record is from the same time period as the third accelerogram and is tentatively linked to a magnitude, 2.4 event (from Talwaini et al, 1980) that occurred earlier in the same day. This correlation is consistent with the trigger to S wave intervals as compared to the hypocentral distances. All three hypocentral distances are less than 2 km. The pertinent hypocentral parameters are given in table 4.

Figure 7 shows the corrected accelerations, velocity, and displacements of the four events using the procedures desribed in Fletcher et al. (1980). S-wave pulse shapes in displacement are high-frequency short-duration pulses (e.g. the 180° component of the Aug 27, 1978 event) with a maximum peak acceleration of 347 cm/sec^2 and a maximum peak displacement of 0.12cm. The duration of strong ground shaking is about 1/2 second for the first two events but about one second for the third and largest of the three events.

Source parameters for these events were calculated using the formulae applied to the digital event recordings except that the long-period asymptotic level of the displacement spectra (shown in fig. 8) is used in place of the area of the displacement pulse shape and an RMS average of the radiation pattern correction takes the place of the computed corrections as no focal mechanisms have been calculated for these events. Table 5 lists the source parameters derived for the four strong motion accelerograms by component. If an average of the moment estimates is used, the seismic moments range from 1.7×10^{20} dyne-cm to 3.4×10^{20} dyne-cm. The stress drop estimates from the two horizontal components for the August 27, 1978 event and the October 27, 1978 16.27 event show a large discrepancy, illustrating the errors that are possible when using single station data. Three of the estimates of stress drop are at about 13 bars with two others extending up to about 100 bars. If the highest value is omitted (it is about two standard deviations from an average of all 8 values), then the average of the stress drops is 39 bars. Clearly the lack of consistency in these stress drop estimates suggests these data can only be used to infer that the stress drop of these larger events is a few tens of bars or one order of magnitude larger than the smaller digitally recorded events.

In-situ Stress Measurements

Zoback and Hickman, (1981) reports on a series of in-situ stress measurements using the hydrofracture technique at Monticello. Magnitudes of the greatest and least compressive stress are given for four depths between 0.16 km and 0.96 km in the northern hole (called Mont-1) and at 7 depths to .65 km in the southern hole (called Mont-2). Directions of the maximum

compressive stress are not given. Figure 9 shows the stress data versus depth and the shear stress that results from a Mohr-Coulomb failure criteria on a 45° dipping fault plane at the given focal depths. Note that although thrust faulting is consistent with the relative magnitudes of stresses at shallow depths, strike-slip, and even normal faulting are indicated at greater depths. This contradicts the observation that the earthquakes all appear to have thrust-faulting mechanisms from close to the surface to below one km.

Even with this inconsistency in the stress data at the deeper locations, about 45 bars of shear stress in Mont-1 and 15-20 bars in Mont-2 is available for faulting at the shallowest depths. Between 30 and 70 bars might be available at 0.96 km, depending on how the inconsistency is resolved. At .48 km depth, if σ_3 is equal to the lithostat, the faulting mechanism is constrained to be thrust faulting. There are 38 bars of shear stress, but if strike-slip is allowed, 43 bars are available. This simple approach to bounding the stress is not appropriate for normal faulting but, at a depth of 0.96 km, a thrust mechanism would have 32 bars of shear stress and 66 bars for strike-slip. Similar arguments also apply to the stress measurements below .2 km in Mont-2. Thus the data suggest that between 30 and 70 bars of shear stress is available between 0.16 and 1 km depth.

For figure 9, the horizontal principal stresses at 0.7 km depth are substantially smaller than would be expected from the other three measurements at 0.16 km, 0.48 km and 0.96 km depth in Mont-1. A pronounced absence of seismic activity (J. Boatwright. p,c.) at a depth of approximately 0.4 km to 0.6 km in figure 4 may be a result of the reduction in stress available for faulting at 0.7 km depth. This stress reduction and the seismic gap at 0.4 to 0.6 km depth do not precisely coincide, but considering the error of the depth estimates of 0.3 to 0.5 km, the depths of the stress anomaly and the seismic gap are remarkably close.

It is also interesting to speculate on the cause of the stress anomaly. As the largest of the earthquakes at Monticello have stress drops that are of the same order as the available shear stress, could this stress anomaly be caused by an earthquake Zoback and Hickman, (1981) shows that the maximum compressive stress will be reduced by about twice the stress drop in the vicinity of the earthquake. If we make the assumption that earthquakes with approximately the same moment have about the same stress (which is certainly true in a general sense for the data presented here), then the 80 bar

reduction in the maximum principal stress could have been caused by an earthquake similar to the three recorded on the strong-motion instrument as these events have stress drops ranging from about 10 to 40 bars. In fact, five events with magnitudes greater than 2.4 (Talwani et al., 1980) did occur near the location of the well between February 10, 1978 and February 15, 1978. These events appear to be large enough to have released enough stress. As the depths are not well-determined, it must remain a conjecture that the events did have appropriate source depths.

Discussion

We can now compare the shear stress determined seismically and in-situ at Monticello with similar data from the East Rand Proprietary Mines (ERPM) of McGarr et al. (1979). The shear stress data from Monticello suggest a ratio of about .04 (2/45) or less for the ratio of stress released seismically to the total shear stress available for the smaller digitally recorded earthquakes but a value of about .87 is appropriate for the larger events. These data suggest that the larger events occurring at Monticello are releasing a greater portion of the stress available for driving the failure process. The data from ERPM suggested that the shear stress available for faulting is largely absorbed in creating the fault zone as evidenced by: 1) the similarity of the in-situ shear stress and the driving stress calculated from the surface area of the gouge and 2) the dissimilarity of the previous values and the seismically determined stress drops. (Less than one tenth of the 700 bars of shear stress ended up in seismic waves.)

The most relevant differences between these two tectonic regimes are that: 1) the Monticello events appear to be occurring on previously existing fractures (Talwani et al., 1979) whereas the ERPM events are creating new fault zones in quartzite and 2) where the pore pressure appears to have "triggered" the events at Monticello and therefore is an important factor in the failure process of these earthquakes, there is no pore water in the country rock at ERPM (McGarr et al., 1975). This comparison suggests that the increase of pore pressure has reduced the normal stress on the fault (Zoback

and Hickman, 1981; Hubbert and Rubey, 1959) and the fault friction causing the sudden failure. The pore pressure also allows larger displacements and a lower final stress than where the effective stress is high. This hypothesis is tentative, however, as no earthquakes were recorded before the increase in pore pressure. Thus we do not know if the characteristics of the Monticello events are common to all or most events in the eastern United States. The apparent dependence of stress drop on moment would suggest that an upper limit to the magnitude of the events observed at Monticello. Interestingly, 3 years after the beginning of the major phase of induced seismicity at Monticello, there does appear to be an upper limit to the magnitude of events at around M $\cong$ 3 as documented in b-value curves (Talwani, personal communication).

The Monticello events may be analyzed using the model of inhomogeneous faulting recently developed by McGarr (1981). His model yields an estimate of the degree of inhomogeneity of the faulting process (magnitude and relative source radius of a subevent). The impetus for constructing this model stems in part from the apparent dichotomy in frequency content between the wavelet that usually produces the peak acceleration ($\geq$ 100 Hz) and the displacement pulse ($\leq$ 100 Hz), suggesting that failureis occurring over at least two different length scales. The data at Monticello, however, appear as simple pulses and exhibit a large degree of homogeneity. Our instrumentation is too band-limited at the high frequencies to explore this question definitively, but the broader-band data from the single component station suggest the same conclusion.

The differences in stress drop between the smaller digitally-recorded events and the larger events with magnitudes of about 3.0 suggest an increase in stress drop with increasing moment, at least over the range in moment studied here. Fundamentally, this derives from a scaling between corner frequency and the asymptotic long-period level of the displacement spectra such that the corner frequency is only changing by a factor of 2 to 2.5 while the moment has increased by 2 orders of magnitude. Using the Brune model, this scaling becomes one where the source radius is increasing from the 50 to 80 meter range to a 150 to 250 meter range as the moment has increased from 10^{18} dyne-cm. to 10^{20} dyne-cm. This is similar to the results from an analysis of source parameters of events from the Mammoth Lakes, California sequence in late May and June of 1980 (Archuleta et al., 1981). The increase

in stress drop for the Monticello events can also be related to an increase in seismic efficiency (Hanks and Thatcher, 1972). Assuming that the final stress is equal to the frictional stress, the smaller events at Monticello have efficiencies of 0.02 and 0.76 for the larger events.

Acknowledgement

The author is grateful to Pradeep Talwani, Chas Duc, and David Amick at the University of South Carolina for assistance in the field program. Chas Duc was also helpful in processing the cassette recordings. Jack Boatwright altered the inversion program for determining the focal mechanism to include the corrections of P-SV coupling at the free-surface. During the course of this investigation, I had many valuable discussions with Pradeep Talwani and A. McGarr. John C. Coakley was largely responsible for the success of the field program.

Bibliography

Aki, K. and P. G. Richards, Quantitative Seismology Theory and Methods, vols. I and II, W. H. Freeman and Company, San Francisco, 1980.

Archuleta, R. J., P. Spudich, E. Cranswick, and C. Mueller, Source Parameters of the 1980 Mammoth Lakes, California, Earthquake Sequence, in press J.G.R., 1981.

Brune, J. N., Tectonic Stress and the Spectra of Seismic Shear Waves from Earthquakes, J. Geophys. Res., 75, 4977-5009, 1970.

Brune, J. N., Tectonic Stress and the Spectra of Seismic Shear Waves from earthquakes (correction). J. Geophys. Res. 76, 5002, 1971.

Caterina, V., and A. G. Lindh, D. M. Boore, A New Inversion Technique for Computing Focal Mechanisms of Local Earthquakes, 1980, in preparation, 1981

Evans, D. M., Man-Made Earthquakes in Denver, Geotimes, May-June, 11-18, 1966.

Evans, D. M., The Denver Area Earthquakes and the Rocky Mountain Arsenal Disposal Well, The Mountain Geologist, 3, 23-36, 1966.

Fitch, T. J., and C. H. Scholz, Mechanism of Underthrushing in Southwest Japan: A model of Convergent Plate Interactions. Jour. Geophys. Res., 76, 7260, 1971.

Fletcher, J. B., and A. G. Brady, T. C. Hanks, Strong-Motion Accelerograms of the Oroville, California Aftershocks: Data Processing and the Aftershock of 0350 August 6, 1975. Bull. Seis. Soc. Amer., 70, 243-267, 1980.

Hanks, T. C., The kuril trench-Hokkaido rise system: Large shallow earthquakes and simple models of deformation, Geophys. J. Roy. Astron. Soc. 23, 173-189, 1971.

Hanks, T. C., and W. Thatcher, A graphical representation of seismic source parameters, J. Geophy. Res. 77, 4393-4405, 1972.

Hanks, T. C., and M. Wyss, The Use of Body-Wave Spectra in the Determination of Seismic Source Parameters, Bull. Seism. Soc. of Amer., 62, 561-589, 1972.

Hanks, T. C., and H. Kanamori, A Moment Magnitude Scale, Jour. Geophys. Res., 84, 2348-2350, 1979.

Healy, J. H., W. W. Rubey, D. T. Griggs, and C. B. Raleigh, The Denver Earthquakes, Science, 161, 1301-1310, 1968.

Hubbert, M. K., and W. W. Rubey, Role of Fluid Pressure in Mechanics of Overthrust Faulting 1, Mechanics of Fluid-Filled Porous Solids and its Application to Overthrust Faulting, Geol. Soc. Amer. Bull., 70, 115-166, 1959.

Klein, F. W., Hypocenter Location Program Hypoinverse Part 1: Users Guide to Versions 1, 2, 3, and 4. U.S. Geological Survey Open File Report 78-694, 1978.

Lachenbruch, A. H., and J. H. Sass, Heat flow and energetics of the San Andreas fault zone, J. Geophys. Res., 85, 6185-6222, 1980.

Marion, G. E., and L. T. Long, Microearthquake Spectra in the Southeastern United States, Bull. Seis. Soc. Amer., 70, 1037-1054, 1980.

McGarr, A., Analysis of Peak Ground Motion in Terms of a Model of Inhomogeneous Faulting, submitted to J. Geophys. Res., 1981.

McGarr, A., S. M. Spottiswoode, N. C. Gay, and W. D. Ortlepp, Observations Relevent to Seismic Driving Stress, Stress Drops, and Efficiency, Jour. of Geophys. Res. 84, 2251-2261, 1979.

McGarr, A., S. M. Spottiswoode, and N. C. Gay, Relationship of Mine Tremors to Induced Stresses and to Rock Properties in the Focal Region, Bull. of Seism. Soc. of Am., 65, 981-993, 1975.

Parsons, B., and P. Molnar, The origin of outer topographic rises associated with trenches, Geophys. J. Roy. Astron. Soc. 45, 707-712, 1976.

Sbar, M. L., J. Armbruster, and Y. P. Aggarwal, the Adirondack, New York earthquake swarm of 1971 and tectonic implications, Bull. Seism. Soc. Am. 62, 1303-1317, 1972.

Sbar, M. L. and L. R. Sykes, Contemporary Compression Stress and Seismicity in Eastern North America: Am Example of Intra-plate Tectonics, Bull. Geol. Soc. Amer., 84, 1861-1882, 1973.

Scholz, C. H., J. Beavan, and T. C. Hanks, Frictional Metamorphism, Argon Depletion, and Tectonic Stress on the Alpine fault, New Zealand, J. Geophys. Res., 84, 6770-6782, 1979.

Spottiswoode, S. M., and A. McGarr, Source Parameters of Tremors in a Deep-Level Gold Mine, Bull. of Seis. Soc. Amer., 65, 93-112, 1975.

Sykes, L. R., and M. L. Sbar, Intraplate Earthquakes, Lithospheric Stresses and the Driving Mechanism of Plate Tectonics, Nature, 245, 298-302, 1973.

Talwani, Pradeep, Induced Seismicity, Earthquake Prediction and Crustal Structure Studies in South Carolina, in Summaries of Technical Reports, Volume IX, US Geological Survey Open-File Report 80-6, 1980.

Talwani, P., B. Rastgi, and D. Stevenson, Induced Seismicity and Earthquake Prediction Studies in South Carolina, Tenth Technical Report Sponsored by the U.S. Geological Survey, April, 1980.

Talwani, P., and others, Seismicity Studies at Lake Jocassee, Lake Keowee and Monticello Reservoir, South Carolina, Summary of Technical Reports, VII, U.S. Geological Survey Report, 1978.

Watts, A. B., and M. Talwani, Gravity anomalies seaward of deep-sea trenches and their tectonic implications, Geophys. J. Roy. Astron. Soc. 36, 57-90, 1974.

Wyss, M. and P. Molnar, Efficiency, Stress Drops, Apparent Stress, Effective Stress, and Frictional Stress of Denver, Colorado, Earthquakes. Jour. of Geophys. Res., 77, 1433-1438, 1972.

Zoback, M. D. and S. Hickman, In-situ Studies of the Physical Mechanisms Controlling Induced Seismicity at Monticello Reservoir, South Carolina, J.G.R. this volume, 1981

Table 1

Recording Statistics

Number of events recorded by each station:

JAB	DON	DUC	DSC	SNK	LKS	CEM	CPL
62	2	198	18	160	19	32	38

3 recordings were obtained for each of 32 events.
4 recordings were obtained for each of 13 events.
5 recordings were obtained for each of 7 events.

Table 2

Pulse Shape Measurements

Station	P-wave						S-wave						Azimuth	distance
	Rise time	Stop time	Duration	$\left(\text{Corner frequency}\right)^{-1}$	Pulse area	Long-period level	Rise time	Stop time	Duration	$\left(\text{Corner frequency}\right)^{-1}$	Pulse area	Long-period level		
SNK	.022	0.21	.043	.044	3×10^{-6}	2.7×10^{-6}	.022	.02	.042	.16	3.5×10^{-6}	8.7×10^{-6}	340	0.3
DUC	.016	.014	.030	.023	7.7×10^{-7}	4.5×10^{-7}	.020	.015	.035	.027	1.2×10^{-6}	1.1×10^{-6}	269	2.4
LKS	.019	.015	.034	.045	5.1×10^{-7}	5.7×10^{-7}	.055	.04	.095	.27	2.4×10^{-6}	6.3×10^{-6}	96	2.7
CEM	.015	.016	.031	.07	9.8×10^{-8}	1.1×10^{-7}	.02	.022	.042	.043	2.5×10^{-6}	2.5×10^{-6}	213	3.0
JAB	.02	.011	.031	.024	1.0×10^{-7}	1.2×10^{-7}	.017	.01	.027	.034	1.2×10^{-6}	1.4×10^{-6}	0	4.0

Table 3

	Event	Source parameters: Moment (dyne-cm) p	Moment (dyne-cm) s	Source Radius (meters) p	Source Radius (meters) s	Stress Drop (bars) P	Stress Drop (bars) S	depth (km)	(1) Quality
145	1429	6.2 (5.5)x10^{17}	6.8 (8.3) x10^{17}	153±87	100±70	0.1	0.3	1.19	08/11
149	2347	1.4 (1.7)x10^{18}	1.2 (3.9) x10^{18}	94±36	72±27	0.7	1.4	0.88	12/12
138	1258	2.5 (2.6)x10^{17}	3.4 (1.8) x10^{17}	106±35	72±56	0.1	0.4	1.37	08/11
151	0433	2.4 (1.9)x10^{17}	3.3 (2.3) x10^{17}	81±47	57±45	0.2	0.8	0.93	08/14
150	1531	1.4 (2.3)x10^{18}	1.1 (1.8) x10^{18}	102±55	75±48	0.6	1.1	0.87	08/12
138	0942	2.6 (2.2)x10^{18}	4.7 (1.5) x10^{18}	111±34	83±16	0.8	3.6	0.51	13/13
150	0714	8.9 (3.1)x10^{17}	6.6 (2.3) x10^{17}	85±40	53±33	0.6	1.9	0.91	11/12
150	2352	5.2 (2.1)x10^{17}	7.4 (1.4) x10^{17}	88±54	67±42	0.3	1.1	1.06	11/12
151	1619	1.6 (1.8)x10^{18}	1.7 (1.8) x10^{18}	92±42	76±60	0.9	1.7	0.95	12/15
141	0026	1.3 (1.4)x10^{18}	1.5 (2.3) x10^{18}	94±29	70±28	0.7	1.9	0.60	10/12

(1) Quality gives the number of amplitudes fit (amplitude ratio between 0.3 and 3.0) by the inversion program by Caterina versus the total number of amplitudes the program tried to fit. In all cases the estimate of the moment from the P wave data was within 1 standard deviation of the moment estimate from the S wave data.

(2) Moments are logarithmic averages of estimates at each station. Errors are a multiplication factor that represents the standard deviation.

Table 4

Magnitude, Hypocentral Coordinates, and Peak Acceleration

Origin[1] Time	Lat.	Lon.	Depth	Peak[2] Acceleration	M[3]
Aug 27, 1978 10.23:07	34° 18.49'	81° 20.06'	0.10 km	291 cm/sec^2	2.8
Oct 27, 1978 07.26:02	34° 17.95'	81° 20.29'	0.20 km	256 cm/sec^2	2.8
Oct 27, 1978 16.27:18	34° 18.20'	81° 19.66'	0.20 km	269 cm/sec^2	3.0
Oct 16, 1979	34° 18.61'	81° 20.10'	0.07 km	347 cm/sec^2	3.0

(1) from Talwani: et al (1980)
(2) from corrected phase II data
(3) Moment magnitude

Table 5

Spectral Data and Source Parameters

	Spectral level (cm:sec)	Corner frequency (hz)	Hypocentral distance (km)	Azimuth (degrees)	Moment (dyne-cm)	Source radius (m)	Stress drop (bars)
Aug. 27, 1978 10.23 GMT							
180°	8.8×10^{-4}	12.7	0.7	123	1.0×10^{20}	100	44
90°	2.3×10^{-3}	5.1	0.7		2.7×10^{20}	248	8
Oct. 27, 1978 07.26 GMT							
180°	4.7×10^{-4}	25.2	1.1	56	8.7×10^{19}	50	304
90°	1.4×10^{-3}	6.1	1.1		2.6×10^{20}	208	13
Oct. 27, 1978 16.27							
180°	6.5×10^{-3}	6.0	0.28	349	3.1×10^{20}	211	14
90°	6.5×10^{-3}	5.6	0.28		3.1×10^{20}	226	12
Oct. 16, 1979 07.06 GMT							
180°	2.2×10^{-3}	11.6	0.90	133	3.5×10^{26}	112	108
90°	2.0×10^{-3}	10.7	0.90		3.2×10^{20}	122	77

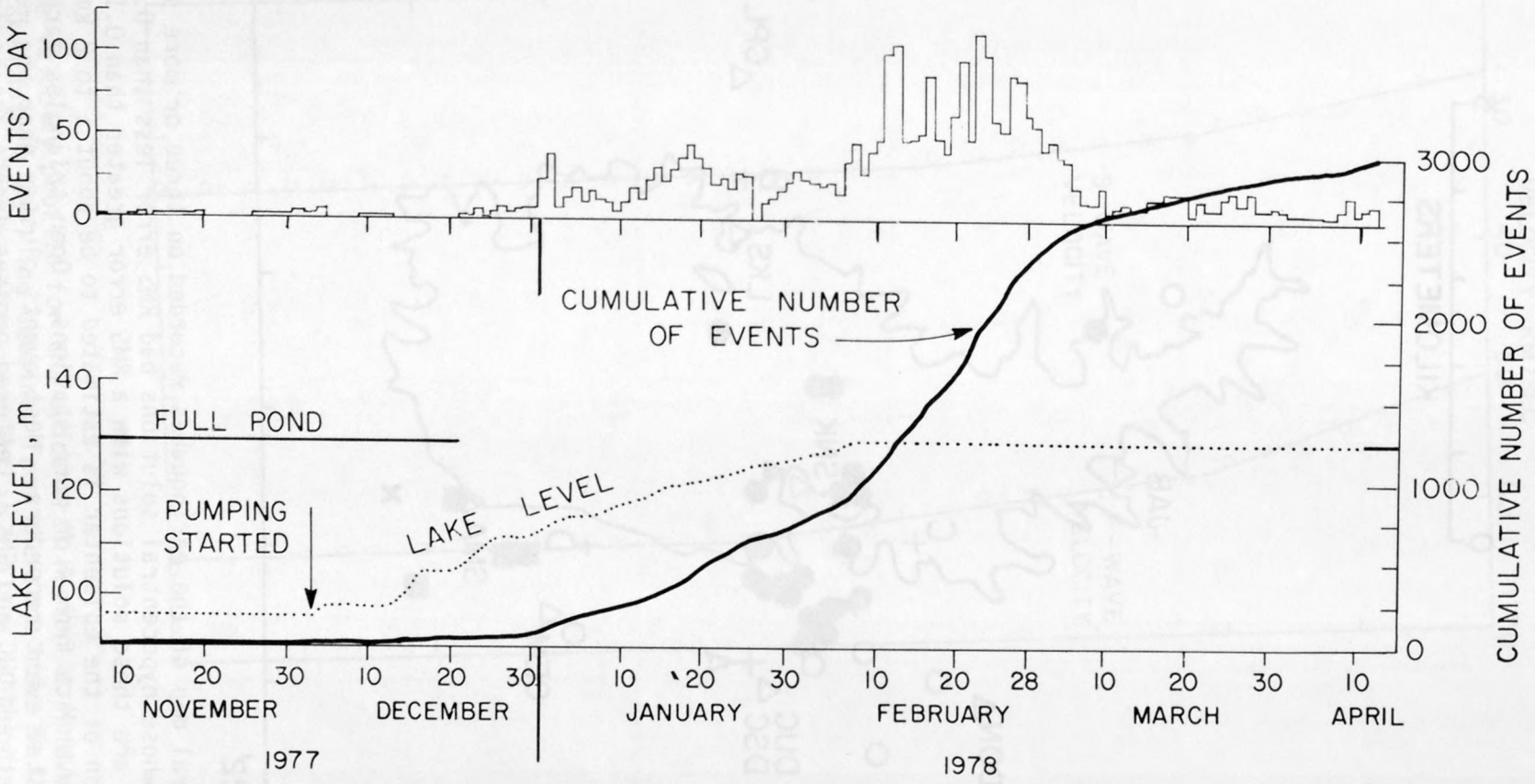

Figure 1) Number of events per day and cumulative number of events versus lake level (after Talwani et al, 1979). Note the close correlation of the increase in seismic activity with lake level and that the high activity in February that sometimes exceeded 100 events per day.

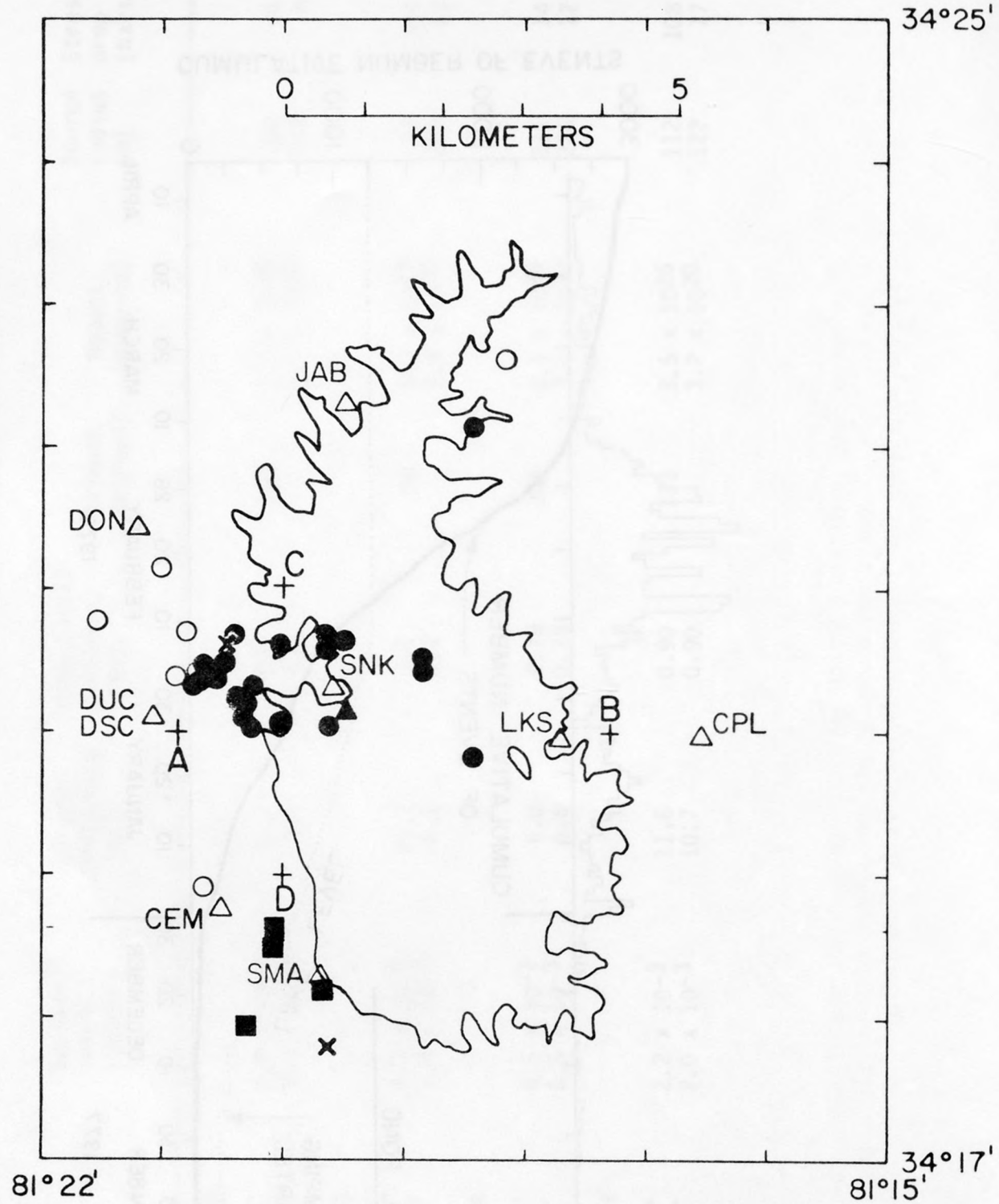

Figure 2) Epicentral map of the earthquakes recorded on three or more stations: dots are those events whose hypocentral solutions had RMS error less than 0.1 sec , and the open circles are those solutions with a RMS error greater than 0.1 sec. One standard deviation of the epicenter is estimated to be about 1 to 2 km for those events with P and S wave data from 4 or more stations. Open triangles mark the sites occupied by the digital event recorders. Most events cluster near the west side of the reservoir near stations DUC and SNK. Lettered crosses denote the horizontal extent of the vertical cross sections shown in fig 4. Station SMA is a strong motion accelerograph. The location of the wells used in measuring the in-situ stresses are noted by crosses; the northern well is Mont-1 and the southern well is Mont-2. The squares are the epicenters of the four largest events recorded by station SMA.

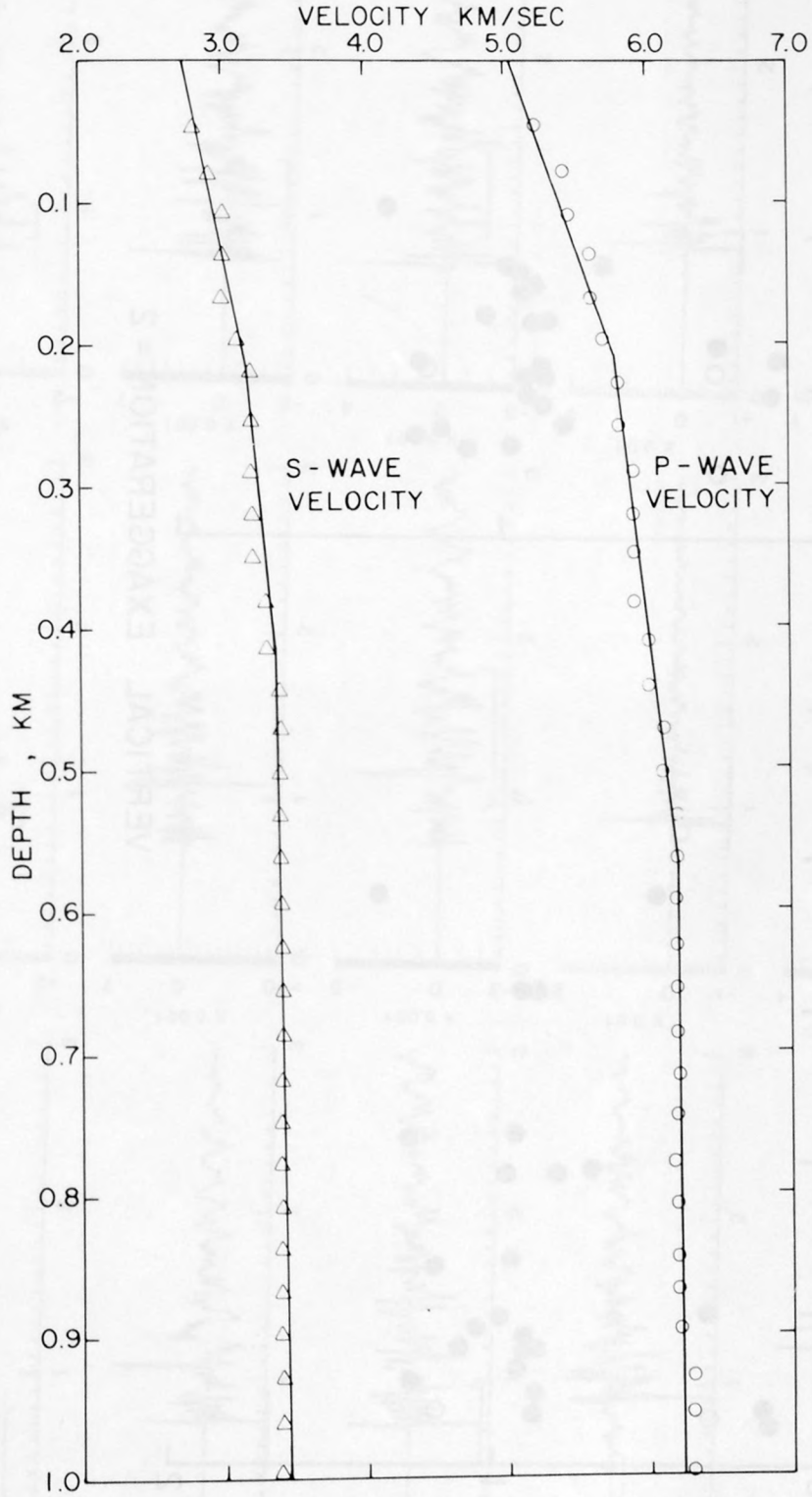

gure 3) P-wave and S-wave velocity profile for the epicentral region at Monticello. Velocities are taken from a well log obtained from the same hole as the hydrofracture stress measurements. Note the moderate gradient at shallow depths (<0.2 km).

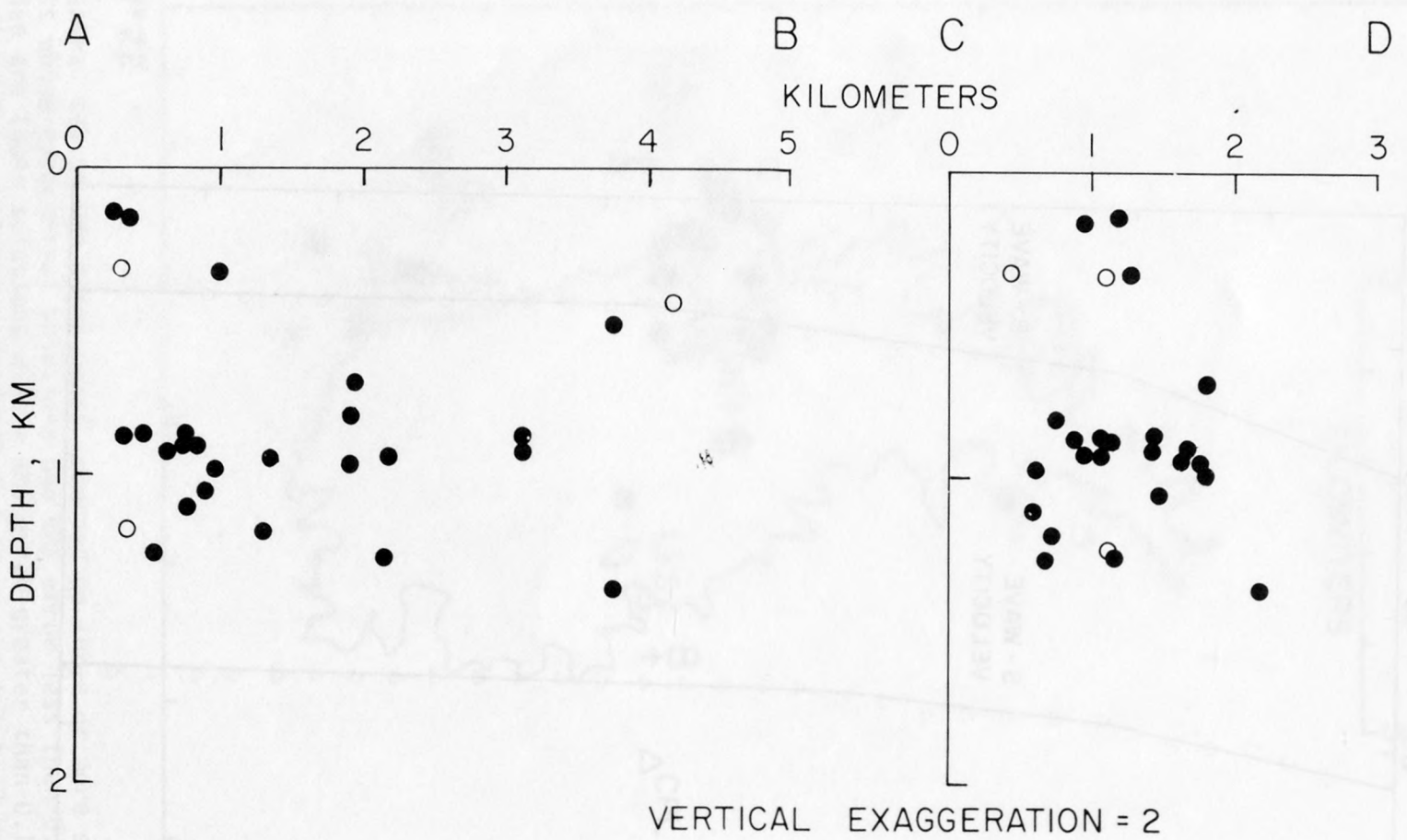

Figure 4) Vertical cross section as noted in fig 2. Events do not seem to form a single through-going fault plane, but rather a zone of activity that extends from near the surface to about 1.5 km depth. One standard deviation in the estimates of the depth is usually several kilometers due to the small number of stations used in the regression. The depth usually changed by only a few tenths of a kilometer when small changes were made in the velocity structure, however, suggesting that the depths are known more precisely than indicated by the formal uncertainty. Open and closed circles denote the same error limits as in fig. 2.

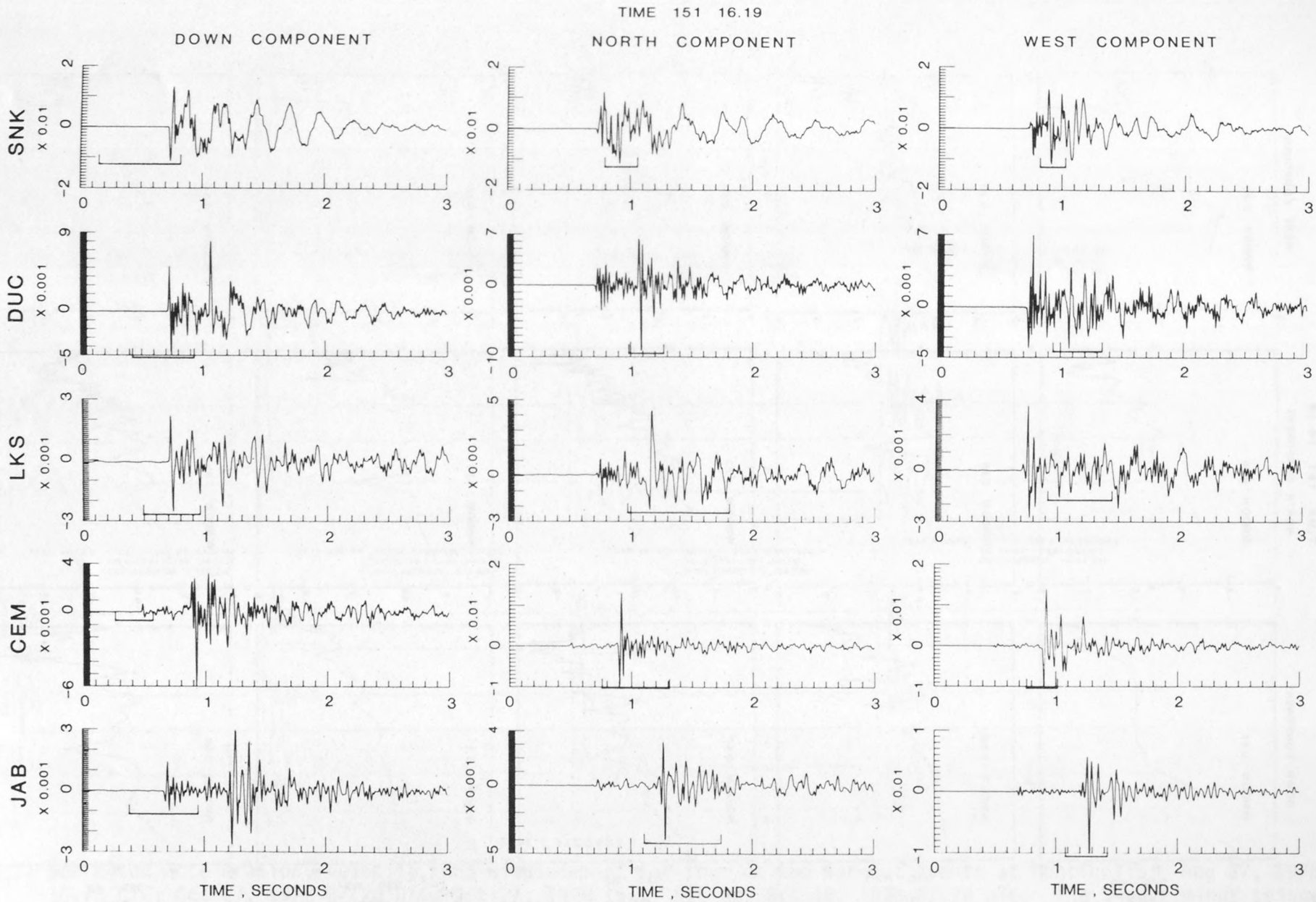

Figure 5) Seismograms for event 151 16.19. Each station has three orthogonal components; Down, North and West. On each record, up is the direction of ground motion described by the component label. The digital seismograph that recorded these traces is approximately flat to velocity from the natural period of the geophones at 2 hz. to the corner of the anti-aliasing filter at 50 or 70 hz. Although the traces are all plotted to the same time scale, the amplitudes have been scaled to fit within a given plot space. The epicentral distances are: SNK; 0.3 km, DUC; 2.4 km, LKS; 2.7 km, CEM; 3.0 km, and JAB; 4.0 km. The depth of event 151 16.19 is 0.95 km.

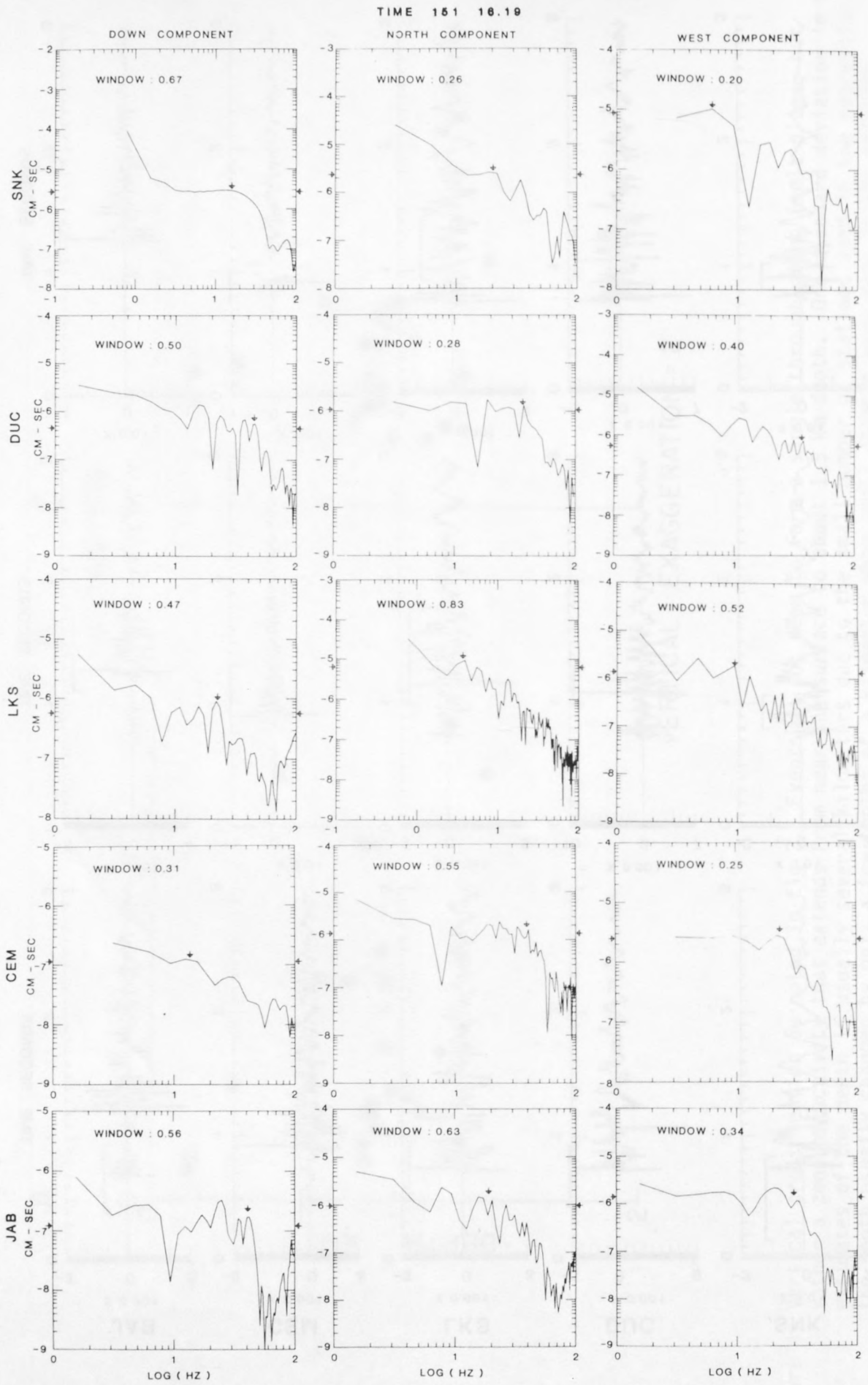

Figure 6) Displacement spectra for event 151 16.19. The section of each time trace used in calculating the spectra is underlined in fig. 5. The corner frequencies used in calculating source parameters as well as the long-period levels used in the time domain spectral comparson are noted by arrows.

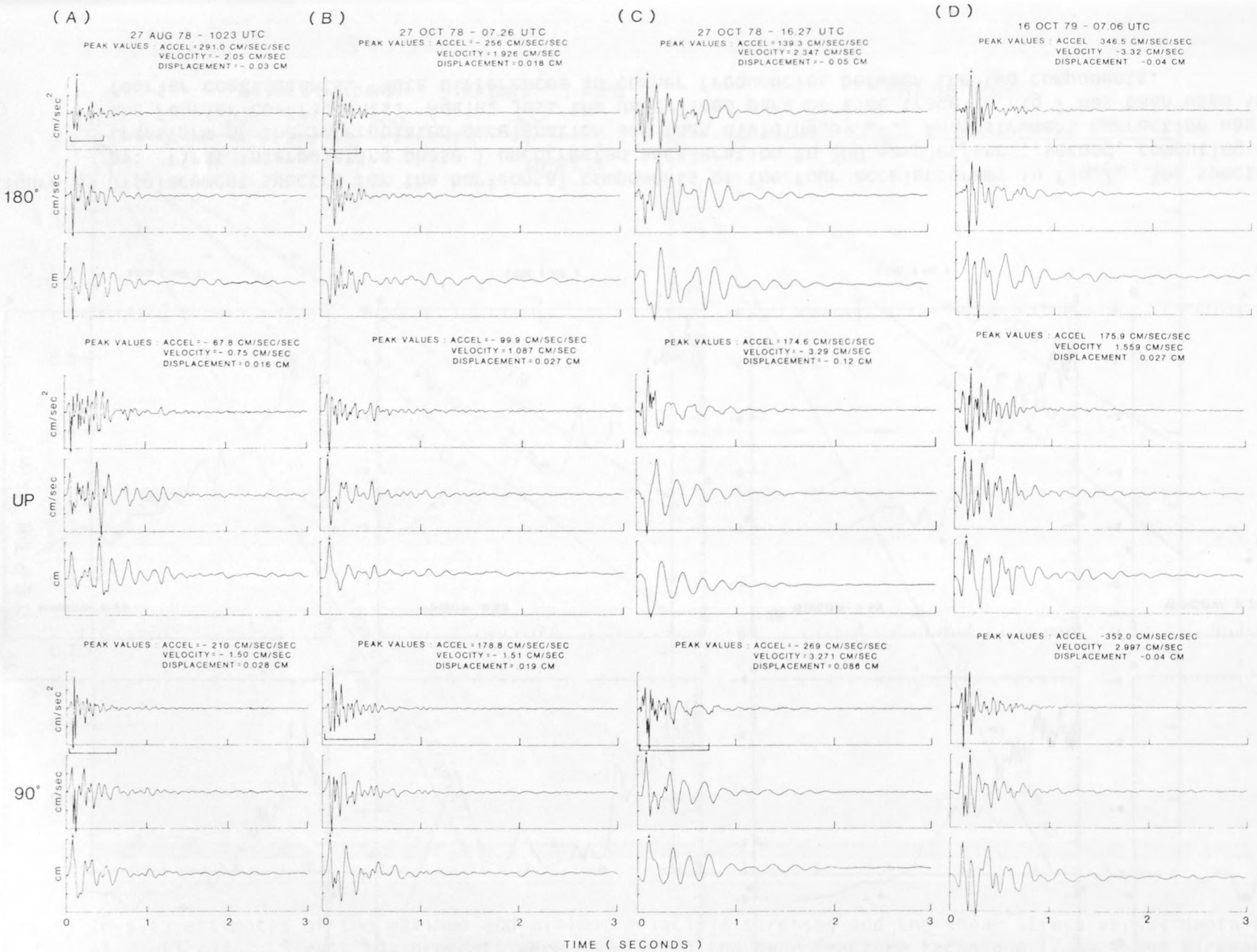

Figure 7) Corrected acceleration, velocity, and displacement for four of the largest events at Monticello: Aug 27, 1978 10.73 UTC, Oct 27, 1978 07.26 UTC, Oct 27, 1978 16.27 UTC and Oct 16, 1979 07.26 UTC. The S-wave minus trigger times suggests that the events are all located near the southern edge of the Reservoir. The phase I traces were interpolated to 500 samples/second to produce these phase II traces. The procedure used is the same as in Fletcher et al. (1980) for the case which used the Butterworth high-pass filter. Note the simple pulse shape of the 180° component for the Aug. 27, 1978 10.23 UTC event.

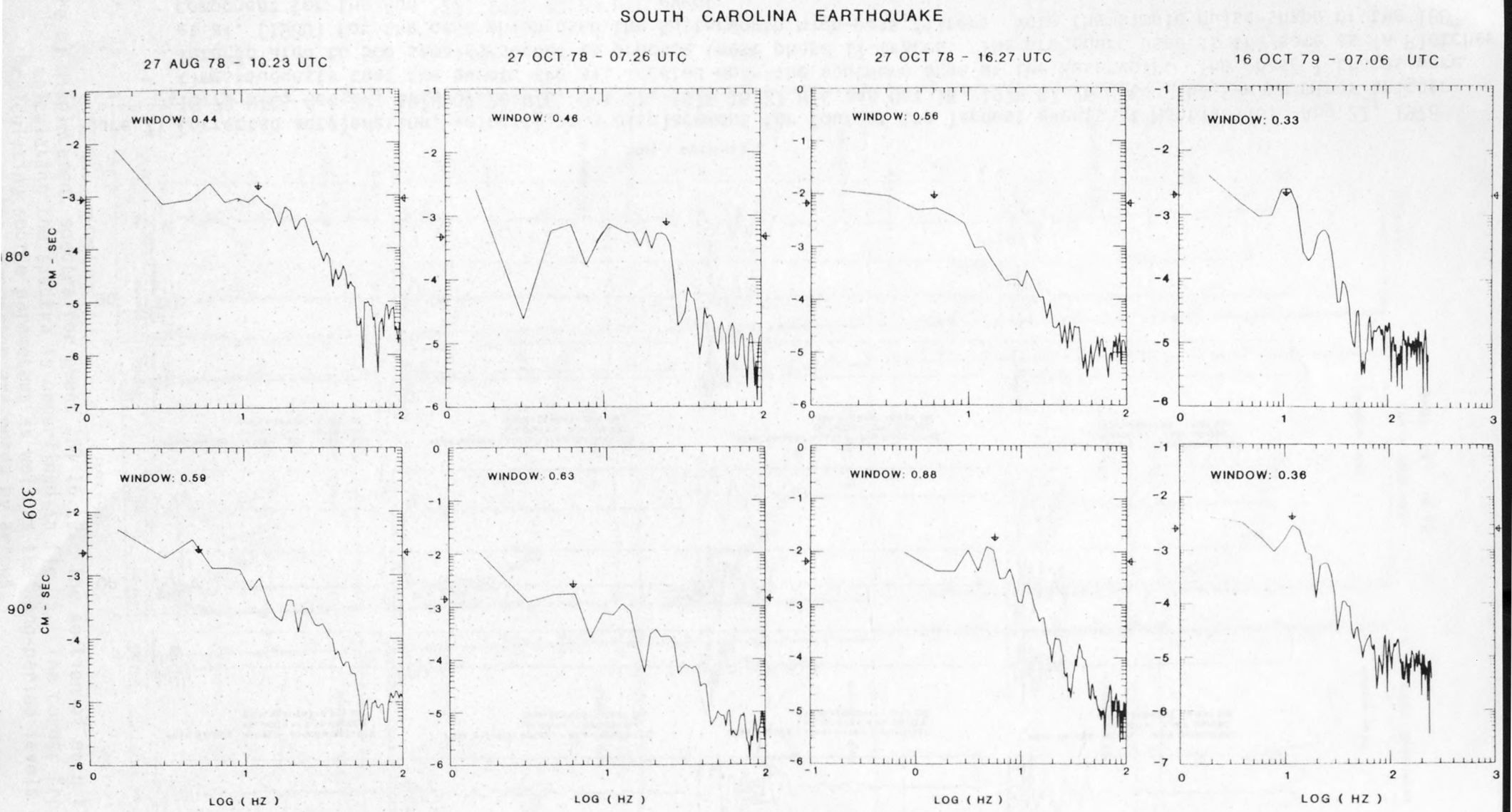

Figure 8) Displacement spectra for the horizontal components of the four accelerograms in fig 7. The spectra was obtained by: first interpolating phase I uncorrected acceleration to 200 samples/sec.; second, computing the fast fourier transform of the interpolated acceleration and then dividing by ω^2. An instrument correction was also applied to the Fourier coefficients. Again, just the underlined part of time trace in fig 7 has been used in calculating the fourier coefficients. Note differences in corner frequencies between the two components.

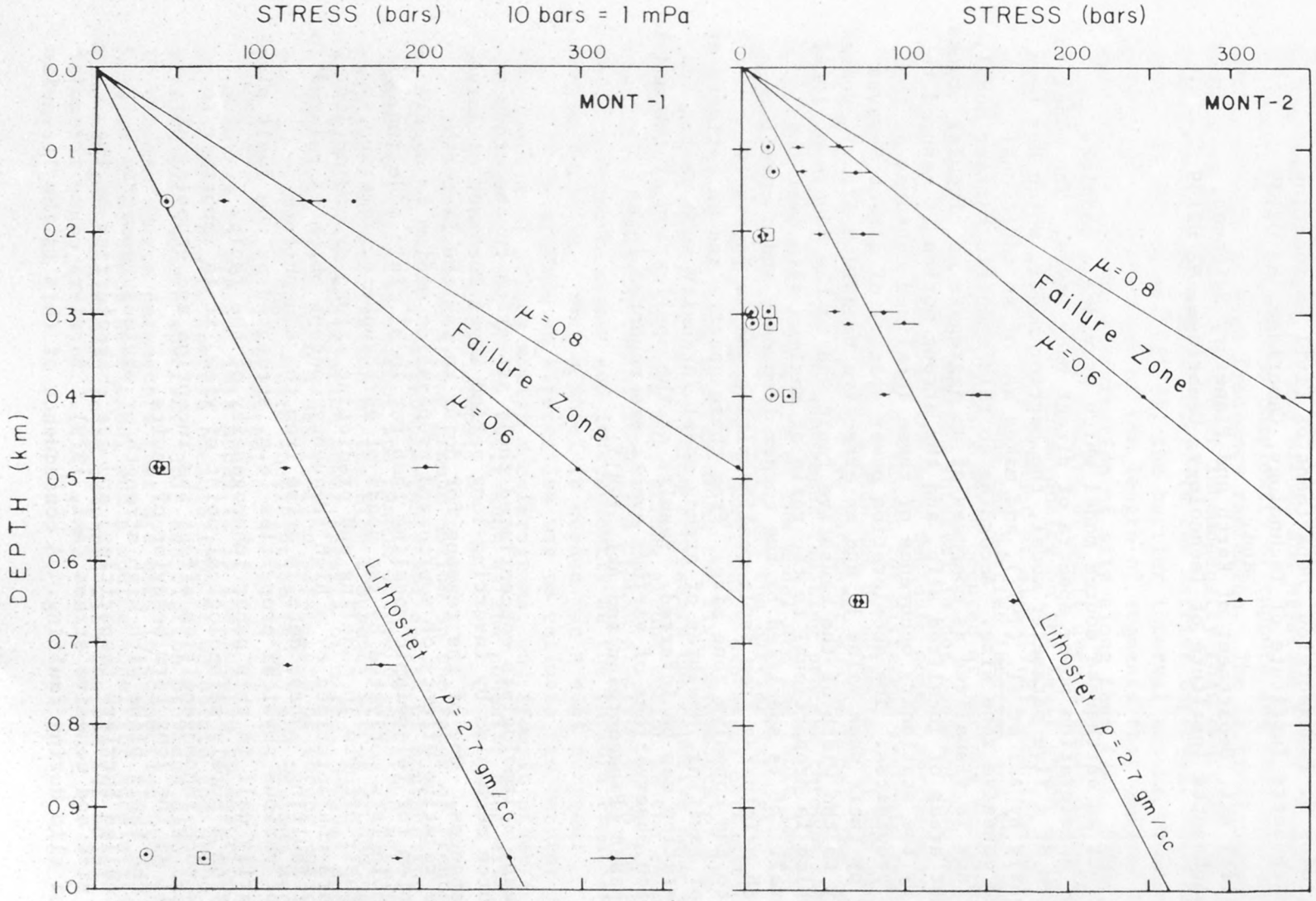

Figure 9) In-situ estimates of the maximum and minimum principle stresses and the shear stress versus depth for the two wells at Monticello. Stress measurements were made using the hydrofracture technique (Zoback and Hickman, 1982). The Mohr-Coulomb failure criteria was used to estimate the shear stress on 45° dipping fault planes. The two estimates of the shear stress shown for the deeper measurements arise from different assumptions made in an attempt to resolve a discrepancy between the mode of the faulting predicted by the relative amplitudes of the principal stresses and the focal mechanisms of the earthquakes: the minimum principal stress is the measured σ_3 with the mode of faulting being thrust only at the 0.16 km depth (represented by squares), and the minimum principal stress is the vertical stress with the mode of faulting assumed to be thrust except at 0.72 km depth in mont-1 (represented by circles).

A SPECIFIC BARRIER MODEL FOR THE QUANTITATIVE DESCRIPTION OF INHOMOGENEOUS FAULTING AND THE PREDICTION OF STRONG GROUND MOTION
I. DESCRIPTION OF THE MODEL

by
Apostolos S. Papageorgiou, Department of Civil Engineering,
Massachusetts Institute of Technology, Cambridge, MA 02139
and
Keiiti Aki, Department of Earth and Planetary Sciences,
Massachusetts Institute of Technology, Cambridge, MA 02139

Abstract

We construct an earthquake source model which provides a complete description of acceleration power spectra of direct body waves. The model is a specific form of a five parameter model, the barrier model, which has been proposed recently by Aki et al. (1977), and makes use of an additional parameter, the cohesive zone size. According to this specific barrier model, the fault surface is visualized as composed of an aggregate of circular cracks which represent areas of localized slip, and the strong motion is assumed to be generated by the stationary occurence of these localized ruptures as the rupture front propagates. The acceleration power spectra of direct S-waves are described by their peak value P_o and an effective bandwidth Δf. P_o scales proportionally to the width of the causative fault and to the square of local stress drop which is proportional to the ratio of maximum slip over the barrier interval. Δf is specified by the corner frequency and a cutoff frequency which originates from fault nonlinearities and is inversely proportional to the cohesive zone size. From these spectra and an estimate of the duration of faulting, measures of strong model intensity such as rms and maximum acceleration can be inferred. Results of the application of the model to strong motion observations of various events are reported in an accompanying paper (Papageorgiou and Aki, 1981).

Introduction

In the past, seismologists concentrated their attention to the study of earthquake source mechanism by inverting long period waves recorded at large epicentral distances. One of the reasons for doing so was the fact that separating the relative effects of source and propagation medium is a more tractable problem for teleseismic modeling than for local field modeling. Recently seismologists motivated by the needs of earthquake engineering, concentrated their efforts in modeling and predicting strong ground motion. Such motions are characterized by a high frequency content which is related to the details of faulting. These details arise from the non-uniform distribution of various physical properties (e.g. strength) on the fault plane which we summarily call in this paper inhomogeneity of the fault. Furthermore, from a purely seismological point of view, it is important to understand how such inhomogeneities affect the inception and stopping of rupture as well as the long term behavior of faults.

Areas on the fault plane with high strength or obvious geometric anomalies are called barriers (asperities) and are characterized by the cohesive zone size and cohesive stress (Aki, 1979). Barriers cause irregular distribution of slip during faulting. A consequence of this is the irregular

distribution of stress drop, with localized high stress drops for the regions that slip smoothly. Such regions are separated from each other by the barriers, which act as stress concentrators because they slip a small amount, if at all, during the faulting process. The numerical experiments performed by Das and Aki (1977a,b) and Mikumo and Miyatake (1978) demonstrated clearly that barriers control the complexity of rupture and they are responsible for the generation of high frequency radiation. The critical parameter which represents the length scale of inhomogeneity that controls the high frequency radiation in a particular event is the barrier interval. As discussed in detail by Aki et al. (1977), the barrier interval can be inferred from geological observations of the length of segments that compose fault traces of past events and the distribution of slip along them (Aki, 1980a), from the scaling law of the source spectra of small events whose dimensions reflect the length scale of strength inhomogeneity on the fault which is important for a certain range of magnitudes (Chouet et al., 1978), and from the rise time. Aki et al. (1977) compiled thus the barrier interval and the corresponding maximum slip of several events which occured at various tectonic regions. They observed that the barrier interval is not constant but varies with maximum slip for events of the same tectonic zone. Furthermore they noticed that this variation may be different for different tectonic regions.

As a unifying basis for a wide set of seismological and geological data, Aki et al. (1977) proposed a five parameter source model, the barrier model, that accounts for the inhomogeneous faulting process through the barrier interval. The five parameters of the model are the fault length and width, the maximum slip, the rupture velocity and the barrier interval.

In this paper we develop a model which expresses mathematically the inhomogeneous faulting process using the five parameters of the barrier model and an additional parameter which represents the cohesive zone size. This model is based on the idea that strong ground motion is the result of the cumulative contribution of localized cracks distributed on the fault plane, which rupture randomly and independently as the rupture front sweeps them during faulting. Such a model is needed for a dual purpose:

(1) To provide an alternative way to estimate the barrier interval from the spectra of strong motion accelerograms, and from it other important physical properties of the fault such as the cohesive zone size, cohesive stress and local stress drops.

(2) To describe strong ground motion in the range of frequencies which is important for the earthquake-resistant design of engineering structures. Given the highly incoherent and random nature of observed accelerograms, a complete characterization of the high frequency strong ground motion may be provided by the acceleration power spectra of direct S-waves and the duration of faulting. From such a description parameters of strong motion intensity such as the root mean square acceleration (a_{rms}) and maximum accelertion (a_{max}) can be easily estimated.

Before we present this model it is instructive to describe the shape of displacement source spectra because from it we obtain the shape of acceleration source spectra. This description provides also the opportunity to discuss source parameters that are used in connection with the specific barrier model to be developed, and a source model for acceleration spectra proposed by Hanks (1979) to be compared with the barrier model.

Shape of the Source Spectrum

The far-field displacement spectrum of a reasonable kinematic source model is expected to have a constant value at low frequencies and a value proportional to a negative power of frequency at high frequencies. When plotted on logarithmic scales, it can be effectively described by two asymptotic lines, one horizontal for the low frequencies and one inclined with a negative slope for the high frequencies (Fig. 1a). The point of intersection of the two asymptotes determines the so-called "corner frequency." This frequency is inversely proportional to a characteristic length that describes the size of the source.

The functional form that conveniently determines this shape is

$$\tilde{\Omega}(f) = \frac{\tilde{\Omega}(0)}{1 + \left(\frac{f}{f_o}\right)^{\gamma}} \qquad (1)$$

where

f_o = the corner frequency

$\tilde{\Omega}(0)$ = the value of the flat part of the displacement spectrum which is proportional to the seismic moment M_o (eq. 2)

γ = the absolute value of the slope of the inclined asymptote

The seismic moment was introduced from the representation of dislocations as double couple sources (Maruyama, 1963; Burridge and Knopoff, 1964). In the far-field and for wavelengths much larger than the source size, the fault appears as a point dislocation. The scalar value of the moment of one of the couples in the double-couple representation of the point dislocation is the seismic moment M_o. This physical quantity, first determined by Aki (1966) for the Niigata earthquake of 1964, is the most important static parameter of the fault that can be reliably inferred from seismic observations such as displacement spectra of long-period surface waves or free oscillations of the earth. Kanamori and Anderson (1975) and Kanamori (1977) listed the seismic moments of about 50 large events and Hanks (1977) summarized the seismic moments of approximately 400 low-to moderate-size events.

For a double couple embedded in an elastic, homogeneous, isotropic, unbounded medium, considering S-waves,

$$\tilde{\Omega}(0) = \frac{1}{4\pi r_o} \cdot \frac{M_o}{\mu} \cdot \frac{1}{\beta} \cdot (F^S) \qquad (2)$$

where

μ = shear modulus (rigidity) of elastic medium

β = shear wave velocity of the medium

r_o = distance from the point source to receiver

(F^S) = double couple radiation pattern for SH or SV waves.

The seismic moment M_o is related to the final slip on the fault by the following relation (Burridge and Knopoff, 1964),

$$M_o = \mu \iint_{\Sigma} \Delta u(\xi) d\Sigma_{\xi} \qquad (3a)$$

where

$\underset{\sim}{\xi}$ = position vector of a point on the fault plane

$\Delta u(\underset{\sim}{\xi})$ = slip at a point $\underset{\sim}{\xi}$ on the fault plane

Σ = total surface of the fault

or, assuming an average slip $\overline{\Delta u}$,

$$M_o = \mu \cdot \overline{\Delta u} \cdot S \tag{3b}$$

where

S = area of fault plane

The corner frequency f_o is related to the source size by the following relation:

$$f_o = (\text{Const}) \cdot \frac{\beta}{\underset{\sim}{L}} \tag{4}$$

where

$\underset{\sim}{L}$ = characteristic length which describes the size of the source

(Const) = proportionality constant of order one, depending on the specific source model under consideration.

Initially proposed by Aki (1967) and recently reaffirmed by Hanks (1979) on an observational basis, the $\gamma = 2$ ("ω-square") model is the one generally, but not always, applicable for crustal earthquakes. Observations such as m_b-M_S relations, peak accelerations near the source ($\leq$10 km), and the San Fernando data with frequencies as high as 100 x f_o, support this model (Hanks, 1979).

Another important parameter of the earthquake source which enters the description of spectra is the stress drop $\Delta\sigma$. This quantity is inferred from the seismic moment and the size of the source. We mentioned above reliable methods to estimate the seismic moment. The size of the source of large events is usually inferred from the aftershock area, extent of surface deformation, tsunami source area (for a submarine earthquake), waveforms, spectra and radiation pattern of body and surface waves. For small events, the size of the source is inferred from the corner frequency (eq. 4).

In order to infer the stress drop (for a planar fault surface, with no barriers) from seismic moment and source size using eq. 3b, we need to relate the average slip Δu with the stress drop $\Delta\sigma$. For that purpose it is assumed that the stress drop is uniform over the fault plane and the average slip is computed for various fault geometries. Solutions of this problem in terms of a shear crack model under uniform stress drop (i.e., difference between tectonic and dynamic frictional stress), are available for various source geometries, e.g., circular (Eshelby, 1957; Keilis-Borok, 1959), two-dimensional in plane (Starr, 1928) or antiplane (Knopoff, 1958). These solutions have the general form

$$\overline{\Delta u} = (\text{Const}) \cdot \frac{\Delta\sigma}{\mu} \cdot \underset{\sim}{L} \tag{5a}$$

where (Const) is a nondimensional shape factor. For a circular crack of radius R the constant is equal to $(16/7\pi)$ and therefore

$$\Delta u = \left(\frac{16}{7\pi}\right) \cdot \left(\frac{\Delta\sigma}{\mu}\right) \cdot R \tag{5b}$$

Substituting this expression for $\overline{\Delta u}$ into eq. 3b we get

$$M_o = \frac{16}{7} \cdot \Delta\sigma \cdot R^3 \tag{6}$$

The value of $\Delta\sigma$ thus inferred is remarkably constant, falling in the range of 10 to 100 bars, for a wide range of magnitudes ($5 \leq M_S \leq 8$) (Aki, 1972; Kanamori and Anderson, 1975). We refer to this stress drop as the "global" stress drop (as opposed to the "local stress drop" which is introduced below). The word "global" implies the fact that the stress drop is assumed to be uniform over the entire fault plane which has no barriers.

Given the shape of displacement spectra described above, the shape of acceleration spectra (for $\gamma = 2$) is obtained by the following relationship:

$$\tilde{a}(f) = (2\pi f)^2 \, \tilde{\Omega}(f)$$

$$= \frac{\tilde{\Omega}(0) \cdot (2\pi f_o)^2}{1 + \left(\frac{f_o}{f}\right)^2} \tag{7}$$

$$= \frac{\tilde{a}_o}{1 + \left(\frac{f_o}{f}\right)^2}$$

where

$$\tilde{a}_o = (2\pi f_o)^2 \, \tilde{\Omega}(0) \tag{8}$$

The shape of acceleration spectra is shown in Fig. 1b. It is described again by two asymptotic lines that intersect at the corner frequency f_o defined above, but now the horizontal asymptote describes the high frequency range.

Hanks' Model

In order to predict strong ground motion, Hanks (1979) used the shape of acceleration spectrum described above, and scaled it according to Brune's source model (Brune, 1970, 1971). He considered for modelling the strongest part of strong motion records, which he assumed to be band-limited white noise with a duration T_d equal to the duration of fault rupture. This is equivalent to modelling the direct S-waves that we consider in this paper.

The corner frequency is related to the radius R of an equivalent circular crack which is used to model the earthquake source by the following relations:

From Brune's (1970, 1971) model,

$$2\pi f_o = \frac{2.34\beta}{R} \tag{9a}$$

This relation was subsequently corrected by Madariaga (1976) who studied the dynamics of a plane circular model of a frictional fault using numerical methods. According to Madariaga's solution (assuming a ratio of the rupture velocity to the shear wave velocity equal to 0.9) the corner frequency is given by

$$2\pi f_o = \frac{1.32\beta}{R} \tag{9b}$$

Since $1/f_o \sim R/v$ and $T_d = R/v$ (v = rupture velocity) then, according to Hanks,

$$T_d \simeq \frac{1}{f_o} \tag{10}$$

is a rough but reasonable estimate of the duration of rupture.

Then Hanks considered the power spectral density function $P(f)$ of the part of ground motion defined above and recorded at a distance r_o from the source. $P(f)$ is related to the Fourier transform $\tilde{a}(f)$ of that part of ground motion by

$$P(f) \simeq \frac{(\tilde{a}(f))^2}{T_d} \tag{11}$$

Using eqs. 7, 10 and 11,

$$P(f) \simeq \frac{\tilde{a}_o^2 \cdot f_o}{\left(1 + \left(\frac{f_o}{f}\right)^2\right)^2} \tag{12}$$

Therefore the value P_o of the flat part of the spectral density of the strong part of ground motion expected at a distance r_o from the source is given by

$$P_o \simeq \tilde{a}_o^2 \cdot f_o \tag{13}$$

Substituting eq. 8 into eq. 13 and making use of eq. 2, eq. 9a and eq. 6 we obtain

$$P_o = (0.61)^2 \cdot R \cdot \frac{(\Delta\sigma)^2}{\beta\rho^2} \cdot \frac{(F^S)^2}{r_o^2} \tag{14}$$

In eq. 14 the term $\frac{(F^S)^2}{r_o^2}$ accounts for the radiation pattern and geometrical spreading of S-waves. P_o scales with the size R of the source. The value of $\Delta\sigma$ is assumed to be (at least formally, according to the derivation) the "global" stress drop discussed above.

The root mean square acceleration a_{rms} observed at a distance r_o from the source is given by

$$a_{rms} = \sqrt{2 \cdot P_o \cdot \Delta f}\ , \tag{15}$$

where Δf is an effective bandwidth to be specified.

In order to specify this effective bandwidth, Hanks assumed that at a distance r_o from the source, the power spectrum of accelerations drops off at high frequencies as shown in Fig. 1b due to anelastic effects of the propagation path. These effects are accounted for by the anelastic attenuation factor

$$\exp\left(-\frac{2\pi f r_o}{Q_\beta \beta}\right)\ , \tag{16}$$

where Q_β is the quality factor of shear waves.

Then he defined a cutoff frequency f_{max} as that frequency where the power spectrum has decreased to e^{-1} of its original value P_o. From eq. 16

$$f_{max} = \frac{Q_\beta \cdot \beta}{2\pi r_o} \tag{17}$$

Therefore

$$\Delta f \simeq f_{max} - f_o = f_{max}\left(1 - \frac{f_o}{f_{max}}\right) \tag{18a}$$

Assuming that $f_{max} >> f_o$, which is a reasonable assumption, for moderate to large events for which f_o is well below 1 Hz as opposed to f_{max} which is above 1 Hz as verified by observations, eq. 18a reduces to

$$\Delta f \simeq f_{max} \tag{18b}$$

Substituting eqs. 14 and 18b into eq. 15 and using eq. 17 we obtain,

$$a_{rms} = \sqrt{2 \cdot (0.61)^2 \cdot R \cdot \frac{(\Delta\sigma)^2}{\beta\rho^2} \frac{(F_s)^2}{r_o^2} \frac{Q_\beta \beta}{2\pi r_o}}$$

$$= 0.34 \cdot (F^s) \cdot \frac{\Delta\sigma}{\rho (r_o)^{3/2}} \cdot \sqrt{Q_\beta R} \tag{19}$$

For comparisons with actual observations, the right-hand side of eq. 19 must be multiplied by the factor $\sqrt{2}$ which accounts for free surface amplification (factor of 2) and vectorial partition of ground motion by the recording device (factor $1/\sqrt{2}$).

Two observations can be made in connection with Hanks' model:

(1) The spectral amplitudes, according to this model, scale with the average stress drop $\Delta\sigma$ over the fault plane.
This is a static parameter obtained from the seismic moment and the source size as described above. For this reason it cannot account properly for the local high stress drops that occur during faulting, which are responsible for the frequencies of ground motion which are higher than the corner frequency f_o. The stress drop $\Delta\sigma$ to be used to scale the acceleration spectra must be estimated in such a way as to reflect these localized stress drops which are caused by the irregular slip on the fault.

Furthermore, the power spectral amplitudes scale proportionally to the radius R of an equivalent circular source. The assumption of an equivalent circular source may not be realistic for elongated sources (e.g. strike-slip events).

(2) Hanks' assumption that the cutoff frequency f_{max} comes from anelastic attenuation implies strong attenuation of high frequencies, i.e., small Q_β, independent of frequency. This may not be correct as it is revealed from analyses of actual data (Aki, 1980b,c; Papageorgiou and Aki, 1981). The Q_β that was inferred from the San Fernando data was found to be strongly frequency-dependent, increasing with frequency. This suggests that the attenuation of high frequencies must not be as strong as initially thought and therefore the cutoff frequency f_{max} may originate primarily from a different cause.

Hanks' assumption about f_{max} implies also that close to the source, where propagation path effects are not so important, f_{max} may be very large, suggesting very large root mean square accelerations (a_{rms}) and equally large maximum accelerations (a_{max}), contrary to what is observed in reality. It is expected that even close to the source f_{max} is limited because materials of the fault zone exhibit strong non-elasticity during the rupture process.

Both observations made above are considered in the specific barrier model to be developed. According to this model, the flat part of the acceleration spectra is scaled by the "local stress drop" inferred from the barrier interval. It is also proposed that f_{max} originates primarily from non-elasticity of the fault.

A Specific Barrier Model (Aggregate of Circular Cracks)

The best example of an actual earthquake that motivates and illustrates the source model to be developed is the Parkfield earthquake of June 1966. With its numerous aftershocks and their accurate determination by Eaton et al. (1970), this event provides an excellent example of a fault plane with distributed barriers and regions that slipped smoothly during the rupture process.

The main event occurred on the central part of the San Andreas fault near Parkfield, and the right lateral slip caused surface breakage that extended over a distance of 30-40 km (Fig. 2a). The fault plane was almost vertical, as shown in Fig. 2b. Most papers that have analyzed this earthquake agree that the rupture started near the northern end of the zone of fault breaks and propagated southward with a velocity in the range of 2.2-2.5 km/sec. This range is confirmed also by the first on-site determination of fault rupture velocity based on the time signal (W.W.V.) recorder at the Golden Hill station (Eaton, 1967).

Fig. 3 shows the projection of the hypocenters of the Parkfield aftershocks on the vertical fault plane. In the barrier model, few aftershocks are expected over a section of the fault that slipped smoothly. On the contrary, areas that act as barriers to the rupture, experience little slip and are stress concentrators. This induced stress increase combined with static fatigue causes a sequence of aftershocks (Mogi, 1962; Aki, 1979). With that reasoning, Aki (1979) drew boundaries between regions with no aftershocks (slipped sections) and regions with aftershocks (unbroken barriers with little slip) as shown in Fig. 3.

Now let us imagine the rupture front sweeping the fault plane as it propagates. Signals are emitted from the localized fractures (regions with no aftershocks). A station at far enough distance receives these signals superimposed in a random manner due to their random position on the fault and the random timing of their slippage.

Let us now assume that the random incidence of fractures described above occurs at an average rate of n per unit time. Within a time interval Δt, $n \cdot \Delta t$ fractures are expected, each of which generates a far-field spectrum. Let us further assume that all cracks have the same dimensions and the same amount of slippage and therefore the same spectrum $G_o(\omega)$, reasoning that we are considering an average crack size contributing to the seismic motion observed at the station. Since the fractures are assumed to occur randomly, and statistically independently of each other, the Fourier transform $G(\omega)$ of the total seismic motion sampled over the time length Δt will be related to the Fourier transform $G_o(\omega)$ of the individual signal by

$$|G(\omega)|^2 = n \cdot \Delta t \cdot |G_o(\omega)|^2 \qquad (20)$$

One can consider eq. 20, which is based on the statistical independence of individual cracks, as the mathematical definition of the average effective crack size.

The power spectrum $P(\omega)$ of a random time series is related to the Fourier transform of a finite sample over time length Δt by

$$P(\omega) \simeq \frac{|G(\omega)|^2}{\Delta t} \qquad (21)$$

Combining eqs. 20 and 21 we get

$$P(\omega) \simeq n\,|G_o(\omega)|^2 \qquad (22)$$

It remains to express (1) $G_o(\omega)$ analytically in terms of the parameters of an individual crack such as the radius and slip or stress drop of the crack, and (2) n in terms of source parameters.

For the first of these two steps, we use a model developed and implemented by Sato and Hirasawa (1973). Even though it is not a solution for the dynamical stress relaxation problem, this model contains all the important aspects of the dynamical process of an expanding circular crack whose rupture propagation is arrested abruptly. We compare the initial behavior of the model to the exact solutions which have been developed for the self-similar growth of rupture after nucleation, of a circular crack with uniform stress drop (Kostrov, 1964). Furthermore, we compare the phases generated by the arrest of rupture propagation (stopping phases) with the asymptotic results obtained by Madariaga (1977). Thus we demonstrate that Sato and Hirasawa's (1973) model is a very good, yet simple, approximation of the solution for the problem of a circular crack with uniform stress drop, which nucleates, expands with constant rupture velocity and stops abruptly. The numerical solution to this problem which has been developed by Madariaga (1976) provides additional support for the model. In what follows, this model is briefly described, and the analytical expression for $C_o(\omega)$ is derived.

Sato and Hirasawa's model has been developed in order to interpret teleseismic body wave spectra. It is a kinematic model whose source function is specified by making use of the static solution of circular cracks. It is constructed by assuming that Eshelby's (1957) static solution holds at every successive instant of rupture propagation for a circular crack under uniform shear stress.

According to Eshelby (1957), in an infinite, homogeneous, isotropic medium with a Poisson's ratio equal to 1/4, the relative slip of the faces of a circular crack of radius ρ_o (Fig. 4) under a uniform shear stress $\Delta\sigma$ is given by

$$\Delta u(\rho) = K(\rho_o^2 - \rho^2)^{1/2} \qquad \rho_o \geq \rho \quad . \tag{23}$$

where

$$K = \left(\frac{24}{7\pi}\right) \cdot \left(\frac{\Delta\sigma}{\mu}\right) \tag{24}$$

Suppose that the rupture initiates at a point at t = 0 and spreads radially outwards at a constant velocity v. Then at time t the radius of the rupture front of the circular fault is vt. According to the assumption made above the relative displacement on the fault surface at time t is:

$$\Delta u(\rho,t) = \left(\frac{24}{7\pi}\right)\cdot\left(\frac{\Delta\sigma}{\mu}\right)\{(vt)^2 - \rho^2\}^{1/2}\, H\left(t - \frac{\rho}{v}\right) \quad , \tag{25a}$$

where H(t) is the Heaviside unit step function.

This is almost identical to the slip function obtained by Kostrov (1964) for the self-similar growth of a circular crack (which was later extended for elliptical cracks by Burridge and Willis (1969)), and which is given by the expression

$$\Delta u(\rho,t) = \frac{\Delta\sigma}{\mu}\, C'\left(\frac{v}{\beta}\right)\{(vt)^2 - \rho^2\}^{1/2}\, H\left(t - \frac{\rho}{v}\right) \tag{25b}$$

The only difference arises from the replacement of the constant $(24/7\pi)$ in eq. 25a by the multiplicative function $C'(v/\beta)$ which decreases monotonically from $C'(0) = (24/7\pi)$ (static solution) to $C'(1) = 8/9$. It might be informative to note that $C'(v/\beta) = (\beta/v)C(v/\beta)$ where $C(v/\beta)$ is a function which has been evaluated by Dahlen (1974) based on Kostrov's (1964) results and is more commonly referred to in the literature. Assuming that the rupture stops abruptly at $\rho = \rho_o$ the slip function is given by:

$$\Delta u(\rho,t) = K[(vt)^2 - \rho^2]^{1/2}\, H(t - \frac{\rho}{v})[1 - H(\rho - \rho_o)] \text{ for } vt < \rho_o \qquad (26)$$
$$= K(\rho_o{}^2 - \rho^2)^{1/2}\, [1 - H(\rho - \rho_o)] \text{ for } vt > \rho_o$$

According to the slip function (eq. 26) of Sato and Hirasawa's model, slip stops simultaneously everywhere over the fault plane. This abrupt freezing of slip enhances the high frequency content of the radiated waves for the generation of which only the stopping at the edge of an expanding crack is important. On the contrary, according to the numerical solution of the dynamical problem of the expansion (with constant rupture velocity) of a circular crack due to a constant stress drop on the fault surface (Madariaga 1976), the slip at a point on the fault ceases to increase only when the reflected P-waves from the outer boundaries of the crack reach that point. That causes a larger slip for the dynamic solution than that obtained from the static solution (eq. 26) by a factor of 1.15 to 1.30 and, together with the finite mesh used in the numerical solution of the dynamical problem, has as an effect the less efficient generation of high frequency phases.

From dislocation theory, the observed seismogram is related to the displacement discontinuity across a fault plane through a space-time convolution with the point impulse response of the elastic space. The far-field displacement waveform of P-and S-waves are described by a simple integral of the form (Aki and Richards, 1980),

$$\Omega(x,t) = \iint_{\Sigma} \Delta\dot{u}\ [\underset{\sim}{\xi}, t - \frac{r_o - (\underset{\sim}{\xi} \cdot \underset{\sim}{\gamma})}{c}]\, d\Sigma \qquad (27)$$

where (Fig. 4)

c = α(P-wave velocity) or β(S-wave velocity)

$\underset{\sim}{\xi}$ and $\underset{\sim}{x}$ = position vectors of a point on the fault and of the point of observation (receiver) respectively for a given set of axes whose origin lies on the fault plane.

Σ = total surface of fault

r_o = distance from the receiver to the origin of axes

$\underset{\sim}{\gamma}$ = unit vector on the direction of r_o

$\Delta\dot{u}[\underset{\sim}{\xi},t]$ = slip velocity at a point $\underset{\sim}{\xi}$ on the fault at time t

Eq. 27 is valid when the following inequality is valid:

$$L^2 \leq \frac{r_o \cdot \lambda}{2} \qquad \text{(Fraunhofer approximation)}$$

where L = maximum dimension of the fault

λ = wavelength of maximum frequency under consideration

Sato and Hirasawa, putting eq. 26 into eq. 27, and carrying out the integration, obtained the following compact result:

$$\Omega(\underset{\sim}{x},t) = 2Kv\rho_o^2\, [\frac{\pi}{(1 - k^2)^2}]\, x^2 \qquad \text{for } 0 < x < 1 - k \qquad (28a)$$

$$= 2Kv\rho_o^2\, (\frac{\pi}{4})\, [\frac{1}{k} - \frac{x^2}{k(1 + k)^2}] \text{ for } 1 - k < x < 1 + k \qquad (28b)$$

where

$$k = \left(\frac{v}{c}\right) \sin\theta \tag{29}$$

$$x = \frac{v}{\rho_o}\left(t - \frac{r_o}{c}\right) \tag{30}$$

The displacement waveform $\Omega(\underset{\sim}{x},t)$ is shown in Fig. 5 for different azimuths.

Equation 28a represents what is called the starting phase of the rupture process which is identical to the parabolic behavior of the far field pulses obtained by Kostrov (1970) and Dahlen (1974) (except again for the multiplicative function $C'(v/\beta)$ which in Sato and Hirasawa's model takes the value $C'(0) = \left(24/7\pi\right)$).

Since we are interested in modelling acceleration spectra, we differentiate the displacement waveform twice to obtain the acceleration waveform. Taking the Fourier transform of the latter and multiplying it with appropriate factors to account for geometric spreading, we obtain the closed form expression for $G_o(\omega)$ that we are looking for.

More explicitly, the derivation is as follows:

We consider two cases: (1) $\theta \neq 0$ ($\leftrightarrow k \neq 0$) and (2) $\theta = 0$ ($\leftrightarrow k = 0$).

(1) $\theta \neq 0 \leftrightarrow k \neq 0$

$$\text{For } 0 < x < 1 - k \leftrightarrow 0 < t < \frac{\rho_o}{v}(1-k) + \frac{r_o}{c}$$

Velocity waveform:

$$\frac{d\Omega}{dt} = 2Kv\rho_o^2 \cdot \frac{\pi}{(1-k^2)^2} \cdot 2x \cdot \frac{v}{\rho_o}$$

Acceleration waveform:

$$\frac{d^2\Omega}{dt^2} = 2Kv\rho_o^2 \cdot \frac{\pi}{(1-k^2)^2} \cdot 2 \cdot \left(\frac{v}{\rho_o}\right)^2 \tag{31a}$$

$$\text{For } 1 - k < x < 1 + k \leftrightarrow \frac{\rho_o}{v}(1-k) + \frac{r_o}{c} < t < \frac{\rho_o}{v}(1+k) + \frac{r_o}{c}$$

Velocity waveform:

$$\frac{d\Omega}{dt} = 2Kv\rho_o^2 \cdot \left(\frac{\pi}{4}\right) \cdot \frac{-2x}{k(1+k)^2} \cdot \frac{v}{\rho_o}$$

Acceleration waveform:

$$\frac{d^2\Omega}{dt^2} = 2Kv\rho_o^2 \cdot \left(\frac{\pi}{4}\right) \cdot \frac{-2}{k(1+k)^2} \cdot \left(\frac{v}{\rho_o}\right)^2 \tag{31b}$$

Let

$$t_1 = \frac{\rho_o}{v}(1-k) + \frac{r_o}{c} \tag{32a}$$

$$t_2 = \frac{\rho_o}{v}(1+k) + \frac{r_o}{c} \tag{32b}$$

Then at $t = t_1$ and $t = t_2$ we obtain the following delta function contributions to the acceleration waveform due to jump discontinuities of the velocity waveform at these points:

At $t = t_1$:

$$\left.\frac{d^2\Omega}{dt^2}\right|_{t=t_1} = -Kv^2\rho_o\pi \cdot \frac{\delta(t-t_1)}{k(1-k)} \tag{33a}$$

At $t = t_2$:

$$\left.\frac{d^2\Omega}{dt^2}\right|_{t=t_2} = Kv^2\rho_o\pi \cdot \frac{\delta(t-t_2)}{k(1+k)} \tag{33b}$$

The displacement, velocity and acceleration waveforms are shown in Fig. 6.

In order to compute the Fourier transform of the acceleration waveform we shift the origin of time axis by r_o/v (i.e., the time it takes for the signal to travel from the fault to the receiver) so that it coincides with the beginning of the signal.

We redefine t_1 and t_2 as

$$t_1 = \frac{\rho_o}{v}(1-k) \tag{34a}$$

$$t_2 = \frac{\rho_o}{v}(1+k) \tag{34b}$$

Let:

$$a_1 = 4Kv^3 \cdot \frac{\pi}{(1-k^2)^2} \tag{35a}$$

$$a_2 = Kv^3 \cdot \frac{\pi}{k(1+k)^2} \tag{35b}$$

These are the heights of the pulses of the acceleration waveform (Fig. 6).

Then:

$$A(\omega) = \int \frac{d^2\Omega}{dt^2} e^{-i\omega t}\, dt \quad .$$

$$= a_1 \int_o^{t_1} e^{-i\omega t}\, dt - a_2 \int_{t_1}^{t_2} e^{-i\omega t} dt - (a_1 + a_2)t_1\, e^{-i\omega t_1} + a_2 t_2\, e^{-i\omega t_2}$$

where the terms $-(a_1+a_2)t_1e^{-i\omega t_1}$ and $a_2t_2e^{-i\omega t_2}$ come from the contributions of the delta functions at t_1 and t_2 respectively (Fig. 6). Performing the integration and after rearranging terms we obtain:

$$A(\omega) = e^{-\frac{i\omega t_1}{2}}\left[a_1 t_1 \frac{2\cdot\sin(\frac{\omega t_1}{2})}{\omega t_1} - a_2(t_2-t_1)\frac{2\sin(\frac{\omega(t_2-t_1)}{2})}{\omega(t_2-t_1)} e^{-\frac{i\omega t_2}{2}}\right.$$

$$\left. - (a_1 + a_2)t_1 e^{-\frac{i\omega t_1}{2}} + a_2 t_2 e^{-i\omega(t_2 - \frac{t_1}{2})}\right] \qquad (36)$$

Let:

$$X = \frac{\omega t_1}{2} \qquad (37a)$$

$$Y = \frac{\omega(t_2 - t_1)}{2} \qquad (37b)$$

Then: $|A(\omega)|^2 =$

$$= \left[a_1 t_1 \frac{\sin X}{X} - a_2(t_2 - t_1)\cdot\frac{\sin Y}{Y}\cdot\cos\frac{\omega t_2}{2}\right.$$

$$\left. - (a_1 + a_2)t_1\cdot\cos\frac{\omega t_1}{2} + a_2 t_2\cdot\cos(\omega t_2 - \frac{\omega t_1}{2})\right]^2$$

$$+ \left[a_2(t_2 - t_1)\cdot\frac{\sin Y}{Y}\cdot\sin\frac{\omega t_2}{2} + (a_1 + a_2)t_1\cdot\sin\frac{\omega t_1}{2}\right.$$

$$\left. - a_2 t_2\cdot\sin(\omega t_2 - \frac{\omega t_1}{2})\right]^2 \qquad (38)$$

(2) $\theta = 0 \rightarrow k = 0$

In this case t_1 and t_2 coincide, causing a step discontinuity in the displacement waveform at $t=t_1=t_2$ and consequently a delta function and a doublet to the velocity and acceleration waveforms respectively as shown in Fig. 7.

Then, $A(\omega) = \int \frac{d^2\Omega}{dt^2}\cdot e^{-i\omega t}\,dt$

$$= a_1\int_0^{t_1} e^{-i\omega t}dt - a_1 t_1\cdot e^{-i\omega t_1} - i\omega e^{-i\omega t_1}\cdot a_1 t_1\frac{t_1}{2}$$

$$= a_1 t_1\cdot\frac{\sin X}{X}\cdot e^{-\frac{i\omega t_1}{2}} - a_1 t_1 e^{-i\omega t_1} - \omega a_1 t_1\frac{t_1}{2} e^{-i(\omega t_1 - \frac{\pi}{2})}$$

$$= e^{-\frac{i\omega t_1}{2}} a_1 t_1\left[\frac{\sin X}{X} - e^{-\frac{i\omega t_1}{2}} - \omega\frac{t_1}{2}\cdot e^{-i(\frac{\omega t_1}{2} - \frac{\pi}{2})}\right] \qquad (39)$$

Therefore: $|A(\omega)|^2 =$

$$= (a_1 t_1)^2 \cdot \left[\frac{\sin X}{X} - \cos\frac{\omega t_1}{2} - \frac{\omega t_1}{2} \cdot \sin\frac{\omega t_1}{2}\right]^2$$

$$+ (a_1 t_1)^2 \cdot \left[\sin\frac{\omega t_1}{2} - \frac{\omega t_1}{2} \cdot \cos\frac{\omega t_1}{2}\right]^2$$

$$= (a_1 t_1)^2 \cdot \left[\left(\frac{\sin X}{X}\right)^2 + 1 + \left(\frac{\omega t_1}{2}\right)^2 - 2\left(\frac{\sin X}{X}\right)\cos\frac{\omega t_1}{2}\right.$$

$$\left. - 2\left(\frac{\sin X}{X}\right) \cdot \frac{\omega t_1}{2} \cdot \sin\frac{\omega t_1}{2}\right] \qquad (40)$$

This result could have been obtained also from eq. 38, derived for the case $\theta \neq 0 (\leftrightarrow k \neq 0)$ by expanding the squares and taking the limit of $|A(\omega)|^2$ as $k \to 0$.

The amplitude $|A(\omega)|$, normalized w.r.t. $\pi K v^2 \rho_o$ is plotted versus the normalized frequency $(\rho_o/v)\omega$ in Figs. 8 and 9 for various azimuthal angles. The general shape of acceleration spectra described above applies for all azimuthal angles except for $\theta = 0$. For this case, i.e., for all observation points lying on the axis which is vertical to the plane of the circular crack at its center, the acceleration waveform has a doublet singularity and the spectral amplitudes exhibit a linear increase as shown in Fig. 9. Since only two points on the focal sphere exhibit such singular behavior, this particular case will not be considered any further. In addition, such singularities can be discounted on physical grounds by arguing that seismic rays are bent and scattered in the heterogenous earth and focusing effects such as this are substantially diminished.

The spectra for all azimuthal directions other than $\theta = 0$ exhibit a periodic oscillatory behavior. Consider eq. 38. Then the asymptotic form of $|A(\omega)|^2$ for large ω is given by

$$|A(\omega)|^2 \underset{(\omega\to\infty)}{\sim} \left[(a_1 + a_2)t_1 \cdot \cos\frac{\omega t_1}{2} - a_2 t_2 \cdot \cos\left(\omega t_2 - \frac{\omega t_1}{2}\right)\right]^2$$

$$+ \left[(a_1 + a_2)t_1 \cdot \sin\frac{\omega t_1}{2} - a_2 t_2 \cdot \sin\left(\omega t_2 - \frac{\omega t_1}{2}\right)\right]^2 \qquad (41)$$

because

$$\lim_{(\omega\to\infty)} \frac{\sin X}{X} = 0 \quad \text{and} \quad \lim_{(\omega\to\infty)} \frac{\sin Y}{Y} = 0 \ .$$

Expanding the square and combining terms in eq. 41 we obtain

$$|A(\omega)|^2 \sim (a_1 + a_2)^2 t_1^2 + (a_2 t_2)^2$$

$$-2(a_1 + a_2)t_1 a_2 t_2 \cos(\omega(t_2 - t_1)) \qquad (42)$$

Eq. 42 reveals that the periodic behavior of the spectra is due to the $\cos(\omega(t_2 - t_1))$ factor. The asymptotic expression of $|A(\omega)|^2$ for $\omega \to \infty$ (eq. 42) attains its minimum value when $\cos(\omega(t_2 - t_1)) = 1$ (valleys of the spectra) and its maximum value when $\cos(\omega(t_2 - t_1)) = -1$ (ridges of the spectra).

The period of the oscillation (i.e., the width of each lobe at the limit as $\omega \to \infty$ and $k \to 0$) is equal to $\frac{2\pi}{(t_2-t_1)} \cdot \frac{\rho_o}{v} = \frac{\pi}{k}$ (in terms of the normalized frequency). But (t_2-t_1) happens to be the time interval between the two impulses of the acceleration waveform. Substituting in (t_2-t_1) the expressions of t_1 and t_2 given by eqs. 34a and 34b, we obtain

$$\begin{aligned} t_2 - t_1 &= \frac{\rho_o}{v}(1+k) - \frac{\rho_o}{v}(1-k) \\ &= \frac{\rho_o}{v} \cdot 2k \\ &= 2 \cdot \frac{\rho_o \sin\theta}{c} \end{aligned} \tag{43}$$

An interpretation of this expression of (t_2-t_1) in terms of the geometry of the circular crack (Fig. 4) reveals that the two impulses originated from the two ends of the diameter S_1S_2 of the circular crack. This diameter is defined by the intersection of the plane of the crack and the plane that is defined by the axis AA' (Fig. 4) which is vertical to the plane of the crack at its center and by the point of observation.

The two impulses are called stopping phases because they are emitted when the crack stops expanding. These impulses are responsible for the flatness of the acceleration spectra at high frequencies (Fig. 8). The beating or holes of the spectra arise from the interference of the two stopping phases which arrive with a time difference (t_2-t_1) between them. Madariaga (1976) observed that the spectra which he obtained with his numerical solution exhibited the same oscillatory behavior, and he correctly attributed it to the interference of the stopping phases.

It is interesting to notice that all these observations are in complete agreement with the results which Madariaga (1977, 1979) obtained in his theoretical study of the high frequency radiation from crack models of faulting. He studied the starting and stopping phases of antiplane and plane cracks and he extended his analysis to three dimensional cracks and in particular circular cracks. He concluded that in the latter case the radiation of high frequencies is entirely controlled by the stopping phases, and he found that his theoretical predictions (Madariaga, 1977) are in excellent agreement with his numerical solution (Madariaga, 1976) for the range of frequencies for which the numerical solution is valid. As he points out, a circular crack which expands with constant rupture velocity and stops abruptly, from the point of view of high frequencies (i.e. frequencies with wavelengths shorter than the radius of the crack), it appears as a circular line source which coincides with the edge of the crack.

To demonstrate this we consider the starting phase given by eq. 28a. This has a displacement spectrum given by (Kostrov, 1970; Dahlen, 1974)

$$\underset{\sim}{\tilde{\Omega}}(x,\omega) = \frac{\Delta\sigma}{\mu} \cdot v^3 \cdot \frac{4\pi \cdot C'\left(\frac{v}{\beta}\right)}{(1-k^2)^2} \cdot (i\omega)^{-3} \tag{44}$$

where again the constant $(24/7\pi)$ has been replaced by $C'(v/\beta)$. Therefore, the acceleration spectrum of the starting phase which is given by $\tilde{\Omega}(\underset{\sim}{x},\omega) \cdot \omega^2$ has a frequency dependence of the ω^{-1} type as opposed to the stopping phases which have a flat acceleration spectrum (i.e. ω^0). Thus the stopping phases

control the high frequency spectrum. This is apparent also from the asymptotic expression of $|A(\omega)|^2$ as $\omega \to \infty$ (eq. 42), which (except for the cosine term that accounts for the interference of the stopping phases as discussed above) gives $|A(\omega)|^2$ only as the sum of the squares of the intensities $(a_1+a_2)t_1$ and a_2t_2 of the two stopping phases at t_1 and t_2 respectively.

Furthermore it is interesting to compare the intensity of the stopping phases of Sato and Hirasawa's (1973) model with those obtained by Madariaga (1977). For Sato and Hirasawa's model the intensities of the stopping phases (eqs. 33a,b) are given by

$$(a_1 + a_2)t_1 = \frac{\Delta\sigma}{\mu} v^2 \cdot \rho_o \cdot \pi \cdot \frac{\left(\frac{24}{7\pi}\right)}{k(1 - k)} \tag{45a}$$

and

$$a_2 t_2 = \frac{\Delta\sigma}{\mu} v^2 \cdot \rho_o \cdot \pi \cdot \frac{\left(\frac{24}{7\pi}\right)}{k(1 + k)} \tag{45b}$$

The corresponding intensities of stopping phases obtained by Madariaga's (1977) analytical study are given by

$$\frac{\Delta\sigma}{\mu} \cdot v^2 \cdot \rho_o \cdot \pi \cdot \frac{4k_i^* \cdot \left(\frac{c}{v}\right)^{1/2} \cdot |F_i(\psi)|}{(1 - k) \cdot k^{1/2}} \qquad \text{with} \quad \psi = \pi/2 - \theta \tag{46a}$$

$$\frac{\Delta\sigma}{\mu} \cdot v^2 \cdot \rho_o \cdot \pi \cdot \frac{4k_i^* \cdot \left(\frac{c}{v}\right)^{1/2} \cdot |F_i(\psi)|}{(1 + k) \cdot k^{1/2}} \qquad \text{with} \quad \psi = \pi/2 + \theta \tag{46b}$$

where i indicates P, SV or SH waves, $k_i^* \simeq 0.5$, and $|F_i(\psi)|$ are smooth functions close to one except for a small range of the azimuthal angle ψ as discussed in detail by Madariaga (1977, 1979).

It should be apparent that eqs. 45a,b and eqs. 46a,b are identical except for the multiplicative factors which account for directivity effects.

We are interested in scaling the flat part of the acceleration spectrum described at the beginning of the paper, and we assume that the stopping phases arrive incoherently. Therefore we consider the mean square of the spectra of the two stopping phases and, averaging over the focal sphere as shown in the Appendix, we obtain

$$\langle A_o \rangle = 2\pi K v^2 \rho_o \cdot (\text{factor}) \tag{47}$$

where the angle brackets stand for the averaging over the focal sphere and (factor) is given by eq. (A.3) of the Appendix.

Considering S waves (i.e., $c = \beta$) and an elastic, isotropic, homogeneous, unbounded medium through which they propagate, we obtain the following expression for the amplitude of the far-field Fourier spectrum of acceleration $|G_o(\omega)|$ radiated by a single crack

$$|G_o(\omega)| = \frac{(F^S)}{4\pi\beta r_o} \cdot \langle A_o \rangle \quad . \tag{48}$$

Finally we need to express the rate n (average number of cracks that fracture per unit time) in terms of the five parameters of the barrier model. We imagine the cracks having the same radius ρ_o and uniformly distributed on the fault plane as shown in Fig. 10. Then as the rupture front propagates

with average rupture velocity V (sweeping velocity) along the fault length L we get

$$N_W = \frac{W}{2\rho_o} \qquad \text{cracks per width}$$

$$N_L = \frac{1}{2\rho_o} \qquad \text{cracks per unit length}$$

$$V = \qquad \text{length traveled by rupture front per unit time}$$

Then $$n = N_W \cdot N_L \cdot V = \frac{WV}{4\rho_o^2} \quad . \tag{49}$$

Therefore considering eq. 22 and substituting the expressions for $|G_o(\omega)|$ (eq. 48) and n (eq. 49) and using eq. 47 we obtain

$$P_o = P(\omega) = n|G_o(\omega)|^2$$

$$= \frac{WV}{4\rho_o^2} \cdot \left(\frac{(F^S)^2}{4\pi\beta r_o}\right) \cdot (2\pi K v^2 \rho_o)^2 \cdot (\text{factor})^2$$

$$= (\text{factor})^2 \cdot W \cdot V \cdot v^4 \cdot (\pi K)^2 \cdot \left(\frac{(F^S)}{4\pi\beta r_o}\right)^2 \quad . \tag{50}$$

It should be noted that the average rupture velocity V (sweeping velocity) with which the rupture front propagates sweeping the fault surface, may be different than the rupture velocity v (spreading velocity) with which the individual circular cracks expand. It can be argued that the sweeping velocity V is controlled by the spacial distribution of the barriers which are effective for a specific event. The distribution of barriers which are effective may be different for events of different sizes, and is expected to be different for various tectonic regions. On the other hand, the spreading velocity v is controlled primarily by the local stress drop. If the local stress drop is approximately constant for a given tectonic region, then the ratio of the spreading velocity v over the shear wave velocity β is expected to be constant.

From eq. 23 the maximum slip Δu_{max} is given by

$$\Delta u_{max} = K\rho_o \quad . \tag{51}$$

and the average slip $\overline{\Delta u}$ over the crack surface is

$$\overline{\Delta u} = \frac{2}{3} \Delta u_{max} \quad . \tag{52}$$

Substituting in eq. 51 the expression of K in terms of $\Delta\sigma$ (eq. 24) we obtain

$$\frac{\Delta u_{max}}{\rho_o} = \left(\frac{24}{7\pi}\right)\left(\frac{\Delta\sigma}{\mu}\right) \quad . \tag{53}$$

Since $\Delta\sigma$ is interpreted as the representative local stress drop, the ratio $\Delta u_{max}/\rho_o$ can be interpreted as the representative local strain drop. Substituting K in eq. 50 in terms of Δu_{max} and ρ_o from eq. 51 we get

$$P_o \simeq (\text{factor})^2 \cdot W \cdot V \cdot v^5 \cdot \left(\pi \cdot \frac{\Delta u_{max}}{\rho_o}\right)^2 \cdot \left(\frac{(F^S)}{4\pi\beta r_o}\right)^2 \tag{54}$$

Interpreting the diameter $2\rho_o$ as the barrier interval, eq. 54 allows us to infer the barrier interval from observed power spectra and maximum slip, or for given estimates of the barrier interval and maximum slip to predict the flat part P_o of power spectra at any distance r_o from the source. Interestingly enough P_o does not depend directly on the barrier interval $2\rho_o$ but on the local strain drop $\Delta u_{max}/\rho_o$ which was found to increase slightly (factor of 2) with earthquake size for a wide range of magnitudes ($5 \leq M \leq 8$) (Aki et al., 1977; Papageorgiou and Aki, 1981).

To infer the barrier interval by fitting eq. 54 to observed spectra, one could use a maximum slip consistent with the distribution of the localized cracks on the fault plane that was proposed above. Such a maximum slip is obtained by equating the sum of the seismic moments of the individual cracks to the total seismic moment

$$\text{i.e.} \qquad \sum_{i}^{N} M_{oi} = M_o^T \,, \tag{55}$$

where

$$N = \frac{W}{2\rho_o} \cdot \frac{L}{2\rho_o} = \frac{WL}{4\rho_o^2} \qquad \text{total number of cracks on the fault plane} \tag{56}$$

The seismic moment of the individual crack is given by

$$M_{o_i} = \mu \cdot \overline{\Delta u_i} \cdot (\pi \rho_o^2)_i \tag{57}$$

Using the assumption that the cracks are of equal dimensions and with equal slip, and eqs. 55, 56 and 57, we obtain

$$\overline{\Delta u'} = \frac{M_o^T}{\frac{\pi}{4} \cdot \mu \cdot S} \tag{58}$$

and therefore

$$\Delta u'_{max} = \frac{M_o^T}{\frac{\pi}{6} \cdot \mu \cdot S} \tag{59}$$

where the prime indicates slip related to the barrier model (Fig. 10), and S is the area of the fault plane. If the stress were assumed to be uniform over the entire fault plane causing an average slip $\overline{\Delta u}$, then $M_o T$ would be given by

$$M_o^T = \mu \cdot \overline{\Delta u} \cdot S \tag{60}$$

From eqs. 58 and 60 we deduce that

$$\overline{\Delta u'} = \frac{4}{\pi} \overline{\Delta u} \tag{61}$$

The difference between $\Delta u'$ and Δu arises from the fact that for a fault with barriers only certain percentage of the total surface area S of the fault slips and in order to release the same seismic moment it is necessary to have a higher slip. This percentage of the total area S in the case of equidimensional circular cracks distributed uniformly on the fault plane as shown in Fig. 10, is equal to $(\pi/4)$.

This reasoning has been used by Aki (1979) in the case of the Parkfield earthquake of 1966, to resolve the outstanding disparity between the seismic moment determined from long-period surface waves and that determined from the aftershock area times the slip estimated from near-source measurements, the latter being larger from the former by a factor of about 3. Aki (1979) concluded that this disparity can be resolved by the barrier model of Fig. 3, because as can be seen in that figure the actually slipped area (regions with no aftershocks) may be one half to one third of the total aftershock area.

Similarly, we can obtain an estimate of the total seismic energy E_s radiated by the fault by summing up the seismic energies E_{s_i} radiated from each individual crack.

The seismic energy E_{s_i} radiated from an individual crack is given (Sato and Hirasawa, 1973) by

$$E_{s_i} = \frac{C'(\frac{v}{\beta})}{16} \cdot \frac{\Delta\sigma . M_{o_i}}{\mu} \cdot \left((\frac{\beta}{\alpha})^2 f(\frac{v}{\alpha}) + g(\frac{v}{\beta})\right) \tag{62}$$

where

$$f(\frac{v}{\alpha}) = \int_0^{\pi/2} \frac{8\sin^2\theta \cdot (1 - \sin^2\theta) \cdot (3\frac{\alpha}{v} - \sin\theta)}{(\frac{\alpha}{v} - \sin\theta) \cdot (\frac{\alpha}{v} + \sin\theta)^2} \, d\theta$$

$$g(\frac{v}{\beta}) = \int_0^{\pi/2} \frac{2(4\sin^4\theta \cdot 5\sin^2\theta + 2) \cdot (3\frac{\beta}{v} - \sin\theta)}{(\frac{\beta}{v} - \sin\theta) \cdot (\frac{\beta}{v} + \sin\theta)^2} \, d\theta$$

α = P-wave velocity, β = S-wave velocity.

For $\alpha=\sqrt{3}\beta$ (i.e., Poisson's ratio equal to 1/4) and $v/\beta = 0.75$ we obtain $(\beta/\alpha)^2 f(v/\beta) + g(v/\beta) = 4.72$ and $C'(v/\beta = 0.75) = 0.94$.

The total seismic energy E_s radiated from the entire fault is given by

$$\begin{aligned} E_s &= \sum_i E_{s_i} \\ &= \frac{3}{14\pi} \cdot \left((\frac{\beta}{\alpha})^2 f(\frac{v}{\alpha}) + g(\frac{v}{\beta})\right) \frac{\Delta\sigma \cdot \sum_i M_{o_i}}{\mu} \\ &= 0.46 \cdot 1/2 \cdot M_o^T \cdot (\frac{\Delta\sigma}{\mu}) \end{aligned} \tag{63}$$

An estimate of E_{s_i} (and therefore of E_s) may be obtained also from Madariaga's results (Madariaga, 1976, eqs. 30 and 32) which were derived from Kostrov's (1974) representations of radiated energy in terms of fault surface traction and particle velocity as opposed to eq. 62 which was derived from the far-field particle velocities. Both approaches to estimating the seismic far-field particle energy are equivalent and give identical results if in Madariaga's model the effective stress (i.e., the stress drop from a constant initial prestress to the kinetic frictional stress) is assumed to be equal to the final static stress drop (i.e., if overshoot is neglected).

Finally, expressing K in eq. 50 in terms of $\Delta\sigma$ using eq. 24 we obtain

$$P_o \simeq (\text{factor})^2 \cdot W \cdot V \cdot v^4 \cdot \left(\pi \cdot \frac{24}{7\pi} \cdot \frac{\Delta\sigma}{\mu}\right)^2 \cdot \left(\frac{(F^S)}{4\pi\beta r_o}\right)^2 \qquad (64a)$$

For $(v/\beta) = 0.86$ and assuming $V=v$, eq. 64a gives

$$P_o \simeq (0.61)^2 \cdot W \cdot \frac{\Delta\sigma^2}{\beta\rho^2} \cdot \frac{(F^S)^2}{r_o^2} \quad , \qquad (64b)$$

which is identical in form to eq. 14 obtained from Hanks' model except that the characteristic dimension of the fault in eq. 64a,b is the width W of the fault instead of the radius R of the equivalent circular crack that represents the entire source in Hanks' model. The important difference in the two expressions lies in the interpretation of $\Delta\sigma$ as it has already been discussed. $\Delta\sigma$ in the specific barrier model developed in this paper represents the local stress drop and may be obtained from the barrier interval and maximum slip using eq. 53, or directly from the value P_o of observed acceleration power spectra of direct S-waves at the source using eq. 64a. It should be emphasized that the local stress drop $\Delta\sigma$ is related to P_o (eq. 64a) and therefore it is not advisable for its inference to use a_{rms} (eq. 15) for which there may be a trade off between P_o and $\Delta f(\simeq f_{max})$ that cannot be resolved by considering only a_{rms}.

The idea on which this specific barrier model is based, i.e. that the strong motion observed at a station is considered to be composed of a random superposition of signals which are assumed to be generated by the stationary occurrence of localized ruptures (subevents) on the fault, is implicit in the work of various investigators who treated the ground acceleration as shot noise (in the limit white noise). Reasoning that seismic waves are initiated by irregular slippage along faults followed by numerous random reflections, refractions and attenuations along the propagation path, various investigators (e.g. Housner, 1947, 1955; Hudson, 1956; Bycroft, 1960; Housner and Jennings, 1964; Jennings et al., 1968) developed stochastic models for the ground motion that were used for the analysis of existing accelerograms or for the computation of synthetic ones. Also studies based on the idea that an event can be considered to be composed of multiple subevents have a long history (Stoneley, 1937; Usami, 1956; Wyss and Brune, 1967; Trifunac and Brune, 1970; Kanamori and Stewart, 1978; Boore et al., 1978; Savy, 1979; Kanamori, 1979).

In order to obtain a rough estimate of a_{rms} using the source model which we developed, we need to define an effective bandwidth Δf or, as we did in connection with Hanks' model, we need to specify a cutoff frequency f_{max}. Let us assume that the cutoff frequency f_{max} is primarily a source effect and not, as argued by Hanks, so much a propagation effect. Then we have to express f_{max} in terms of the fundamental source parameters introduced so far. For that purpose we follow the approach adopted by Aki (1979) who discussed rupture in terms of fracture mechanics concepts.

Let us first state briefly a few fundamental results of the theory of elastic shear crack mechanics pertinent to earthquake rupture (e.g. Freund, 1979; Rice, 1980; Aki and Richards, 1980).

By an elastic shear crack model we understand a model of a crack which is based on two important assumptions: (1) the material outside the crack remains ideally elastic, even near the crack tip and (2) there is an abrupt drop in stress to the dynamic frictional stress immediately behind the crack tip as the cracked region enters into intact material (Fig. 11). These

assumptions lead to stress and strain singularities in the elastic field in front of the crack tip (Fig. 11), as well as to singularities in the slip velocity behind the crack tip. The intensity of the stress singularity is measured by the stress intensity factor K.

Madariaga (1977) demonstrated that the phases which control the high frequency content of the spectrum radiated by the crack, originate from these singularities and are emitted only when there is an abrupt change in rupture velocity. It can be demonstrated, in the context of elastic shear crack theory, that such abrupt changes in rupture velocity occur due to changes of the fracture energy on the fault plane.

Two factors can affect the efficient radiation of high frequencies: (1) the smooth change of fracture energy over regions of the fault plane with dimensions equal or larger than the wavelengths of the frequencies under consideration, and, (2) the existence of a zone of cohesive forces behind the crack tip that removes the stress singularity. This zone is used to model the breakdown process (e.g., small-scale local yielding, microcrack formation, etc.) that takes place over a zone of finite area at the circumference of the crack.

Cohesive zone models have been proposed for a variety of physical processes (e.g., Barenblat, 1959). The most realistic cohesive zone model for a number of geophysical applications is the so-called slip weakening model. According to this model in the simplest case slippage is modelled as rate insensitive. The strength of the fault zone reaches a peak σ_u which corresponds to the onset of slipping for fresh fractures or it is preceded by slip at lower stresses for preexisting faults. The stress to maintain slippage reduces as the amount of slip increases up to a critical amount D, above which the stress to maintain slippage remains constant, equal to the dynamic friction σ_f. Such a constitutive law of the fault gouge is depicted in Fig. 12. The crosshatched area shown in Fig. 12 represents the energy per unit area of crack absorbed at the crack tip by the breakdown process. The region of the crack near the tip where the applied stress is greater than the frictional stress is the cohesive zone. Due to the finite strength of the material which is depicted by the constitutive law, the stress singularity and the slip distribution shown in Fig. 11 have been replaced by a continuous stress distribution and a smooth slip distribution respectively, shown in Fig. 12.

Following Aki (1979), we will assume that the arrest of the expansion of the circular cracks is due to an increase of the fracture energy. Assuming the existence of a cohesive zone at the crack tip, the impulses which are emitted at the instant of rupture arrest (stopping phases) are smoothed.

Aki (1979) used results of fracture mechanics and the slip weakening model to describe quantitatively the arrest of rupture. The various parameters of the problem are related by the following equations:

$$G = \frac{2\sigma^2 d}{\mu\pi C} \tag{65}$$

$$G = \frac{\sigma_c \cdot D}{2} \tag{66}$$

$$G = \frac{(\Delta\sigma)^2 \cdot \rho_o}{\mu\pi C} \tag{67}$$

where:

G = fracture energy per unit area of created new free surface. It represents the fracture energy of the barrier which is necessary to arrest the propagation of rupture of the crack.

d = size of the cohesive zone. It represents the length of the non-elastic zone over which rupture is arrested.

σ_c = average cohesive force distributed on the cohesive zone. It represents the stress necessary to break the barrier. It can also be interpreted as the dynamic stress drop which accelerates the two sides of the crack near the crack tip.

D = average slip in the cohesive zone. It represents the average slip that occurs in the cohesive zone, which is required to break the bond completely.

ρ_o = radius of circular crack

$\Delta\sigma$ = stress drop in the crack

C = constant of order one

We assume that an estimate of f_{max} is given by

$$f_{max} \simeq v/d. \tag{68}$$

The details of the deceleration of the rupture front and the existence of a cohesive zone at the crack tip have an important effect on the generation of waves with frequencies higher than f_{max}. Achenbach and Harris (1978) studied cracks with curvilinear wavefronts which propagate intermittently (i.e. with discrete jumps of the rupture velocity) but with the presence of a cohesive zone at the crack tip. In this case the slip just behind the rupture front is generally described by $C\eta^{\kappa/2}$ (with $\kappa \geq 1$) where η is the distance from the rupture front and κ is a parameter which controls the shape of the slip curve just behind the rupture front. For $\kappa=1$ we obtain the case of brittle fracture (i.e. no cohesive zone present at the crack tip). The acceleration amplitude spectra of the stopping phases are $O(\omega^{-(\kappa-1)/2})$. Therefore the rate of decrease of observed spectra above f_{max} can be used to infer κ.

These results may be used to describe quantitatively the barriers which arrest the localized ruptures.

From eq. 68 it is apparent that the cut off frequency f_{max} varies inversely proportionally with the size of the cohesive zone d. It is necessary therefore to have an estimate of the parameter d of an expected event on a given fault, which together with the five parameters of the barrier model provide a complete description of the acceleration power spectrum at the source. In order to obtain a reliable estimate of the power spectrum of strong ground motion at any site in the vicinity of a potential source it is necessary to know the attenuation characteristics (Q-structure) of the earth medium surrounding the source. The latter can be effectively obtained using the coda method and the S to coda ratio method (Aki, 1969; Aki and Chouet, 1975; Aki, 1980b,c).

The power spectrum of acceleration at a site, combined with an estimate of the duration of the strong part of ground motion (direct S-waves) which may

be assumed to be roughly equal to the duration of faulting, can be used to obtain estimates of a_{rms} and a_{max} which are important parameters for the earthquake resistant design of structures.

At the far field, ground motion may safely be considered to be in general (although there may be exceptions) band-limited, Gaussian, white noise. This is attributed primarily to the inhomogeneity of the source and is enhanced by the inhomogeneous medium. In this case a_{max} can be reliably interpreted as the expected peak amplitude of a stationary process over a finite time interval equal to the faulting duration. On the contrary a_{max} at a site close to the fault may arise from a single crack (probably the nearest one to the station) and therefore may be directly related to the dynamic stress drop σ_c (Aki, 1979). Estimates of peak velocity and acceleration on or near the fault may be obtained by (Ida, 1973),

$$\dot{u}_{max} \sim \frac{\sigma_c}{\mu} v \tag{69}$$

$$\ddot{u}_{max} \sim \left(\frac{\sigma_c}{\mu} v\right)^2 \cdot \frac{1}{D} \tag{70}$$

based on estimates of σ_c, and D. If the values of σ_c and D are based on estimates of ρ_o and $\Delta\sigma$ (eqs. 65 to 67) which are obtained by fitting the specific barrier model to strong motion observation as described above, then they should be interpreted as average values over the fault surface. Therefore one should expect some scatter of actual observations around estimates of peaks of ground motion near the fault, if these estimates are obtained from eqs. 69 and 70 by making use of the average values of σ_c and D. This scatter would reflect local deviations of the physical properties (such as fracture energy) of the fault from the average values obtained based on estimated effective (average) values of ρ_o and $\Delta\sigma$.

Summary and Conclusion

The specific barrier model developed in this paper provides a versatile way to visualize those aspects of the earthquake rupture process which are responsible for the generation of high frequency waves (i.e. waves with frequencies higher than the corner frequency f_o). It provides a complete framework for modeling and interpreting strong ground motion, and it is an effective tool for estimating important physical properties of the fault.

According to the model, strong ground motion is generated by the random and stationary rupture of localized cracks which are distributed on the fault plane. These cracks represent areas which slip smoothly and which are separated from each other by barriers.

The acceleration power spectra of direct body waves are effectively described by (1) the value P_o of their flat part which characterizes frequencies that are larger than the corner frequency f_o and smaller than a cutoff frequency f_{max} and (2) by an effective bandwidth which is specified by these two characteristic frequencies. According to the specific barrier model, the value P_o of the flat part of the spectra, scales proportionally to the width of the fault and to the square of the local stress drop which is proportional to the ratio of the maximum slip over the barrier interval. This ratio was found to increase slightly (factor of 2) with

earthquake size (Aki et al., 1977; Papageorgiou and Aki, 1981). The cutoff frequency is assumed to originate from non-elasticity of the source during the rupture process, and is inversely proportional to a characteristic length scale which, according to the model, is the size of the cohesive zone which arrests the propagation of rupture of the localized cracks.

By fitting the model to strong ground motion observations, important physical parameters of the source (e.g. barrier interval, local stress drop, cohesive zone size and cohesive stress) may be inferred, and their variation with earthquake size and tectonic region may be investigated. Such parameters will form the data base for prediction of the strong ground motion which would be generated by a fault of a specific tectonic region, if this fault were to break.

Acknowledgement

This work was supported by the National Science Foundation under Grant Nos. PFR 8005720 and PFR 7827068.

Appendix

Consider the two stopping phases (eqs. 45a,b) which are radiated from an individual crack. We assume that these phases arrive incoherently and in order to describe the Fourier amplitude spectrum $|G_o(\omega)|$ at high frequencies we consider the mean square of their spectra. Let:

$$A_o = ((a_1 + a_2)^2 t_1^2 + (a_2 t_2)^2)^{1/2} \tag{A.1}$$

Assuming a random distribution of stations over the focal sphere, then the probability of observing the signal between θ and $\theta + \Delta\theta$ is proportional to $\sin\theta$. Therefore the expected value of A_o can be expressed as

$$\langle Ao \rangle = \frac{\int_o^{\pi/2} A_o \cdot \sin\theta \, d\theta}{\int_o^{\pi/2} \sin\theta \, d\theta} \tag{A.2}$$

$$= 2\pi \cdot K \cdot v^2 \cdot \rho_o \cdot (\text{factor})$$

where: $$(\text{factor}) = \frac{1}{\sqrt{2}} \left(\frac{c}{v}\right) \cdot \int_o^{\pi/2} \frac{(1 + k^2)^{1/2}}{1 - k^2} \, d\theta$$

$$k = \left(\frac{v}{c}\right) \sin\theta$$

(factor) is an increasing function of (v/β) and for $(v/\beta) = 0.6$, 0.75 and 0.9 takes the values 2.54, 2.58 and 3.56 respectively.

It would be physically more appropriate to consider A_o^2 for averaging over the focal sphere but the integral

$$\int_0^{\pi/2} A_o^2 \cdot \sin\theta \cdot d\theta$$

does not converge.

References

Achenbach, J.D., and J.G. Harris (1978). "Ray Method for Elastodynamic Radiation From a Slip Zone of Arbitrary Shape," J. Geophys. Res. (83), 2283-2291.

Aki, K. (1966). "Generation and propagation of G waves from the Niigata earthquake of June 16, 1964," Bull. Earthquake Research Inst., Univ. Tokyo (44), 23-88.

Aki, K. (1967). "Scaling law of seismic spectrum," J. Geophys. Res. (72), 1217-1231.

Aki, K. (1969). "Analysis of the seismic coda of local earthquakes as scattered waves," J. Geophys. Res., (74), 615-631.

Aki, K. (1972). "Earthquake mechanism," Tectonophysics, (13), 423-446.

Aki, K. (1979). "Characterization of barriers on an earthquake fault," J. Geophys. Res. (84), 6140-6148.

Aki, K. (1980a). "Reevaluation of stress drop and seismic energy using a new model of earthquake faulting" in "Mechanisme et Prevision des Seismes," Hommage au pro-fessor Jean Coulomb, Publie sons la direction de Claude J. Allegre, Edition du Centre National de la Recherche Scientifique. Aki, K. (1980b). "Attenuation of shear waves in the lithosphere for frequencies from 0.05 to 25 Hz," Phys. Earth Planet. Interiors (21), 50-60.

Aki, K. (1980c). "Scattering and attenuation of shear waves in the lithosphere," J. Geophys. Res. (85), 6496-6504.

Aki, K., And B. Chouet (1975). "Origin of coda-waves: source, attenuation, and scattering effects," J. Geophys. Res. (80), 3322-3342.

Aki, K., M. Bouchon, B. Chouet, and S. Das (1977). "Quantitative prediction of strong motion for a potential earthquake fault," Annali di Geogisica, Vol. XXX, N. 3-4, 341-368. Aki, K., and P.G. Richards (1980). Quantitative Seismology: Theory and Methods, W.H. Freeman Co.

Barenblat, G.I. (1959). "The formation of equilibrium cracks during brittle fracture: General ideas and hypothesis, axially symmetric cracks," J. Appl. Math. Mech. (23), 434-444.

Boore, D.M., and W.B. Joyner (1978). "The influence of rupture incoherence on seismic directivity," Bull. Seism. Soc. Am. (68), 283-300.

Brune, J.N. (1970). "Tectonic stress and the spectra of seismic shear waves from earthquakes ," J. Geophys. Res. (75), 4997-5009.

Brune, J.N. (1971). "Correction," J. Geophys. Res. (76), 5002.

Burridge, R., and L. Knopoff (1964). "Body force equivalents for seismic dislocations," Bull. Seism. Soc. Am. (54), 1875-1888.

Burridge, R., and Willis, J. (1969). "The self-similar problem of the expanding elliptical crack in an anisotropic solid," Proc. Cambridge Phil. Soc. (66), 443-468. Bycroft, G.N. (1960). "White noise representation of earthquakes," J. Eng. Mech. Div., ASCE (86), 1-16.

Chouet, B., K. Aki, and M. Tsujiura (1978). "Regional variation of the scaling law of earthquake source spectra," Bull. Seismol. Soc. Am. (68), 49-80.

Dahlen, F.A. (1974). "On the ratio of P-wave to S-wave corner frequencies for shallow earthquake sources," Bull. Seismol. Soc. Am. (64), 1159-1180.

Das, S., and K. Aki (1977a). "A numerical study of two-dimensional spontaneous rupture propagation," Geophys. J. Roy. Astron. Soc., 50, 643-668.

Das, S., and K. Aki (1977b). "Fault plane with barriers: A versatile earthquake model," J. Geophys. Res., 82, 5648-5670.

Eaton, J.P. (1967). "Instrumental seismic studies, the Parkfield-Cholame, California earthquakes of June-August 1966," U.S. Geol. Surv. Prof. Pap., 579, 57-65.

Eaton, J.P., M.E. O'Neill, and J.N. Murdock (1970). "Aftershocks of the 1966 Parkfield-Cholame, California earthquake: A detailed study," Bull. Seism. Soc. Am. (60), 1151-1197.

Eshelby, J.D. (1957). "The determination of the elastic field of an ellipsoidal inclusion and related problems," Proc. Roy. Soc. London, A, 241, 376-396.

Freund, L.B. (1979). "The mechanics of dynamic shear crack propagation," J. Geophys. Res. (84), 2199-2209.

Hanks, T.C. (1977). "Earthquake stress drops, ambient tectonic stress, and stresses that drive plate motions," Pure Appl. Geophys. (115), 441-458.

Hanks, T.C. (1979). "b-values and seismic source models: implications for tectonic stress variations along active crustal fault zones and the estimation of high-frequency strong ground motion," J. Geophys. Res. (84), 2235-2242.

Housner, G.W. (1947). "Characteristics of strong-motion earthquakes," Bull. Seism. Soc. Am. (37), 19-31.

Housner, G.W. (1955). "Properties of strong-motion earthquakes," Bull. Seism. Soc. Am. (45), 197-218.

Housner, G.W., and P.C. Jennings (1964). "Generation of artificial earthquakes," J. Eng. Mech. Div., ASCE (90), 113-150.

Hudson, D.E. (1956). "Response spectrum techniques in engineering seismology," Proc. 1st World Conf. on Earthquake Eng., Berkeley, Calif.

Ida, Y., (1973). "The maximum acceleration of seismic ground motion," Bull. Seismol. Soc. Am. (63), 959-968.

Jennings, P.C., G.W. Housner, and N.C. Tsai (1968). "Simulated earthquake motions," Earthquake Eng. Research Lab., Calif. Inst. of Tech., Pasadena.

Kanamori, H. (1977). "The energy release in great earthquakes," J. Geophys. Res. (82), 2981-2987.

Kanamori, H. (1979). "A semi-empirical approach to prediction of long period ground motions from great earthquakes," Bull. Seism. Soc. Am. (69), 1645-1670.

Kanamori, H., and D.L. Anderson (1975). "Theoretical basis for some empirical relations in seismology," Bull. Seism. Soc. Am. (65), 1073-1095.

Keilis-Borok, V.I. (1959). "On the estimation of the displacement in an earthquake source and of source dimensions," Annali di Geofisica (12), 205-214.

Knopoff, L. (1958). "Energy release in earthquakes," Geophys. J. Roy. Astr. Soc. (1), 44-52.

Kostrov, B.V., (1964). "Selfsimilar problems of propagation of shear cracks," J. Appl. Math. Mech. (PMM) (28), 1077-1087.

Kostrov, B.V., (1970). "The theory of the focus for tectonic earthquakes," Izv., Solid Earth Physics (4), 84-101.

Kostrov, B.V. (1974). "Seismic Moment and Energy of Earthquakes and Seismic Flow of Rocks," Izv. Fizika Zemli, 1, 23-40.

Madariaga, R. (1976). "Dynamics of an expanding circular fault," Bull. Seism. Soc. Am. (66), 639-666.

Madariaga, R. (1977). "High frequency radiation from crack (stress drop) models of earthquake faulting," Geophys. J. Roy. Astron. Soc. (51), 625-651.

Madariaga, R. (1979). "Seismic radiation from earthquake models based on fracture mechanics," SIAM-AMS Proceedings Vol. 12, 59-77.

Maruyama, T. (1963). "On force equivalents of dynamic elastic dislocations with reference to the earthquake mechanism," Bull. Earthq. Res. Inst. Univ. Tokyo. (41), 467-486.

Mikumo, T., and T. Miyatake (1978). "Dynamical rupture process on a three-dimensional fault with non-uniform frictions and near field seismic waves," Geophys. J. Roy. Astron. Soc. (54), 417-438.

Mogi, K. (1962). "Study of elastic shocks caused by the fracture of heterogeneous material and its relation to earthquake phenomena," Bull. Earthq. Res. Inst. Tokyo Univ. (40), 125-173.

Papageorgiou, A.S., and K. Aki (1981). "A Specific Barrier Model for the Quantitative Description of Inhomogeneous Faulting and the Prediction of Strong Ground Motion - II. Applications of the Model," Submitted for Publication in Bull. Seismol. Soc. Am.

Rice, J.R. (1980). "The mechanics of earthquake rupture," Proc. Intern. School of Physics "Enrico Fermi," Italian Physical Society, Course LXXVIII (1979, Varenna on Lake Como, Italy) on Physics of the Earth's Interior, edited by E. Boschi and A.M. Dziewonski, North-Holland Publishing Co., 555-649.

Sato, T., and T. Hirasawa (1973). "Body wave spectra from propagating shear cracks," J. Phys. Earth (21), 415-431.

Savy, J. (1979). "Determination of the seismic design parameters: A stochastic approach," Ph.D. Thesis, Stanford University., Stanford, California.

Starr, A.T. (1928). "Slip in a crystal and rupture in a solid due to shear," Proc. Camb. Phil. Soc. (24), 489-500.

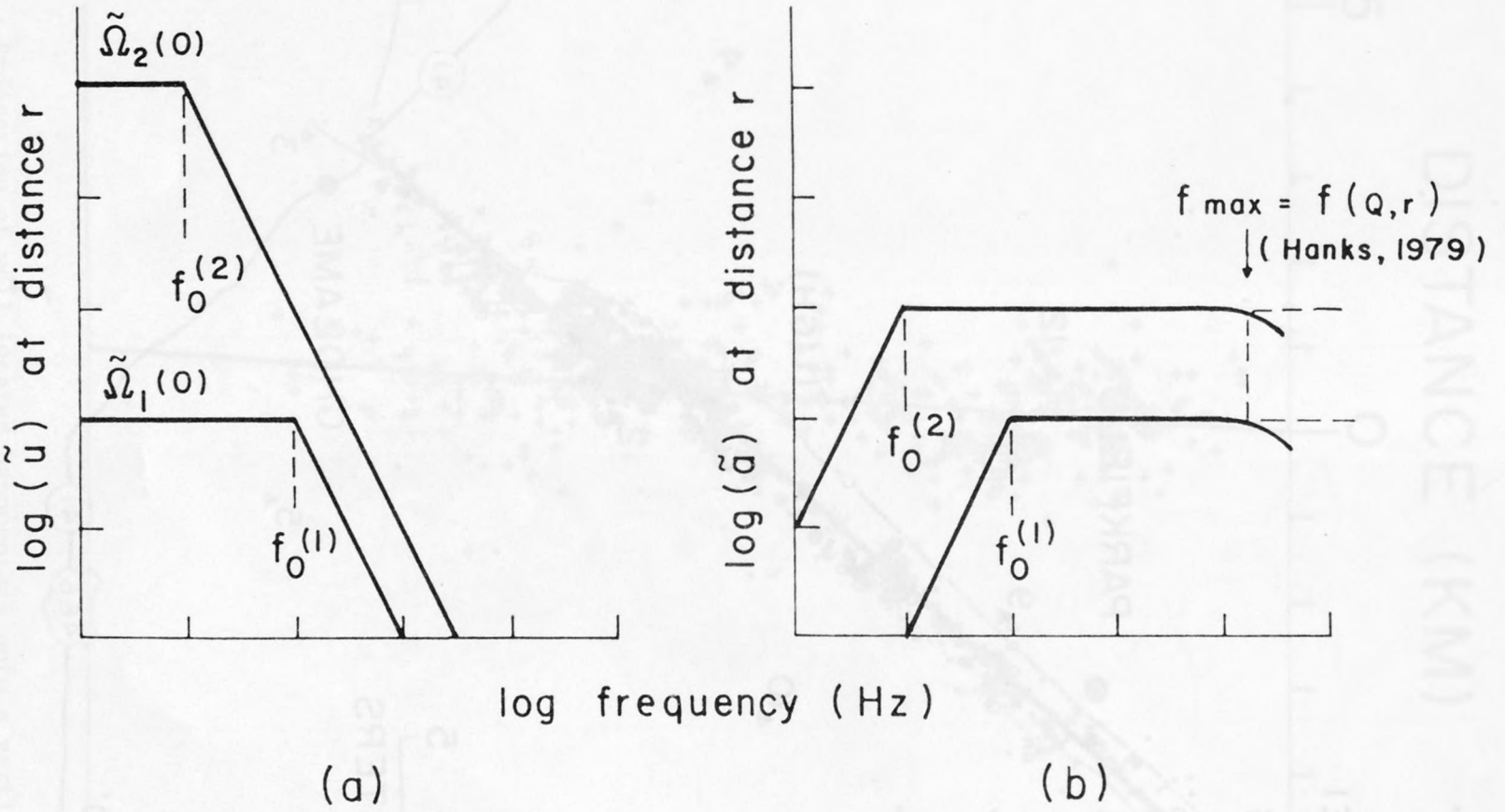

Figure 1. (a) Displacement and (b) acceleration amplitude spectra of the "ω-square" source model for two constant stress drop earthquakes observed at the same distance r_o in an elastic, homogeneous, isotropic, unbounded medium.

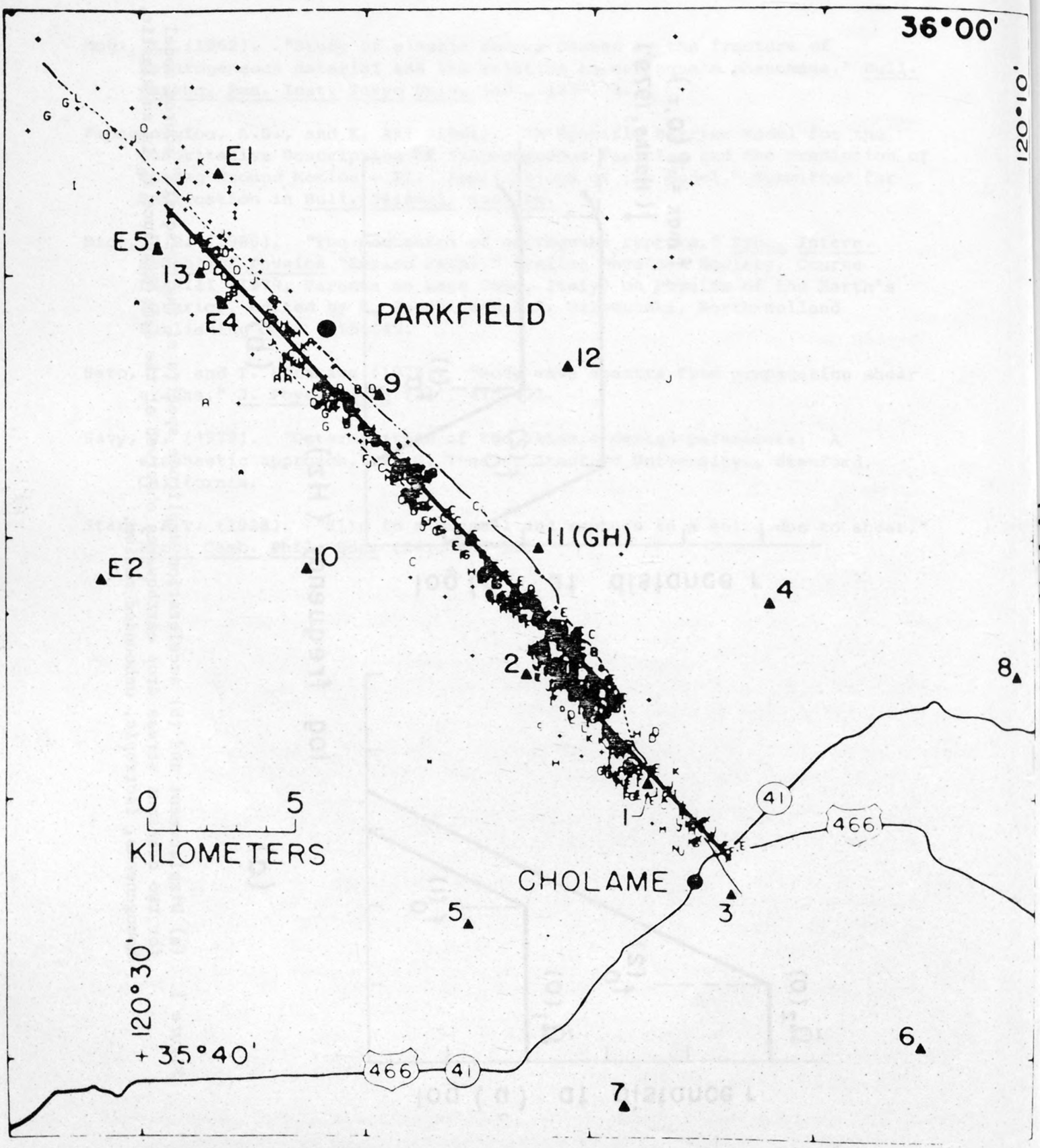

Figure 2a. Map of the fault trace and aftershock epicenters of the Parkfield earthquake of 1966, reproduced from Eaton et al. (1970). Both the fault trace and the fault plane at depth, identified by the aftershock zone, jump from one side of the Cholame Valley to the other. Two lines were drawn by Aki (1979), fitting the two zones of aftershock epicenters.

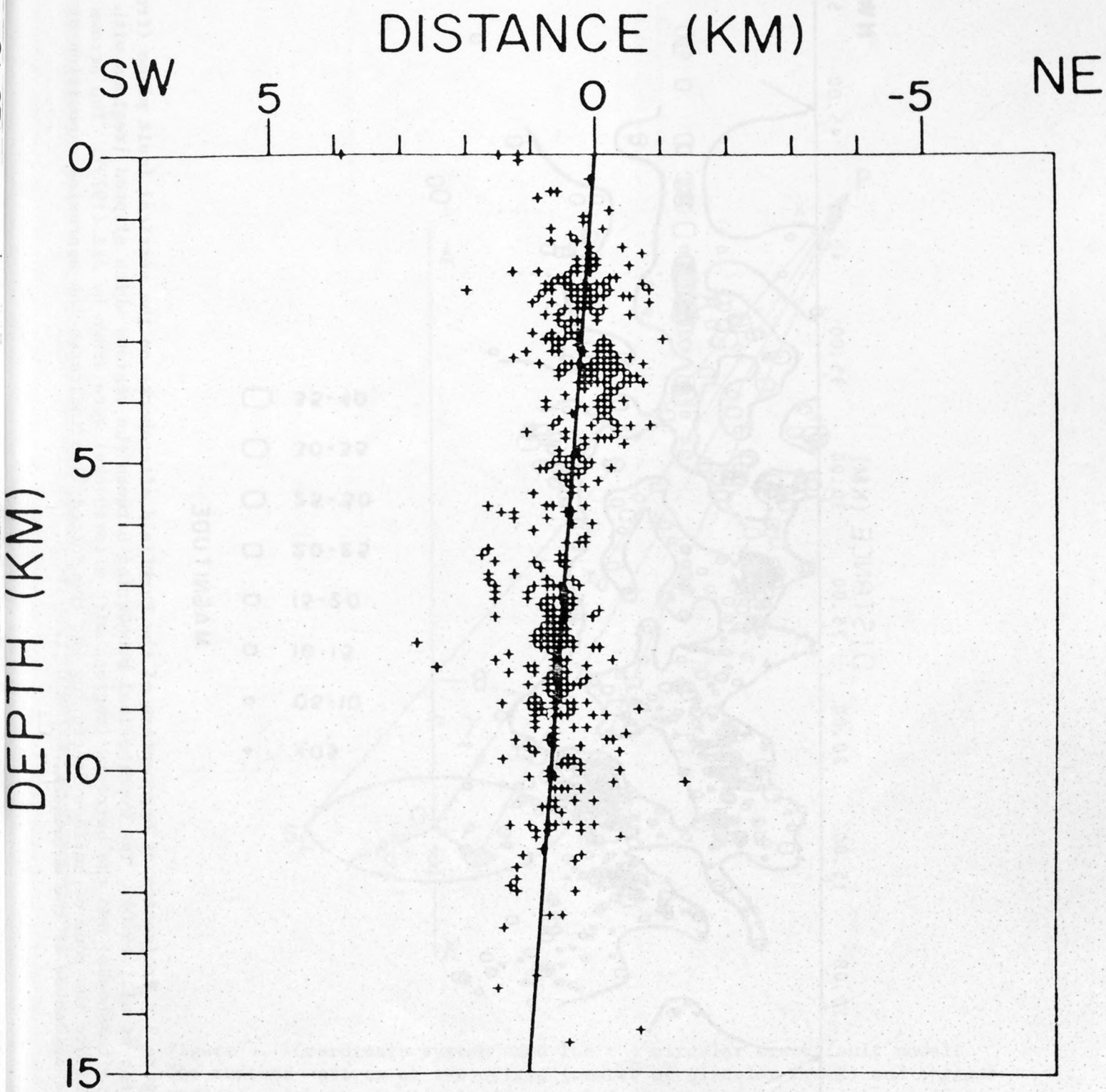

Figure 2b. Projection of well located hypocenters onto a vertical plane perpendicular to the strike of the fault (from Eaton et al., 1970).

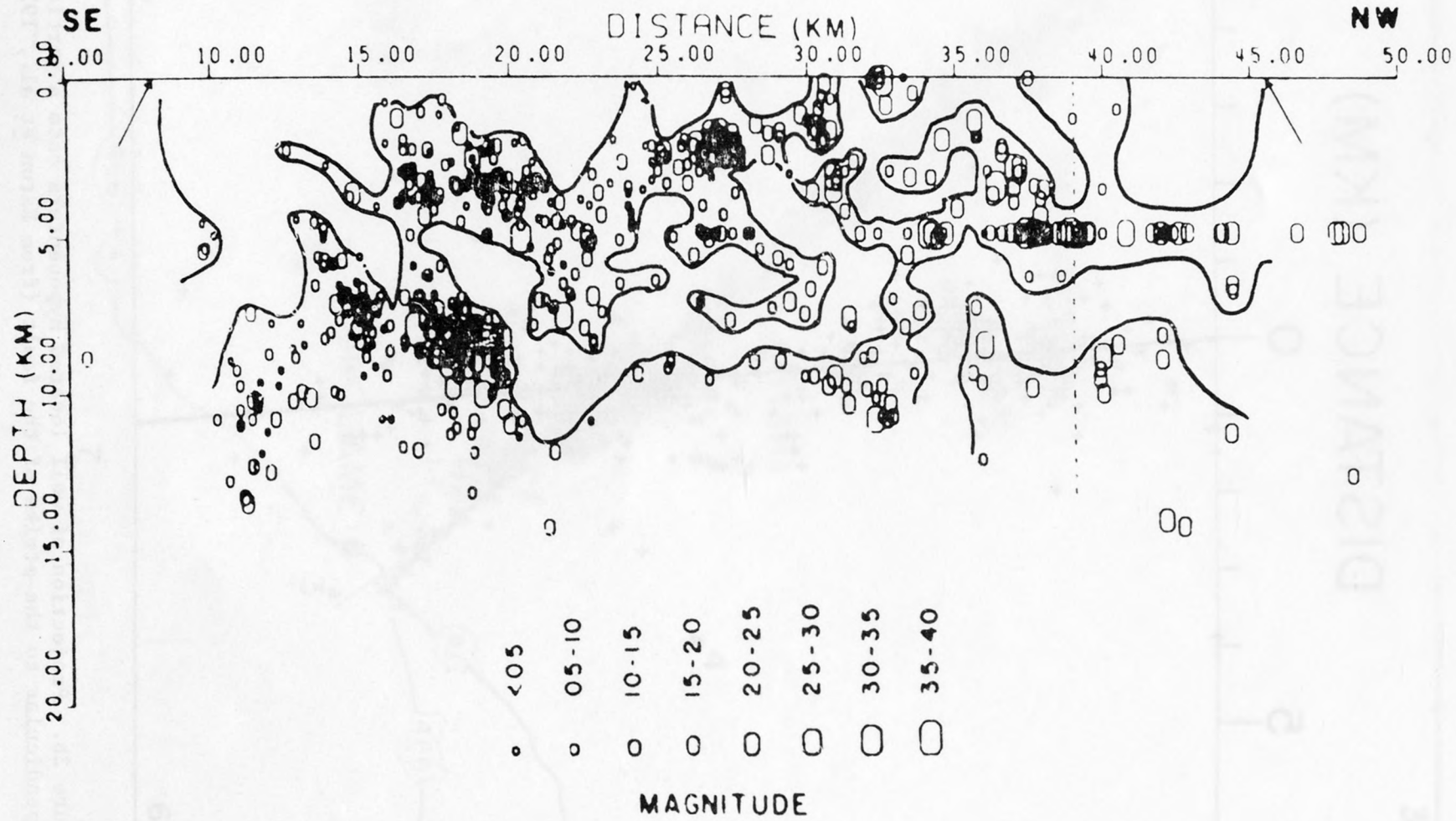

Figure 3. Projection of hypocenters of the Parkfield aftershocks on the vertical fault plane (from Eaton et al., 1970). The hypothetical boundaries between the regions which slipped (regions with no aftershocks) and the barriers (regions with aftershocks) were drawn by Aki (1979). The arrows indicate the zone of surface fracturing and the dotted line indicates the approximate position of the epicenter of the mainshock.

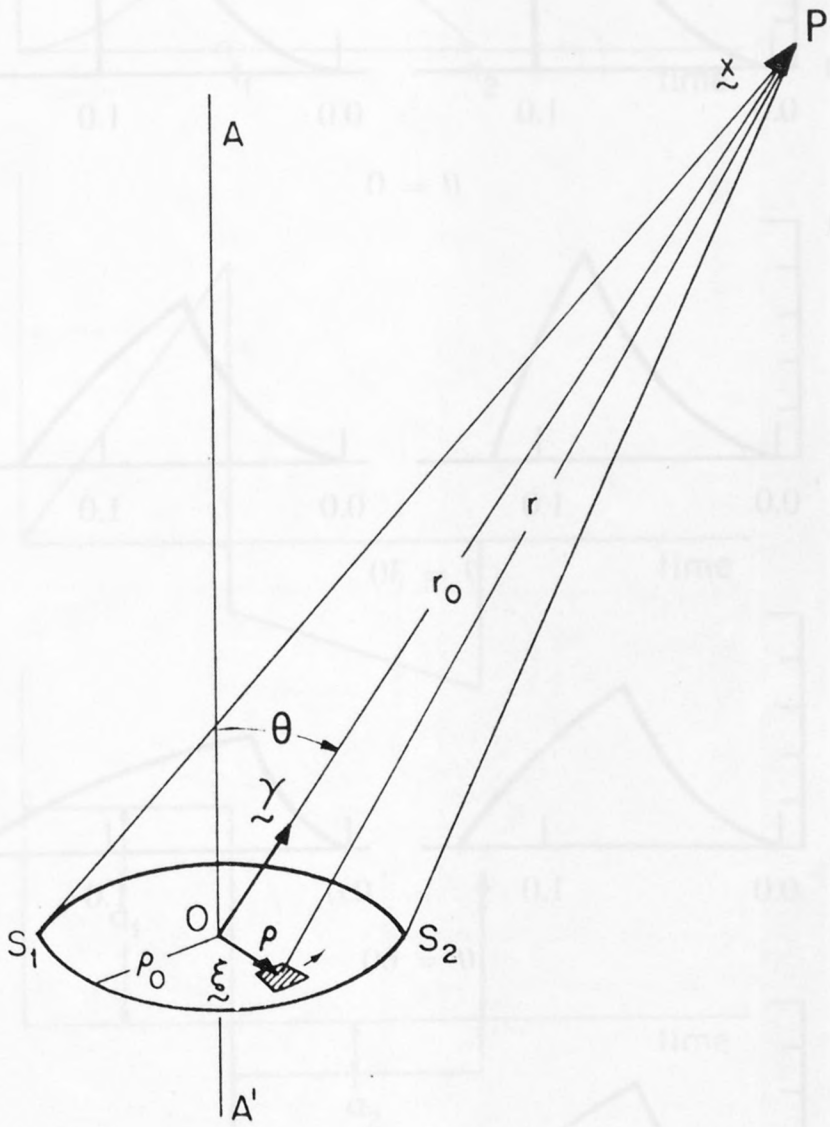

Figure 4. Coordinate system used for the circular crack fault model. The rupture starts at the origin (center of circular crack) and spreads radially with constant velocity v. P is an observation point and $d\Sigma$ is an element of the fault area.

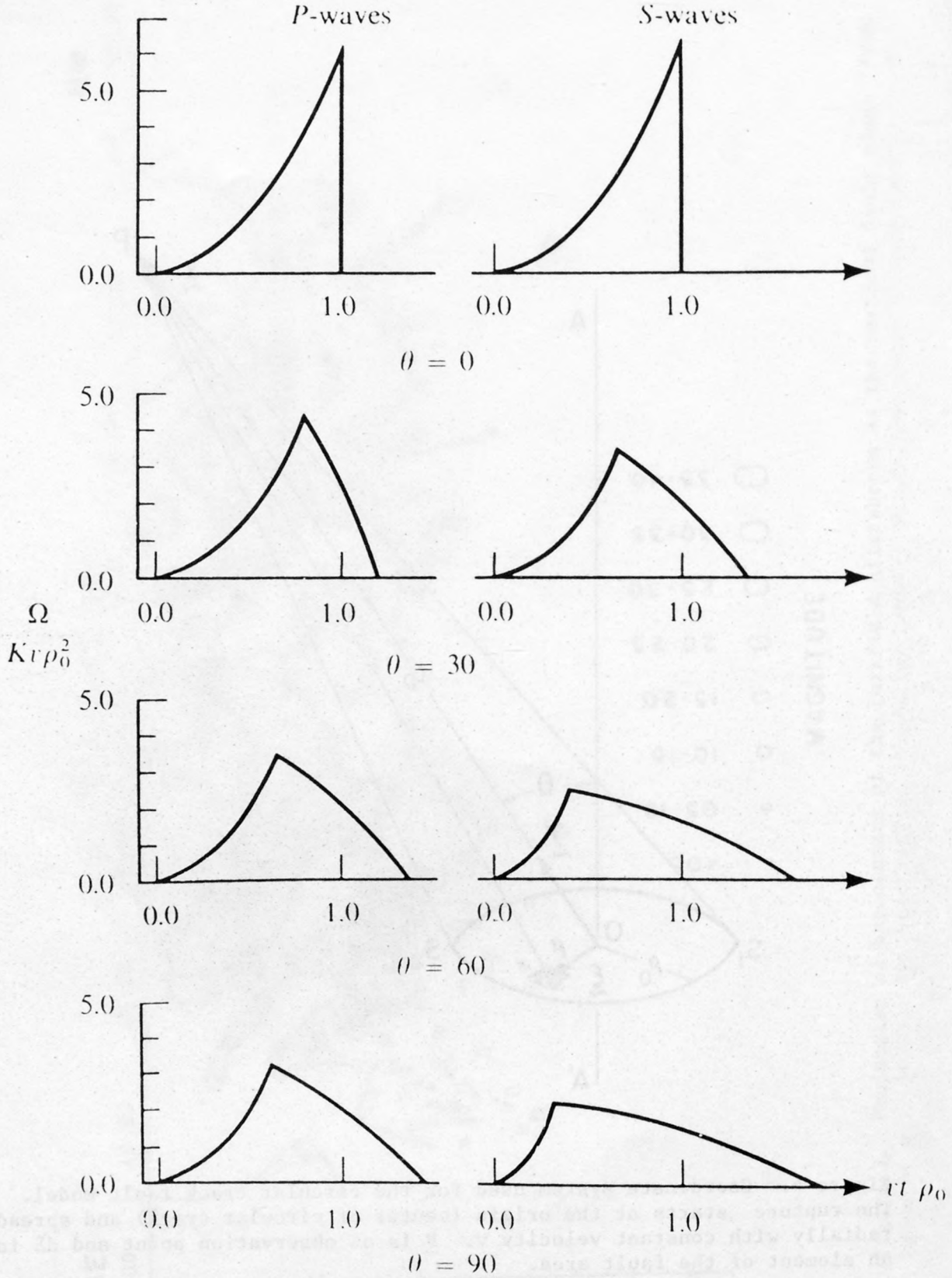

Figure 5. Far-field displacement wave forms (eq. 28); θ is defined in Figure 4 (v/β = 0.75 has been assumed). (From Sato and Hirasawa, 1973.)

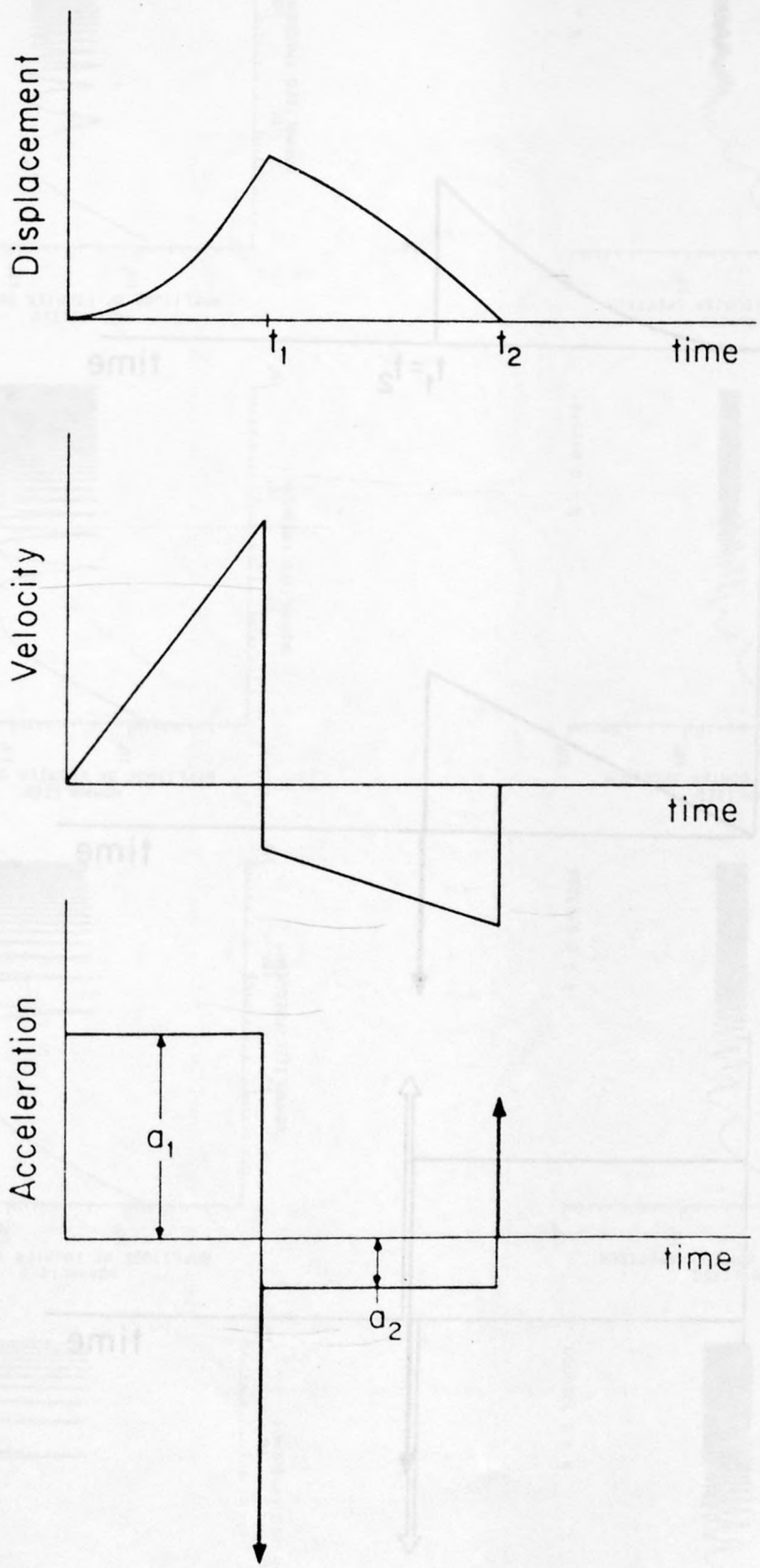

Figure 6. Displacement, velocity and acceleration waveforms of the Sato and Hirasawa (1973) model for the case $k \neq 0$ ($\theta \neq 0$).

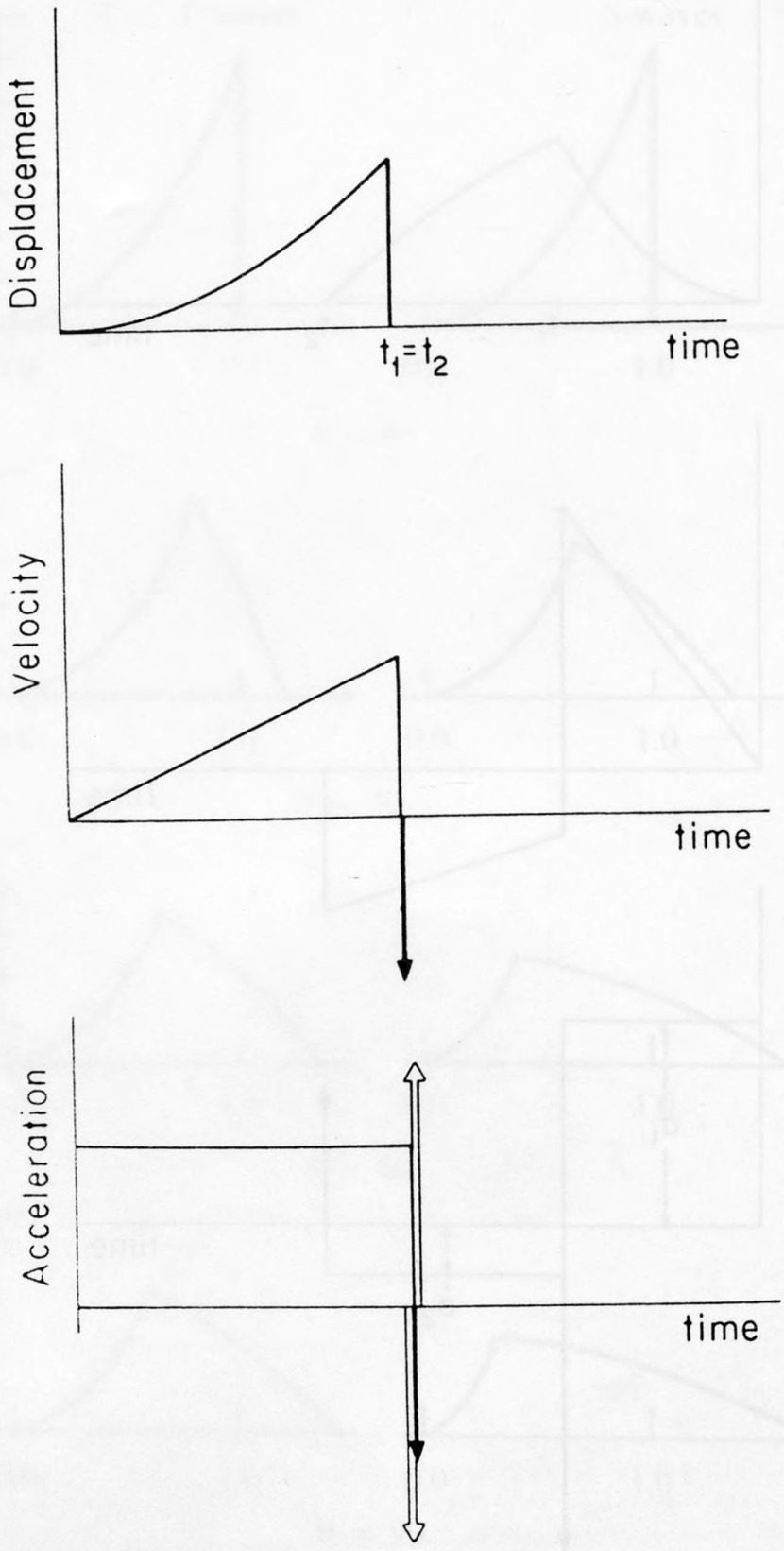

Figure 7. Displacement, velocity and acceleration waveforms of the Sato and Hirasawa (1973) model for the case k = 0 (θ = 0).

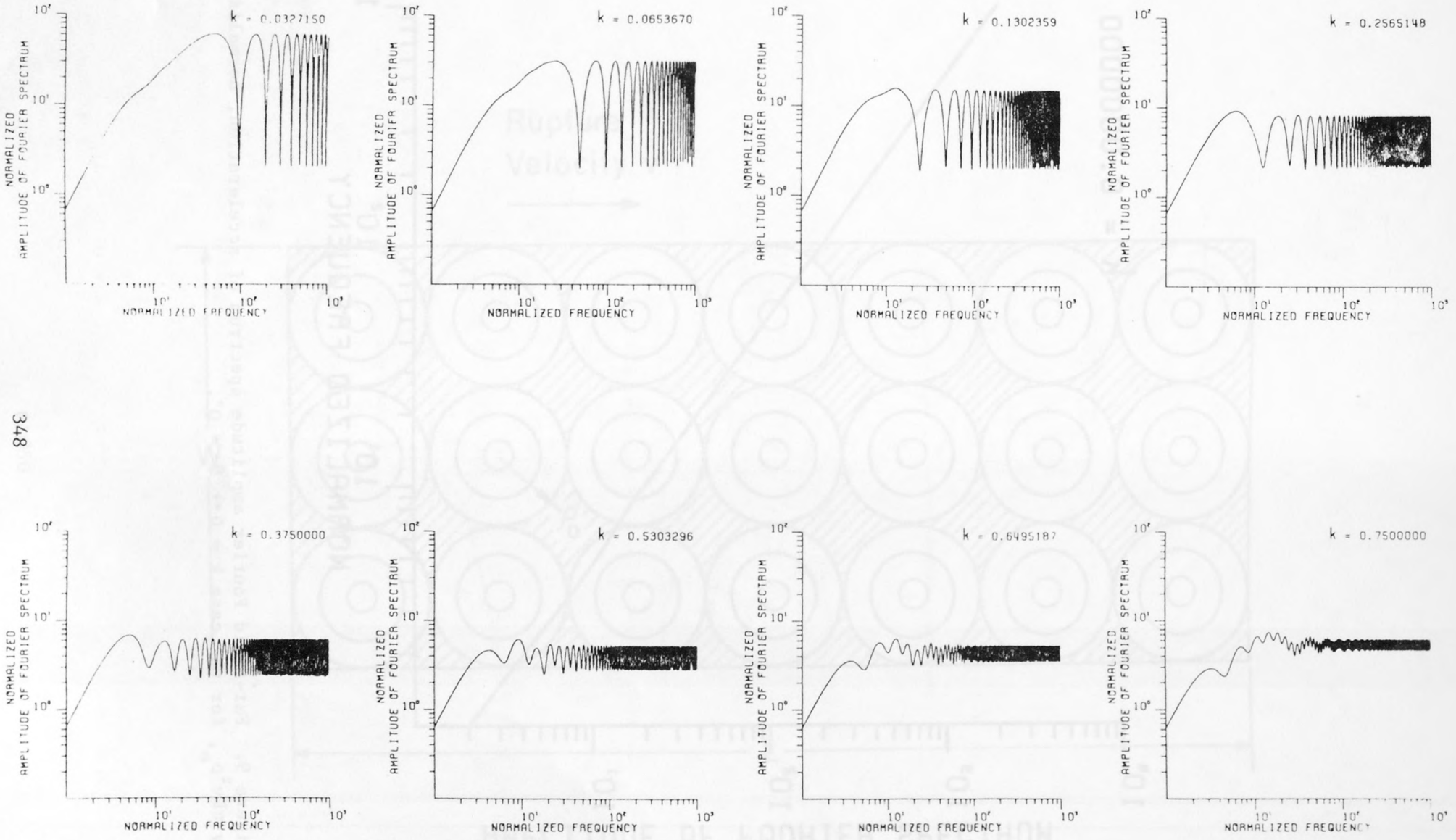

Figure 8. Far-field Fourier amplitude spectra of acceleration, normalized by $\pi K v^2 \rho_o$, for the cases: k = 0.032715, 0.065367, 0.1302359, 0.256515, 0.375, 0.53033, 0.649519 and 0.75. Assuming v/c = 0.75, these values of k correspond to θ = 2.5°, 5°, 10°, 20°, 30°, 45°, 60° and 90°, respectively.

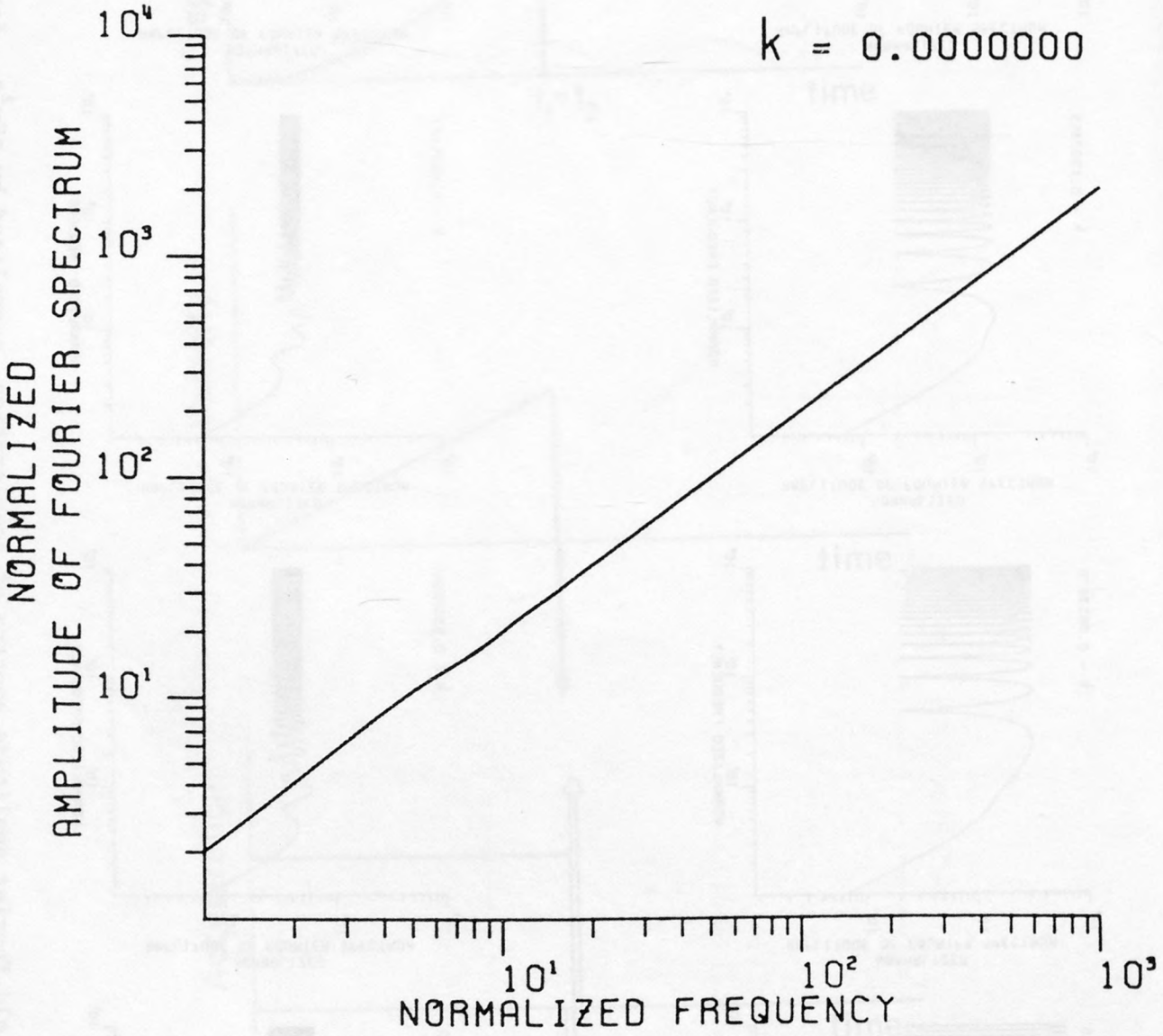

Figure 9. Far-field Fourier amplitude spectrum of acceleration, normalized by $\pi K v^2 \rho_o$, for the case $k = 0 \leftrightarrow \theta = 0°$.

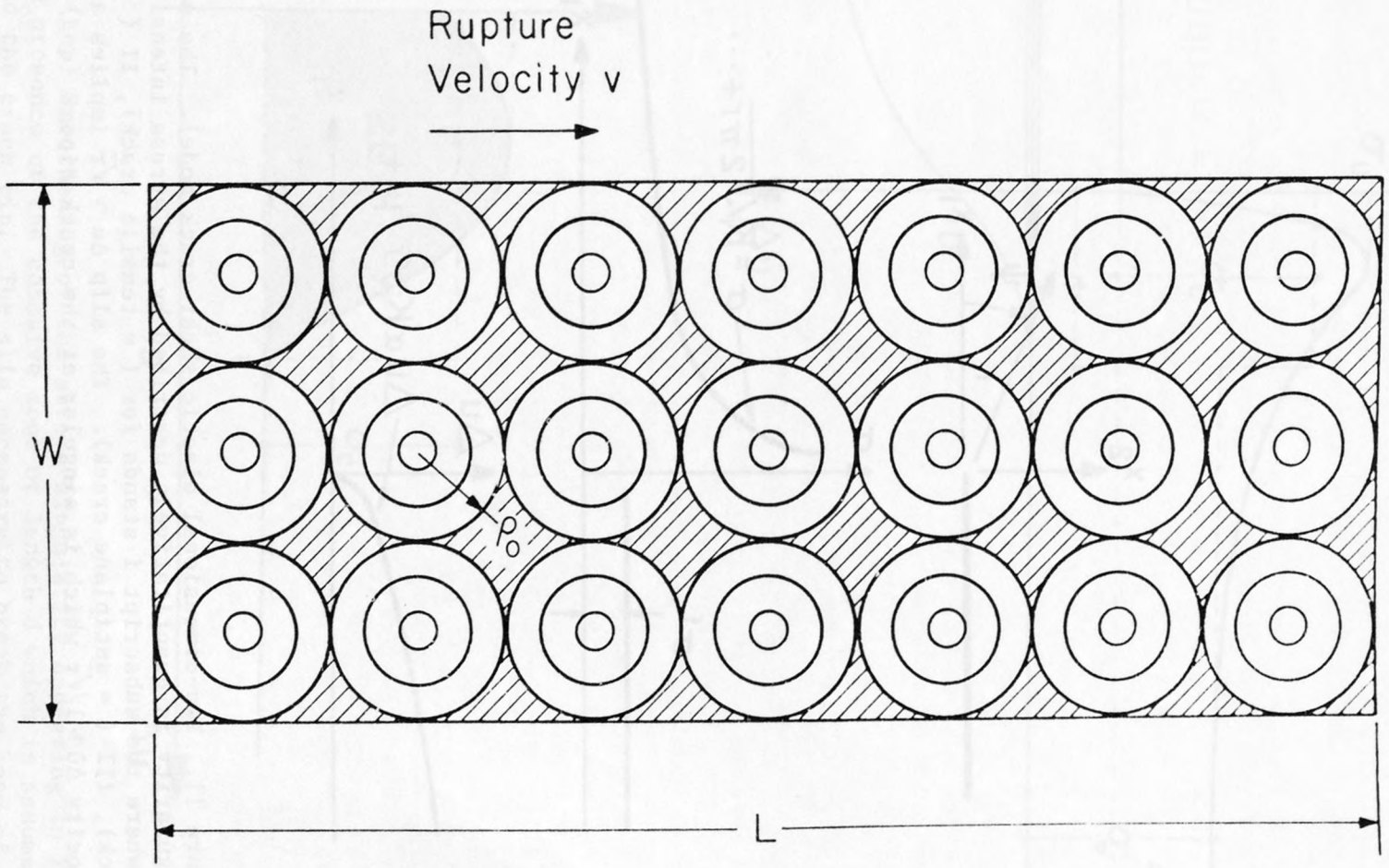

Figure 10. Assumed distribution of circular cracks on the fault plane for the specific barrier model (aggregate of circular cracks) considered in the present paper.

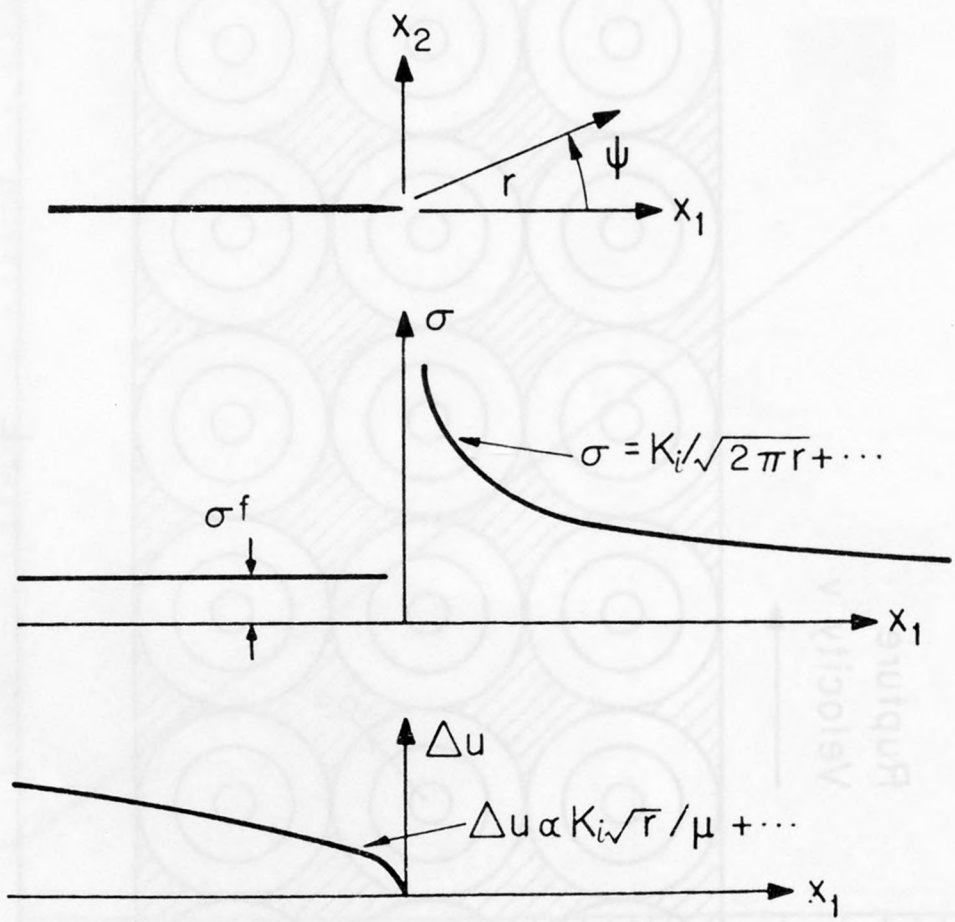

Figure 11. Two-dimensional elastic shear crack model. The stress singularity is quantitatively described by the stress intensity factor K_i where the subscript i stands for (= tensile crack), II (= in plane crack), III (= antiplane crack). The slip $\Delta u \sim \sqrt{r}$ implies a slip velocity $\Delta\dot{u} \sim 1/\sqrt{r}$ which is singular at the crack tip.

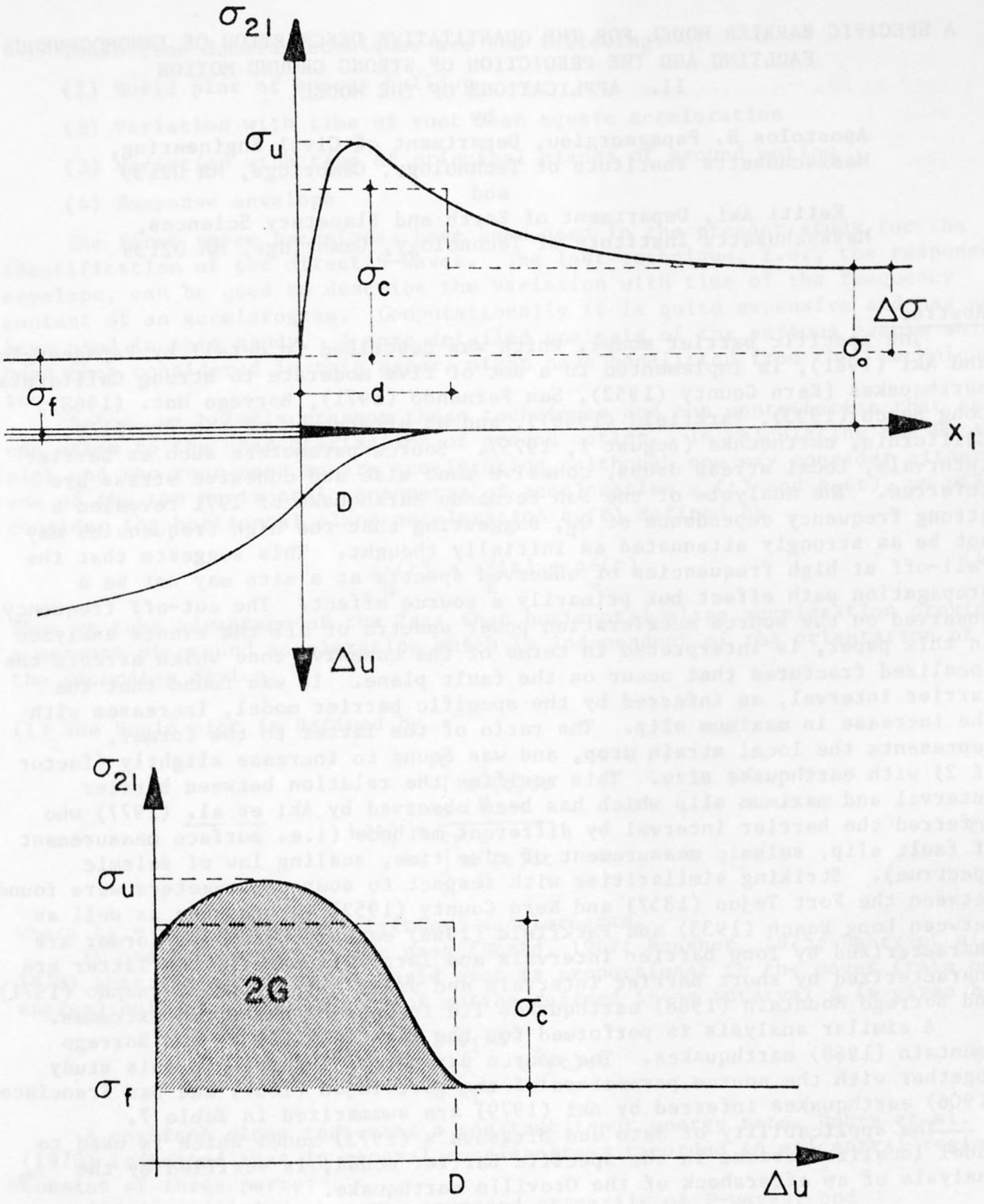

Figure 12. (top) Smoothening of the stress singularity appearing in Fig. 11 due to the presence of the cohesive zone of length d which is assumed to exist just behind the crack tip. The slip necessary to break the bond of the cohesive zone completely is denoted by D. The average value of the cohesive stress, assuming the latter to be uniformly distributed over the cohesive zones, is denoted by σ_c.

(bottom) A schematic representation of the constitutive law (cohesive force diagram) of the "slip weakening" model.

A SPECIFIC BARRIER MODEL FOR THE QUANTITATIVE DESCRIPTION OF INHOMOGENEOUS FAULTING AND THE PREDICTION OF STRONG GROUND MOTION
II. APPLICATIONS OF THE MODEL

by

Apostolos S. Papageorgiou, Department of Civil Engineering,
Massachusetts Institute of Technology, Cambridge, MA 02139

and

Keiiti Aki, Department of Earth and Planetary Sciences,
Massachusetts Institute of Technology, Cambridge, MA 02139

Abstract

The specific barrier model, which was described in detail by Papageorgiou and Aki (1981), is implemented to a set of five moderate to strong Californian earthquakes (Kern County (1952), San Fernando (1971), Borrego Mnt. (1968), Long Beach (1933), Parkfield (1966)), and an aftershock of the Oroville, California, earthquake (August 1, 1975). Source parameters such as barrier intervals, local stress drops, cohesive zone size and cohesive stress are inferred. The analysis of the San Fernando earthquake of 1971 revealed a strong frequency dependence of Q_β, suggesting that the high frequencies may not be as strongly attenuated as initially thought. This suggests that the fall-off at high frequencies of observed spectra at a site may not be a propagation path effect but primarily a source effect. The cut-off frequency observed on the source acceleration power spectra of all the events analyzed in this paper, is interpreted in terms of the cohesive zone which arrests the localized fractures that occur on the fault plane. It was found that the barrier interval, as inferred by the specific barrier model, increases with the increase in maximum slip. The ratio of the latter to the former, represents the local strain drop, and was found to increase slightly (factor of 2) with earthquake size. This verifies the relation between barrier interval and maximum slip which has been observed by Aki et al. (1977) who inferred the barrier interval by different methods (i.e. surface measurement of fault slip, seismic measurement of rise time, scaling law of seismic spectrum). Striking similarities with respect to source parameters were found between the Fort Tejon (1857) and Kern County (1952) earthquakes as well as between Long Beach (1933) and Parkfield (1966) earthquakes. The former are characterized by long barrier intervals and large slips while the latter are characterized by short barrier intervals and small slips. San Fernando (1971) and Borrego Mountain (1968) earthquakes lie in between these two extremes.

A similar analysis is performed for the Parkfield (1966) and Borrego Mountain (1968) earthquakes. The source parameters inferred in this study together with the source parameters of the Fort Tejon (1857) and San Francisco (1906) earthquakes inferred by Aki (1979) are summarized in Table 7.

The applicability of Sato and Hirasawa's (1973) model which is used to model localized cracks in the specific barrier model, is verified by the analysis of an aftershock of the Oroville earthquake.

Identification of direct S-waves

Bond et al. (1980), in a study of the engineering characteristics of the San Fernando earthquake of 1971, integrated a set of time domain techniques that can be used to identify the direct S-waves of earthquake strong motion accelerograms.

These time domain techniques are the following:

(1) Husid plot of energy buildup

(2) Variation with time of root mean square acceleration

(3) Variation with time of principal planes of ground motion

(4) Response envelope

The first three techniques have been used in the present study for the identification of the direct S-waves. The last technique, i.e., the response envelope, can be used to describe the variation with time of the frequency content of an accelerogram. Computationally it is quite expensive and has not been used in this study. A more detailed analysis of the various events which have been considered in this paper, might have benefitted from that technique too.

Below, we briefly present these techniques and the contribution that each one makes to the characterization of ground motion. In calculating the Husid plot and the root mean square acceleration, although one may consider either one of the two horizontal components of acceleration $a_x(t)$ and $a_y(t)$, we will consider the horizontal plane acceleration $a_H(t)$ defined by

$$a_H^2(t) = a_x^2(t) + a_y^2(t) \tag{1}$$

Thus we take advantage of the fact that horizontal plane acceleration provides a measure of ground acceleration which is independent of the orientation of the recording device.

(1) The Husid plot is defined by

$$h(t) = \frac{\int_0^t a_H^2(t)dt}{\int_0^{t_f} a_H^2(t)dt} \tag{2}$$

where t_f = time length of digitized accelerogram.

It has been noted in the past (Husid, 1967; Housner, 1975; Dobry et al., 1978) that the slope of the Husid plot is proportional to the power (rate of energy) buildup. The power P of motion defined in an interval Δ is given by

$$P = \frac{1}{\Delta}\int_{t_1}^{t_1+\Delta} a_H^2(t)dt \tag{3}$$

A constant slope indicates a constant input energy rate. Dobry et al. (1978) indicated that in general accelerograms recorded in epicentral regions consist of three parts:

(i) An initial weak part, composed primarily of P-waves, and corresponding to an initial flat slope of the Husid plot.

(ii) An intermediate strong part, composed primarily of S-waves, and corresponding to the steep slope of the Husid plot.

(iii) A final part, corresponding to indirect (scattered) body waves and/or surface waves. This part of the record is weak for rock sites and moderately strong for soil sites.

(2) Root mean square acceleration:

Closely related to the Husid plot is the root mean square acceleration defined in the time interval Δ. It is given by

$$\bar{a}_H = \sqrt{P} = \sqrt{\frac{1}{\Delta}\int_{t_1}^{t_1+\Delta} a_H^2(t)dt} \tag{4}$$

The variation of the root mean square acceleration with time can be investigated by employing a moving time window as follows:

$$\bar{a}_H(t) = \int_{t-\delta/2}^{t+\delta/2} a_H^2(t)dt \tag{5}$$

where δ = width of the moving time window.

Peaks of the $\bar{a}_H(t)$ plot versus time correspond to bursts of energy arriving at the station. Therefore an examination of the shape of the $\bar{a}_H(t)$ graph allows one to identify on the record these wave packets. Bond et al. (1980) examined the $\bar{a}_H(t)$ graphs of the San Fernando earthquake records and interpreted them in terms of the details of the source mechanism.

(3) Principal planes of ground motion

The time variation of the principal planes of ground motion is used to distinguish between the types of seismic waves that arrive at the site.

We define a moving time window intensity tensor, [G(t)], for a set of ground acceleration, $a_x(t)$, $a_y(t)$, $a_z(t)$ defined along three mutually perpendicular axes:

$$[G(t)] = [g_{ij}(t)] \tag{6}$$

where

$$g_{ij}(t) = g_{ji}(t) = \int_{t-\delta/2}^{t+\delta/2} a_i(t)a_j(t)dt \quad (i,j = x,y,z)$$

This definition of [G(t)] was initially proposed by Penzien (Penzien and Watabe, 1975; Kubo and Penzien, 1976; Kubo and Penzien, 1977). Penzien used this procedure to determine the types of seismic waves arriving at a site and their approximate direction of travel at the site.

The eigenvalues and eigenvectors of the tensor [G(t)] may be found as a function of time. The eigenvectors correspond to the principal directions and the eigenvalues to the principal values of the moving time window intensity of ground motion. The principal directions of intensity correspond to the direction of principal earth ground motions. That way one can distinguish phases in which different types of seismic waves and directions of travel at the recording site are prevalent.

Following Bond et al. (1980), for the easier interpretation of the variation with time of the principal planes of motion, we rotate the components of acceleration as shown in Fig. 1, and the directions of the eigenvectors are described in terms of the polar coordinate angles θ and ϕ. Due to refraction near the surface of the earth, P-waves produce particle motions predominantly in the vertical direction ($\phi = 0°$) while S-waves exhibit motions primarily in the horizontal plane ($\phi = 90°$). Therefore it is reasonable to expect a shift in the angle of the maximum principal plane from 0° to 90° at the initial arrival of S-waves at a site (this presupposes that the recording device was triggered by one of the initial P-wave arrivals).

A small time window (0.5 sec adopted in this study) allows a sharp determination (±0.25 sec) of the time of the first S-wave arrivals.

The Husid plot and the time variation of the direction of the maximum principal intensity provide accurate determination of the time t_1 of the first S-wave arrivals on an accelerogram. The time t_2, corresponding to the time of the last arrival of direct S-waves is rather clearly determined for rock sites by the Husid plot. For soil sites the Husid plot is rounded at the transition from direct to indirect (scattered) body waves and/or surface waves. This makes difficult the determination of t_2. Similarly the time variation of the ϕ-angle of the principal planes does not demonstrate the abrupt transitions that it does for t_1. The only plot that can be used with more confidence to determine t_2 for soil sites is the moving time window root mean square acceleration which at t_2 shows visually a clearer transition from high values to lower values.

Typical horizontal components of ground acceleration and the corresponding Husid plot, moving time-window root mean square acceleration plot and ϕ-angle plot are shown in Fig. 2.

Having identified t_1 and t_2, the duration Δ of the direct S-waves corresponding to the steep slope of the Husid plot is given by

$$\Delta = t_2 - t_1 \tag{7}$$

Bond et al. (1980) succeeded in identifying t_1 and t_2 for 68 of the 97 stations that recorded the San Fernando earthquake at the epicentral region. The time t_1 of onset of S-waves as identified by Bond et al. (1980) is for all practical purposes identical to that found by Hanks (1975). They found that the duration Δ was 3 to 4 seconds for the stations north of the epicenter and 6 to 8 seconds for the stations south of the epicenter. Except for this strong azimuthal variation, which is going to be discussed further in connection with the analysis of the San Fernando earthquake, Bond et al. (1980) did not observe any strong variations of the duration Δ with distance. They point out only that the determination of t_2 becomes increasingly difficult with distance. This can be explained by the fact that with increasing epicentral distance surface waves become more important than body waves obscuring the transition from direct body waves to indirect (scattered) body waves and/or surface waves. Also, at large epicentral distances, dispersion becomes an important factor.

Processing of the direct S-waves

The horizontal components of ground motion at each station were vectorially rotated to obtain the radial (along the ray path) and the transverse (90° counterclockwise from the radial) components. The direct S-waves, which were identified by the time domain techniques, were windowed, cosine tapered (10 percent at each end of the time window) and were used to obtain Fourier spectra F(f). Estimates of the power spectral density P(f) of the direct S-waves were obtained by dividing the square of the amplitude of the Fourier spectrum by the duration Δ as follows:

$$P(f) = \frac{|F(f)|^2}{\Delta} \tag{8}$$

In order to estimate the source power spectrum from the observed power spectra at various stations, we assume that the earthquake source is a point source described by the power spectrum S(f). The direct S-waves that we consider for analysis are subject to two types of attenuation: geometric attenuation which for body waves (and therefore for S-waves) is described by

the factor (1/r) and attenuation due to material nonlinearities and/or scattering, which for Fourier amplitudes of shear waves is described by the factor $\exp(-\pi f r/Q_\beta \cdot \beta)$, where r = source-to-station distance, f = frequency, Q_B = quality factor of shear waves, β = shear wave velocity.

Therefore the predicted value of the power spectrum at a frequency f_i and distance r_j is given by

$$\bar{P}(f_i,r_i) = \frac{S(f_i)}{r_j^2} \cdot \exp\left(-\frac{2\pi f_i r_i}{Q_{\beta_i} \cdot \beta}\right) \tag{9}$$

Let P_{ij} denote an observed value of the power spectrum for a frequency f_i and a source-to-station distance (epicentral or hypocentral) r_j. Let us define a factor k^P as follows:

$$k^P_{ij} = \frac{P_{ij}}{\bar{P}(f_i,r_j)} \tag{10}$$

Berill (1975) defined a similar factor k^F_{ij} as the ratio of the observed Fourier amplitude to the estimated Fourier amplitude of acceleration for a frequency f_i and a source-to-station distance r_j. He studied the high frequency attenuation of strong motion from the San Fernando earthquake by investigating the decay of Fourier amplitudes of a 10-second time window of strong motion on each record which he considered to be composed primarily of direct S-waves. He considered separately northern and southern stations w.r.t. the epicenter and he observed that in each group the scatter of observed Fourier amplitudes was roughly the same with respect to distance and frequency variations. He noted that for a given frequency f_i the distribution of $\ln(k^F_{ij})$ was approximately Gaussian. This is consistent with the observation (e.g., McGuire, 1974) that the scatter of peak acceleration data has a log-normal distribution.

Since $\ln(k^P_{ij}) = 2\ln(k^F_{ij})$, we conclude that the observations made above for k^F_{ij} apply also for k^P_{ij}.

Therefore, for a set of m discrete sampling frequencies and a set of n stations (i.e., 2n records, since each station provides two horizontal components of motion), the best (maximum likelihood) estimates of the parameters $S(f_i)$ and $Q_{\beta_i} = Q_\beta(f_i)$ (assuming in general a frequency dependent quality factor) at the sampling frequencies are those that minimize

$$\Phi = \sum_{i=1}^{m} \sum_{j=1}^{2n} (\ell n\, k^P_{ij})^2 \tag{11}$$

over the data set (Tukey, 1965), where (2nm) is the number of data. The data have been given equal weight in eq. 11 because any anomalous data can be excluded and because the scatter, as discussed above, remains approximately the same with respect to variations in distance and frequency.

The thus inferred source power spectrum S(f) is used in connection with the specific barrier model (Papageorgiou and Aki, 1981) to infer the barrier interval and local stress drop.

Inference of source parameters of recorded earthquakes

The San Fernando earthquake of 1971

Several investigators have analyzed the source mechanism of the 1971 San Fernando earthquake (Bolt, 1972; Mikumo, 1973; Trifunac, 1974; Hanks, 1974; Boore and Zoback, 1974; Niazi, 1975; Bouchon and Aki, 1977; Bouchon, 1978; Langston, 1978; Heaton and Helmberger, 1979; Shakal, 1979). It is an important event for the study of strong ground motion because having occurred virtually in the center of the southern California strong motion instrumentation network, it provided a large number of strong motion accelerograms. In addition, abundant teleseismic body-wave and surface-wave data and also static offset data, provide the opportunity to cross-check various different methods of studying the slip on the fault.

The thrust fault produced an earthquake with a local magnitude $M_L = 6.35$ (Kanamori and Jennings, 1978). Analysis of the event revealed a complex rupture process. Strong directivity effects, manifested in strong azimuthal dependence of duration and amplitudes of strong ground motion, are apparent in the San Fernando records. These effects are expected and predictable for thrust faults.

Analyses of both teleseismic and local records and the distribution of aftershocks indicate a fault plane steepening with depth. Fig. 3 shows the geometry of the fault plane, adopted from Bouchon (1978). The general characteristics of this geometry are included in most modelling studies.

Studies of both local (Hanks, 1974; Trifunac, 1974) and teleseismic (Bouchon, 1978; Langston, 1978) data agree that faulting initiated on the steeper plane of the fault with a massive but localized rupture with a radius that varies from 1.5-2 km (Bouchon, 1978; Langston, 1978) to 3-6 km (Hanks, 1974). Rupture subsequently propagated upwards and to the south until it reached the surface.

Bouchon (1978) provides the best explanation for the rupture process of the shallower plane of the fault (Fig. 3). He introduced barriers along this segment of the fault, which caused irregular slip and high frequency acceleration pulses. This was confirmed by Shakal (1979) who modelled the initial part of the velocity records obtained from two stations which are located south of the epicenter and at distances less than 40 km from the center of the fault. In harmony are also the models arrived at by Trifunac (1974) and Heaton and Helmberger (1979) which indicate a massive localized fracture near the surface. Such a fracture at shallow depth explains also the part of the velocity records obtained from two stations which are located south of the epicenter and at distances less than 40 km from the center of the fault. In harmony are also the models arrived at by Trifunac (1974) and Heaton and Helmberger (1979) which indicate a massive localized fracture near the surface. Such a fracture at shallow depth explains also the Rayleigh wave detected in the San Fernando Valley propagating in a northeast-southwest direction (Shakal, 1979; Bond et al., 1980).

Interesting observations were also made by Bond et al. (1980) who correlated the shape of the moving time window r.m.s. acceleration and the arrival times of peak accelerations with localized fractures on the fault plane. Bond et al. (1980) observed that the records to the north and east of the up-thrust block were less energetic and of smaller duration (3-4 sec) than those obtained from stations located to the south and west. The latter were more energetic and had a larger duration (6-8 sec).

They observed that the shape of the moving time window r.m.s. acceleration of the northern stations is simple, exhibiting a single peak. On the contrary, that of several southern stations which were selected over a fairly extended area is more complex exhibiting two prominent peaks at 3 sec and 6 sec from the onset of S-waves. They also noticed that the arrival times of peak accelerations coincided with the peaks of the moving time window r.m.s. acceleration.

An explanation of the above observations which is in harmony with the other studies is the following. Due to strong directivity effects, which were demonstrated in numerical experiments by Shakal (1979), the northern stations sampled primarily the radiation emitted by the steeper segment of the fault plane (i.e., the initiation of rupture). On the contrary the southern stations sampled equally well the radiation emitted by the entire fault plane. The two peaks of the moving time window r.m.s. acceleration and the corresponding peak accelerations were attributed by Bond et al. (1980) to the inferred localized fractures which are located at the initiation of rupture and near the surface.

Therefore from all the records that Bond et al. (1980) analyzed in order to identify the direct S-waves, in this study we considered only those which were recorded at southern stations and have a discernible strong motion part (direct S-waves). The 56 stations that we considered are listed in Table 1a.

The identified direct S-waves of all the records were processed following the procedure described in the previous section. The selected sampling frequencies are 1,2,4,8 and 16 Hz. Around each sampling frequency we averaged the spectral amplitudes over a frequency bandwidth equal to 0.9 Hz. We found that the selection of this bandwidth is not very crucial for the parameters to be inferred by least squares fitting. As expected, the smaller the frequency bandwidth of averaging the higher the dispersion of the observation points around the fitted curves.

The decay of the averaged amplitudes of observed power spectra together with the fitted curves which are described by eq. 9 are shown in Figs. 4a-e.

The data points which are indicated in Figs. 4a-e by their Caltech reference numbers, were excluded from the regressions for the following reasons (Berrill, 1975): The Fourier spectra of the horizontal components of the ground motion recorded at the Glendale Municipal Services Building (F088) exhibited pronounced narrow band peaks between 1 and 1.5 Hz. Other ground level spectra recorded at approximately the same source-to-station distance and azimuth, did not exhibit such peaks. We excluded the spectral amplitudes at frequencies 1 and 2 Hz, following Berrill (1975) who attributed the peaks to the motion transmitted from an adjacent, massive, concrete shear-wall structure, the Public Services Building.

Similarly, we excluded spectral amplitudes of the records obtained from the instruments located on the crests of the Whittier Narrows dam (N186) and the Carbon Canyon dam (N185). Berrill (1975) estimated the fundamental frequencies of the two dams to be 5.5 Hz and 3.1 Hz respectively. To account for the uncertainty of the estimates he excluded the spectral amplitudes at 8 and 16 Hz for the Whittier Narrows dam and those at 4, 8 and 16 Hz for the Carbon Canyon dam.

Finally, the spectral amplitude at 16 Hz of the 4000 W. Chapman Avenue Basement station (M180) was excluded because the data point was found to be at the digitization noise level.

Three cases of the frequency dependence of Q_β were considered:

(1) Q_β is assumed to be constant, independent of frequency.

(2) Q_β follows the power law $Q_\beta = Q_o f^m$ which has been suggested by Aki (1980b,c) for the description of the attenuation of S-waves. Q_o and m are parameters to be estimated.

(3) $Q_{\beta_i} = Q_\beta(f_i)$ varies freely at each sampling frequency.

The inferred values of the parameters for these three cases are listed in Table 1b. The following observations can be made in connection with Figs. 4a-e:

(1) It is clear that there is a considerable scatter around the fitted curves. As expected this scatter is approximately uniform with distance and frequency variations.

(2) Figs. 4a-e clearly demonstrate that the assumption that Q_β is constant is wrong because it does not provide a good fitting to the observations. For the estimated value of $Q_\beta \simeq 700$, eq. 9 overestimates the spectral amplitudes of the frequencies 1 and 2 Hz at large distances (Figs. 4a,b). This implies that $Q_\beta \simeq 700$ is too large for these frequencies which in turn implies that Q_β is frequency-dependent. This can be verified by observing the good fitting which is provided by the other two assumptions on Q_β.

The variation of Q^{-1}_β with frequency as that was inferred by allowing Q_β to vary freely at each sampling frequency is shown in Fig. 5. We observe a strong frequency dependence of Q_β, similar to that inferred by other studies on the attenuation of shear waves using the S to coda ratio method (Aki, 1980b,c). Such a strong frequency dependence of Q_β may explain the generally observed tendency of acceleration spectra obtained during strong earthquakes to show similar shapes independent of the distance from the epicenter (Trifunac, 1976, 1978; Trifunac and Anderson, 1977).

It is interesting to compare the variation with frequency of Q_β^{-1} with that of Q^{-1} of the coda waves of small ($M \leq 3$) events which occurred in the San Fernando area and were analyzed by Chouet (1976) (Fig. 5). Coda waves are the tail of a seismogram (after the arrival of major wave types such as P,S and surface waves) recorded at short distances from an earthquake. The first systematic study of coda waves was done by Aki (1969) who suggested that coda waves are waves back-scattered from randomly distributed inhomogeneities in the earth. The Q of coda waves is determined by fitting the formula $t^{-1} \exp(-\pi f t/Q)$ (where t is time measured from the time of occurrence of the event) to the envelope of amplitudes of band-pass filtered coda waves. It has been observed in the past (Rautian and Khalturin, 1978; Aki, 1980b,c) and is verified by Fig. 5 within the uncertainty of measurements, that Q_β of shear waves agrees very well with Q of coda waves.

It is evident that the power spectrum at the source exhibits for all cases of frequency dependence of Q_β a cutoff frequency f_{max}. This, combined with the strong frequency dependence of Q_β, justifies the assumption of Papageorgiou and Aki (1981) that the cutoff frequency f_{max} observed on the acceleration power spectra at any distance from the fault should be attributed primarily to source effects.

Let us infer the barrier interval for the San Fernando earthquake from the observed spectra using the specific barrier model described by Papageorgiou and Aki (1981).

The source parameters of the San Fernando earthquake of 1971 are listed below (Kanamori and Anderson, 1975; Geller, 1976).

Surface wave magnitude $M_S = 6.6$ ($M_L = 6.35$, $m_b = 6.2$)

Seismic moment $M_o = 0.12 \times 10^{27}$ dyn-cm

Fault length $L = 20$ km $\rightarrow S = 280$ km^2

Fault width $W = 14$ km

Average slip $\overline{\Delta u} = 1.4$ m

Average sweeping velocity V = spreading velocity v = 2.4 km/sec (Geller, 1976) (See Papageorgiou and Aki for definitions of V and v.)

Shear wave velocity $\beta = 3.2$ km/sec (i.e., $v = 3/4\ \beta$)

As discussed by Papageorgiou and Aki (1981) we will consider two cases for Δu_{max}:

$$\Delta u_{max} = \frac{M_o}{\frac{\pi}{6} \cdot \mu \cdot S} \tag{12}$$

$$= \frac{0.12 \cdot 10^{27}}{\frac{\pi}{6} \cdot 3 \cdot 10^{11} \cdot 280 \cdot 10^{10}} = 273 \text{ cm}$$

$$\Delta u_{max} = \frac{3}{2} \overline{\Delta u} \tag{13}$$

$$= \frac{3}{2} \cdot 140 = 210 \text{ cm}.$$

Consider eq. 54 of Papageorgiou and Aki (1981):

$$P_0 \simeq (\text{factor})^2 \cdot W \cdot V \cdot v^4 \cdot \frac{(\Delta u_{max})^2}{\rho_0^2} \cdot \frac{(F^S)^2}{16\beta^2 r_0^2} \tag{14}$$

and assume that $F^S = 1$ (McGuire and Hanks, 1980). This is a reasonable assumption since we are considering southern stations only and the maximum of F^S modulated by rupture propagation lies to the south. From Fig. 6 (considering the case $Q_\beta = Q_o \cdot f^m$), $\rho_o \simeq 8.5 \cdot 10^5 (\text{cm/sec})^2/\text{sec} \cdot (\sqrt{2}/2)^2$ where the factor $(\sqrt{2}/2)$ accounts for free surface amplification (factor 2) and vectorial partition of the recording device (factor $\sqrt{2}$). Then from eq. 14,

$$\rho_0^2 \simeq (\text{factor})^2 \cdot W \cdot V \cdot v^4 \cdot \frac{(\Delta u_{max})^2}{P_0} \cdot \frac{(F^S)^2}{16\beta^2 r_0^2} \tag{15}$$

$$\simeq (2.6)^2 \cdot 14 \cdot (2.4)^5 \cdot \frac{(\Delta u_{max})^2}{\left(\frac{\sqrt{2}}{2}\right)^2 \cdot 8.5 \cdot 10^5} \cdot \frac{(1)^2}{16 \cdot 3.2^2 \cdot (1)^2}$$

Substituting the values of Δu_{max} obtained above we get:

(i) for $\Delta u_{max} = 273$ cm $\rightarrow \rho_0 \simeq 2.8$ km $\rightarrow 2\rho_0 \simeq 5.6$ km

(ii) for $\Delta u_{max} = 210$ cm $\rightarrow \rho_0 \simeq 2.2$ km $\rightarrow 2\rho_0 \simeq 4.4$ km

The local stress drop can be obtained from eq. 53 of Papageorgiou and Aki (1981), as follows:

$$\Delta\sigma = \left(\frac{7\pi}{24}\right) \cdot \mu \cdot \left(\frac{\Delta u_{max}}{\rho_o}\right) \tag{16}$$

$$= \left(\frac{7\pi}{24}\right) \cdot 3 \cdot 10^{11} \cdot (98 \cdot 10^{-5})$$

$$\simeq 300 \cdot 10^{6} \ (\mathrm{dyn/cm^2})$$

$$\simeq 300 \text{ bars.}$$

The total number of cracks which are distributed on the fault plane can be inferred from the assumption that the circular cracks which generate the strong ground motion, are of equal radius and are uniformly distributed on the rectangular fault plane of length L and width W as shown in Fig. 10 of Papageorgiou and Aki (1981).

Therefore, total number of cracks $= \frac{L}{2\rho_o} \cdot \frac{W}{2\rho_o} = \frac{S}{4\rho_o{}^2} = \frac{480}{4\rho_o{}^2}$

(i) for $\rho_o \simeq 2.8$ km $\rightarrow \frac{S}{4\rho_o{}^2} \simeq 9$ cracks

(ii) for $\rho_o \simeq 2.2$ km $\rightarrow \frac{S}{4\rho_o{}^2} \simeq 14$ cracks.

The total energy of seismic waves is given by eq. 63 of Papageorgiou and Aki (1981):

$$E_s = \frac{1}{2} \cdot M_o \cdot \left(\frac{\Delta\sigma}{\mu}\right) \cdot 0.46 \tag{17}$$

$$= \frac{1}{2} \cdot 0.12 \cdot 10^{27} \cdot \left(\frac{300}{3 \cdot 10^{5}}\right) \cdot 0.46$$

$$\simeq 28 \cdot 10^{21} \text{ erg.}$$

An estimate of the same quantity obtained using the Gutenberg-Richter relation is

$$\log E_s = 1.5 M_S + 11.8 \tag{18}$$

$$\simeq 1.5 \cdot 6.6 + 11.8$$

$$E_s \simeq 5 \cdot 10^{21} \text{ erg.}$$

Having obtained an estimate of ρ_o and assuming that f_{max} is approximately equal to 5 Hz, we can apply eqs. 65-68 of Papageorgiou and Aki (1981) to estimate the parameters that characterize the barriers which arrest the rupture of the cracks.

For $\rho_o \simeq 2.5$, $f_{max} \simeq 5$ Hz and $C \simeq 1$, we obtain:

$$d \simeq 500 \text{ m}, \ G \simeq 2.4 \cdot 10^{10} \frac{\text{erg}}{\text{cm}^2}, \ \sigma_c \simeq 480 \text{ bars}, \ D \simeq 1 \text{ m}.$$

Aki (1979) estimated the specific fracture energy G of the barriers of the Parkfield (1966), Fort Tejon (1857), and San Francisco (1906), earthquakes. For these events he found G to span the range 10^9-10^{11} ergs. The value we obtained for the San Fernando earthquake falls in this range.

The stress σ_c required to break the bond at the barrier is only 480 bars as compared with the stress drop $\Delta\sigma$ which is ~300 bars. The value of D ≃ 1m suggests that at the end zone approximately 50% of the average slip Δu is necessary to break the bond (see Fig. 12 of Papageorgiou and Aki, 1981).

It is interesting to compare the barrier interval $2\rho_o \simeq$ 5km inferred in this study for the San Fernando earthquake with the size of localized regions of high slip inferred by Shakal (1979). He considered the part of the velocity records of two bedrock stations (CIT, Seismological Laboratory and Griffith Park Observatory) which corresponds to the arrival of direct S-waves and he modelled it in terms of localized regions of high slip on the fault plane. The final model of the fault plane which Shakal arrived at, is shown in Fig. 7. The size of the cracks varies from 2 to 6 km in agreement with what we obtained. The maximum slip and the stress drop that he inferred are larger by a factor of 2 to 3 compared to the slip that we inferred. This may be attributed to the fact that Shakal considered 5-6 cracks as opposed to the specific barrier model that we used, which gives 9-14 cracks since it assumes that the entire fault plane is covered with cracks which slip the same amount.

Finally, it is interesting to predict the r.m.s. accelerations of the various stations and their attenuation with distance. Fig. 8 compares a regression curve of the form $\bar{a}_H = cr_o^d$ for the horizontal r.m.s. acceleration $\bar{a}_H$ of direct S-waves versus source-to-station distance r_o fitted to the observations, with predictions obtained by the specific barrier model and Hanks' model (Hanks, 1979; McGuire and Hanks, 1980). As expected the barrier model provides excellent fitting to the data using the inferred source spectra, as opposed to Hanks' model which predicts values lower by a factor of 3 as compared to the data. Hanks was puzzled by this discrepancy (Hanks, 1980; McGuire and Hanks, 1980). He attributed it to the use of the "global" stress drop $\Delta\sigma$. Reasoning that the events which he considered for analysis appear to be more energetic as they are viewed from strong ad hoc constant stress (which he called "dynamic stress drop") of the order of 100 bars to account for this. In the barrier model this stress drop follows naturally from the barrier interval. It is a static quantity but it reflects the local stress drop as opposed to the "global" stress drop which is assumed to be uniform over the fault plane and is estimated using the characteristic dimension of the entire fault plane.

It is worth mentioning the excellent correlation of r.m.s. acceleration a_{rms} with peak accelerations a_{max} which was pointed out by Bond et al. (1980) for the San Fernando earthquake (see also McGuire and Hanks, 1980). They found that on the average $a_{max} \simeq 3a_{rms}$. This suggests that, for this particular event, a_{max} is as good a measure of ground motion intensity as a_{rms}. These observations must be verified by other events before generalizations can be made with confidence.

The Kern County earthquake of 1952

One of the most signficant earthquakes that occurred in the western United States after the 1906 San Francisco event is the Kern County earthquake of July 21, 1952. It has a surface wave magnitude M_S = 7.4 to 7.7 (Gutenberg, 1955) and a local magnitude M_L = 7.2 (Kanamori and Jennings, 1978; Bolt, 1978).

It occurred on the White Wolfe fault to the north of the intersection of the Garlock fault with the San Andreas fault.

Recently, Dunbar, Boore and Thatcher (1980), fitted a dislocation model to coseismic (1952 to 1953) triangulation data, supplemented by leveling data, and obtained the following characteristics:

dip $\delta = 60°$ SE, strike ϕ_S = N50°E, length = 70 km, left lateral strike-slip = 2.4 ± 0.1 m, reverse dip-slip = 1.9 to 0.6m (decreasing to the NE) (Fig. 9) and seismic moment $\geq 0.9 \times 10^{27}$ dyn-cm.

The inferred fault plane described above is in agreement with the fault plane inferred using the location of epicenters of the aftershocks of the Kern County earthquake by Cisternas (1963).

These data suggest that the Kern County earthquake has important characteristics in common with the San Fernando earthquake.

The source parameters of this event given by Kanamori and Anderson (1975) are as follows:

$$M_o = 2.0 \times 10^{27} \text{ dyn-cm}$$

$$L = 70 \text{ km}$$

$$W = 20 \text{ km} \rightarrow S = L \times W = 1400 \text{ km}^2$$

(According to Geller, 1976, L = 60 km and W = 18 km)

$$\overline{\Delta u} = 4.6 \text{ m}$$

Average sweeping velocity V = 2.9 km/sec (Kanamori and Anderson, 1975). We assume that spreading velocity v = 2.5 km/sec and $\beta = 4/3\ v$.

Then

(i) Eq. 12 $\rightarrow \Delta u_{max} \simeq 9\text{m}$ ($\rightarrow \Delta u \simeq 6\text{m}$)

(ii) Eq. 13 $\rightarrow \Delta u_{max} \simeq 7\text{m}$ ($\rightarrow \overline{\Delta u} \simeq 4.7\text{m}$).

Both estimates of Δu are larger than the estimates obtained by geodetic measurements (Dunbar, et al., 1980) by a factor of 2. Dunbar et al. (1980) noted that the estimate of seismic moment ($M_o \simeq 0.9 \times 10^{27}$ dyn-cm) using the geodetic data is in remarkable agreement with various other estimates of the seismic moment of this event. Boore and Kanamori (unpublished data) found $M_o \simeq 1\text{-}2 \times 10^{27}$ dyn-cm using records from a low magnification instrument in Pasadena and teleseismic shear waves, Ben-Menahem (1978) obtained $M_o \simeq 0.9 \times 10^{27}$ dyn-cm from a simplified analysis of 20 sec surface waves and Hanks et al. (1975) obtained $M_o \simeq 2 \times 10^{27}$ dyn-cm from an analysis of the isoseismals. This is in contrast to the outstanding disparity observed, in the case of the Parkfield earthquake of 1966, between the seismic moment determined from long-period surface waves and that determined from the aftershock area times the slip estimated from near-source measurements, the latter being larger from the former by a factor of about 3 (Aki, 1979).

The stations which recorded this event and were considered for analysis are listed on Table 2. The attenuation of spectral amplitudes with distance and the inferred source power spectra are shown in Fig. 10 and Fig. 11, respectively. Since the stations are distributed around the source we consider the RMS average over the spherical surface of the shear displacement radiation pattern $[\langle F^S \rangle]^{1/2}$ which is equal to $(0.4)^{1/2}$. From Fig. 11

$$P_o \simeq 10^6 \left(\frac{cm}{sec}\right)^2 / sec \cdot \left(\frac{\sqrt{2}}{2}\right)^2$$

Therefore,

(i) for $\Delta u_{max} \simeq 9m \rightarrow 2\rho_o \simeq 14$ km

(ii) for $\Delta u_{max} \simeq 7m \rightarrow 2\rho_o \simeq 11$ km

Eq. 16 $\rightarrow \Delta\sigma \simeq 350$ bars

Total number of cracks = $\frac{S}{4\rho_o^2}$.

(i) for $2\rho_o \simeq 14$ km $\rightarrow$ 7 cracks

(ii) for $2\rho_o \simeq 11$ km $\rightarrow$ 11 cracks

For $2\rho_o = 13$ km, $\Delta\sigma = 350$ bars and $f_{max} \simeq 2.5$ Hz (Fig. 11) we obtain

$d \simeq 1$ km, $G \simeq 10^{11}$ erg, $\sigma_c \simeq 680$ bars, $D \simeq 3m$.

The values of these parameters are in excellent agreement with those inferred for the 1857 Fort Tejon earthquake by Aki (1979).

An estimate of the total seismic energy obtained from eq. 17 is $E_S = 5.4 \cdot 10^{23}$ erg.

The Gutenberg-Richter relation (eq. 18) gives $E_S = 2.24 \times 10^{23}$ erg.

The Long Beach Earthquake of 1933

The 1933 Long Beach earthquake ($M_S = 6.25$) was the first event to be recorded by strong motion instruments in the western U.S. It occurred on the Newport-Inglewood fault zone which runs parallel to the shore line, south of Los Angeles. The strong motion records used in this study, together with the duration of the direct S-waves, are listed in Table 3. The attenuation of spectral amplitudes with distance is shown in Fig. 12. The spectral amplitudes of Vernon station (B021) are apparently large, especially at frequencies 4, 8 and 16 Hz. This may be due to a local soil effect. Shakal (1979) compared the attenuation of amplitudes of acceleration records obtained from the Borrego and San Fernando earthquakes. He noticed that the Vernon station records exhibited for both events large amplitudes which did not conform with the attenuation of the rest of the records. Shakal (1979) attributed this to local soil effects. This is in agreement with what we observe in connection with the Long Beach records. Therefore we performed the regression analysis twice, first including all data points and second ignoring the spectral amplitudes of Vernon records, at frequencies 4, 8 and 16 Hz. The winnowing of data had as an effect the slight increase of the inferred source spectrum. The inferred (after winnowing) source power spectrum of acceleration is shown in Fig. 13.

The source parameters of the event, taken from Kanamori and Anderson (1975) are the following:

$M_o = 2.8 \times 10^{25}$ ($M_L = 6.43$; Kanamori and Jennings, 1978)

$L = 30$ km

$W = 15$ km

$S = L \times W = 450$ km^2

$\overline{\Delta u} = 20$ cm

V = 2.3 km/sec (from Geller, 1976)

We assume that $V = v = 3/4\ \beta$.

Then, assuming that the rupture started near the south end of the fault and propagated northward (Richter, 1958), towards the stations, $F^S = 1$. From Fig. 13 $P_o \simeq 5 \times 10^5$ (cm/sec)^2/sec $\cdot (\sqrt{2}/2)^2$.

(i) Eq. 12 $\rightarrow \Delta u_{max} \simeq 40$ cm $\rightarrow 2\rho_o \simeq 1$ km

(ii) Eq. 13 $\rightarrow \Delta u_{max} \simeq 30$ cm $\rightarrow 2\rho_o \simeq 0.8$ km.

Eq. 16 $\rightarrow \Delta\sigma \simeq 220$ bars

Number of cracks:

(i) for $2\rho_o \simeq 1$ km $\rightarrow$ ~450 cracks

(ii) for $2\rho_o \simeq 0.8$ km $\rightarrow$ ~700 cracks.

It is interesting to note the small barrier interval inferred for this event which is due to the small slip used in eq. 15. This is related to the small "global" stress drop (7 bars) inferred for this event . The Parkfield earthquake of 1966 (M_S = 6.4) has an equally small barrier interval and small slip. This might be a common feature of strike slip earthquakes in California for that range of magnitudes. Bouchon (1981) made a similar observation on another strike slip event, the Coyote Lake earthquake of 1979. He modeled the displacement records obtained from two stations located in the immediate vicinity of the causative fault. He noticed that he was getting very good agreement between observed and synthetic records even though he was using a simple dislocation model with zero rise time. He attributed this to the small slip of localized areas, which is in harmony to the results obtained from our analysis.

The local stress drop is a more stable parameter than the barrier interval. The barrier interval spans a range of values which differ by an order of magnitude depending on the amount of slip as opposed to the local stress drop which is of the order of a few hundred bars. This is simply due to the fact that $\Delta\sigma$ is the ratio of two quantities which change approximately in proportion to each other.

Finally, comparing the peak values of the source spectra of Kern County (M_L = 7.2) and San Fernando (M_L = 6.35) earthquakes, we observe that they differ only by a factor of 2. This confirms Aki's (1968, 1972) conclusion that the near field ground motion depends neither on the fault length nor on the fault width once they exceed certain limits, but is determined mostly by the dislocation time function (source function) and velocity of rupture propagation. The dislocation time function is described by the final slip and by the slip velocity. The latter is controlled by the accelerating stress which in the barrier model may be approximated by the cohesive stress σ_c (dynamic stress drop which was found to be slightly larger (only 50%) as compared to the local stress drop), and is expected to be bounded by the strength of the materials at the fault gauge.

This observation agrees with the observed saturation of peak ground accelerations recorded near the source ($\lesssim$5 km) for magnitudes greater than $M_S \simeq 6.5$.

This is of great importance for earthquake engineering because it provides upper bounds for the seismic motion near the causative fault, a fact which is a serious consideration in the design of nuclear power plants, dams and other critical facilities.

The aftershock of 0350, August 6, 1975, of the Oroville, earthquake (August 1, 1975; $M_L = 5.7$)

As a confirmation of the applicability of Sato and Hirasawa's model to represent localized fractures we considered the aftershock of 0350, August 6, 1975, of the Oroville earthquake. This event was one of the largest aftershocks ($M_L = 4.7$, depth = 9.3 km) and was recorded by ten strong motion accelerograms. Fletcher et al. (1980) analyzed the displacement records of the event and inferred the following source parameters:

$$M_o = 4.0 \cdot 10^{23} \text{ dyn-cm}$$

$$\Delta\sigma = 410 \text{ bars.}$$

Radius of an equivalent circular source $\rho_o = 0.83$ km

$$\Delta u_{max} = \left(\frac{24}{7\pi}\right) \cdot \left(\frac{\Delta\sigma}{\mu}\right) \cdot \rho_o = 124 \text{ cm}$$

$$v = 2.78 \text{ km/sec}$$

$$\beta = 3.7 \text{ km/sec.}$$

Since we assume the source of this small earthquake to be a single crack, we use eq. 48 of Papageorgiou and Aki (1981) which provides estimates of the Fourier amplitude spectra of a single crack. For $[\langle F^S \rangle^2]^{1/2} = (0.4)^{1/2}$ and multiplied by the factor $(\sqrt{2}/2)$ to account for free surface amplification and vectorial partition, eq. 48 of Papageorgiou and Aki (1981) gives 156 cm/sec as an estimate of the Fourier amplitude at the source. This is in very good agreement with the Fourier amplitude at the source (Fig. 14) obtained by analyzing the direct S-waves recorded at the stations listed on Table 4.

An analysis similar to that performed for the San Fernando, Kern County and Long Beach earthquakes, has been performed for the Borrego Mountain earthquake and the Parkfield earthquakes. The results are summarized below.

The Borrego Mountain earthquake of 1968

The Borrego Mountain earthquake ($M_L = 6.8$, $M_S = 6.7$, $m_b = 6.1$) is a strike slip event which occurred on the Coyote Creek fault in southern California. The surface rupture was composed of three well-defined segments of fracture (north, central, and south) and extended over a distance of 31 km. A maximum right-lateral offset of 38 cm was observed on the north segment and right lateral offsets of 25 to 30 cm and 8 to 14 cm were measured on the central and south segments respectively.

Burdick and Mellman (1976) point out the complexity of stress release during the event. They base their argument (1) on the tectonic setting which is composed of many parallel faults (zones of weakness) which contribute to the complexity of stress pattern on the Coyote Creek fault, (2) offsets caused by the event on the nearby faults (i.e., Imperial, Superstition Hills and San Andreas faults) and (3) on the diffuse pattern of aftershock distribution which did not define a single plane but a three dimensional region.

Burdick and Mellman (1976), who used teleseismic data, and Heaton and Helmberger (1977), who modelled the displacement record at El Centro agree that there was a massive rupture at the north segment which also caused the strong impulse observed on the acceleration record at the El Centro station. Few aftershocks and very little postseismic slip was observed along this segment as opposed to the larger number of aftershocks and the small coseismic slip and equal amount of postseismic slip that was observed along the south segment.

The attenuation of spectral amplitudes with distance and the source spectrum are shown in Fig. 15 and Fig. 16, respectively. They are based on the analyses of records obtained from stations listed on Table 5. The San Diego Light and Power Building station was excluded from the analysis because it may be on a node of the radiation pattern. The data could support regressions only with constant Q_β.

With the following source parameters (Geller, 1976)

$$M_o = 6.3 \times 10^{25} \text{ dyn-cm}$$
$$L = 33 \text{ km}$$
$$W = 11 \text{ km}$$
$$\overline{\Delta u} = 58 \text{ cm (assume: } V = v = 2.4 \text{ km/sec, } \beta = 3.2 \text{ km/sec)}$$

and $\left[\langle F^S \rangle^2\right]^{1/2} = (0.4)^{1/2}$, $P_o = 2 \cdot 10^5$ (cm/sec)^2 / sec($\sqrt{2}/2$) we obtain

$2\rho_o \simeq 2. - 3.$ km and $\Delta\sigma \simeq 200-300$ bars.

The Parkfield earthquake of 1966

The disposition of the stations which recorded this event, and their proximity to the source do not allow reliable correction by the present method based on the far-field assumption. The records which were included in the analysis were obtained from the stations listed on Table 6. The data could support regressions only with constant Q_β. The attenuation with distance of spectral amplitudes and the inferred source spectrum are shown in Fig. 17 and Fig. 18 respectively. It is not possible from these data to identify the origin of the corner frequency observed at 2 Hz, i.e., whether it is a genuine feature of the earthquake or whether it originates from the unreliable correction.

With the following source data (Aki, 1979)

$$M_o = 1.4 \times 10^{25} \text{ dyn-cm}$$
$$L = 35 \text{ km} \quad \rightarrow S = 525 \text{ km}^2$$
$$W = 15 \text{ km}$$
$$V = 2.2 \text{ km/sec}$$

we obtain $\Delta u_{max} = 51$ cm, $2\rho_o \simeq 1-2$ km and $\Delta\sigma \simeq 200-300$ bars and total number of cracks $\simeq 200$. These numbers are in very good agreement with those obtained for the Long Beach earthquake of 1933.

Aki (1979) considered a shallow slipped section near station 2 on the fault plane of the Parkfield earthquake of 1966 (Fig. 3 of Papageorgiou and Aki, 1981 reproduced from Aki, 1979). From the size of this slipped section which is roughly a circle of diameter $2\rho_o \simeq 6$ km he inferred a local stress drop of 50 bars. The size of this local fracture is larger than the barrier interval $2\rho_o \simeq 1-2$ km which we inferred in this study. This is due to the fact that Aki (1979) considered a particular crack which happens to be also the largest one and therefore is not expected to be representative of the average size of local fractures.

Table 7 summarizes the source parameters inferred in this study together with those inferred by Aki (1979). Striking are the similarities between the parameters inferred for the Fort Tejon and Kern County earthquakes as well as for the Parkfield and Long Beach earthquakes. The source parameters inferred in this paper confirm the barrier interval vs. maximum slip relationship proposed by Aki et al. (1977) for the California region (Fig. 13 of Aki et al., 1977).

Discussion and Conclusion

The specific barrier model, which was described in detail by Papageorgiou and Aki (1981), is implemented in the analysis of a set of six earthquake events of California, spanning a large range of magnitudes (M_L = 4.7 to 7.2).

It was found that the barrier interval (i.e. the parameter which measures the length scale of inhomogeneity of the fault which is effective during a particular event), as inferred by the specific barrier model, is not constant for a given fault zone, but varies roughly proportionally to the maximum slip. The ratio of the maximum slip over the barrier interval is proportional to the local stress drop, with constant of proportionality the rigidity of the material of the fault. The local stress drop was found to vary in the range of 200 to 400 bars, increasing slightly with earthquake size. Therefore, the local stress drop is an order of magnitude greater than the "global" stress drop which is proportional to the ratio of the maximum slip to the dimension which describes the size of the entire fault plane that breaks (Papageorgiou and Aki, 1981). This is in agreement with the ad hoc constant stress drop of 100 bars which is used by Hanks in his model in order to account for the discrepancies between measured and predicted root mean square accelerations that he observed when he used the "global" stress drop.

These observations confirm the barrier interval versus maximum slip relationship obtained by Aki et al. (1977) for the tectonic region of California, based on estimates of the barrier interval obtained from the scaling law of displacement spectra (Chouet et al., 1978), from surface measurements of fault slip (Aki, 1980a), and from seismic measurements of rise time. The agreement of the results of the variation of the barrier interval with maximum slip, arrived at by so different methods, is a further confirmation of the applicability of the barrier model.

Analysis of the attenuation of spectral amplitudes of the San Fernando earthquake of 1971, revealed that the Q_β of shear waves is strongly frequency dependent. The observed agreement between Q_β of shear waves and Q of coda waves supports the conjecture that coda waves are scattered shear waves (Aki, 1980b,c; Rautian and Khalturin, 1978). Frequency dependent Q_β was inferred also from the analysis of Kern County (1952) and Long Beach (1933) earthquakes. For all the events analyzed in the present paper, it was found that the attenuation of high frequency ($f \geq 3$ Hz) shear waves is not as strong as initially thought. This suggests that the cut-off frequency f_{max} observed on S-wave spectra of recorded strong ground motion at a site, should be attributed primarily to source effects rather than propagation path effects. For this reason f_{max} is interpreted in terms of the non-elasticity of the source that are caused by the rupture process. As discussed in detail by Aki (1979) and Papageorgiou and Aki (1981), f_{max} is inversely proportional to the cohesive zone size.

Various interesting observations can be made in connection with the cut-off frequencies of the spectra of the events which were analyzed in this paper. The cut-off frequency f_{max} of the earthquake events of San Fernando

(1971), Borrego Mountain (1968), Long Beach (1933) and Parkfield (1966) ($5.5 \leq M_L \leq 6.4$), was found to be practically the same, equal to ~5 Hz, as opposed to f_{max} of the Kern County earthquake of 1952 ($M_L = 7.2$) which is equal to 2.5 Hz. Interestingly enough, the corner frequencies of the displacement spectra of small events ($M \leq 3$) which occurred in Central California (Stone Canyon and San Fernando areas) fall in the range 5 to 10 Hz (see Fig. 25 of Chouet et al., 1978). In particular, the corner frequencies of the displacement spectra of small events ($1 \leq M \leq 3$) which occurred in the San Fernando area, are equal to 5 Hz (see Fig. 21 of Chouet et al., 1978), i.e. equal to the cut-off frequency of the acceleration power spectrum at the source, of the San Fernando earthquake of 1971.

It should also be noted that, for frequencies which are larger than f_{max}, the acceleration power spectra at the source of all the events considered fall off as $\omega^{-3 \sim -4}$ except for the Long Beach (1933), which decreases as $\omega^{-2 \sim -2.5}$.

Finally, striking similarities with respect to the source parameters were found between the Fort Tejon (1857) and Kern County (1952) earthquakes and between Long Beach (1933) and Parkfield (1966) earthquakes. The former are characterized by long barrier intervals, large slip and strong barriers while the latter are characterized by short barrier intervals, small slip and comparatively weaker barriers. The San Fernando (1971) and the Borrego Mountain (1968) are characterized with fault parameters which lie in between these two extremes.

TABLE 1a

RECORDS OF THE SAN FERNANDO EARTHQUAKE OF 1971
USED FOR ANALYSIS

RECORD NUMBER*	STATION	r_o(km)
C051	250 E. First Street Basement, LA	45.
C054	445 Figueroa Street, Sub-basement, LA	44.
D057	Hollywood Storage Basement, LA	39.
D058	Hollywood Storage P.E. Lot, LA	39.
D059	1901 Ave. of the Stars Sub-basement, LA	42.
D062	1640 S. Marengo Street 1st Floor, LA	45.
D065	3710 Wilshire Blvd. Basement, LA	42.
D068	7080 Hollywood Blvd. Basement, LA	37.
E075	3470 Wilshire Blvd. Sub-basement, LA	42.
E078	Water and Power Building Basement, LA	45.
E083	3407 6th Street Basement, LA	42.
F086	Vernon, CMD Building	51.
F088	633 E. Broadway, Glendale	37.
F089	808 S. Olive Street, Street Level, LA	46.
F095	120 N. Robertson Blvd. Sub-basement, LA	40.
F098	646 S. Olive Avenue Basement, LA	45.
F105	UCLA Reactor Laboratory, LA	41.
G106	Caltech Seismological Lab., Pasadena	38.
G107	Caltech Athenaeum, Pasadena	42.
G108	Caltech Millikan Library Basement, Pasadena	42.
G110	Jet Propulstion Lab. Basement, Pasadena	34.
G112	611 W. Sixth Street Basement, LA	45.
H115	15250 Ventura Blvd. Basement, LA	32.
H121	900 S. Fremont Avenue Basement, Alhambra	45.
I128	435 N. Oakhurst Ave. Basement, Beverly Hills	39.
I131	450 N. Roxbury Dr. First Floor, Beverly Hills	40.
I134	1800 Century Park East Basement, (P-3), LA	41.
J148	616 S. Normandie Avenue Basement, LA	42.
L166	3838 Lankershim Blvd. Basement, LA	33.
M176	1150 S. Hill Street Sub-basement, LA	45.
M180	4000 W. Chapman Avenue Basement, Orange	85.
M183	6074 Park Drive Ground Level, Wrightwood	72.
M184	6074 Park Drive Ground Level, Wrightwood	72.
N185	Carbon Canyon Dam	77.
N186	Whittier Narrows Dam	56.
N188	1880 Century Park East 1st Level Parking, LA	41.
N192	2500 Wilshire Blvd. Basement, LA	43.
O198	Griffith Park Observatory, LA	36.
O199	1625 Olympic Blvd. Ground Floor, LA	44.
P214	4867 Sunset Blvd. Basement, LA	39.
P217	3345 Wilshire Blvd. Basement, LA	42.
P221	Santa Anita Reservoir, Arcadia	45.
P223	Puddingston Reservoir, San Dimas	66.
Q233	14724 Ventura Blvd. First Floor, LA	32.

Q236	1750 N. Orchid Avenue Ground Floor, Hollywood	37.
Q239	9100 Wilshire Blvd. Basement, Beverly Hills	41.
Q241	800 W. First Street First Floor, LA	44.
R244	222 Figueroa Street First Floor, LA	44.
R246	6464 Sunset Blvd. Basement, LA	38.
R249	1900 Avenue of the Stars Basement, LA	41.
R251	234 Figueroa Street Basement, LA	44.
R253	535 S. Fremont Avenue Basement, LA	44.
S255	6200 Wilshire Blvd. Ground Floor, LA	41.
S258	3440 University Avenue Basement, LA	47.
S265	3411 Wilshire Blvd. 5th Basement, LA	42.
S266	3550 Wilshire Blvd. Basement, LA	42.

* See California Institute of Technology (1973).

TABLE 1b

THE SOURCE POWER SPECTRUM OF ACCELERATION, OF THE SAN FERNANDO EARTHQUAKE OF 1971 INFERRED FOR THREE CASES OF FREQUENCY DEPENDENCE OF Q_β

Parameter		Value		90% Confidence Interval		
Q_β=Const	Q_β	700.0		550.0 - 1000.0		
	S_1	2.3		2.0 - 2.6		
	S_2	2.8		2.4 - 3.3		
	S_3	2.6	x 10^5	2.1 - 3.2		x 10^5
	S_4	1.0		0.74 - 1.4		
	S_5	0.08		0.043 - 0.15		
$Q_\beta=Q_o f^m$	Q_o	61.0		45.0 - 93.0		
	m	1.0		0.85 - 1.3		
	S_1	8.5		5.1 - 14.0		
	S_2	8.1	x 10^5	5.7 - 12.0		x 10^5
	S_3	5.4		3.9 - 7.4		
	S_4	1.2		0.81 - 1.8		
	S_5	0.032		0.019 - 0.053		
Q_β=free	Q_1	50.0		40.0 - 70.0		
	Q_2	220.0		100.0 - 600.0		
	Q_3	430.0		200.0 - 2600.0		
	Q_4	610.0		400.0 - 1300.0		
	Q_5	890.0		600.0 - 1600.0		
	S_1	12.4		7.0 - 23.0		
	S_2	5.4		2.8 - 10.0		
	S_3	3.5	x 10^5	1.8 - 6.8		x 10^5
	S_4	1.2		0.64 - 2.2		
	S_5	0.051		0.025 - 0.1		

Note: The subscripts 1,2,3,4 and 5 refer to the frequencies 1,2,4,8 and 16Hz respectively. S_i's in $(cm/sec)^2/sec$.

TABLE 2

RECORDS OF THE KERN COUNTY EARTHQUAKE OF 1952 USED FOR ANALYSIS

Station*		t_1 (sec)	t_2 (sec)	Δ (sec)	r_o (km)	$\bar{a}_H$ (cm/sec^2)
A003	Pasadena CIT Athenaeum	11.5	27.	15.5	126.	22.6
A004	Taft Lincoln School (tunnel)	2.5	15.	12.5	43.	66.2
A005	Santa Barbara Courthouse	6.5	20.5	14.	89.5	42.9
A006	Hollywood Storage (basement)	9.	22.	13.	119.5	23.2
A007	Hollywood Storage (P.E. Lot)	9.	22.	13.	119.5	23.6

TABLE 3

RECORDS OF THE LONG BEACH EARTHQUAKE OF 1933 USED FOR ANALYSIS

	Station*	t_1 (sec)	t_2 (sec)	Δ (sec)	r_o (km)	$\bar{a}_H$ (cm/sec^2)
B021	Vernon CMD Bldg.	0.5	5.5	5.0	47.8	55.5
V314	L.A. Subway Terminal (Sub-Bsmt) Los Angeles, Cal.	1.0	7.0	6.0	54.9	33.7
V315	Public Utilities Bldg. Long Beach, Cal.	0.5	7.5	7.0	27.2	83.9

* See California Institute of Technology (1973).

TABLE 4

RECORDS OF THE AFTERSHOCK OF 0350, August 6, 1975, OF THE OROVILLE EARTHQUAKE USED FOR ANALYSIS

	Station	t_1 (sec)	t_2 (sec)	Δ (sec)	r_o (km)
DJR	D. Johnson Branch	1.50	2.50	1.00	11.7
OAP	Oroville Airport	1.50	2.25	0.75	12.7
OMC	Medical Center	1.00	1.88	0.88	9.5
003	CMDG Station 3 Oroville, Cal.	1.63	2.88	1.25	9.6
002	CMDG Station 2 Oroville, Cal.	1.63	2.88	1.25	15.6
EBH	E. Broadbeck Station Oroville, Cal.	1.25	2.5	1.25	10.9
001	CMDG Station 1 Oroville, Cal.	1.25	2.5	1.25	13.6
004	CMDG Station 4 Oroville, Cal.	1.25	2.5	1.25	12.7
005	CMDG Station 5 Oroville, Cal.	1.25	2.5	1.25	11.7

TABLE 5

RECORDS OF THE BORREGO MOUNTAIN EARTHQUAKE OF 1968
USED FOR ANALYSIS

	Station*	t_1 (sec)	t_2 (sec)	Δ (sec)	r_o (km)	$\bar{a}_H$ (cm/sec^2)
A019	El Centro Site Imperial Valley	6.5	11.0	4.5	69.8	42.2
A020	San Diego Light & Power Bldg.	7.0	12.0	5.0	109.9	14.5
B040	San Onofre Sce Power Plant	15.5	22.0	6.5	134.4	17.9
Y370	S. Cal. Edison Co. Colton, Cal.	8.5	15.0	6.5	146.2	10.9

TABLE 6

RECORDS OF THE PARKFIELD EARTHQUAKE OF 1966
USED FOR ANALYSIS

	Station*	t_1 (sec)	t_2 (sec)	Δ (sec)	r_o (km)	a_H (cm/sec^2)
B034	Cholame, Shandon Cal. Array No. 5	4.5	9.5	5.0	27	126.2
B035	Cholame, Shandon Cal. Array No. 8	1.5	7.0	5.5	29	76.0
B036	Cholame, Shandon Cal. Array No. 12	2.0	8.0	6.0	31	22.6
B037	Temblor, Cal. No. 2	2.0	5.5	3.5	36	109.

* See California Institute of Technology (1973).

TABLE 7

EARTHQUAKE SOURCE PARAMETERS

EVENT	M_S	M_L	m_b	$M_o \times 10^{27}$ (dyn-cm)	L (km)	W (km)	$\Delta\sigma^*$ (pars)	ΔU_{max} (m)	$2\rho_o$ (km)	d (km)	f_{max} (Hz)	$G \times 10^{10}$ (erg/cm^2)	σ_c (bars)	D (m)
San Francisco, 1906	8.25			~3.5-4.3	~300.	~15-20.		~4.-6.	15.			2.		
Fort Tejon, 1857				~5.3-9.0	~300.	~15-20.	~370.	10.	15.	~1.-2.		10	~500-700.	~3.-4.
Kern Country, 1952	7.7	7.2		2.0	70.	20.	~350.	7.-9.	~13.	1.0	2.5	10	~680	~3
San Fernando, 1971	6.6	6.35	6.2	0.12	20.	14.	~300.	2.-3.	~5.	0.5	5.0	2.4	~480	~1.
Borrego Mountain, 1968	6.7	6.8	6.1	0.063	33.	11.	~200-300.	~0.90	~2.-3.	0.6	4.0	~1-2	~300-400.	~0.4
Long Beach, 1933	6.25	6.43		0.028	30.	15.	~220.	0.30	~1.	0.6	4.0	~0.3	~200	~0.4
Parkfield, 1966	6.5	5.5	5.9	0.014	35.	15.	~200-300 (~50[1])	0.51	~1.-2. (~6.[1])	0.5	5.0	~0.3-0.5	~200	~0.4
The aftershock of 0350, August 6, 1975 of the Oroville Cal. earthquake.		4.7		0.0004	equivalent radius R=0.83km		410	1.24	1.6	0.2	10.0	1.5	~600	~0.5

*Local stress drop

(1) Aki (1979)

REFERENCES

Aki, K. (1966). "Generation and propagation of G waves from the Niigata earthquake of June 16, 1964, "Bull. Earthquake Research Inst., Univ. Tokyo (44), 23-88.

Aki, K. (1968). "Seismic displacements near a fault," J. Geophys. Res. (73), 5359-5376.

Aki, K. (1969). "Analysis of the seismic coda of local earthquakes as scattered waves," J. Geophys. Res., (74), 615-631.

Aki, K. (1972). "Scaling law of earthquake source time-function," Geophys. J. Roy. Astr. Soc. (31), 3-25.

Aki, K. (1979). "Characterization of barriers on an earthquake fault," J. Geophys. Res., (84), 6140-6148.

Aki, K. (1980a). "Reevaluation of stress drop and seismic energy using a new model of earthquake faulting" in "Mechanisme et Prevision Seismes," Hommage au professeur Jean Coulomb, Publie sous la direction de Claude J. Allegre, Edition du Centre National de la Recherche Scientifique.

Aki, K. (1980b). "Attenuation of shear waves in the lithosphere for frequencies from 0.05 to 25 Hz," Phys. Earth Planet. Interiors (21), 50-60.

Aki, K. (1980c). "Scattering and attenuation of shear waves in the lithosphere," J. Geophys. Res. (85), 6496-6504.

Aki, K., M. Bouchon, B. Chouet, and S. Das (1977). "Quantitative prediction strong motion for a potential earthquake fault," Annali di Geophisica, Vol. XXX, N. 3-4, 341-368.

Aki, K., and Richards, P.G. (1980). Quantitative Seismology: Theory and Methods, W.H. Freeman Co.

Ben-Menahem, . (1978). "Source mechanism of the 1906 San Francisco earthquake," Phys. Earth Planet. Interiors (17), 163-181.

Berrill, J.B. (1975). "A study of high-frequency strong ground motion from the San Fernando earthquake," Ph.D. thesis, California Institute of Technology, Pasadena.

Bolt, B.A. (1972). "San Fernando rupture mechanism and the Pacoima strong-motion record," Bull. Seism. Soc. Am. (62), 1053-1061.

Bolt, B.A. (1978). "The local magnitude M_L of the Kern County earthquake of July 21, 1952," Bull. Seism. Soc. Am. (68), 513-515.

Bond, W.E., Dobry, R., O'Rourke, M.J. (1980), "A study of the engineering characteristics of the 1971 San Fernando earthquake records using time domain techniques," Research Report, Rensselaer Polytechnic Institute, Department of Civil Engineering.

Boore, D.M., and M.D. Zoback (1974). "Two-dimensional kinematic fault modelling of the Pacoima Dam strong-motion recordings of the February 9, 1971 San Fernando earthquake," Bull. Seism. Soc. Am. (64), 555-570.

Bouchon, M. (1978). "A dynamic source model for the San Fernando earthquake," Bull. Seism. Soc. Am. (68), 1555-1576.

Bouchon, M. (1981). "The Rupture Mechanism of the Coyote Lake Earthquake of August 6, 1979 Inferred From Near-Field Data", submitted for publication to the Bull. Seism. Soc. Am.

Bouchon, M., and K. Aki (1977). "Discrete wave-number representation of seismic-source wavefields," Bull. Seism. Soc. Am. (67), 259-277.

Brune, J.N. (1968). "Seismic moment, seismicity, and rate of slip along major fault zones," J. Geophys. Res. (73), 777-784.

Burdick, L.J. and G.R. Mellman (1976). "Inversion of the body waves from the Borrego Mountain earthquake to the source mechanism," Bull. Seism. Soc. Am. (66), 1485-1499.

California Institute of Technology (1973). "Strong-motion earthquake accelerograms - digitized and plotted data," Earthquake Eng. Res. Lab., Calif. Inst. of Tech., Pasadena, pt. C and subsequent pts. D through S. Chouet, B. (1976). "Source, scattering and attenuation effects on high frequency seismic waves," Ph.D. Thesis, Massachusetts Institute of Technology, Cambridge.

Chouet, B., K. Aki, and M. Tsujiura (1978). "Regional variation of the scaling law of earthquake source spectra," Bull. Seism. Soc. Am. (68), 49-80).

Cisternas, A. (1963). "Precision determination of focal depths and epicenters of local shocks in California," Bull. Seism. Soc. Am. (53), 1075-1083.

Dobry, R., Idriss, I.M., and Ng, E. (1978). "Duration characteristics of horizontal components of strong motion earthquake records," Bull. Seism. Soc. Am. (68), 1487-1520.

Dunbar, W.S., Boore, D.M., and W. Thatcher (1980). "Pre-, co-, postseismic strain changes associated with the 1952 M_L = 7.2 Kern County, California earthquake," Bull. Seism. [Kei: something seems to be missing here.--j]

Fletcher, J.B., Brady, A.G., and T.C. Hanks (1980). "Strong motion accelerograms of the Oroville, California aftershocks; data processing and the aftershocks of 0350, August 6, 1975," Bull. Seism. Soc. Am. (70), 243-268.

Geller, R.J. (1976). "Scaling relations for earthquake source parameters and magnitudes," Bull. Seism. Soc. Am. (66), 1501-1523.

Gutenberg, B. (1955). "Magnitude determination for larger Kern County shocks, 1952; effects of station azimuth and calculation methods," Bull. 171, Calif. Div. Mines and Geol., 171-175.

Hanks, T.C. (1974). "The faulting mechanism of the San Fernando, California earthquake," J. Geophys. Res. (79), 1215-1229.

Hanks. T. C. (1975). "Strong ground motion of the San Fernando, California earthquake: ground displacements," Bull. Seism. Soc. Am. (65), 193-225.

Hanks, T.C. (1977). "Earthquake stress drops, ambient tectonic stress, and stresses that drive plate motions," Pure Appl. Geophys. (115), 441-458.

Hanks, T.C. (1979). "b-values and seismic source models: implications for tectonic stress variations along active crustal fault zones and the estimation of high-frequency strong ground motion," J. Geophys. Res. (84), 2235-2242.

Hanks, T.C. (1980). "Crustal earthquake stress drops," Proc. of Conference IX, Magnitude of Deviatoric Stress in Earth's Crust and Upper Mantle, v. II, 491-518.

Hanks, T.C., T. Hileman, and W. Thatcher (1975). "Seismic moments of the larger earthquakes of the southern California region," Bull. Geol. Soc. Am. (86), 1131-1139. Heaton, T.H., and D.V. Helmberger (1977). "A study of the strong ground motion of the Borrego Mountain, California earthquake," Bull. Seism. Soc. Am. (67), 315-330.

Heaton, T.H., and D.V. Helmberger (1979). "Generalized ray models of the San Fernando earthquake," Bull. Seism. Soc. Am. (69), 1311-1341.

Housner, G.W. (1975). "Measures of Severity of Earthquake Ground Shaking," Proceedings, U.S. National Conference on Earthquake Engineering, Ann Arbor, Michigan.

Husid, P. (1967). "Gravity effects on the earthquake response of yielding structures," Report of Earthquake Engineering, Research Laboratory, California Institute of Technology, Pasadena.

Kanamori, H., and D.L. Anderson (1975). "Theoretical basis for some empirical relations in seismology," Bull. Seism. Soc. Am. (65), 1073-1095.

Kanamori, H., and P.C. Jennings (1978). "Determination of local magnitude, M_L, from strong motion accelerograms," Bull. Seism. Soc. Am. (68), 471-485.

Kanamori, H., and G.S. Stewart, "Seismological aspects of Guatemala earthquake of February 4, 1976," J. Geophys. Res., (83), 3427-3434, 1978.

Kubo, T., and Penzien, J. (1977). "Characteristics of three-dimensional ground motions along principal axes, San Fernando earthquake," Proceedings, 6th World Conference on Earthquake Engineering, New Delhi, India.

Kubo, T., and Penzien, J. (1976). "Time and frequency domain analysis of three-dimensional ground motion, San Fernando earthquake," EERC 76-6, University of California, Berkeley.

Langston, C.A. (1978). "The February 9, 1971 San Fernando Earthquake: A study of source finiteness in teleseismic body waves," Bull. Seism. Soc. Am. (68), 1-29.

McGuire, R.K. (1974). "Seismic structural response risk analysis, incorporating peak response regressions on earthquake magnitude and distance," Ph.D. thesis, Massachusetts Institute of Technology, Cambridge, Mass.

McGuire, R.K., and T.C. Hanks (1980). "RMS accelerations and spectral amplitudes of strong ground motion during the San Fernando, California earthquake," Bull. Seism. Soc. Am. (70), 1907-1919.

Mikumo, T. (1973). "Faulting process of the San Fernando earthquake of February 9, 1971 inferred from static and dynamic near-field displacements," Bull. Seism. Soc. Am. (63), 249-269.

Niazy, A. (1975). "An exact solution for a finite, two-dimensional moving dislocation in an elastic half-space with application to the San Fernando earthquake of 1971," Bull. Seism. Soc. Am. (65), 1797-1826.

Orowan, E. (1960). "Mechanism of seismic faulting in rock deformation," Geol. Soc. Am. Mem. (79), 323-345.

Papageorgiou, A.S. and K. Aki (1981). "A specific barrier model for the quantitative description of inhomogeneous faulting and the prediction of strong ground motion. - I. Description of the model," submitted for publication to the Bull. Seism. Soc. Am.

Penzien, J. and Watabe, M. (1975). "Characteristics of 3-dimensional earthquake ground motions," International Journal of Earthquake Engineering and Structural Dynamics, Vol. 3.

Rautian, T.G. and V.I. Khalturin (1978). "The use of coda for determination of the earthquake source spectrum," Bull. Seism. Soc. Am. (68), 923-948.

Richter, C.F. (1958). Elementary Seismology, San Francisco, W.H. Freeman Co.

Sato, T. and T. Hirasawa (1973). "Body wave spectra from propagating shear cracks," J. Phys. Earth (21), 415-431. Shakal, A.F. (1979). "Analysis and modelling of the effects of the source and medium on strong motion," Ph.D. thesis, Massachusetts Institute of Technology, Cambridge, Mass.

Stoneley, R., "The Mongolian earthquake of 1931, August 10," Rep 42, 5-6, Brit. Ass. of Seism., London, 1937.

Trifunac, M.D. (1974). "A three-dimensional dislocation model for the San Fernando, California earthquake of February 9, 1971," Bull. Seism. Soc. Am. (64), 149-172.

Trifunac, M.D. (1976). "Preliminary empirical model for scaling Fourier amplitude spectra of strong ground acceleration in terms of earthquake magnitude, source to station distance and recording site conditions," Bull. Seism. Soc. Am. (66), 1343-1373.

Trifunac, M.D. (1978). "Response spectra of earthquake ground motion," J. Eng. Mech. Division, ASCE (104), EM5, 1081-1097.

Trifunac, M.D., and Anderson, J.G. (1977). "Preliminary empirical models for scaling absolute acceleration spectra," Report No. 77-03, Department of Civil Engineering, University of Southern California, Los Angeles.

Trifunac, M.D. and J.N. Brune, "Complexity of energy release during the Imperial Valley, Calfornia earthquake of 1940," Bull. Seis. Soc. Am. (60), 137-160, 1970.

Tukey, J.W. (1965). "Data analysis and the frontiers of geophysics," Science (148), 1283-1289.

Usami, T., "Seismometrical study of Boso-Oki earthquake of November 26, 1953," Quart. J. Seism., Tokyo (21), 3, 1956.

Wyss, M. (1970). "Stress estimates for South American shallow and deep earthquakes," J. Geophys. Res. (75), 1529-1544.

Wyss, M. and J.N. Brune, "The Alaska earthquake of 28 March 1964: A complex multiple rupture," Bull. Seis. Soc. Am. (57), 1017-1023, 1967.

$$\theta = \text{arctg}\left(\frac{y}{x}\right)$$

$$\phi = \left|\text{arctg}\left(\frac{x}{z \cdot \cos\theta}\right)\right|$$

$$-90° \leq \theta \leq 90°$$

$$0° \leq \phi \leq 90°$$

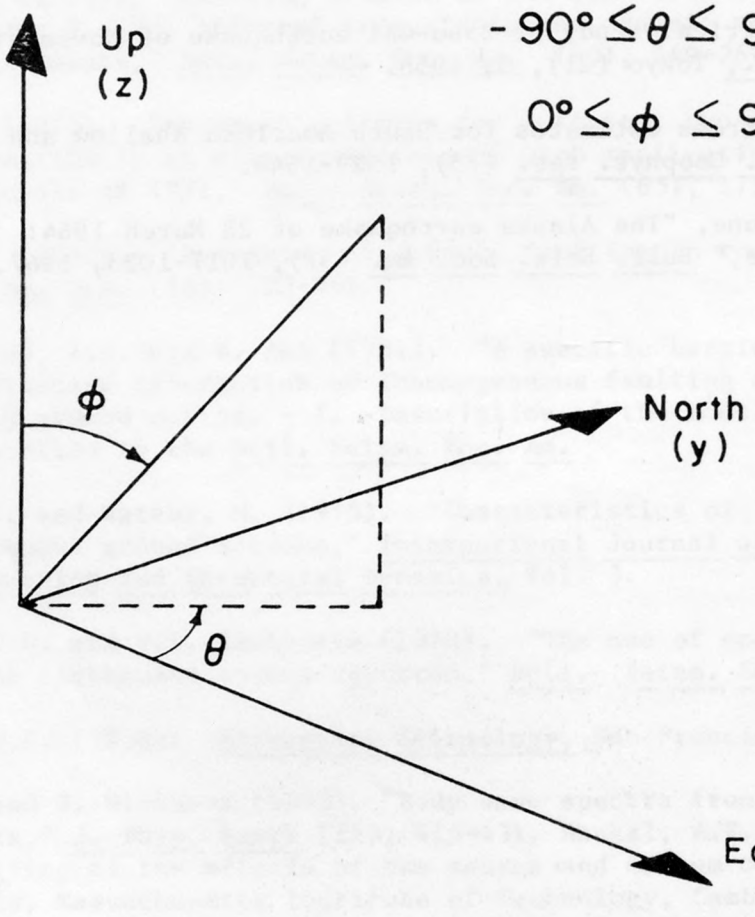

Fig. 1. Coordinate system used for the interpretation of the time variation of the maximum principal plane of ground motion.

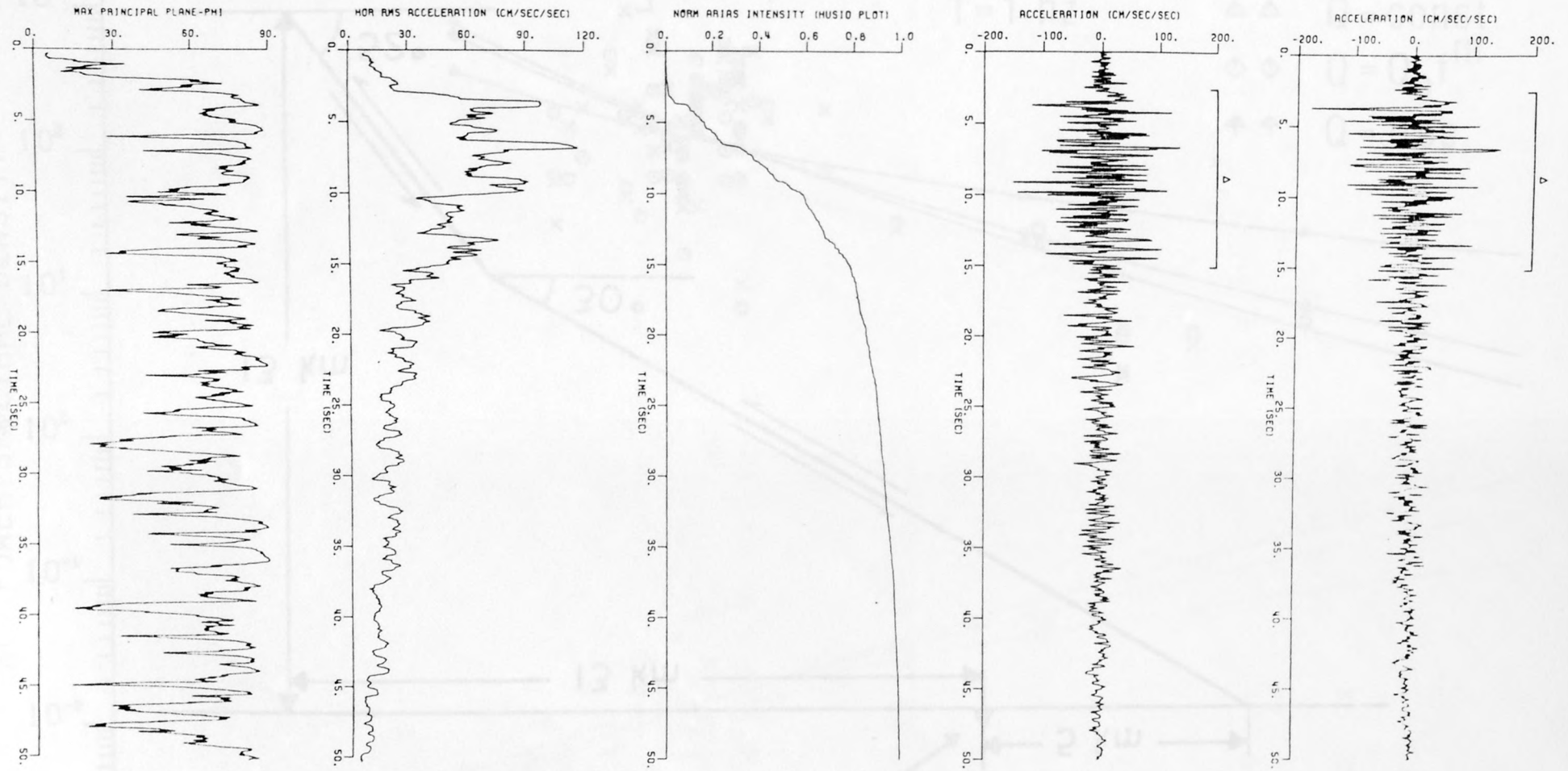

Figure 2. Radial and transverse accelerograms (w.r.t. epicenter) of the ground motion recorded at the Taft Lincoln School station during the Kern County earthquake of 1952, and the correspondin g Husid plot, moving time window root mean square acceleration, and time variation of maximum principal plane (ϕ-angle).

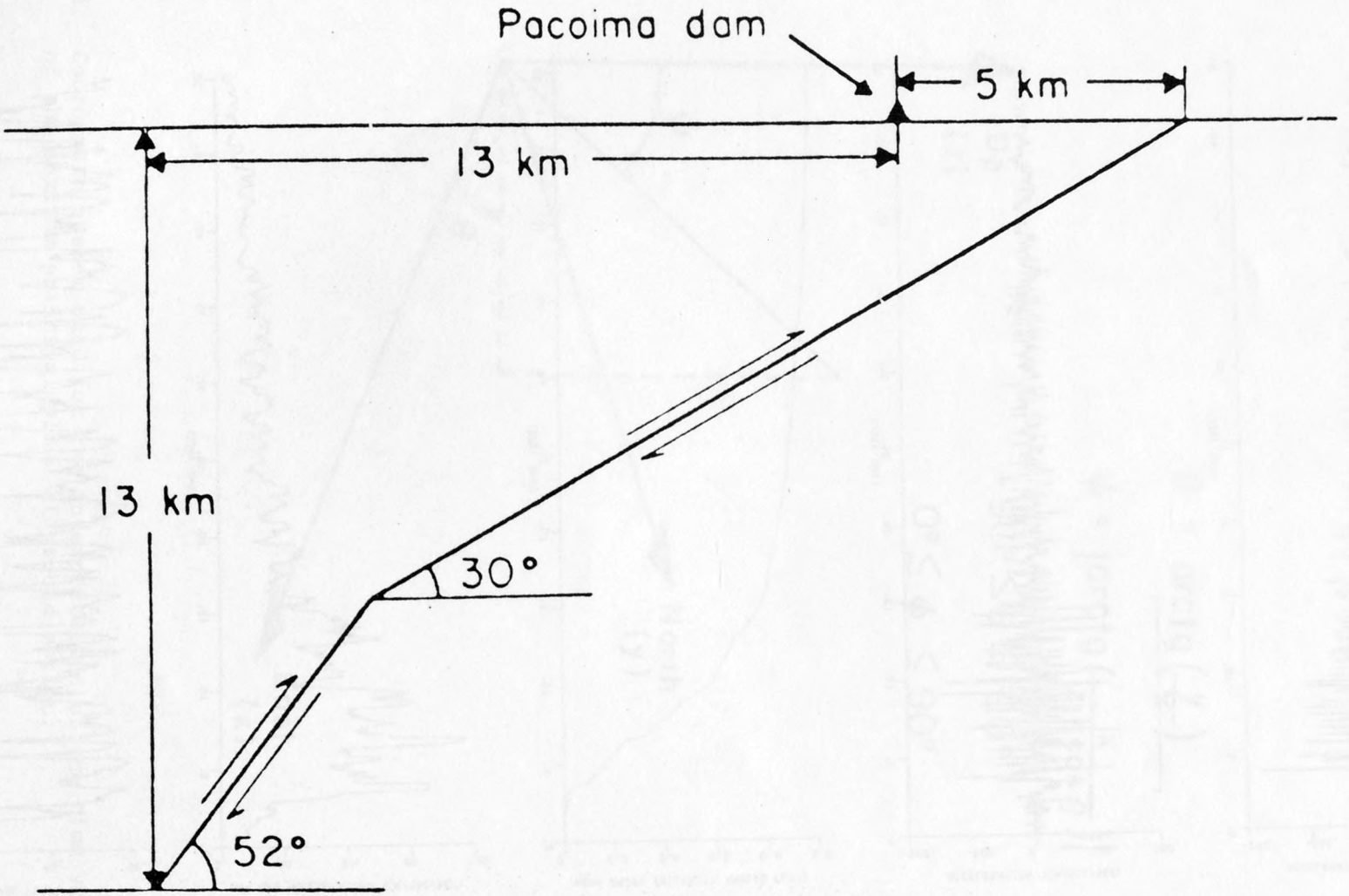

Fig. 3. The fault configuration used by Bouchon (1978) to model the San Fernando earthquake of 1971. The rupture started on the steepest plane and propagated upwards and to the south until it reached the ground surface.

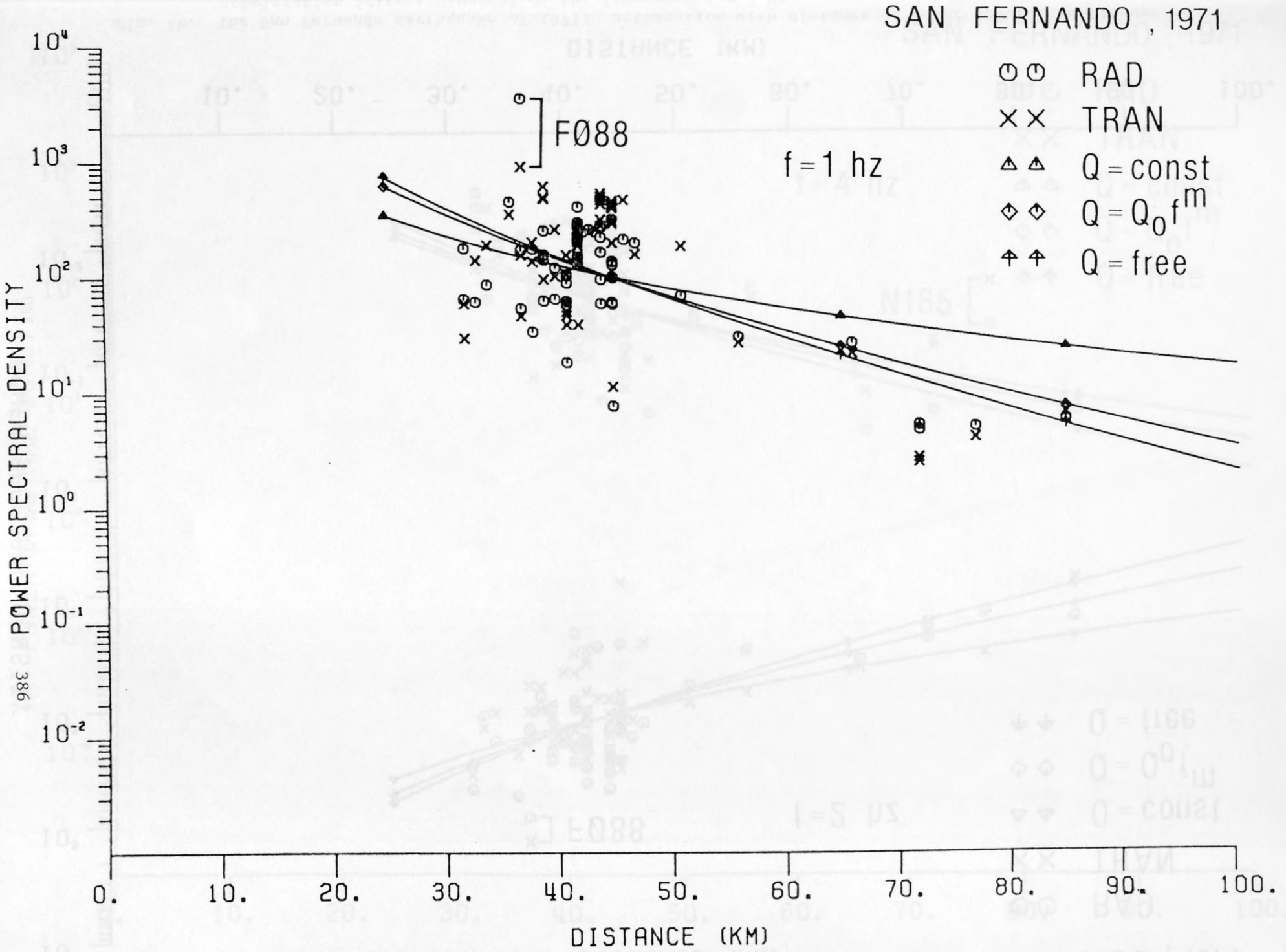

Fig. 4a. The San Fernando earthquake of 1971: attenuation with distance of power spectral amplitudes of acceleration (direct S-waves) of the frequency f = 1 Hz.

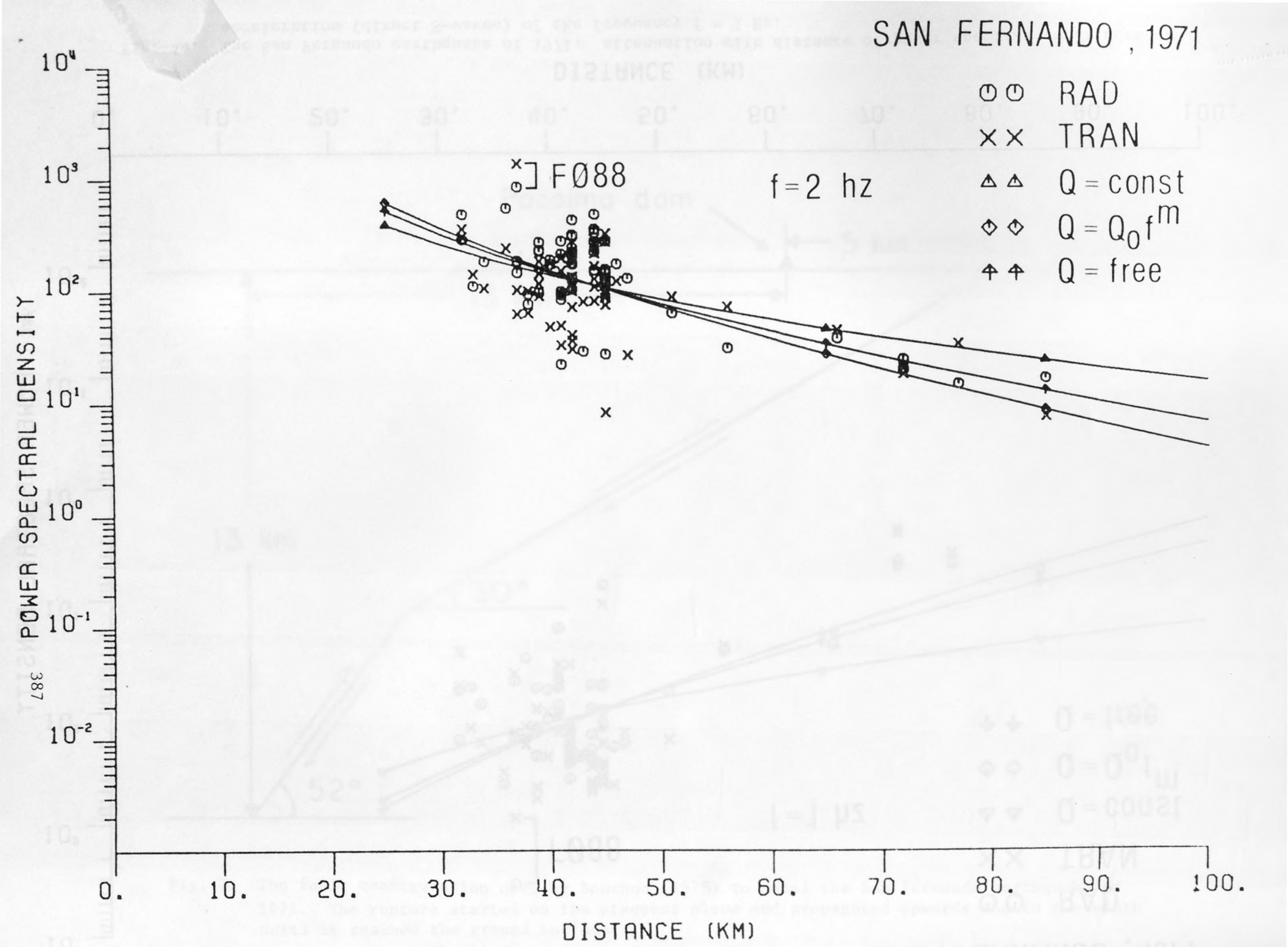

Fig. 4b. The San Fernando earthquake of 1971: attenuation with distance of power specral amplitudes of acceleration (direct S-waves) of the frequency f = 2 Hz.

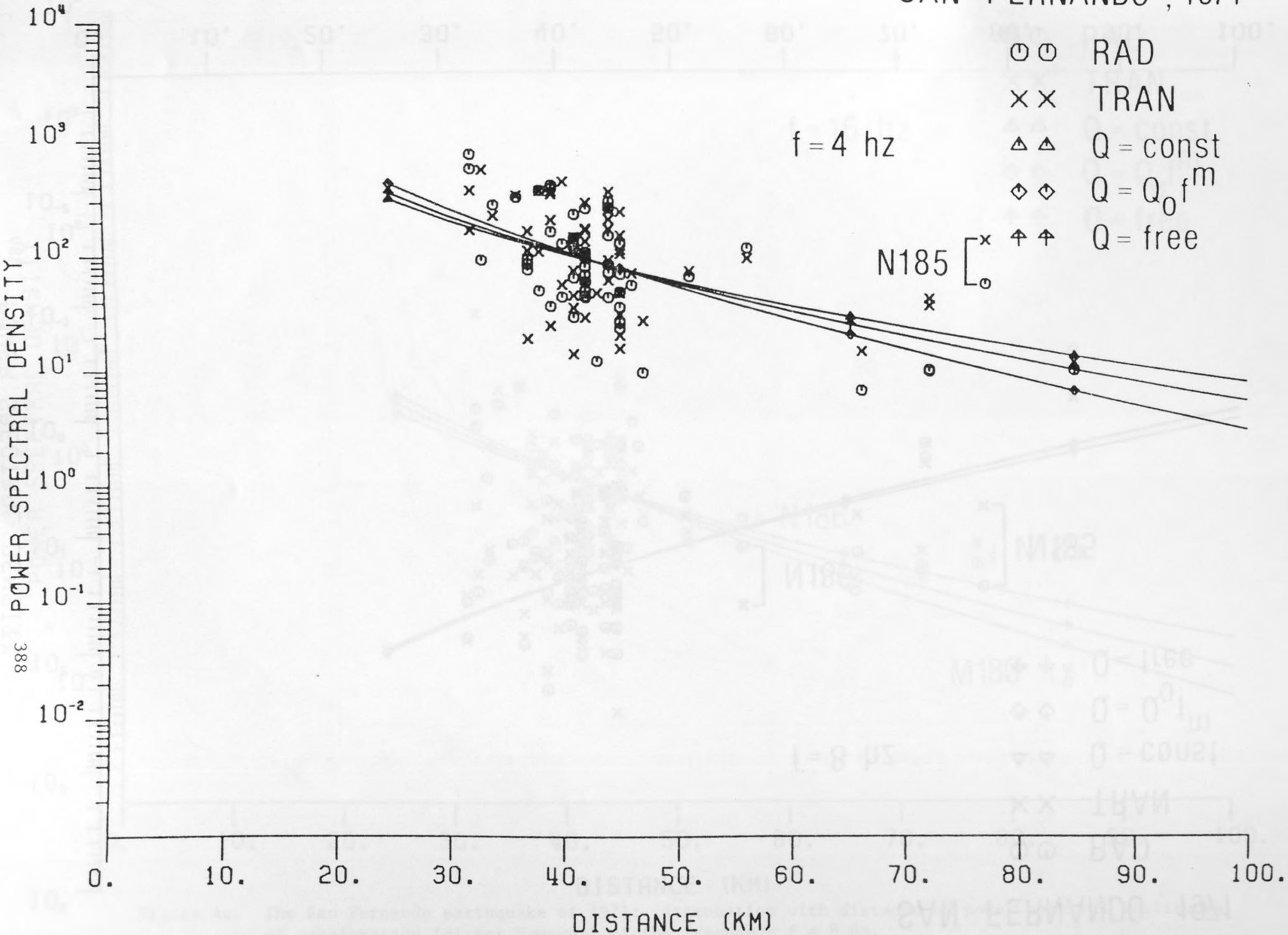

Figure 4c. The San Fernando earthquake of 1971: attenuation with distance of power spectral amplitudes of acceleration (direct S-waves) of the frequency f = 4 Hz.

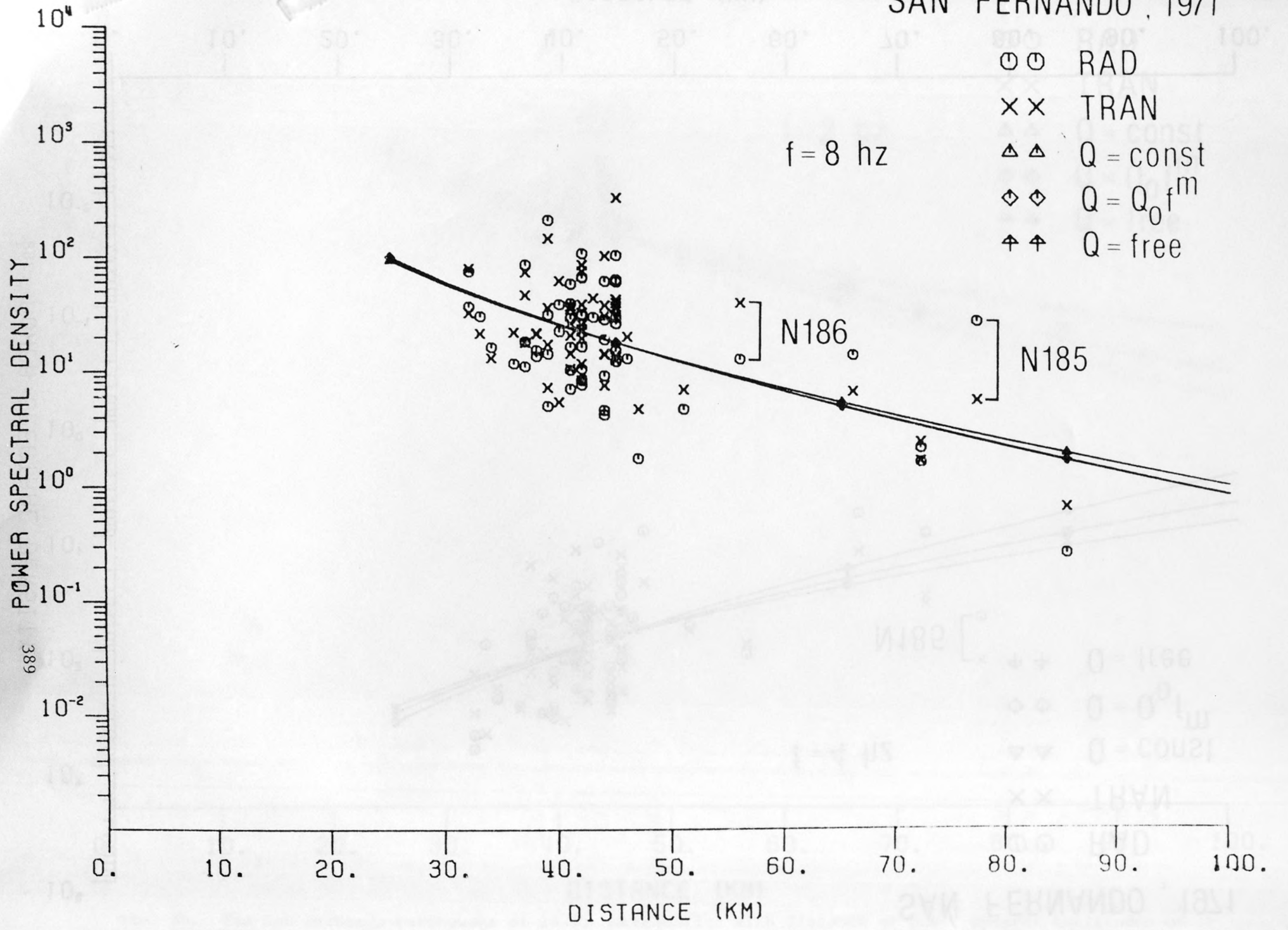

Figure 4d. The San Fernando earthquake of 1971: attenuation with distance of power spectral amplitudes of acceleration (direct S-waves) of the frequency f = 8 Hz.

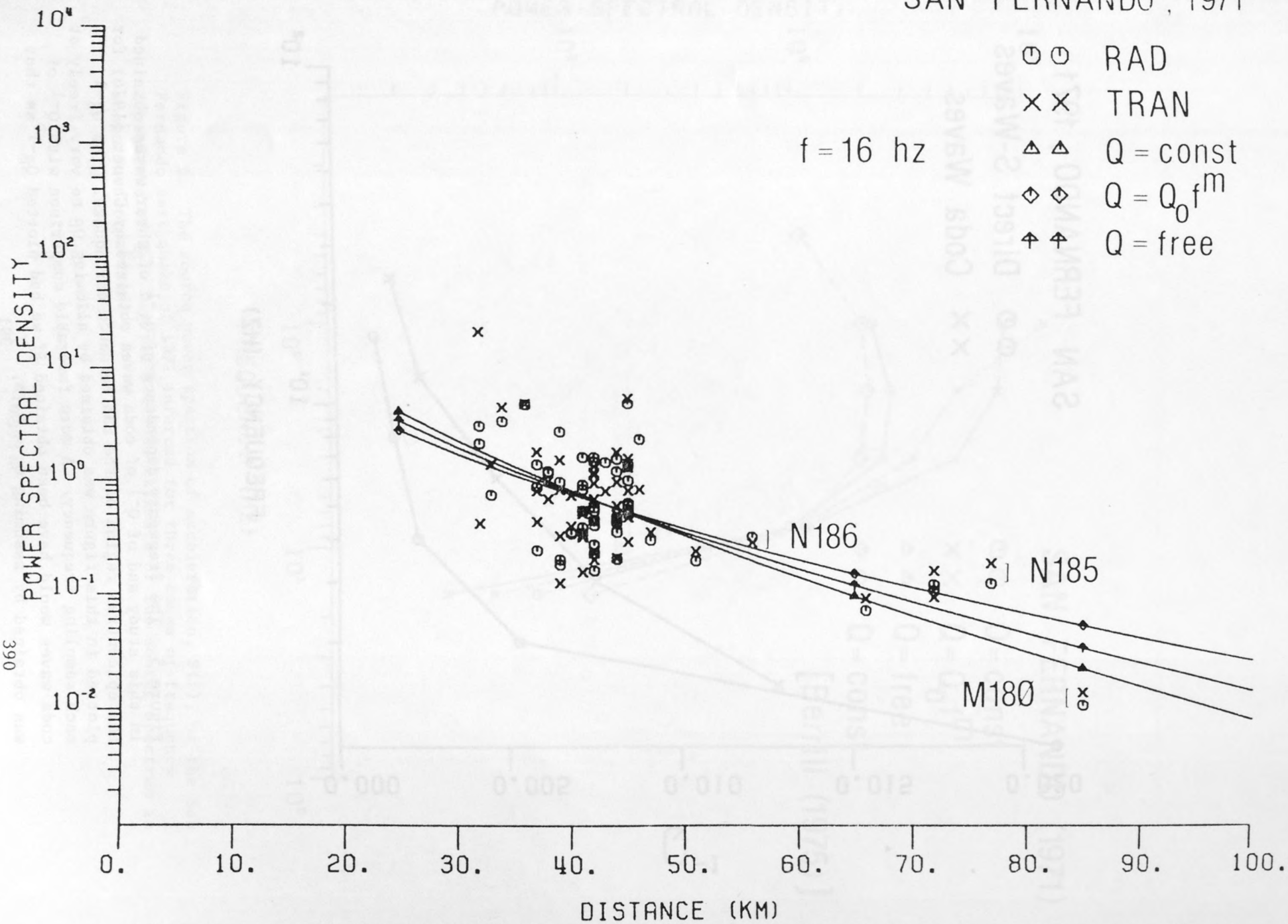

Figure 4e. The San Fernando earthquake of 1971: attenuation with distance of power spectral amplitudes of acceleration (direct S-waves) of the frequency f = 8 Hz.

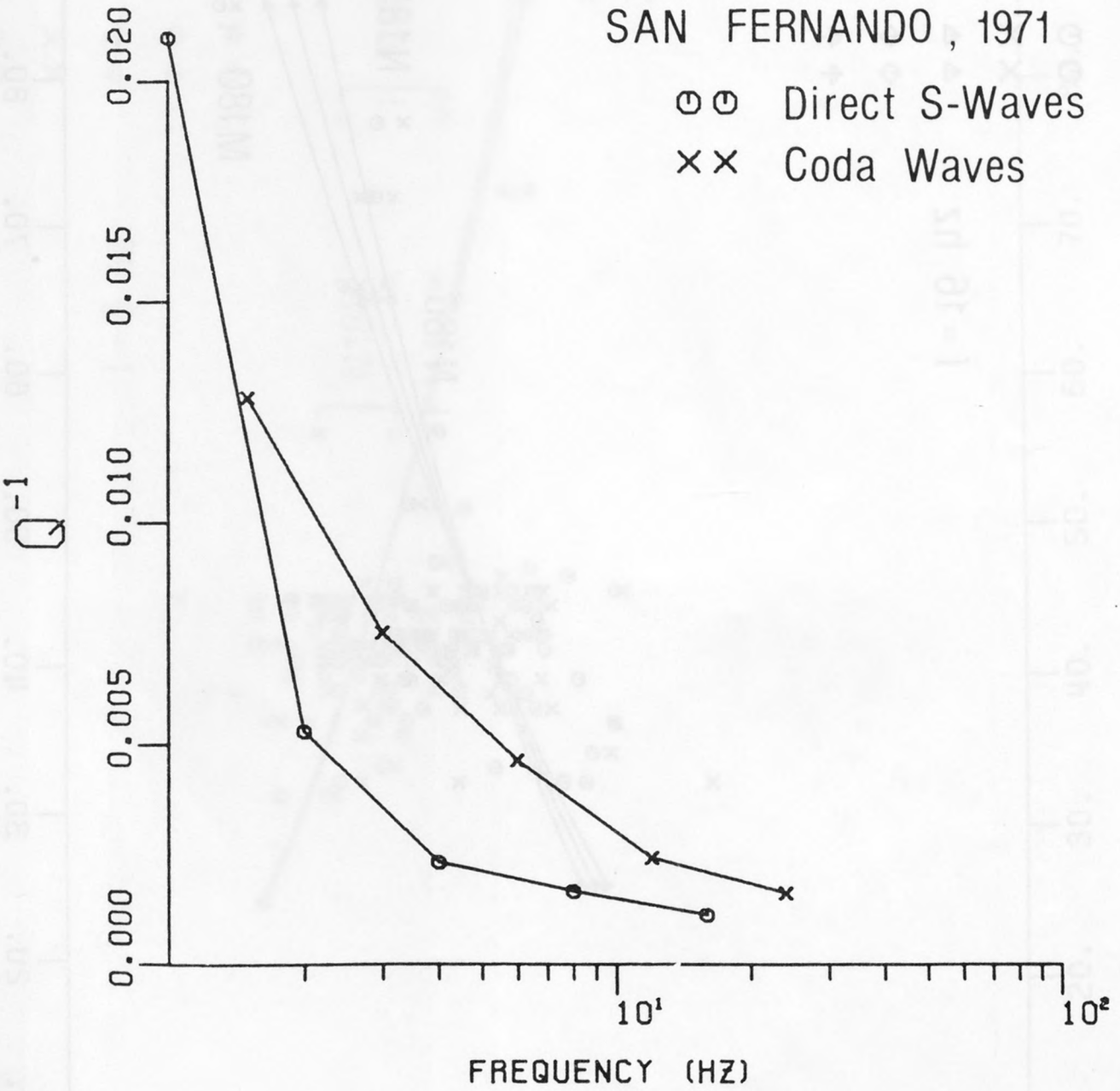

Figure 5. The frequency dependence of Q_β^{-1} of shear waves obtained in this study and of Q^{-1} of coda waves obtained by Chouet (1976) for the epicentral region of the San Fernando earthquake. The Q_β^{-1} plotted in this figure was obtained by allowing $Q\beta$ to vary freely at each sampling frequency. A more favorable comparison with Q^{-1} of coda waves would have been obtained if we had plotted Q_β^{-1} as that was obtained by assuming $Q_\beta = Q_o f^m$.

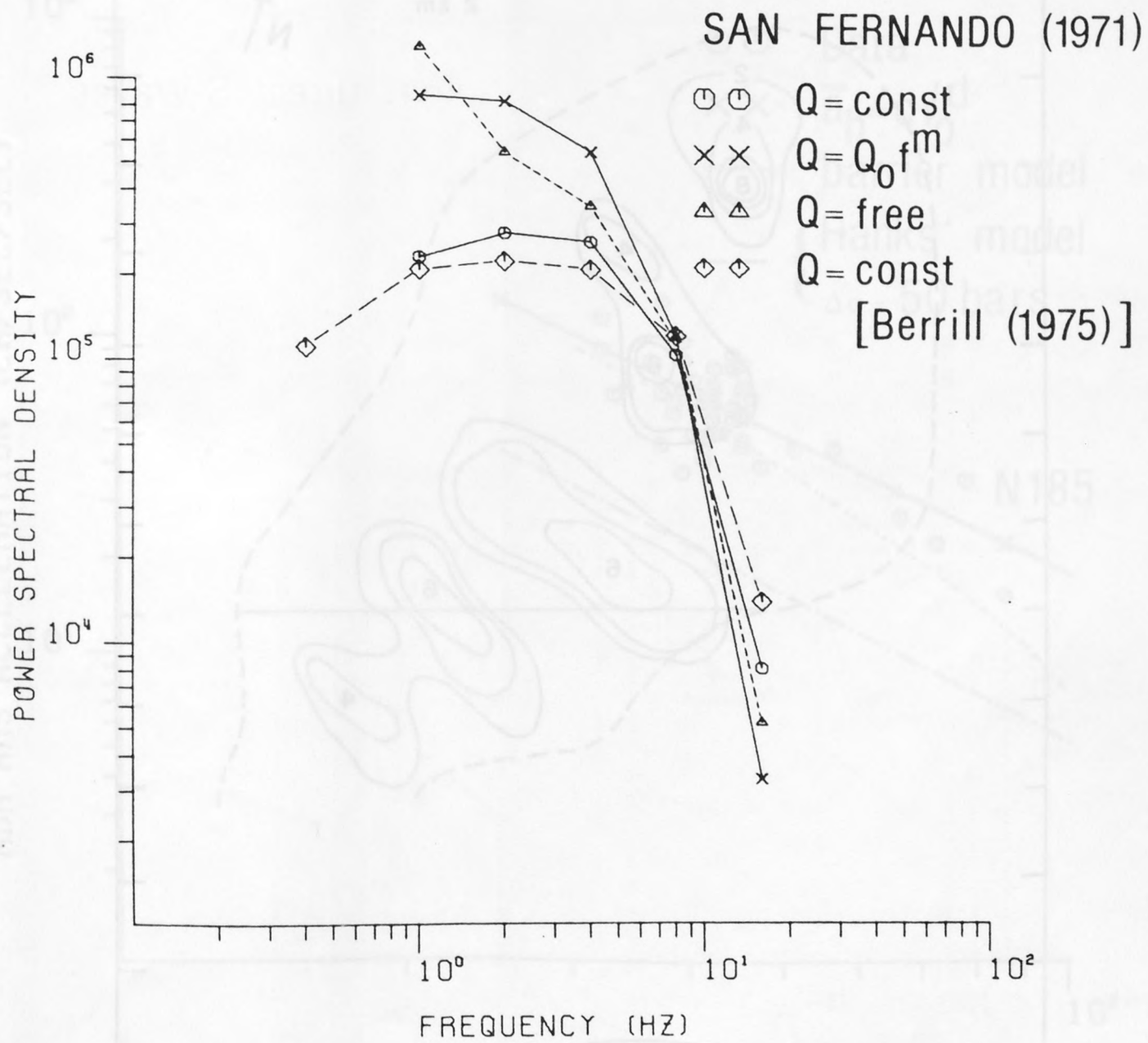

Figure 6. The source power spectrum of acceleration, S(f), of the San Fernando earthquake of 1971 inferred for three cases of frequency dependence of Q_β. Berrill's (1975) estimate of the source spectrum is shown for comparison.

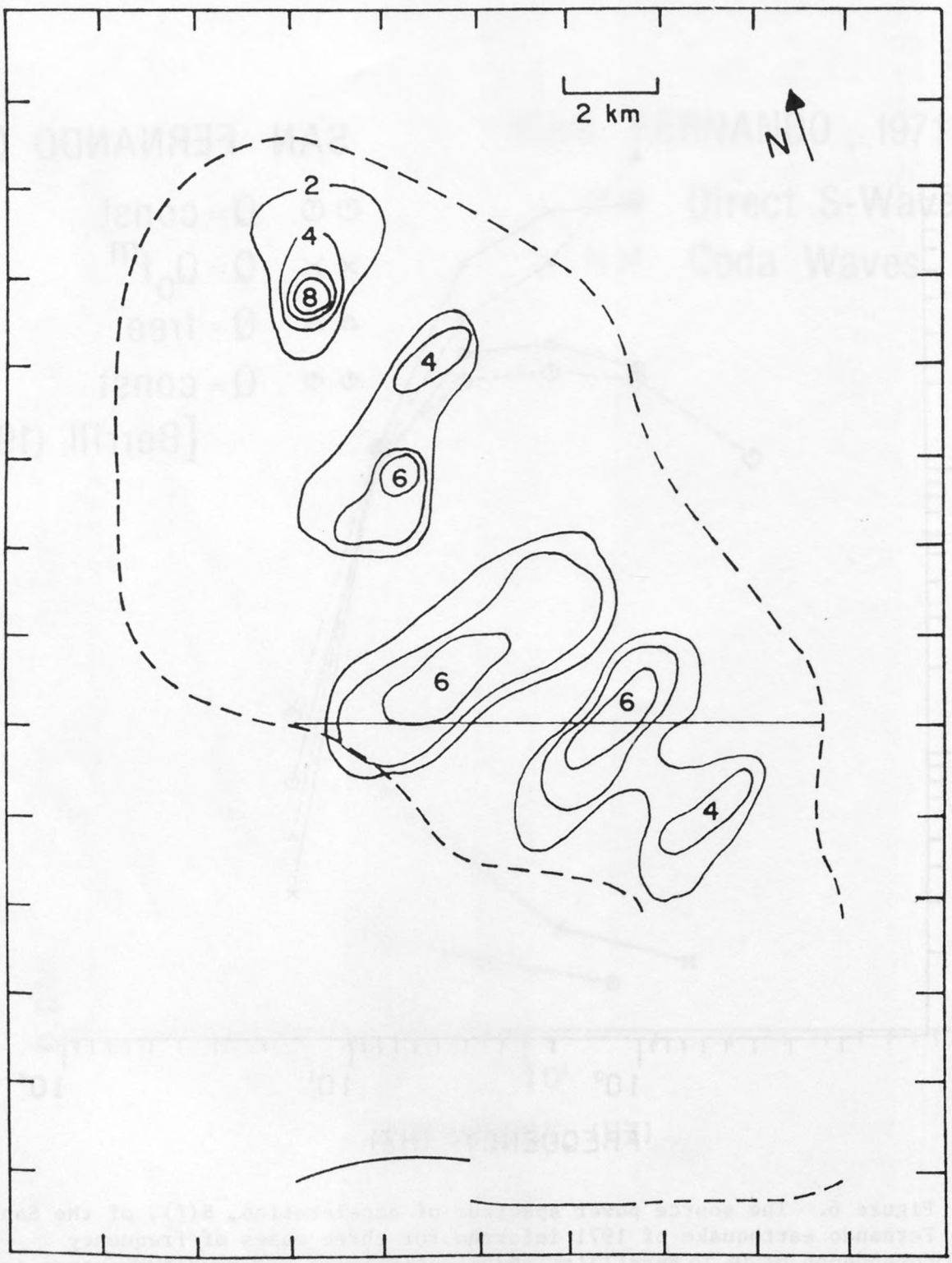

Figure 7. Localized areas of large slip on the fault plane, inferred by Shakal (1979) for the San Fernando earthquake of 1971. (Reproduced from Shakal, 1979.)

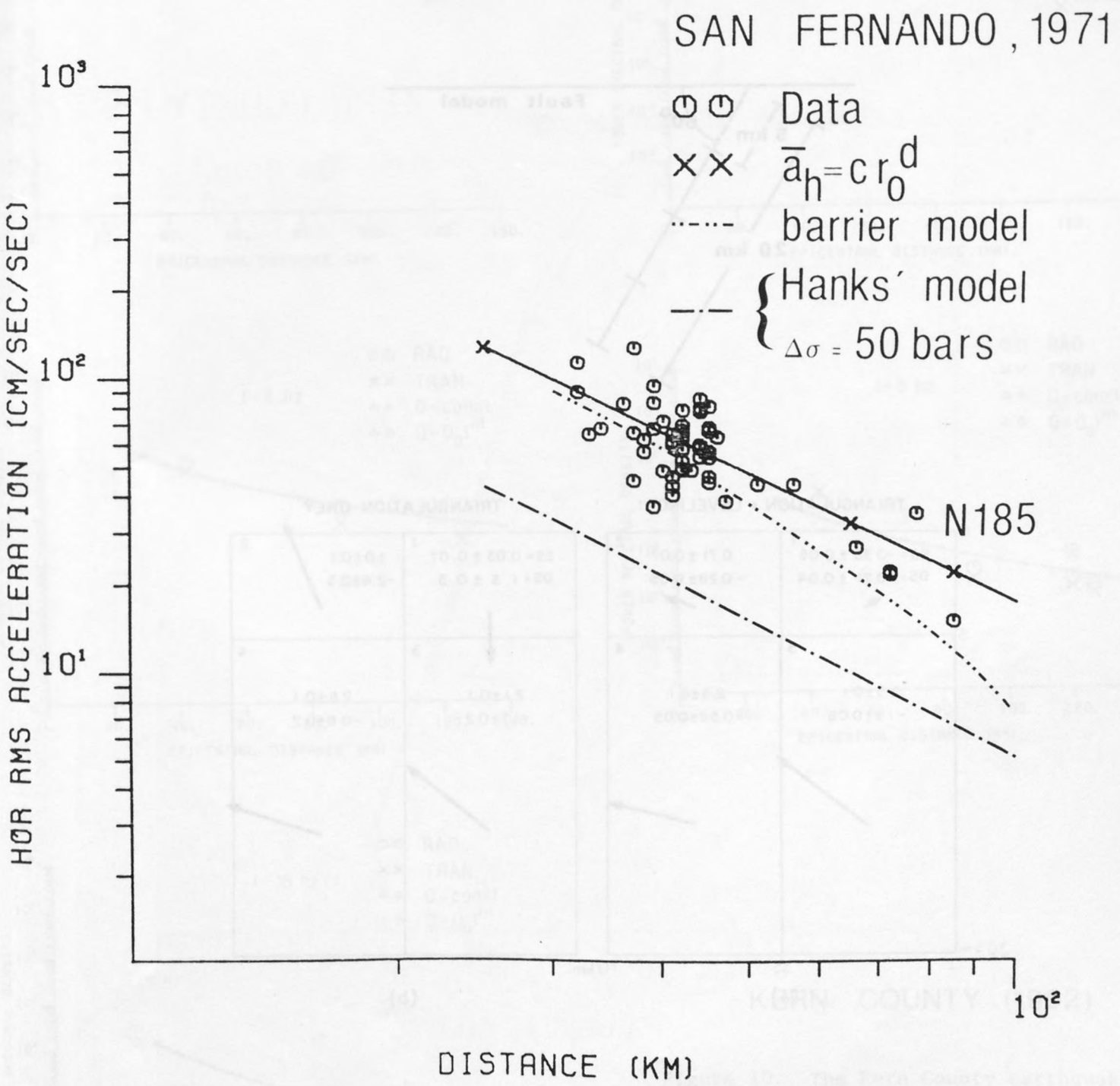

Figure 8. Attenuation of r.m.s. accelerations of direct S-waves of the San Fernando earthquake obtained from stations listed in Table 1a. Predictions obtained using Hanks' model (with "global" stress drop) and the specific barrier model are compared with a regression line of the form $a_H = cr_o^d$ fitted to the observations.

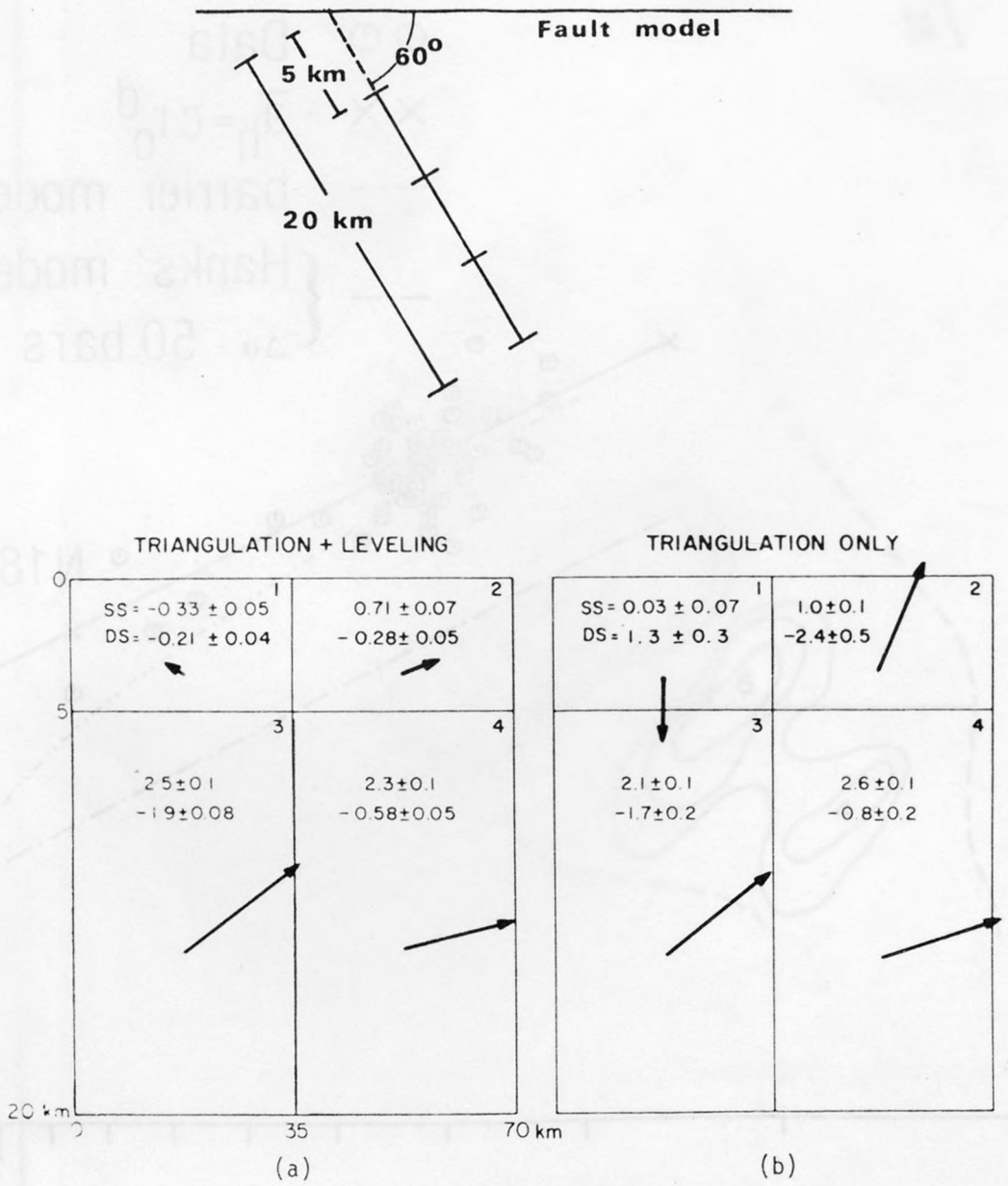

Figure 9. (top) Fault model used by Dunbar et al. (1980) in modeling geodetic measurements associated with the Kern County earthquake of 1952.
(bottom) Slip estimates obtained by Dunbar et al. (1980).
(Reproduced from Dunbar et al., 1980.)

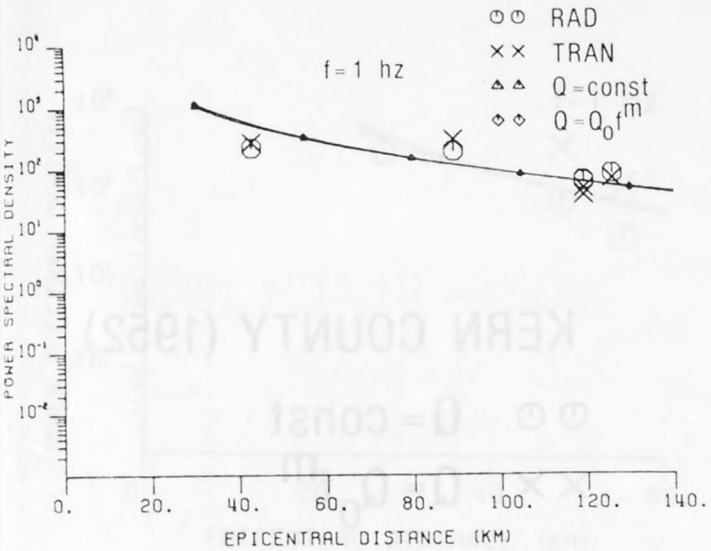

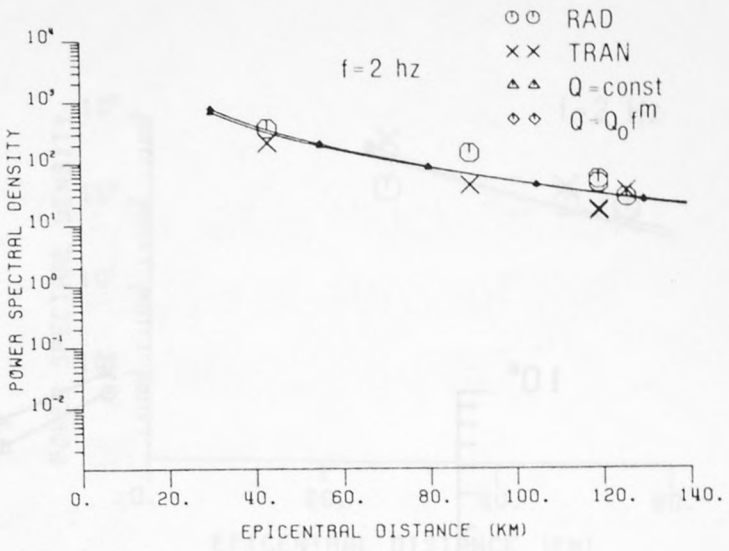

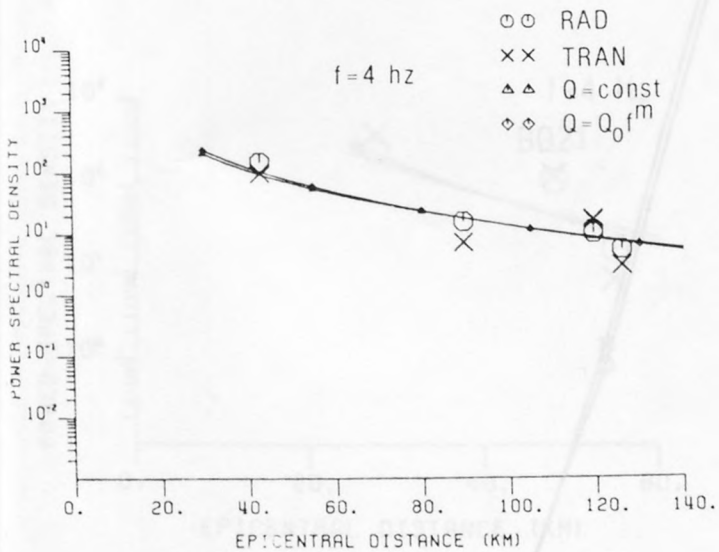

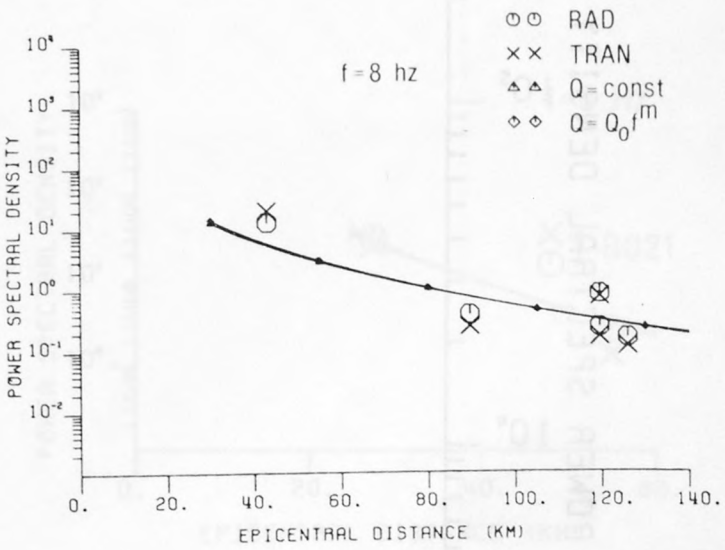

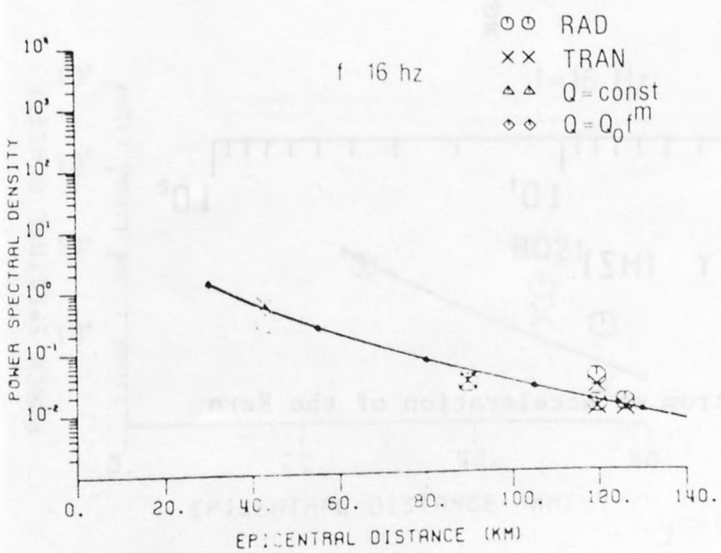

KERN COUNTY (1952)

Figure 10. The Kern County earthquake of 1952: attenuation with distance of power spectral amplitudes of acceleration (direct S-waves) of the frequencies f = 1, 2, 4, 8 and 16 Hz.

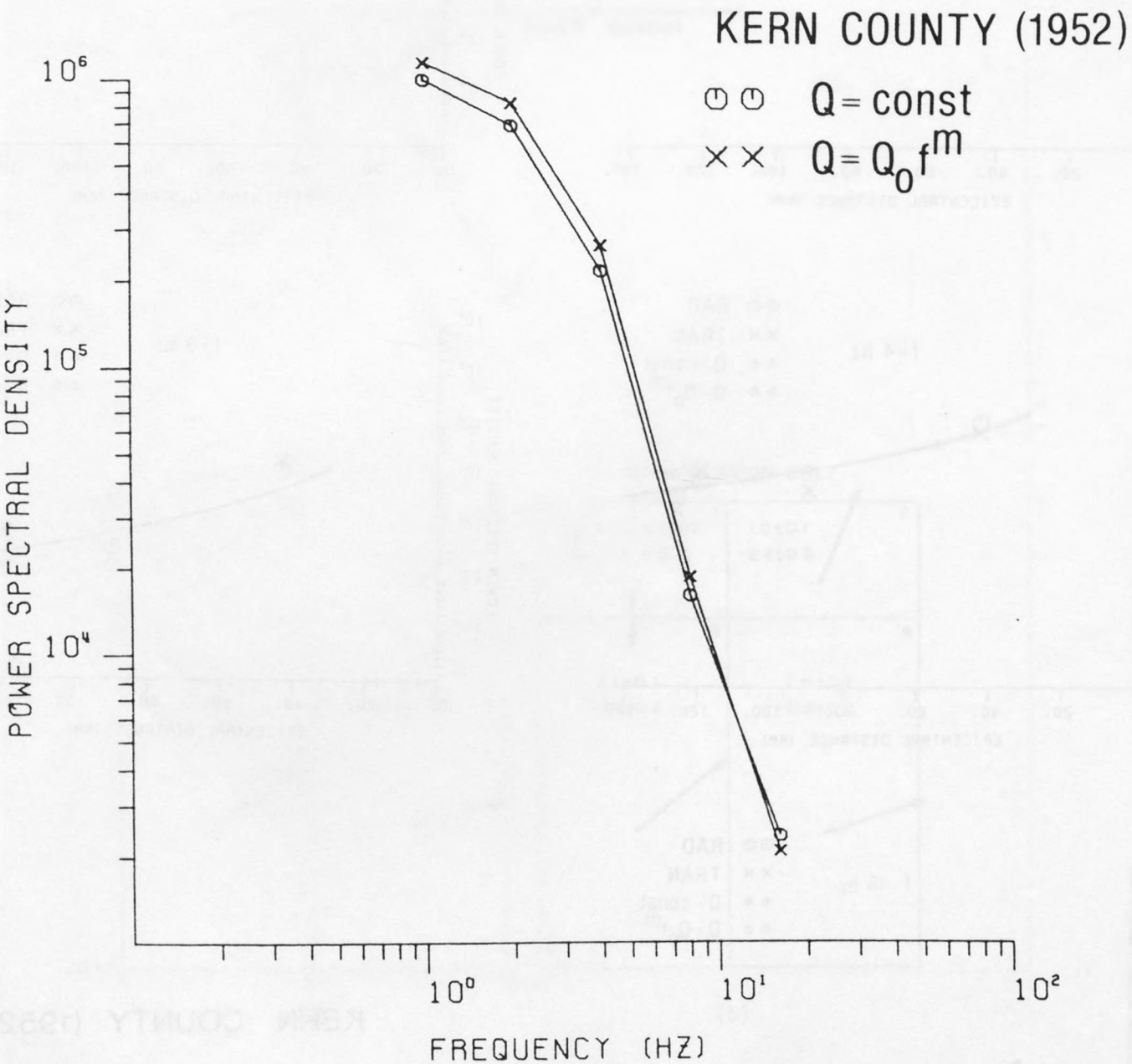

Figure 11. The source power spectrum of acceleration of the Kern County earthquake of 1952.

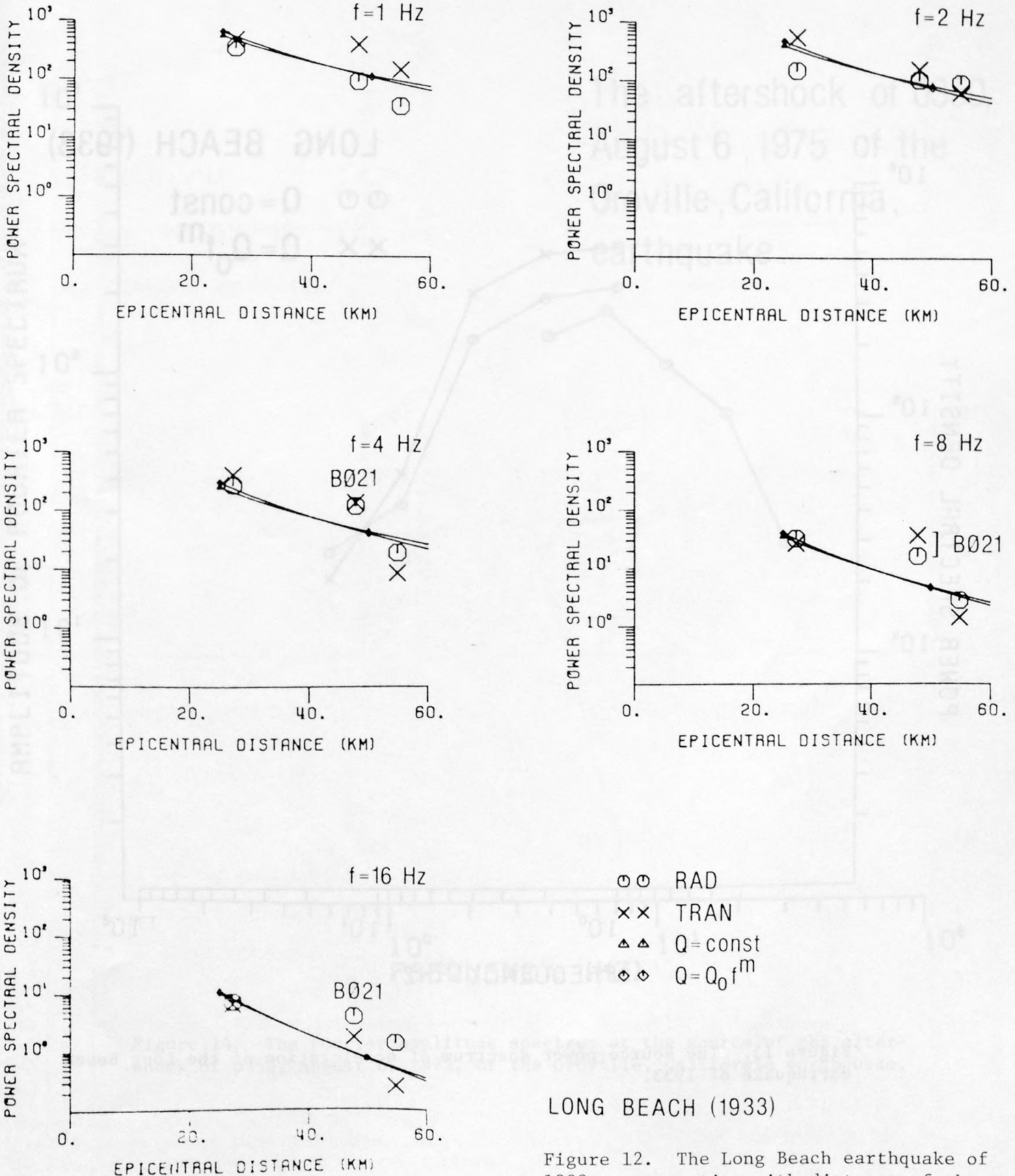

Figure 12. The Long Beach earthquake of 1933: attenuation with distance of the power spectral amplitudes of acceleration (direct S-waves) of the frequencies f = 1, 2, 4, 8 and 16 Hz.

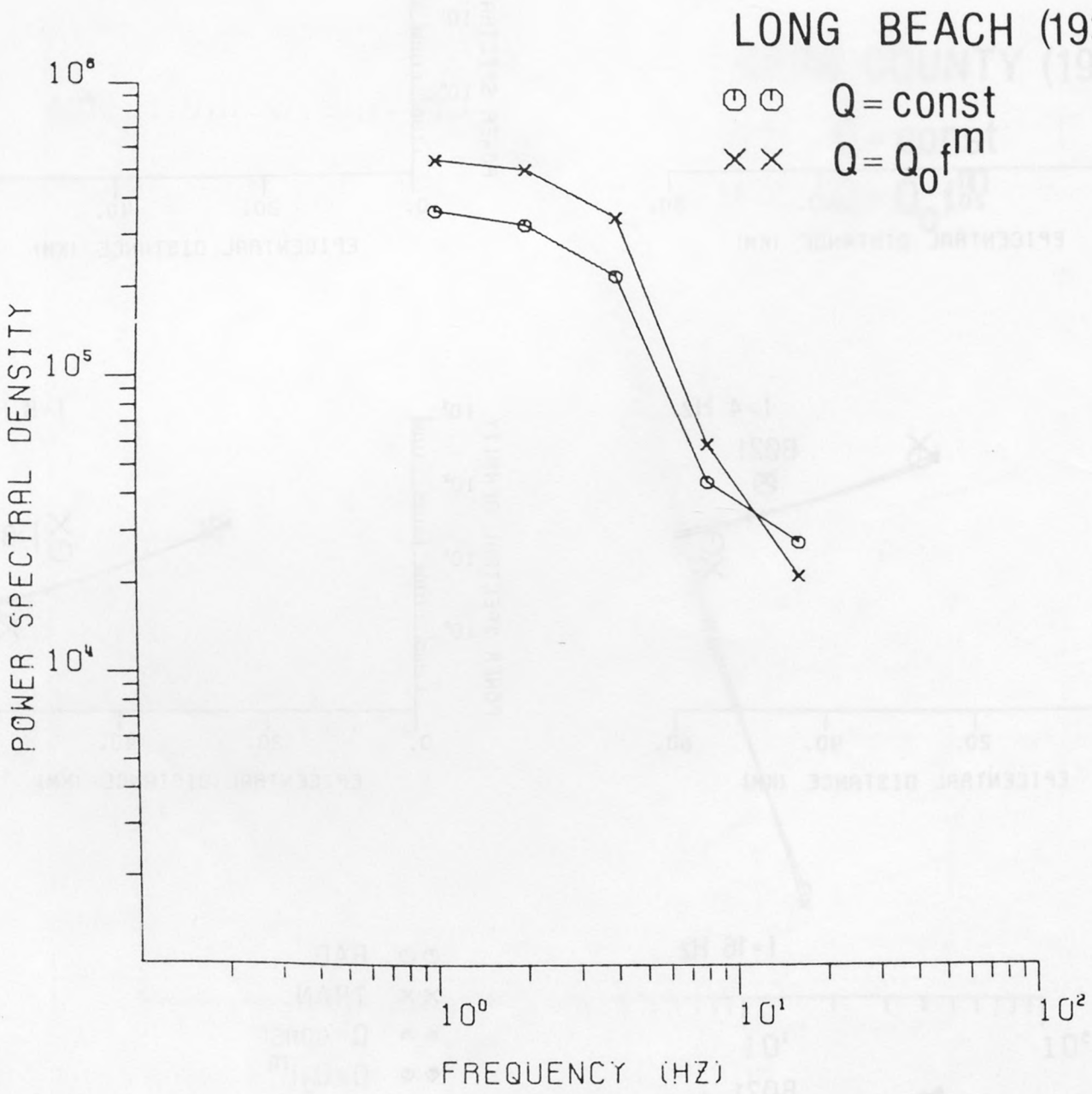

Figure 13. The source power spectrum of acceleration of the Long Beach earthquake of 1933.

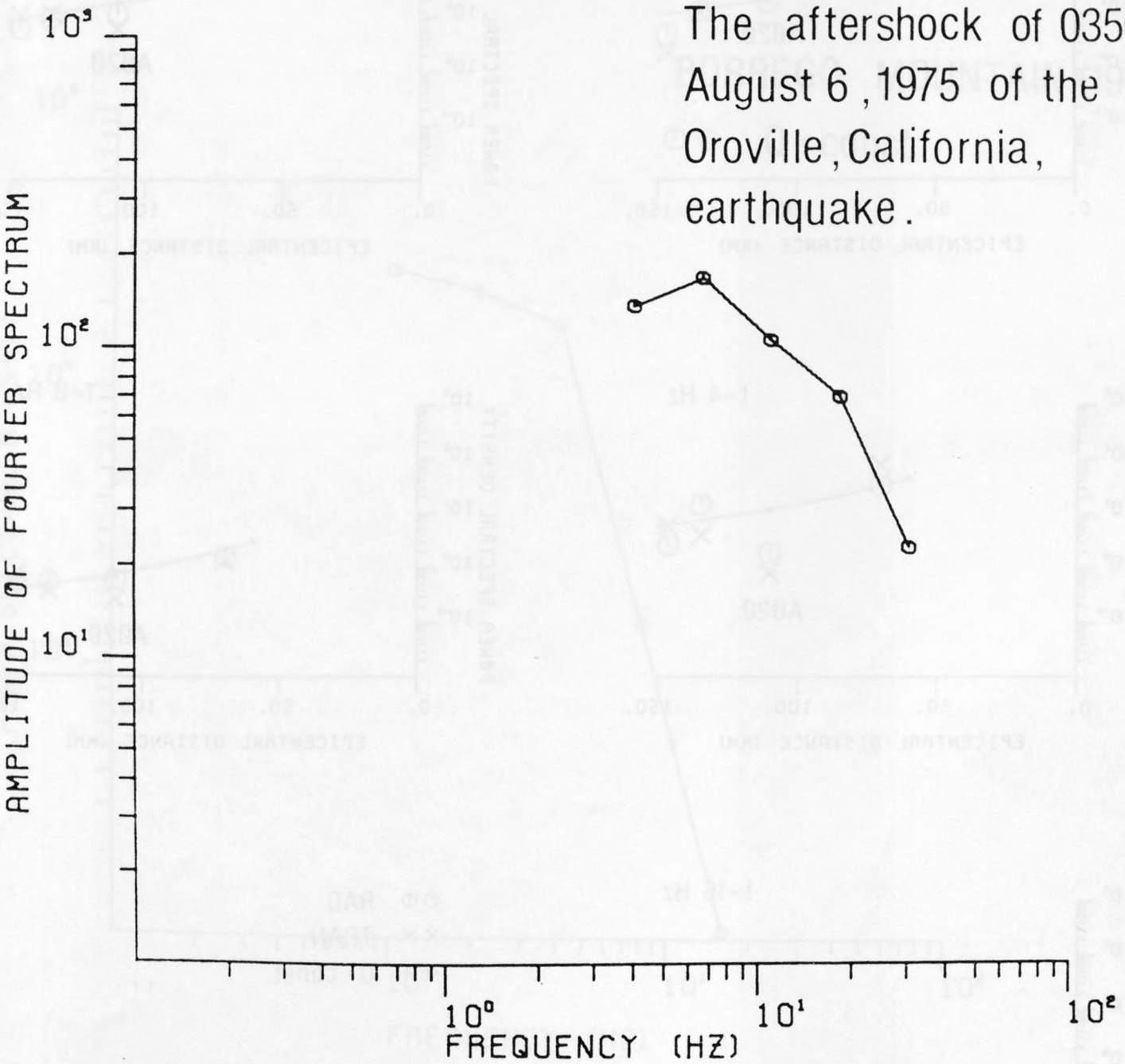

Figure 14. The Fourier amplitude spectrum at the source of the aftershock of 0350, August 6, 1975, of the Oroville, California earthquake.

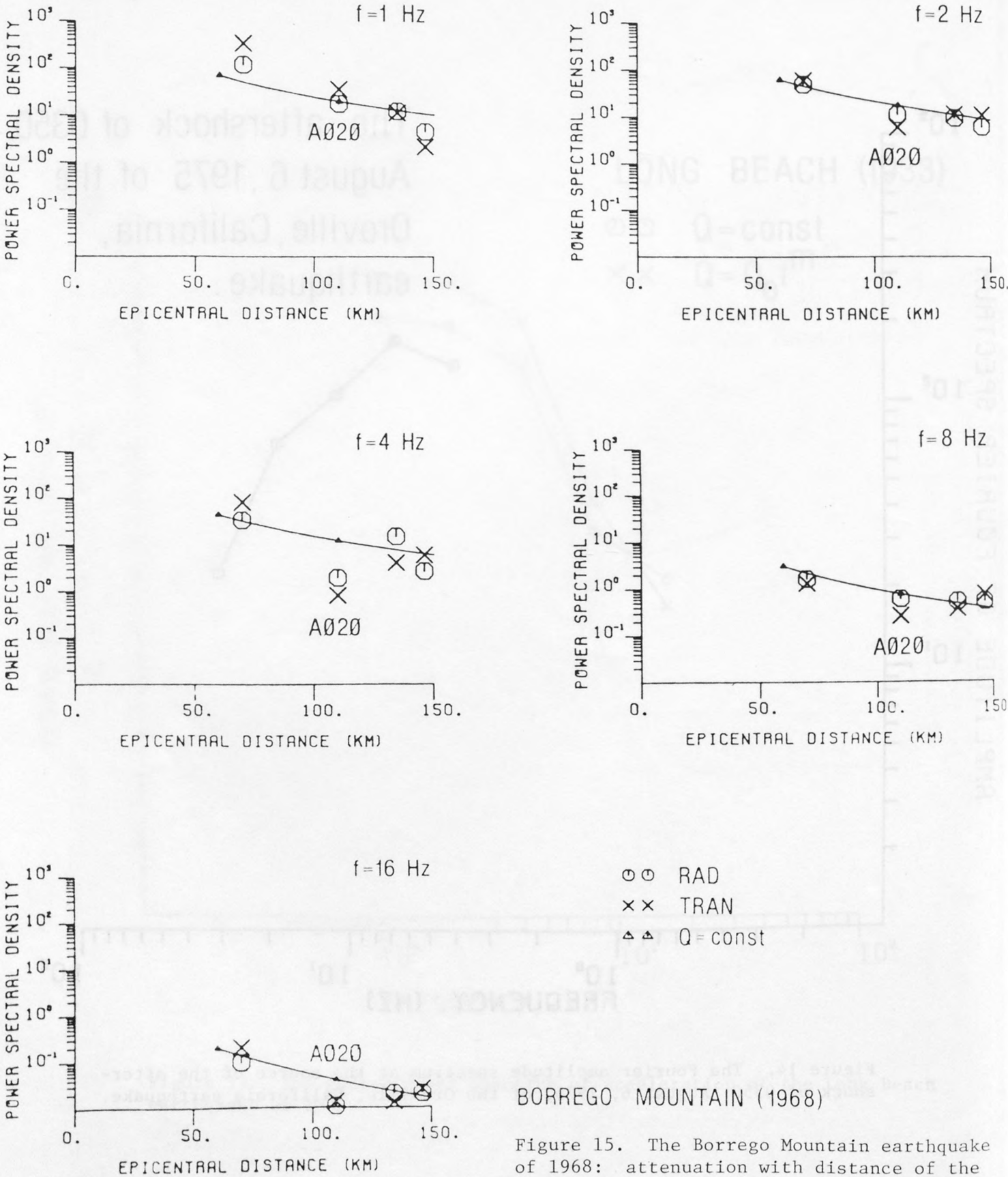

BORREGO MOUNTAIN (1968)

Figure 15. The Borrego Mountain earthquake of 1968: attenuation with distance of the power spectral amplitudes of acceleration (direct S-waves) of the frequencies f = 1, 2, 4, 8 and 16 Hz.

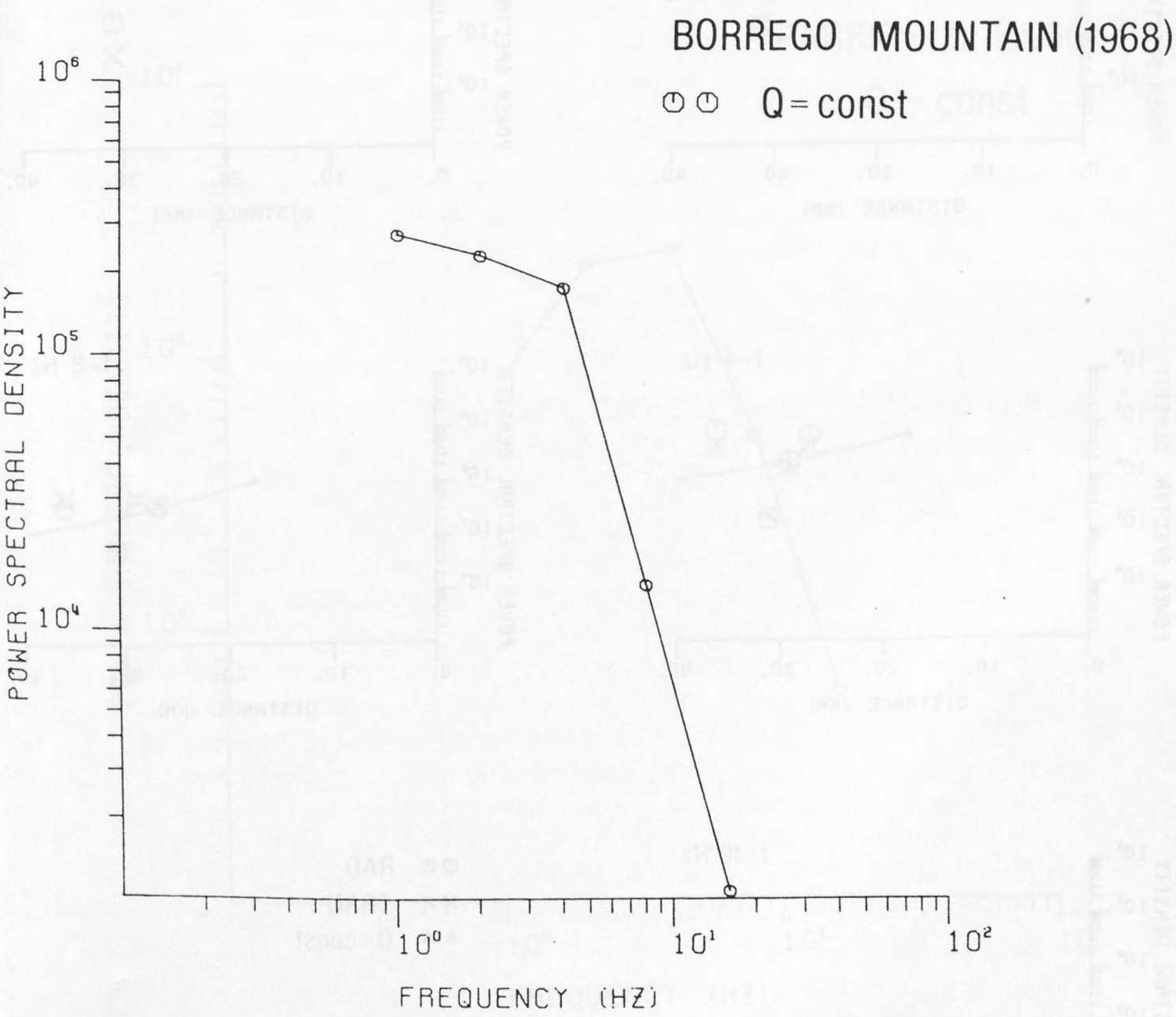

Figure 16. The source power spectrum of acceleration of the Borrego mountain earthquake of 1968.

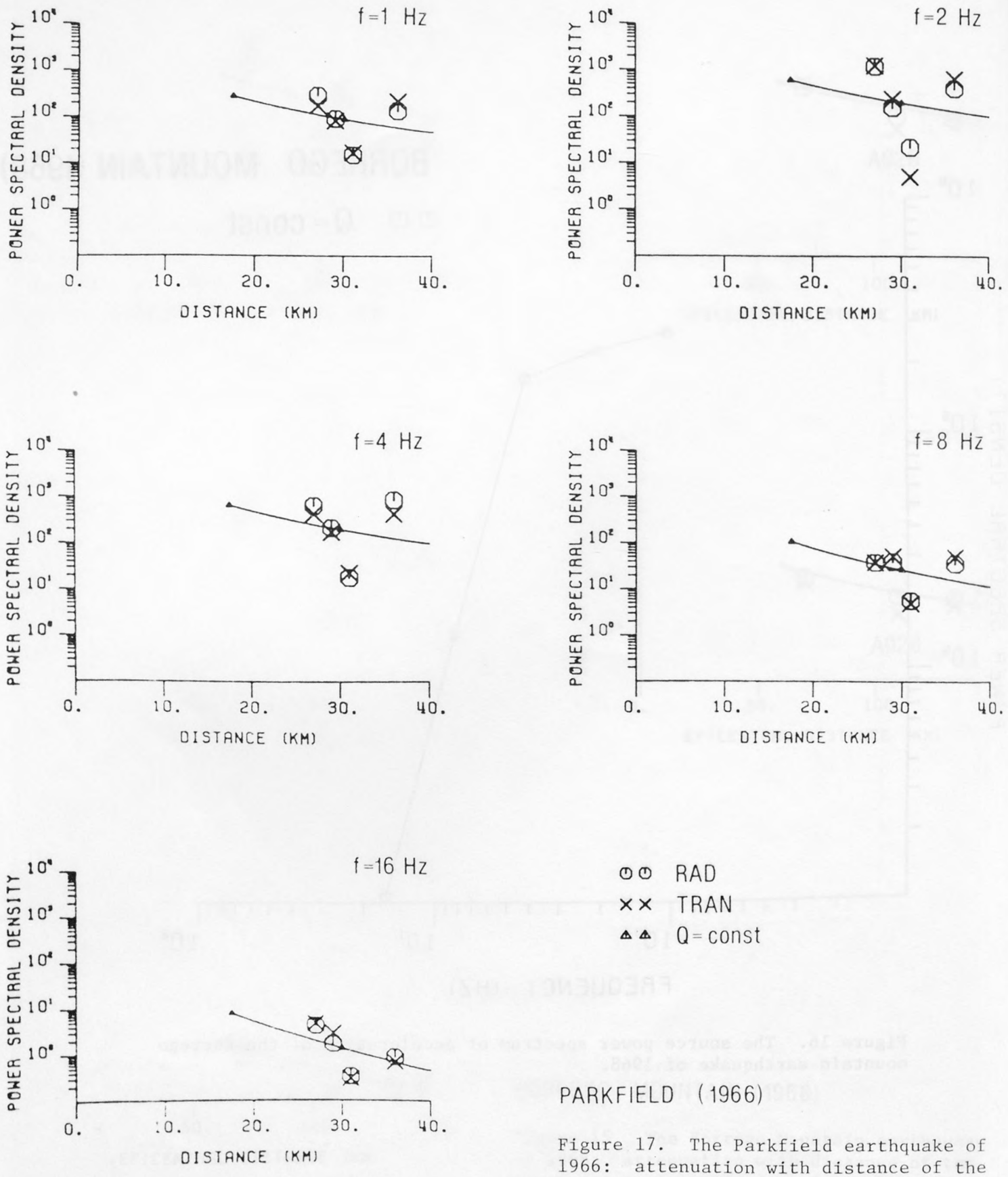

Figure 17. The Parkfield earthquake of 1966: attenuation with distance of the power spectral amplitudes of acceleration (direct S-waves) of the frequencies f = 1, 2, 4, 8 and 16 Hz.

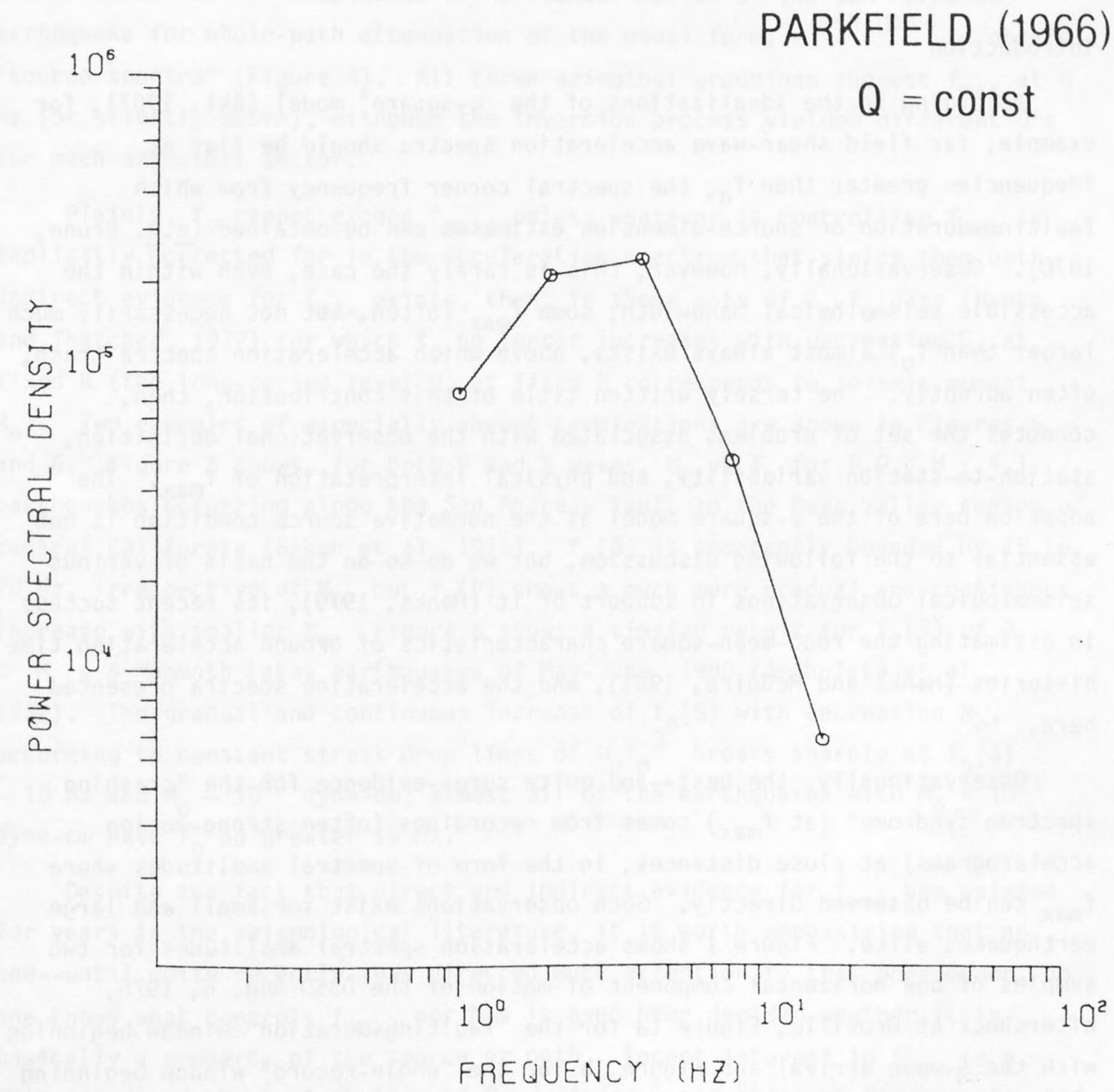

Figure 18. The source power spectrum of acceleration of the Parkfield earthquake of 1966.

f_{max}

Thomas C. Hanks
U.S. Geological Survey
345 Middlefield Road
Menlo Park, California 94025

Introduction

According to the idealizations of the "ω-square" model (Aki, 1967), for example, far field shear-wave acceleration spectra should be flat at frequencies greater than f_0, the spectral corner frequency from which faulting-duration or source-dimension estimates can be obtained (e.g. Brune, 1970). Observationally, however, this is rarely the case, even within the accessible seismological bandwidth; some f_{max} (often, but not necessarily much larger than f_0) almost always exists, above which acceleration spectra crash, often abruptly. The tersely written title of this contribution, then, connotes the set of problems associated with the observational definition, station-to-station variability, and physical interpretation of f_{max}. The adoption here of the ω-square model as the normative source condition is not essential to the following discussion, but we do so on the basis of various seismological observations in support of it (Hanks, 1979), its recent success in estimating the root-mean-square characteristics of ground acceleration time histories (Hanks and McGuire, 1981), and the acceleration spectra presented here.

Observationally, the best--and quite sure--evidence for the "crashing spectrum syndrome" (at f_{max}) comes from recordings (often strong-motion accelerograms) at close distances, in the form of spectral amplitudes where f_{max} can be observed directly. Such observations exist for small and large earthquakes alike. Figure 1 shows acceleration spectral amplitudes for two samples of one horizontal component of motion of the 0350 Aug. 6, 1975, aftershock at Oroville, Figure 1a for the "faulting-duration" window beginning with the S-wave arrival and Figure 1b for the "whole-record" window beginning with the S-wave arrival. In both cases, f_{max} is fairly well-determined at 14 Hz although f_0 = 1.3 Hz for this earthquake is more clearly defined in the whole-record spectrum. There is very little difference (at the 50% level) between the two spectra, the unsurprising consequence of the ground motion's being dominated--in this case--by the direct shear arrival. Similarly,

Figures 2 and 3 show acceleration records and their whole-record spectra from the San Fernando earthquake (at Pacoima Dam) and the Kern County earthquake (at Taft), respectively. In both cases, f_{max}'s near 10 Hz are suggested, as are f_0's of about 0.1 Hz. Berrill (1975) has corrected spectral amplitudes of acceleration for 190 components of horizontal motion of the San Fernando earthquake for whole-path attenuation of the usual form, $e^{-\pi fR/Q\beta}$ to obtain "source spectra" (Figure 4). All three azimuthal groupings suggest f_{max} at 8 Hz (or slightly above), although the inversion process yielded different Q's for each azimuthal sector.

Plainly, f_0 cannot exceed f_{max}, unless whatever is controlling f_{max} is explicitly corrected for in the acceleration spectrum that yields them both. Indirect evidence for f_{max} exists, then, in those sets of Ω_0-f_0 data (Hanks and Thatcher, 1972) for which f_0 no longer increases with decreasing Ω_0 at fixed R (the long-period level Ω_0 at fixed R corresponds to seismic moment M_0). Two examples of especially abrupt terminations are shown in Figures 5 and 6. Figure 5 shows, for both P and S waves, M_0 vs f_0 for $0.9 \leq M \leq 4.1$ earthquakes occurring along the San Andreas fault in the Bear Valley region of central California (Bakun et al, 1976). $f_0(S)$ is apparently bounded by 15 to 20 Hz, irrespective of M_0, but $f_0(P)$ shows a much more gradual and continuous increase with smaller M_0. Figure 6 shows a similar result for $f_0(S)$ of $3 \lesssim M_L \lesssim 6$ Mammoth Lakes earthquakes of May-June, 1980 (Archuleta et al., 1982). The gradual and continuous increase of $f_0(S)$ with decreasing M_0, according to constant stress drop lines of $\Omega_0 f_0^3$ breaks sharply at $f_0(S) \tilde{-} 10$ Hz and $M_0 \tilde{-} 10^{21}$ dyne-cm; almost all of the earthquakes with $M_0 \leq 10^{21}$ dyne-cm have f_0 no greater 15 Hz.

Despite the fact that direct and indirect evidence for f_{max} has existed for years in the seismological literature, it is worth emphasizing that no one--until quite recently--has directed much attention to this phenomenon, no one knows what controls f_{max}, nor has it even been decided whether it is basically a property of the source or path. Recent interest in f_{max} (e g. this paper and the contribution of D. J. Andrews and those of Papageorgiou and Aki to this meeting) has arisen through its explicit relationships to root-mean-square and peak accelerations (Hanks and McGuire, 1981) and the possibility that it may be observational evidence for the "barrier model which has been developed by seismologists at MIT since 1977" (Aki, 1981).

Although the weight of opinion to date sides with f_{max}'s being a property of the source, not path (e.g. Bakun et al., 1976; Papageorgiou, 1981; Archuleta et al., 1982), it must be true that deciding what the cause of f_{max} may be will be a tricky business, because it is the absence of signal that must be interpreted, not its definitive presence. That is, all one really knows is that at frequencies > f_{max}, there is little if any physically meaningful ground motion. Moreover, f_{max} evidently occurs in a band ($f \geq 10$ Hz) about which very little is known for propagation distances of $R \tilde{-} 10$ km. Specifically, the observations summarized above suggest that f_{max} occurs in a very narrow bandwidth indeed, 8 to 15 Hz, without regard to a wide range in source strength, tectonic setting, or recording site condition.

That said, there are seemingly only three possible factors that can control f_{max}, at least in broad outline. First, it can be controlled by properties of the source, barrier end zones for example. The idea here is that there are characteristic dimensions in the Earth below which seismogenic excitation is sharply diminished. Archuleta et al. (1982) discuss several of the posibilities here, in addition to those arising from the barrier model (e.g. Papageorgiou, 1981, for an at-length discussion). The very important implication of this possibility is the breakdown of earthquake similarity at $M_0 \tilde{-} 10^{21}$ dyne-cm ($M_L \tilde{-} 3$) and $f_0 \tilde{-} 10$ Hz, a breakdown that nowhere seems manifest in b-values. The second possibility is a whole-path anelastic attenuation effect, but this seems remote, at least at close distances, unless one invokes a sharply reduced Q for frequencies at and above f_{max}; there is no evidence for this proposition. The third possibility involves a differential attenuation effect in the last kilometer or so of the propagation path, through that part of the crust that is especially heterogeneous by virtue of shallow structure and tectonic shattering. If such differential attenuation is somehow due to the presence of joints or cracks and frictional losses across them, the resulting aneleastic attenuation could be considerably different from the standard $e^{-\pi fR/Q\beta}$ type.

The first possibility can never be conclusively eliminated, short of routinely measuring seismic radiation at arbitrarily small distances and to arbitrarily high frequencies: a source-controlled f_{max} can always exist at or above the one that actually materializes, for whatever other reason, at the recording point. The third possibility is eminently testable, however, with

matched instrumentation at the top and bottom of holes drilled to ~1 km depth in whatever areas are of interest.

My view on these matters is that, while a source-controlled f_{max} (as actually observed) is always theoretically possible, many f_{max} observations as they have actually materialized nevertheless bear a strong imprint of properties of the path. In the first place, source mechanism studies at even closer distances ($R \leq 5$ km) have yielded corner frequencies of up to 40 Hz for small earthquakes ($1 \lesssim M \lesssim 2$) at Oroville, California, (Fletcher, 1980) and Monticello Reservoir, South Carolina (Fletcher, 1981). Small mining-induced tremors recorded at very close distances (hundreds of meters) have yielded corner frequencies up to 200 Hz (McGarr et al., 1981). Since f_{max} in all three cases is at least as large as f_o, one concludes that f_{max} can be quite high for seismic radiation traversing especially competent rock and observed at progressively closer distances. On the other hand, the shocks involved are of progressively smaller magnitude so a magnitude dependence of f_{max} cannot be ruled out--but any such dependence at larger magnitude ($M \gtrsim 3$) must be much weaker. Secondly, there is a great body of evidence to indicate, at least qualitatively, that f_{max} depends on local site conditions. Any observational seismologist knows that records from competent crystalline rock almost always contain higher frequency radiation than records obtained from otherwise equivalent alluvial or sedimentary-rock sties. Similarly it is my impression, though be it without first-hand experience, that one records higher frequency motion at depth than at the surface of the Earth. Thus, there is much reason to believe that local site conditions, both laterally and vertically, condition observed f_{max}'s. The next section documents this effect for the 0548 Aug. 16, 1975, Oroville aftershock, with f_{max} estimates obtained from 17 horizontal components across a range of local site conditions.

f_{max} for Strong-Motion Accelerograms of Oroville Aftershocks

We begin with f_{max} estimates for a single aftershock (0548 Aug. 16, 1978; $M_L = 4.0$) recorded across the array of 11 strong-motion accelerographs deployed in the Oroville area at that time. This earthquake occurred at $39^o28.2'$N, $121^o31.7'$W at 8.5 km depth; it has $M_o = 3 \times 10^{22}$ dyne-cm and $f_o(S) = 3$ Hz. Figure 7 shows the location of this earthquake, together with the

instrumental locations. The least hypocentral distance is 9 km at stations EBH, OMC, 7, and 6, and the greatest hypocentral distance is 12 km at stations OAP and 1. Stations 2 and 3 were discontinued prior to the occurrence of this aftershock, and records from Stations DWR and DJR are not analyzed here for reasons given in Hanks and McGuire (1981), namely strong site resonances at frequencies high enough that f_{max} estimates may be biased by their presence.

f_{max} values are estimated from shear-wave acceleration spectra corrected only for instrument response. Table 1 gives 2 values of f_{max} for each horizontal component for each of eight stations and for one component of motion for EBH; one value is estimated for the "faulting-duration" sample (approximately 1/2 second), and one value for the "whole-record" sample (approximately 9 seconds), as in Figure 1. Parentheses enclose the values I judge to be less certain. Figures 8 and 9 show the four acceleration spectra and the four f_{max} estimates for Stations 5 (an alluvial site) and 6 (a hard-rock site), respectively.

As has always been the case in parameter estimation of body-wave spectra, estimating f_{max} involves some subjective judgment, and what I have developed here is perhaps worth recounting. First, with the exceptions of OMC S66W and 6 N35E, f_{max} estimates from the two sample lengths agree within 30%. At this level of uncertainty, we can regard the f_{max} estimates to be observationally stable (for 15 of 17 components), that is independent of the sample window (but perhaps not independent of my judgment). Also for these 15 components, it seems that back-scattering (into the coda) of any high-frequency ($f \geq f_{max}$) energy lost from the direct arrival is negligibly important. For the two components with f_{max} differences greater than 30%, the whole-record value is less than the faulting-duration value. Indeed for all estimates, the whole-record value is greater than the faulting duration value in just three cases--and only nominally so.

Secondly, estimating f_{max} is generally less certain with the whole-record samples than with the faulting-duration samples. This is evident in the preponderance of whole-record values enclosed by parentheses, due in part, I think, to the "rounding" of whole-record spectra between f_o and f_{max} that can occur when significant energy is contained in the coda (e.g. Fig. 8d).

Now, the point of Table 1, in which the recording sites have been arranged from west to east, is that f_{max} shows a clear distinction between

sites west of and including EBH as opposed to sites east of EBH. With the exception of Station 1, f_{max} at the five western sites is approximately 15 Hz, but at the four eastern sites, f_{max} is not less than 20 Hz except for one component of Station 8. This division is probably not coincidental since the five western sites are all situated on Pleistocene or younger, probably water-saturated, gravels and alluvium, while east of EBH the four sites are located either on crystalline bedrock of Mesozoic age or on a thin veneer of Tertiary gravels filling a pre-existing drainage in the crystalline rock (Figure 7).

I conclude that, in the case of the data of Table 1, local site conditions have conditioned the f_{max} values as observed in the acceleration spectra. These results, however, do not preclude the possiblility of a source-controlled f_{max} at some higher frequency, namely ~30 Hz or above. What would have happened if one had tried to extract source parameters from spectral representations of seismograms written by small earthquakes at sites west of EBH? I suspect that an upper limit to f_o would have been realized at 15 to 20 Hz, irrespective of any further decrease in M_o. East of EBH, one might have done better, ~30 Hz or better, depending both on the site and on the performance of the strong-motion accelerographs at frequencies greater than their natural instrumental frequency. Fletcher (1980) estimated S-wave spectral corner frequencies as high as 40 Hz for small earthquakes at the site marked W in Figure 7.

How, stable, then are f_{max} estimates for several earthquakes recorded at the same site? Table 2 presents f_{max} estimates for the seven well-recorded $M_L \geq 4$ aftershocks, as observed at OAP. With the sole exception of 0103 N90W, whole-record values again agree well with the faulting-duration values. Nineteen of the 28 values in Table 2 are 15 Hz ± 20%, that is between 12 and 18 Hz. At OAP, then, an expectable value of f_{max} is near 15 Hz with a statistically plausible range of 10 to 20 Hz. Again in the sense of how these values would limit corner frequencies of small earthquakes irrespective of decreasing M_o, both the expectable value and its likely range are in remarkable accord with the observations of Bakun et al. (1976) (Figure 5) and Archuleta et al., (1976) (Figure 6), their results, of course, being for completely different areas. What is the magic of this very narrow bandwidth $10 \leq f \leq 20$ Hz?

While much work remains to be done in estimating f_{max} for the other aftershocks at the other stations, the results of this preliminary study are hardly surprising. In gross form, a clear site-dependence of f_{max} is indicated, perhaps 15 to 20 Hz on the young sediments in the western part of Figure 7 and perhaps 20 to 30 Hz (or greater) in the eastern part of Figure 7. The f_{max} stability of the seven aftershocks of OAP does not allow much possiblity that f_{max} would exceed 20 Hz at this site, given ordinary conditions of recording earthquakes at ordinary crustal depths. While source-controlled f_{max}'s may yet exist for any or all of these aftershocks, they would be difficult if not impossible to find in these data.

For the purposes of estimating theoretical rms-accelerations or stress differences from record rms-accelerations, however, this range in f_{max} is not of much consequence, at least at Oroville. The $\Delta\sigma$ estimates in Table 2 of Hanks and McGuire (1981) could be corrected by a factor of $\sqrt{\frac{f_{max}}{25}}$, a number varying between 0.8 and 1 for most of the values given in Table 1 and 2 here, but such fine-tuning, of course, would require knowing f_{max} in advance for each source-site pair.

Anelastic Attenuation of High-Frequency Strong Ground Motion

This final section addresses the possibility that f_{max} estimates obtained from records in the 50 to 150 km range can be seriously biased by whole-path attenuation effects if there are large uncertainties in Q. It has been motivated by two recent results, both curious and contradictory. The first is from Joyner and Boore (1981), who find that the attenuation coefficient γ(of $e^{-\gamma R}$) is the same for both peak velocities (0.00256) and peak accelerations (0.00255). This, of course, implies that Q is linearly dependent on frequency through the band contributing to the peak values studied by Joyner and Boore (1981), assuming that any peak is formed monochromatically from the same frequency, independent of distance. This assumption is naive, certainly, but for the moment we will accept it. At frequencies of 0.5, 1, 2, and 4 Hz, Q then works out to be 90, 180, 350, and 700 respectively.

The second result is from Papageorgiou (1981), reproduced at this meeting in Figure 5 of Papageorgiou and Aki (II). In an analysis of strong-motion accelerograms of the San Fernando earthquake at southern azimuths,

Hz was in the range of several hundred. While a frequency-dependent Q at 2 Hz and above is possible, it is not well-resolved. The difference in Q between 1 Hz and 2 Hz is (or it should be; otherwise we have some real problems).

Figure 10 presents a similar analysis performed earlier by Berrill (1975) and illustrates the problem. Smoothed spectral amplitudes of a 15-second window (beginning with direct S) of ground accelerations at six frequencies are calculated for the transverse (x) and radial (o) components of motion of the San Fernando earthquake at southern azimuths. The smooth curves are of the form

$$a(f,R) = a_o(f, 1\ km)\ \frac{e^{-\frac{\pi f R}{Q\beta}}}{R}$$

where $a_o(f, 1\ km)$ is the "source excitation" (Figure 4), and Q in all cases is 330. Exclusive of the labeled data (denoting sites where resonances at the appropriate frequencies seem likely), the theoretical predictions are in reasonable agreement with the observations--and provide at the same time a very believable source excitation--except at 0.4 and 1 Hz for $60 \leq R \leq 100$ km. Here, stronger attenuation (Q lower than 330) seems called for. One will pay for this, however, by increasing the source excitation at these frequencies over values that are already high (by a factor of 2 at southern azimuths) with respect to a conventional ω^{-2} model (heavy line in Figure 4), and Figure 6 of Papageorgiou and Aki (II) indicates the magnitude of the increase. But this restriction should not be taken too literally, since it has been known for years that the San Fernando earthquake is especially energetic at frequencies of 0.5 to 1 Hz (Hanks, 1974, and numerous more recent studies, several by participants at this meeting).

Fortunately, there is yet another data set pertinent to the anelastic attenuation of 0.5-2 Hz shear waves in southern California, and it is truly enormous. We know that tens of thousands of Wood-Anderson peak amplitudes are consistent with the -log $A_o(R)$ attenuation relationship used to determine local magnitude M_L (Richter, 1935, 1958). What does -log $A_o(R)$ imply for anelastic attenuation of peak amplitudes, assuming a predominant frequency near 1 Hz? Figure 11 indicates the range of possibilities, and it is not large.

The heavy curve is a smoothed version of the -log $A_0(R)$ tabulations of Richter (1958), minus 1.7 to zero it at R = 20 km. The other curves are all of the form

$$\log \text{amp} = \log a_0 - \log R - 0.42\, f/Q\, R.$$

For f = 1 Hz, the top of these three curves is for Q = 180 and is the distance-attenuation relation of Joyner and Boore (1981); the middle curve is for Q = 100, and the bottom curve is for Q = 50.

Several features of Figure 11 are apparent. First at $R \lesssim 50$ km, the -log $A_0(R)$ curve of Richter cannot be matched unless the frequencies controlling the peak Wood-Anderson amplitude are in fact very high (5 to 10 Hz) or Q is very low (10 to 20). Complicating matters, however, is the fact that relatively little M_L data is available for $R < 50$ km, and prior to the advent of low-gain, 0.8-second torsion instruments in southern California following the Kern County earthquake, all earthquakes recorded on-scale on a Wood-Anderson at $R \leq 50$ km are necessarily small, $M_L \lesssim 4$. For progressively smaller shocks at close R, the maximum amplitude would be at progressively higher frequencies (near f_0), frequencies not forming the maximum amplitude at greater distances. On the other hand, Kanamori and Jennings (1978) have estimated M_L's for larger events at $R \leq 50$ km from strong-motion accelerograms and have found no distance bias.

For $50 \lesssim R \leq 200$ km, however, matters are simpler. This is the range where M_L is easily defined, the decay in log $A_0(R)$ is gradual and smooth, and where a 1 Hz approximation for the predominant frequency of the maximum amplitude is the most easily justified. The Q = 50 curve is badly off the -log $A_0(R)$ curve; any such difference in trend would have been easily detectable as a distance-dependent magnitude. I do not see how Papageorgiou's result of Q = 48 can possibly be representative of southern California as a whole. The curve of Joyner and Boore (1981) is the best match in trend to -log $A_0(R)$; had I "zeroed" the curves at R = 50 km, it would have matched -log $A_0(R)$ everywhere between 50 and 200 km to 0.1 log unit. Since approximately half of the data of Joyner and Boore (1981) is for southern California sources and sites, it would seem that Q for 1 Hz in this region is no lower than 150 to 200, lower by a factor of 2 from Berrill's (1975) estimate but higher by a factor of 3 to 4 than Papageorgiou's (1981) value.

References

Aki, K., 1967, Scaling law of seismic spectrum, J. Geophys. Res. 72, 1217-1231.

Aki, K., 1981, Strong motion prediction based on the barrier model, IASPEI Abstracts, A3.21.

Andrews, D. J., 1981, Separation of source and propagation spectra of seven Mammoth Lakes aftershocks, this meeting.

Archuleta, R. J., Spudich, P., Cranswick, E., and Mueller, C., 1982, Source parameters of the 1980 Mammoth Lakes, California, earthquake sequence, J. Geophys. Res., in press.

Bakun, W. H., Bufe, C. G., and Stewart, R. M., 1976, Body-wave spectra of central California earthquakes, Bull. Seism. Soc. Am. 66, 363-384.

Berrill, J. B., 1975, A study of high-frequency strong ground motion from the San Fernando earthquake, Ph.D. Thesis, California Institute of Technology, Pasadena.

Brune, J. N., 1970, Tectonic stress and the spectra of seismic shear waves from earthquakes, J. Geophys. res. 75, 4997-5009.

Fletcher, J. B., 1980, Spectra from high-dynamic range digital recordings of Oroville, California aftershocks and their source parameters, Bull. Seism. Soc. Am. 70, 735-755.

Fletcher, J. B., 1981, A comparison between the tectonic stress measured in situ and stress parameters from induced seismicity at Monticello Reservoir, South Carolina, J. Geophys. Res., in press.

Hanks, T. C., 1974, The faulting mechanism of the San Fernando earthquake, J. Geophys. Res. 79, 1215-1229.

Hanks, T. C., 1979, b-values and $\omega^{-\gamma}$ seismic source models: implications for tectonic stress variations along active crustal fault zones and the estimation of high-frequency strong ground motion, J. Geophys. Res. 84, 2235-2242.

Hanks, T. C. and McGuire, R. K., 1981, The character of high-frequency strong ground motion, Bull. Seis. Soc. Am. 71, 2071-2095.

Hanks, T. C., and Thatcher, W., 1972, A graphical representation of seismic source parameters, J. Geophys. Res. 77, 4393-4405.

Joyner, W. B., and Boore, D. M., 1981, Peak horizontal acceleration and velocity from strong-motion records including records from the 1979 Imperial Valley, California, earthquake, this meeting.

Kanamori, H., and Jennings, P. C., 1978, Determination of local magnitude, M_L, from strong-motion accelerograms, Bull. Seism. Soc. Am. 68, 471-485.

McGarr, A., Green, R. W. E., and Spottiswoode, S. M., 1981, Strong ground motion of mine tremors: some implications for near-source ground motion parameters, Bull. Seism. Soc. Am. 71, 295-319.

Papageorgiou, A. S., 1981, On an earthquake source model of inhomogeneous faulting and its applications to earthquake engineering, Ph.D. Thesis, MIT.

Papageorgiou, A. S., and Aki, K., 1981, A specific barrier model for the quantitative description of inhomogeneous faulting and the prediction of strong ground motion I. Description of the model, this meeting.

Papageorgiou, A. S., and Aki, K., 1981, A specific barrier model for the quantitative description of inhomogeneous faulting and the prediction of strong ground motion II. Applications of the model, this meeting.

Richter, C. F., 1935, An instrumental earthquake magnitude scale, Bull. Seism. Soc. Am. 25, 1-32.

Richter, C. F., 1958, Elementary Seismology, 768 pp., W. H. Freeman, San Francisco.

FIGURE CAPTIONS

Fig. 1: Shear-wave acceleration spectra of the aftershock 0350 Aug. 6, 1975 (M_L = 4.7) at Station OAP (located in Figure 7). (a) faulting-duration sample; (b) whole-record sample. f_{max} is indicated by vertical arrow.

Fig. 2: Whole-record spectra of the San Fernando earthquake at Pacoima Dam (S16E component). f_o and f_{max} are estimated as indicated.

Fig. 3: Whole-record spectra of the Kern County earthquake at Taft (N21E component). f_o and f_{max} are estimated as indicated.

Fig. 4: "Source spectra" of the San Fernando earthquake, as inferred from observations at three separate azimuths (uncorrected for radiation pattern). From Berrill (1975).

Fig. 5: Ω_o -f_o data for earthquakes in Bear Valley, central California; P-wave observations on the left, S-Wave observations on the right. From Bakun et al. (1976).

Fig. 6: Ω_o-f_o data (S waves) for earthquakes of the Mammoth lakes sequence. From Archuleta et al. (1982).

Fig. 7: The epicentral region of the Oroville earthquake (Aug. 1, 1975; M_L = 5.7). The larger aftershocks recorded by the strong-motion accelerographs (solid triangles) occurred within or near the dashed box. The aftershock 0548 (Aug. 16, 1975; M_L = 4.0) is specifically located. W marks the instrument location of Fletcher (1980). In the eastern half of the region, crystalline bedrock of Mesozoic age (horizontal lines) is covered locally by a thin veneer of tertiary gravels (open circles) filling an ancient drainage. In the western half of the region, cover is young, unconsolidated sediments, the thickness of which is contoured in meters.

Fig. 8: Shear-wave acceleration spectral of aftershock 0548 at station 5 (Figure 7). (a) S00E, faulting-duration sample; (b) S00, whole-record sample; (c) N90E, faulting-duration sample; (d) N90E, whole-record sample; f_{max} is estimated by vertical arrows.

Fig. 9: Shear-wave acceleration spectra of aftershock 0548 at station 6 (FIgure 7). (a) S55E, faulting-duratin sample; (b) S55E, whole-record sample; (c) N35E, faulting-duration sample; (d) N35E, whole-record sample f_{max} is estimated by vertical arrows.

Fig. 10: Shear-wave acceleration spectral amplitudes of the San Fernando earthquake at 0.4, 1.0, 2, 4, 8, and 16 Hz for a 15-second window beginning with the S-Wave arrival at southern azimuths. The smooth curves are explained in the text; circles are radial components; x's are transverse components.

Fig. 11: The-log $A_o(R)$ curve of Richter (1958), "zeroed" at R = 20 km, together with curves of the form $e^{-\pi fR/Q\beta}$, also "zeroed" at R = 20 km, for f = 1 Hz, and three choices of Q.

Table 1

f_{max} Estimates for 0548

OAP		1		4		5		EBH	OMC		7		6		8	
12[a]		12		11		10		9	9		9		9		11	
N90W	S00E	N90E	N00E	N35W	S55W	S00E	N90E	N90E	N24W	S66W	N90W	S00W	S55E	N35E	N90W	S00E
(15)[b]	10	19	20	11	(14)	16	13	14	20	(29)	28	21	26	28	21	16
16[c]	(10)	(19)	20	(13)	(13)	17	(13)	(13)	20	(18)	26	20	21	(20)	(20)	16

[d]

a. Hypocentral distance in km
b. Faulting-duration sample
c. Whole-record sample
d. S-wave arrival complicated by strong S P conversion

Table 2

f_{max} Estimates for Seven Aftershocks at OAP

	0103		0247		0350		0700		0548		0231		2234	
	4.6[a]	12[b]	4.1	12	4.7	12	4.9	12	4.0	12	4.0	13	4.6	13
N90W	(9)[c]	(15)[d]	(8)	(8)	14	14	14	17	(15)	16	17	17	12	13
S00E	22	23	17	(15)	(16)	17	22	22	10	(10)	16	(15)	(15)	(18)

a. M_L
b. Hypocentral distance in km
c. Faulting-duration sample
d. Whole-record sample

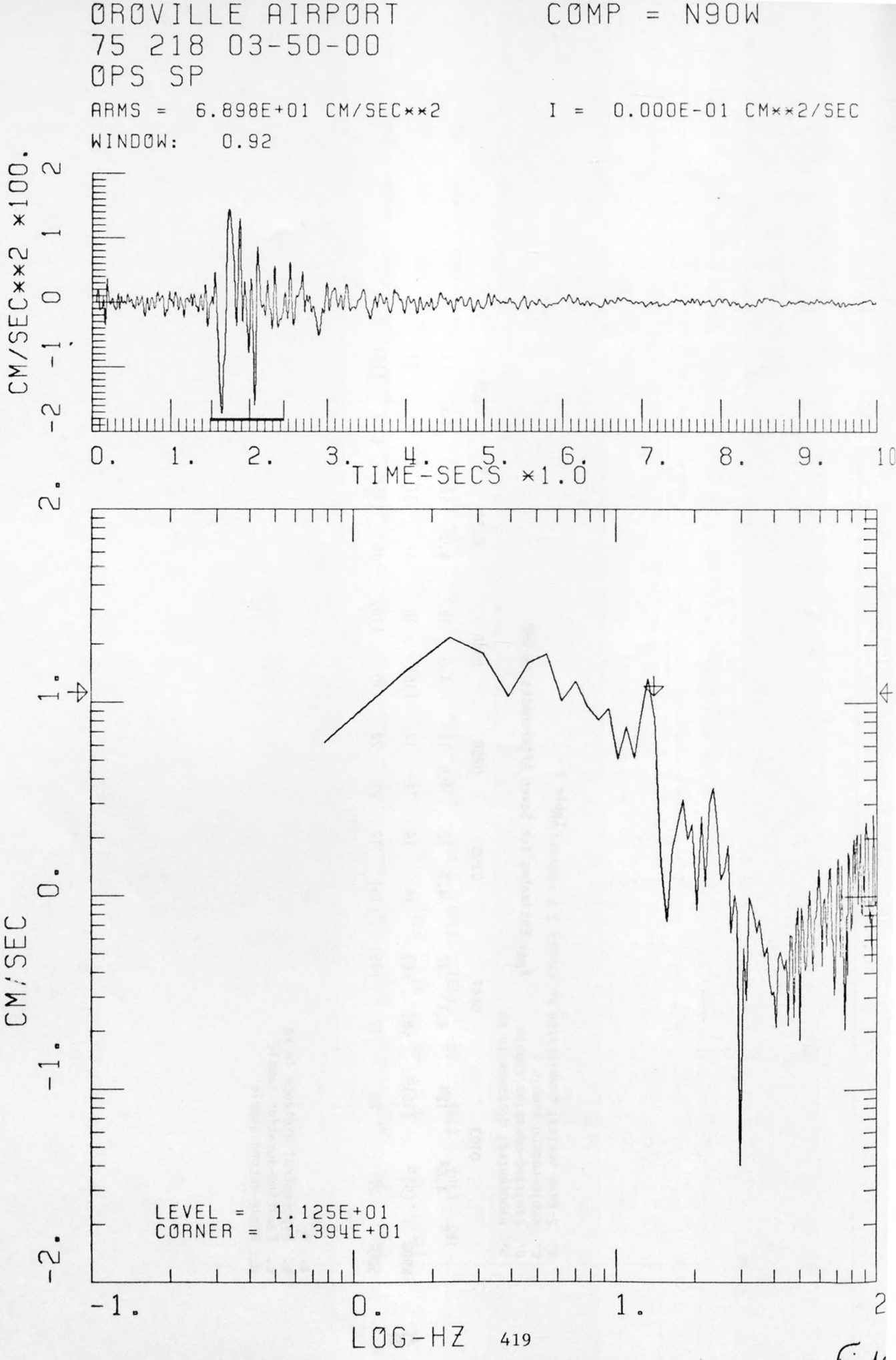
OROVILLE AIRPORT
75 218 03-50-00
OPS SP
COMP = N90W
ARMS = 6.898E+01 CM/SEC**2
I = 0.000E-01 CM**2/SEC
WINDOW: 0.92
CM/SEC**2 *100.
TIME-SECS *1.0
CM/SEC
LEVEL = 1.125E+01
CORNER = 1.394E+01
LOG-HZ

Fig 1a

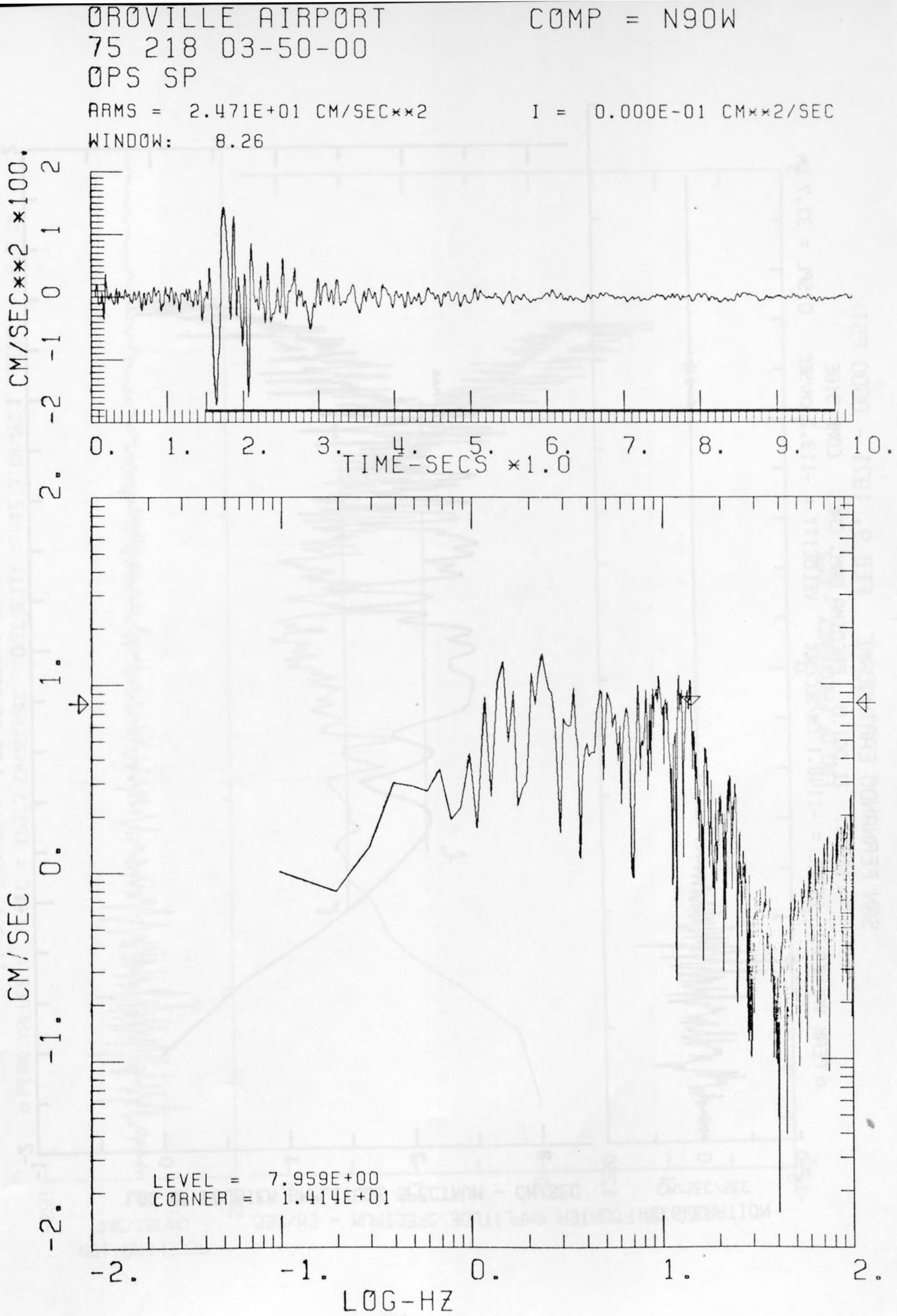
OROVILLE AIRPORT
COMP = N90W
75 218 03-50-00
OPS SP
ARMS = 2.471E+01 CM/SEC**2
I = 0.000E-01 CM**2/SEC
WINDOW: 8.26
CM/SEC**2 *100.
2
1
0
-1
-2
0. 1. 2. 3. 4. 5. 6. 7. 8. 9. 10.
TIME-SECS *1.0
CM/SEC
2.
1.
0.
-1.
-2.
LEVEL = 7.959E+00
CORNER = 1.414E+01
-2. -1. 0. 1. 2.
LOG-HZ

Fig 16

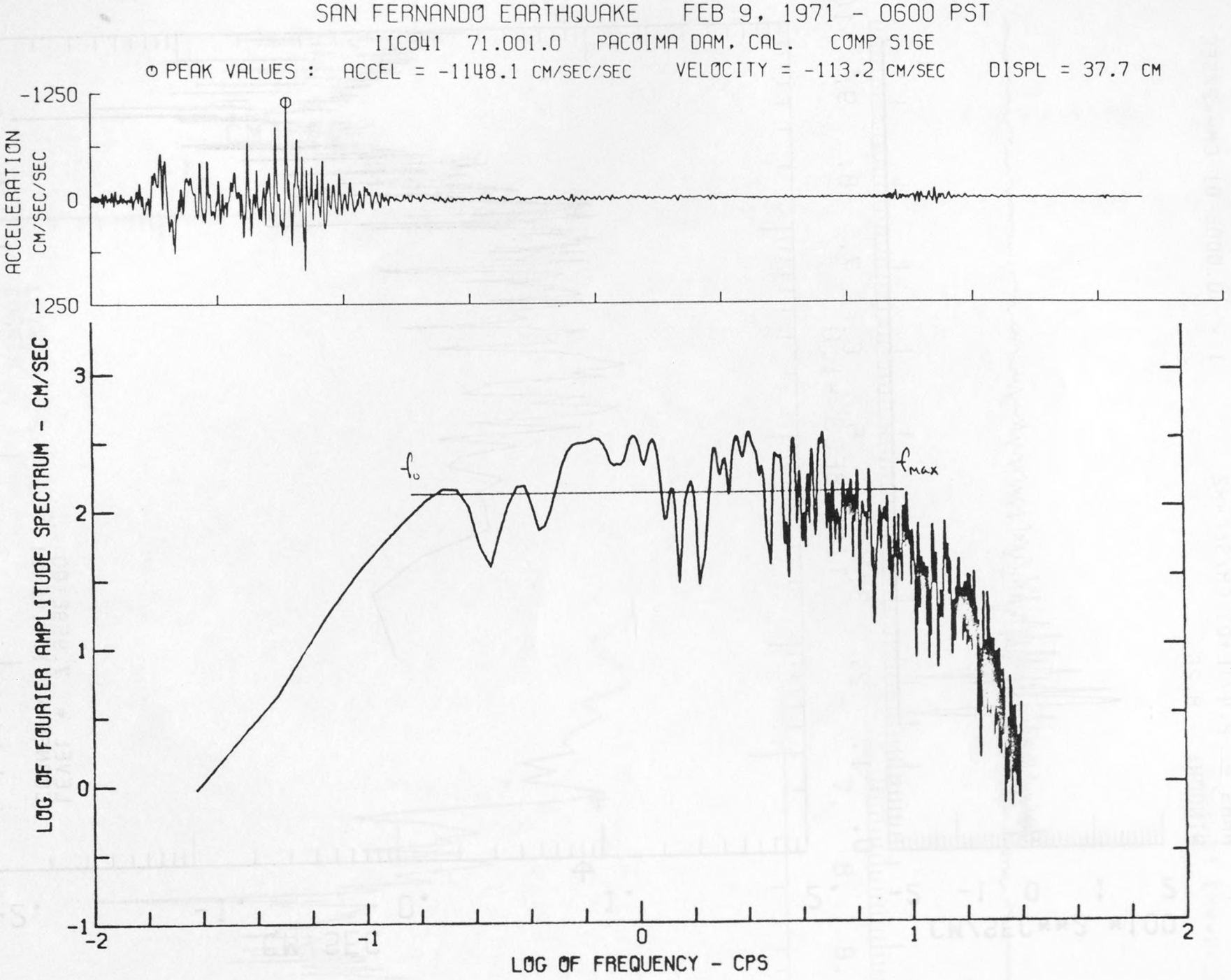
SAN FERNANDO EARTHQUAKE FEB 9, 1971 - 0600 PST
IIC041 71.001.0 PACOIMA DAM, CAL. COMP S16E
⊙ PEAK VALUES : ACCEL = -1148.1 CM/SEC/SEC VELOCITY = -113.2 CM/SEC DISPL = 37.7 CM
ACCELERATION CM/SEC/SEC
-1250
0
1250
LOG OF FOURIER AMPLITUDE SPECTRUM - CM/SEC
3
2
1
0
-1
-2
-1
0
1
2
LOG OF FREQUENCY - CPS
f_o
f_{max}

KERN COUNTY, CALIFORNIA EARTHQUAKE JULY 21, 1952 - 0453 PDT

IIA004 52.002.0 TAFT LINCOLN SCHOOL TUNNEL COMP N21E

⊙ PEAK VALUES : ACCEL = 152.7 CM/SEC/SEC VELOCITY = -15.7 CM/SEC DISPL = -6.7 CM

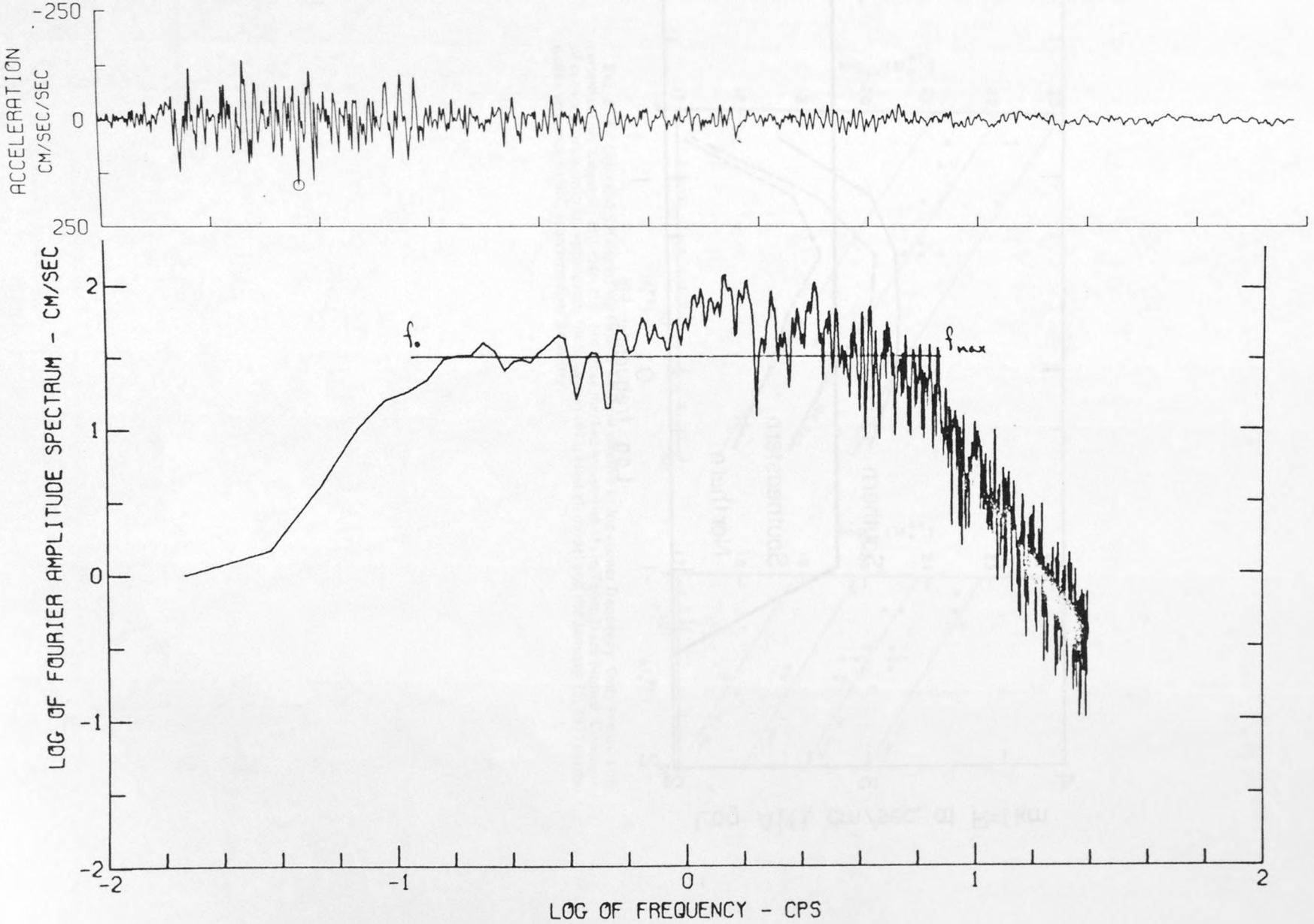

Fig. 3

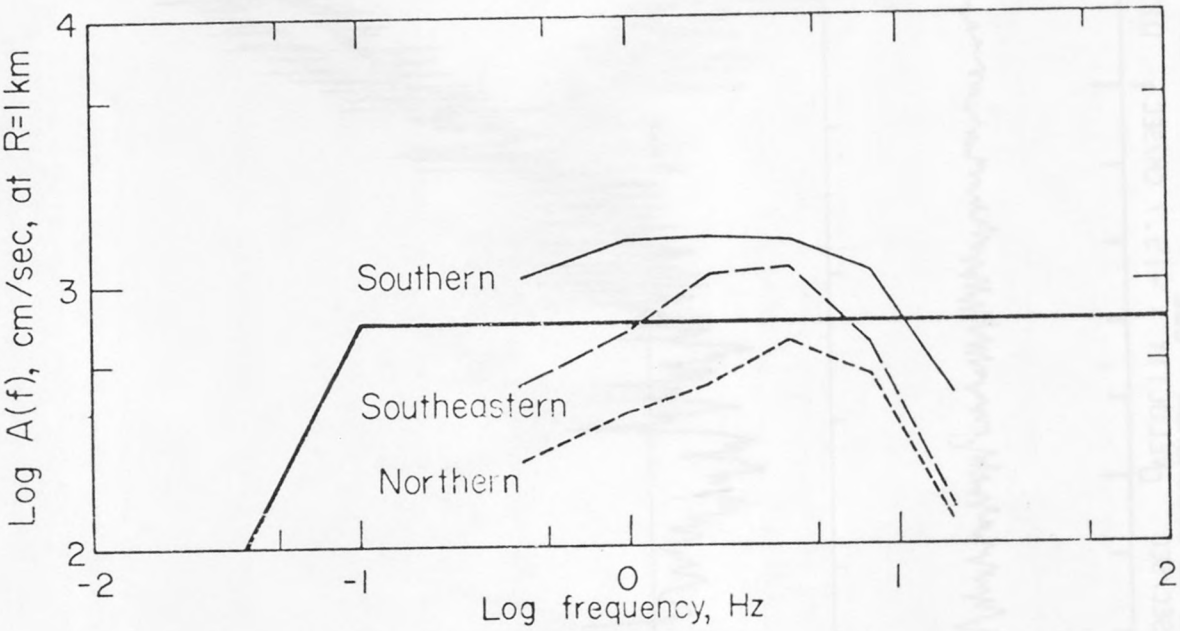
Log A(f), cm/sec, at R=1 km
4
3
2
Southern
Southeastern
Northern
-2
-1
0
1
2
Log frequency, Hz

Fig 4

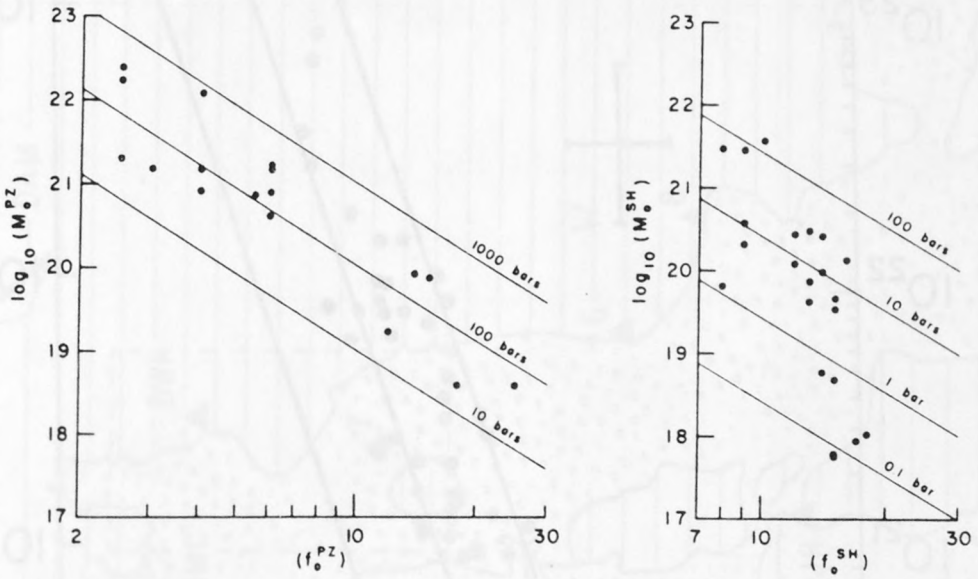

FIG. 6. *PZ* (*left*) and *SH* (*right*) log seismic moment relative to log corner frequency. Only events with certain corner-frequency estimates (i.e., not those marked by asterisk (*) in Table 2) are plotted. Contours of constant stress drop are appropriate for Savage's (1972) Haskell model and the January 15, 1973 earthquake sequence to BIC source-receiver geometry.

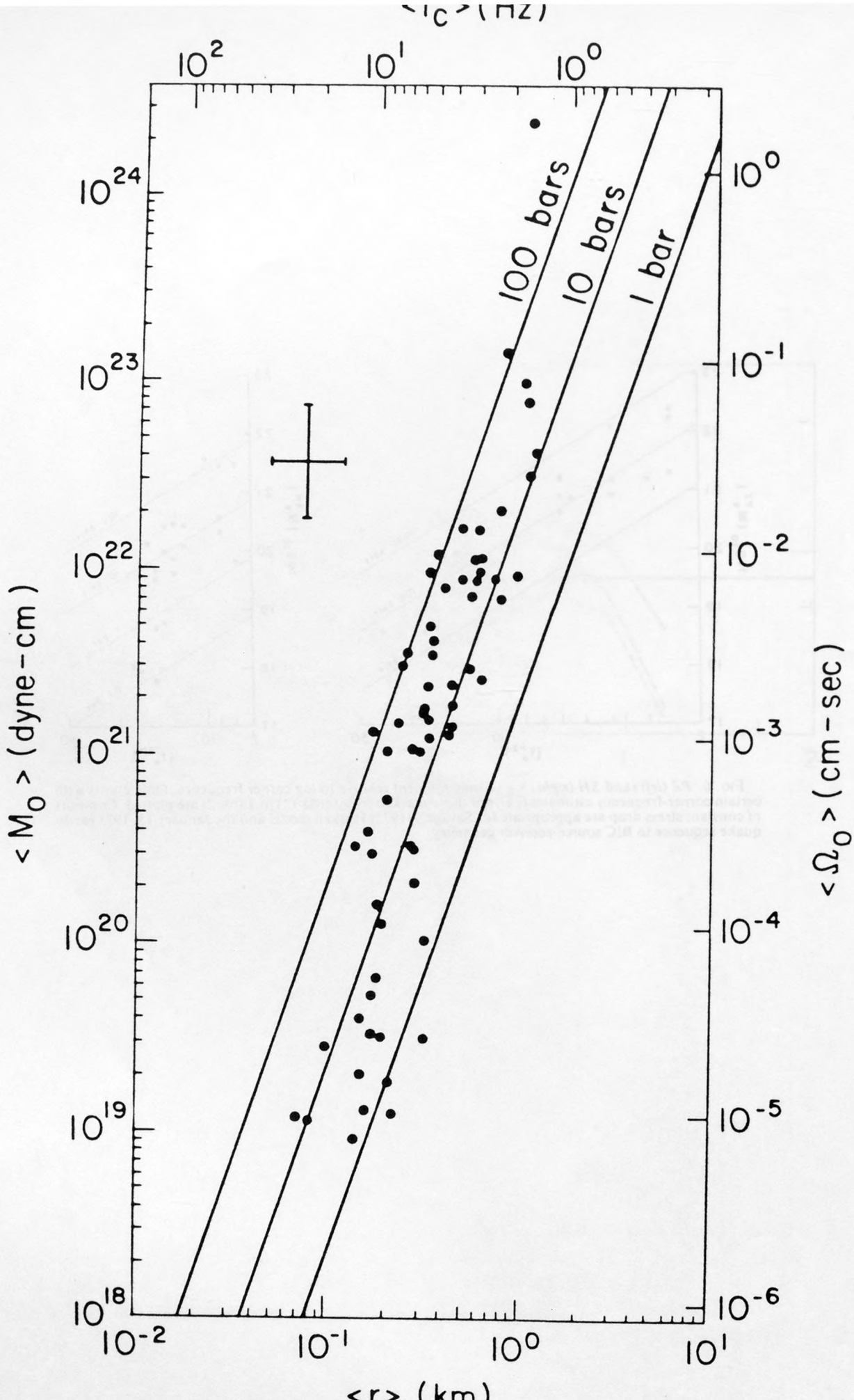
$\langle f_c \rangle$ (Hz)
10^2
10^1
10^0
100 bars
10 bars
1 bar
10^{24}
10^{23}
10^{22}
10^{21}
10^{20}
10^{19}
10^{18}
10^0
10^{-1}
10^{-2}
10^{-3}
10^{-4}
10^{-5}
10^{-6}
10^{-2}
10^{-1}
10^0
10^1
$\langle M_0 \rangle$ (dyne-cm)
$\langle \Omega_0 \rangle$ (cm-sec)
$\langle r \rangle$ (km)

Fig 6

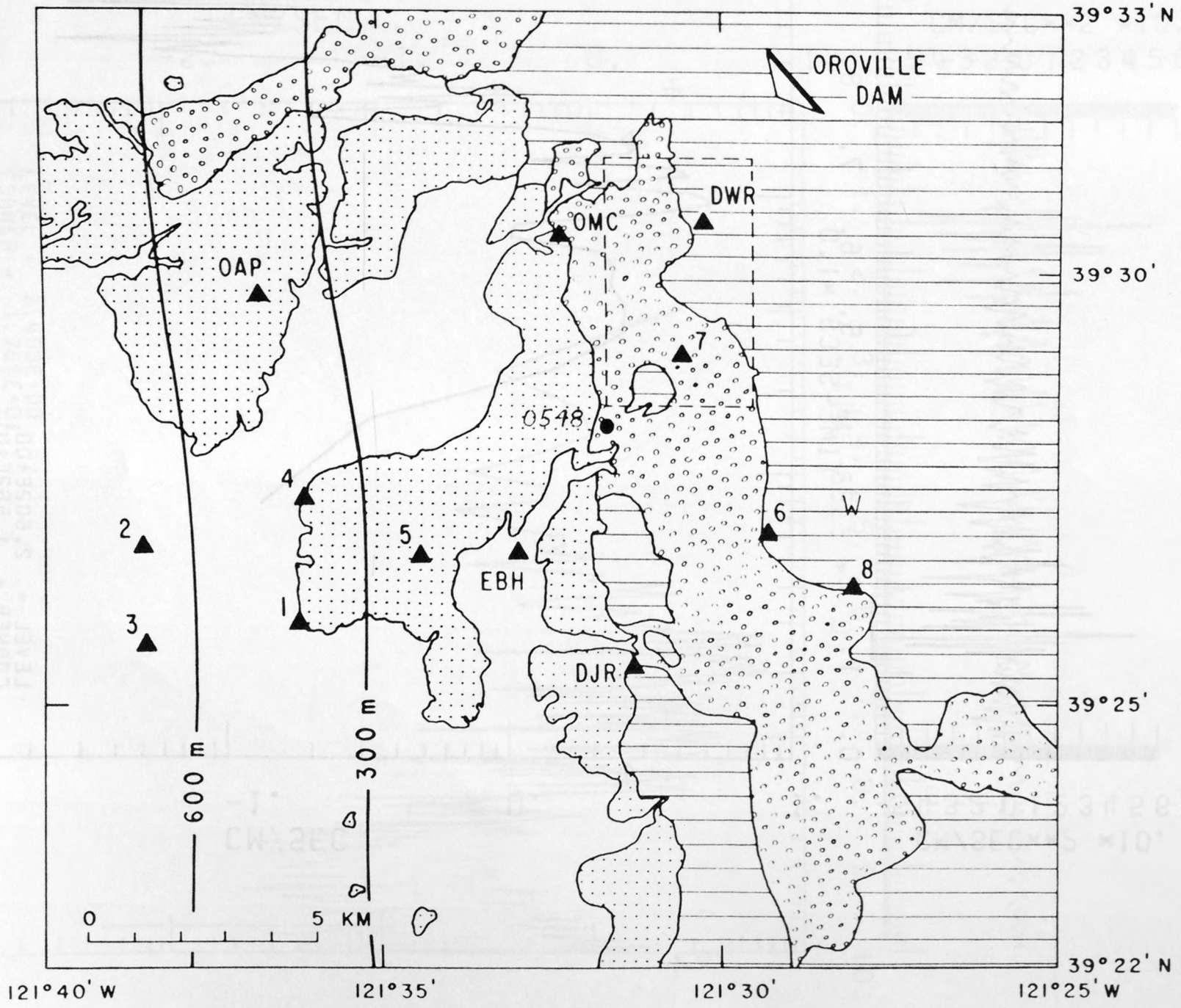
39°33'N
OROVILLE
DAM
DWR
OMC
OAP
39°30'
7
0548
4
2
5
6
W
EBH
8
1
3
DJR
39°25'
600 E
300 E
0
5 KM
39°22'N
121°40'W
121°35'
121°30'
121°25'W

Fig. 7

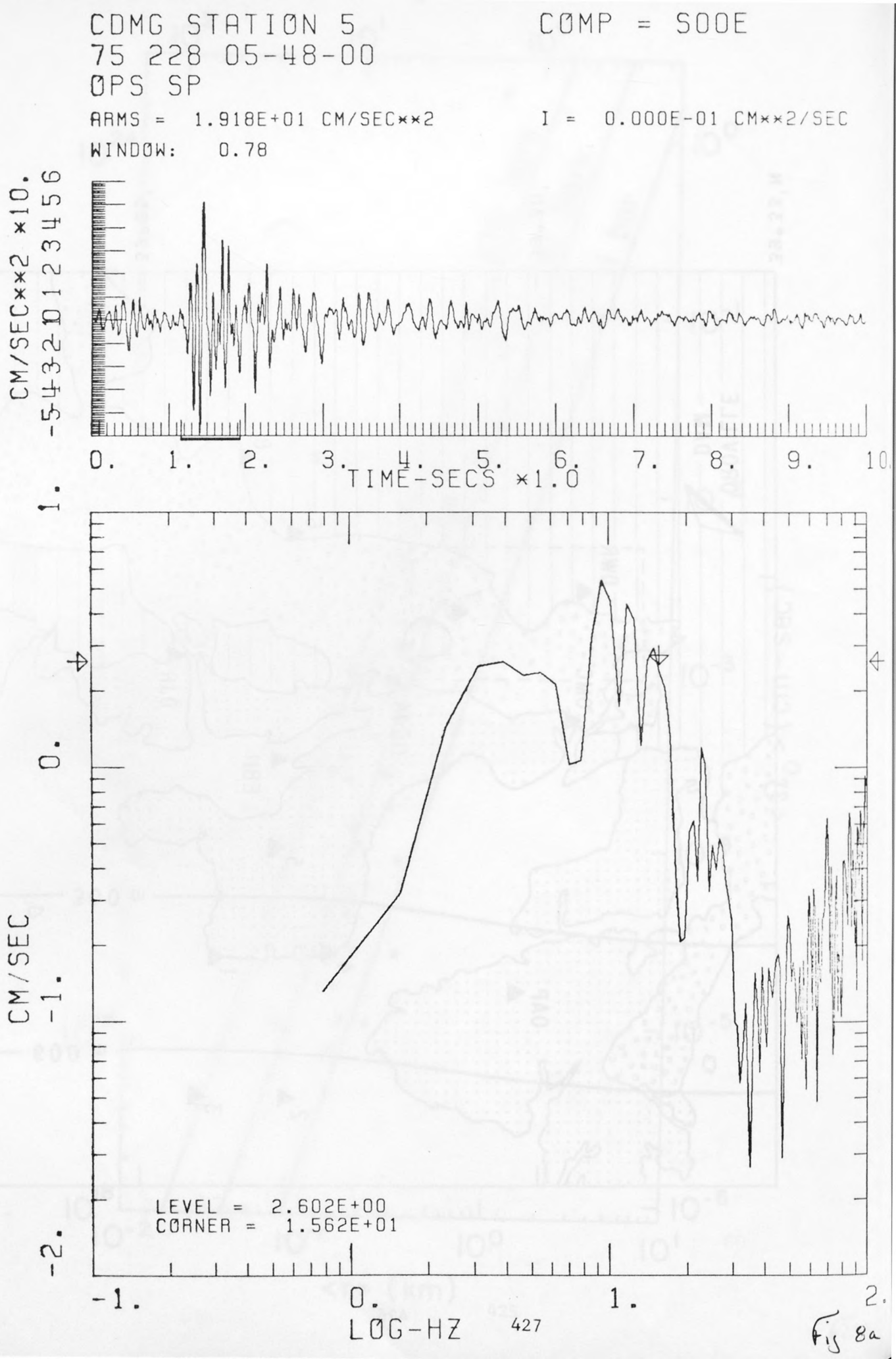
CDMG STATION 5
75 228 05-48-00
OPS SP
COMP = SOOE
ARMS = 1.918E+01 CM/SEC**2
I = 0.000E-01 CM**2/SEC
WINDOW: 0.78
CM/SEC**2 *10.
-5 -4 -3 -2 -1 0 1 2 3 4 5 6
0. 1. 2. 3. 4. 5. 6. 7. 8. 9. 10.
TIME-SECS *1.0
CM/SEC
1. 0. -1. -2.
LEVEL = 2.602E+00
CORNER = 1.562E+01
-1. 0. 1. 2.
LOG-HZ

Fig 8a

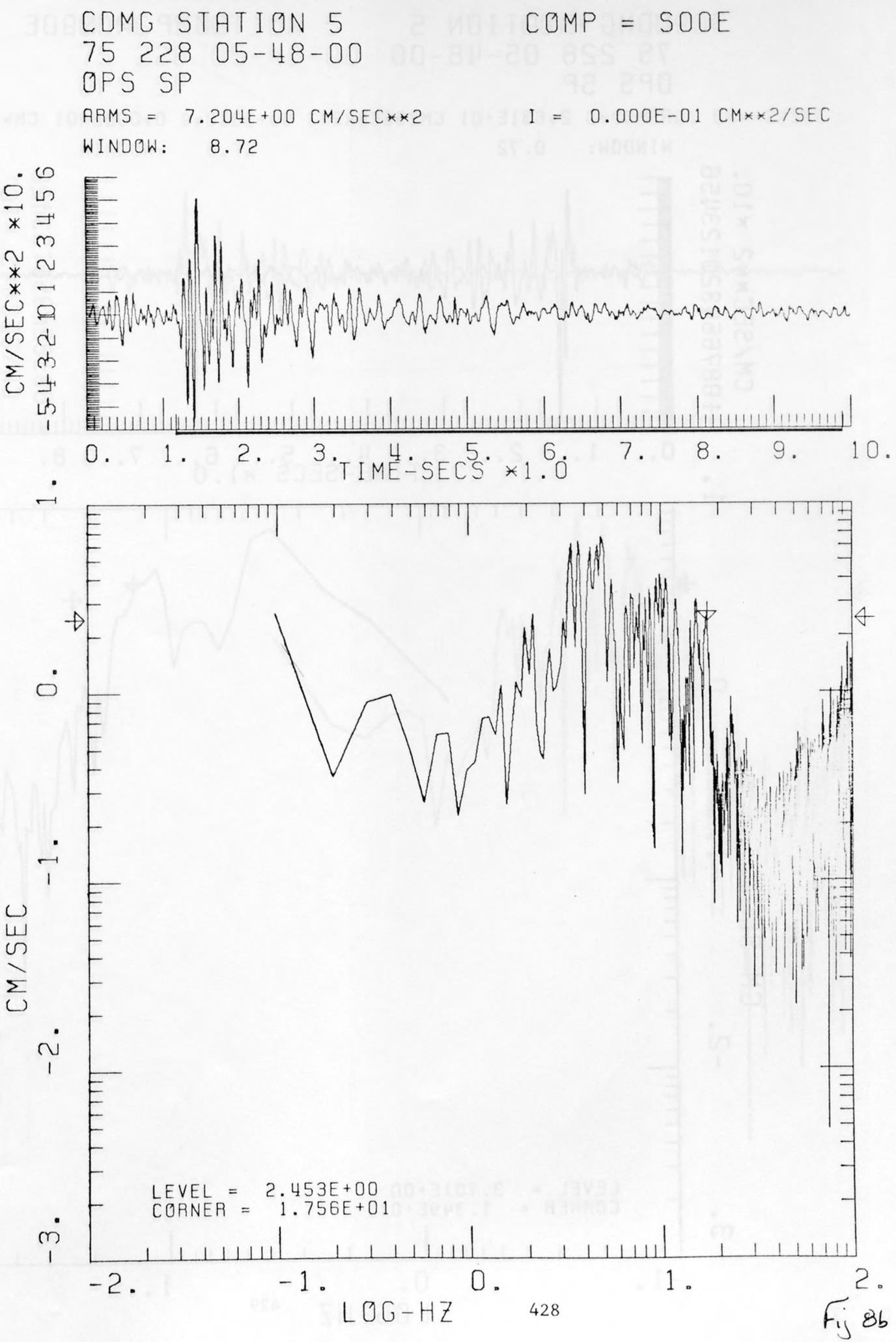
CDMG STATION 5
COMP = SOOE
75 228 05-48-00
OPS SP
ARMS = 7.204E+00 CM/SEC**2
I = 0.000E-01 CM**2/SEC
WINDOW: 8.72
CM/SEC**2 *10.
-5 -4 -3 -2 -1 0 1 2 3 4 5 6
0. 1. 2. 3. 4. 5. 6. 7. 8. 9. 10.
TIME-SECS *1.0
CM/SEC
1. 0. -1. -2. -3.
LEVEL = 2.453E+00
CORNER = 1.756E+01
-2. -1. 0. 1. 2.
LOG-HZ

Fig 86

CDMG STATION 5 COMP = N90E
75 228 05-48-00
0PS SP
ARMS = 2.631E+01 CM/SEC**2 I = 0.000E-01 CM**2/SEC
WINDOW: 0.72

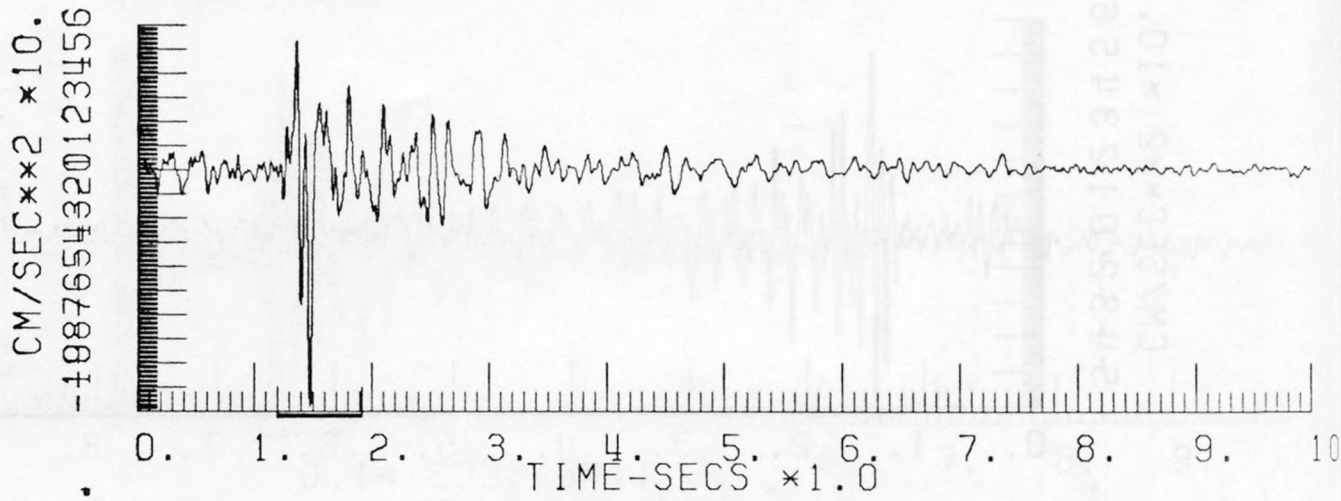

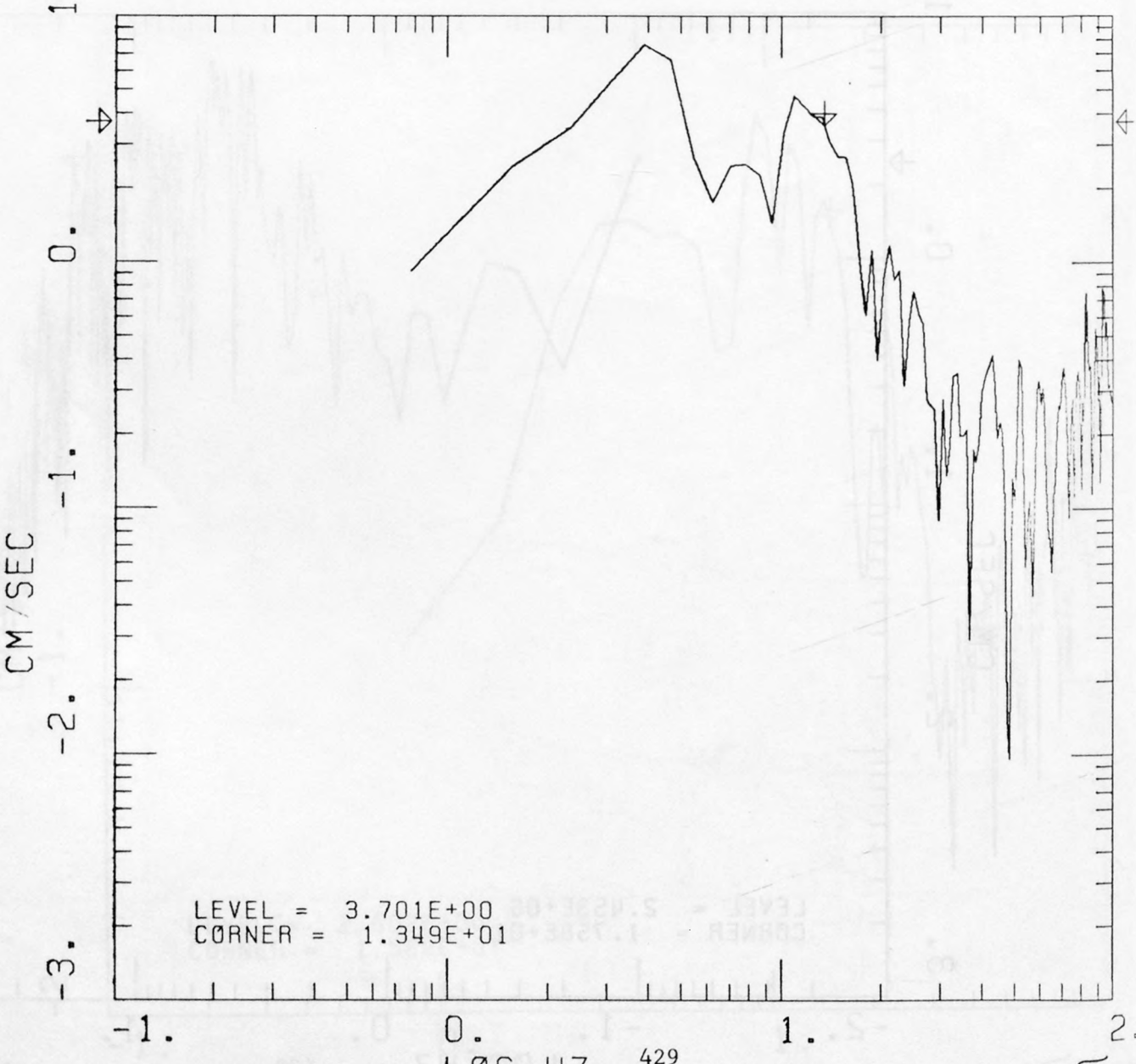

Fig 8c

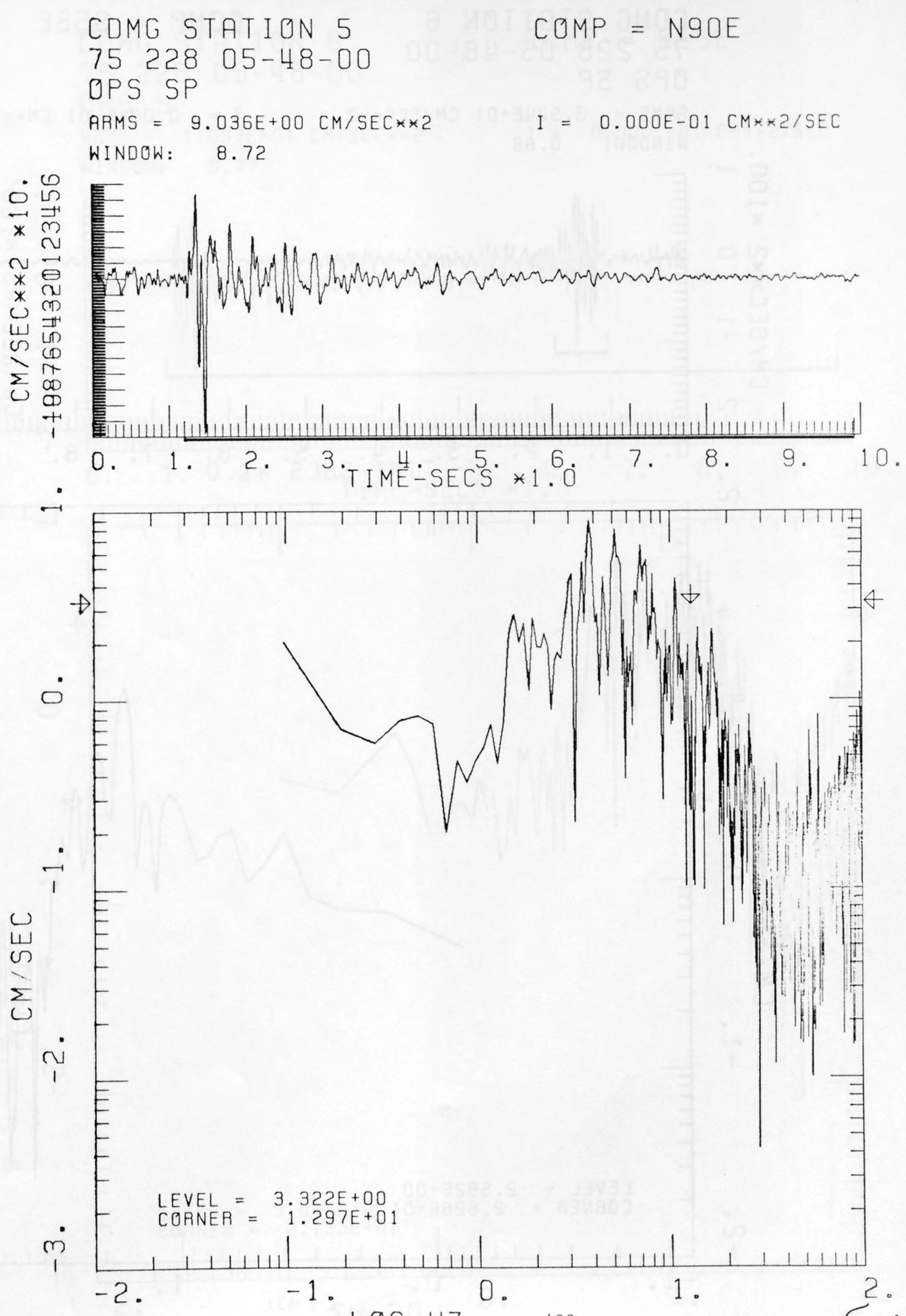
CDMG STATION 5
75 228 05-48-00
0PS SP
COMP = N90E
ARMS = 9.036E+00 CM/SEC**2
I = 0.000E-01 CM**2/SEC
WINDOW: 8.72
CM/SEC**2 *10.
-10 -9 -8 -7 -6 -5 -4 -3 -2 -1 0 1 2 3 4 5 6 7 8 9 10
0. 1. 2. 3. 4. 5. 6. 7. 8. 9. 10.
TIME-SECS *1.0
1.
0.
-1.
-2.
-3.
CM/SEC
LEVEL = 3.322E+00
CORNER = 1.297E+01
-2. -1. 0. 1. 2.
LOG-HZ

Fig 8d

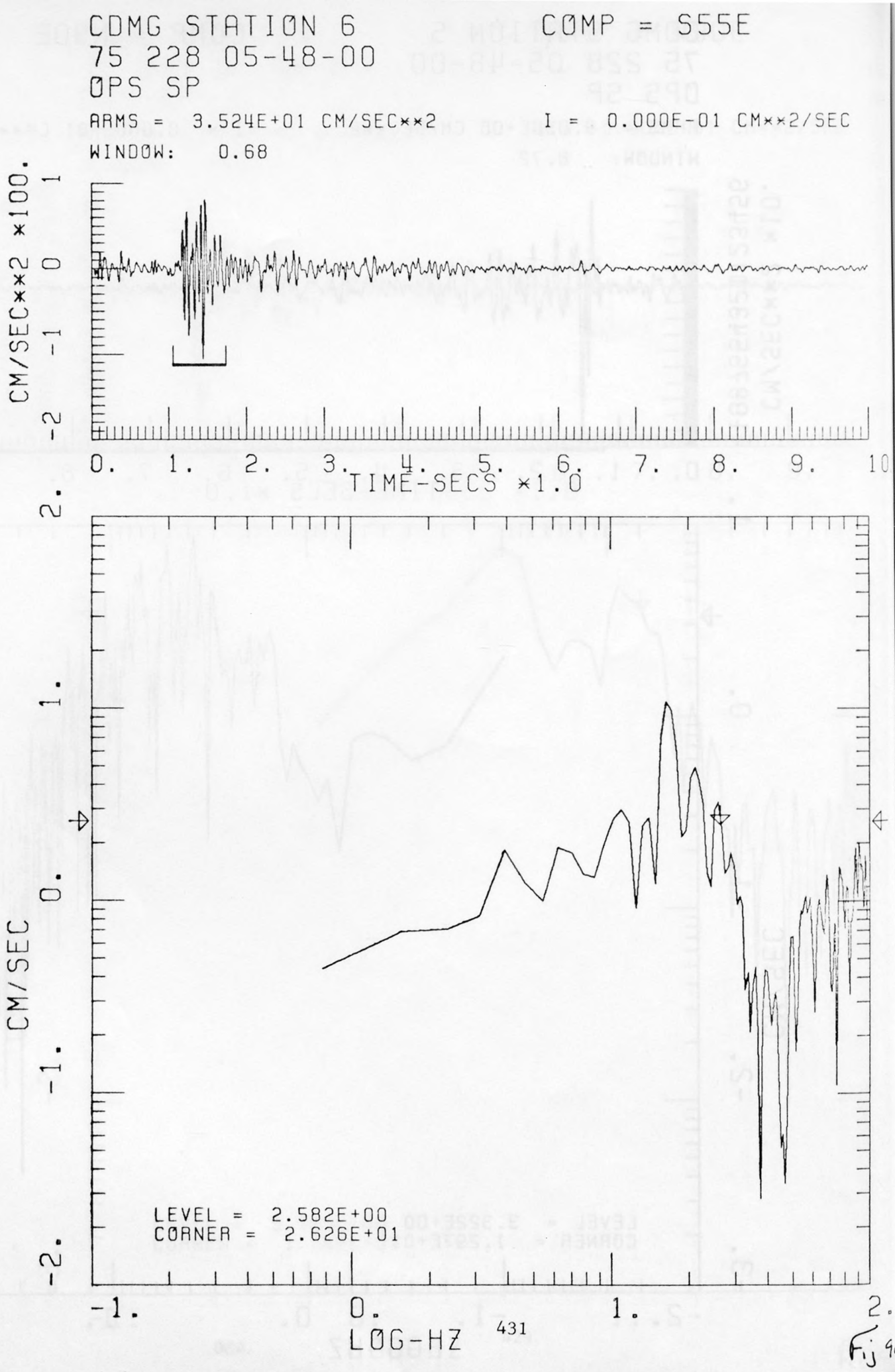
COMG STATION 6
COMP = S55E
75 228 05-48-00
OPS SP
ARMS = 3.524E+01 CM/SEC**2
I = 0.000E-01 CM**2/SEC
WINDOW: 0.68
CM/SEC**2 *100.
1
0
-1
-2
0. 1. 2. 3. 4. 5. 6. 7. 8. 9. 10
TIME-SECS *1.0
2.
1.
0.
-1.
-2.
CM/SEC
LEVEL = 2.582E+00
CORNER = 2.626E+01
-1. 0. 1. 2.
LOG-HZ

Fig 94

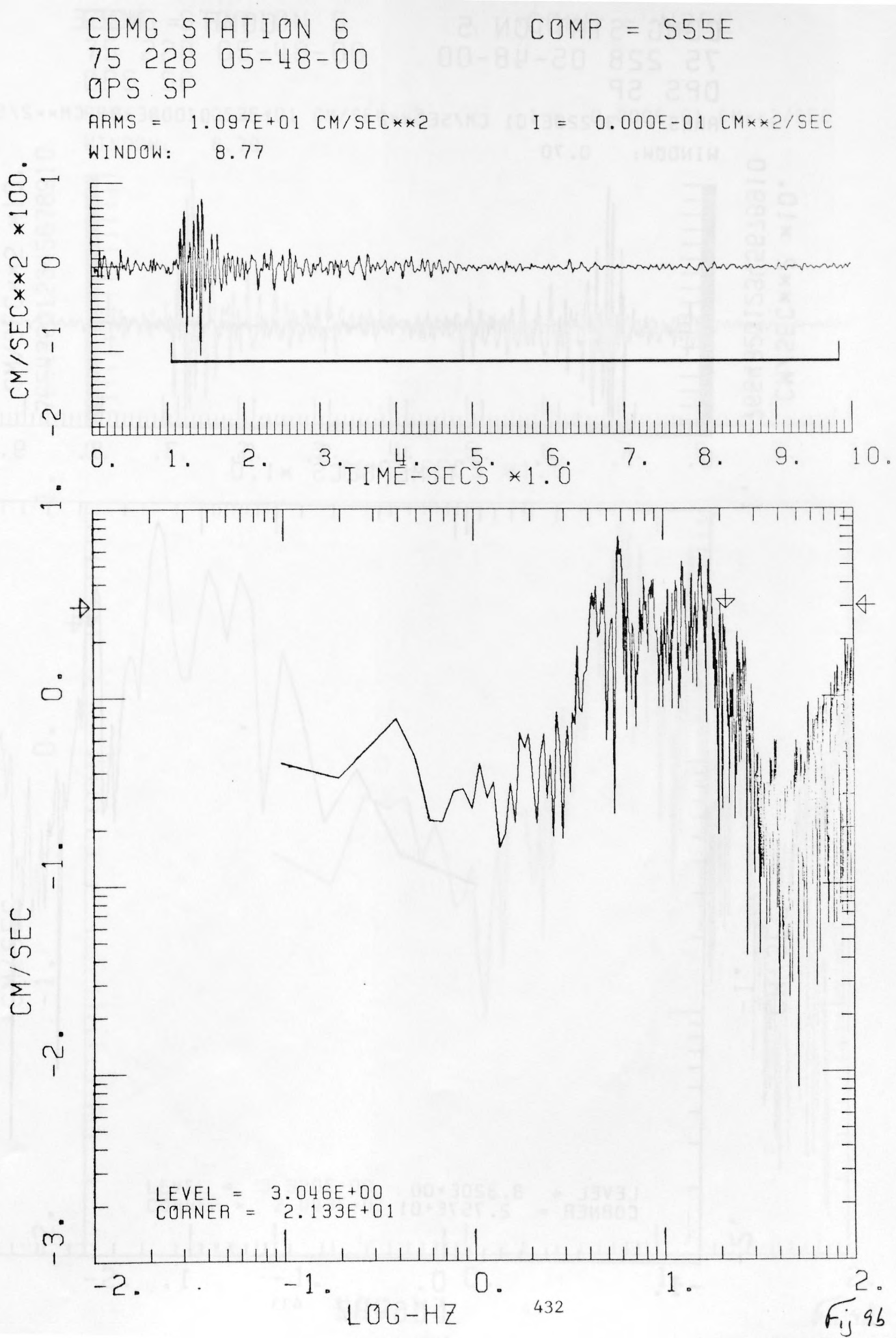
CDMG STATION 6
COMP = S55E
75 228 05-48-00
0PS SP
ARMS = 1.097E+01 CM/SEC**2
I = 0.000E-01 CM**2/SEC
WINDOW: 8.77
CM/SEC**2 *100.
1
0
-1
-2
0. 1. 2. 3. 4. 5. 6. 7. 8. 9. 10.
TIME-SECS *1.0
1.
0.
-1.
-2.
-3.
CM/SEC
LEVEL = 3.046E+00
CORNER = 2.133E+01
-2. -1. 0. 1. 2.
LOG-HZ

Fig 96

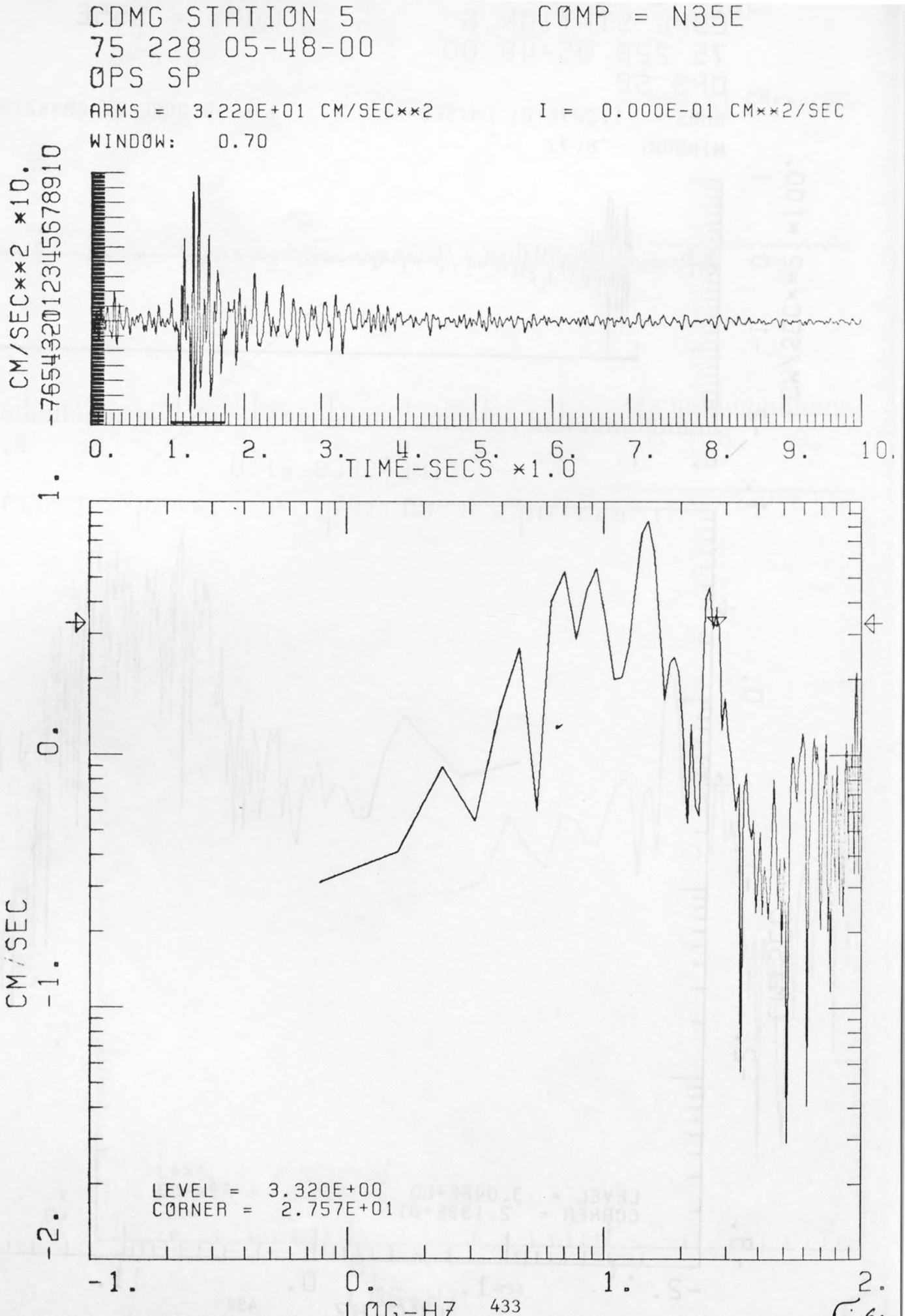
CDMG STATION 5
COMP = N35E
75 228 05-48-00
OPS SP
ARMS = 3.220E+01 CM/SEC**2
I = 0.000E-01 CM**2/SEC
WINDOW: 0.70
CM/SEC**2 *10.
-7654320123456789 10
0. 1. 2. 3. 4. 5. 6. 7. 8. 9. 10.
TIME-SECS *1.0
CM/SEC
1. 0. -1. -2.
LEVEL = 3.320E+00
CORNER = 2.757E+01
-1. 0. 1. 2.
LOG-HZ

Fig 9a

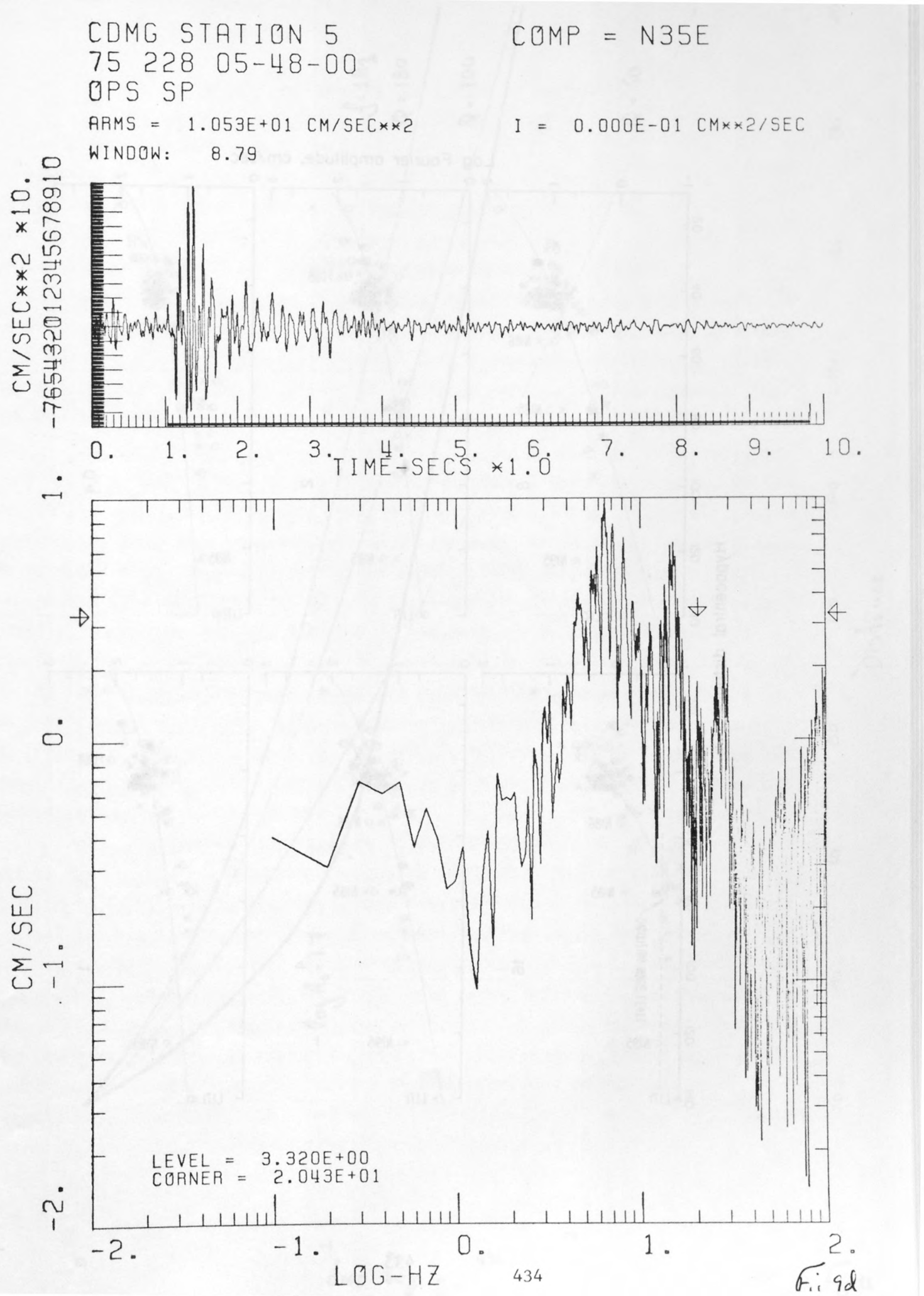
CDMG STATION 5
75 228 05-48-00
OPS SP
COMP = N35E
ARMS = 1.053E+01 CM/SEC**2
I = 0.000E-01 CM**2/SEC
WINDOW: 8.79
CM/SEC**2 *10.
-7654320123456789 10
0. 1. 2. 3. 4. 5. 6. 7. 8. 9. 10.
TIME-SECS *1.0
CM/SEC
1. 0. -1. -2.
LEVEL = 3.320E+00
CORNER = 2.043E+01
-2. -1. 0. 1. 2.
LOG-HZ

Fig 9d

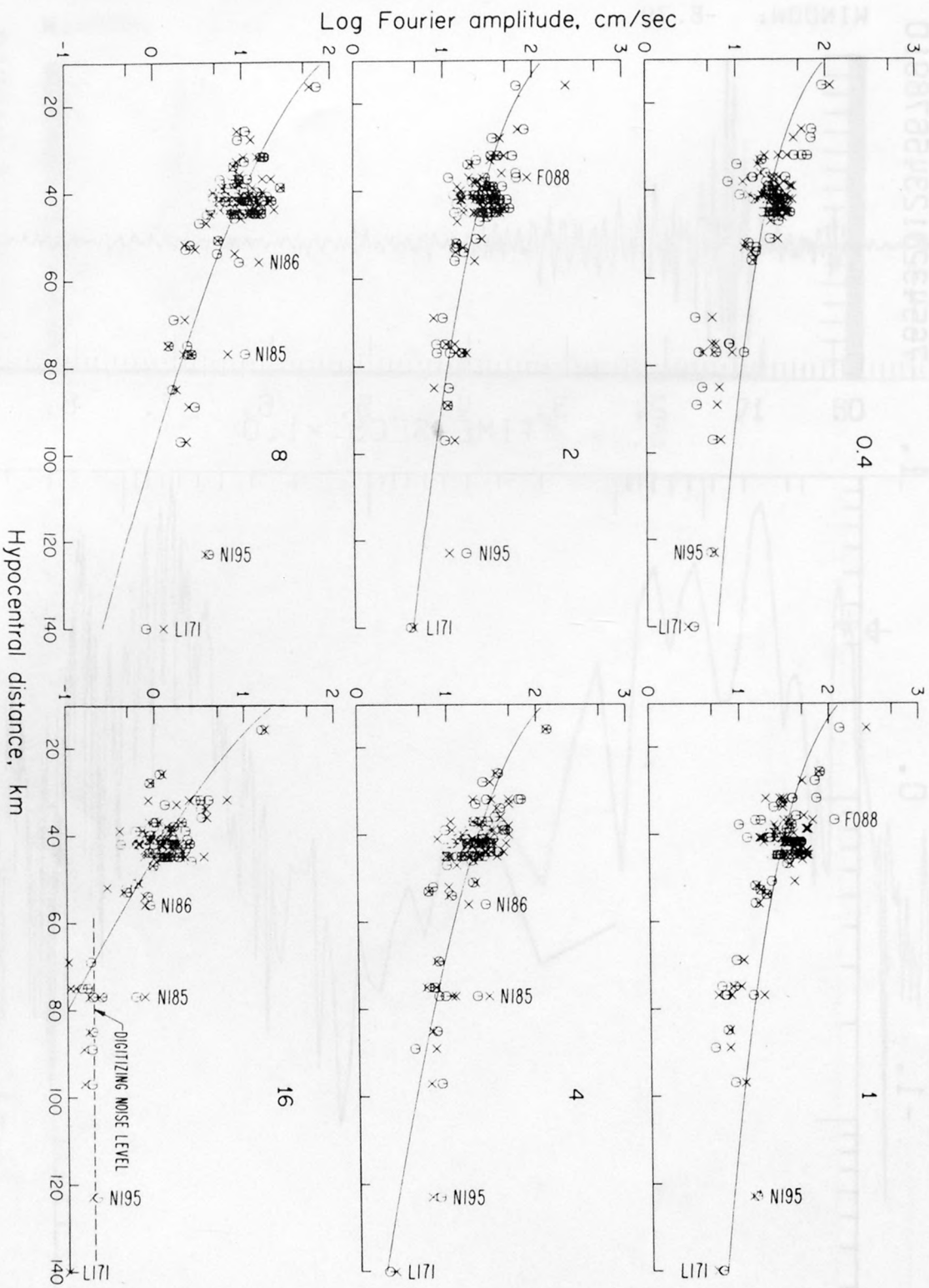
Log Fourier amplitude, cm/sec
Hypocentral distance, km
8
2
0.4
16
4
1
N186
N185
N195
L171
F088
DIGITIZING NOISE LEVEL

fig 19

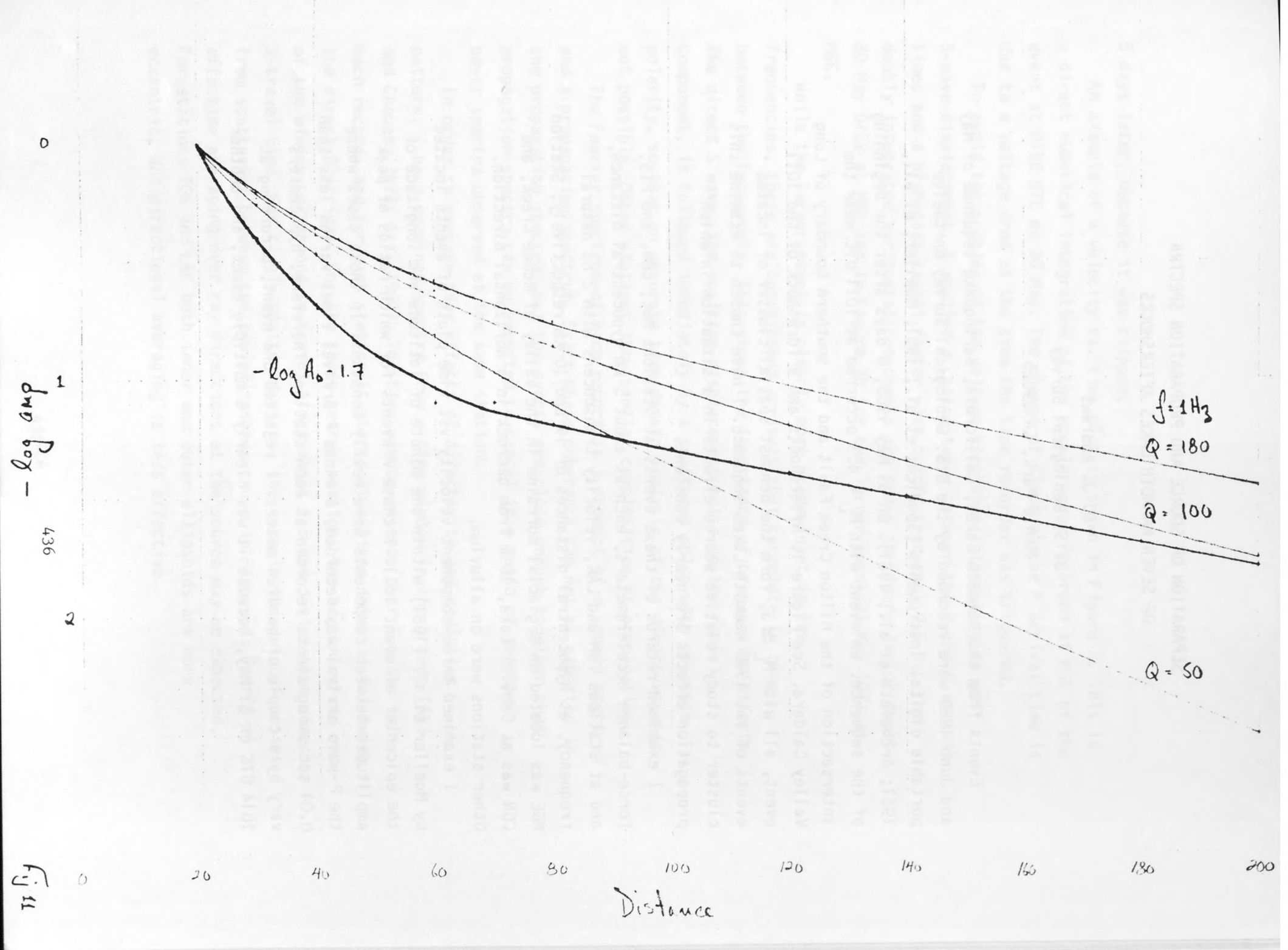
0
1
2
− log amp
436
−log A₀ - 1.7
f = 1 Hz
Q = 180
Q = 100
Q = 50
0
20
40
60
80
100
120
140
160
180
200
Distance

Fig 11

SEPARATION OF SOURCE AND PROPAGATION SPECTRA OF SEVEN MAMMOTH LAKES AFTERSHOCKS

D. J. Andrews
U. S. Geological Survey
Menlo Park, CA 94025

Events from the Mammoth Lakes, California, earthquake sequence of May and June 1980 were recorded by the U.S. Geological Survey on twelve portable digital instruments (Spudich, et al., 1981; Mueller, et al., 1981; Archuleta et al., 1981). On 31 May 1980, 6 days after the beginning of the sequence, an event with M_L = 4.3 occurred at 1011 UTC near the intersection of the Hilton Creek Fault and the southern boundary of Long Valley Caldera. See Figure 1. Aftershocks and a foreshock of the 1011 event, all with $M_L \simeq 3$, form the densest spatial cluster of located events of the 1980 Mammoth Lakes sequence. I have chosen to examine this cluster to study relative source effects in a situation in which propagation effects are nearly constant.

I examined records of these events at stations MGE, CON, and FIS, force-balance accelerometers, each at about 5 km hypocentral distance, and at stations TOM and LAK, velocity transducers with 2 Hz natural frequency, at hypocentral distances of 14 and 10 km respectively. Station MGE was located on a glacial morraine in the valley of McGee Creek, and CON was at Convict Lake, 10 m from bedrock in a horizontal direction. Other stations were on alluvium.

I examined three-component velocity vs. time plots of events located by Mueller et al. (1981) within one minute of latitude and longitude of the epicenter of event 1011. I chose 7 events for which ratios of peak amplitudes between components were nearly constant. In those cases where the P-wave arrival was recorded, S minus P arrival times varied less than 0.04 sec among events recorded at each station. Therefore, hypocenters vary by a couple of hundred meters. I rejected one event, occurring at 1014 UTC on 31 May, because it was clearly a multiple event, and another

5 days later, because it was clipped.

An example of a velocity vs. time plot is shown in Figure 2. This is a direct numerical integration of the accelerogram recorded at MGE of the event at 0752 UTC on 30 May. The change of slope at the P arrival time is due to a voltage drop at the time the tape recorder was triggered.

To avoid the problem of the voltage step when integrating to get S-wave displacement, I applied a cosine taper between the P and S arrival times and a high-pass causal filter with cutoff frequency 0.5 Hz. The doubly integrated horizontal components are shown in Figure 3a for event 30 May 0752 at MGE and in Figure 3b for the larger event 31 May 1011 at MGE.

While the larger event is clearly more predominant in low frequencies, there are conspicuous arrivals that correlate in time between the two events. This shows the importance of propagation effects. The direct S wave, the positive displacement pulse on the radial component, is followed immediately by a scattered pulse with opposite polarity, so that an accurate time-domain analysis of the direct wave is not possible. Other stations show similar complexities of propagation.

The Fourier spectrum of each record is a product of a source spectrum and a propagation spectrum. Exact phase coherence can not be expected in the propagation spectra, but the events are close enough together that propagation spectra can be expected to cancel in a ratio of smoothed power spectra observed at the same station.

In order to average over effects of directivity and radiation pattern, I have examined spectra from a time window in the S coda (Aki and Chouet, 1975; Aki, 1980). The time window extends over 2.8 sec for each record, and for each station it starts at a fixed interval following the direct S arrival. For the three nearer stations the beginning and end of the window correspond to travel times about 1.5 and 3 times the direct S travel time. For singly scattered waves, the coda in this window arises from scatterers between the two ellipsoids shown in Figure 4. Fairly effective averaging over ray directions at the source may be expected. For stations TOM and LAK both inner and outer ellipsoids are more eccentric, and directional averaging is less effective.

A stationary random function may be specified by its expected power spectrum. The Fourier transform of a windowed sample of the random function will, at each frequency, have real and imaginary parts having Gaussian probability distributions with zero mean. The squared magnitude of the Fourier transform, normalized to the window length, has an expected value termed the power spectrum by statisticians, but it is not a deterministic quantity; its standard deviation is equal to its expected value. A better estimate of the power spectrum than that given by the squared transform of a single sample is needed, especially if spectral ratios are used (Aki and Richards, 1980, p. 636). A seismogram is transient rather than stationary, but its random character suggests the similar need to eliminate random scatter in spectral analysis.

I have chosen to use a time window that is a composite of four overlapping time windows, as shown in Figure 5. Each individual window function is a full cosine bell extending over 1.75 sec. Squared magnitudes of Fourier transforms found with the four windows are averaged to get an estimate of the power spectrum.

In order to reduce the number of frequency values to be dealt with in the inversion and to further smooth the spectra at high frequencies, each power spectrum is averaged over a geometric sequence of frequency intervals. Each interval spans a factor of $2^{1/4}$ in frequency, a minor third in musical terminology. The averaging method conserves the integral of the power spectrum.

As a final step in smoothing, power spectra from each pair of horizontal components are summed.

Smoothed velocity power spectra observed at MGE from the 7 selected events are shown in Figure 6.

For the 7 events and 5 stations, 28 of the possible 35 event-station combinations have usable records. Each observed power spectrum is assumed to be the product of the source spectrum of the event and the propagation spectrum appropriate to the station. Let O_{jk} be the logarithm of the observed power spectrum of event j at station k. Let S_j be the logarithm of the source spectrum of event j, and P_k be the logarithm of the propagation spectrum for station k. At each frequency value there is

a separate set of linear equations to be inverted:

$$S_j + P_k = O_{jk}$$

There are 28 equations relating observed spectral values to 12 parameters, 7 source spectra and 5 propagation spectra. There is one unconstrained degree of freedom: at each frequency all propagation spectra may be divided by a constant and all source spectra may be multiplied by the same constant without affecting the fit. Upon adding the arbitrary constraint that the logarithms of the propagation spectra must sum to zero

$$\sum P_k = 0$$

the system of equations becomes well-conditioned (condition number = 3.5), and a least-squares solution may be found.

The resulting source spectra (velocity power spectra) are shown in Figure 7, and the propagation spectra are shown in Figure 8. Only ratios of these curves are determined by the data; all curves may be shifted by a single arbitrary function of frequency.

The propagation spectra in Figure 8 show the relative effects of local site structure and of varying propagation distances. The regional scattering spectrum relating coda spectra to direct-wave spectra is not determined.

The velocity power spectra shown in Figure 7 trend as frequency to the -7 power between 10 and 20 Hz. This corresponds to displacement Fourier amplitude trending as frequency to the -4.5 power, much steeper than is reasonable according to any theoretical source model. This suggests that the regional scattering spectrum for coda waves decreases toward higher frequency.

The lower four of the 7 source spectra are bunched closely together. Their geometric mean is chosen as the base for plotting source power spectral ratios in Figure 9. The ratio of power spectra between events 1011 and 0752 at 2 Hz is about 750, indicating a ratio of seismic moments

of 27. The ratio of seismic moments determined in the time domain from the area of the direct S pulse at the 3 nearer stations is 24.

The most interesting feature of these source spectra is perhaps the consistency of their trends at high frequency; the curves cross by only minor amounts. Perhaps there is hope that high-frequency spectral levels (related to damaging ground motion in large earthquakes) are predictable from low and intermediate frequency parameters, such as moment and energy.

Moments and radiated energies were determined in the time domain for events 0752 and 1343 from the first S-wave displacement pulse recorded at the three nearer stations. When the source spectra in Fig. 7 are normalized at 1 Hz to match the moments, energies found by integrating the spectra are a factor of 10 smaller than values found in the time domain. Therefore the regional scattering spectrum for coda waves seriously biases estimates of source parameters from coda spectra.

To illustrate this last point, a common function is removed from all the source spectra to make the spectra for events 0752 and 1343 have Brune ω^{-2} spectra with appropriate moments and energies. The adjusted source spectra are shown in Fig. 10 and the propagation spectra are shown in Fig. 11. Apparent stress is shown in Fig. 12. Points indicated by diamonds are from unadjusted spectra, and plus signs are from adjusted spectra. Therefore it is possible, but not proved, that apparent stress is relativelely constant for these events.

Acknowledgement

I am grateful to all those who worked in the field at Mammoth Lakes to gather the data and to all those who worked to put it into readily-accessible computer files. Edward Cranswick, Joanne Vinton, and Jon Fletcher helped me get started in my work. Ralph Archuleta and Paul Spudich have gladly offerred information and advice.

REFERENCES

Aki, K., Attenuation of shear waves in the lithosphere for frequencies from 0.05 to 25 Hz, Phys. Earth and Plan. Interiors, 21, 50-60, 1980.

Aki, K. and B. Chouet, Origin of coda waves: source, attenuation, and scattering effects, J. Geophys. Res., 80, 3322-3342, 1975.

Aki, K. and P. G. Richards, Quantitative Seismology: Theory and Methods, W. H. Freeman, San Francisco, 1980.

Archuleta, R. J., P. Spudich, E. Cranswick, and C. Mueller, Source parameters of the 1980 Mammoth Lakes, California, earthquake sequence, submitted to J. Geophys. Res., 1981.

Mueller, C., P. Spudich, E. Cranswick, and R. J. Archuleta, Preliminary analysis of digital seismograms from the Mammoth Lakes, California, earthquake sequence of May-June, 1980, U.S. Geological Survey Open-File Report 81-155, 1981.

Spudich, P., E. Cranswick, J. Fletcher, E. Harp, C. Mueller, R. Navarro, J. Sarmiento, J. Vinton, and R. Warrick, Acquisition of digital seismograms during the Mammoth Lakes, California, earthquake sequence of May-June 1980, U.S. Geological Survey Open-File Report 81-38, 1981.

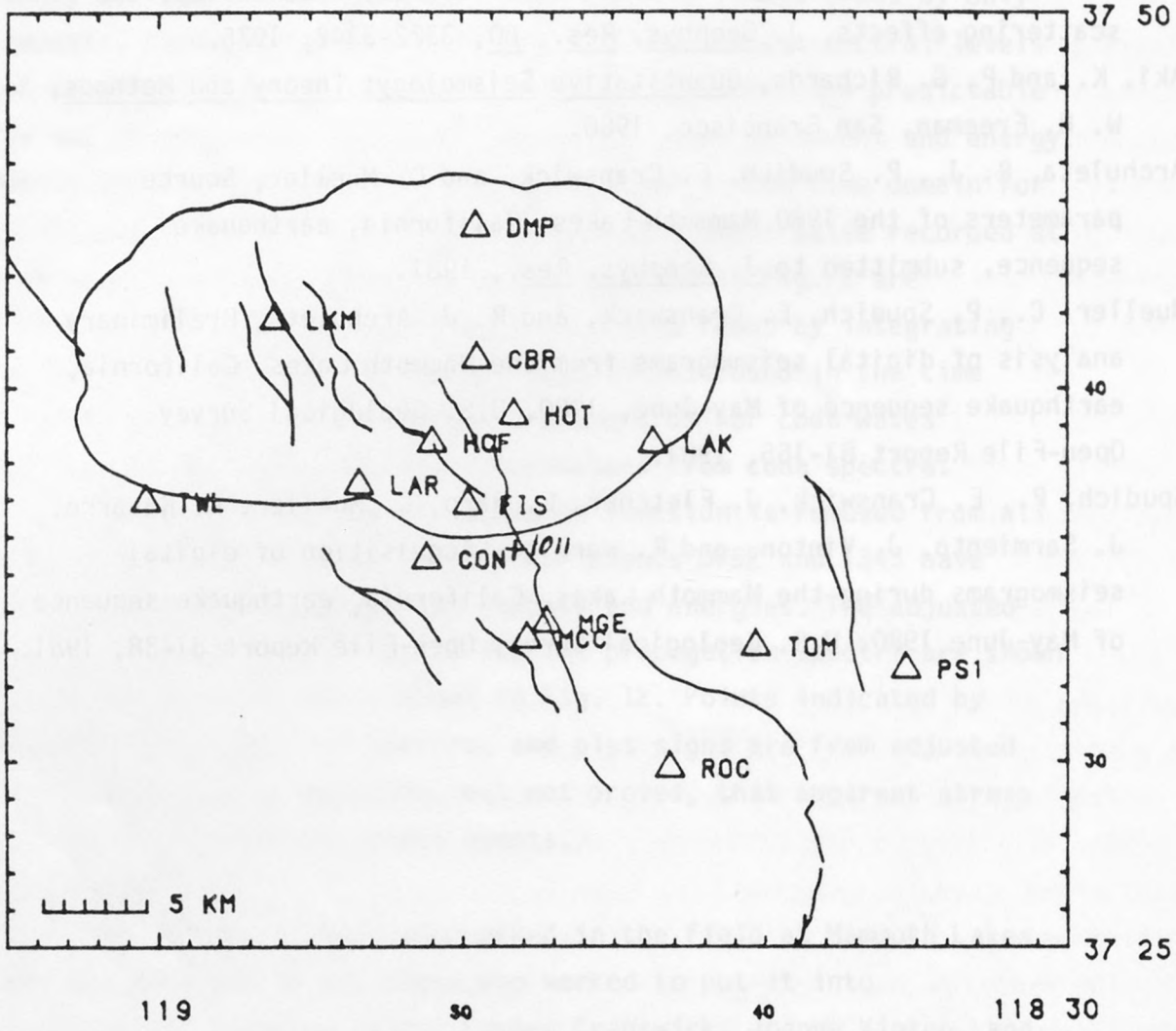

MAMMOTH LAKES STATION LOCATIONS

Figure 1. Locations of digital seismometers which recorded earthquakes during the Mammoth Lakes earthquake sequence. (From Spudich, et al., 1981)

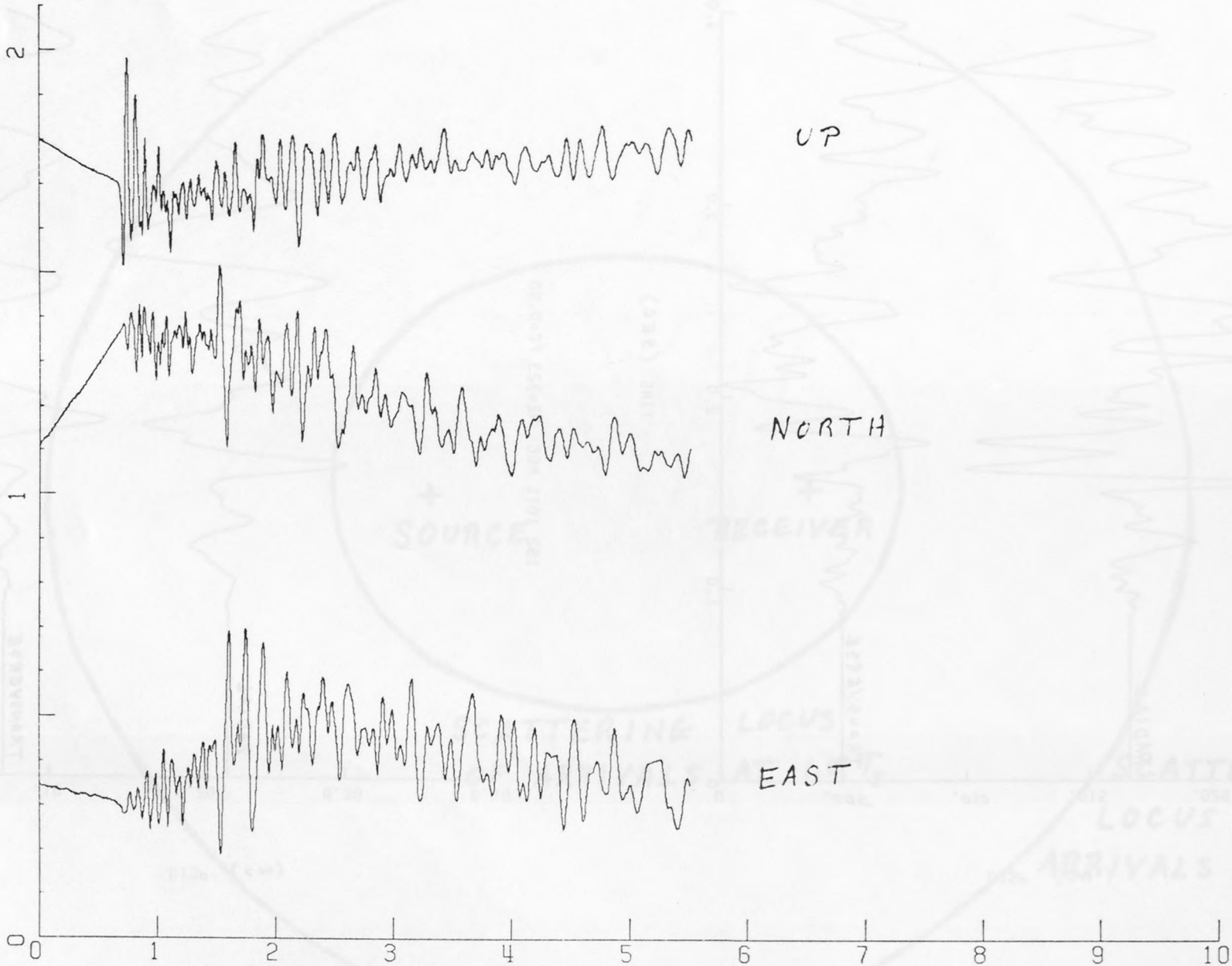

FIG. 2

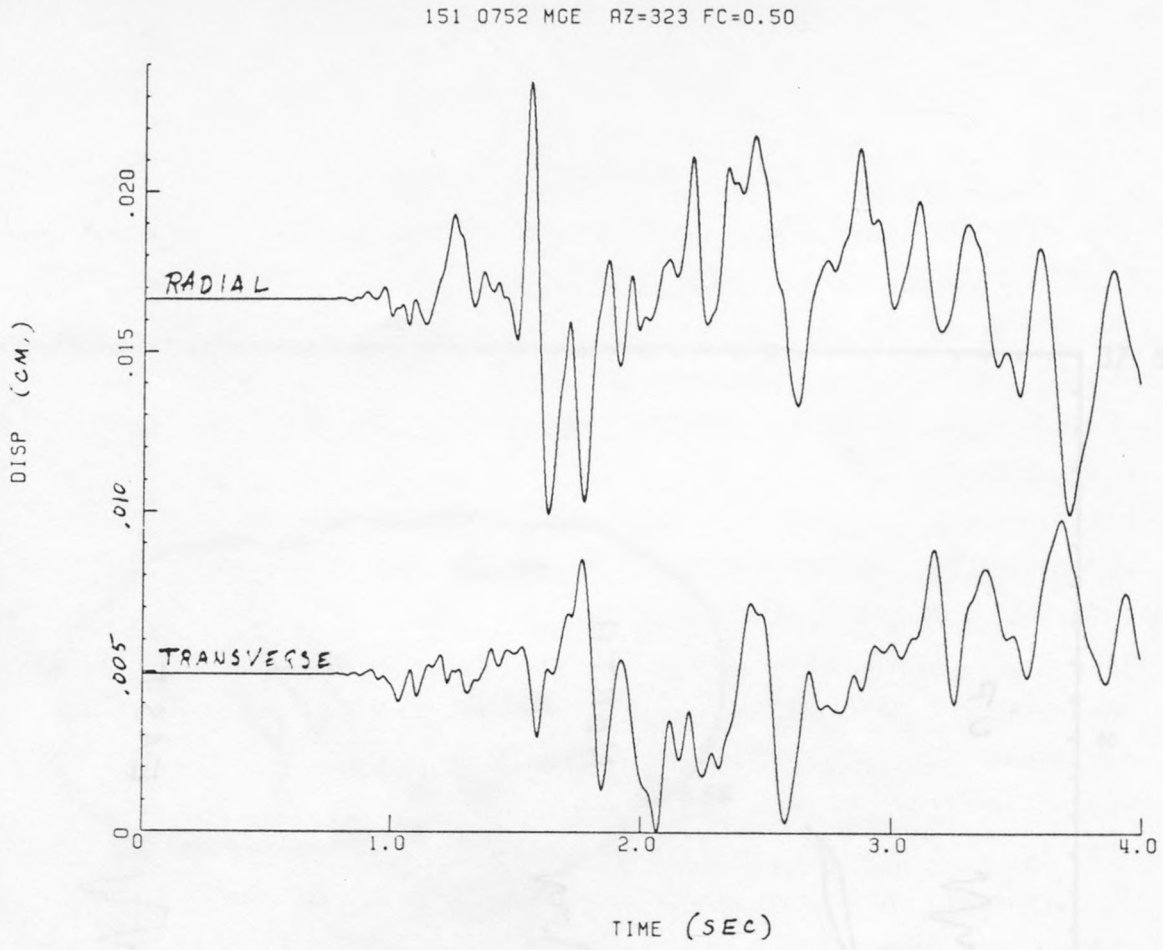
151 0752 MGE AZ=323 FC=0.50
DISP (CM.)
.020
.015
.010
.005
0
RADIAL
TRANSVERSE
0
1.0
2.0
3.0
4.0
TIME (SEC)

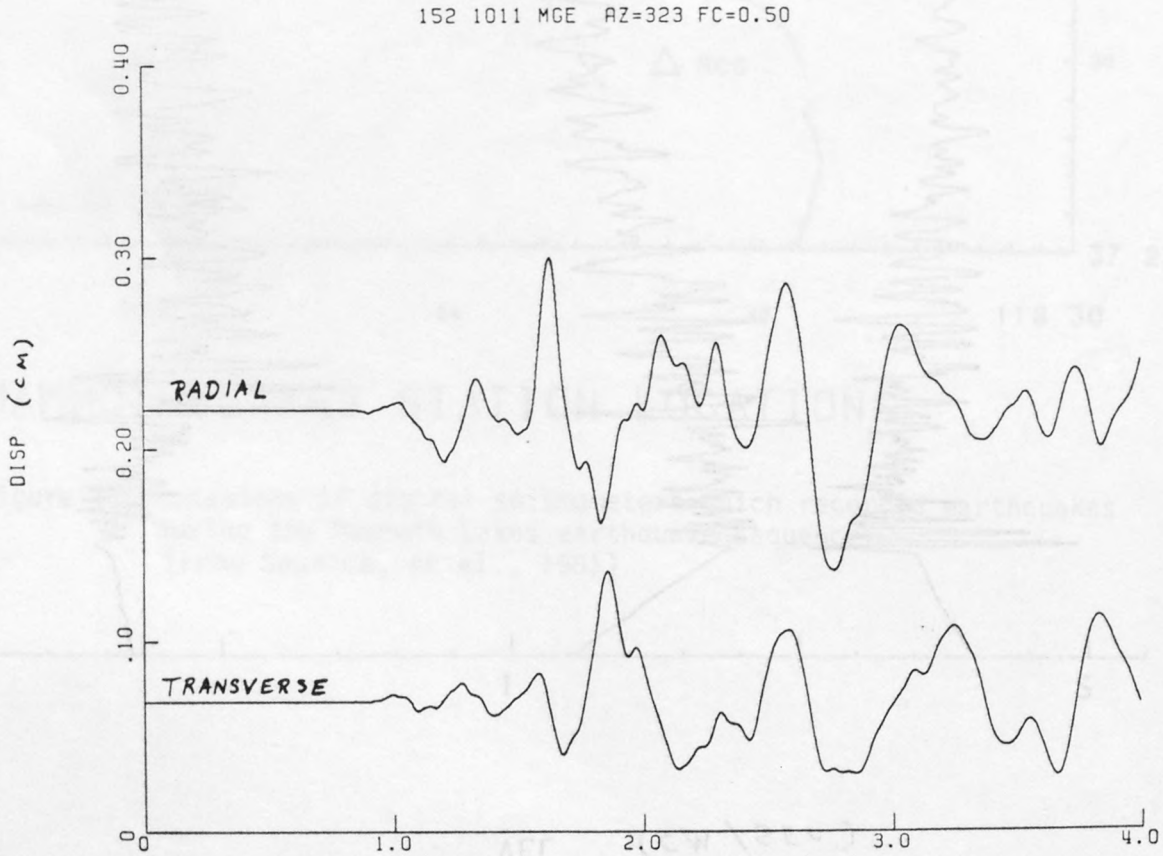
152 1011 MGE AZ=323 FC=0.50
DISP (CM)
0.40
0.30
0.20
.10
0
RADIAL
TRANSVERSE
0
1.0
2.0
3.0
4.0
TIME (SEC)

FIG. 3

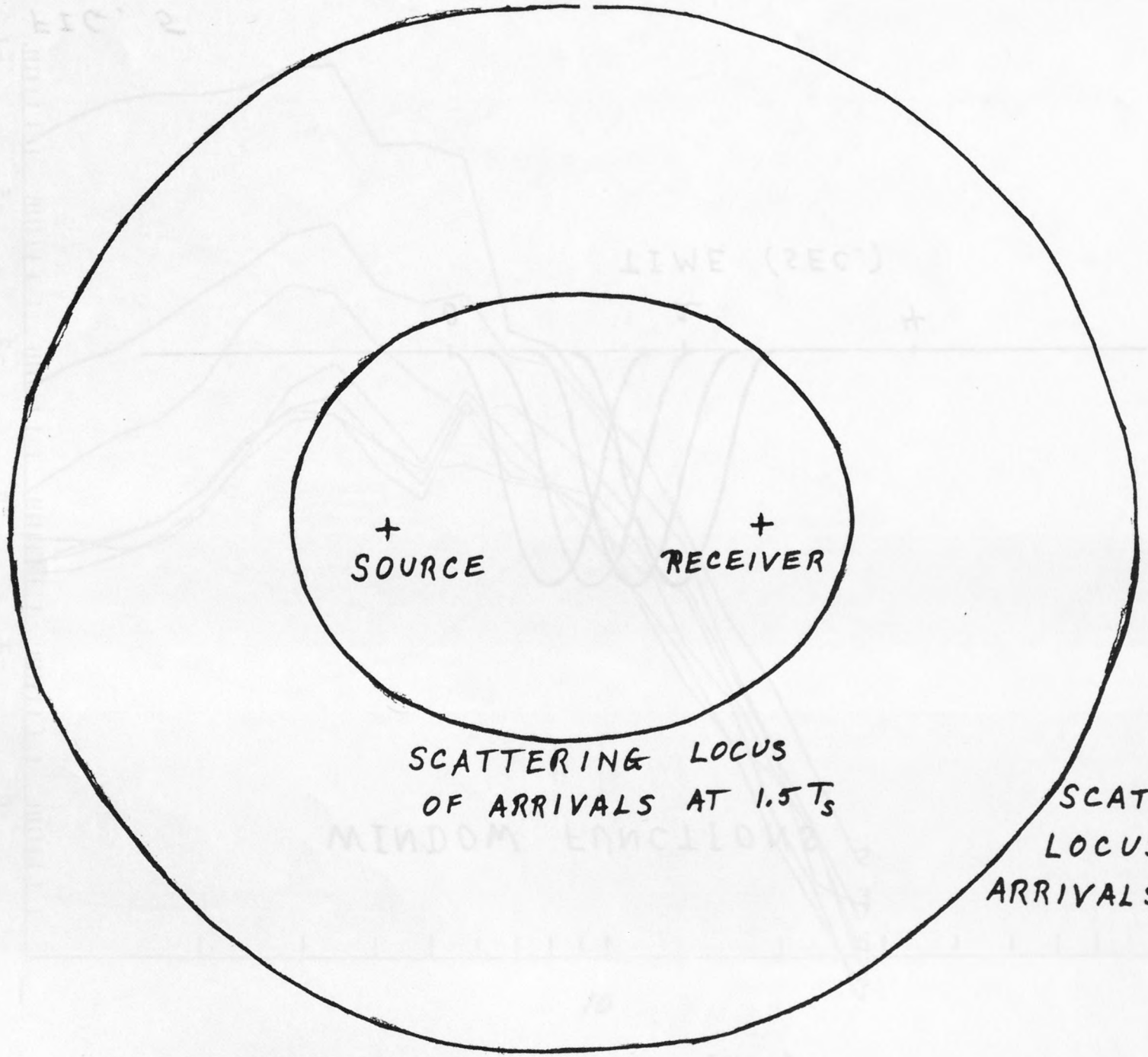
SOURCE
RECEIVER
SCATTERING LOCUS OF ARRIVALS AT 1.5 T_s
SCATTERING LOCUS OF ARRIVALS AT 3 T_s

FIG. 4

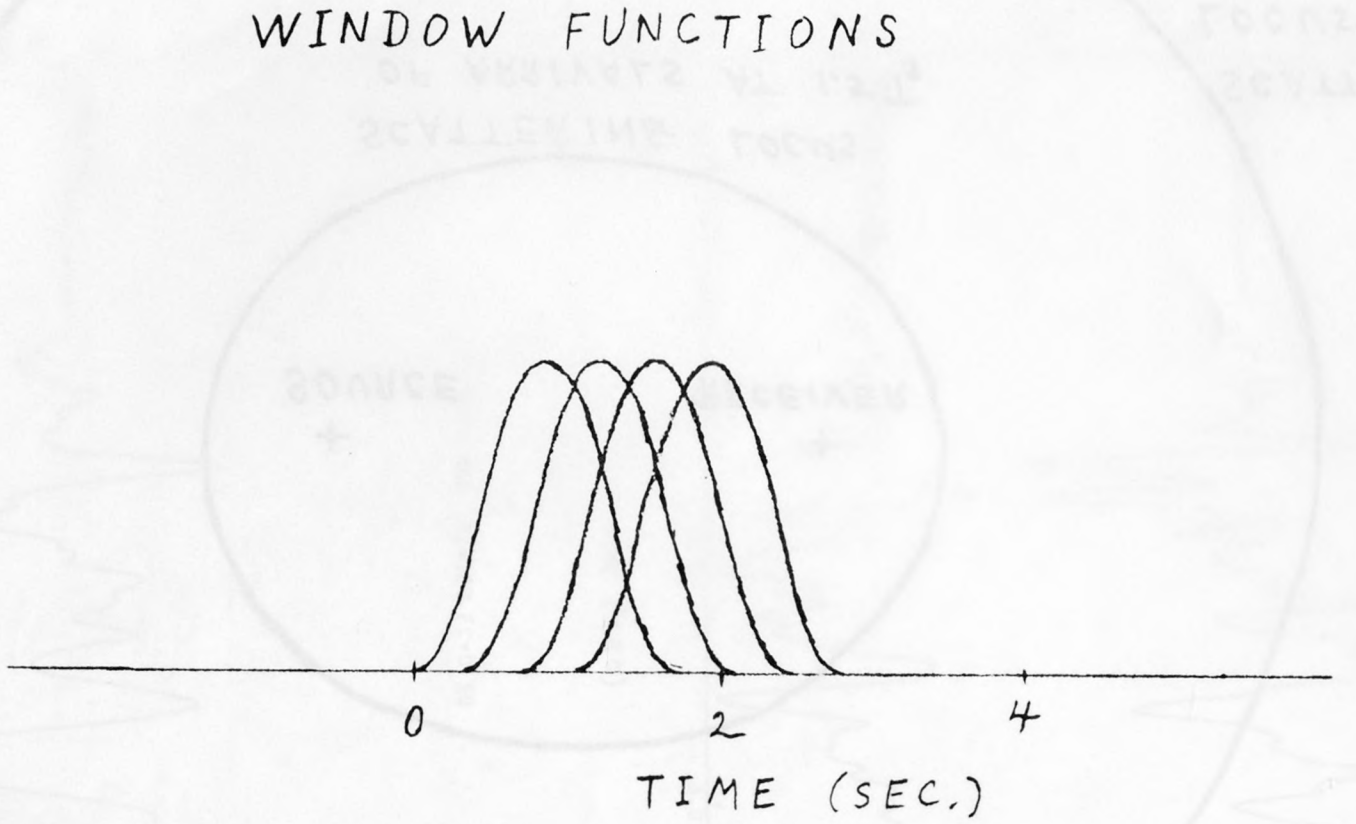

FIG. 5

VELOCITY POWER SPECTRA

LOG10 VELOCITY POWER

-6.0 -5.0 -4.0 -3.0 -2.0 -1.0

1 10 100

FREQUENCY (HZ)

5 4 3 2

SOURCE SPECTRA

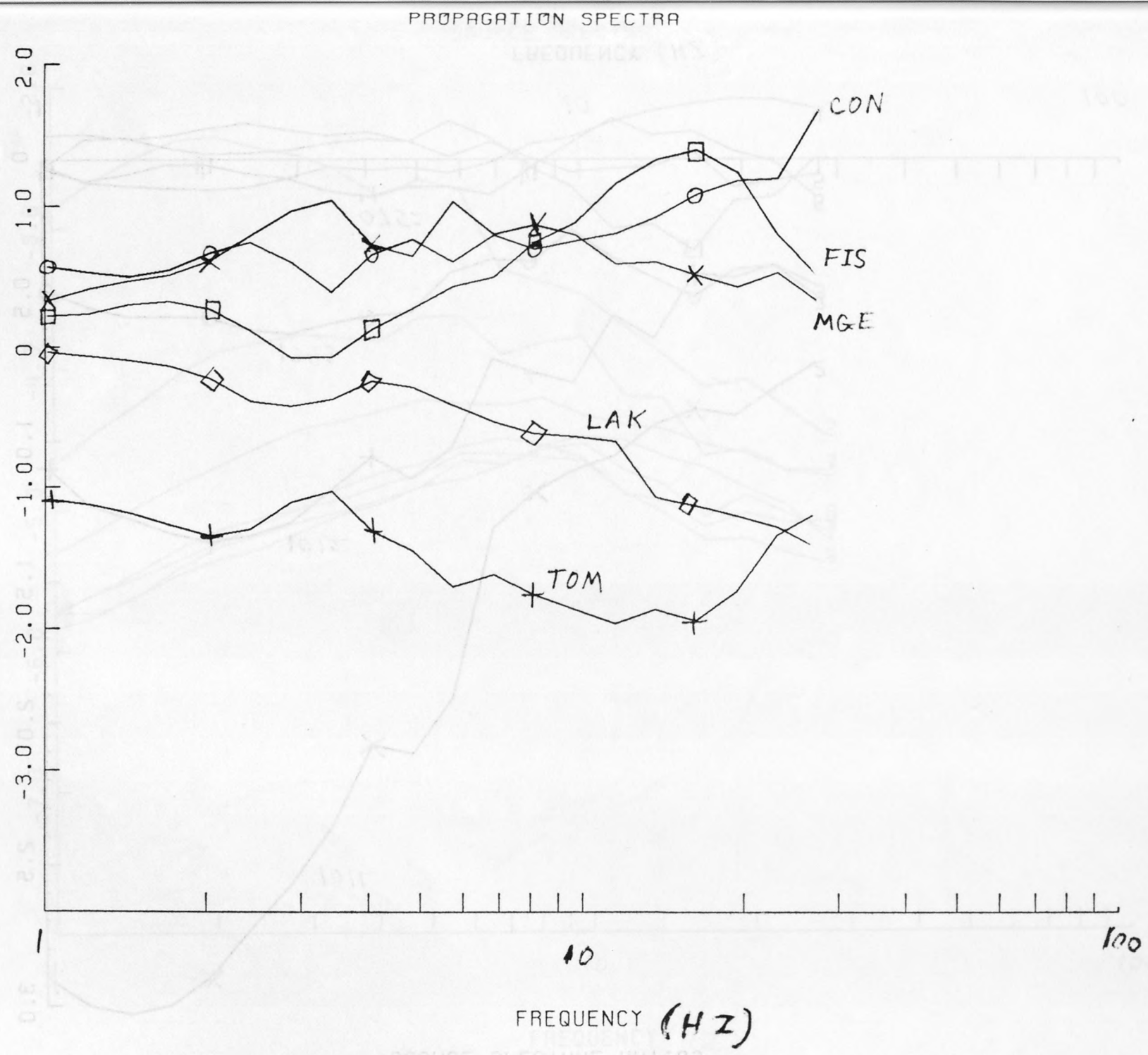
PROPAGATION SPECTRA
2.0
1.0
0
-1.0
-2.0
-3.0
LOG10 POWER SPECTRA
CON
FIS
MGE
LAK
TOM
1
10
100
FREQUENCY (HZ)

450

FIG. 8

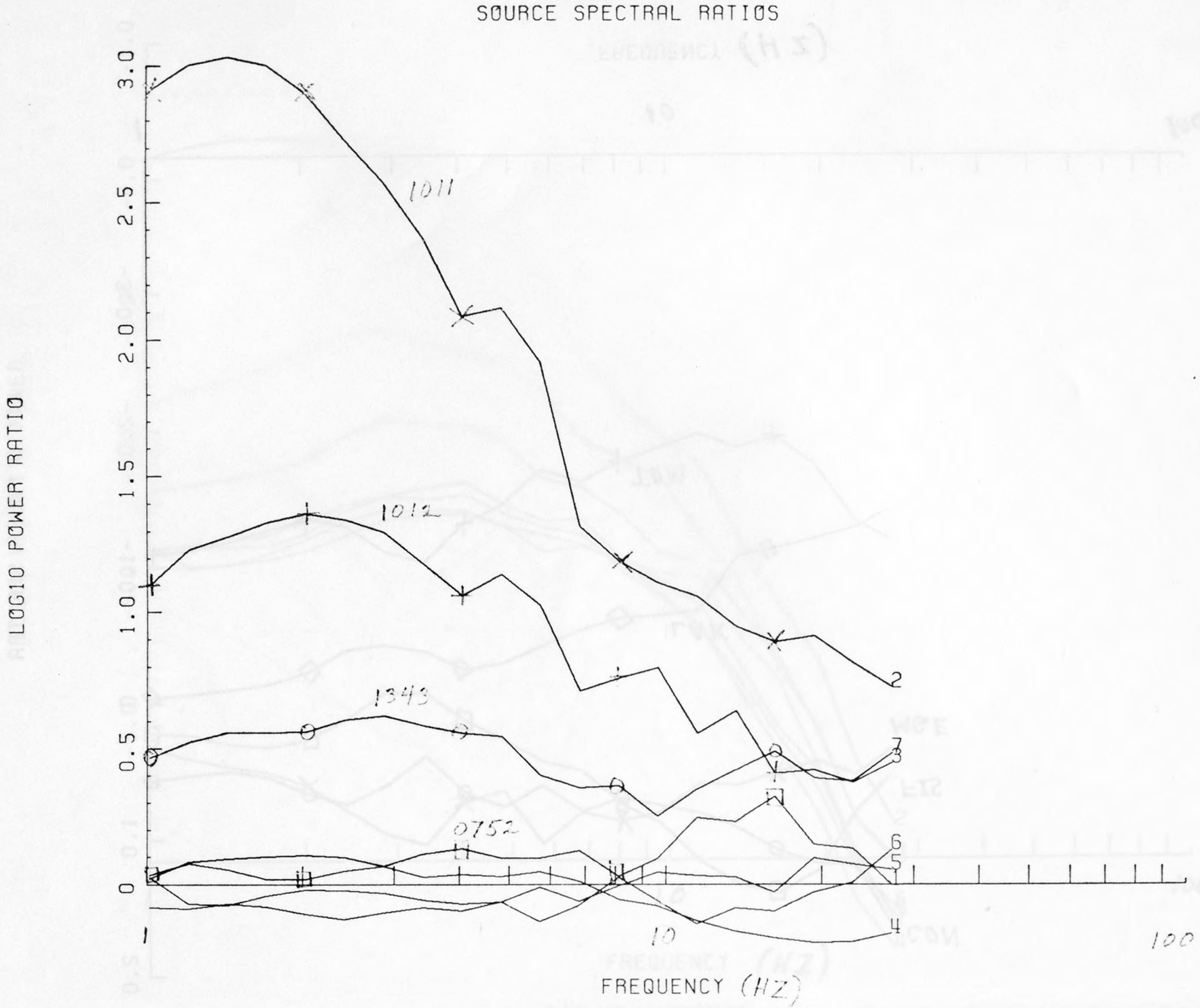
SOURCE SPECTRAL RATIOS
LOG10 POWER RATIO
3.0
2.5
2.0
1.5
1.0
0.5
0
1011
1012
1343
0752
2
3
6
5
4
1
10
100
FREQUENCY (HZ)

LOG10 VELOCITY POWER

SOURCE SPECTRA

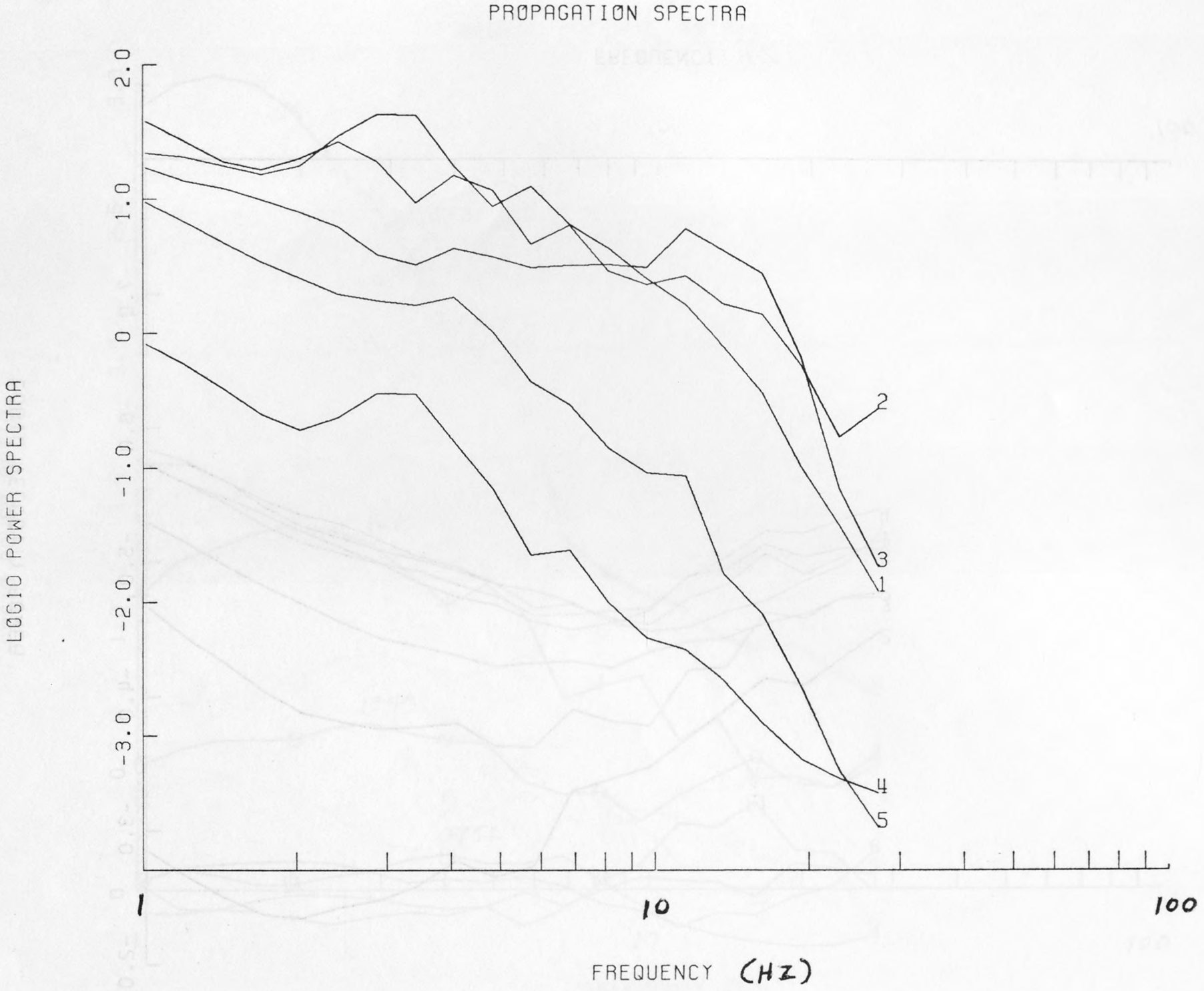
PROPAGATION SPECTRA
LOG10 POWER SPECTRA
2.0
1.0
0
-1.0
-2.0
-3.0
1
10
100
FREQUENCY (HZ)
1
2
3
4
5

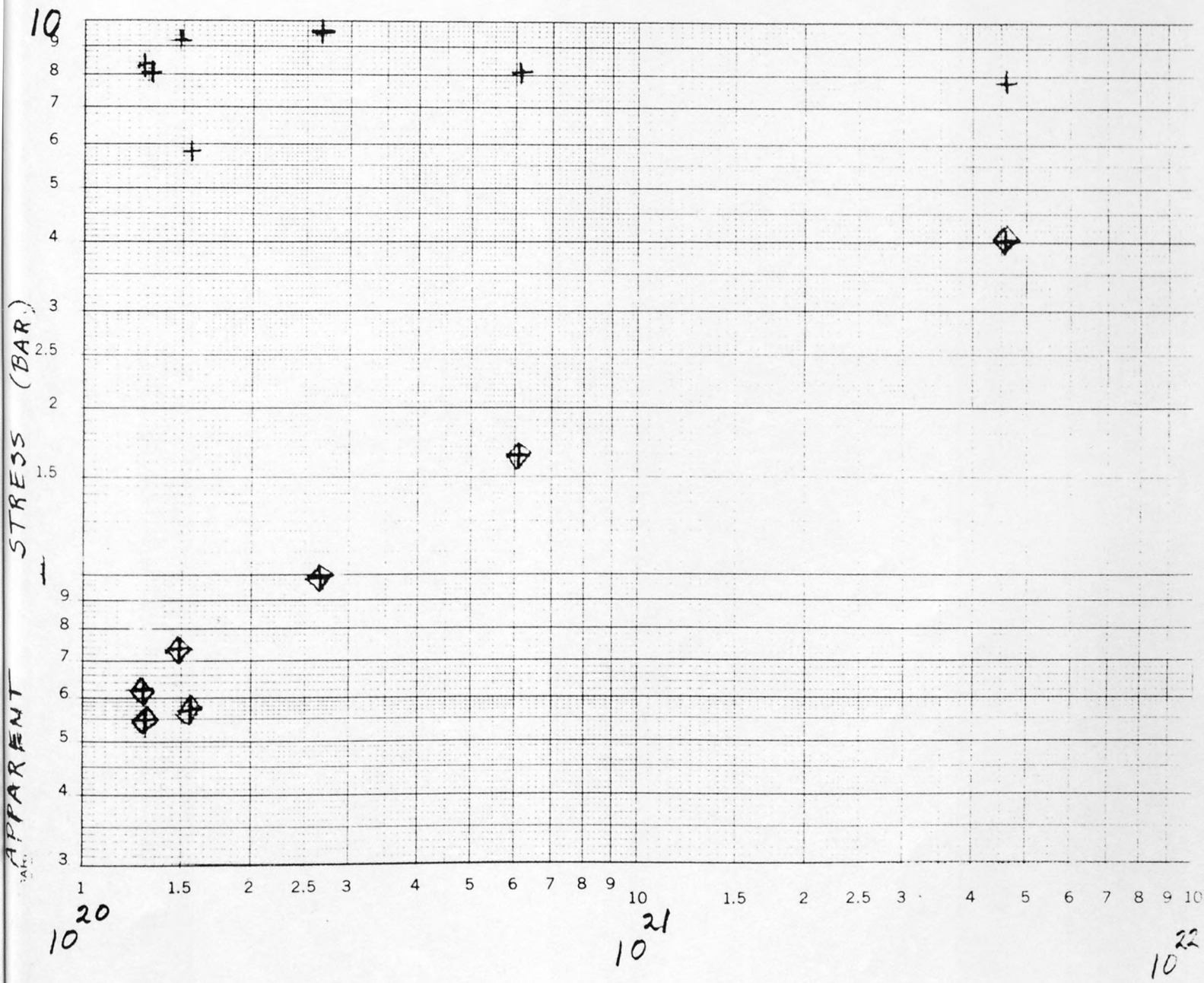
APPARENT STRESS (BAR)
10
9
8
7
6
5
4
3
2.5
2
1.5
1
9
8
7
6
5
4
3
1
1.5
2
2.5
3
4
5
6
7
8
9
10
1.5
2
2.5
3
4
5
6
7
8
9
10
10^20
10^21
10^22
SEISMIC MOMENT (DYNE-CM)

FIG. 12

GPO 587-041/45